ANNALS OF A FORMER WORLD:

THE REMNANTS OF WATER AT GUSEV CRATER AND EBERSWALDE CRATER, MARS

A Dissertation

Presented to the Faculty of the Graduate School

of Cornell University

In Partial Fulfillment of the Requirements for the Degree of

Doctor of Philosophy

by

Melissa S. Rice

January 2012

ANNALS OF A FORMER WORLD:
THE REMNANTS OF WATER AT GUSEV CRATER AND EBERSWALDE CRATER, MARS

Melissa S. Rice, Ph. D.

Cornell University 2012

Understanding the past and present distribution, form, and behavior of water on Mars is critical to assessing whether the planet is, or was ever, a habitable world. This thesis examines the evidence for a more water-rich past that is preserved at two key locations on Mars: (1) Gusev crater, the landing site of the Mars Exploration Rover (MER) Spirit; and (2) Eberswalde crater, a candidate landing site for the Mars Science Laboratory (MSL) Curiosity.

At Gusev Crater, the discovery of hydrated silica- and sulfate-rich soils in the Columbia Hills was one of most significant results of the MER Spirit mission. In visible to near infrared (Vis-NIR) spectra from the Pancam instrument, an H_2O and/or OH absorption feature near 1000 nm is characteristic of the silica-rich materials. This spectral feature has been used to developed a ‘‘hydration signature” for mapping the distribution of hydrated materials at Gusev crater. An extensive study of the Vis-NIR spectra of natural and synthetic silica-rich materials has been performed to help interpret observations of silica on Mars. Temporal observations of the silica- and sulfate-rich soil spectra reveal that no statistically significant spectral changes occurred, implying that the minerals have not undergone dehydration after their exposure.

Eberswalde Crater is famous for the spectacularly preserved delta near its western wall, which indicates an aqueous sedimentary environment. Five additional fluvio-deltaic systems in the crater are identified and described in this work. The identification and mapping of a fault system in and around the crater has revealed the topography as being largely controlled by dip-slip faulting. A detailed geologic characterization of the entire Eberswalde crater basin has also been performed, and maps of stratigraphic and geomorphic units have been produced. The results reveal a complex relationship between deposition and exhumation within Eberswalde crater, and a more complex history of aqueous activity than had previously been acknowledged.

BIOGRAPHICAL SKETCH

Melissa Rice was born and raised in the shadow of Mt. Rainier in Sammamish, Washington, where she graduated from Forest Ridge School of the Sacred Heart in 2000. She credits Mr. Fenoli's 11th grade astronomy elective and Carl Sagan's novel *Contact* with inspiring her to pursue astronomy during high school. As an undergraduate, she participated in research internships at the Geophysical Institute of the University of Alaska Fairbanks, the Arecibo Observatory and the Cerro Tololo Interamerican Observatory. She received her B.A. degree in Astrophysics from Wellesley College in 2004, after which she worked as a research assistant at the Harvard Smithsonian Center for Astrophysics and the NASA Ames Research Institute. Before starting her graduate work, she spent a year traveling to Mars analog sites (Rio Tinto, Spain; the Bolivian Altiplano; the Australian Outback; and Houghton Crater in the Canadian High Arctic) as a Wellesley College Susan Rappaport Knafel Traveling Fellow. She met her husband, Casey Dreier, at the 2005 Division for Planetary Science meeting; they were married in the summer of 2009. Melissa earned her M.S. in Astronomy from Cornell University in 2009, and her Ph.D. in 2012, with minors in Geology and Communication.

Dedicated to Steve Rice, who brought me to Red Rock Canyon and ignited my love of rocks; and to Marcia Rice, who brought me into this world and loved me like a rock.

ACKNOWLEDGMENTS

I would like to extend my most sincere thanks to the many, many people who contributed to this work and made its completion possible:

Coauthors who contributed to the submitted and published versions of the chapters contained in this work: Ryan Anderson, Dan Bailey, Jim Bell, Dave Bish, Ed Cloutis, Mike Craig, Bjarni Gautason, Kate Goddard, Sanjeev Gupta, Bill Farrand, Ken Herkenhoff, Briony Horgan, Jeff Johnson, Stan Mertzman, Bruce Mountain, Robin Renaut, Steve Ruff, Paulo de Souza, Rob Sullivan, Alian Wang, Nick Warner, and James Wray;

Colleagues who provided reviews, insights, analysis and/or samples for the chapters contained in this work: Ray Arvidson, Sue Atkinson, Josh Bandfield, Annabelle Batista, Bill Buhay, Larry Cathles, Shoshe Cole, Larry Crumpler, Tim Glotch, Jonathan Joseph, Ross Irwin, Suniti Karunatillake, Dick Morris, Ian Nicklin, Anya Portyankina, Leah Roach, Matt Smith, Kim Tait, M. Vincendon, Wes Watters, and three anonymous reviewers;

Colleagues on the Mars Exploration Rover and MRO HiRISE teams at the Jet Propulsion Laboratory, Cornell University, USGS/Flagstaff, University of Arizona, and other partner institutions for enabling us to study the surface of Mars from microscopic to orbital scales;

The endlessly helpful staff of the Department of Astronomy and Graduate School: Monica Armstrong, Sue Clark, Sherry Falletta, Patricia Fernandéz de Castro, Sarah

Hale, Bill Hoffman, Erica Miles, Mary Mulvanerton, Danielle O'Connor, Lynda Sovocool and Shirley Weaver;

The agencies that provided me the funding to make this journey possible, in the form of fellowships, assistantships and travel grants: the National Science Foundation, the Cornell University Department of Astronomy, the Knight Institute for Writing in the Disciplines, the Cornell University Graduate School, the New York Space Grant, the Wellesley College Center for Work and Service, Zonta International, the NASA Mars Program Office, and the Lunar and Planetary Institute;

Dr. James F. Bell III, my thesis advisor, for teaching me to perform scientific inquiries with rigor and integrity; and for always reminding me what the most important thing is to get out of graduate school (answer: myself);

The highly-educated and intellectually-fierce women in my family, in whose footsteps I follow: Marcia Rice, Dr. Alphoretta Fish, Hazel Rice, Joan Headrick and Taura McMeekin;

My father, Devereux Rice, who has always encouraged (and often financed) my educational pursuits;

And finally Casey Dreier, the love of my life, whose unwavering support and home-cooked dinners (especially spaghetti and turkey meatballs) indubitably made every step of this journey possible.

TABLE OF CONTENTS

PART II:
The remnants of water at Eberswalde crater

PREFACE

> *Unlike the other worlds that scientists create with their imaginations and instruments – the worlds of molecular dynamics and of inflationary cosmology and the rest of them – this one is on the edge of being a world in the oldest, truest, sense. A world of places and views, a world that would graze your knees if you fell on it, a world with winds and sunsets and the palest of moonlight.*
>
> - Oliver Morton, *Mapping Mars*

When John McPhee published the tome *Annals of the Former World*, a collection of his books detailing the geologic history of North America, in 1998, his use of "the" was easily justified. His readers knew of nine planets but only one world – the Earth – to which the title could refer. In the intervening years, however, I believe things have changed. Mars is a world now too. Anyone who has looked – really *looked* – at photographs from the Spirit and Opportunity rovers will understand what I mean. In homage to John McPhee, and in honor of Mars' promotion in our imagination, I have titled this thesis *Annals of a Former World*.

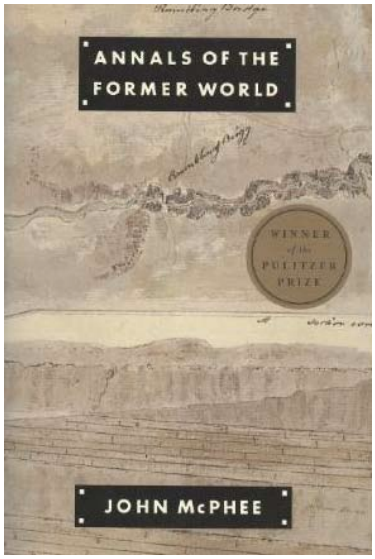

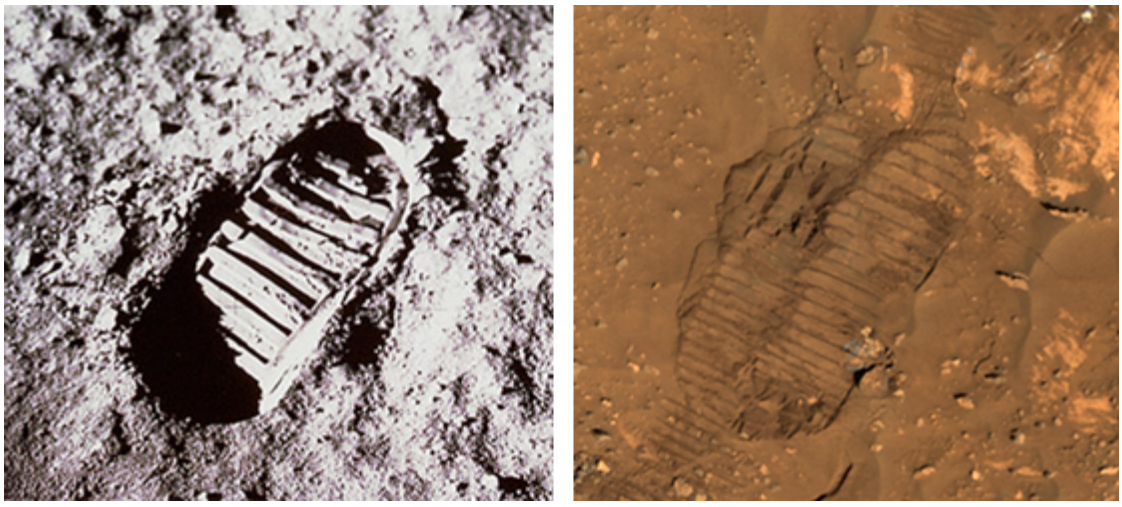

Footprints on other worlds

Left: Neil Armstrong's footprint on the Moon, 20 July 1969

Right: Spirit's "footprint" on Mars, 20 April 2006

CHAPTER 1

INTRODUCTION

The history of major discoveries in astronomy has been a history of what Carl Sagan called "great demotions"; each has made our position in the universe less privileged and unique. We have discovered that our Earth is not at the center of the universe, that our Sun is but one of hundreds of billions of stars in the Milky Way, and that the Milky Way is but one of hundreds of billions of galaxies. To date, 645 planets outside our solar system have been discovered, including one in the habitable zone of a Sun-like star (Borucki et al., in press). The next – and perhaps the greatest – demotion in this series may be the discovery that our Earth is not the only planet with a history of life.

The question of life beyond Earth is inextricably linked to the history of water on other planets and satellites. The goal of this dissertation is to add to our understanding of the history of water on Mars so that we can better understand the potential for life to have arisen on another planet. Two key locations on Mars, both of which are targets for NASA's Mars Exploration Program, have been the focus of this work: Gusev crater and Eberswalde crater. Each of these sites preserve evidence for a unique and complex history of water at the surface, and both may have been habitable at some point in Mars' past.

1. The context of water at Gusev crater

The main science objective of the Mars Exploration Rover (MER) mission is

to explore two sites on the martian surface where water may once have been present, and to assess past environmental conditions at those sites and their suitability for life (Squyres et al., 2004). Gusev crater was selected as the landing site for MER Spirit based on the presence of Ma'adim Vallis, a ~900 km valley that breaches the crater's southern rim, suggesting that the rover could study fluvial and/or lacustrine processes at this location (Cabrol et al., 2003). However, the first images from Spirit's Panocramic Camera (Pancam) revealed that the plains on which the rover landed were covered with basaltic soils and rocks, not lakebed sediments (e.g., Bell et al., 2004). In its entire mission 7-year mission, Spirit found no definitive evidence for the former presence of a lake.

Two years into its mission, however, a different story of aqueous alteration within Gusev crater began to unfold. Spirit's right wheel motor failed, and the rover had to be driven backwards for the remainder of its traverse, digging a ~5-10 cm deep trench as the stuck wheel was dragged through the soil. Serendipitously, subsurface deposits of bright soils with yellowish to whitish hues – unlike any soils that had previously been observed on Mars – were discovered in the wheel tracks in eight distinct locations (e.g., Yen et al., 2008; Ruff et al., 2011). These soils, which contain abundant hydrated silica and sulfate minerals, provided the first compelling evidence for significant amounts of water having interacted with the surface of Gusev crater (Squyres et al., 2007; 2008).

This dissertation aims to resolve several outstanding issues surrounding the composition, origin, and stability of the bright soils discovered by MER Spirit, and to understand their implications for the past and present behaviors of water at Gusev

crater. The major questions addressed here are:

1. *What are the visible to near-infrared spectral characteristics of the silica-rich materials at Gusev crater?*
2. *What is the distribution of hydrated materials at Gusev crater, and what constraints does this place on how and when they formed?*
3. *What can reflectance spectra tell us about the formation, water content, and current environmental conditions of silica-rich materials on Mars?*
4. *What processes are currently effecting the silica- and sulfate-rich soils on Mars?*

2. The context of water at Eberswalde crater

The flow and ponding of liquid water on the surface of Mars has been studied since the Mariner 9 and Viking missions, which observed abundant evidence for valleys and channels scouring the ancient martian terrain (e.g., Carr, 1986). Whether fluvial and lacustrine activity was persistent or sporadic, however, has always been difficult to infer. Perhaps the first "smoking gun" evidence for a long-lived lake on Mars was the discovery of the spectacularly preserved delta in Eberswalde crater. As described in the discovery paper by Malin and Edgett (2003), the location, form and structure of this landform "uniquely reflect materials deposited within an aqueous sedimentary environment."

Eberswalde crater was selected as one of four finalist landing sites for the Mars Science Laboratory (MSL) mission, which launched on 26 November 2011 and is scheduled to land on 5 August 2012 (Grant et al., 2011). The primary objective of the

MSL mission is to search for past and present habitable environments on Mars (Grotzinger 2009). The selection of a candidate landing sites was based in part on their potential for having preserved biomarkers (Grant et al., 2011); sediment deposition in a low-energy environment, such as a quiescent lake, typically has very high preservation potential (Summons et al., 2011). After a series of five community MSL Landing Site Workshops, the MSL team ranked Gale Crater and Eberswalde Crater as the top two sites. Gale Crater was selected as the final landing site over Eberswalde Crater in July 2011.

This work has been motivated by the landing site selection process described above, and its major goal has been to assess the science potential of Eberswalde crater for the Mars Science Laboratory mission. Therefore, this dissertation aims to resolve major outstanding questions about the aqueous history of Eberswalde crater, its past habitability, its biopreservation potential, and its relevance to the larger geologic history of Mars. The major questions addressed here are:

1. *What was the full extent of deltaic activity in Eberswalde crater, and what constraints can this place on the size and duration of an Eberswalde lake?*
2. *What specific factors controlled the pattern of delta development?*
3. *What other aqueous processes have occurred at Eberswalde crater?*
4. *What was the sequence of major events in the geologic history of Eberswalde crater, and what do these imply for the ancient habitability of the site?*
5. *What is the diversity of outcrops that the Curiosity rover could investigate in Eberswalde crater?*

3. Outline of the following chapters

Part I: The remnants of water at Gusev crater

Chapter 2 characterizes the Pancam spectra of the silica-rich soils and outcrops discovered by MER Spirit at Gusev crater. The major result of this work is that Pancam has detected an absorption near 1000 nm that is attributed to the substantial amounts of H_2O and/or OH, either bound in the mineral structure of the silica, trapped in fluid inclusions, or adsorbed onto the surface. This Pancam feature has allowed for the development of a "hydration signature," which has been used to map the distribution of putative hydrated materials along Spirit's traverse. This work has been peer reviewed and published in full in the journal *Icarus* (Rice et al., 2010a).

In Chapter 3, an extensive laboratory characterization of the spectral diversity of terrestrial silica-rich materials is described. Spectra have been acquired of a variety of natural and synthetic materials at different grain sizes, temperatures, pressures and humidity conditions. The goal of this work is to describe the effects of silica formation processes and environmental conditions on diagnostic absorption features, and the results show that the H_2O content and form of H_2O/OH present in silica-rich materials can have significant effects on their Vis-NIR spectra. How these results can aid in the interpretation of silica detections on Mars made by Pancam (and other rover- and orbiter-based spectrometers) is also addressed. This chapter has been submitted to the journal *Icarus* and is currently undergoing peer review.

Chapter 4 examines the repeated Pancam observations made by Spirit at the bright silica- and sulfate-rich soil exposures, specifically to test the hypothesis from Wang et al. (2008) that spectral changes have occurred due to mineralogic phase

transitions accompanying dehydration. The main finding is that, at all bright soil exposures, no statistically significant spectral changes have occurred that are uniquely diagnostic of dehydration and/or mineralogic phase changes. However, textural changes have occurred, consistent with aeolian sorting and/or minor amounts of airfall dust deposition. This chapter was peer reviewed and published in full in a MER Special Issue of *Geophysical Journal of Research – Planets* (Rice et al., 2011a).

Part II: The remnants of water at Eberswalde crater

Chapter 5 explores the structure of the Eberswalde crater as a sedimentary basin. The identification and mapping of a fault system in and around the crater has revealed the topography as being largely controlled by dip-slip faulting. Using key morphologic criteria, five fluvio-deltaic systems in the crater have been identified, in addition to the famous "Eberswalde delta." The mapping of the fluvio-deltaic systems suggests that delta development was controlled by this preexisting topography. This chapter has been peer reviewed and published in full in the journal *Geophysical Research Letters* (Rice et al., 2011b).

In Chapter 6, a detailed geologic characterization of Eberswalde crater has been performed, and maps of stratigraphic and geomorphic units have been produced. Observations of the stratigraphy, geomorphology, topography and crater densities imply a complex relationship between deposition and exhumation within Eberswalde crater. The major result of this work is an inferred sequence of geologic events: the emplacement of impact ejecta; fracturing and fluid circulation; extensive faulting; a period of fluvio-lacustrine activity; erosion of the crater floor occurring

simultaneously with the deposition of an airfall mantling. This chapter has been presented at the Fourth and Fifth MSL Landing Site Workshops, and is currently undergoing peer review for publication in the *Mars Journal*.

Chapter 7 synthesizes these results and their implications for the larger history of water on Mars, and provides a summary of the new techniques developed and their applicability for future missions.

REFERENCES

Bell, J.F. III, and 42 colleagues, 2004. Pancam multispectral imaging results from the Spirit Rover at Gusev crater. Science 305, 5685, 800–806.

Borucki, W.J., and 82 colleagues, 2011. Kepler-22b: A 2.4 Earth-radius Planet in the Habitable Zone of a Sun-like Star. Astrophys. J., in press.

Cabrol, N.A., and 19 colleagues, 2003. Exploring Gusev Crater with Spirit: Review of science objectives and testable hypotheses. J. Geophys. Res. 108, E12, 8076. doi: 10.1029/2002JE002026.

Carr, M., 1986. Mars: A water-rich planet. Icarus 68, 187-216.

Grant, J. A. et al., 2011. The science process for selecting the landing site for the 2011 Mars Science Laboratory Planetary and Space Science, v. 59, Issue 11, 1114-1127 doi:10.1016/j.pss.2010.06.016.

Grotzinger, J., 2009. Beyond water on Mars Nature Geoscience, Volume 2, Issue 4, pp. 231-233 (2009). doi:10.1038/ngeo480.

Malin, M. C. and Edgett, K. S., 2003. Evidence for Persistent Flow and Aqueous Sedimentation on Early Mars Science 302, 1931-1934. doi:10.1126/science.1090544.

Rice, M.S., Bell, J.F. III, Cloutis, E.A., Wang, A., Ruff, S., Craig, M.A., Bailey, D.T., Johnson, J.R., de Souza Jr., P.A., Farrand, W.H., 2010a. Silica-rich deposits and hydrated minerals at Gusev crater, Mars: Vis-NIR spectral characterization and regional mapping. Icarus 205, 375–395. doi:10.1016/j.icarus.2009.03.035.

Rice, M.S., Batista, A., Bell, J.F. III, 2010b. Searching for “Home Plates” Near Gusev Crater, Mars: Spirit's Regional Context in an Area of Explosive Volcanism. AGU Fall Meeting, , abstract #P11B-1338.

Rice, M.S., Bell, J.F. III, Cloutis, E.A., Wray, J.J., Herkenhoff, K.E., Sullivan, R., Johnson, J.R., Anderson, R.B., 2011a. Temporal observations of bright soil exposures at Gusev crater, Mars. J. Geophys. Res. 116, E00F14. doi:10.1029/2010JE003683.

Rice, M. S., Gupta, S., Bell, J. F., III, Warner, N. H., 2011b. Influence of fault-controlled topography on fluvio-deltaic sedimentary systems in Eberswalde crater, Mars. Geophys. Res. Lett. 38, 16. doi:10.1029/2011GL048149.

Ruff, S.W., and 10 colleagues, 2011. Characteristics, distribution, origin, and significance of opaline silica observed by the Spirit rover in Gusev crater,

Mars, J. Geophys. Res. 116, E00F23. doi:10.1029/2010JE003767.

Squyres, S.W., and 49 colleagues, 2004. The Spirit Rover's Athena Science Investigation at Gusev Crater, Mars. Science 305, 794. doi:10.1126/science.3050794.

Squyres, S.W., and 27 colleagues, 2007. Pyroclastic activity at Home Plate in Gusev Crater, Mars. Science 316, 738–742. doi:10.1126/science.1139045.

Squyres, S.W.and 17 colleagues, 2008. Detection of silica-rich deposits on Mars. Science 320, 1063–1067. doi:10.1126/science.1155429.

Wang, A., and 15 colleagues, 2008. Light-toned salty soils and coexisting Si-rich species discovered by the Mars Exploration Rover Spirit in the Columbia Hills. J. Geophys. Res. 113, E12S40. doi:10.1029/2008JE003126.

Yen, A.S., and 13 colleagues, 2008. Hydrothermal processes at Gusev Crater: An evaluation of Paso Robles class soils. J. Geophys. Res. 113, E12. doi:10.1029/2007JE002978.

CHAPTER 2

SILICA-RICH DEPOSITS AND HYDRATED MINERALS AT GUSEV CRATER, MARS: VIS-NIR SPECTRAL CHARACTERIZATION AND REGIONAL MAPPING[1]

0. Abstract

The Mars Exploration Rover (MER) Spirit has discovered surprisingly high concentrations of amorphous silica in soil and nodular outcrops in the Inner Basin of the Columbia Hills. In Pancam multispectral observations, we find that an absorption feature at the longest Pancam wavelength (1009 nm) appears to be characteristic of these silica-rich materials; however, spectral analyses of amorphous silica suggest that the ~1009 nm spectral feature is not a direct reflection of their silica-rich nature. Based on comparisons with spectral databases, we hypothesize that the presence of H_2O or OH, either free (as water ice), adsorbed or bound in a mineral structure, is responsible for the spectral feature observed by Pancam. The Gertrude Weise soil, which is nearly pure opaline silica, may have adsorbed water cold-trapped on mineral grains. The origin of the ~1009 nm Pancam feature observed in the silica-rich nodular outcrops may result from the presence of additional hydrated minerals (specific sulfates, halides, chlorides, sodium silicates, carbonates or borates). Using the ~1009 nm feature with other spectral parameters as a "hydration signature" we have mapped the occurrence of hydrated materials along the extent of Spirit's traverse across the

[1] Reprinted from Icarus, Vol. 205, M.S. Rice, J.F. Bell III, E.A. Cloutis, A. Wang, S. Ruff, M. Craig, D. Bailey, J.R. Johnson, P.A. de Souza Jr., W.H. Farrand Silica-Rich Deposits and Hydrated Minerals at Gusev Crater, Mars: Vis-NIR Spectral Characterization and Regional Mapping, Pages 375–395, Copyright 2009, with permission of Elsevier.

Columbia Hills from West Spur to Home Plate (sols 155 to 1696). We have also mapped this hydration signature across large panoramic images to understand the regional distribution of materials that are spectrally similar to the silica-rich soil and nodular outcrops. Our results suggest that hydrated materials are common in the Columbia Hills.

1. Introduction

In the past decade, the search for water on Mars has focused on the identification of aqueous alteration products such as carbonate, sulfate, phyllosilicate, and opaline silica minerals. While sulfate and phyllosilicate minerals have been detected across the planet by multiple instruments (e.g., Bibring et al., 2006; Mustard et al., 2008), discoveries of carbonates and hydrated silica minerals have been elusive in orbital measurements. Carbonates have only been identified in small (2-5%) concentrations in martian dust (Bandfield et al., 2003), and recent observations at high spatial resolution by the Mars Reconnaissance Orbiter (MRO) Compact Reconnaissance Imaging Spectrometer for Mars (CRISM) suggest the presence of magnesium carbonates in a rock layer in the Nili Fossae region (Ehlman et al., 2008).

Discoveries of opaline silica on Mars have been anticipated for many years based on geochemical arguments (McLennan, 2003) and evidence for past hydrothermal activity (Farmer, 1996; Bishop et al., 2004). Amorphous silica is also of astrobiological importance because its precipitation from fluids can provide a mechanism for preserving evidence of microbes (Cady and Farmer, 1996). Several authors have studied thermal emission spectra of silica-rich coatings on basalts (Crisp

et al., 1990), silica polymorphs (Michalski et al., 2003) and silica sinter deposits (Preston et al., 2008) to constrain their remote sensing applications for Mars. Until recently, however, no unambiguous discoveries of opaline silica on Mars had been made.

Thermal infrared spectra from the Mars Global Surveyor (MGS) Thermal Emission Spectrometer (TES) have been interpreted in some locations to exhibit signatures of high-silica glass (Bandfield et al., 2000; Michalski et al., 2005; Bandfield, 2008); however, Wyatt and McSween, (2002) have noted that these spectral interpretations are not unique, and Rogers and Christensen (2007) suggest that surface alteration is the primary control in areas where high-silica phases are observed with TES. Chemical measurements from Mars Pathfinder suggested the presence of sedimentary silica in rocks at the landing site (McLennan, 2003), and Miniature Thermal Emission Spectrometer (Mini-TES) analyses from the Mars Exploration Rover (MER) Opportunity suggest that Al-rich opaline silica could be a component of light-toned sedimentary outcrops at Meridiani Planum (Glotch et al., 2006). The CRISM instrument has detected possible spectral signatures of opal and chalcedony in the near-infrared (Mustard et al., 2008; Milliken et al., 2008), although abundances have not been constrained.

The Spirit rover has recently made the only unequivocal detection of nearly pure silica on Mars (Squyres et al., 2008). During its traverse through the Columbia Hills, Spirit's front right wheel motor failed, and the rover has since been driving backwards, digging a trench as the stuck wheel drags through the soil. Serendipitously, a subsurface deposit of bright, whitish silica-rich soil has been discovered within this

trench in a topographic lowland called the Eastern Valley (Squyres et al., 2008). Observations of the brightest exposure of soil (a spot called Kenosha Comets within the Gertrude Weise trench) by the rover's Alpha Particle X-Ray Spectrometer (APXS) instrument show that its composition is 90.1 wt.% SiO_2 (~98 wt.% SiO_2 when corrected for dust contamination). Mini-TES measurements from Gertrude Weise are consistent with the presence of opaline silica (Squyres et al., 2008).

Light-toned nodular outcrops in the Eastern Valley region also have high silica compositions; four nodular outcrops measured by APXS contain 63-73 wt.% SiO_2 (Ming et al., 2008). Comparisons of Mini-TES spectra of the nodular outcrops to that of Gertrude Weise show highly consistent features, implying that the subsurface soil may be derived from these nodular outcrops, possibly by aeolian weathering (Ruff et al., 2008b). Based on chemical differences seen by APXS, however, Wang et al. (2008) suggest that the nodular outcrops have formed by a different process than the silica-rich soil. Nodular outcrops enriched in silica have been identified in the vicinity of sulfate-rich light-toned soils as well. For example, Mini-TES spectra have revealed that the light-toned nodular outcrop near the Tyrone light-toned soil exposure has the same infrared spectral characteristics of those in the Eastern Valley (Squyres et al., 2008). Analyses of the silica-rich nodular outcrops (Wang et al., 2008) suggest that their formation process may be related to that of the sulfate deposits, many of which are likely hydrothermal in origin with a large range of water to rock ratios (Yen et al., 2008; Wang et al., 2008).

Squyres et al. (2008) interpret the silica-rich soil and outcrops discovered by Spirit to have formed under hydrothermal conditions. On Earth, deposits of amorphous

silica are common surface manifestations of high-temperature geothermal systems (e.g. Ellis and Mahon, 1977; Farmer, 1996), and studies of terrestrial hydrothermal sites show that fragments of silica-rich outcrops near extinct vents have strikingly similar textures and morphologies to the nodular outcrops imaged by Spirit's Pancam instrument (Preston et al., 2008). The silica-rich soil targets (Kenosha Comets and Lefty Ganote, both within the Gertrude Weise soil trench) at Gusev Crater are also enriched in TiO_2. This enrichment supports the hypothesis proposed by Squyres et al. (2008) that the silica forms from the remnants of former basaltic materials after extensive open-system leaching of metallic cations by acidic fluids, because both TiO_2 and SiO_2 are relatively insoluble at low pH and can be concentrated by leaching processes (Rodgers et al., 2002). Such alteration caused by acidic solutions does not necessarily require hydrothermal temperatures, however; theoretical models show that abundant silica can precipitate from low pH fluids below 0^oC at water/rock ratios of 10^2 - 10^4 (McAdam et al., 2008).

To further constrain the depositional environment of silica-rich outcrops and soils, it is important to understand the regional distribution of silica-rich species and the related deposits formed by similar processes. Highly localized distributions could imply the formation of amorphous silica by alteration of local rocks near a fumarolic vent, while more widespread distributions could indicate transportation and precipitation of silica sinters from hydrothermal fluids (e.g., White et al., 1956; Rodgers et al., 2004). If the deposits are constrained to topographic lows, their emplacement could even be consistent with precipitates from standing bodies of water. While it appears unlikely given the available data that the high-silica materials at the

Spirit site formed in a lacustrine environment (Arvidson et al., 2006), this possibility still warrants further investigation.

Wang et al. (2008) identified a spectral feature in the visible to near-infrared (Vis-NIR) Pancam data (a spectral downturn near 1000 nm) that is associated with the soil and nodular outcrops that are known to be silica-rich. In this work, we present a comparison of the Pancam spectra from typical Gusev silica-rich species (the soil and nodular outcrops characterized by APXS and Mini-TES) with the spectra obtained from a series of laboratory experiments and from those in current Vis-NIR spectral databases. We aim to link this specific Pancam spectral feature to one or more specific mineralogical properties. In addition, we have extracted a set of spectral indices based on more detailed Pancam spectral analyses and have used them to map the distributions of the materials that bear these spectral characteristics along Spirit's traverse through the Columbia Hills. We offer interpretations of the nature of these materials by combining Pancam observations with observations made by the rest of Spirit's science payload. The ultimate goal of our study is to map the distribution of potential alteration deposits within the Columbia Hills region and to constrain models for their formation and evolution.

2. Pancam spectral features and chemical/mineralogic origins

2.1. Pancam instrument and data overview

The Pancam instrument consists of two cameras at a 30 cm stereo separation, each using a 1024 x 1024 pixel charge-coupled device (CCD) with 0.27 mrad per pixel resolution (Bell et al., 2003; Bell et al., 2006). Pancam's 13 narrowband geology

filters cover 11 unique wavelengths in the visible and near infrared (434 to 1009 nm); the effective band center of each filter and the associated camera (right or left) is given in Table 1. Some of the images used in this study were acquired using lossy wavelet-based ("ICER") compression (Maki et al., 2003) and/or 2x2 pixel averaging to reduce the downlinked data volume. Based on pre-launch tests, compression effects on radiometric precision at the typical compression bit rates employed using the ICER compressor were estimated to be less than 1% (Bell et al., 2006).

We use near-simultaneous observations of the Pancam calibration target, as well as pre-launch calibration and modeling, to derive estimated reflectances of the scene relative to the standard reflectance materials on the calibration target (Bell et al., 2003; Bell et al., 2006). To correct for dust contamination of the calibration target, Pancam data are calibrated using a two-layer radiative transfer model (Sohl-Dickstein et al., 2005; Bell et al., 2006; Kinch et al., 2007). The Pancam reflectance products are called "IOF" (I over F) images, where IOF (also known as the "radiance factor" (Hapke, 1993)), is defined as the ratio of the bidirectional reflectance of a surface to that of a normally illuminated, perfectly diffuse surface. Dividing the Pancam IOF images by the cosine of the solar incidence angle at the time of each observation gives the relative reflectance (R*) (Reid et al., 1999; Bell et al., 2006) (also known as the "reflectance factor" or "reflectance coefficient" (Hapke, 1993)). Bell et al. (2006) have estimated the relative filter-to-filter uncertainties in R* to be 1-5%, and the absolute reflectance levels to be accurate to within ~10%. Because diffuse component corrections are relatively minor at the solar incidence angles of our dataset (6^{o}-19^{o};

Table 1. Pancam filter data.

Filter	Effective Wavelength (nm)[a]	Band Pass (nm)[a]	Camera
L7	432	32	LEFT
R1	436	37	RIGHT
L6	482	30	LEFT
L5	535	20	LEFT
L4	601	17	LEFT
L3	673	16	LEFT
L2	753	20	LEFT
R2	754	20	RIGHT
R3	803	20	RIGHT
R4	864	17	RIGHT
R5	904	26	RIGHT
R6	934	25	RIGHT
R7	1009	38	RIGHT

[a] from Bell et al. (2003)

Table 2) (Johnson et al., 2006), we have not corrected further for diffuse illumination in this study.

2.2. Pancam spectra of silica-rich soil and nodular outcrops

To characterize the spectral behavior of the silica-rich materials at Gusev Crater, we have collected spectra from every 13-filter Pancam observation of targets confirmed by APXS and/or Mini-TES analyses to be silica-rich (Ming et al., 2008; Ruff et al., 2008b). We exclude Pancam sequences with any image saturation. These observations include a total of eight Pancam image sequences: three of the Gertrude Weise soil (which include the Kenosha Comets and Lefty Ganote targets) and five of

Table 2. Pancam imaging sequences used for spectral characterization of known silica-rich targets.

Name[a]	Feature Type	Sol	Site[b]	Position[b]	Sequence ID	Local True Solar Time	Incidence Angle (degrees)	Emission Angle (degrees)[c]	Phase Angle (degrees)	First exposure by wheels (sol)	SiO_2 content (wt.%)[d]	934 to 1009nm slope x 10^{-4} nm^{-1}
Tyrone Nodular outcrops	Nodule	1101	128	316	P2552	12:49	19	68	75	---	---	-3.7
Elizabeth Mahon	Nodule	1160	128	1318	P2582	13:18	19	17	20	---	72.4	-3.7
		1174	129	25	P2588	12:25	6	56	50			-3.7
Kenosha Comets	Soil Trench	1158	128	1318	P2581	12:32	8	78	75	1148	90.1	-5.9
		1187	129	112	P2533	12:19	7	70	64			-4.1
		1198	129	140	P2539	12:14	8	48	55			-3.6
Lefty Ganote	Soil Trench	1158	128	1318	P2581	12:32	8	78	75	1148	74.6	-3.2
		1187	129	112	P2533	12:19	7	70	64			-2.5
Nancy Warren	Nodule	1190	129	135	P2534	12:18	7	72	67	---	72.7	-3.2
Innocent Bystander	Nodule	1294	130	201	P2581	11:09	14	33	39	1234	63.1	-3.3
Norma Luker	Nodule	1294	130	201	P2581	11:09	14	33	39	1234	69.2	-3.3

[a] Feature names are informal and not formally accepted by the International Astronomical Union;
[b] The surface coordinate frames utilized by MER (Maki et al., 2003);
[c] The INSTRUMENT_ELEVATION parameter stored in the image label;
[d] (Ming et al., 2008)

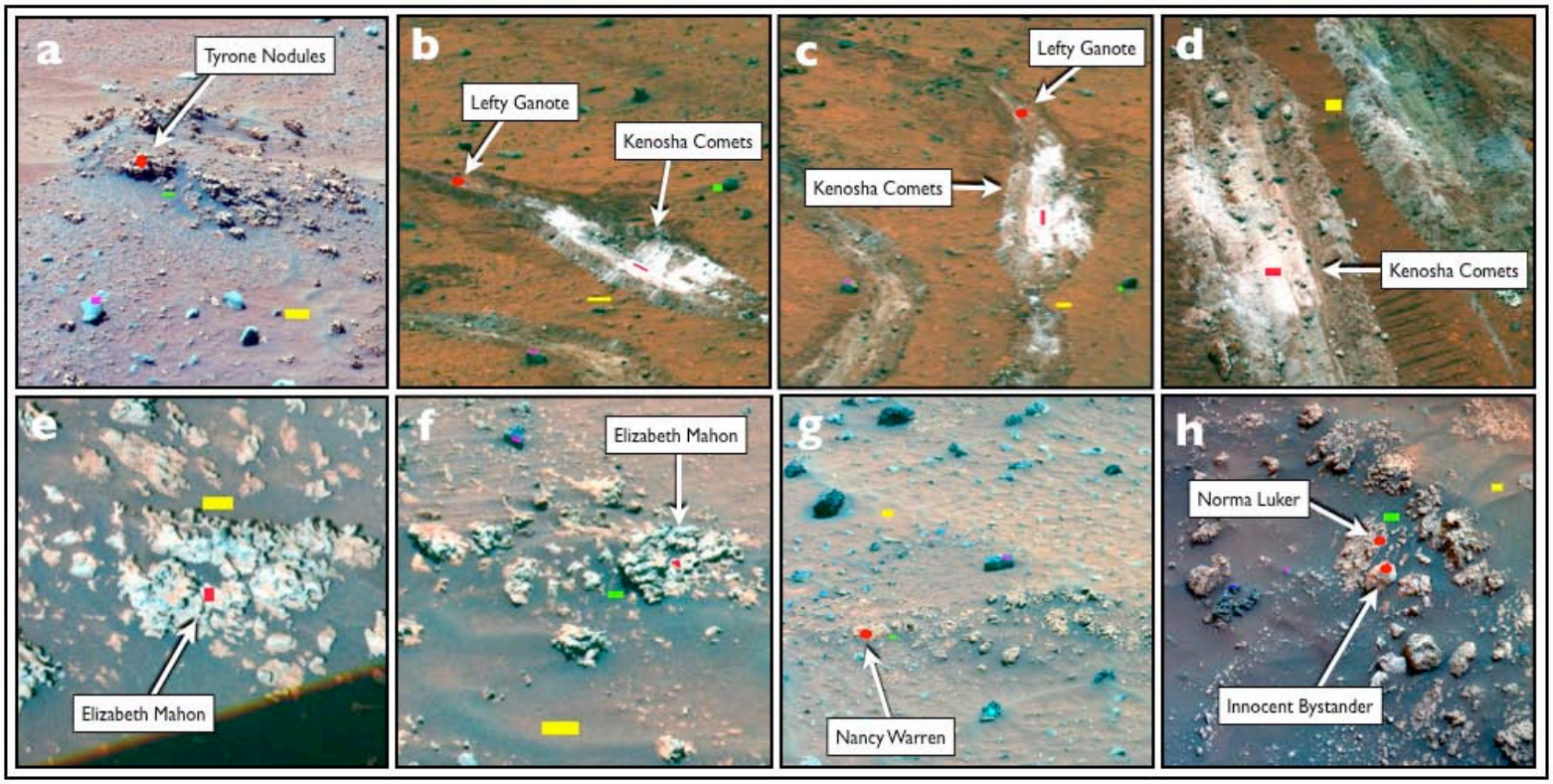

Figure 1. False color Pancam images (blue = 432 nm, green = 535 nm, red = 753 nm) of the targets confirmed by APXS and/or Mini-TES to be silica-rich: a) Tyrone Nodular outcrops (sol 1101, P2552), the extent of the outcrop is ~ 75 cm; b) Gertrude Weise (sol 1158, P2581), the width of the wheel tracks are ~16 cm; c) Gertrude Weise (sol 1187, P2533); d) Gertrude Weise (sol 1198, P2539); e) Elizabeth Mahon (sol 1160, P2582), the nodule is ~10 cm; f) Elizabeth Mahon (sol 1174, P2588), the extent of the outcrop is ~ 60 cm; g) Nancy Warren (sol 1190, P2534), the extent of the outcrop is ~140 cm; h) Innocent Bystander and Norma Luker (sol 1294, P2581), the size of Innocent Bystander is ~ 6 cm. ROIs from which spectra were acquired are overlaid on each image as: red = silica-rich target(s); yellow = "light" soil; green = "dark" soil; purple = "smooth" basalt; blue = vesicular basalt.

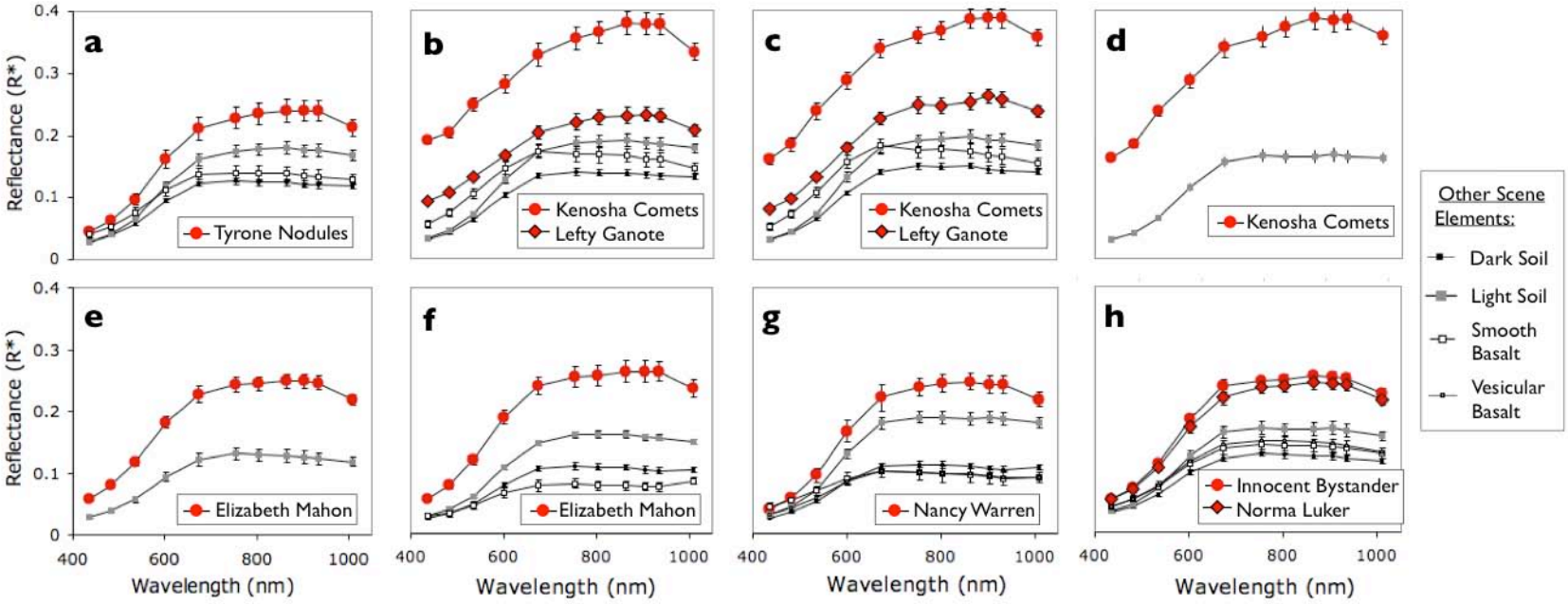

Figure 2. Pancam relative reflectance spectra of silica-rich targets (red) and other scene materials extracted from the ROIs shown in Fig. 1. Error bars represent the standard deviations of the group of pixels sampled for each ROI, not formal instrumental uncertainties (which are generally lower).

the nodular outcrops (Table 2). Unfortunately, no 13-filter Pancam observations were taken of the Mini-TES confirmed silica-rich nodule called Kobal.

Vis-NIR spectra of the high-silica targets were acquired by manually selecting pixels from common regions in the right and left camera datasets and averaging the R* values of those regions for each filter. The regions of interest (ROIs; typically 50-200 pixels) include the portions of each target with the highest relative reflectance in the R2 filter and exclude pixels within shadows. For comparison to the spectra of high-silica soils and nodular outcrops, we also extracted representative spectra from other materials in each image ("light" soil, "dark" soil, "smooth" basalt float rocks and vesicular basalts). Figure 1 shows the Pancam images and ROIs chosen for our analysis.

For the blue (432 and 436 nm) and red (753 and 754 nm) stereo filters, we have used the R* values acquired by the right camera (436 and 754 nm). We estimate the uncertainty of R* from the variance among the selected ROI pixels, rather than from the formal instrumental noise (which is generally much lower). The resulting spectra for the ROIs within each Pancam image are shown in Fig. 2.

2.3 Spectral characterization of silica-rich species at Gusev Crater

The high-silica soils and nodular outcrops imaged by Spirit are spectrally distinct from other materials in the Columbia Hills. Wang et al. (2008) have identified a strong spectral downturn from 934 to 1009 nm that characterizes the spectra of all the known high-silica targets (Fig. 2); this spectral feature is not seen, however, in any of the other soils or basaltic rocks in the immediate vicinity (including those within the

same imaging sequences as the high-silica targets). To quantify the magnitude of the 934 to 1009 nm downturn in Vis-NIR spectra extracted from many Pancam observations, we measure the spectral slope between the R6 and R7 filters, where the slope, S, between the R* values measured by two Pancam filters i and j is given by:

$$S_{ij} = \frac{R^*_j - R^*_i}{\lambda_j - \lambda_i},$$

where R* is the relative reflectance, and λ is the wavelength of the filter's effective band center (Table 1).

We observe a correlation between the magnitude of this spectral slope and the abundance of silica; indeed, the Kenosha Comets target, observed by APXS to be the most silica-rich material yet observed by Spirit at 90.1 ± 0.83 wt.% SiO_2 (Ming et al., 2008), exhibits the most negative 934 to 1009 nm slope (-5.9 x10^{-4} nm^{-1}; Table 2). The Kenosha Comets target lies within the Gertrude Weise soil feature, which was excavated by Spirit's inoperative right front wheel on sol 1148. Spectra from the three Pancam observations of this feature (sols 1158, 1187 and 1198; Fig. 2) show that the 934 to 1009 nm slope becomes slightly less pronounced with time (-5.9, -4.1, and -3.2 x10^{-4} nm^{-1}), suggesting that changes in dust contamination between observations may be affecting the spectrum (although no dust storm activity was observed between sols 1158 and 1198), or that the deposit is undergoing a chemical or mineralogical change upon exposure to surface conditions.

The 934 to 1009 nm negative slope was also observed by Wang et al. (2008) and Johnson et al. (2007) in Pancam spectra from the whitish sulfate-rich Tyrone soil and by Wang et al. (2008) in spectra from the soil patches at the sites where high

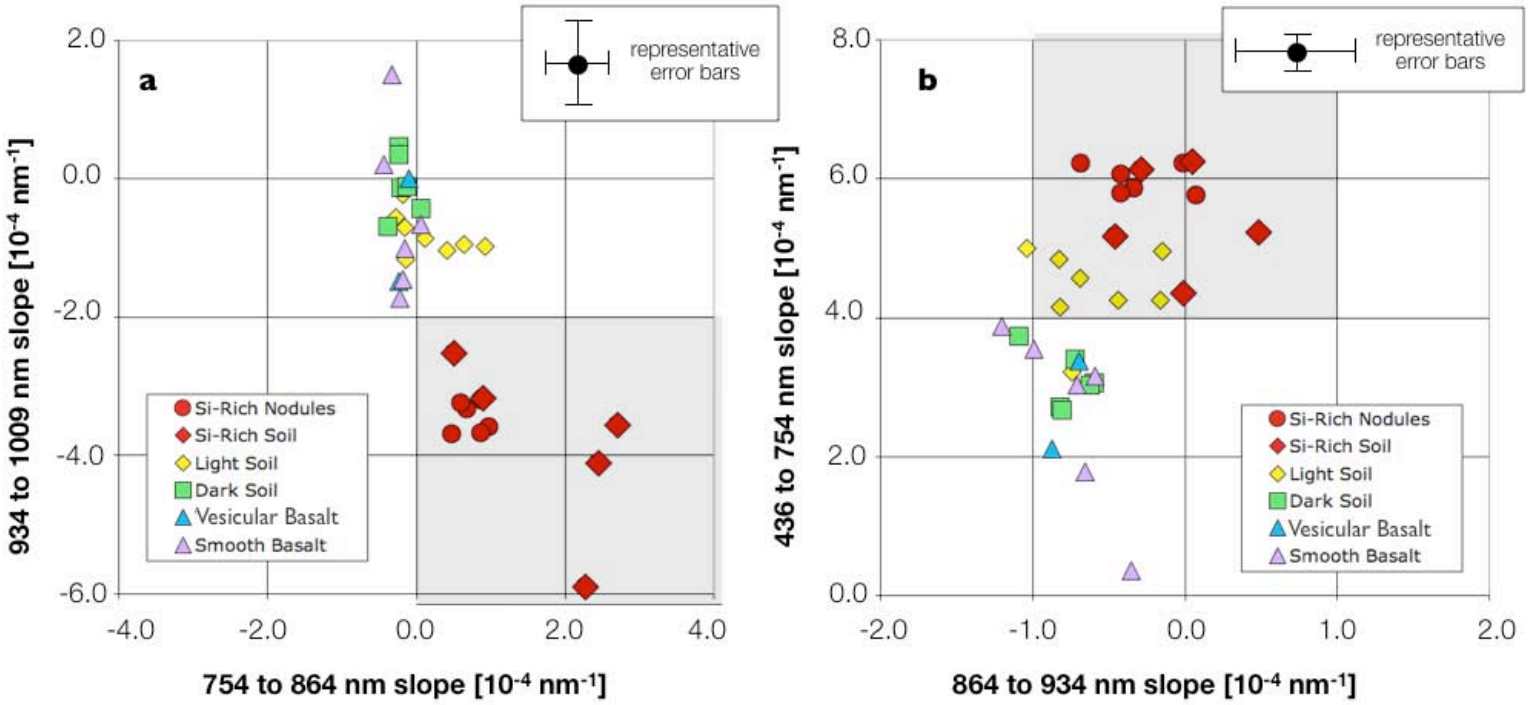

Figure 3. Parameter-space plots showing how the spectra of silica-rich targets are characterized in comparison to the spectra of other scene materials from Fig. 1 and 2. The shaded regions represent our Pancam-based spectral parameterization of high-silica materials: a) silica-rich targets (soil and nodular outcrops) are characterized by a 934 to 1009 nm slope less than -2.0 x 10^{-4} nm^{-1}, and a 754 to 864 nm slope greater than 0.0 nm^{-1}; b) silica-rich targets are characterized by a 436 to 754 nm slope greater than 4.0 x 10^{-4} nm^{-1}, and a 864 to 934 nm slope between -1.0 x 10^{-4} nm^{-1} and 1.0 x 10^{-4} nm^{-1}. Spectral slope is defined in Section 2.2.2. Representative error bars are shown above.

spatial heterogeneity was observed. For example, a few yellowish soil patches at the Dead Sea site (including the Samra target, which contains 37.7 ± 0.26 wt.% excess SiO_2; (Yen et al., 2008)), a few soil patches at the Hank's Hollow site, and a few near the Champagne-Penny targets, exhibit the 934 to 1009 nm negative slope (Wang et al., 2008).

To more generally characterize more generally the Pancam spectra of high-silica targets, we have examined a wide range of spectral parameters, including band depths at specific wavelengths, slopes between wavelength bands, and relative reflectance values. We have found that, in addition to the 934 to 1009 nm negative slope, a positive 754 to 864 nm slope characterizes the high-silica materials as well. Figure 3a shows that, in a 934 to 1009 nm slope vs. 754 to 864 m slope parameter space, the silica-rich soils and nodular outcrops plot in a region distinct from the other materials imaged in the same scene. The high-silica targets also exhibit a relatively flat spectrum from 864 to 934 nm. A parameter space plot of the 436 to 754 nm slope vs. 864 to 934 nm slope for the silica-rich materials, basaltic rocks and surface soils, shown in Fig. 3b, indicates that the silica-rich soils and nodular outcrops are spectrally distinct from the other elements in the scene.

We acknowledge that the 864 to 934 nm slopes of the silica-rich materials may not be statistically distinct from the other materials imaged in these sequences given the size of the error bars (Fig. 3b). Nonetheless, we choose to characterize the silica-rich materials with the 864 to 934 nm slope in order to constrain a "flat" spectral slope in this wavelength region. While no surface materials imaged in the same scene as the silica-rich soil and nodules have 864 to 934 nm slopes of large magnitude, we

anticipate that other materials in Gusev Crater may exhibit significantly negative slopes across this wavelength region. For example, many Fe-bearing minerals such as olivine have a wide absorption feature near 1 μm, the edge of which would be detected not only by Pancam's R7 (1009 nm) filter, but by the R6 (934 nm) and possibly R5 (904 nm) filters as well, which would exhibit a negative 864 to 934 nm slope.

Compared with the other materials imaged in each Pancam scene, the silica-rich materials are highly reflective in red and near infrared wavelengths, causing strongly positive 436 to 754 nm slopes. Wang et al. (2008) have suggested that, because this blue to red slope is greater than that of common Gusev surface dust, the spectra of the silica-rich targets at these wavelengths are not dominated by dust contamination. We observe that the Lefty Ganote target within the Gertrude Weise soil trench exhibits the lowest magnitude 436 to 754 nm slopes of all the silica-rich materials, equivalent to those of the surrounding light-toned surface material. As this specific target is small and has been intimately mixed with surface soils by Spirit's wheels, its shallower blue to red slope is likely due to contamination by other materials.

We find few differences between the observed Pancam spectra of the silica-rich soil and nodular outcrops. Fig. 3a shows that some spectra from the Kenosha Comets target (within the Gertrude Weise soil trench) have larger 754 to 864 nm slopes than the nodule spectra, as well as the most negative 934 to 1009 nm slopes; the spectral slopes from the Lefty Ganote target within Gertrude Weise, however, cluster with the silica-rich nodular outcrops in this parameter space. At all wavelengths the

Kenosha Comets spectra also exhibit higher absolute reflectances than the other silica-rich materials (Fig. 2), while the Lefty Ganote spectra exhibit similar reflectances to the nodular outcrops. While APXS data show that the Kenosha Comets and Lefty Ganote soil targets are chemically equivalent except for a higher level of dust contamination at Lefty Ganote (Ming et al., 2008), the silica-rich nodular outcrops are chemically distinct as observed by APXS (Ming et al., 2008) and may have an origin separate from than the silica-rich soil (Wang et al., 2008). Therefore the Vis-NIR spectral differences between the Kenosha Comets target and the other silica-rich materials (including Lefty Ganote and the nodular outcrops) reflect contamination of surface materials more so than chemistry, and so we do not treat the soil targets separately from the nodular outcrops in terms of our Pancam spectral parameterization.

2.4 The origin of the observed Vis-NIR features

As the 934 to 1009 nm negative slope is the most distinctive Vis-NIR spectral feature of the silica-rich soil and nodular outcrops in the East Valley, it is important that we understand its chemical/mineralogical origin. As stated by Wang et al. (2008), the Pancam spectral features found to be diagnostic of silica-rich materials, especially the negative slope from 934 to 1009 nm, are not a direct reflection of their silica-rich nature because Si-bearing phases are not particularly "spectrally active" in the Vis-NIR spectral range (e.g., Clark et al., 2007b). The 934 to 1009 nm slope may be a reflection of more general properties of silica-rich materials produced from a specific process, such as transition metal substitutions and/or possession of water or hydroxyl.

2.4.1 Comparisons with Vis-NIR spectra of known chemical components

Except for 90.1 wt.% of SiO_2, and 1.2 wt.% of TiO_2, no other elements were detected by APXS to be above 1 wt.% in the Gertrude Weise soil (Ming et al., 2008). Based on Mini-TES observations, Squyres et al. (2008) suggested that hydrous opaline silica accounts for the high concentration of SiO_2 in the Gertrude Weise soil. To understand the potential contributions of these chemical/mineralogical components to the observed Pancam spectra, we have examined high-resolution Vis-NIR reflectance spectra of hydrous amorphous silica (as sinter, opal, silicic acid, and silica gel, all with varying water/ice contents), titanium dioxide (as anatase and rutile), and other high-silica materials (sodium metasilicates). Table 3 lists the TiO_2 and silica-rich samples for which we have acquired laboratory spectra. While anatase, rutile and opal are available in spectral databases, we have also performed our own laboratory measurements of these minerals for consistency with our other laboratory measurements.

Reflectance spectra (350 to 2500 nm) were measured at the University of Winnipeg with the HOSERLab (Cloutis et al., 2006a) Analytical Spectral Devices (ASD) Field Spec Pro HR spectrometer, at $i = 30^o$ and $e = 0^o$ and a spectral resolution of between 2 and 7 nm at 1 nm intervals. Incident light was provided by a 50 W quartz-tungsten-halogen collimated light source. Sample spectra were measured relative to a Spectralon disk and corrected for minor (<2%) irregularities in its absolute reflectance. The spectra were also corrected for small occasional offsets at 1000 nm and 1830 nm where detector changeovers occurred (Cloutis et al., 2008). In

every case, 1000 spectra of dark current, standard, and sample were acquired. Wavelength calibration was ensured through periodic measurements of a holmium oxide-doped Spectralon® puck. Except for the opal and silica gel samples, all measurements were acquired at standard temperature and pressure.

Synthetic TiO_2 samples (anatase and rutile; Table 3) were crushed by hand and dry sieved to < 45 μm. We find that the spectra of anatase and rutile are spectrally flat at wavelengths greater than 900 nm (Fig. 4a); there are no features at this wavelength region that could contribute to a negative 934 to 1009 nm slope in Pancam wavelengths.

Our hydrous amorphous silica samples include silicic acid ($SiO_2 \cdot xH_2O$), opal, and silica gel, which were crushed by hand and dry sieved to <45 μm, < 250 μm, and < 1mm grain sizes, respectively. We acquired spectra of the opal at room temperature and after being frozen to -13^o C (the lowest temperature setting of the available laboratory freezer). The silica gel sample was also frozen to -13^o C, and spectra were taken immediately after removal from the freezer and every 2 minutes thereafter, until the sample equilibrated with room temperature (~20^o C after one hour). Spectra were acquired at both ambient and cold temperatures because it is known that liquid water and water ice spectra exhibit different spectral properties (e.g. Irvine and Pollack, 1968). By freezing and thawing the samples while performing continuous spectral measurements, we can trace the spectral changes accompanying thawing. These observations also allowed us to acquire spectra at a range of temperatures consistent with temperatures measured at the CCD during Pancam observations of silica-rich

targets (-21.5 to 8.9^{o} C). Spectra from the first and last observation in this series are given in Fig. 4b and summarized in Table 3.

We measured the water contents of the opal and silica gel samples to be 3.22 and 16.69 wt. % H_2O, respectively. These numbers are the weight losses upon heating the samples to 950^{o} C for 1 hour, as described by Mertzman (2000). During our sample preparation (grinding and sieving), we observed no physical change in any of the hydrated silica materials that would indicate a change in water content.

To make comparisons with silica precipitates from terrestrial environments, we acquired spectra of silica sinter samples from a thermal vent in Wairakei, New Zealand, from the Great Geysir silica terrace at the Geysir hydrothermal region, Iceland, and from a cold spring solution chimney at the Mafeking Quarry in Manitoba, Canada. The water contents of these sinters are 9.69, 6.46 and 3.64 wt. % H_2O, respectively. For direct comparison with the Pancam observations of nodular outcrops in the East Valley, we acquired spectra of these sinters as whole rock samples (i.e., not crushed and sieved); example spectra are shown in Fig. 4c and summarized in Table 3.

All of the amorphous silica example spectra (Fig. 4) are featureless in the near-infrared except for a shallow absorption band centered at ~970 nm resulting from a combinational mode ($2\nu_1+\nu_3$) of water (Herzberg, 1945), which could be contributed by the water molecules present in the interstitial spaces within the amorphous silica structure. As listed in Table 3, band centers of this feature occur between ~955 and 970 nm. By convolving the high-resolution laboratory spectra to Pancam bandpasses (Bell et al., 2003), shown by the colored symbols in Fig. 4, we find that the ~955 to 970 nm absorption band falls at the mid-point between the effective band centers of

Table 3. Examples of minerals containing the chemical components identified by APXS in the high-silica soils and nodular outcrops (TiO_2 and $SiO_2 \cdot nH_2O$), and other Si-rich minerals.

Sample[a]	Origin	Formula[d]	934 to 1009nm slope (x 10^{-4} nm^{-1})	Location of band minimum (nm)
Anatase	Synthetic	TiO_2	0.6	---
Magadiite	Lake Magadi, Kenya	$NaSi_7O_{13}(OH)_3 \cdot 4H_2O$	1.3	963
Opal	unknown	$SiO_2 \cdot nH_2O$	0.4	960
Opal (-13°C)	unknown	$SiO_2 \cdot nH_2O$	0.3	959
Rutile	Synthetic	TiO_2	1.4	---
Silica Gel (-13°C)[b]	Synthetic	$SiO_2 \cdot nH_2O$	-1.4	966
Silica Gel[c]	Synthetic	$SiO_2 \cdot nH_2O$	0.0	959
Silica Sinter	Great Geysir, Iceland	$SiO_2 \cdot nH_2O$ and unknown components	-2.2	962
Silica Sinter	Mafeking Quarry, Manitoba, Canada	$SiO_2 \cdot nH_2O$ and unknown components	-0.2	---
Silica Sinter	Wairkei Thermal Valley, New Zealand	$SiO_2 \cdot nH_2O$ and unknown components	0.1	968
Silicic Acid	Synthetic	$SiO_2 \cdot nH_2O$	-1.7	967
Sodium Metasilicate Nonahydrate	Synthetic	$Na_2SiO_3 \cdot 9H_2O$	-7.0	1001
Sodium Metasilicate Pentahydrate	Synthetic	$Na_2SiO_3 \cdot 5H_2O$	-2.8	---

[a] Reflectance spectra from these samples were acquired at room temperature unless otherwise noted. Details of the laboratory procedure are given in Section 2.3;
[b] Exposed to 100% relative humidity for 22 hours before freezing;
[c] Observed one hour after freezing;
[d] (Deer et al., 1997).

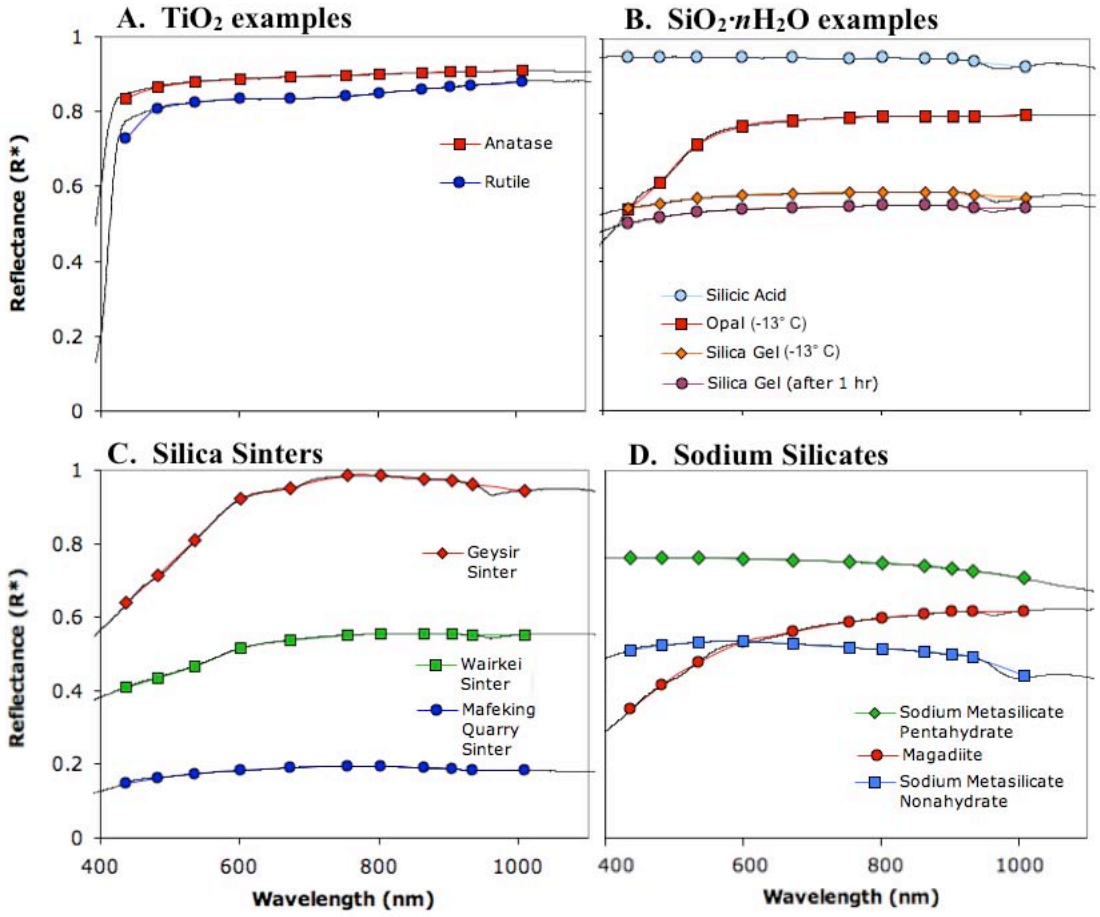

Figure 4. Example spectra of minerals containing the chemical components identified by APXS in the high-silica soils and nodular outcrops (TiO_2 and $SiO_2{\cdot}nH_2O$) and other silica-rich minerals from Table 3: a) TiO_2 examples: anatase and rutile; b) $SiO_2{\cdot}nH_2O$ examples: silicic acid, opal (-13°C) and silica gel (immediately after being frozen to -13°C, and after one hour); c) silica sinter examples from: Icleand (Geysir), New Zealand (Wairkei) and Canada (Mafeking Quarry, Manitoba); and d) natural and synthetic sodium silicate examples: magadiite ($NaSi_7O_{13}(OH)_3{\cdot}4H_2O$), sodium metasilicate pentahydrate ($Na_2SiO_3{\cdot}5H_2O$) and sodium metasilicate nonahydrate ($Na_2SiO_3{\cdot}9H_2O$). All spectra for this study were acquired at room temperature unless otherwise noted; details of the laboratory methods are given in Section 2.2.

the R6 and R7 filters; thus, in most samples this band cannot induce a reduction of reflectnce through the R7 filter. While this band contributes to slightly negative 934 to 1009 nm slopes in the silicic acid, frozen silica gel, and Geysir sinter samples (-1.7, -1.4 and -2.2 x 10^{-4} nm^{-1}, respectively; Table 3), it cannot account for the magnitude of the slopes observed in Pancam spectra of silica-rich soil and nodular outcrops (-2.5 to -6 2 x 10^{-4} nm^{-1}; Table 2).

We observe that the position of the ~970 nm band in silica gel shifts towards shorter wavelengths with time as the frozen sample warms from -13^{o} C to ambient temperatures. Subsequently, the observed 934 to 1009 nm slope changes from negative (-1.4 x 10^{-4} nm^{-1} immediately after removal from the freezer) to flat (~0.0 one hour after removal). We observe no significant change in the band center or the 934 to 1009 nm slope of opal between the observations at -13^{o} C and room temperature. Further laboratory studies are needed, however, to fully constrain the effects of both temperature and pressure on the ~970 nm band in silica-rich materials.

We have also acquired spectra of a suite of sodium silicate minerals (magadiite ($NaSi_7O_{13}(OH)_3 \cdot 4(H_2O)$), sodium metasilicate pentahydrate ($Na_2SiO_3 \cdot 5H_2O$), and sodium metasilicate nonahydrate ($Na_2SiO_3 \cdot 9H_2O$)] as potential geologically reasonable silica-rich material components that could cause a negative 934 to 1009 nm slope (Fig. 4d). Because sodium is at the edge of the APXS spectrum and has the largest error (Rieder et al., 2003), it is possible that a small component of a sodium silicate mineral could be present in the silica-rich soil and nodular outcrops without being detected by the APXS instrument. We find that the sodium silicate with the highest H_2O content (sodium metasilicate nonahydrate) exhibits a very strong negative

934 to 1009 nm slope (-7.0 x 10^{-4} nm^{-1}; Table 3) due to the position of the $2\nu_1+\nu_3$ H_2O combination band. The center of the absorption band is at a longer wavelength (1001 nm) than observed in the amorphous silica spectra for two reasons: 1) the position of the band is dependent upon nearest-neighbor cations, and the presence of Na shifts the ~970 nm band towards longer wavelengths; and 2) strong water bands at longer wavelengths (e.g., the ~1200 nm combination band) serve to "drag down" the long-wavelength edge of the ~1000 nm band, imparting a negative slope to the spectrum longward of ~1000 nm.

We hypothesize that the 934 to 1009 nm spectral feature seen in Pancam observations of silica-rich targets is not necessarily a direct contribution from water-bearing amorphous silica (opal, sinter, or others). Rather, it may be a signature of other mineral phases or chemical species produced together with the high-silica materials. These species must have the correct cation arrangements to exhibit the $2\nu_1+\nu_3$ H_2O combination band centered at long wavelengths (~1000 nm) and/or strong enough bands at longer wavelengths to affect the edge of the ~970 nm band, as observed in the sodium metasilicate nonahydrate spectrum. Below we discuss our searches of spectral databases to identify additional mineral candidates that exhibit these spectral effects.

2.4.2 Comparisons with Vis-NIR features in spectral databases

We have performed comparisons of the Pancam silica-rich soil and nodular outcrop spectra to a total of 1880 laboratory spectra of minerals from the USGS Digital Spectral Library (Clark et al., 2007b), the CRISM Spectral Library (Murchie

et al., 2007), as well as the spectra from other studies of sulfate minerals (Cloutis et al., 2006b), playa evaporite minerals (Crowley, 1991), and ices (Roush et al., 1990). We have also acquired reflectance spectra of fresh snow (measured at -25^{o} C) and hydrated sodium metasilicates (experimental methods were described in Section 2.4.1).

To simulate Pancam observations of these minerals and ices on the martian surface, we multiplied the high-resolution laboratory spectra by the solar spectrum, convolved the resulting radiance spectra to the Pancam spectral bands (Table 1), and divided the radiance value at each band by the solar spectrum convolved to that band. From the convolved spectra, we have calculated the 864 to 934 nm and 934 to 1009 nm slope values and identified the minerals that fit the slope criteria shown by the grey regions in Fig. 3 (864 to 934 nm slopes between -1.0 x 10^{-4} nm^{-1} and 1.0 x 10^{-4} nm^{-1}; 934 to 1009 nm slopes less than -2.0 x 10^{-4} nm^{-1}). This approach enables the potential identification of minerals with an absorption band in the near-infrared spectral range (~1000 nm) that would be detected by Pancam's R7 filter and thus could be consistent with the 934 to 1009 nm negative slope seen in the spectra from high-silica soils and nodular outcrops.

Of the 1880 mineral spectra examined, we have identified 18 spectra that exhibit a 934 to 1009 nm slope less than -2.0 x 10^{-4} nm^{-1} when convolved to Pancam bandpasses. Details of these samples are listed in Table 4. These minerals include borates, carbonates, chlorides, garnet, halides, silicates, sulfates, and water ice. Figure 5 shows plots of the matching mineral spectra with the steepest 934 to 1009 nm slope: natron ($Na_2CO_3 \cdot 10H_2O$); (Crowley, 1991)), sanderite ($MgSO_4 \cdot 2H_2O$; (Crowley,

Table 4. Mineral library spectra that exhibit Pancam spectral parameters like those seen in high-silica materials at Gusev Crater.

Group	Mineral	Formula[a]	wt% H_2O or OH[a]	Library[b]	934 to 1009nm slope (x 10^{-4} nm^{-1})
Borate	Datolite	$CaBSiO_4(OH)$	19	1	-3.0
Borate	Pinnoite	$MgB_2O_4 \cdot 3H_2O$	33	2	-2.5
Borate	Teepleite	$Na_2(BO_2)Cl \cdot 2H_2O$	22	2	-2.1
Carbonate	Natron	$Na_2CO_3 \cdot 10H_2O$	63	2	-2.7
Carbonate	Trona	$Na_3(CO_3)(HCO_3) \cdot 2H_2O$	20	1	-2.5
Chloride	Antarcticite	$CaCl_2 \cdot 6H_2O$	49	2	-3.9
Chloride	Sinjarite	$CaCl_2 \cdot 2H_2O$	25	2	-3.2
Garnet	Grossular	$Ca_3Al_2(SiO_4)_3$	0	1	-2.1
Halide	Kainite	$MgSO_4 \cdot KCl \cdot 3H_2O$	22	2	-4.3
Silicate	Sodium Metasilicate Nonahydrate	$Na_2SiO_3 \cdot 9H_2O$	45	5	-7.0
Sulfate	Alunite	$KAl_3(SO_4)_2(OH)_6$	26	1	-4.6
Sulfate	Epsomite	$MgSO_4 \cdot 7H_2O$	51	4	-2.5
Sulfate	Gypsum	$CaSO_4 \cdot 2H_2O$	21	2	-2.5
Sulfate	Sanderite	$MgSO_4 \cdot 2H_2O$	13	2	-4.1
Sulfate	Mirabilite	$Na_2SO_4 \cdot 10H_2O$	56	2	-2.5
Sulfate	Pentahydrite	$MgSO_4 \cdot 5H_2O$	43	2	-3.1
Water Ice	Fine grained water ice	H_2O	100	3	-2.0
Water Ice	Snow	H_2O	100	5	-2.3

[a]wt.% H_2O and OH values are calculated from standard mineral formulae (Deer et al., 1997).

[b]Spectral libraries and databases included in our analysis:

1) USGS Mineral Database (Clark et al., 2007b).
2) Playa Evaporite Minerals (Crowley, 1991).
3) Ices (Roush et al., 1990).
4) CRISM Spectral Library (Murchie et al., 2007).
5) This study.

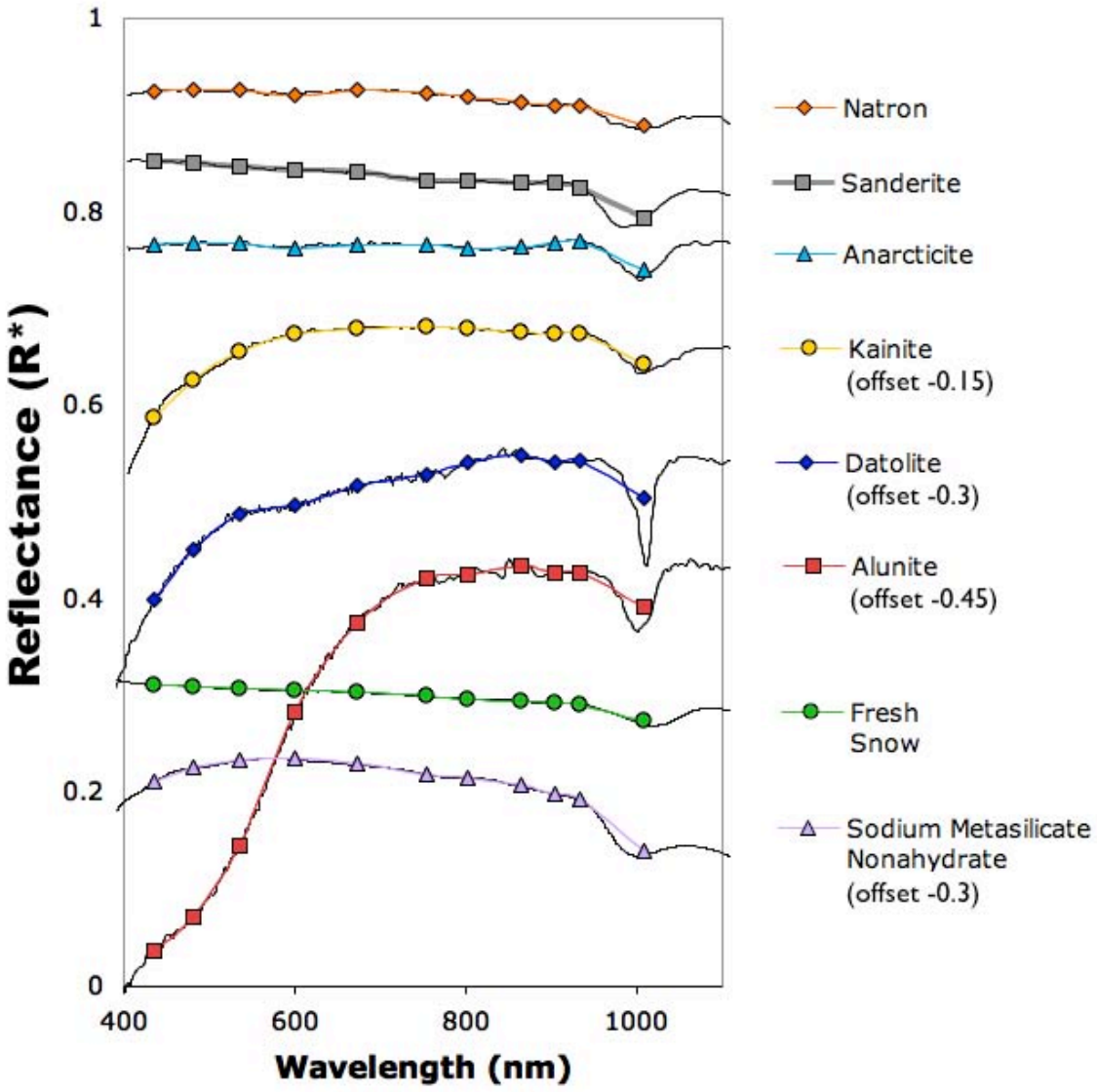

Figure 5. Examples of laboratory spectra of minerals from Table 4 that exhibit a strong negative slope from 934 to 1009 nm. Black lines are the high-resolution laboratory spectra, and colored symbols are the spectra convolved to Pancam wavelengths. The negative 934 to 1009 nm slopes (values given in Table 4) result from a water overtone whose position varies slightly depending on its bonding to nearest-neighbor atoms.

1991)), anarcticite ($CaCl_2 \cdot 6H_2O$; (Crowley, 1991)), kainite ($MgSO_4 \cdot KCl \cdot 3H_2O$; (Crowley, 1991)), datolite ($CaBSiO_4(OH)$; (Clark et al., 2007b)), alunite ($KAl_3(SO_4)_2(OH)_6$; (Clark et al., 2007b)), fresh snow (H_2O; from our laboratory observations), and sodium metasilicate nonahydrate ($Na_2SiO_3 \cdot 9H_2O$; from our laboratory observations). Rice et al. (2008) discuss additional minerals with a steeply negative 934 to 1009 nm slope, but those do not share the "flat" spectrum between 864 and 934 nm (values between -1.0 x 10^{-4} nm^{-1} and 1.0 x 10^{-4} nm^{-1}) that we also use here to characterize the silica-rich materials observed by Spirit.

A common theme among our spectral matches is that, with the exception of grossular, they all possess structurally bonded H_2O or OH. The water molecules have absorption bands centered near 1000 nm, likely from the combinational mode $2\nu_1+\nu_3$ (Herzberg, 1945). Because the centers of the absorption bands from those species occur near 1000 nm, some with a large band depth, they can induce the negative slope from 943 to 1009 nm when the spectra are convolved into the Pancam spectral resolution (Fig. 5). A similar absorption band was seen in spectra of hydrated amorphous silica samples (Fig. 4), but the band minimum occurs at wavelengths too short to be detected by Pancam's R7 filter. In the candidate mineral spectra shown in Fig. 5, the absorption band minima occur within the effective band center of the R7 filter and are narrow enough that the short-wavelength tails of the absorption bands are not detected by the R6 filter.

Only one spectrum fits our spectral criteria without possessing H_2O or OH in its structure: Grossular HS113 from the USGS Spectral Library (Clark et al., 2007b). We note that four additional grossular spectra were included in our analysis, none of

which exhibit a negative 934 to 1009 nm slope. The ~1000 nm absorption seen in the one specific Grossular HS113 sample appears to be caused by the substitution of some ferrous iron for calcium in the garnet structure; however, we do not observe similar ferrous iron substitutions contributing to a negative 934 to 1009 nm slope in any other of the database spectra. Because of the anomalous nature of this grossular spectrum, and because the presence of grossular at Gusev Crater is highly unlikely (given that, in terrestrial environments, grossular is typically found in contact with metamorphosed limestone (Deer et al., 1997)), we do not further consider it as a reasonable mineral candidate in this study.

2.5 Candidate Minerals that may contribute to the ~1000 nm absorption band in the silica-rich soil

Based on the spectral comparisons described above, we hypothesize that the steeply negative slope from 934 to 1009 nm observed in the spectra from silica-rich soil and nodular outcrops at Eastern Valley is an indication of hydration, in the form of H_2O or OH, either free, adsorbed, or bound in a mineral structure. While each mineral phase given in Table 4 could produce a spectrum that fits the slope criteria extracted from the Pancam observations of silica-rich species, most of them apparently have compositions inconsistent with the elemental chemistry of silica-rich soil (Gertrude Weise) measured by APXS. The detection limit of the APXS instrument is 0.5-1.0 wt.%, depending on the element (Rieder et al., 2003). In a linear mixing model with pure amorphous silica (the spectrum of silica gel shown in Fig. 5), 5% Gusev surface dust (an average spectrum of the surface dust shown in Fig. 2) and

a spectrum from each of the candidate minerals in Table 4, we found that the lowest concentration of any single mineral that would create a 934 to1009 nm slope below 2.0 x 10^{-4} nm^{-1} would be 10% sodium metasilicate nonahydrate ($Na_2SiO_3 \cdot 9H_2O$). At this concentration, there would be roughly 1-2 wt.% Na in the sample, which is near the APXS detection limit. We note that linear mixing models cannot be used definitively to find absolute abundances due to non-linear effects induced by intimate mixing (e.g., Clark and Roush, 1984; Mustard and Pieters, 1987; Poulet and Erard, 2004), thus we only use these models as first-order approximations of possible mineral concentrations.

It is feasible that a component of sodium metasilicate nonahydrate in the silica-rich soil (Gertrude Weise) could be at low enough concentrations to be undetected by APXS but still affect the near-infrared spectrum, especially as Na is at the edge of the APXS spectrum and has the largest error. However, we have found no other minerals for which this kind of situation is plausible. For all other minerals listed in Table 4, our mixing model approximations show that in order to cause the observed 934 to 1009 nm negative slope, the concentrations of candidate minerals required would make one or more elements detectable to APXS (besides Si and Ti) in excess of 5 wt.%. This would be inconsistent with the observed APXS chemistry of the Gertrude Weise soil.

While hydrous sodium silicate is the most likely mineral contributor to the negative slope from 934 to 1009 nm in the spectra of silica-rich soil among our available library of samples, the presence of such materials is not particularly consistent with the proposed low pH depositional environment for the silica-rich

materials observed in Gusev Crater (Squyres et al., 2008). In terrestrial environments, sodium silicate minerals are often found in alkaline playa evaporite sequences (e.g., Eugster, 1967; Sheppard et al., 1970), and are unstable under acidic conditions. However, the composition of the silica-rich deposits at Gusev does not uniquely constrain the pH of associated fluids, and precipitation of sinter deposits from alkali chloride brines is possible at high pH (Squyres et al., 2008).

The candidate minerals listed in Table 4 are not a unique set of solutions. Our spectral comparisons are highly sensitive to the exact position and depth of the ($2\nu_1+\nu_3$) H_2O combination band, which can vary slightly with temperature and pressure (e.g., Clark, 1981; Grundy and Schmitt, 1998). It is possible that a mineral with a ~1000 nm absorption band too weak to be included in this study could exhibit a negative 934 to 1009 nm slope at lower temperatures and pressures, and, conversely, that candidate spectra from Table 4 with narrow absorption bands may not exhibit the same negative 934 to 1009 nm slope under different experimental conditions. We also note that the mineral spectral libraries used in this study are not comprehensive in terms of particle sizes, crystallinity, the presence of thin coatings, and the level of hydration of minerals that can hold variable amounts of water (such as expanding layer phyllosilicates and polyhydrated sulfates). The observed 934 to 1009 nm slope could thus be due to one of these or other factors that has not yet been properly measured and/or characterized. Further laboratory spectroscopy work with H_2O and/or OH-bearing minerals under martian surface conditions and with varying particles sizes (and other factors) is needed to understand the full suite of candidate minerals that could be consistent with the Pancam observations.

2.6 Potential mineralogical differences between silica-rich soil and nodular outcrops

Aside from their high concentrations of SiO_2, the silica-rich nodular outcrops are otherwise chemically quite different from the silica-rich soil (Ming et al., 2008). On the basis of the nodule compositions, the presence of one or more of the mineral candidates in Table 4 (with amorphous silica and remnants of basaltic materials) cannot be excluded as contributors to the negative 934 to 1009 nm slope in their Pancam spectra. For example, the nodule "Innocent Bystander" is enriched in MgO with a small SO_3 component, and so the magnesium sulfate candidates (epsomite, sanderite and pentahydrite) and the borate pinnotite listed in Table 4 could be present in large enough quantities to produce the observed 934 to 1009 nm slope in this sample and also be consistent with the observed APXS chemistry.

Squyres et al. (2008) discussed two potential processes that can produce high concentrations of opaline silica in hydrothermal settings, both of which involve hydrothermal fluids: 1) the silica precipitates directly from hydrothermal fluids after the fluid temperature decreases (silica sinter); or 2) the silica forms from the remnants of former basaltic materials after extensive open-system leaching of metallic cations by acidic fluids. The first hypothesis requires a relatively high original fluid temperature so that it can retain high concentration of SiO_2 and can then deposit silica abruptly upon cooling (e.g., >98 wt.% SiO_2 in one sample). The second hypothesis requires high acidity of the original fluid, enabling the leaching of metal cations from the local rocks and thus allowing high SiO_2 concentrations in the rock residue. While high temperature would increase the efficiency and rate of the second process, it is not

required (e.g., McAdam et al., 2008). Squyres et al. (2008) favor the second process mainly based on the elevated TiO_2 levels in silica-rich targets of the Home Plate region; however, because TiO_2 enrichments have also been observed in terrestrial sinters (Preston et al., 2008), this enrichment may not necessarily uniquely identify a leaching process.

Wang et al. (2008) suggested that the silica-rich soil and nodular outcrops in Eastern Valley are genetically related to the S-rich soil at Tyrone, and that relatively large amounts of acidic hydrothermal fluids were involved in their formation. Their arguments were based on Vis-NIR properties of Tyrone sulfate-rich soils (two layer structures, spectral homogeneity within each layer, and non-equilibrium of the deeper layer with surface atmospheric conditions), and the existence of silica-rich nodular outcrops throughout the topographical lowland where the most S-rich (Tyrone soil) and the most silica-rich (Gertrude Weise soil) deposits both occur (separated by a distance of ~75 meters). They proposed that the Tyrone soil and Gertrude Weise soil are two endmember products of the same process, but that the two soils were chemically sorted, aqueously transported, and deposited at different stages of the process.

The studies by Squyres et al. (2008) and Wang et al. (2008) suggest that the silica-rich nodular outcrops are remnants of local outcrops after the Mg, Fe, Ca, Al (etc.) cations were leached out by low-pH hydrothermal fluids. We notice that the silica-rich nodular outcrops have a typical surface morphology similar to broken-off-pieces from the clastic texture of Riquelme type outcrops found on Low Ridge or on Mitcheltree Ridge (Lewis et al., 2008). Hydrothermal fluids and a temperature

gradient could have assisted in producing the Si-enriched species observed in the East Valley, to carry $(SO_4)^{2-}$ and leached cations (Ca, Mg, Fe, and even Al) over some distance, followed by the precipitation of sulfates (as well as halides, bromides, etc.) at lower temperatures at the Tyrone site. It is worth noting that the large range of SiO_2 contents of the East Valley materials (48 to 90 wt.% SiO_2) is a potential indication of various degrees of leaching and fine scale temperature and pH gradients.

Given the compositional character of local outcrops (e.g., the Ca-enriched Halley outcrops; Ming et al., 2008) and the highly porous surface/interior morphology of silica-rich nodular outcrops, the formation of Mg-, Ca-, and even Al-bearing hydrous salts (similar to those in Table 4) during or after the acidic leaching process is possible, and perhaps even likely. Although no definitive mineralogy can be derived from the measurements made on the nodular outcrops, we know that the steep 436 to 754 nm slope in Pancam Vis-NIR spectra suggests a high oxidation state of Fe-species (high Fe^{3+}/Fe_{Total}); a 6 μm feature in Mini-TES spectra of nodular outcrops is indicative of the presence of hydrous species (Ruff et al., 2008b); and the compositions of silica-rich nodular outcrops revealed by APXS (Ming et al., 2008) and Mössbauer (MB) (Morris et al., 2008) supports the contention that they are very different from (and likely altered remains of) other local outcrops. This evidence supports the hypothesis that some alteration products remain as a component of the nodular outcrops, which (in addition to the properties seen by APXS, MB, and Mini-TES) could also be a potential source of the distinct negative slope from 934 to 1009 nm observed by Pancam.

3. Regional Mapping of a Characteristic Hydration Signature

We argue that four slope parameters extracted from the Pancam Vis-NIR spectra of typical silica-rich species in the East Valley can be used as a "hydration signature" based on our hypothesis that the 934 to 1009 nm slope is caused by an H_2O combination mode. This hydration signature can be used to search for other potential silica-rich or hydrated species along Spirit's traverse. However, we could only characterize materials as "silica-rich" by a comprehensive evaluation of multiple lines of evidence, including composition, mineralogy, and morphology (as with the multi-instrument analyses of silica-rich species at Hank's Hollow by Wang et al. (2008), for example). In the following analysis, we use solely our Pancam spectral parameters to map the potential distribution of hydrated materials in the Columbia Hills region.

3.1 Mapping methodology

We can use the spectral characteristics of the known silica-rich targets to remotely identify potentially similar deposits in places where in situ chemical measurements have not been made. To identify regions in Pancam images that are spectrally similar to the high-silica materials, we search for pixels with the following four characteristic hydration signature parameters: 1) 934 to 1009 nm slopes less than -2.0×10^{-4} nm^{-1}; 2) 754 to 864 nm slopes greater than 0.0 nm^{-1}; 3) 436 to 754 nm slopes greater than 4.0×10^{-4} nm^{-1}; and 4) 864 to 934 nm slopes between -1.0 and 1.0 $\times 10^{-4}$ nm^{-1}. The shaded areas in the parameter space plots of Fig. 3 illustrate how we restrict the spectra in our mapping, and show that of all the materials in each Pancam image, only the hydrated opaline silica targets meet these spectral criteria.

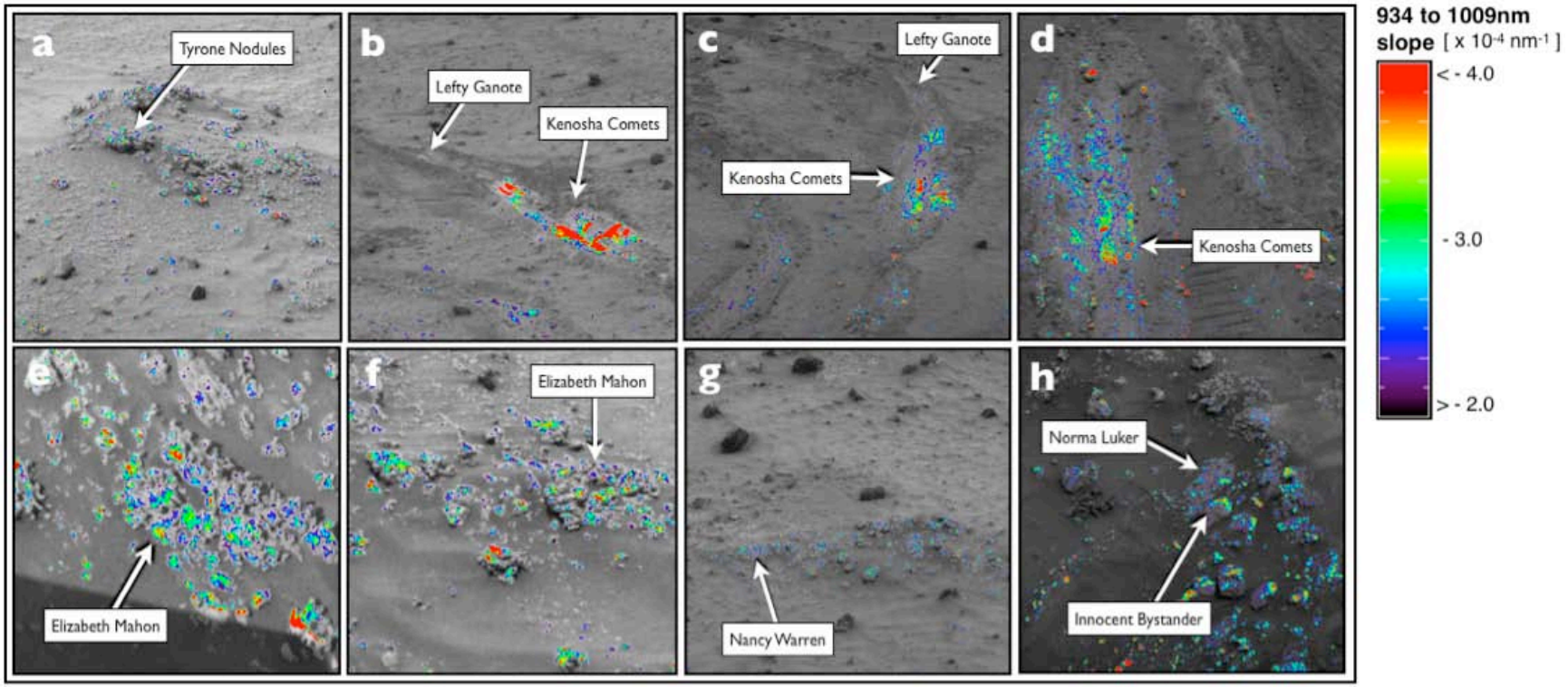

Figure 6. Maps of the hydration signature (defined by four spectral parameters: 1) 934 to 1009 nm slopes less than -2.0 x 10^{-4} nm^{-1}; 2) 754 to 864 nm slopes greater than 0.0 nm^{-1}; 3) 436 to 754 nm slopes greater than 4.0 x 10^{-4} nm^{-1}; and 4) 864 to 934 nm slopes between -1.0 and 1.0 x 10^{-4} nm^{-1}; see Fig. 3). The color scale corresponds to the magnitude of the 934 to 1009 nm slope, with purple indicating slopes at our limit of -2.0 x 10^{-4} nm^{-1} and red indicating slopes less than -4.0 x 10^{-4} nm^{-1}. Maps are overlain on R2 (754nm) Pancam images of the targets confirmed by APXS and/or Mini-TES to be silica-rich: a) Tyrone Nodular outcrops (sol 1101, P2552), the extent of the outcrop is ~ 75 cm; b) Gertrude Weise (sol 1158, P2581), the width of the wheel tracks are ~16 cm; c) Gertrude Weise (sol 1187, P2533); d) Gertrude Weise (sol 1198, P2539); e) Elizabeth Mahon (sol 1160, P2582), the nodule is ~10 cm; f) Elizabeth Mahon (sol 1174, P2588), the extent of the outcrop is ~ 60 cm; g) Nancy Warren (sol 1190, P2534), the extent of the outcrop is ~140 cm; h) Innocent Bystander and Norma Luker (sol 1294, P2581), Innocent Bystander is ~ 6 cm.

To determine how well our four hydration signature parameters correlate with the known silica exposures, we have mapped our criteria over the eight Pancam 13 filter image sequences containing silica-rich nodular outcrops and soil. Figure 6 shows where the four spectral criteria are met in each scene, and are mapped over the images taken by Pancam's R2 filter. The color scale in these maps indicates the magnitude of the 934 to 1009 nm slope.

We find that the hydration signature is well correlated with the soils and nodular outcrops that are known to be silica-rich in each image. The hydration signature is not seen over the entire extent of each nodule, however; this variability could indicate compositional heterogeneities within the deposits, variable dust coverage, or illumination effects such as shadowing. Also, the hydration signature is only seen over a small portion of the Lefty Ganote target within the Gertrude Weise soil trench (Fig. 6b-c), which is likely due to the limited extent of bright silica material within this segment of the trench. Based on these mapping tests, we hypothesize that we can use maps of the hydration signature in other Pancam 13 filter image sequences along Spirit's traverse to remotely identify deposits similar to the silica-rich materials observed in the East Valley.

3.2 Mapping the hydration signature along Spirit's traverse

To understand the distribution of deposits that are spectrally similar to the silica-rich soil, nodular outcrops, and other hydrated alteration materials, we have performed our mapping of the hydration signature (defined by the four spectral parameters discussed in Section 3.1) over every 13-filter Pancam image sequence

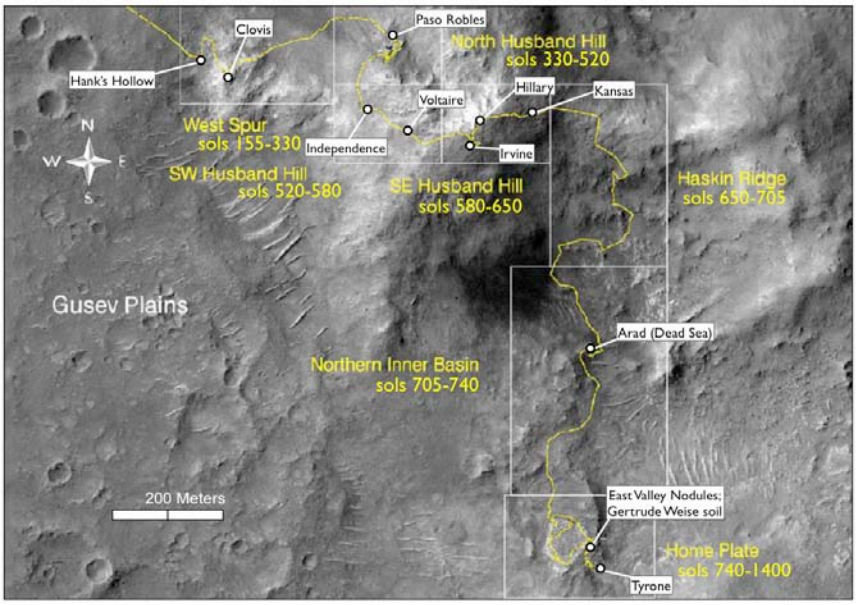

Figure 7. Spirit's traverse (yellow line) in the Columbia Hills shown over HiRISE image PSP_001513_1655_RED. Boxed regions adapted from Arvidson et al. (2008).

taken from the West Spur to Home Plate (sols 155-1400), excluding calibration sequences, observations of the rover deck, or sequences exhibiting image saturation. This analysis includes 702 image sequences from Spirit's ascent out of the Gusev Plains into the Columbia Hills, its traverse across Husband Hill, its descent into the Northern Inner Basin, and its exploration of the East Valley and the Home Plate vicinity (Fig. 7; a mission narrative for these sols is given by Arvidson et al. (2008)).

Our initial analysis of these data sets showed that the hydration signature is falsely detected in image sequences acquired at very low Sun angles. That is, in image sequences of the same target acquired at identical emission angle geometries but at largely different incidence angles (times of sol), the low-Sun observations generally exhibit spectra with more steeply negative 934 to 1009 nm slopes (e.g., the sol 316 observations of Spirit's wheel tracks, P2558 and P2559, taken at 12:31 and 16:29 local true solar time (LTST), respectively; Fig. 8a-b). This effect is likely due to calibration

inaccuracies at low solar elevations: the Pancam calibration model (Bell et al., 2003, 2006; Kinch et al., 2007) assumes that the calibration target behaves as a Lambertian scatterer, an assumption that, for the specific calibration target materials used on the rovers, is increasingly incorrect as incidence angles get closer to 90° or at strongly forward scattering geometries (see Fig. 21 in Bell et al., 2003). To avoid complications at low Sun angles, here we restrict our discussion to image sequences acquired within the same range of LTST as the observations of silica-rich materials listed in Table 2 (11:00 to 13:30 LTST).

While variations in local incidence angles may have an affect on the observed spectra, when there are multiple image sequences of a target acquired within this range of LTST just cited, we observe that the hydration signature maps are nearly identical. For example, we have looked for changes in seven separate observations of the Tyrone soil exposure (sols 864, 922, 959, 982, 1005, 1036, and 1062) and find no systematic changes in the location or intensity of the hydration signature parameters (Fig. 8c-d). The maximum differences in LTST, solar incidence angle, solar azimuth, and atmospheric opacity between these Pancam image sequences are 60 minutes, 28.3^{o}, 14.8^{o}, and 0.6, respectively (observations are summarized in Table 2 of Wang et al. (2008)), and the seven observations have nearly identical emission angle viewing geometries. The consistency of the hydration signature maps made from these observations provides additional support for our assertion that the spectral components that define our hydration signature are not affected by illumination and atmospheric differences within these ranges.

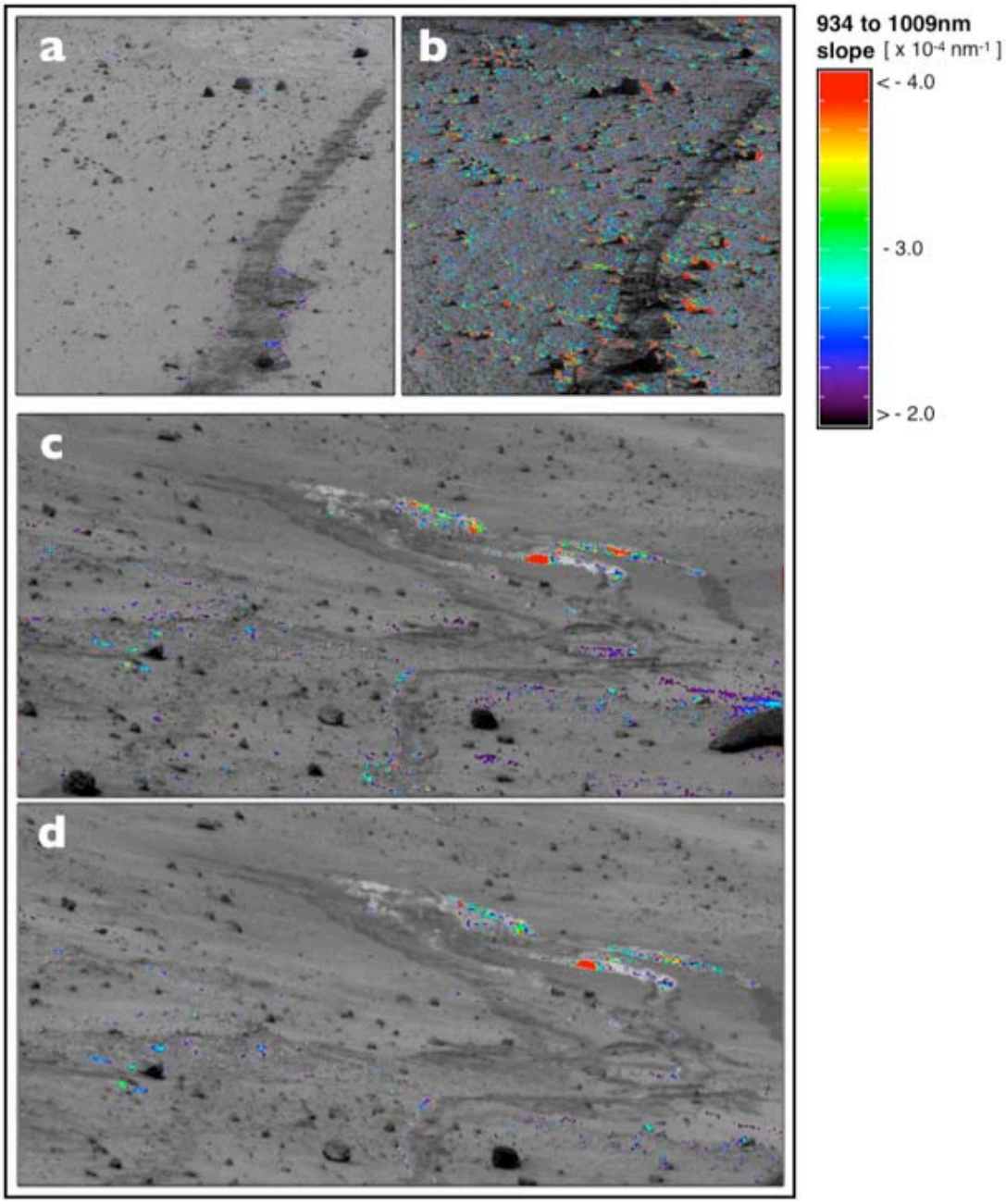

Figure 8. Examples of hydration signature maps from Pancam observations acquired at different local true solar times (LTST), mapped over R2 (754 nm) images: a) Spirit's wheel tracks, sol 316, P2558, starting LTST 12:31:17; b) Sprit's wheel tracks, sol 316, P2559, starting LTST 16:29:57. Note the increased prevalence of the hydration signature due to effects at low Sun angles (see text); c) Tyrone soil, sol 864, P2547, starting LTST 12:37:47; and d) Tyrone soil, sol 1005, P2546, starting LTST 12:33:12. Note that the hydration signature occurrence over Tyrone does not change within this range of LTST over 141 sols.

Geometric factors may be responsible for the elevated hydration signature that we observe on some rocks at high local incidence angles (see Section 3.2.4). While we find no preferred absolute geographic orientation of the hydration signature across these rock faces, we note that the hydration signature may occur most often on dusty surfaces that are tilted relatively away from the rover's line of sight (i.e., at higher emission angles). See Section 4 for further discussion.

Below, we summarize the results of our mapping across the segments of Spirit's traverse shown in Fig. 7, and we then offer interpretations of these hydration signature exposures in Section 4. We find occurrences of the hydration signature to be rare and highly localized across Husband Hill, Haskin Ridge, and the Northern Inner Basin, but widespread at West Spur and in the Home Plate vicinity. Many of our results are unexpected, in that possible hydrated mineral detections correspond to outcrops that we would not necessarily otherwise have expected to be compositionally similar to the high-silica deposits in the East Valley.

3.2.1 Sols 155-425: West Spur

From Spirit's ascent out of the Gusev Plains to the West Spur, we find that the hydration signature is prevalent across a variety of outcrops, float rocks, and clasts (Fig. 9). Near Hank's Hallow, the friable, nodular outcrop rock called Pot of Gold exhibits the hydration signature across its weathered surface (but not on the "fresh" surface exposed by Spirit's Rock Abrasion Tool (RAT); Fig. 9a,e). The hydration signature is also manifested along the edges of the angular outcrop Breadbox (Fig. 9b,f); Wang et al. (2008) have observed a downturn at 1009 nm along these rock edges

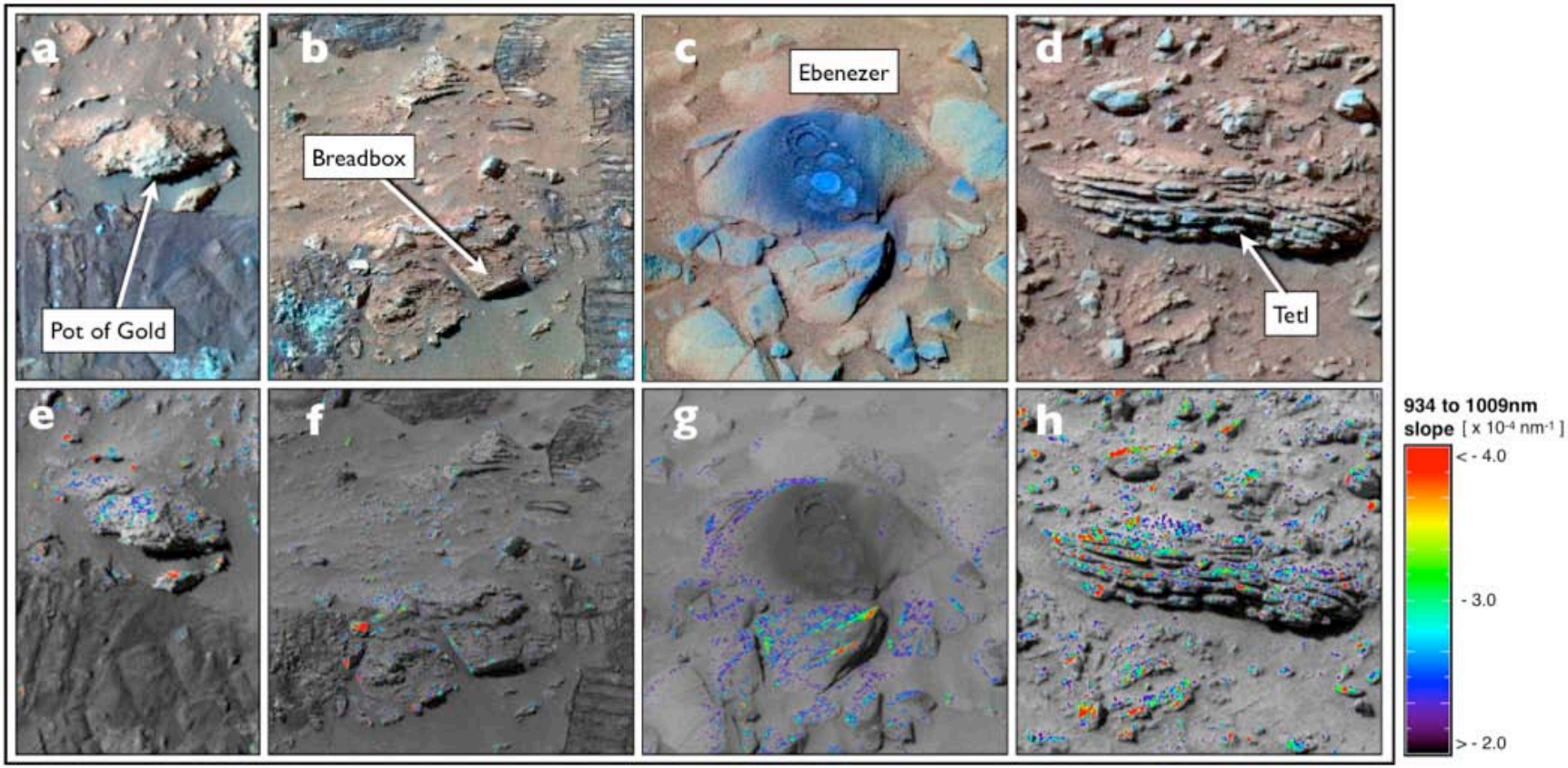

Figure 9. Occurrences of the hydration signature along Spirit's traverse at West Spur: False color Pancam images (blue = 432 nm, green = 535 nm, red = 753 nm; note that false-color images are not all at the same stretch) of a) Pot of Gold (sol 158, P2595), size of the rock is ~16 cm; b) Breadbox (sol 166, P2530), the width of the wheel track is ~16 cm for scale; c) RAT brushes on Ebenezer (sol 238, P2585), the diameter of the RAT grind is ~4.5 cm; d) Tetl (sol 264, P2598), the width of the outcrop is ~40 cm; and corresponding hydration signature maps over R2 (754 nm) Pancam images (e-h).

as well, which they argue may be from a silica coating along these rock "cases". While Wang et al. (2008) have also observed the ~1009 nm spectral feature in spots of light-toned, disturbed soil near Breadbox, and later at the Champagne/Penny site, we note that Pancam images of this soil were acquired later in the afternoon (LTST > 14:30) and were not included in our analysis due to possible calibration complications at low Sun angles (see Section 3.2).

We find that the majority of outcrops imaged through sol ~340 exhibit the hydration signature across some part of their surface. On all targets with "fresh" surfaces exposed by RAT brushes and grinds, however, we find no occurrences of the hydration signature; for example, Fig. 9g shows the rock Ebenezer (sol 238, P2585), which only exhibits the hydration signature on its weathered surface. As discussed in more detail in Section 4, these superficial occurrences of the hydration signature may result from dust covered surfaces viewed at high emission angles.

The layered outcrops Uxmal and Tetl (sol 264, P2598; Fig. 9d,h), which are exposed on the flank of the West Spur, also exhibit the hydration signature across their surfaces. In observations from Spirit's ascent to Husband Hill after leaving the West Spur, however, the hydration signature becomes less prevalent across rock surfaces. Additional occurrences of the hydration signature are seen in parts of the outcrops Peace and Watchtower, however, which have a hydration feature in Mini-TES observations (Ruff et al., 2006).

3.2.2 Sols 425-520: North Husband Hill

On the northern side of Husband Hill, we find that spots within the Paso

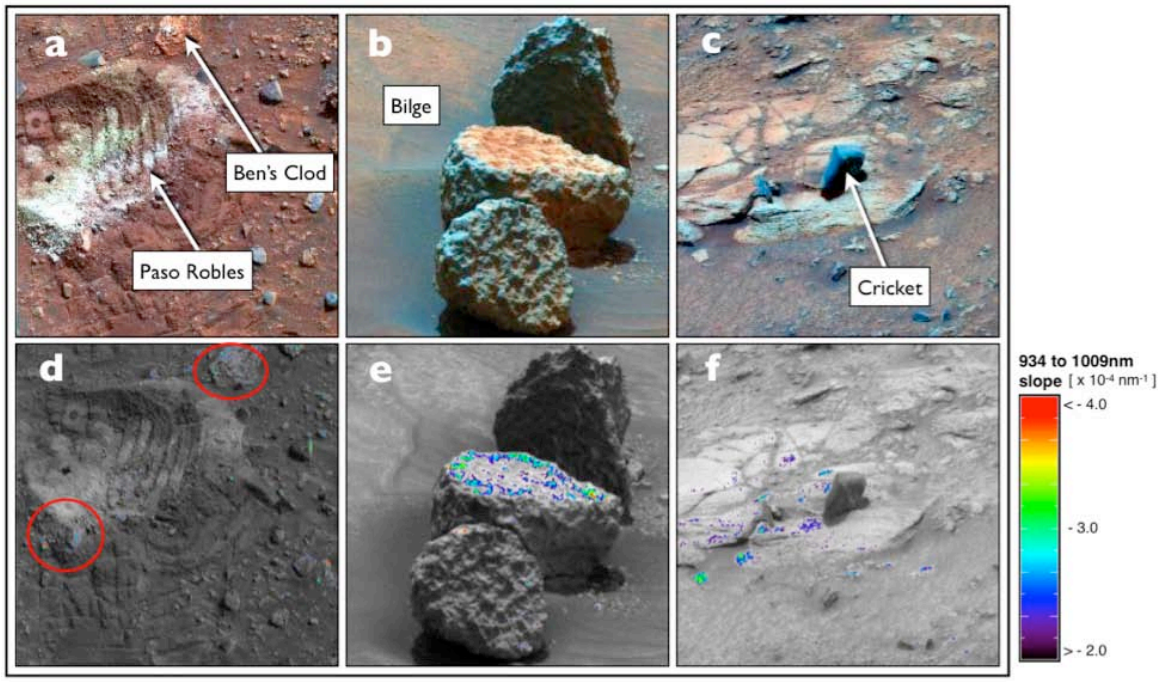

Figure 10. Occurrences of the hydration signature along Spirit's traverse over North Husband Hill: False color Pancam images (blue = 432 nm, green = 535 nm, red = 753 nm; note that false-color images are not all at the same stretch) of a) Paso Robles (sol 431, P2530), the width of the wheel track is ~16 cm; b) Bilge Rock (sol 506, P2556), the size of the rock is ~45 cm; c) Outcrop near the float rock Cricket (sol 514, P2571), the size of Cricket is ~20 cm; and corresponding hydration signature maps over R2 (754 nm) Pancam images (d-f). Red circles in (d) indicate locations where the hydration signature occurs over light-toned nodular outcrops.

Robles soil exposure, as well as nodular outcrops in the vicinity of this soil target, exhibit the hydration signature characteristic of the East Valley high-silica materials (Fig. 10). APXS, MB, and Pancam measurements of the Paso Robles soil, which was exposed by Spirit's wheels on sol 425, are consistent with the deposit being enriched in ferric sulfates (Gellert et al., 2006; Morris et al., 2006; Ming et al., 2006; Johnson et al., 2007; Lane et al., 2008). The soil has been interpreted to have formed in a hydrothermal environment (e.g., Yen et al., 2008). Wang et al. (2008) have performed

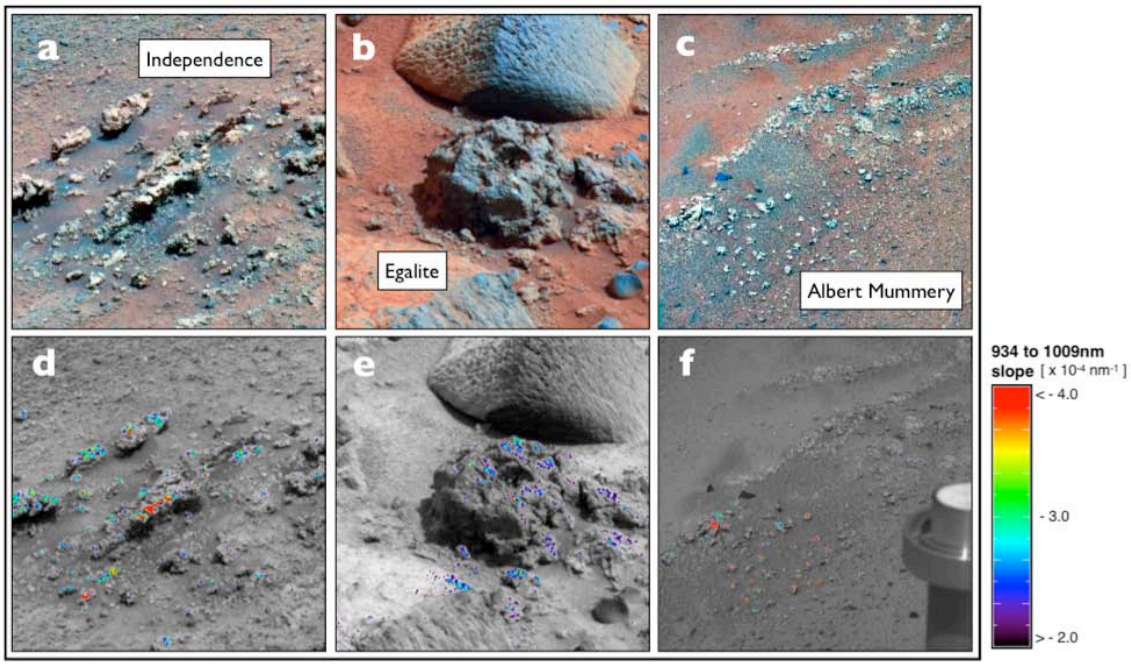

Figure 11. Occurrences of the hydration signature along Spirit's traverse over Southwest Husband Hill: False color Pancam images (blue = 432 nm, green = 535 nm, red = 753 nm; note that false-color images are not all at the same stretch) of a) Independence Outcrop (sol 541, P2549), field of view is ~65 cm; b) Egalite Rock at the Voltaire Outcrop (sol 553, P2559), the size of the rock is ~45 cm; c) Albert Mummery nodular outcrops (sol 580, P2549), the visible extent of the nodular outcrops is ~160 cm; and corresponding hydration signature maps over R2 (754 nm) Pancam images (d-f).

Pancam spectral comparisons of the Paso Robles deposit with the nearby nodule called Ben's Clod, which is enriched in silica (Clark et al., 2007a), and have observed a spectral downturn in Pancam's R7 (1009 nm) filter.

We find a few other occurrences of the hydration signature elsewhere on the northern side of Husband Hill, including the tops of the textured basalt rocks Bilge (sol 506; Fig. 10e) and Minnow (sol 508), as well as the light-toned outcrop below the float rock Cricket (sol 514; Fig. 10f). In-situ APXS or MB measurements were not made at any of these targets. We note that the brightest portions of several other probably basaltic float rocks along this stretch exhibit the hydration signature as well,

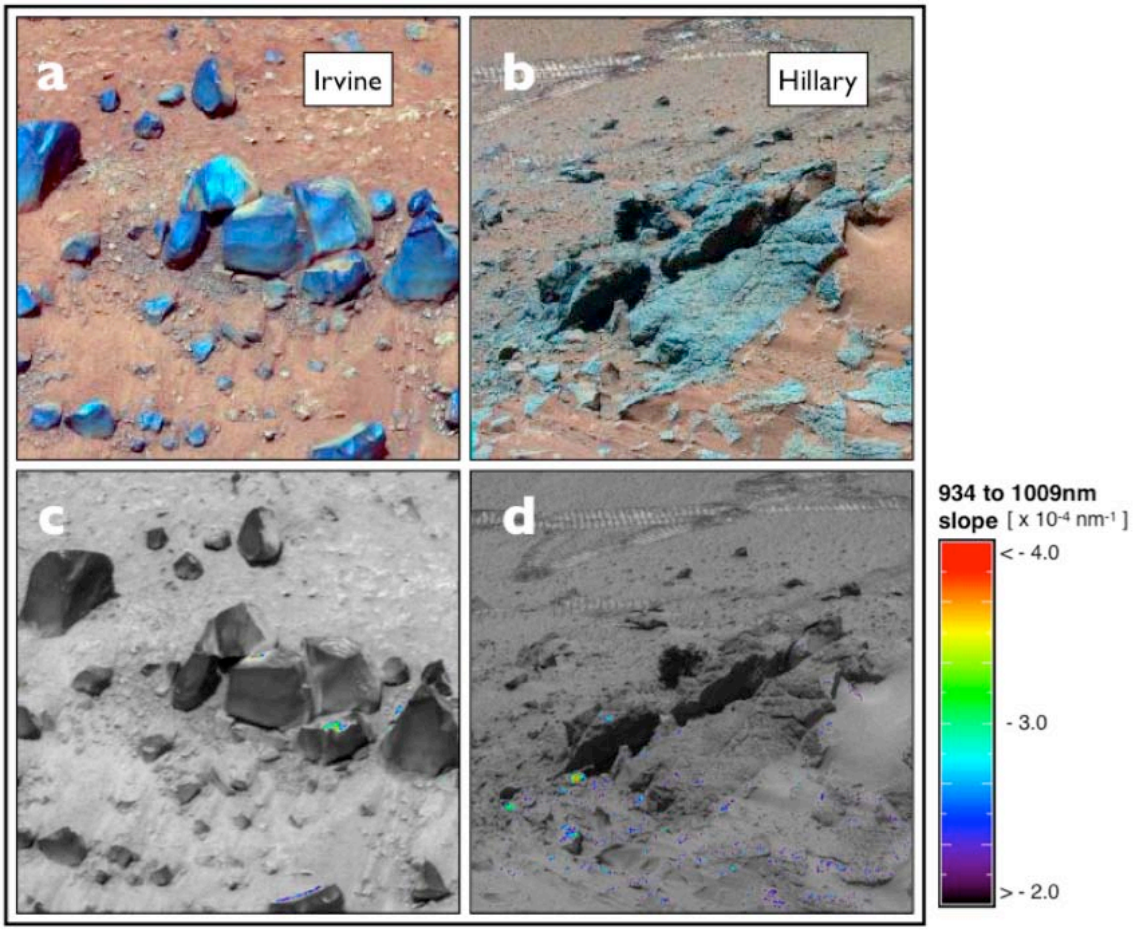

Figure 12. Occurrences of the hydration signature along Spirit's traverse over Southeast Husband Hill: False color Pancam images (blue = 432 nm, green = 535 nm, red = 753 nm; note that false-color images are not all at the same stretch) of a) the cluster of rocks near Irvine (sol 603, P2577), the field of view is ~50 cm; b) Hillary Outcrop (sol 624, P2532), the widths of the wheel tracks are ~16 cm for scale; and corresponding hydration signature maps over R2 (754 nm) Pancam images (c-d).

but because these all have some degree of image saturation in one or more filters, we cannot uniquely credit these occurrences as true detections.

3.2.3 Sols 520-580: Southwest Husband Hill

The layered outcrop called Independence exhibits the hydration signature with a steep 934 to 1009 nm slope in places where there is little dust and/or soil

accumulation on the outcrop (e.g. Fig. 11a,d). APXS measurements of Independence show that it is unusual in its low Fe content and its Al enrichment, and Ming et al. (2008) interpret the outcrop to have been altered in an open hydrologic system. Clark et al. (2007a) have proposed that the outcrop contains smectites; in our spectral database comparisons (Section 2.2.2), however, we find no smectite minerals as candidates with the necessary ~1000 nm absorption band to trigger the hydration signature.

Along this portion of the traverse, the hydration signature appears non-uniformly over the outcrops Egalité (sol 553; Fig. 11e), Vendemiaire (sol 561) and Assemblee (sol 572) in the Voltaire outcrop region. These outcrops are all of the Assemblee class (Arvidson et al., 2008) that is characterized by a nodular or crumbly appearance, low Fe content, and higher concentrations of SiO_2, Cr_2O_3, Ni, and Ge relative to other Voltaire APXS targets (Ming et al., 2008). Clark et al. (2007a) have shown compositional similarities between Assemblee class rocks and Independence. The thermal emission spectra of these targets suggest the presence of glassy or amorphous silicate phases, which suggests that the outcrop may have been emplaced as an impact melt (Arvidson et al., 2008).

An outcrop of partially buried, light-toned nodular outcrops imaged by Pancam on sol 580 (called Albert Mummery; Fig. 11c,f) also exhibits the hydration signature, as do bright spots in a wheel track made nearby on sol 583. The nodular outcrop has a similar morphology and albedo to the silica-rich nodular outcrops observed at the Tyrone site (Fig. 1a), but unfortunately no in-situ APXS or MB measurements were made at this site.

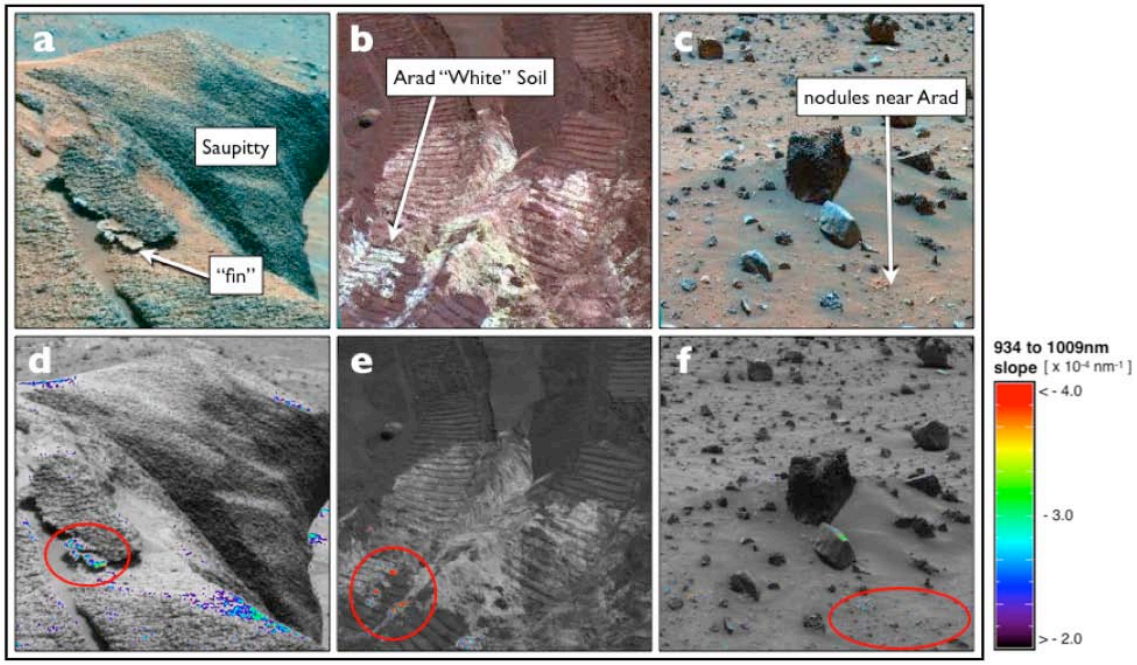

Figure 13. Occurrences of the hydration signature along Spirit's traverse over Haskin Ridge and the Northern Inner Basin: False color Pancam images (blue = 432 nm, green = 535 nm, red = 753 nm; note that false-color images are not all at the same stretch) of a) Saupitty Outcrop (sol 701, P2597), the size of the "fin" is ~20 cm; b) Arad soil at the Dead Sea site (sol 725, P2547), the width of the wheel track is ~16 cm; c) Nodular outcrops near the Arad soil (sol 725, P2544), the size of the dark rock in the center of the image is ~55 cm; and corresponding hydration signature maps over R2 (754 nm) Pancam images (d-f). Red circles show where the hydration signature occurs over: d) the Saupitty "fin"; e) the Arad "white" soil; and f) nodular outcrops near the Arad soil.

3.2.4 Sols 580-650: Southeast Husband Hill

On the southeast side of Husband Hill, we observe the hydration signature on the dustiest surfaces of basaltic rock fragments with massive textures along this portion of the traverse, including some rocks in the vicinity of the target Irvine (sol 603; Fig. 12a,c), which has been classified as an alkaline basalt (McSween et al., 2006).

Near the Hillary outcrop, we find the hydration signature across light-toned portions of the outcrop (sol 624; Fig. 12b,d), as well as on light-toned spots that may be crushed rock fragments within Spirit's wheel tracks. The hydration signature appears again at the Kansas outcrop (sol 642), which is morphologically similar to Hillary. Both Kansas and Hillary are of the Watchtower class, which is characterized from APXS and Mini-TES observations by a large degree of alteration and the presence of a significant amorphous silica phase (Ming et al., 2006; Ruff et al., 2006).

3.2.5 Sols 650-705: Haskin Ridge and Northern Inner Basin

The only prominent occurrence of the hydration signature found along Haskin Ridge is at the Saupitty outcrop (sol 701; Fig. 13a,d), where a fin (possibly a fracture fill?) is visible in the Pancam image. No in-situ APXS or MB measurements were made at this site.

As Spirit descended into the Inner Basin of the Columbia Hills, a comprehensive series of Pancam observations were made of the "El Dorado" sand dunes on the southeast flank of Husband Hill; we observe no occurrences of the hydration signature at this site. At the nearby Dead Sea site, however, we find that some spots within the Arad bright soil deposit exhibit the hydration signature (sol 725; Fig. 13e), as do nodular outcrops in the vicinity (sol 725; Fig. 13f). Like the Paso Robles soil exposure, Arad is also enriched in ferric sulfates (Gellert et al., 2006; Morris et al., 2006; Ming et al., 2006; Johnson et al., 2007) and has coexisting nodular outcrops which may be genetically related (Wang et al., 2008). We observe no other nodular outcrops in Pancam images along this portion of the traverse.

3.2.6 Sols 740-1400: Home Plate Vicinity

The Home Plate structure is a layered plateau of volcaniclastic sediments with east-west chemical variations observed across its surface (Squyres et al., 2007; Schmidt et al., 2008; Lewis et al., 2008). The layered sequences observed on the northwest side are called the Barnhill class, which have high concentrations of volatile elements (i.e., Cl, S, Br) that suggest alteration by vapors or waters rich in these elements (Ming et al., 2008). The outcrops on the eastern side, called Pesapallo class materials, may not have been subjected to the same degree of alteration (Ming et al., 2008; Schmidt et al., 2008). We observe the four-parameter hydration signature extensively over both Barnhill (sol 754; Fig. 14a,e) and Pesapallo class outcrops (sol 1214; Fig. 14d,h). On Home Plate, the hydration signature occurs over portions of outcrop, but not on the dark, likely basaltic float rocks.

The hydration signature also occurs over exposures of Halley class rocks, which are platy, buff-colored outcrops on the floor of the East Valley (Arvidson et al., 2008). APXS measurements of the target Halley (sol 814; Fig. 16) suggest the presence of a calcium-sulfate such as gypsum (Ming et al., 2008). The rock Montalva (sol 1088; Fig. 14c,g), which lies stratigraphically above Halley in the East Valley, also exhibits the hydration signature; Montalva is a layered outcrop enriched in hematite, and no sulfate component has been suggested for its composition (Ming et al., 2008).

The Tyrone bright soil deposit appears to exhibit a layered structure (Wang et al., 2008), with whitish soils immediately beneath the surface dust, and yellowish soils below a depth of ~5 cm. We observe the hydration signature to be well correlated with

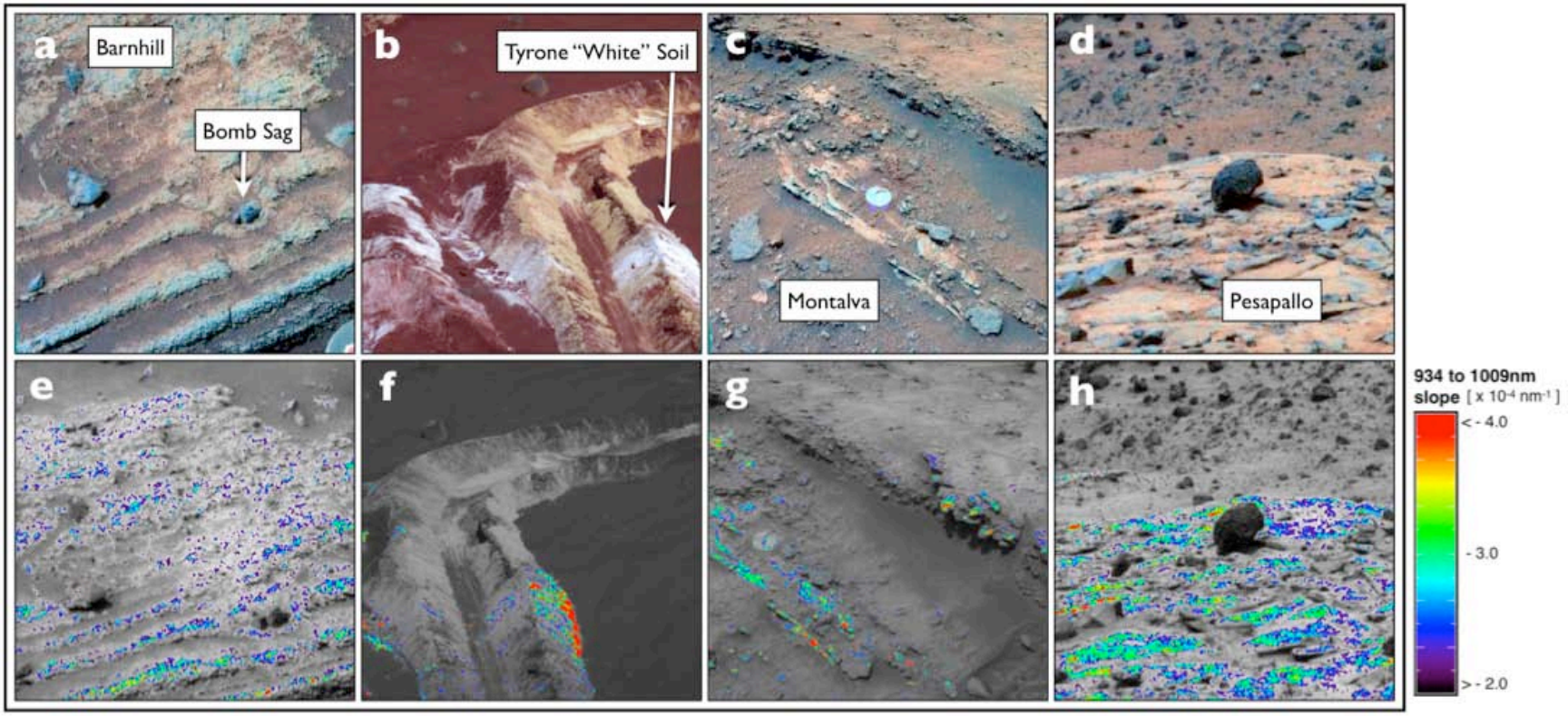

Figure 14. Occurrences of the hydration signature along Spirit's traverse in the Home Plate vicinity: False color Pancam images (blue = 432 nm, green = 535 nm, red = 753 nm; note that false-color images are not all at the same stretch) of a) Barnhill Outcrop at Home Plate (sol 754, P2584), field of view is ~57 cm; b) Tyrone Soil (sol 790, P2531), the width of the wheel track is ~16 cm; c) Montalva Outcrop (sol 1073, P2584), the width of the circular RAT brush is ~4.5 cm; d) Pesapallo Outcrop on the top of Home Plate (sol 1214, P2550), the size of the dark float rock in the center of the image is ~38 cm; and corresponding hydration signature maps over R2 (754 nm) Pancam images (e-g).

exposures of the Tyrone "white" soil, both in the main soil exposure (sol 790; Fig. 14b,f) and in the trail of whiteish soil dragged by Spirit's inoperative right-front wheel as it drove away from the Tyrone site. In-situ measurements could not be made at Tyrone, but the Mt. Berkner target within the whiteish soil trail (sol 814; Fig. 16) was observed by APXS to be enriched in sulfur, similar to the Paso Robles and Arad soils (Yen et al., 2008).

Wang et al. (2008) described color changes observed for the Tyrone "yellow" soil in seven Pancam images of the same scene over a period of 200 sols, and hypothesized that the color changes observed in the "yellow" soil are due to the dehydration of the "yellow" material upon being exposed to martian surface conditions.

We observe the hydration signature to be correlated with several nodular outcrops in the East Valley that have not been studied by in-situ measurements but which we hypothesize could be silica-rich. We do not find any occurrence of the hydration signature to correlate with the dark rock Fuzzy Smith on the north edge of Home Plate, which has been observed by APXS to be enriched (68.4 wt.%) in SiO_2 (Ming et al., 2008). The alteration history of Fuzzy Smith is likely different than the acid leaching process proposed for East Valley soils and nodular outcrops, however, because Fuzzy Smith is enriched in K and Zn (elements which are highly mobile in acid sulfate systems) (Ming et al., 2008).

3.3 Mapping the hydration signature over 360^o Panoramic Images

Spirit acquired two 360^o observations with all 13 Pancam filters during its

traverse through the Columbia Hills and the Inner Basin: 1) the McMurdo panorama (sols 814-932); and 2) the Bonestell panorama (sols 1477-1696). These large panoramas were acquired over Spirit's second and third winter campaigns, when the rover was parked on the north-facing slopes of Low Ridge and the north edge of Home Plate, respectively. Because of their high resolution and wide spatial and spectral coverage, these observations allow us to map the regional distribution of materials that exhibit the hydration signature in the Inner Basin of the Columbia Hills.

Both of these panoramas exhibit some effects of minor dust contamination on the front sapphire windows of the Pancam instruments. The effect is too small to be observed in mosaics made from individual filters, but it is enhanced in ratio or difference images, such as maps of the 934 to 1009 nm slope, creating noticeable seams between individual panorama frames. We account for this effect by first creating 934 to 1009 nm slope maps from the individual R6 and R7 images comprising each panorama, applying an empirical ~10% top-to-bottom brightness gradient "delta flatfield" correction to each slope map, and then mapping the individual corrected slope map images into a full 360° mosaic. We use this corrected slope mosaic along with mosaics made from R* values for individual filters to calculate the slope parameters discussed in Section 3.1 and to map locations where the criteria of the hydration signature are met.

3.3.1 The McMurdo Panorama

We have mapped the occurrence of the hydration signature over the 360° McMurdo panorama, which consists of 111 individual 13-filter image sequences. Fig.

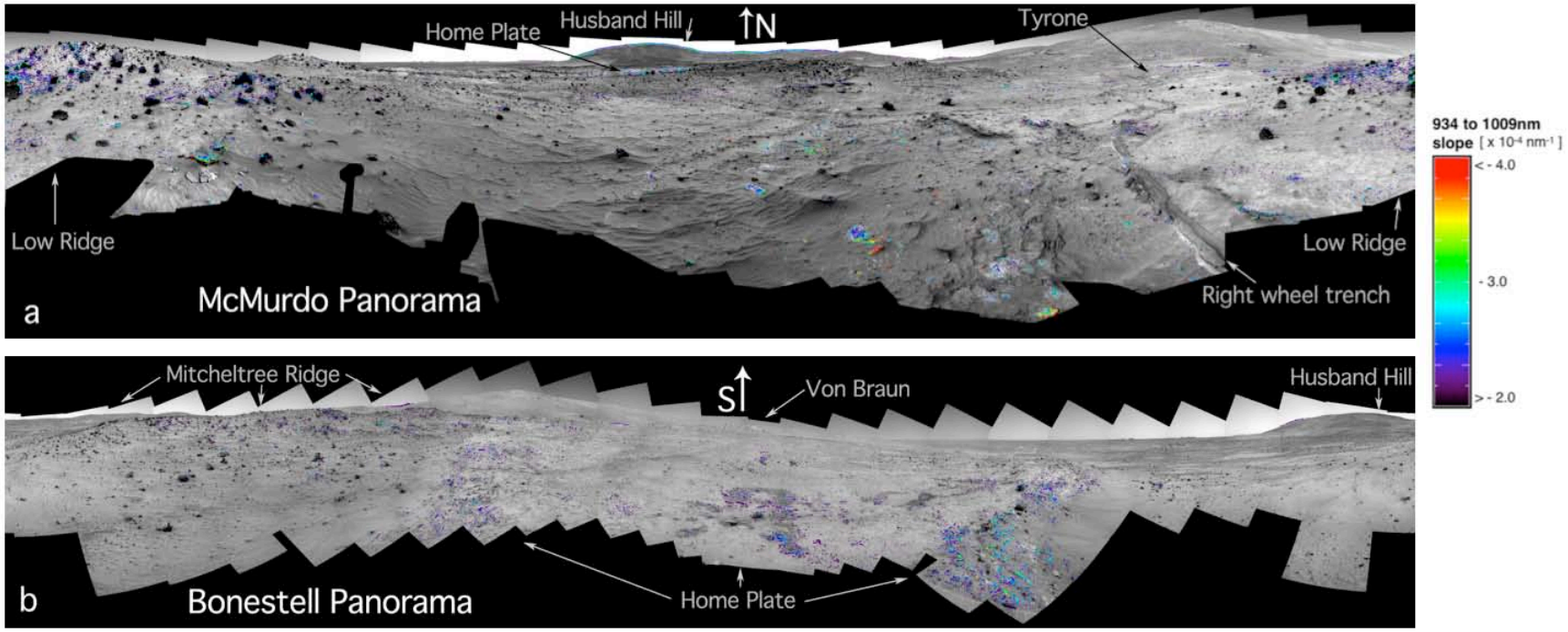

Figure 15. Results of mapping the hydration signature for a) the 360° McMurdo Panorama acquired during Spirit's second Winter Campaign (sols 814-932); and b) the 360° Bonestell Panorama acquired during Spirit's third Winter Campaign (sols 1477-1696. Maps are shown over mosaics made from R2 (754nm) Pancam images, and the centers of both mosaics face due south.

15a shows our detections mapped over the full McMurdo panorama, and Fig. 16 shows a vertical projection of the hydration signature map shown in Fig. 15a, but just out to ~5 m from the rover deck. The scene in Fig. 15a includes Low Ridge immediately behind the rover, the eastern edge of Home Plate with Husband Hill on the horizon, the southern edge of Mitcheltree Ridge, and the Tyrone site with McCool Hill behind it. This view shows the hydration signature aligned with several occurrences of Halley Class outcrops exposed in the vicinity of the rover. A map of the Home Plate vicinity showing the terrain visible in the entire panorama is shown in Fig. 17.

We have used Pancam stereo images with 3D visualizations of a digital elevation model of the Home Plate vicinity (Kirk et al., 2007) to correlate the occurrences of the hydration signature seen in the McMurdo panorama with features seen in HiRISE orbital images. The red regions shown in Fig. 17 indicate the spatial distributions of materials that we find to be spectrally similar to the known silica-rich soils and nodular outcrops studied by APXS. The occurrences are widespread, and include the visible extent of Home Plate, portions of the South Promontory feature southeast of Home Plate, the surface of Low Ridge that is not covered by vesicular basalts (where platy outcrops and soil ripples are visible), visible portions of the East Valley floor (including the Halley and King George Island targets labeled in Fig. 16), exposures of nodular outcrops in the vicinity of Tyrone, and light-toned outcrops at the base of McCool Hill.

3.3.2 The Bonestell Panorama

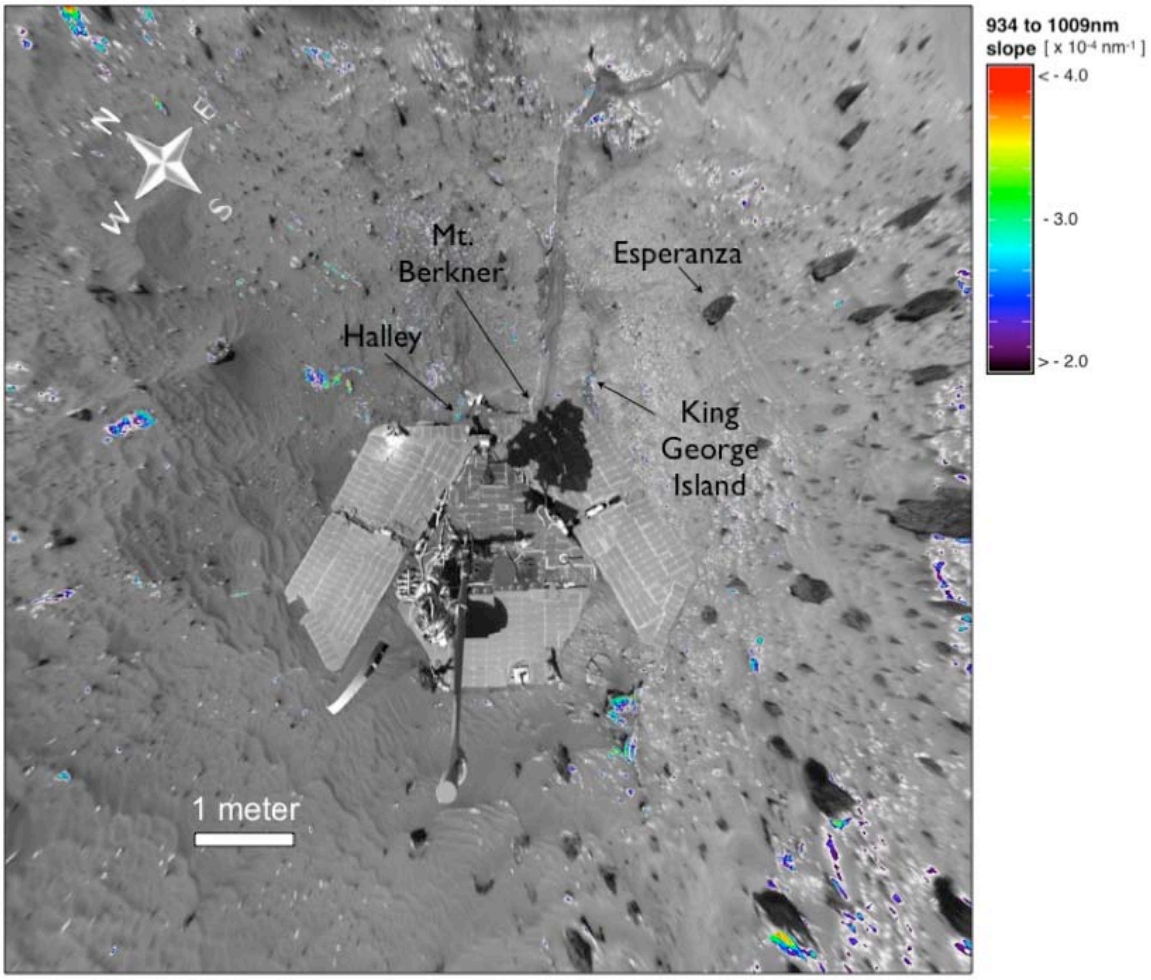

Figure 16. Vertical projection of the hydration signature map in Fig. 15a out to ~5 m from Spirit (the location of the scene is indicated by the yellow box in Fig. 17). Targets for which Spirit has made in situ geochemical measurements are labeled. Metallic sunglint-induced signatures on the rover deck have been removed.

The Bonestell Panorama consists of 87 13-filter Pancam images. The scene includes the entire north slope and much of the top of Home Plate visible to the south, the western edge of Mitcheltree Ridge visible to the east, Husband Hill (with the El Dorado dune field) visible to the northwest, and portions of the plains west of Home Plate, to the southwest (Fig. 15b).

As described for the McMurdo panorama above, we have correlated the

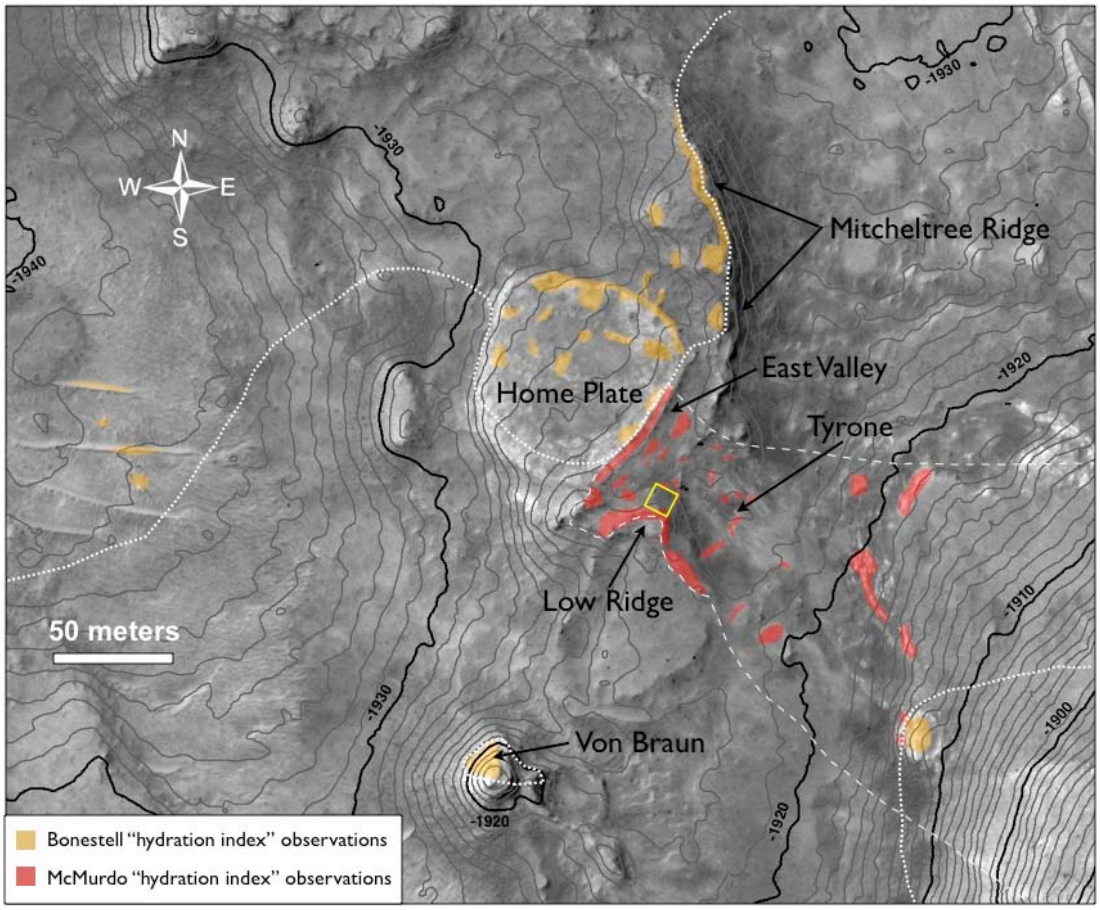

Figure 17. Regions where the hydration signature is seen in the McMurdo (red) and Bonestell (orange) panoramas (Fig. 15), overlain on HiRISE image PSP_001513_1655_red. Contours are taken from the USGS HiRISE digital terrain model [Kirk et al., 2007]. The dotted and dashed lines indicate the terrain visible in the McMurdo and Bonestell mosaics, respectively. The yellow box shows the region covered in Fig. 16.

occurrences of the hydration signature seen in the Bonestell panorama with features seen in HiRISE orbital images (orange regions in Fig. 17). We find the hydration signature across the visible portions of Mitcheltree Ridge that are not covered by vesicular basalts (where platy outcrops and soil are visible, similar to the occurrences at Low Ridge). While APXS measurements have not been made directly on these Mitcheltree Ridge outcrops and soils, measurements of the rock Torquas at the base of

Mitcheltree Ridge show enrichments of Cl, Ni, Zn and Br that suggest alteration by hydrothermal fluids or vapors (Schmidt et al., 2008).

The hydration signature is strongest (exhibits the most negative 934 to 1009 nm slopes) across the entire sequence of layered outcrops on the north face of Home Plate. The hydration signature is also widespread across the top of Home Plate, aligned with platy outcrops that are not covered by float rocks; these observations confirm many of the hydration signature occurrences from Spirit's traverse acros Home Plate discussed in Section 3.2.6. We note that the hydration signature is particularly well correlated with Home Plate rocks that have been scuffed, overturned, or otherwise disturbed by Spirit's wheels, but is not observed within the darker soil materials or rocks exposed by the wheel tracks.

Where the area imaged by the Bonestell panorama overlaps with areas visible in the McMurdo panorama (outlined in Fig. 17), we find agreement in the occurrences of the hydration signature. These regions include light-toned outcrops at the base of McCool Hill and the top of Home Plate's eastern edge. Other occurrences visible in the Bonestell panorama include the Von Braun feature south of Home Plate, which is a hill capped with light-toned outcrops. We also observe the hydration signature aligned with light-toned, linear aeolian bedforms visible beyond Home Plate, in the plains to the west.

4. Discussion

We find that a distinct spectral feature at the longest Pancam wavelengths (primarily characterized by a negative 934 to 1009 nm slope) appears to be diagnostic

of the silica-rich soil and nodular outcrops discovered by Spirit in the East Valley of the Columbia Hills Inner Basin. Analyses of the Vis-NIR spectra of materials with chemistries and inferred mineralogies confirmed by APXS to be present in the East Valley soils and nodular outcrops (hydrous opaline silica and TiO_2) suggest that the Pancam spectral feature is not a direct reflection of their Si- or Ti-rich nature. Instead, based on comparisons with spectral databases, we hypothesize that the presence of H_2O or OH, either free (as water ice), adsorbed, or bound in a mineral structure, is responsible for the spectral feature observed by Pancam.

Because the Gertrude Weise soil is nearly pure opaline silica (~98 wt.% after the removal of dust contamination (Squyres et al., 2008)), it is highly unlikely that additional hydrated mineral components are present in large enough quantities to produce the observed Pancam feature (except for perhaps sodium metasilicate nonahydrate, as discussed in Section 2.5). Free water (as fine-grained water frost or fluid inclusions) could potentially create the negative slope from 934 to 1009 nm and not be inconsistent with APXS observations or the proposed depositional environment for the Gertrude Weise soil. Although the ice spectra of Roush et al. (1991) and this study (Fig. 5) do not exhibit negative 934 to 1009 nm slopes as strong as those observed by Pancam, the exact band depths of the ($2\nu_1+\nu_3$) combinational mode of water ice vary significantly with temperature and grain size (Clark, 1981; Grundy and Schmitt, 1998). Frost is unlikely to be stable at the surface of Gusev Crater under current martian conditions (e.g., Clifford and Hillel, 1983; Mellon and Jakosky, 1993), but water ice in fluid inclusions could be isolated from the martian atmosphere and remain stable for extended periods (Roedder, 1984). It is possible that pore spaces

(voids) in the translucent silica-rich material contain H_2O ice that is shielded from the martian atmosphere but which is still able to interact with solar radiation. This hypothesis is preliminary, and future work will include modeling and experimental studies to understand the long-term stability of ice potentially trapped in translucent mineral voids under martian surface conditions.

Another hypothesis is that adsorbed water on mineral grains causes the observed ~1000 nm absorption feature in the Gertrude Weise soil. It is possible that Spirit's wheels exposed a water source at several centimeters depth below the surface (perhaps on or in the hydrous opaline silica, but not tightly bound) that, as it sublimates and migrates towards the surface, gets cold-trapped on mineral grains. Such a supply of water vapor would diffuse towards the surface until the supply is exhausted, as has been modeled extensively for studies of ground ice stability (e.g. Aharonson and Schorghofer, 2005; Hudson et al., 2008; Hudson et al., 2009). To test this adsorption hypothesis, laboratory spectroscopy studies of fine-grained opaline silica with monolayers of adsorbed water are needed to understand if adsorbed water can exhibit a strong enough ~1000 nm absorption.

The Pancam feature observed at the silica-rich nodular outcrops may have the same origin as the feature observed in the Gertrude Weise soil, but because the nodular outcrops have different chemistries than the soil, the presence of additional hydrated minerals could contribute to the spectrum as well. Possible additional phases include sulfates, halides, chlorides, sodium silicates, carbonates, or borates. The presence of these minerals, however, may not be consistent with proposed acid-leaching formation processes for the nodular outcrops (e.g., Squyres et al., 2008).

We have found the hydration signature associated with the silica-rich soil and nodular outcrops to be present at a wide variety of outcrops, float rocks, and soils along Spirit's traverse. Because there are significant geochemical differences among the materials that exhibit the hydration signature (summarized in Section 3.2), it is possible that there could be several different mineralogic origins of the ~1009 nm hydration feature in the Columbia Hills. Based on Mini-TES, APXS and MB observations, we can make reasonable estimates of the origin of the hydration signature in some locations, such as the rocks across the West Spur. For example, all rocks observed by Mini-TES at the West Spur have a distinctive thermal infrared feature that Ruff et al. (2006) have used to group them into a single class called Clovis. Farrand et al. (2008) also grouped these rocks into a single class based on their Vis-NIR spectra and inferred ferrous mineralogy. Deconvolutions of their Mini-TES spectra and APXS measurements suggest that Clovis Class rocks consist mainly of basaltic glass with a Ca- and/or Mg- sulfate component up to ~25 wt.% (Ruff et al., 2006; Ming et al., 2006; Squyres et al., 2006). Such a potential abundance of gypsum, epsomite, and/or other of the sulfates listed in Table 4 could easily contribute to the strong negative 934 to 1009 nm slope that triggers our hydration signature across the surface of Clovis Class rocks. Our results suggest that the mineral contributor to the hydration signature is only present as a rock coating or alteration rind, however, because in all Clovis Class rocks with RAT grinds, the hydration signature does not appear in the abraded portion of the rock. If that interpretation is correct, then the coating must be hydrated and less than ~5 mm thick, which is the typical RAT hole depth.

The majority of our observed hydration signature occurrences in the Columbia Hills correlate with materials that are suggested to have undergone aqueous alteration, such as Clovis Class rocks, Assemblee Class rocks, Watchtower Class rocks (e.g., Hillary and Kansas), Halley Class rocks, Home Plate, and the rocks Breadbox, Independence and Peace (e.g., Ruff et al., 2006; Squyres et al., 2006; Clark et al., 2007a; Squyres et al., 2007; Arvidson et al., 2008; Ming et al., 2008; Wang et al., 2008). For these rocks it is possible that alteration by water, as a liquid or vapor, may have resulted in the formation of hydrated minerals (such as those listed in Table 4). For the rock Irvine, however, which has been classified as a relatively unaltered alkaline basalt (McSween et al., 2006), the presence of the hydration signature is more enigmatic. We observe the hydration signature on the dust-covered surfaces of several other massive, probably basaltic float rocks near Irvine in the Southeast Husband Hill region as well. These rocks exhibit the hydration signature most prominently at high local emission angles (on surfaces tilted away from the rover's line of sight, such on the rock facets near Irvine seen in Fig. 12c).

It is possible that hydration signature occurrences on some high emission angle facets may result from the dust itself. Martian dust has been known for decades to contain some bound water phase (e.g., Sinton 1967; Houck et al., 1973; Pimentel et al., 1974; Bell and Crisp, 1993). Orbital observations from TES confirmed the hydrated nature of the bright fine-grained dust that blankets low thermal inertia regions on Mars and further suggested that the dust contains minor carbonates as well (Bandfield et al., 2003). Mini-TES observations of the airfall dust that is ubiquitous at Gusev Crater show the same hydration features as those seen in TES dust spectra

(Christensen et al., 2004). While we have not observed veneers of airfall dust exhibiting the hydration signature on flat-lying surface soils (including the Mini-TES Gusev dust end-member (Christensen et al., 2004; Ruff et al., 2008a) imaged by Pancam on sol 77, sequence P2573), it is possible that increased multiple scattering through hydrated dust grains at high emission angle geometries could result in an increase in the strength of the ~1000 nm absorption of bound water. This possibility needs to be explored much further in order to gain a better understanding of the possible sources of the hydration signature that we observe on some rocks with heavily dust-coated surfaces.

The main goal of our mapping exercise was to understand the regional distribution of silica-rich materials similar to those observed in the Eastern Valley in order to better constrain their depositional environment. Unfortunately we have found no occurrences of light-toned soils along Spirit's traverse with a hydration signature similar to that seen at Gertrude Weise. While other subsurface deposits of nearly-pure opaline silica may exist elsewhere in the Columbia Hills, we have found no surface expression of such soils in Pancam spectra.

We have identified patches of nodular outcrops that exhibit the hydration signature at Albert Mummery on southwest Husband Hill, near the Paso Robles and Dead Sea soil sites, and at additional locations within the Eastern Valley. Although no APXS, MB or Mini-TES measurements have been made of these targets, their morphologies, albedos, and Vis-NIR spectra imply that they may be chemically similar to the silica-rich nodular outcrops. The Eastern Valley nodular outcrops are located in a topographic depression, as are those at Dead Sea and the nodular outcrops

near the Tyrone site confirmed by Mini-TES to be silica-rich. The nodular outcrops near Paso Robles, however, are on a slope (Wang et al., 2008), and those observed at Albert Mummery are near the top of Husband Hill. Based on these observations, it seems unlikely that the silica-rich nodular outcrops formed from a process that is restricted to any one geomorphologic setting (such as precipitation from standing bodies of water). Rather, the observations may be more consistent with highly localized alteration of emplaced rocks by, for example, hydrothermal vents, and/or precipitation of silica from fluids transported within the Inner Basin. We note that some light-toned outcrops that appear morphologically similar to the silica-rich nodular outcrops, such as those seen in the near field of the Bonestell Panorama immediately north of Home Plate (Fig. 15b, 17), do not exhibit the hydration signature. We cannot rule these out as potential silica-rich nodular outcrops, however; these nodule-like outcrops are largely covered by what may be relatively more anhydrous dust and soil, which may be obscuring their spectral signatures.

While there are very few potentially silica-rich soils and nodular outcrops observed along Spirit's traverse, our analysis indicates that hydration in general appears to be widespread throughout the Columbia Hills. We have observed occurrences of the hydration signature at various stages of Spirit's traverse; the hydration signature is localized across Husband Hill and into the Northern Inner Basin, but nearly ubiquitous across the West Spur and in the Home Plate vicinity. In our analyses of the McMurdo and Bonestell Panoramas (Fig. 17), which cover regions of the Inner Basin beyond where Spirit has yet traversed, we find that manifestations of the hydration signature extend to the flanks of McCool Hill, into the plains west of

Home Plate, and south to the Von Braun feature. Because these features have been imaged at large distances, however, we are not able to characterize in detail the coverage of dust on their surfaces and its potential contribution to the observed hydration signature. We find no overall correlation of these occurrences with topography. The variety of materials that exhibit the hydration signature along Spirit's traverse, as well as their wide range of geomorphic settings and extended regional coverage, seems to suggest a complicated history of alteration across the Columbia Hills.

5. Conclusions

In Pancam multispectral observations of the silica-rich soil and nodular outcrops at Gusev Crater, we find a characteristic absorption feature at the longest Pancam wavelength (1009 nm). We have used the negative 934 to 1009 nm slope, along with other spectral parameters, as a hydration signature to search for other compositionally similar materials in Pancam multispectral images along Spirit's traverse. While this hydration signature does not uniquely identify silica-rich materials, it appears most likely to be an indicator of hydrated minerals, adsorbed water on mineral grains, or interstitial water/ice in mineral pore spaces.

We find that the hydration signature is widespread along Spirit's path through the Columbia Hills (sols 155-1696) and correlates with a wide variety of features, including (in chronological order):

1. The edges of angular outcrops (e.g., Breadbox) at Hank's Hollow;
2. Clovis Class rocks across West Spur;

3. Assemblee Class rocks at the Voltaire outcrop on Southwest Husband Hill;
4. Altered rocks across Husband Hill (e.g., Independence, Hillary, Kansas, Peace);
5. Dust-coated facets of Irvine and similar massive basalts;
6. Light-toned nodular outcrops (at Albert Mummery on southwest Husband Hill, near the Paso Robles and Dead Sea soil sites, and at other locations within the East Valley);
7. Scattered portions of light-toned, S-rich soil deposits (Paso Robles, Dead Sea, and Tyrone "white" soil);
8. Platy, thinly-bedded, light-toned outcrops in the Home Plate vicinity (e.g., Halley, King George Island, Low Ridge and Mitcheltree Ridge outcrops);
9. Portions of the layered Home Plate outcrop.

Analyses of two 360° Pancam panoramas taken from the vicinity of Home Plate show that the hydration signature extends to regions of the Columbia Hills Inner Basin where Spirit has not yet traversed. Most intriguing is the identification of putative hydrated materials at the Von Braun feature, which Spirit might be able to characterize with Pancam, Mini-TES, and in-situ measurements during its future exploration. These observations of possible widespread hydration along Spirit's traverse (and beyond) add to the growing body of evidence that aqueous alteration has played a significant role in the complex geologic history of the Columbia Hills.

REFERENCES

Arvidson, R. E., and 62 colleagues, 2006. Overview of the Spirit Mars Exploration Rover Mission to Gusev Crater: Landing site to Backstay Rock in the Columbia Hills, J. Geophys. Res. 111, E02S01, doi:10.1029/2005JE002499.

Arvidson, R. E., and 32 colleagues, 2008. Spirit Mars Rover Mission to the Columbia Hills, Gusev Crater: Mission overview and selected results from the Cumberland Ridge to Home Plate, J. Geophys. Res., 113, doi:10.1029/2008JE003183.

Bandfield, J.L., 2008. High-silica deposits of an aqueous origin in western Hellas Basin, Mars. Geophys. Res. Lett. 35, 12205, doi:10.1029/2008GL033807.

Bandfield, J.L., Hamilton, V.E., Christensen, P.R., 2000. A global view of martian surface compositions from MGS-TES. Science 287, 1626-1630, doi:10.1126/science.287.5458.1626.

Bandfield, J.L., Glotch, T.D., Christensen, P.R., 2003. Spectroscopic identification of carbonate minerals in the martian dust. Science 301, 1084-1087. doi:10.1126/science.1088054.

Bell, J.F., III, and Crisp, D., 1993. Groundbased Imaging Spectroscopy of Mars in the Near-Infrared: Preliminary Results, Icarus 104, 2-19.

Bell, J.F., III, and 24 colleagues, 2003. Mars Exploration Rover Athena Panoramic Camera (Pancam) investigation. J. Geophys. Res. 108, E12, doi:10.1029/2003JE002070.

Bell, J.F., III, Joseph, J., Sohl-Dickstein, J.N., Arneson, H.M., Johnson, M.J., Lemmon, M.T., Savransky, D., 2006. In-flight calibration and performance of the Mars Exploration Rover Panoramic Camera (Pancam) instruments. J. Geophys. Res. 111, E2, doi 10.1029/2005JE002444.

Bibring, J., Langevin, Y., Mustard, J.F., Poulet, F., Arvidson, R., Gendrin, A., Gondet, B., Mangold, N., Pinet, P., Forget, F., 2006. Global mineralogical and aqueous Mars history derived from OMEGA/Mars express data. Science 312, 400-404, doi:10.1126/science.1122659.

Bishop, J.L., Murad, E., Lane, M.D., Mancinelli, R.L., 2004. Multiple techniques for mineral identification on Mars: A study of hydrothermal rocks as potential analogues for astrobiology sites on Mars. Icarus 169, 311-323, doi:10.1016/j.icarus.2003.12.025.

Cady, S.L., Farmer, J.D., 1996. Fossilization processes in siliceous thermal springs: trends in preservation along thermal gradients, in: Bock, G., Goode, J. (Eds.), Evolution of hydrothermal ecosystems on Earth (and Mars?). Wiley, New

York, pp. 150-170.

Christensen, P.R. and 26 colleagues, 2004. Initial results from the Mini-TES experiment in Gusev Crater from the Spirit rover. Science 305, 837-842, doi: 10.1126/science.1104909.

Clark, B.C., and 15 colleagues, 2007a. Evidence for montmorillonite or its compositional equivalent in Columbia Hills, Mars. J. Geophys. Res. 112, doi:10.1029/2006JE002756.

Clark, R.N., 1981. The spectral reflectance of water-mineral mixtures at low temperatures. J. Geophys. Res. 86, 3074-3086, doi:10.1029/JB086iB04p03074.

Clark, R.N., 1981. Water frost and ice - the near-infrared spectral reflectance 0.65-2.5 microns. J. Geophys. Res. 86, 3087-3096, doi:10.1029/JB086iB04p03087.

Clark, R.N. and Roush, T.L., 1984. Reflectance spectroscopy - quantitative analysis techniques for remote sensing applications. J. Geophys. Res. 89, 6329-6340, doi:10.1029/JB089iB07p06329.

Clark, R.N., Swayze, G. A., Wise, R., Livo, E., Hoefen, T., Kokaly, R., Sutley, S. J., 2007b. USGS digital spectral library splib06a: U.S. Geological Survey, Digital Data Series 231.

Cloutis, E., Craig, M., Kaletzke, L., McCormack, K., Stewart, L., 2006. HOSERLab: A New Planetary Spectrophotometer Facility. 37th Annual Lunar and Planetary Science Conference 37, 2121.

Cloutis, E.A., Craig, M.A., Kruzelecky, R.V., Jamroz, W.R., Scott, A., Hawthorne, F.C., Mertzman, S.A., 2008. Spectral reflectance properties of minerals exposed to simulated Mars surface conditions. Icarus 195, 140-168, doi: 10.1016/j.icarus.2007.10.028.

Cloutis, E.A., and 11 colleagues, 2006. Detection and discrimination of sulfate minerals using reflectance spectroscopy. Icarus 184, 121-157, doi:10.1016/j.icarus.2006.04.003.

Crisp, J., Kahle, A.B., Abbott, E.A., 1990. Thermal infrared spectral character of Hawaiian basaltic glasses. J. Geophys. Res. 95, 21657-21669, doi:10.1029/JB095iB13p21657.

Crowley, J.K., 1991. Visible and near-infrared (0.4–2.5 μm) reflectance spectra of playa evaporite minerals. J. Geophys. Res. 96, 16231, doi:10.1016/0016-7037(91)90320-5.

Deer, W.A., Howie, R.A., Zussman, J., 1997. Rock-Forming Minerals. The Geological Society, London, UK.

Ehlmann, B.L., and 13 colleagues, 2008. Orbital identification of carbonate-bearing rocks on Mars. Science 322, 1828. doi:10.1126/science.1164759.

Ellis, A.J., Mahon, W.A.J., 1977. Chemistry and geothermal systems. Academic Press, New York.

Eugster, H.P., 1967. Hydrous sodium silicates from Lake Magadi, Kenya: Precursors of bedded chert. Science 157, 1177-1180, doi:10.1126/science.157.3793.1177.

Farmer, J.D., 1996. Hydrothermal systems on Mars: an assessment of present evidence, in: Bock, G., Goode, J. (Eds.), Evolution of hydrothermal ecosystems on Earth (and Mars?). Wiley, New York, pp. 273-295.

Farrand, W.H., Bell, J.F., III, Johnson, J.R., Arvidson, R.E., Crumpler, L.S., Hurowitz, J.A., Schröder, C., 2008. Rock spectral classes observed by the Spirit rover's Pancam on the Gusev Crater plains and in the Columbia Hills. J. Geophys. Res. 113, doi:10.1029/2008JE003237.

Gellert, R., and 11 colleagues, 2006. Alpha particle X-ray spectrometer (APXS): Results from Gusev Crater and calibration report. J. Geophys. Res. 111, doi:10.1029/2005JE002555.

Glotch, T.D., Bandfield, J.L., Christensen, P.R., Calvin, W.M., McLennan, S.M., Clark, B.C., Rogers, A.D., Squyres, S.W., 2006. Mineralogy of the light-toned outcrop at Meridiani Planum as seen by the Miniature Thermal Emission Spectrometer and implications for its formation. J. Geophys. Res. 111, doi:10.1029/2005JE002671.

Grundy, W.M. and Schmitt, B., 1998. The temperature-dependent near-infrared absorption spectrum of hexagonal H_2O ice. J. Geophys. Res. 103, 25809-25822, doi:10.1029/98JE00738.

Hapke, B., 1993. Theory of Reflectance and Emittance Spectroscopy. Cambridge Univ. Press, Cambridge, UK.

Herzberg, G., 1945. Infrared and Raman Spectroscopy. Von Nostrand Reinhold Company, Inc., New York.

Houck J.R., Pollack J.B., Sagan C., Schaack D., and Decker J., 1973. High altitude infrared spectroscopic evidence for bound water on Mars. Icarus 18, 470-480, doi:10.1016/0019-1035(73)90156-5.

Hudson, T.L, Aharonson, O., Schorghofer, N., Farmer, C.B., Hecht, M.H., and Bridges, N.T., 2007. Water vapor diffusion in Mars subsurface environments. J. Geophys. Res. 112, 27, doi:10.1029/2006JE002815.

Hudson, T.L. ,Aharonson, O., and Schorghofer, N., 2009. Laboratory experiments and models of diffusive emplacement of ground ice on Mars. J. Geophys. Res. 114, 21, doi:10.1029/2008JE003149.

Irvine, W.M. and Pollack, J.B., 1968. Infrared optical properties of water and ice spheres. Icarus 8, 324-360, doi:10.1016/0019-1035(68)90083-3.

Johnson, J.R., and 12 colleagues, 2006. Spectrophotometric properties of materials observed by Pancam on the Mars Exploration Rovers: 1. Spirit. J. Geophys. Res. 111, doi:10.1029/2005JE002494.

Johnson, J.R., Bell, J.F., III, Cloutis, E., Staid, M., Farrand, W.H., McCoy, T., Rice, M., Wang, A., Yen, A., 2007. Mineralogic constraints on sulfur-rich soils from Pancam spectra at Gusev Crater, Mars. Geophys. Res. Lett. 34, 13202, doi:10.1029/2007GL029894.

Kinch, K.J., Sohl-Dickstein, J., Bell III, J.F., Johnson, J.R., Goetz, W. and Landis, G.A., 2007. Dust deposition on the Mars Exploration Rover Panoramic Camera (Pancam) calibration targets, J. Geophys. Res., 112, CiteID E06S03, doi:10.1029/2006JE002807.

Kirk, R.L., and 10 colleagues, 2007. Ultrahigh resolution topographic mapping of Mars with HiRISE stereo images: Methods and first results. LPI Contributions 1353, 3381.

Lane, M.D., Bishop, J.L., Dyar, M.D., King, P.L., Parente, M., Hyde B.C., 2008. Mineralogy of the Paso Robles soils on Mars. Amer. Min. 93, 728-739, doi:10.2138/am.2008.2757.

Lewis, K.W., Aharonson, O., Grotzinger, J.P., Squyres, S.W., Bell III, J.F., Crumpler, L.S., and Schmidt, M.E., 2008. Structure and stratigraphy of Home Plate from the Spirit Mars Exploration Rover. J. Geophys. Res. 113, E12S36, doi:10.1029/2007JE003025.

Maki, J.N., and 21 colleagues, 2003. Mars exploration rover engineering cameras. J. Geophys. Res. 108, 8071, doi:10.1029/2003JE002077.

McAdam, A.C., Zolotov, M.Y., Mironenko, M.V., Sharp, T.G., 2008. Formation of silica by low-temperature acid alteration of martian rocks: Physical-chemical constraints. J. Geophys. Res. 113, 08003, doi:10.1029/2007JE003056.

McLennan, S.M., 2003. Sedimentary silica on Mars. Geology 31, 315-318, doi:10.1130/0091-7613(2003)031<0315:SSOM>2.0.CO;2.

McSween, H.Y., and 13 colleagues, 2006. Alkaline volcanic rocks from the Columbia Hills, Gusev Crater, Mars. J. Geophys. Res. 111, doi:10.1029/2006JE002698.

Mertzman, S.A., 2000. K-Ar results from the southern Oregon-northern California cascade range. Oregon Geol. 62, 99-122.

Michalski, J.R., Kraft, M.D., Diedrich, T., Sharp, T.G., Christensen, P.R., 2003. Thermal emission spectroscopy of the silica polymorphs and considerations for remote sensing of Mars. Geophys. Res. Lett. 30, 1, doi:10.1029/2003GL018354.

Michalski, J.R., Kraft, M.D., Sharp, T.G., Williams, L.B., Christensen, P.R., 2005. Mineralogical constraints on the high-silica martian surface component observed by TES. Icarus 174, 161-177, doi:10.1016/j.icarus.2004.10.022.

Milliken, R.E., and 11 colleagues, 2008. Spectral Evidence for Sedimentary Silica on Mars. Lunar and Planetary Institute Conference Abstracts 39, 2025.

Ming, D.W., and 16 colleagues, 2006. Geochemical and mineralogical indicators for aqueous processes in the Columbia Hills of Gusev Crater, Mars. J. Geophys. Res. 111, doi:10.1029/2005JE002560.

Ming, D.W., and 19 colleagues, 2008. Geochemical properties of rocks and soils in Gusev Crater, Mars: Results of the Alpha Particle X-Ray Spectrometer from Cumberland Ridge to Home Plate, J. Geophys. Res., 113, E12S39, doi:10.1029/2008JE003195.

Morris, R.V., and 19 colleagues, 2006. Mössbauer mineralogy of rock, soil, and dust at Gusev Crater, Mars: Spirit's journey through weakly altered olivine basalt on the plains and pervasively altered basalt in the columbia hills. J. Geophys. Res. 111, doi:10.1029/2005JE002584.

Morris, R.V., and 19 colleagues, 2008. Iron mineralogy and aqueous alteration from Husband Hill through Home Plate at Gusev Crater, Mars: Results from the Mössbauer instrument on the Spirit Mars Exploration Rover. J. Geophys. Res. 113, E12S42, doi:10.1029/2008JE003201.

Murchie, S., and 49 colleagues, 2007. Compact Reconnaissance Imaging Spectrometer for Mars (CRISM) on Mars Reconnaissance Orbiter (MRO). J. Geophys. Res. 112, E11, doi: 10.1029/2006JE002682.

Mustard, J.F. and Pieters, C.M., 1987. Quantitative abundance estimates from bidirectional reflectance measurements. J. Geophys. Res. 92, 617, doi:10.1029/JB092iB04p0E617.

Mustard, J.F., and 35 colleagues, 2008. Hydrated silicate minerals on Mars observed by the Mars Reconnaissance Orbiter CRISM instrument. Nature 454, 305-309, doi:10.1038/nature07097.

Pimentel G.C., Forney, P.B., and Herr, K.C., 1974. Evidence about hydrate and solid

water in the martian surface from the 1969 Mariner infrared spectrometer. J. Geophys. Res. 79, 1623-1634.

Poulet, F. and Erard, S., 2004. Nonlinear spectral mixing: Quantitative analysis of laboratory mineral mixtures. J. Geophys. Res. 109, 02009, doi:10.1029/2003JE002179.

Preston, L.J., Benedix, G.K., Genge, M.J., Sephton, M.A., 2008. A multidisciplinary study of silica sinter deposits with applications to silica identification and detection of fossil life on Mars. Icarus 198, 331-350, doi:10.1016/j.icarus.2008.08.006.

Reid, R.J., Rueffer, P., Gliem, F., Johnson, J.R., Maki, J.N., Herkenhoff, K.E., Singer, R.B., 1999. Imager for Mars Pathfinder (IMP) image calibration. J. Geophys. Res. 104, 8907-8926, doi: 10.1029/1998JE900011.

Rice, M.S., Bell, J. F., Wang, A., Cloutis, E. A., 2008. Vis-NIR spectral characterization of Si-rich deposits at Gusev Crater, Mars. Lunar and Planetary Institute Conference Abstracts 39, 2138.

Rieder, R., Gellert, R., Brückner, J., Klingelhöfer, G., Dreibus, G., Yen, A., Squyres, S.W., 2003. The new Athena Alpha Particle X-ray Spectrometer for the Mars Exploration Rovers. J. Geophys. Res. 108, 8066, doi:10.1029/2003JE002150.

Rodgers, K.A., Cook, K.L., Browne, P. R. L., Campbell, K.A., 2002. The mineralogy, texture and significance of silica derived from alteration by steam condensate in three New Zealand geothermal fields. Clay Miner. 37, 299, doi:10.1180/0009855023720035.

Rodgers, K.A., and 13 colleagues, 2004. Silica phases in sinters and residues from geothermal fields of New Zealand. Earth Sci. Rev., 66, 1-61, doi:10.1016/j.earscirev.2003.10.001.

Rogers, A.D. and Christensen, P.R., 2007. Surface mineralogy of Martian low-albedo regions from MGS-TES data: Implications for upper crustal evolution and surface alteration. J. Geophys. Res. 112, E01003, doi:10.1029/2006JE002727.

Roedder, E., 1984. Fluid Inclusions: An Introduction to Studies of All Types of Fluid Inclusions, Gas, Liquid, or Melt, Trapped in Materials from Earth and Space, and their Application to the Understanding of geologic processes. Mineralogical Society of America, Washington, D.C.

Roush, T.L., Pollack, J.B., Witteborn, F.C., Bregman, J.D., Simpson, J.P., 1990. Ice and minerals on callisto - A reassessment of the reflectance spectra. Icarus 86, 355-382.

Ruff, S.W., Christensen, P.R., Blaney, D.L., Farrand, W.H., Johnson, J.R., Michalski,

J.R., Moersch, J.E., Wright, S.P., Squyres, S.W., 2006. The rocks of Gusev Crater as viewed by the Mini-TES instrument. J. Geophys. Res. 111, doi:10.1029/2006JE002747.

Ruff, S.W., Christensen, P.R., Glotch, T.D., Blaney, D.L, Moersch, J.E., Wyatt, M.B., 2008a. The mineralogy of Gusev crater and Meridiani Planum derived from the Miniature Thermal Emission Spectrometers on the Spirit and Opportunity rovers, in: Bell III, J.F. (Ed.), The Martian Surface – Composition, Mineralogy, and Physical Properties, Cambridge Univ. Press, Cambridge, UK, pp. 315-338.

Ruff, S.W., Farmer, J. D., Arvidson, R. E., Squyres, S. W., Christensen, P. R., Athena Science Team, 2008b. The nature and distribution of silica at Home Plate in Gusev Crater, Mars: Evidence for a hydrothermal system. Lunar and Planetary Institute Conference Abstracts 39, 2213.

Schmidt, M.E., and 10 colleagues, 2008. The hydrothermal origin of halogens at Home Plate, Gusev Crater. J. Geophys. Res. 113, E12, doi: 10.1029/2007JE003027.

Schorghofer, N. and Aharonson, O. ,2005. Stability and exchange of subsurface ice on Mars. J. Geophys. Res. 110, E9, doi: 10.1029/2004JE002350.

Sheppard, R.A., Gude, A.J., I., Hay, R.L., 1970. Makatite, a new hydrous sodium silicate mineral from Lake Magadi, Kenya. Am. Mineralogist 55, 358-366.

Sinton, W.M., 1967. On the composition of martian surface materials. Icarus, 6, 222-228.

Sohl-Dickstein, J., Johnson, J. R., Grundy, W. M., Guinness, E. A., Graff, T., Shepard, M. K., Arvidson, R. E., Bell, J. F.,III, Christensen, P. R., Morris, R. V., 2005. Modeling visible/near-infrared photometric properties of dustfall on a known substrate. Lunar Planet. Sci. XXXVI, Abstract 2235.

Squyres, S.W., and 15 colleagues, 2006. Rocks of the Columbia Hills. J. Geophys. Res. 111, doi:10.1029/2005JE002562.

Squyres, S.W., and 27 colleagues, 2007. Pyroclastic activity at Home Plate in Gusev Crater, Mars. Science 316, 738-742, doi:10.1126/science.1139045.

Squyres, S.W., and 17 colleagues, 2008. Detection of silica-rich deposits on Mars. Science 320, 1063, doi:10.1126/science.1155429.

Wang, A., and 15 colleagues, 2008. Light-toned salty soils and coexisting Si-rich species discovered by the Mars Exploration Rover Spirit in the Columbia Hills. J. Geophys. Res. 113, E12S40, doi:10.1029/2008JE003126.

White, D.E., Brannock, W.W., Murata, K.J., 1956. Silica in hot-spring waters.

Geochimica Et Cosmochimica Acta, 10, 27-59.

Wyatt, M.B. and McSween, H.Y., 2002. Spectral evidence for weathered basalt as an alternative to andesite in the northern lowlands of Mars. Nature 417, 263-266.

Yen, A.S., and 13 colleagues, 2008. Hydrothermal processes at Gusev Crater: An evaluation of Paso Robles class soils. J. Geophys. Res. 113, E12, doi:10.1029/2007JE002978.

CHAPTER 3

SPECTRAL DIVERSITY OF SILICA-RICH MATERIALS[1]

0. Abstract

Hydrated silica-rich materials have recently been discovered on the surface of Mars by the Mars Exploration Rover (MER) Spirit, the Mars Reconnaissance Orbiter (MRO) Compact Reconnaissance Imaging Spectrometer for Mars (CRISM), and the Mars Express Observatoire pour la Minéralogie, l'Eau, les Glaces, et l'Activité (OMEGA) in several locations. Having been interpreted as hydrothermal deposits and aqueous alteration products, these materials have important implications for the history of water on the martian surface. Spectral detections of these materials in visible to near infrared (Vis-NIR) wavelengths have been based on a H_2O absorption feature in the 934 to 1009 nm region seen with Spirit's Pancam instrument, and on Si–OH absorption features in the 2.21 to 2.26 μm range seen with CRISM. Our work aims to determine how the spectral reflectance properties of silica-rich materials in Vis-NIR wavelengths vary as a function of environmental conditions and formation. Here we present laboratory reflectance spectra of a diverse suite of silica-rich materials (chert, opal, quartz, natural sinters and synthetic silica) under a range of grain sizes and temperature, pressure, and humidity conditions. We find that the H_2O content and form of H_2O/OH present in silica-rich materials can have significant effects on their Vis-NIR spectra. Our main findings are that the position of the ~1.4

[1] An edited version has been submitted for publication in *Icarus* as: M.S. Rice, E.A. Cloutis, J.F. Bell III, S.A. Mertzman, D.L. Bish, B. Horgan, M. Craig, R.W. Renaut, B. Gautason, B. Mountain, Reflectance Spectra Diversity of Silica-Rich Materials: Sensitivity to Environment and Implications for Detections on Mars.

μm OH feature and the symmetry of the ~1.9 μm feature can be used to discern between various forms of silica-rich materials, and that the ratio of the ~2.2 μm (SiOH) and ~1.9 μm (H_2O) band depths can aid in distinguishing between silica phases (opal-A vs. opal-CT) and formation conditions (low vs. high temperature). We also discuss how these results can aid in the interpretation of silica detections on Mars made by the MER Panoramic Camera (Pancam) and Mars Science Laboratory (MSL) Mast-mounted Camera (Mastcam) instruments.

1. Introduction

Determining the extent and form of water on the surface of Mars is crucial to understanding the planet's evolutionary history and habitability. Identifying aqueous minerals at the surface is an important aspect of the search for evidence of past and present water. In the past decade, sulfate and phyllosilicate minerals have been detected across the planet by multiple investigations (*e.g.,* Bibring, 2006; Mustard et al., 2008). Discoveries of carbonates have been more elusive in orbital measurements, but they have been identified in small (2-5%) concentrations in martian dust (Bandfield et al., 2003) and more recently within rocks in the Nili Fossae region (Ehlmann et al., 2008) and in the Columbia Hills within Gusev crater (Morris *et al.,* 2010). Opaline silica ($SiO_2 \cdot nH_2O$) is the most recent addition to the classes of known hydrated minerals on Mars, having been detected from orbit by multiple instruments (*e.g.* Bandfield et al., 2008; Milliken et al., 2008) and with rover-based observations (Squyres et al., 2008).

On Earth, hydrated silica-rich materials can occur in a variety of forms, such as the weathering products of volcanic rocks under a wide range of conditions (e.g., Ugolini, 1986), as coatings and rinds on volcanic materials (Minitti et al., 2007), as sedimentary silica (McLennan, 2003), or as precipitates from high- and low-temperature geothermal fluids (e.g., Ellis and Mahon, 1977; Farmer, 1996; Channing and Butler, 2007). Discoveries of opaline silica on Mars have been anticipated for many years based on evidence for past hydrothermal activity (Farmer, 1996; Bishop, 2004) and geochemical arguments (Gooding and Keil, 1978; Burns and Fisher, 1993; McLennan, 2003). Because the precipitation of silica from fluids can provide a mechanism for preserving evidence of microbes, detections of silica on Mars may have astrobiological significance as well (*e.g.* Cady and Farmer, 1996; Konhauser *et al.*, 2003).

The Mars Exploration Rover (MER) Spirit discovered the first unequivocal occurrence of silica on Mars (Squyres et al., 2008). This subsurface deposit of bright, whitish silica-rich soil (Figure 1b) was exposed within the rover's wheel trench in a topographic lowland called the Eastern Valley in the Inner Basin of the Columbia Hills of Gusev Crater, and it has been interpreted to have formed under hydrothermal conditions (Squyres et al., 2008; Ruff et al., 2011). Observations of the brightest exposure by the rover's Alpha Particle X-Ray Spectrometer (APXS; Gellert et al., 2006) instrument show that its composition is 90.1 wt.% SiO_2 (~98 wt.% SiO_2 when corrected for dust contamination; Squyres et al., 2008). Spectra of this trench from Spirit's Miniature Thermal Emission Spectrometer (Mini-TES; Christensen et al., 2003) are consistent with the presence of opaline silica (Ruff et al., 2011). Other light-

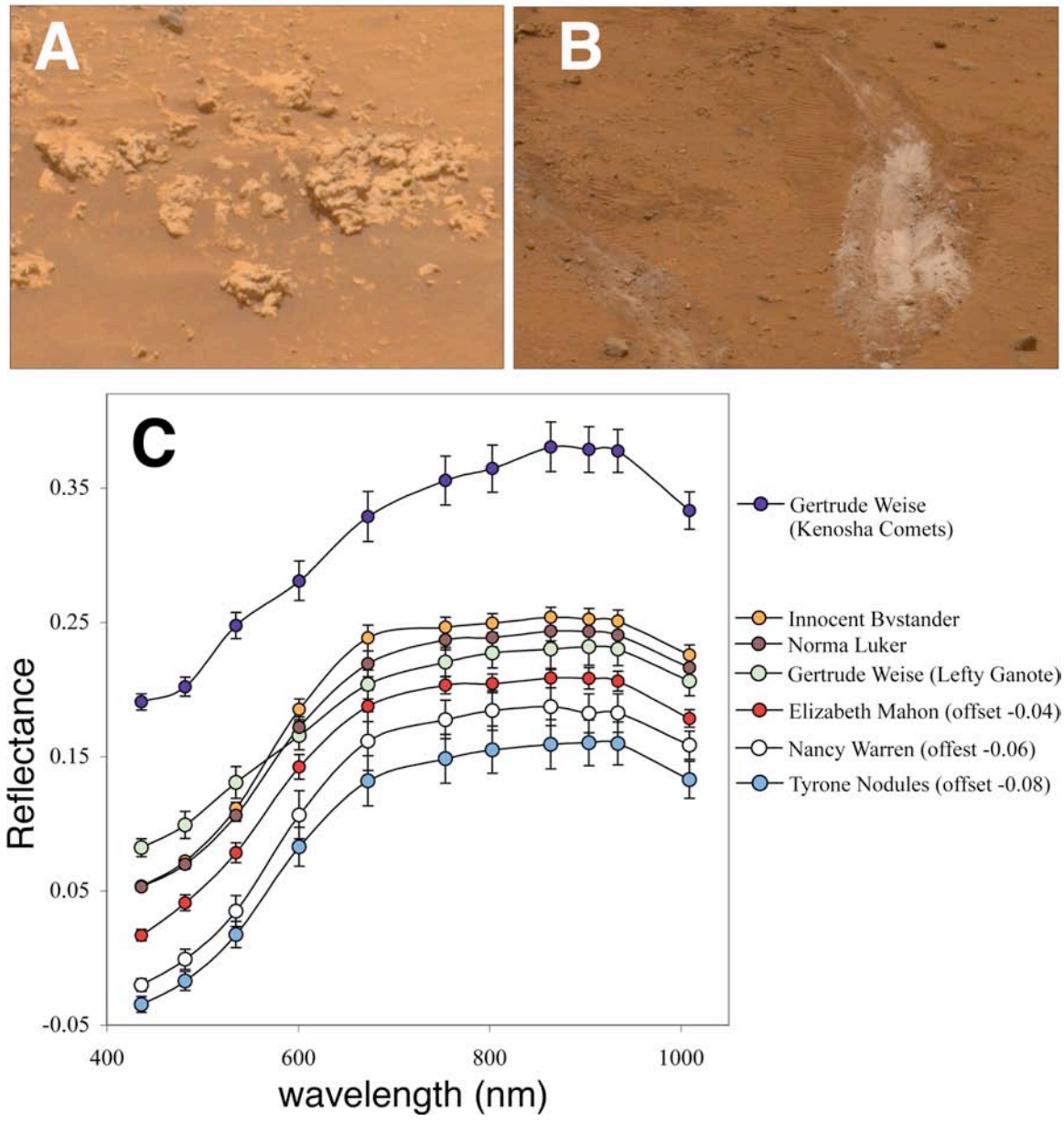

Figure 1. Silica-rich materials in the Columbia Hills of Gusev Crater, discovered by the Mars Exploration Rover (MER) Spirit: (a) Panoramic Camera (Pancam) approximate true color (ATC) image (blue = 482 nm, green = 535 nm, red = 601 nm) of the Elizabeth Mahon nodular outcrop (sol 1174, P2588), which contains ~72% SiO_2 (Ming et al., 2008). The extent of the outcrop is ~60 cm; (b) Pancam ATC image of the Gertrude Weise soil (sol 1187, P2533), which contains ~98% SiO_2 (Squyres et al., 2008). The width of the wheel track is ~16 cm; (c) Pancam relative reflectance spectra of silica-rich targets (see Rice et al., 2010 for further discussion). All spectra exhibit a relatively flat near-infrared profile (864 to 934 nm) and a characteristic downturn in the longest-wavelength filter (1009 nm) due to H_2O and/or OH absorptions near ~1000 nm (Rice et al., 2010).

toned nodular outcrops (e.g., Figure 1a) in the Eastern Valley region also have high silica compositions; for example, four nodular outcrops measured by APXS contain 63-73 wt.% SiO_2 (Ming et al., 2008b).

Observations by Spirit's Pancam multispectral imager (Bell et al., 2003) indicate that the silica-rich soil and outcrops exhibit unique spectral properties in visible to near-infrared (Vis-NIR) wavelengths. In addition to a much higher reflectivity, another major spectral difference between the silica-rich materials and the surrounding terrain is the presence of a reflectance downturn in the last two Pancam channels, from 934 to 1009 nm (Wang et al., 2008; Rice et al., 2010) (Figure 1c). A similar spectral feature was also associated with exposures of subsurface ice imaged by the Surface Stereo Imager (SSI) on the Phoenix spacecraft (Smith et al., 2009). Because this downturn is also associated with a generally flat reflectance spectrum in the 864 nm to 934 nm region, the source of the spectral downturn must be confined to wavelengths longer than 934 nm. Pure silica, in its various forms, does not exhibit an absorption feature in the 934-1009 nm region (*e.g.* Clark et al., 2007), although Elliot and Newns (1970) noted the occurrence of a weak ~938 nm feature in the spectrum of H_2O dissolved in fused silica. Many minerals, including the abundant mafic silicates at the Gusev site, do exhibit absorption bands in the 1000 nm region that could potentially be detectable in a multispectral imaging system such as Pancam (e.g., Cloutis and Bell, 2003; McSween et al., 2006); however, these bands are wide enough that the downturn in reflectance begins shortward of 934 nm, and thus they are not viable candidates to explain the ~1009 nm Pancam feature. Rice et al. (2010) suggested that the ~1009 nm feature arises from the presence of H_2O and/or OH, as

H_2O ice, adsorbed H_2O/OH, or H_2O/OH bound in the structure of an additional mineral component. H_2O exhibits an absorption band near ~950 nm that is attributable to a combination of the $2v_1$ and v_3 vibrations (e.g., Herzberg, 1945; Bayly *et al.*, 1963), and a vibrational overtone of OH ($3v_{OH}$) occurs in this wavelength region as well.

Silica has also been detected from orbit by the Mars Global Surveyor (MGS) Thermal Emission Spectrometer (TES) in outcrops exposed in western Hellas Basin (Bandfield, 2008), by the Mars Express Observatoire pour la Minéralogie, l'Eau, les Glaces, et l'Activité (OMEGA) in Acidalia Planitia and in the north polar region (Horgan and Bell, in press), and by the Mars Reconnaissance Orbiter (MRO) Compact Reconnaissance Imaging Spectrometer for Mars (CRISM) instrument near the Valles Marineris canyon system (Milliken et al., 2008; Bishop et al., 2009; Weitz et al., 2010; Wendt et al., 2011), in the Syrtis Major region (Mustard et al., 2008; Ehlmann et al., 2009, Skok et al., 2009, Marzo et al., 2010), Mawrth Vallis (e.g., Bishop et al., 2008; McKeown et al., 2009; Noe Dobrea et al., 2010), Terra Sirenum (Wray et al., 2011) and Antoniadi crater (Smith et al., 2011). The CRISM detections of silica are based on the position and width of an OH overtone band at ~1.41 μm, an H_2O overtone band at ~1.9 μm, and Si-OH bands near ~2.2 μm (Figure 2a). In some CRISM observations, where the ~1.41 and ~1.9 μm features are weak or absent, detections of silica have been based solely on the ~2.2 μm bands (Figure 2b), as OH and H_2O features may have been lost during dehydration of silica, or they may be obscured by additional constituents such as iron oxides (Skok et al., 2010). Phyllosilicates have also been identified on Mars based on absorption bands centered near ~2.2 μm (e.g., Murchie et al., 2009), and sulfate minerals exhibit features in this wavelength region as well (e.g.,

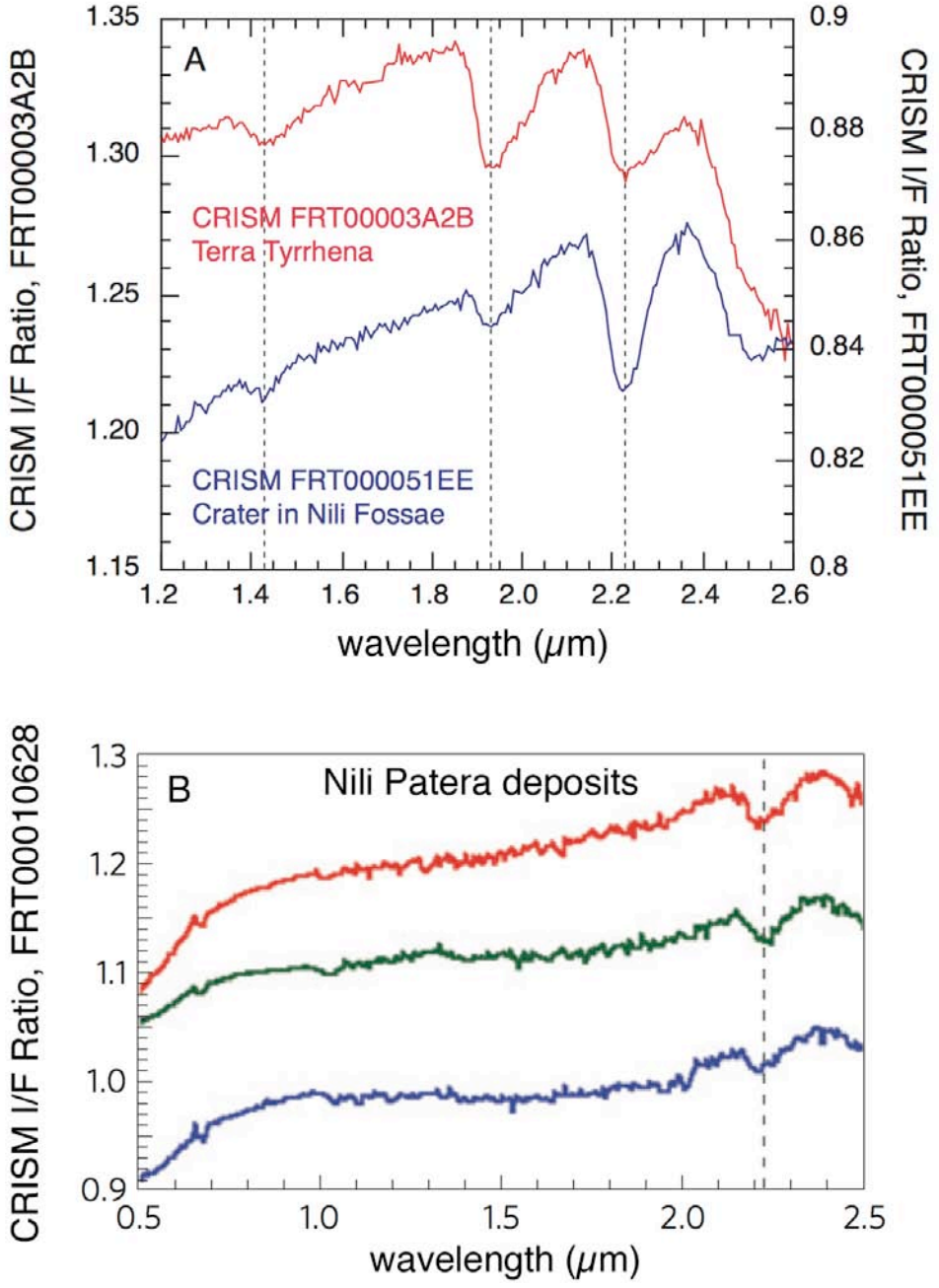

Figure 2. Examples of hydrated silica detections in CRISM spectra: (a) CRISM ratio spectra for deposits in Terra Tyrrhena (image FRT00003A2B) and Nili Fossae (image FRT000051EE) from Milliken et al. (2008). Both spectra exhibit diagnostic features in the 1.4, 1.9 and 2.2 μm regions; (b) CRISM ratio spectra for Nili Patera cone with deposits (image FRT00010628) from Skok et al. (2010). The detection at this location was made based solely on the position of the ~2.2 μm feature, as the ~1.4 and ~1.9 μm bands are absent or unresolvable.

Clark et al., 1990); therefore the width, symmetry, and number of local minima of these bands must be used to distinguish between Si-OH in opaline silica and bonds in other minerals.

Absorption bands in the Vis-NIR spectra of hydrated silica are sensitive to environmental conditions during and since the mineral's genesis. Understanding how these factors affect reflectance spectra will aid interpretations of recent and future detections of opaline silica on Mars. In this study we have undertaken a comprehensive examination of how silica formation, as well as variations in the physical forms of H_2O/OH and OH associated with silica-rich materials, can affect reflectance spectra. First we present a review of the spectral properties of terrestrial silica and H_2O speciation in silica-rich materials (*Section 2*). We then describe our acquisition of spectra of a diverse suite of silica-rich materials, including cherts, opals, quartzes, natural sinters, and synthetic silica at varying grain sizes and temperature and humidity conditions (*Section 3.1-3.3*). We have also subjected a silica-rich sinter (opal-A) to a simulated Mars surface environment for more than one year and have recorded its spectral changes while equilibrating (*Section 3.4*).

Because of their significance to recent Pancam, OMEGA, and CRISM detections of opaline silica on Mars, as well as for potential detections by the Mars Science Laboratory (MSL) Mast-mounted Cameras (Mastcams), we focus our analysis on the H_2O absorption near ~1 μm, which has not been previously studied in detail, and on the OH, H_2O and Si-OH absorptions near ~1.4 μm, ~1.9 μm and ~2.2 μm (*Section 4*). The goal of this study is to identify ways in which the band depths, positions, and widths of these features can constrain the depositional environment of

silica-rich materials. In *Section 5* we discuss correlations we have found between our measured spectral parameters and the content and form of H_2O. *Section 6* outlines our plans for future work and implications of this study for future spectral detections of silica on Mars.

2. Background

The spectral reflectance properties of H_2O - and OH-bearing silica-rich materials can be largely interpreted from the perspective of the spectral properties of H_2O and OH and how these molecules interact with and bind to a Si-O framework. In this section we provide an overview of the spectral properties of H_2O and OH, the structure of silica, the nature of H_2O in silica, and the Vis-NIR spectral properties of silica.

2.1 Spectral properties of H_2O and OH

Because H_2O is a polar molecule, it can interact with adjacent H_2O molecules or to solids with which it is in contact. For example, H_2O in different states shows differences in the wavelength position of the H-O-H bending (ν_2) fundamental vibration: 6.27 μm in the vapor state, 6.08 μm in the liquid state, and between 6.10 and 6.12 μm when adsorbed on silica gel (e.g., Irvine and Pollack, 1968; Eisenberg and Kauzmann, 1969). When examined in more detail, H_2O exhibits a large number of fundamental, combination, and overtone bands (e.g., Herzberg, 1945; Bayly *et al.*, 1963) (Table 1) which show variations in spectral shape depending on the number of hydrogen bonds in each H_2O molecule (Van Thiel et al.,1957; Buijs and Choppin

Table 1. Wavelength position of H_2O absorption bands (from Bayly et al., 1963).

Mode* ($v_1v_2v_3v_L$)	**Wavelength (μm)**	**Intensity (cm^{-1} mol^{-1})**
0001	~13-20	--
0100	6.079	20.8
0101	4.706	3.23
1000/0200	3.048	54.54
0010	2.865	62.7
0011	2.551	0.83
0110	1.934	1.05
0111	1.787	0.095
0020/1010/0210	1.449	0.28
1110	1.219	0.01
2010	0.981	0.0044
2110/0130	0.880	0.0011
3010	0.749	0.0007

* v_1: symmetrical stretching; v_2: symmetrical bending; v_3: antisymmetric stretching; v_L: libration.

1963). With increasing temperature, the number of hydrogen-bonded H_2O molecules decreases, and the average band position of various overtones and combinations moves to shorter wavelengths (Bayly et al.,1963). In addition, different types of anions and cations can either increase or decrease the amount of ordering (hydrogen bonding) in liquid H_2O (Choppin and Buijs 1963). These variations explain, in large part, the minor disagreements between the laboratory analyses of different investigators (e.g., Hornig 1964; Buijs and Choppin, 1964).

The wavelengths of the fundamental bands in liquid H_2O are intermediate between those of solid and vapor, consistent with differences in the degree of hydrogen bonding between these three phases (Irvine and Pollack 1968; Eisenberg and Kauzmann 1969) (Table 2). Solid H_2O shows diagnostic shifts in absorption band positions and changes in band intensities as a function of temperature (e.g., Grundy

Table 2. Absorption band positions for H_2O (from Irvine and Pollack, 1968; Eisenberg and Kauzmann, 1969)

Mode* ($\nu_1\nu_2\nu_3\nu_L$)	Solid (μm)	Liquid (μm)	Vapor (μm)
1000/0200	~3.12	~2.86	~2.66 and 2.73
0100	~6.06	~6.08	~6.27

* ν_1: symmetrical stretching; ν_2: symmetrical bending; ν_3: antisymmetric stretching; ν_L: libration.

and Schmitt, 1998), and the absorption bands in amorphous H_2O ice are weaker and at shorter wavelengths than for crystalline solid H_2O (e.g., Mastrapa et al., 2008). The implications of these observations are that reflectance spectra of the same target at different temperatures may show differences in H_2O band positions that could be due to changes in the degree of hydrogen bonding or to phase changes.

In addition to H_2O, many minerals also possess OH in the form of "structural OH" or hydroxyl. Technically, such phases are anhydrous rather than hydrated minerals (see Ming et al., 2008a for a review of hydrated mineral terminology), even though they are still formed by aqueous processes. The OH^- anion in minerals is necessarily bonded to adjacent atoms to preserve charge neutrality, and because it is diatomic, it does not possess bending vibrations except in the context of the adjacent atoms to which it is bound. The only stretching vibration of OH appears in minerals near 2.8 μm (sometimes as high as 3.45 μm), and its overtones are present near 1.4 μm ($2\nu_{OH}$) and 0.95 μm ($3\nu_{OH}$) (e.g., Clark et al.,1990).

2.2 Structure of silica-rich materials

Silica occurs in the Earth's crust in a variety of mineral forms, and this has

given rise to a broad range of names for materials that are composed essentially of a three dimensional network of Si-O. The type of silica-rich materials that form by various processes can be sensitive indicators of petrogenesis, diagenesis, and/or biological processes; a summary of different silica-rich materials and their formation environments is provided in Table 3. Factors such as abundance of accessory elements and presence and abundance of fluid inclusions can also be affected by formation conditions (Wang and Merino, 1990). Chemical factors, such as the presence of organic material, can also affect silica crystallization reactions as well (Hinman, 1990).

In Table 3 and in the sample descriptions for this study, we categorize "opals" as the natural non-crystalline silica samples that were deposited in rock fissures at low temperatures (e.g. Jones and Segnit, 1966). However, "opal" can more generally indicate any hydrated silica ($SiO_2 \bullet nH_2O$) without crystalline order (as opposed to macro- or microcrystalline SiO_2 polymorphs), as determined by X-ray diffraction (XRD), and with H_2O contents higher than 1 wt. % (e.g., Langer and Flörke, 1974). Although the term "opaline" has often been used synonymously with "amorphous" (e.g. Jones and Segnit, 1966), there is an ongoing debate in the literature about the appropriate use of "amorphous" in reference to silica (Smith, 1998; Rodgers et al., 2004). In this study we adopt the terminology of Rodgers et al. (2004) and use "non-crystalline" or "X-ray amorphous, where appropriate, in place of "amorphous."

Over a dozen distinct varieties of opals have been identified in the literature, which differ largely in the arrangement and size of voids located between silica spheres (e.g., King, 1986). Gem-quality and other opals do not differ in terms of

Table 3. Descriptions of silica-rich materials used in this study

Material	Representative Chemical Formula	Formation Environment	Description	Selected References
amethyst	SiO_2 with Fe impurities	occurs as geodes in sedimentary and volcanic rocks; deposited from groundwater or hydrothermal solutions rich in dissolved silicates	a variety of quartz; violet crystals found within hollow rock chambers	Proust and Fontaine, 2007
chalcedony	SiO_2	occurs as nodules within rock cavities, typically volcanics; can precipitate from low-temperature (<100^o C) solutions	a fibrous cryptocrystalline variety of quartz; called "agate" when concentrically banded	Frondel, 1982; Graetsch et al., 1985; 1987
chert	SiO_2	forms in layers and nodules in sedimentary rocks as a replacement mineral; can be recrystallized from siliceous grains of biological origin (e.g., diatoms)	consists of microcrystalline or cryptocrystalline quartz	Laschet, 1984; Knauth, 1994; McDowell et al., 2009
chrysoprase	SiO_2 with Ni impurities	results from weathering of ultramafic rocks (e.g., serpentine)	a green, gemstone variety of chalcedony; consists of cryptocrystalline quartz	Graetsch, 1985; 2011
cristobalite	SiO_2	a low-pressure, high-temperature polymorph of silica; occurs in volcanic rocks and converted diatomaceous deposits	white octahedral crystals or spherulites; persists as metastable phase at low temperatures;	Reich et al., 2009; Flörke et al., 2000
flint	SiO_2	occurs as nodules and masses in chalk and limestone formations as a replacement of calcium carbonate with silica	a variety of chert, but typically darker in color; consists of microcrystalline or cryptocrystalline quartz	Laschet, 1984; Knauth, 1994
lechatelierite	SiO_2	natural glass formed from high pressure shock metamorphism (e.g., meteorite impacts) or from lightening strikes in SiO_2-rich sediments (e.g., quartz sand fulgerite)	amorphous silica; a component of tektites; varieties include Dakhleh glass and Darwin glass (impactites)	Moroz et al., 2009; Bouška and Bell, 1993
novaculite	SiO_2	siliceous layers found in the Ouachita Mountains, may be a product of low-grade metamorphism of chert beds	a variety of chert; consists of microcrystalline or cryptocrystalline quartz; rock is particularly hard and dense due to interlocking structure	Lowe, 1975
opal	$SiO_2 \cdot nH_2O$	deposited from silica-rich solutions at low temperatures in rock fissures; can replace organic remains	referred to as "precious" when a play of color is displayed, otherwise called "common" or "potch" and has a milky appearance; composed of spheres of amorphous silica (close-packed for precious opals, irregularly packed for potch opals)	Bayliss and Males, 1965; Segnit et al., 1965; Jones and Segnit, 1966; Gaillou et al., 2008

Table 3 cont'd.

Material	Representative Chemical Formula	Formation Environment	Description	Selected References
quartz	SiO_2	one of the main products of slowly cooled, silica-rich magmas (e.g., granites and granodiorites); also a primary mineral of pegmatites and hydrothermal veins formed during late stages of magmatic processes; a major constituent of metamorphic rocks	made up of a continuous framework of SiO_4 tetrahedra; colorless and transparent; few impurities, but water can be incorporated in concentrations from hundreds to several thousands of parts per million	Kekulawala et al., 1981; Paterson et al., 1982; Flörke et al., 1982; Cordier and Doukhan, 1991
rose quartz	SiO_2 with Fe and Ti in nanoinclusions	occurs in pegmatites; forms at high temperatures (400-700^o C); sometimes occurs in hydrothermal veins	a variety of quartz; rose-pink colored due to submicroscopic mineral fiber inclusions; hazy to translucent character; occurs as massy aggregates rather than as single crystals	Flörke et al., 2000; Goreva et al., 2001
silica gel	$SiO_2 \cdot nH_2O$	synthetic silicon dioxide prepared by the neutralization of aqueous alkali metal silicate with acid	solid, amorphous; distinguished by its microporosity and hydroxylated surface; an interconnected random array of spherical, polymerized silicate particles called "micelles"	Flörke et al., 2000
silica residue	$SiO_2 \cdot nH_2O$	forms when H_2S emissions (e.g., from fumaroles) oxidize and condense to produce low pH (<2) solutions that react with volcanic rocks, producing alteration assemblages enriched in silica	amorphous silica (opal-AG, opal-CT and/or opal-C); morphologically similar to silica sinter; can preserve primary structures and textures of the original rock; can contain kaolinite, sulfates like jarosite and alunite, TiO_2 and other components	White et al., 1988; Rodgers et al., 2002; Ruff et al., 2011
silicic acid	$SiO_2 \cdot nH_2O$	synthetic silicon dioxide, formed by the acidification of silicate salts (e.g., sodium silicate) in aqueous solution	white solid in powder form	Flörke et al., 2000
sinter	$SiO_2 \cdot nH_2O$	precipitates from high-temperature solutions in volcanic settings	Deposited as spheres of opal-AG with disordered packing; typically porous and friable; called "geyserite" when found in proximity to a hydrothermal vent; can incorporate large amounts of water; can preserve fossil evidence of organic material; transitions to more crystalline polymorphs (opal-CT and/or opal-C) with age and/or due to high temperature	Herdianita et al., 2000a; 2000b; Jones and Renaut, 2004; Konhauser et al., 2003; Cady and Farmer, 1996; Preston et al., 2008
tektite	SiO_2	natural glass formed during meteorite impacts; precursor material is the impact target	amorphous silica with very low water contents; range in color from green to brown	Koeberl, 1990; Bouška and Bell, 1993

many common properties such as X-ray diffraction pattern, trace element content, and thermogravimetry (Bayliss and Males, 1965); however, nuclear magnetic resonance can provide limited discrimination (e.g., Adams et al.,1991), as can XRD discrimination for some silica polymorphs (e.g., Herdianita et al.,2000b).

Opals are generally divided into four groups, listed here in order of increasing structural order: (1) opal-AN, sometimes referred to as "hyalite," which is X-ray amorphous and has a network-like structure similar to glass; (2) opal-AG, which includes "precious" and "potch" opals and consists of aggregated spheres of non-crystalline silica (a gel-like structure) with H_2O filling the gaps between spheres; (3) opal-CT, which exhibits the beginnings of short-range ordering; and (4) opal-C, which consists of short-range cristobalite-like order (e.g., Langer and Flörke, 1974; Herdianita et al., 2000a; Gaillou et al., 2008). Groups (1) and (2) are both commonly referred to as "opal-A." Opal-A and opal-CT are easily distinguishable in thermal infrared spectra (Michalski et al., 2003) but are significantly more difficult to discern in Vis-NIR wavelengths (e.g., Milliken et al., 2008).

When deposited, most opal consists largely of non-crystalline silica spheres of opal-A with disordered packing, low densities, high porosities and large H_2O contents. Over typical timescales of tens of thousands of years, opals can incrementally crystallize to become opal-CT and/or opal-C . Therefore, as these materials age, changes to silica properties (e.g., H_2O content, void size) accompanying increases in order are amenable to characterization by reflectance spectroscopy; as a result, these spectral changes can potentially be used for relative age dating (Herdianita et al., 2000a). However, transitions can sometimes occur more rapidly; for example, Jones

and Renaut (2007) and Jones et al. (2007) reported opal-CT in the sinter mound at Geysir, Iceland that was < 10^3 years old based on stratigraphic relationships to known volcanic ash horizons. The original opal-A was altered rapidly by dissolution-reprecipitation reactions a few meters below the surface (Jones and Renaut, 2007).

2.3 The nature of H_2O in silica

H_2O is ubiquitous in both natural and synthetically produced silica, and can occur in a variety of forms related to formation conditions and subsequent diagenesis (e.g., Anderson and Wickersheim 1964). H_2O content can also be indicative of silica formation conditions, as it can be related to the rate of precipitation (Jones and Renaut, 2004). H_2O can also enter silica via diffusion and can react with silica to form Si-OH complexes (e.g., Doremus, 1998).

The total H_2O content (wt. % H_2O) in a hydrated silica phase is the sum of the H_2O present in the form of molecular H_2O and in the form of SiOH-groups. Silanol (Si-O-H) can be present in three broad forms: (1) vicinal (hydrogen-bonded); (2) geminal (two silanol groups attached to the same Si); or (3) isolated (no hydrogen bonds) (e.g., Hockey and Pethica, 1961; Anderson, 1964; Graetsch, 1994; Dijkstra et al., 2002), each of which exhibits absorption bands at different wavelengths. H^+ in the form of OH may also be present to balance the charge when cations such as Al^{3+} substitute for Si^{4+} in the silica framework (Webb and Finlayson, 1987).

The size of any voids or bubbles that contain H_2O is also a significant factor in controlling the spectral properties of silica. This arises from the fact that, at a minimum, the first monolayer of H_2O molecules lining a void are strongly affected by

strong hydrogen bonding to the underlying silica; in the case of voids that are 60 nm in diameter, approximately one-third of the H_2O molecules comprise this monolayer (e.g., Kekulawala et al., 1981; Tables 1 and 2). In larger voids, multilayers of adsorbed H_2O can build up on the silanol surface by hydrogen bonding to the surface hydroxyls, and these multilayers then grade into capillary adsorbed H_2O (Segnit et al., 1965). If the voids are sufficiently large, some of the H_2O molecules exist as liquid H_2O and can freeze upon exposure to low temperatures to result in the appearance of solid H_2O (ice) absorption bands (Aines et al., 1984). However, some H_2O that may be present in silica cannot be "frozen" into an ice structure because it occurs in monolayer-size films that are adsorbed on and reacting with the silica surface (Kekulawala et al.,1981). H_2O adsorbed on silica gel is spectrally similar to liquid H_2O (Benesi and Jones 1959).

2.4 Vis-NIR spectral properties of silica

The presence of H_2O in silica gives rise to a broad absorption feature between ~2.8 and 3.3 μm with superimposed absorption bands near 3.05 and 3.12 μm due to O-H stretching in H_2O (Kekulawala et al.,1981). Spectral variations between different silica-rich materials, which can be related to petrogenetic conditions, are present in this wavelength region (Paterson 1982). When OH is present, a series of sharp additional bands (in transmission spectra) can appear in the 2.76- 2.99 μm region (Kekulawala et al.,1981; Aines and Rossman, 1984). The way in which nearest-neighbor silanol groups interact affects the wavelength position and intensity of the

associated O-H stretching vibrations in the 2.70-3.12 μm region, and likely the combination bands in the 2.2-2.3 μm region (Langer and Flörke 1974).

Effects such as heating lead to changes in spectral properties associated with H_2O/OH absorption bands, as H_2O in fluid inclusions can be lost and silanol-associated spectral features become more apparent (Frondel, 1982). Some structural/compositional changes accompanying diagenesis of silica-rich materials appear to be irreversible, thus potentially providing a record of past conditions that can be accessed spectroscopically (e.g., Hambleton et al.,1966). Differences in the appearance of the H_2O/OH fundamental bands in the 2.7-3.2 μm region and Si-OH combination bands in the 2.2-2.3 μm region are associated with different types of silica-rich materials and are affected by factors such as sample heating and the temperature at which the spectra are measured (e.g., Segnit et al.,1965; Langer and Flörke, 1974; Graetsch et al.,1985). Because different types of H_2O (e.g., adsorbed, capillary) are lost at different temperatures upon heating and may have different spectral properties (depending on degree and nature of hydrogen bonding), analysis of the constituent H_2O absorption bands may be useful for constraining initial H_2O contents and/or subsequent diagenesis (Thompson, 1965).

The ~2.2 μm region in spectra of hydrated silica exhibits two overlapping absorption features near ~2.21 and ~2.26 μm (Table 4). Both are attributable to Si-OH rotation plus stretching, but with differences in hydrogen bonding. The constituent band near ~2.21 μm (type-A) has been reported as being the strongest in opal-A (consistent with isolated OH present within the silica matrix), whereas the band near ~2.26 μm (type-B) is strongest in opal-C (consistent with geminal SiOH-groups with

Table 4. Expected Vis-NIR absorption features of H_2O, OH and Si-OH (from Herzberg, 1945; Bayly et al., 1963; Langer & Flörke, 1974).

Band Position	Band Attribution*		Notes
~0.95 μm	H_2O	$2v_1 + v_3$	
	OH	$3v_{OH}$	
~1.14 μm	H_2O	$v_1 + v_2 + v_3$	
~1.36 μm	H_2O	$v_1 + v_3$	
~1.41 μm	OH	$2v_{OH}$	
~1.46 μm	H_2O	$2v_2 + v_3$	
~1.78 μm	H_2O	$2\delta + v_1$ or v_3 or v_L	
	OH	$2\delta + v_{OH}$	
~1.91 μm	H_2O	$v_2 + v_3$	type A; attributed to H_2O molecules in silica cages (almost free from hydrogen bonding)
~1.96 μm			type B; attributed to hydrogen-bonded H_2O molecules in voids or films on silica surfaces
~2.21 μm	Si-OH	$\delta + v_{OH}$	type A; isolated SiOH present within the silica matrix
~2.26 μm			type B; geminal (two silanol groups) SiOH-groups with stronger hydrogen bonding

* v_1: symmetrical stretching; v_2: symmetrical bending; v_3: antisymmetric stretching; v_{OH}: OH-stretching; δ: SiOH-bending (in plane).

stronger hydrogen bonds) (Langer & Flörke, 1974). The ~1.9 μm region is similarly characterized by two overlapping bands due to differences in hydrogen bonding. The higher energy (type-A) band at ~1.91 μm is attributed to isolated H_2O molecules encased in the silica structure, and the broader, lower energy (type-B) band at ~1.96 μm is attributed to H_2O molecules in larger voids that are hydrogen-bonded to other H_2O molecules as in liquid water (Langer & Flörke, 1974). Similar to the ~2.2 μm behavior, the strength of the ~1.9 μm B band relative to the A band tends to increase from non-crystalline to partially ordered opal (Langer & Flörke, 1974).

The ~1.4 μm region exhibits fine structure as well, due to the H_2O combination band near ~1.46 μm and the OH overtone near ~1.41 μm (Table 4). A weaker H_2O combination band near ~1.36 μm can add structure to this region as well. Another weak band that appears near ~1.8 μm has been assigned to an O-H stretching combination band (Kats 1962), but it is likely due to a combination of an O-H stretch and H-O-H bend and O-H libration (Table 4). Fine structure in the lower-wavelength bands (near ~0.95 μm and ~1.14 μm) has previously not been examined in as much detail. In the visible region, the presence of substitutional or interstitial components other than Si, or exposure to heat or ionizing radiation can also give rise to additional absorption features (e.g., Rossman 1994).

From this brief overview, it is evident that silica-rich materials yield a variety of OH, H_2O, and SiOH absorption bands that can potentially provide clues to both formation and environmental conditions. Conditions such as desiccation and freezing (Aines et al., 1984) should have variable effects on Vis-NIR reflectance spectra. For example, the loss of readily removed H_2O molecules should change the structure of the ~1.9 and ~2.2 μm regions; specifically, band depths in the 1.94 and 2.26 μm (type-B) regions should decrease relative to those near 1.91 and 2.21 μm (type-A). Upon freezing, spectral changes are expected in all of the H_2O-associated absorption bands except for the ~1.91 and ~2.22 μm features; i.e., all of the H_2O bands where H_2O is present in clusters significantly large to form an ice-like structure (Aines et al., 1984). It is worth noting that the first few layers of H_2O molecules in contact with silanol groups may not be capable of forming an ice-like structure at lower temperatures due

to strong hydrogen bonding with the underlying silanol groups (e.g., Kekulawala et al.,1981).

3. Experimental procedures

In order to address the effects of various sample properties on reflectance spectra of H_2O /OH-bearing silica-rich materials, we measured the Vis-NIR spectra of a wide range of naturally-occurring and synthetic samples, including four cherts, four glasses, seven opals, seven quartzes, eleven naturally occurring silica sinters, and three synthetic silica materials. Tables 5-7 provide details on the samples and experimental measurements used in this study.

3.1 Collection of laboratory spectra

Reflectance spectra were measured with an Analytical Spectral Devices FieldSpec Pro HR spectrometer at the University of Winnipeg HOSERLab (Cloutis et al., 2006). This instrument acquires data from 0.35 to 2.5 μm, with a spectral resolution of between 2 nm and 7 nm. The data are internally resampled by the instrument, which ultimately produces data at 1 nm intervals. All spectra were measured at a viewing geometry of i=30° and e=0°. Incident light was provided by an in-house 50W quartz-tungsten-halogen collimated light source. Sample spectra were measured relative to a Spectralon® standard and corrected for minor (<2%) irregularities in its absolute reflectance. The spectra were also corrected for small occasional offsets at 1000 nm and 1830 nm where detector changeovers occur (Cloutis et al., 2008a). The offsets are due to the fact that different fibers in the spectrometer's

fiber optic bundle have overlapping, but not identical, fields of view. These offsets are minor and do not affect the spectral interpretations. In every case, 1000 spectra of the dark current, standard, and sample were acquired, to provide sufficient signal to noise for subsequent interpretation.

Each sample was crushed by hand and dry sieved to several grain sizes (provided in Table 5). For direct comparison with the Pancam observations of nodular outcrops in Gusev Crater (Rice et al., 2010), spectra of natural sinters were also acquired on whole-rock samples (i.e., not crushed and sieved). For these rocks, which have large surface texture variations, the distance between the sample and the spectrometer can vary slightly depending on the specific spot analyzed. This distance varied during the pressure-controlled (*Section 3.4*) experiments as well, as the sample surface can drop during dehydration and desiccation (Cloutis et al., 2008a). Because the sample-spectrometer distance can affect absolute reflectance, we analyzed all of our results as scaled reflectance. All spectra were normalized to unity at a featureless wavelength position of 1.6 μm for glasses and 1.25 μm for all other samples.

All samples were characterized by X-ray fluorescence (XRF), and H_2O contents (wt. % H_2O) were measured as the weight losses upon heating the samples to 950^o C for 1 hour, as described by Mertzman (2000). During our sample preparation (grinding and sieving), we observed no physical change in any of the hydrated silica materials that would indicate a change in H_2O content. The compositions and H_2O contents of each sample are provided in Table 8. The samples were structurally characterized using X-ray diffraction (XRD) to ascertain the phases present in the samples (specifically to categorize the silica samples as predominantly opal-A, opal-

Table 5. Details of samples used in this study for grain size analyses

Material	Sample ID	Origin	Grain Sizes (µm)
CHERTS			
chert	SIL105	Mississippian Period, Boone Formation, Jefferson City, MO, USA; from Minerals Unlimited	<45 ; 90-1000
chert	SIL208	Lake Magadi, Kenya; from Robin Renaut, University of Saskatchewan	<45 ; 90-1000
flint	SIL103	White Cliffs of Dover, England; from Minerals Unlimited	<45 ; 90-1000
novaculite	SIL112	Hot Springs, Garland Co., Arkansas, USA; from Minerals Unlimited	<45 ; 90-1000
GLASSES			
Dakhleh glass	SIL131	Dakhleh, ROM #M48024	<45 ; 90-1000
Darwin glass	IMP001	Mount Darwin, Tasmania, Australia; from S. Atkinson	<45 ; 90-1000
lechatelierite	SIL130	Libya; ROM #M26692	<45 ; 90-1000
tektite	TEK001	Indochina; from Houston Museum	<45 ; 90-1000
tektite	TEK003	Australia; from Collector's Marketing Corp.	<45 ; 90-1000
OPALS			
opal-CT	OPA001	locality unknown, U. Winnipeg Dept. of Geography	<45 ; <250; 90-1000
opal-CT	OPA002c	locality unknown, U. Winnipeg Dept. of Geography	<45 ; <250; 90-1000
opal-CT	OPA002r	locality unknown, U. Winnipeg Dept. of Geography	<45 ; <250; 90-1000
opal-CT	OPA002o	locality unknown, U. Winnipeg Dept. of Geography	<45 ; <250; 90-1000
opal-CT	OPA002y	locality unknown, U. Winnipeg Dept. of Geography	<45 ; <250; 90-1000
opal-A	SIL115	Coober Pedy, Australia; from Bill Buhay	<45 ; 90-1000
opal-CT	SIL106	North Edwards, Kramer Hills, Kern Co., CA, USA; from Minerals Unlimited	<45 ; 90-1000
QUARTZ AND CRITOBALITE			
amethyst	QUA108	locality unknown; from Mineral Society of Manitoba	<45 ; 90-1000
chalcedony	SIL113	near El Sueco, Chihuahua, Mexico; from Minerals Unlimited	<45 ; 90-1000
chrysoprase	SIL108	Minas Gerais, Brazil; from Minerals Unlimited	<45 ; 90-1000
cristobalite	SIL114	Glass Mountain, near Coso, Inyo Co., CA, USA; from Minerals Unlimited	<45 ; 90-1000
quartz	QUA101	locality unknown; from National Museum of Nature, Ottawa	<45 ; 90-1000
rose quartz	QUA107	locality unknown; from Mineral Society of Manitoba	<45 ; 90-1000
sulfur-bearing quartz	SIL104	Kalahari Desert, Namibia; from Minerals Unlimited	<45 ; 90-1000
SINTERS			
effluent sinter	SIL206	Wairakei geothermal power station, New Zealand; from Robin Renaut, University of Saskatchewan #NZ092	<45 ; 90-1000 ; whole rock
laminated sinter	SIL302	Rotokawa, New Zealand; from Bruce Mountain	<45 ; 90-1000 ; whole rock
silica sand	SIL303	West of Champagne Pool, Waiotapu, New Zealand; from Bruce Mountain	<45 ; 90-1000 ; whole rock
sinter	ICE102	Reykjanes Gullbringusýsla, Iceland; from Bjarni Gautason	<45 ; 90-1000 ; whole rock
sinter	Geysir-02	Geysir, Iceland; collected by M. Rice	<45 ; 90-1000 ; whole rock
sinter	Geysir-04	Geysir, Iceland; collected by M. Rice	<45 ; 90-1000 ; whole rock
sinter	SIL200	Wairakei, New Zealand; from Robin Renaut, University of Saskatchewan #NZ007	<45 ; 90-1000 ; whole rock
sinter	SIL201	Wairakei, New Zealand; from Robin Renaut, University of Saskatchewan #NZ042	<45 ; 90-1000 ; whole rock
sinter	SIL203	Wairakei, New Zealand; from Robin Renaut, University of Saskatchewan #NZ028	<45 ; 90-1000 ; whole rock
silica residue on rhyolite	SIL306	Rotokawa, New Zealand; from Bruce Mountain	<45 ; 90-1000 ; whole rock
SYNTHETIC SILICA			
silicic acid	SIL002	synthetic; from Alfa Aesar stock #33270, lot #H03S028; CAS #7699-41-4	<45 ; unsorted
silica gel	SGE001	synthetic; from Guangyi Food Additive Co. Ltd.	<250 ; 250-1000
humidified silca gel	SGE001	synthetic; from Guangyi Food Additive Co. Ltd.	<90 ; <1000

Table 6. Details of samples used in this study for temperature analyses

Material	Sample ID	Grain Size (μm)	Temperatures	Notes on Spectra Acquisition
milky quartz	MIS015	<250	-13 °C 23 °C	
quartz	QUA103	<250	-13 °C 23 °C	
quartz vein	MSI-A2-05	<250	-13 °C 23 °C	
opal	OPA001	<250	-13 °C 23 °C	
opal	OPA002c	<250	-13 °C 23 °C	
humidified silica gel[b]	SGE001	<90	-13 °C 23 °C	0, 3, 5, and 7 minutes after exposure to 23 °C
humidified silica gel[c]	SGE001	<1mm	-13 °C 23 °C	0, 1, 3, 5, 8, 17, 19, 38, and 62 minutes after exposure to 23 °C
silica gel	SGE001	<250	-13 °C 23 °C	0, 2, 10, and 17 minutes after exposure to 23 °C
silica gel	SGE001	250-1000	-13 °C 23 °C	0, 2, 11, and 16 minutes after exposure to 23 °C
fresh snow	fresh snow	unsorted	-10 °C	Every 30s for 5 minutes after seconds after exposure to 23 °C
silica gel slurry[a]	SGE002	unsorted	-13 °C	0, 3, 5, 9, and 20 minutes after exposure to 23 °C
quartz slurry[a]	QUA101	<45	-13 °C	0, 3, 5, 20, and 22 minutes after exposure to 23 °C

[a] Saturated with water prior to freezing
[b] Exposed to 100% relative humidity for 1 hour
[c] Exposed to 100% relative humidity for 22 hour

CT or opal-C) and to verify the phases determined by XRF; results are given in Table 9. XRD data were measured using a Bruker D-8 diffractometer with CuKa radiation and an energy-dispersive SolX detector. Data were generally measured on sample powders mounted in 1-mm deep cavities, collecting data from 2 to 70° 2θ with 0.02° steps. Phase identification was accomplished by comparison with standard patterns measured in our laboratory and with data in the ICDD database. Diffraction patterns for opal-A, opal-C, and opal-CT were distinguished as described by Jones and Segnit (1971) and Guthrie et al. (1995)

3.2 Temperature-controlled experiments

We acquired spectra of eleven high-silica samples at room temperature and after being frozen to -13° C (the lowest temperature setting of the available laboratory

Table 7. Details of samples used in this study for humidity analyses

Material	Sample ID	Grain Size (µm)	RH Conditions	Notes on Spectra Acquisition
opal	OPA002c	<250	ambient	
			100%[a]	
quartz	QUA101	<45	ambient	
			bathed in water	0, 2, 5, 7 minutes after sample preparation
quartz vein	MSI-A2-05	<250	ambient	
			100%[a]	
silica gel	SGE002	unsorted	ambient	
			100%[a]	1, 4 min after sample preparation

[a] Exposed to 100% relative humidity for 1 hour

freezer). For comparison with a pure H_2O spectrum, we also included observations of freshly fallen snow (-10^o C). For select samples, after freezing to -13^o C, spectra were taken immediately after removal from the freezer and periodically thereafter, until the sample equilibrated with room temperature (23^o C); details of these experimental runs are given in Table 6. Spectra were acquired at both ambient and cold temperatures because liquid H_2O and H_2O ice exhibit different spectral properties (*e.g.,* Irvine and Pollack, 1968; Table 2). By freezing and thawing the samples while performing continuous spectral measurements, we can trace the spectral changes accompanying the phase changes. These observations also allowed us to acquire spectra over a range of temperatures consistent with temperatures measured at the CCD during Pancam observations of silica-rich targets on Mars (-21.5 ^{o} C to 8.9^o C; Rice et al., 2010).

3.3 Humidity-controlled experiments

To examine the effects of humidity on the spectra of silica-rich materials, we collected spectra of an opal, quartz, and synthetic silica sample in ambient conditions

and after exposure to a water-saturated atmosphere (100% relative humidity) for one hour. With our driest quartz sample (QUA101, 0.2 wt.% H_2O), we created a quartz "slurry" by bathing the sample in water and observed the spectra as the "slurry" desiccated after sample preparation. Table 7 provides details of these experiments.

3.4 Pressure-controlled experiments

One silica sinter sample (SIL203 ground and sieved to <45 μm) was exposed to simulated Mars surface conditions using the University of Winnipeg's miniature Mars Environment (mini-ME) chamber (Craig et al., 2001). A constant atmospheric pressure was maintained at 660 Pa CO_2 (0.0065 atm; 5 Torr), and the sample temperature was restricted to a maximum close to maximum surface temperatures on present-day Mars (~20^o C), as described by Cloutis et al. (2008a) and Rice et al. (2011). We note that the partial pressure of water vapor (pH_2O) was not monitored during the experiment; however we maintained a continuous flow of dry carbon dioxide to ensure that any liberated H_2O was carried away from the sample. Reflectance spectra of the sample were acquired through a 10 mm-thick sapphire window every few days for the first month, and then on a roughly monthly basis (19 spectra acquired over 442 days of exposure). After the sample appeared to have equilibrated to 5 Torr CO_2 conditions (i.e., when spectral differences between measurements were no longer observed), we irradiated the sample with UV light using two 25 W deuterium lamps. The incident UV radiation during one day of laboratory irradiation was determined to equal approximately one decade of UV flux as presently

Table 8a-b. Composition of samples used in this study

	CHERTS				GLASSES				
Wt. %	chert SIL105	chert SIL208	flint SIL103	novaculite SIL112	Dakhleh glass SIL131	lechatelierite SIL130	Darwin glass IMP001	tektite TEK001	tektite TEK003
SiO_2	99.01	96.81	97.88	99.17	56.22	97.44	84.25	71.47	72.54
TiO_2	0.02	0.01	0.01	0.04	0.71	0.16	0.58	0.80	0.78
Al_2O_3	0.99	1.29	1.29	0.55	11.29	2.01	8.41	14.15	13.29
(Fe_2O_3)[a]	(0.00)	(0.01)	(0.00)	(0.08)	(4.59)	(0.15)	(2.90)	(5.60)	(5.20)
FeO					0.56	0.12	2.38	4.67	4.10
Fe_2O_3					4.69	0.02	0.25	0.42	0.64
MnO	0.002	0.004	0.002	0.002	0.11	0.01	0.03	0.11	0.09
MgO	0.04	0.04	0.04	0.04	4.96	0.08	1.40	2.22	2.12
CaO	0.08	1.24	0.16	0.06	17.11	0.09	0.28	1.98	2.08
Na_2O	0.03	0.29	0.04	0.04	2.29	0.02	0.13	1.37	1.54
K_2O	0.05	0.06	0.02	0.03	1.78	0.02	1.92	2.57	2.51
P_2O_5	0.02	0.03	0.03	0.02	0.52	0.04	0.09	0.07	0.08
SO_3	0.03	0.08	0.03	0.03					
Total[b]	100.27	99.86	99.50	100.06	100.24	100.01	99.72	99.83	99.77
LOI[c] (wt. %)	0.68	2.6	1.41	0.24	2.81	0.5		0.50	0.71
Sr (ppm)	53	146	29	39	454	44	33	146	146
Zr (ppm)	18	62	18	47	339	167	418	271	303
V (ppm)	22	22	23	28	133	31	70	110	108
Co (ppm)	<1	<1	2	<1	2	<2	3	4	4
Cr (ppm)	<1	1	<1	<1	88	14	193	71	76
Cu (ppm)	715	3730	690	425					
Ni (ppm)	<1	25	<1	30					

	SYNTHETIC SILICA			OPALS				
Wt. %	silica gel SGE001	silica gel SGE002	silicic acid SIL002	OPA001	OPA002r	OPA002y	SIL115	SIL106
SiO_2	98.57	98.99	98.43	98.60	98.71	98.64	96.40	64.26
TiO_2	0.08	0.02	0.03	0.02	0.01	0.01	0.01	0.01
Al_2O_3	0.27	0.08	0.53	0.52	0.39	0.40	1.94	0.16
(Fe_2O_3)[a]	(0.15)	(0.01)	(0.00)	(0.01)	(0.32)	(0.19)	(0.10)	(0.04)
MnO	0.00	0.00	0.00	0.00	0.00	0.00	0.00	0.00
MgO	0.06	0.05	0.05	0.07	0.06	0.08	0.08	0.60
CaO	0.13	0.14	0.07	0.13	0.11	0.09	0.52	35.11
Na_2O	0.30	0.08	0.30	0.04	0.03	0.02	0.27	0.13
K_2O	0.01	0.00	0.00	0.02	0.00	0.01	0.18	0.00
P_2O_5	0.02	0.02	0.01	0.02	0.02	0.03	0.02	0.03
SO_3	0.08	0.04	0.03	0.03	0.03	0.03	0.06	0.03
Total[b]	99.67	99.43	99.45	99.46	99.68	99.5	99.58	100.37
LOI[c] (wt. %)	16.69	5.7	59.71	3.67	3.22	3.09	6.37	22.17
Sr (ppm)	39	26	26	29	28	25	223	408
Zr (ppm)	165	89	65	13	16	16	163	18
V (ppm)	31	23	29	34	32	33	27	32
Co (ppm)	>1	2	<1	<1	<1	<1	<1	<1
Cr (ppm)	8	<1	<1	<1	10	<1	<1	1
Cu (ppm)	155	15	110	535	465	335	385	230
Ni (ppm)	<1	<1	<1	<1	10	<1	<1	<1

[a] All Fe expressed as Fe_2O_3

[b] Total expressed on a volatile-free basis and with all Fe as Fe_2O_3.

[c] Loss on ignition after heating sample to 950°C; a measure of the H_2O content of the sample.

Table 8c-d. Composition of samples used in this study

QUARTZ AND CRISTOBALITE

Wt. %	amethyst QUA108	chalcedony SIL113	chrysoprase SIL108	cristobalite SIL114	milky quartz MIS015	quartz QUA101	quartz QUA103	rose quartz QUA107	sulfur-bearing quartz SIL104
SiO_2	99.13	98.31	95.04	75.78	99.29	98.98	98.60	98.12	98.85
TiO_2	0.01	0.01	0.01	0.07	0.01	0.02	0.01	0.01	0.01
Al_2O_3	0.50	1.21	0.22	12.71	0.43	0.95	0.43	1.02	0.86
(Fe_2O_3)[a]	0.19	(0.01)	(0.61)	(1.17)	0.08	(0.24)	0.00	0.12	(0.04)
MnO	0.003	0.00	0.02	0.03	0.003	0.01	0.002	0.006	0.00
MgO	0.05	0.05	2.78	0.15	0.06	0.03	0.04	0.10	0.06
CaO	0.05	0.17	0.11	0.58	0.04	0.04	0.04	0.13	0.05
Na_2O	0.03	0.17	0.10	5.05	0.03	0.01	0.04	0.05	0.08
K_2O	0.01	0.01	0.00	3.56	0.00	0.00	0.00	0.00	0.01
P_2O_5	0.01	0.03	0.02	0.08	0.02	0.02	0.01	0.01	0.02
SO_3		0.08	0.02	0.08		0.02			0.03
Total[b]	99.981	100.05	98.93	99.26	99.963	100.32	99.172	99.566	100.01
LOI[c] (wt. %)	0.34	1.06	2.82	0.68	0.12	0.2	0.17	0.46	0.3
Sr (ppm)	15	30	26	39	8	27	10	12	24
Zr (ppm)	15	59	15	144	12	18	10	10	15
V (ppm)	10	28	31	29	8	26	5	5	27
Co (ppm)	<1	<1	20	<1	<1	<1	<1	<1	5
Cr (ppm)	33	<1	125	<1	25	1	<2	154	<1
Cu (ppm)		415	415	510		365			440
Ni (ppm)	<5	<1	10200	<1	<5	<1	<5	<5	<1

SINTERS

Wt. %	SIL206	SIL302	SIL303	ICE102	Geysir-02	Geysir-04	SIL200	SIL201	SIL203	SIL306
SiO_2	95.89	94.22	97.62	99.30	97.72	82.54	96.69	96.93	96.13	98.51
TiO_2	0.01	0.17	0.44	0.01	0.06	2.34	0.04	0.12	0.03	0.59
Al_2O_3	0.84	5.01	1.37	0.07	0.99	12.25	1.56	1.36	0.68	0.79
(Fe_2O_3)[a]	(1.50)	(0.19)	(0.00)	0.31	(0.30)	(1.55)	(0.35)	(0.39)	(0.18)	(0.00)
FeO						0.54				
Fe_2O_3						0.95				
MnO	0.03	0.00	0.00	0.003	0.01	0.02	0.03	0.02	0.01	0.00
MgO	0.17	0.09	0.05	0.06	0.17	0.36	0.12	0.13	0.15	0.05
CaO	0.29	0.07	0.07	0.08	0.53	0.30	0.59	0.24	1.91	0.06
Na_2O	0.42	0.10	0.04	0.07	0.27	0.32	0.10	0.20	0.48	0.03
K_2O	0.24	0.11	0.02	0.00	0.18	0.11	0.21	0.08	0.41	0.03
P_2O_5	0.03	0.06	0.01	0.01	0.02	0.03	0.02	0.02	0.02	0.02
SO_3	0.07	0.03	0.07		0.04	0.03	0.06	0.08	0.08	0.05
Total[b]	99.49	100.05	99.69	99.913	100.29	99.85	99.77	99.57	100.08	100.13
LOI[c] (wt. %)	6.4	11.09	1.91	5.82	6.46	8.55	7.82	4.88	9.69	1.83
Sr (ppm)	43	140	39	13	46	37	66	37	79	38
Zr (ppm)	27	110	299	10	19	128	26	49	23	306
V (ppm)	24	40	28	5	33	131	34	28	38	28
Co (ppm)	<1	<1	<1	<1	<1	5	<1	<1	<1	<1
Cr (ppm)	<1	10	2	35	<1	225	<1	<1	<1	1
Cu (ppm)	1950	665	2050		375	310	520	560	685	490
Ni (ppm)	<1	<1	<1	<5	<1	<1	<1	<1	<1	<1

[a] All Fe expressed as Fe_2O_3

[b] Total expressed on a volatile-free basis and with all Fe as Fe_2O_3.

[c] Loss on ignition after heating sample to 950°C; a measure of the H_2O content of the sample.

Table 9. Sample mineralogy from XRD

Material	Sample ID	Mineralogy	Notes
CHERTS			
chert	SIL105	quartz	
chert	SIL208	quartz, calcite, sulfur	
flint	SIL103	quartz, microcrystalline	
novaculite	SIL112	well-ordered quartz	
GLASSES			
Dakhleh glass	SIL131	amorphous silica, augite,	trace calcite
Darwin glass	IMP001	opal-A	
lechatelierite	SIL130	opal-A	
tektite	TEK001	opal-A	
tektite	TEK003	opal-A	
OPALS			
opal	OPA001	opal-CT	
opal	OPA002c	opal-CT	All OPA002 specimens
opal	OPA002r	opal-CT	are from the same hand
opal	OPA002o	opal-CT	sample
opal	OPA002y	opal-CT	
opal	SIL115	opal-A	
opal	SIL106	opal-CT + quartz + major calcite	
QUARTZ			
amethyst	QUA108	quartz	
chalcedony	SIL113	microcrystalline quartz	
chrysoprase	SIL108	microcrystalline quartz, serpentine	trace smectite
cristobalite	SIL114	cristobalite, sanidine	
quartz	QUA101	quartz, well-ordered	
rose quartz	QUA107	quartz	
sulfur-bearing quartz	SIL104	quartz	sulfur not detected
SINTERS			
effluent sinter	SIL206	opal-A	
laminated sinter	SIL302	opal-A, sulfur, kaolinite	
silica sand	SIL303	almost pure quartz + minor cristobalite	
sinter	ICE102	opal-CT	
sinter	Geysir-02	opal-A	
sinter	Geysir-04	kaolinite + quartz + opal-CT	
sinter	SIL200	opal-A	
sinter	SIL201	opal-A	
sinter	SIL203	opal-A	
silica residue	SIL306	major quartz + opal-C	
SYNTHETIC SILICA			
silicic acid	SIL002	opal-A	
silica gel	SGE001	opal-A	
humidified silca gel	SGE001	n/a.	

Table 10. Shoulder positions used for the continuum lines for band depth analysis

Band (μm)	Left Shoulder (μm)	Right Shoulder (μm)
~0.95	0.800	1.050
~1.14	1.050	1.250
~1.41	1.250	1.700
~1.78	1.700	1.820
~1.91	1.820	2.125
~2.21	2.125	2.350

received on the martian surface (Cloutis et al., 2008a). UV irradiation began on day 259 of the experiment and ended on day 319.

3.5 Analysis of spectral features

Spectral analysis involved measuring the positions and depths of the H_2O, OH and SiOH bands expected for hydrated silica materials given in Table 4. Band depth D_B was measured by constructing a straight line continuum on either side of the absorption feature of interest and measuring the depth as described by Eq. (32) of Clark and Roush (1984):

$$D_B \equiv \frac{R_C - R_B}{R_C} \tag{1}$$

where R_B is the reflectance at the band center and R_C is the reflectance of the continuum at the band center (Figure 3). The band center in Eq. (1) was defined as the wavelength of the minimum reflectance of the feature of interest after dividing out the continuum line. The left and right "shoulder" wavelength positions used for each continuum line are shown graphically in Figure 3. The same shoulder wavelengths were used for each spectrum (Table 10) and were chosen as locations that are

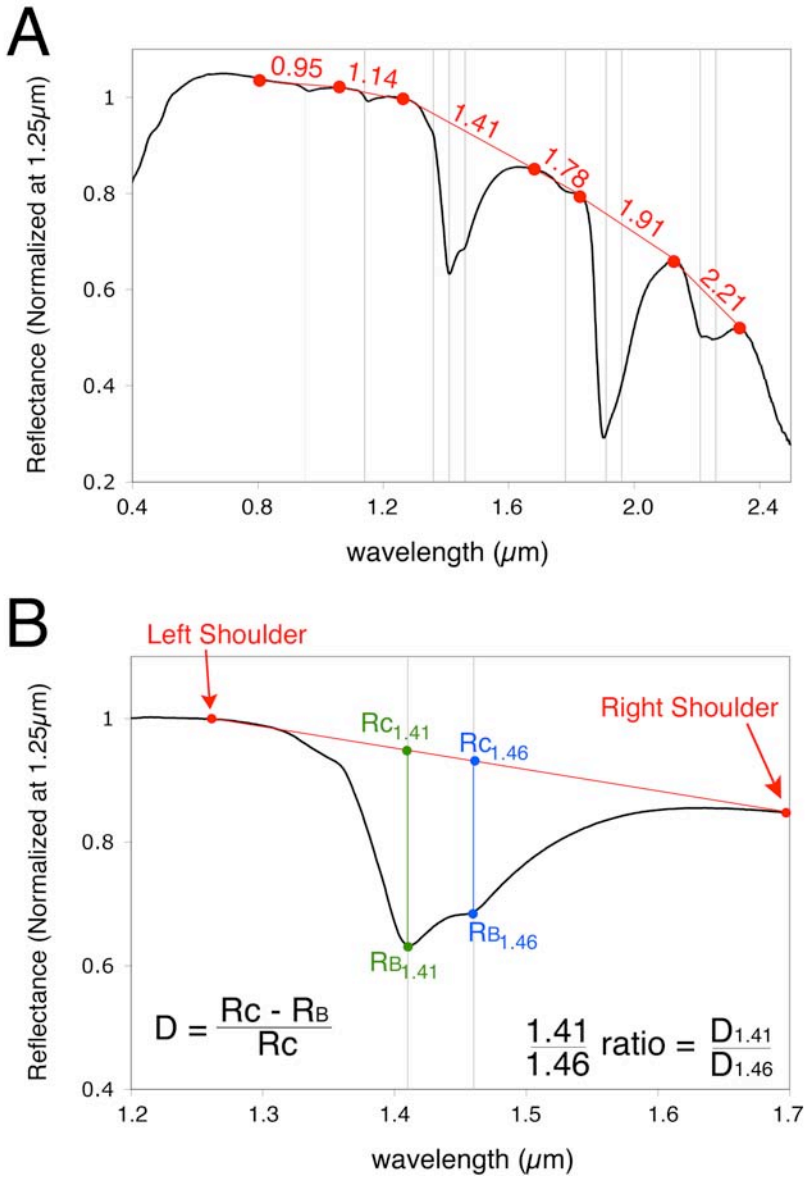

Figure 3. Illustrations of spectral parameters used in the band analyses for this study: (a) Straight-line continua (red) drawn for H_2O, OH and SiOH absorption bands in the spectrum of opal (black; sample OPA001; grain size 90-1000 μm). Shoulder positions (red dots) are provided in Table 10; (b) Band depth measurements for the 1.41 and 1.46 μm features. Equations for the band depth *D* and the 1.41/1.46 ratio are provided.

unaffected by the bands of interest in all of our sample spectra.

Because we were unable to resolve the minima and depths of the lower energy features of overlapping bands in the ~1.4, ~1.9, and ~2.2 μm regions, we measured the ratio of the depths at 1.41 and 1.46 μm, 1.91 and 1.96 μm, and 2.21 and 2.26 μm, respectively. These ratios provide us with the relative strengths of the type-A and type-B bands that comprise the ~1.9 and ~2.2 μm features (similarly to the "relative band areas" measured by Langer and Flörke, 1974), and the relative strengths of the OH and H_2O features in the ~1.4 μm region (Figure 3). These ratios also allow us to quantify the symmetry of the broad features in these wavelength regions; for example, a perfectly symmetrical feature with two overlapping H_2O bands at 1.91 and 1.96 μm will have a 1.91/1.96 band depth ratio of 1.0.

To approximate the ratio of SiOH to H_2O in the samples, we also calculate the ratio of the ~2.2 μm band depth to the ~1.9 μm band depth for each spectrum. Langer and Flörke (1974) quantitatively determined the abundances of SiOH and H_2O in opals from the integral absorbances of the ~2.2 μm and ~1.9 μm features, respectively, in transmission spectra. We used the ~2.2/1.9 μm band depth ratio as a crude estimate of the relative abundances of these different types of hydration that can be inferred directly from the reflectance spectra.

To simulate Pancam observations of these minerals on the martian surface, we multiplied the high-resolution laboratory spectra by the solar spectrum, convolved the resulting radiance spectra to the 13 Pancam spectral bands (Bell et al., 2003), and divided the radiance value at each band by the solar spectrum convolved to that band. We also performed the same procedure for the nine Mastcam spectral bands (Ghaemi,

2009; Malin et al., 2010) in order to address the implications of our results for future observations by the Mars Science Laboratory (MSL) rover.

4. Results

We have measured the positions and depths of each band listed in Table 4 (all Vis-NIR H_2O, OH, and SiOH features) for each spectrum acquired, and our results are provided in Tables 11-14. The formation environments of the samples used for this study, and descriptions of their silica structure, are provided in Table 3. Details of spectral features observed under varying conditions (grain size, temperature, humidity and pressure) are discussed below.

4.1 Grain-size experiments

The results of our band position and depth analyses for the samples listed in Table 5 for varying grain sizes are provided in Table 11 and discussed in detail below.

4.1.1 Cherts

In all fine-grained (<45 μm) chert samples (Figure 4), the features at wavelengths below ~1.4 μm are unresolvable, and those at longer wavelengths are very weak (band depths < 0.04; Table 11a). At coarser grain sizes (90-1000 μm), however, the ~1.4, ~1.9 and ~2.2 μm features are prominent in the chert and flint spectra (SIL105, SIL208 and SIL103 (chert and flint). The novaculite (SIL112) spectrum is largely featureless, except for the shallow, narrow bands at 1.41 and 2.21

Table 11a. Band position and depth analyses for chert, glass and opal samples at all grain sizes. All spectra were acquired at standard temperature and pressure.

Material	Sample ID	Grain Size (µm)	~ 0.95 µm Position	~ 0.95 µm Depth	~ 1.14 µm Position	~ 1.14 µm Depth	~ 1.41 µm Position	~ 1.41 µm Depth	1.41/1.46 Ratio	~ 1.78 µm Position	~ 1.78 µm Depth	~ 1.91 µm Position	~ 1.91 µm Depth	1.91/1.96 Ratio	~ 2.21 µm Position	~ 2.21 µm Depth	2.21/2.26 Ratio	~2.2/1.9 Ratio
chert	SIL105	<45	0.917	0.000	1.150	0.004	1.418	0.009	1.592	1.820	0.000	1.925	0.016	1.280	2.198	0.010	1.919	0.636
		90-1000	0.918	-0.002	1.150	0.000	1.419	0.040	1.313	1.820	0.000	1.917	0.118	1.336	2.205	0.048	1.886	0.405
chert	SIL208	<45	0.925	0.022	1.150	0.008	1.406	0.010	2.156	1.815	0.001	1.912	0.015	1.226	2.202	0.014	1.545	0.932
		90-1000	0.968	0.003	1.152	0.008	1.418	0.113	1.590	1.772	0.000	1.903	0.265	1.607	2.217	0.105	1.205	0.396
flint	SIL103	<45	0.942	0.000	1.146	0.003	1.418	0.018	1.776	1.820	0.000	1.912	0.038	1.715	2.213	0.034	1.232	0.890
		90-1000	0.981	-0.012	1.156	-0.003	1.420	0.232	1.285	1.789	0.001	1.912	0.409	1.430	2.219	0.275	1.123	0.673
novaculite	SIL112	<45	0.989	-0.001	1.145	0.002	1.372	0.005	6.864	1.819	0.000	1.943	0.006	0.720	2.204	0.003	-5.344	0.526
		90-1000	0.916	0.006	1.100	0.000	1.414	0.024	-14.490	1.820	0.000	1.934	0.009	1.398	2.206	0.031	-5.999	3.312
Dakhleh glass	SIL131	<45	0.980	0.006	1.103	0.006	1.373	-0.008	0.653	1.816	0.000	1.936	0.019	0.928	2.194	0.004	1.678	0.203
		90-1000	0.947	0.007	1.152	0.003	1.414	0.022	3.255	1.760	0.003	1.932	0.061	1.129	2.171	-0.011	0.736	-0.183
Darwin glass	IMP001	<45	0.949	0.012	1.150	0.016	1.373	-0.018	0.764	1.803	0.001	1.949	0.013	0.779	2.200	0.006	3.117	0.476
		90-1000	0.952	0.053	1.150	0.043	1.370	-0.051	0.792	1.762	0.003	1.940	0.021	0.860	2.209	0.015	1.996	0.737
lechatelierite	SIL130	<45	0.955	0.000	1.163	0.004	1.386	0.005	0.025	1.816	0.000	1.943	0.009	0.887	2.211	0.032	1.695	3.706
		90-1000	0.945	0.008	1.148	0.011	1.384	0.021	0.275	1.762	0.001	1.932	0.008	0.901	2.210	0.129	1.722	15.648
tektite	TEK001	<45	0.938	0.031	1.145	0.025	1.370	-0.027	0.813	1.762	0.001	1.936	0.013	0.810	2.194	0.002	-0.122	0.162
		90-1000	0.922	0.131	1.159	0.051	1.370	-0.045	0.736	1.757	0.004	1.945	0.034	0.883	2.211	0.009	4.035	0.278
tektite	TEK003	<45	0.945	0.024	1.152	0.022	1.373	-0.022	0.815	1.762	0.001	1.950	0.011	0.843	2.229	0.002	0.171	0.188
		90-1000	0.939	0.112	1.158	0.057	1.370	-0.049	0.789	1.778	0.003	1.932	0.032	0.797	2.233	0.008	0.834	0.258
opal	OPA001c	<45	0.968	0.000	1.150	0.004	1.410	0.044	1.544	1.780	0.001	1.901	0.141	1.638	2.215	0.036	1.308	0.252
		<250	0.963	0.000	1.150	0.007	1.409	0.127	1.659	1.778	0.001	1.901	0.284	1.689	2.209	0.167	1.240	0.271
		90-1000	0.961	0.013	1.152	0.018	1.411	0.331	1.271	1.777	0.012	1.903	0.618	1.337	2.216	0.092	1.424	0.324
opal	OPA002c	<45	0.919	0.019	1.154	0.005	1.409	0.029	1.649	1.820	0.000	1.901	0.099	1.784	2.209	0.027	1.616	0.274
		<250	0.980	-0.006	1.150	0.007	1.410	0.125	1.343	1.776	0.002	1.903	0.304	1.465	2.213	0.151	1.229	0.253
		90-1000	0.960	0.016	1.152	0.017	1.411	0.308	1.229	1.780	0.011	1.903	0.596	1.322	2.213	0.079	1.268	0.260
opal	OPA002r	<45	0.914	0.014	1.150	0.004	1.407	0.035	1.624	1.820	0.000	1.901	0.104	1.678	2.211	0.038	1.523	0.367
		<250	0.913	0.023	1.150	-0.002	1.409	0.101	1.372	1.774	0.001	1.901	0.245	1.462	2.213	0.171	1.214	0.317
		90-1000	0.936	0.041	1.150	0.005	1.409	0.276	1.242	1.780	0.008	1.901	0.538	1.329	2.213	0.076	1.170	0.309
opal	OPA002o	<45	0.941	0.006	1.147	0.003	1.407	0.029	1.746	1.820	0.000	1.901	0.102	1.689	2.210	0.040	1.551	0.392
		<250	0.949	0.015	1.150	0.003	1.411	0.138	1.221	1.775	0.003	1.903	0.301	1.365	2.213	0.166	1.307	0.338
		90-1000	0.936	0.033	1.150	0.003	1.409	0.249	1.233	1.781	0.006	1.901	0.492	1.353	2.212	0.073	1.199	0.243
opal	OPA002y	<45	0.946	0.007	1.150	0.003	1.408	0.048	1.565	1.820	0.000	1.901	0.133	1.653	2.211	0.050	1.395	0.378
		<250	0.960	0.005	1.150	0.006	1.411	0.132	1.186	1.776	0.003	1.903	0.296	1.338	2.215	0.145	1.330	0.336
		90-1000	0.957	0.014	1.150	0.008	1.409	0.217	1.237	1.780	0.005	1.901	0.432	1.364	2.211	0.068	1.183	0.229
opal	SIL115	<45	0.963	0.003	1.150	0.007	1.410	0.116	1.702	1.820	0.000	1.901	0.290	1.797	2.213	0.062	1.343	0.216
		90-1000	0.962	0.023	1.152	0.037	1.411	0.481	1.317	1.780	0.012	1.903	0.753	1.315	2.215	0.175	1.199	0.232
opal	SIL106	<45	0.923	0.001	1.154	0.003	1.411	0.021	1.322	1.820	0.000	1.907	0.067	1.518	2.192	0.007	12.158	0.108
		90-1000	0.959	0.003	1.152	0.009	1.418	0.182	1.090	1.779	0.005	1.907	0.375	1.276	2.211	0.031	2.139	0.082

Table 11b. Band position and depth analyses for grain size experiments, continued (quartz and sinter samples).

Material	Sample ID	Grain Size (µm)	~ 0.95 µm Position	~ 0.95 µm Depth	~ 1.14 µm Position	~ 1.14 µm Depth	~ 1.41 µm Position	~ 1.41 µm Depth	1.41/1.46 Ratio	~ 1.78 µm Position	~ 1.78 µm Depth	~ 1.91 µm Position	~ 1.91 µm Depth	1.91/1.96 Ratio	~ 2.21 µm Position	~ 2.21 µm Depth	2.21/2.26 Ratio	~2.2/1.9 Ratio
amethyst	QUA108	<45	0.945	0.000	1.107	0.004	1.378	0.005	3.429	1.820	0.000	1.945	0.007	0.994	2.170	0.002	2.416	0.342
		90-1000	0.948	0.011	1.100	0.002	1.425	0.008	1.382	1.818	0.000	1.925	0.048	1.134	2.204	0.007	2.319	0.142
chalcedony	SIL113	<45	0.969	0.002	1.160	0.004	1.418	0.014	1.810	1.818	0.000	1.912	0.035	1.547	2.211	0.021	1.516	0.596
		90-1000	0.965	0.010	1.160	0.004	1.421	0.147	1.245	1.791	0.001	1.912	0.314	1.349	2.214	0.145	1.208	0.463
chrysoprase	SIL108	<45	0.989	-0.002	1.150	0.008	1.391	0.040	-10.113	1.820	0.000	1.909	0.042	1.808	2.200	0.036	1.267	0.853
		90-1000	0.990	-0.014	1.151	0.025	1.412	0.243	1.819	1.820	0.000	1.908	0.374	1.655	2.206	0.373	1.196	0.997
cristobalite	SIL114	<45	0.953	0.011	1.150	0.000	1.370	0.003	-1.429	1.820	0.000	1.943	0.007	1.235	2.202	0.003	47.049	0.419
		90-1000	0.944	0.035	1.171	-0.003	1.408	0.005	-3.300	1.820	0.000	1.901	0.030	1.588	2.208	0.006	3.603	0.209
quartz	QUA101	<45	0.924	0.000	1.150	0.003	1.370	0.006	2.485	1.819	0.000	1.945	0.003	0.159	2.194	0.003	-2.761	1.083
		90-1000	0.914	0.003	1.156	0.003	1.372	0.002	-2.117	1.819	0.000	1.936	0.006	1.169	2.202	0.005	-10.073	0.825
rose quartz	QUA107	<45	0.951	0.000	1.100	0.002	1.400	0.006	2.290	1.820	0.000	1.892	0.005	1.009	2.200	0.002	-0.321	0.377
		90-1000	0.949	-0.002	1.132	0.004	1.409	0.009	2.015	1.815	0.000	1.936	0.019	1.024	2.188	0.005	-0.275	0.262
S-bearing quartz	SIL104	<45	0.914	0.017	1.139	0.006	1.370	0.006	7.952	1.820	0.000	1.947	0.004	0.509	2.212	0.002	-6.962	0.673
		90-1000	0.910	0.003	1.152	0.004	1.438	0.018	0.845	1.820	0.000	1.929	0.077	1.017	2.196	-0.001	0.399	-0.016
effluent	SIL206	<45	0.951	0.003	1.150	0.002	1.405	0.030	2.966	1.820	0.000	1.897	0.081	2.381	2.209	0.068	1.398	0.839
sinter		90-1000	0.955	0.021	1.149	0.002	1.406	0.149	1.960	1.820	0.000	1.898	0.272	1.923	2.211	0.165	1.250	0.608
		whole	0.955	0.015	1.152	0.003	1.408	0.109	1.848	1.773	0.001	1.899	0.237	1.827	2.209	0.095	1.187	0.400
sinter	SIL302	<45	0.990	-0.006	1.107	0.000	1.413	0.024	158.666	1.820	0.000	1.897	0.039	3.213	2.206	0.091	2.210	2.323
		90-1000	0.990	-0.006	1.150	-0.002	1.413	0.079	6.463	1.820	0.000	1.898	0.146	2.554	2.206	0.185	2.065	1.267
		whole	0.955	0.000	1.150	0.002	1.414	0.080	3.374	1.820	0.000	1.899	0.135	2.095	2.206	0.118	2.432	0.877
silica sand	SIL303	<45	0.936	0.016	1.146	0.007	1.403	0.004	-3.303	1.820	0.000	1.899	0.012	1.495	2.216	0.011	1.595	0.896
		90-1000	0.990	-0.006	1.154	0.002	1.414	0.042	1.377	1.814	0.000	1.908	0.139	1.347	2.215	0.029	1.151	0.206
		whole	0.964	-0.007	1.162	0.000	1.420	0.064	1.194	1.772	0.001	1.914	0.180	1.297	2.213	0.021	1.126	0.116
sinter	ICE102	<45	0.962	0.002	1.152	0.005	1.427	0.084	1.000	1.781	0.002	1.918	0.232	1.285	2.212	0.001	-0.271	0.005
		90-1000	0.961	0.003	1.152	0.007	1.425	0.136	1.045	1.781	0.004	1.914	0.311	1.280	2.211	0.022	2.374	0.070
		whole	0.963	0.011	1.156	0.018	1.431	0.192	0.972	1.779	0.008	1.920	0.346	1.202	2.206	0.001	0.120	0.001
sinter	Geysir-02	<45	0.925	0.010	1.152	0.004	1.407	0.052	2.129	1.772	0.000	1.899	0.169	2.129	2.213	0.067	1.251	0.394
		90-1000	0.959	0.008	1.150	0.009	1.408	0.191	1.826	1.782	0.001	1.899	0.405	1.798	2.213	0.158	1.224	0.390
		whole	0.961	0.027	1.150	0.034	1.408	0.312	1.354	1.779	0.011	1.901	0.444	1.424	2.213	0.140	1.115	0.315
sinter	Geysir-04	<45	0.912	0.005	1.150	0.002	1.413	0.091	2.800	1.818	0.000	1.903	0.134	1.675	2.206	0.137	17.204	1.022
		90-1000	0.968	0.006	1.150	0.004	1.413	0.154	3.215	1.820	0.000	1.901	0.186	1.642	2.206	0.231	-213.77	1.243
		whole	0.968	0.019	1.162	0.030	1.446	0.529	0.930	1.781	0.038	1.923	0.725	1.058	2.206	0.034	0.120	0.048
sinter	SIL200	<45	0.961	0.000	1.150	0.003	1.407	0.080	2.305	1.820	0.000	1.899	0.193	2.172	2.209	0.104	1.399	0.396
		90-1000	0.962	0.002	1.150	0.009	1.408	0.222	1.933	1.793	0.000	1.899	0.417	1.867	2.209	0.228	1.323	0.244
		whole	0.961	0.015	1.152	0.019	1.411	0.358	1.451	1.780	0.010	1.901	0.553	1.430	2.209	0.197	1.246	-0.187
sinter	SIL201	<45	0.965	-0.002	1.150	0.002	1.405	0.044	2.851	1.820	0.000	1.898	0.126	2.267	2.209	0.077	1.406	0.539
		90-1000	0.962	-0.002	1.150	0.004	1.406	0.142	2.064	1.820	0.000	1.898	0.333	1.881	2.209	0.184	1.274	0.546
		whole	0.961	-0.004	1.150	0.004	1.406	0.167	1.806	1.780	0.001	1.898	0.346	1.709	2.211	0.174	1.238	0.355
sinter	SIL203	<45	0.962	-0.002	1.150	0.004	1.406	0.142	2.064	1.820	0.000	1.898	0.333	1.881	2.209	0.184	1.274	0.611
		90-1000	0.961	0.010	1.151	0.014	1.409	0.301	1.566	1.781	0.005	1.901	0.527	1.545	2.214	0.191	1.156	0.553
		whole	0.961	0.023	1.152	0.034	1.409	0.437	1.332	1.777	0.018	1.901	0.593	1.346	2.217	0.177	1.045	0.503
leached basalt	SIL306	<45	0.951	0.003	1.148	0.004	1.408	0.019	1.738	1.820	0.000	1.901	0.054	1.672	2.209	0.025	1.546	0.553
		90-1000	0.965	-0.001	1.150	0.005	1.409	0.113	1.364	1.770	0.000	1.901	0.262	1.423	2.211	0.100	1.374	0.362
		whole	0.955	-0.001	1.153	0.001	1.414	0.024	1.558	1.772	0.001	1.905	0.077	1.496	2.213	0.020	1.078	0.299

Table 11c. Band position and depth analyses for grain size experiments, continued (synthetic silica samples).

Material	Sample ID	Grain Size (µm)	~ 0.95 µm Position	~ 0.95 µm Depth	~ 1.14 µm Position	~ 1.14 µm Depth	~ 1.41 µm Position	~ 1.41 µm Depth	1.41/1.46 Ratio	~ 1.78 µm Position	~ 1.78 µm Depth	~ 1.91 µm Position	~ 1.91 µm Depth	1.91/1.96 Ratio	~ 2.21 µm Position	~ 2.21 µm Depth	2.21/2.26 Ratio	~2.2/1.9 Ratio
silicic acid	SIL002[b]	<45	0.961	0.013	1.152	0.013	1.409	0.164	1.234	1.780	0.005	1.899	0.337	1.491	2.250	0.072	0.841	0.212
		unsorted	0.966	0.021	1.157	0.032	1.435	0.307	0.960	1.776	0.015	1.916	0.553	1.149	2.248	-0.048	1.340	-0.087
silica gel	SGE001[c]	<250	0.963	0.021	1.152	0.029	1.411	0.401	1.229	1.776	0.017	1.901	0.624	1.356	2.246	0.242	0.935	0.388
		250-1000	0.963	0.073	1.152	0.097	1.412	0.720	1.105	1.778	0.050	1.903	0.821	1.162	2.246	0.400	0.940	0.486
humidified silica gel	SGE001	<90	0.962	0.009	1.150	0.014	1.409	0.261	1.347	1.778	0.009	1.901	0.473	1.497	2.225	0.206	1.011	0.435
		<1000	0.964	0.044	1.152	0.061	1.414	0.578	1.108	1.778	0.036	1.903	0.765	1.195	2.250	0.265	0.860	0.346

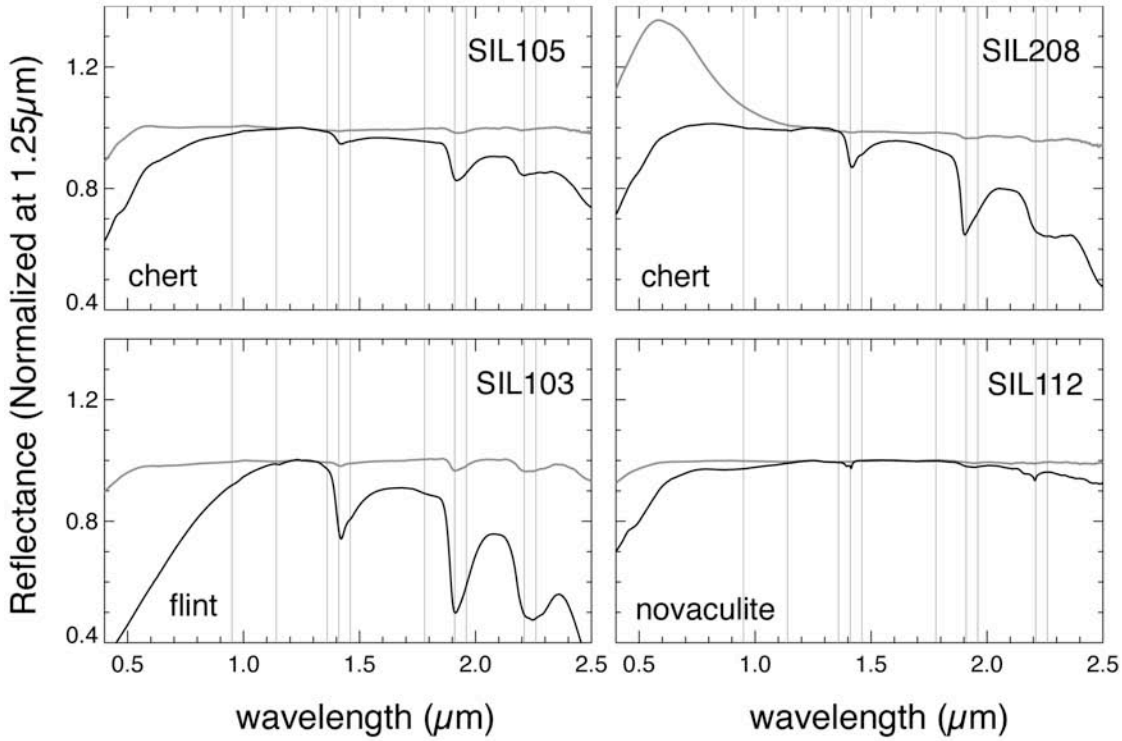

Figure 4. Scaled reflectance spectra (0.35-2.5 μm; normalized to 1 at 1.25 μm) of chert samples at varying grain sizes: 90-1000 μm (solid black line) and <45 μm (solid gray line). Sample information provided in Table 5.

μm. The absence of strong H_2O and OH features is likely due to the low H_2O content of the sample (~0.24 wt. % H_2O; Table 8a).

The ~1.4 μm region displays at least two partially overlapping absorption bands, near 1.41 and 1.46 μm, in spectra of the coarser-grained chert and flint samples. The shorter-wavelength band is assigned to the $2\nu_{OH}$ overtone, and the longer-wavelength band is associated with the H_2O $2\nu_2 + \nu_3$ combination/overtone (Table 4). The OH band (1.406-1.420 μm) is most prominent, with 1.41/1.46 band depth ratios between ~1.3 and ~1.6 (Table 11a). The ~1.9 μm feature is similarly wide, with overlapping absorption bands centered near 1.91 and 1.96 μm. The shorter-

wavelength type-A band (1.903-1.925 μm) is dominant, with 1.91/1.96 ratios ranging between ~1.3 and 1.6 (Table 11a). The behavior in the ~2.2 μm region varies considerably between samples, where two bands occur at ~2.21 and ~2.26 μm from the SiOH-bending and OH-stretch combination ($\delta + \nu_{OH}$). For example, the type-A band (centered at 2.198 μm) in the spectra of the chert sample SIL105 is predominant (2.21/2.26 band depth ratio ~1.9), whereas in the flint sample SIL103, the broad ~2.2 μm feature is nearly symmetrical (2.21/2.26 band depth ratio ~ 1.1).

The reflectance maximum near 0.6 μm in the spectra of the fine-grained SIL208 sample (Figure 4) is also observed in spectra the finest-grained (<45 μm) fraction of several other samples (e.g., SIL104 in Figure 7; SIL303 in Figure 8). Spectra of the finer-grained samples are, in general, less red than spectra of the coarser-grained samples. Shortward of~0.6 μm, the influence of the UV metal-oxygen charge transfers is observed (e.g., Cloutis et al., 2008b). The reflectance maximum near 0.6 μm may be due to the short wavelength wing of long wavelength absorptions coupled with the long wavelength wing of the UV charge-transfer.

4.1.2 Glasses

The most notable features in the spectra of glasses (Figure 5) are the broad bands centered near ~1.1 μm. All glass samples examined contain some iron (Table 8a), and the ~1.1 μm features likely correspond to spin-allowed crystal-field transitions in octahedrally coordinated Fe^{2+} ions, as has been observed in spectra of natural and synthetic glasses (e.g., Adams et al., 1974; Minnitti et al., 2007; Moroz et al., 2009). In our samples, this band is superimposed by a much broader Fe^{3+}

absorption that extends throughout the entire wavelength range observed (Moroz et al., 2009), and is responsible for the positive continuum slope in the near-infrared for samples IMP001, TEK001 and TEK003 (the impactites). The depths of these bands, and hence the slopes of the near-infrared continua, are greater in spectra of the coarse-grained (90-1000 μm) samples than in those of the finer-grained (<45 μm) fraction. The spectra of the impactites lack features due to H_2O and structural OH bound to metal cations, indicating an absence of hydrated or hydroxylated phases in these samples.

The spectra of lechatelierites (SIL131 and SIL130) do, however, exhibit weak OH and H_2O bands in spectra of the coarse-grained fraction (Figure 5). The ~1.4 μm region exhibits the narrow OH feature centered at 1.48-1.49 μm (Table 11a) but lacks the H_2O combination 1.46 μm that broadens this feature in the spectra of other silica-rich materials. The 1.41/1.46 band depth ratios for the lechatelierites are therefore large (up to ~3.3). The Dakhleh glass sample (SIL131) is hydrated (2.81 wt. % H_2O; Table 8a) and its spectra contain a broad and nearly symmetrical ~1.9 μm H_2O feature (1.91/1.96 band depth ratios between 0.9 and 1.1). A distinct band near 2.31 μm appears in the spectrum of coarse-grained Dakhleh glass, but no ~2.2 μm feature is observed; this sample contains a large fraction of calcium (17.11 wt. % CaO; Table 8a) and contains calcite (Table 9), and the longer-wavelength absorption is consistent with the calcite band between 2.30 and 2.35 μm (e.g., Clark et al., 1990). Dakhleh glass is known to contain calcite (Osinski et al., 2007). The spectra of the lechatelierite sample SIL130, however, exhibit the overlapping SiOH bands at 2.21 and 2.26 μm; the prominence of the ~2.21 feature (2.21/2.26 band depth ratio ~ 1.7) is consistent

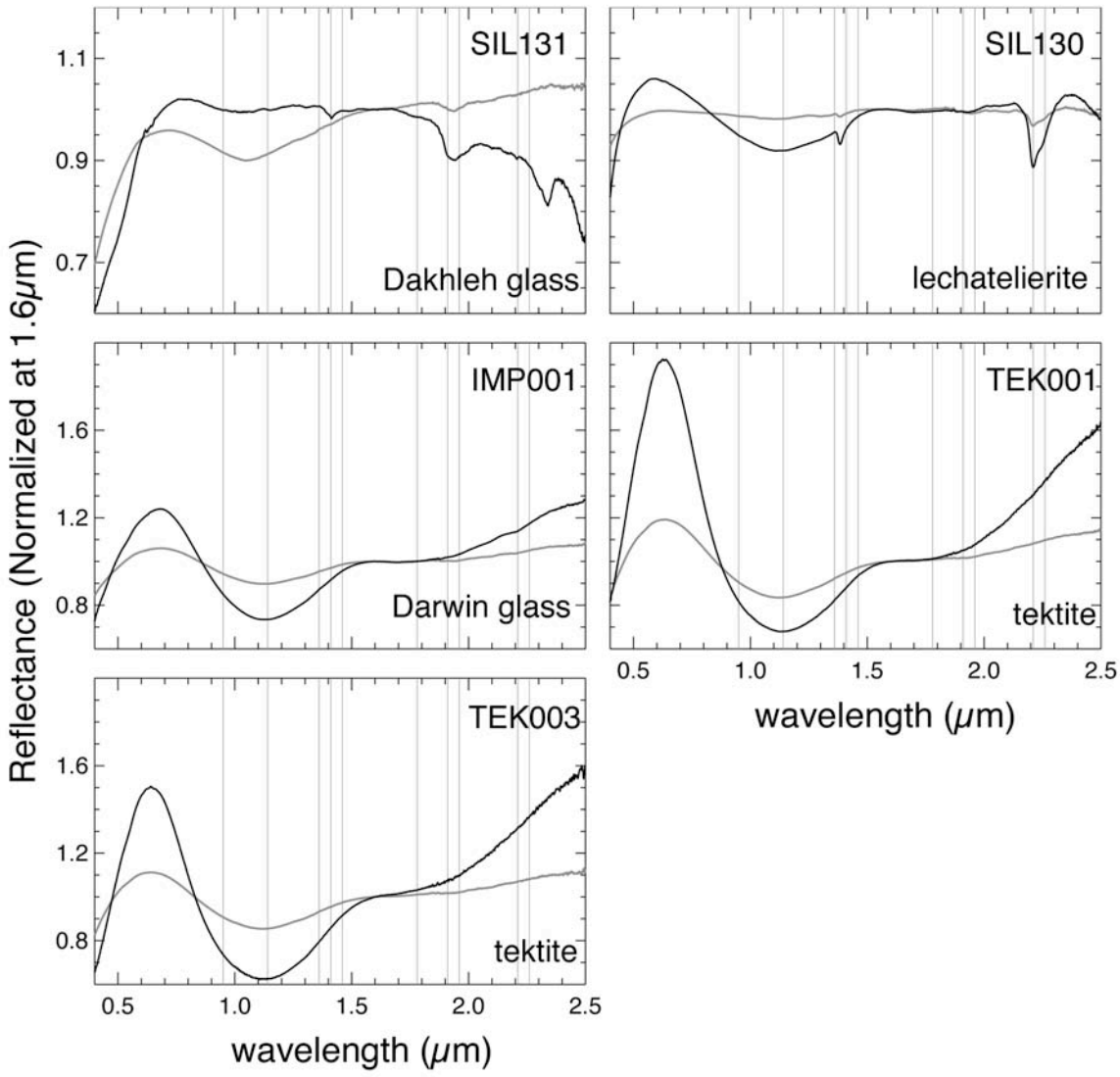

Figure 5. Scaled reflectance spectra (0.35-2.5 μm; normalized to 1 at 1.6 μm) of glass samples at varying grain sizes: 90-1000 μm (solid black line) and <45 μm (solid gray line). Sample information provided in Table 5.

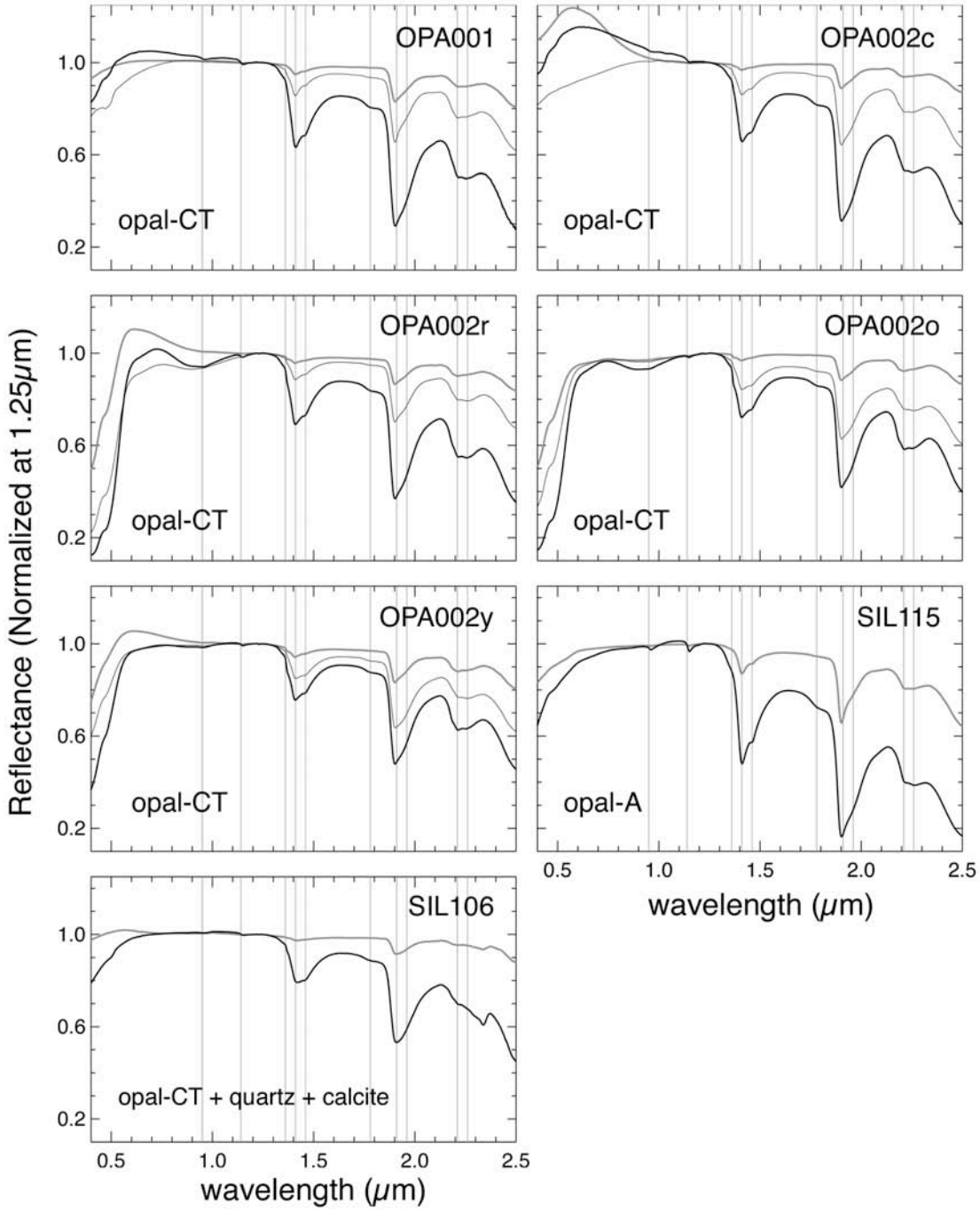

Figure 6. Scaled reflectance spectra (0.35-2.5 μm; normalized to 1 at 1.25 μm) of opal samples at varying grain sizes: 90-1000 μm (solid thick black line), <250 μm (solid thin black line) and <45 μm (solid gray line). The silica polymorph identified by XRD (Table 9) is provided for each sample. Sample information provided in Table 5.

with the spectra of impact glass from Haughton Crater measured by Craig et al. (2011).

4.1.3 Opals

The opal spectra shown in Figure 6 provide good illustrations of the characteristic spectral features of silica-rich materials. The ~1.4 μm region exhibits the two overlapping bands near 1.41 and 1.46 μm, and the separate minima of these features are resolvable in all spectra except those of SIL106. In the OPA002 spectra, the H_2O combination near ~1.36 μm contributes to the width and asymmetry of the ~1.4 μm feature, adding a shoulder to the short-wavelength limb of the band. The separate 1.91 and 1.96 μm H_2O features are not clearly resolvable in any opal spectrum, as they overlap to form a wide, asymmetric feature with a band minimum near 1.91 μm. Similarly, the 2.21 and 2.26 μm SiOH bands contribute to a single, wide, asymmetric feature with a band minimum near 2.21 μm; only in the spectra of the coarse-grained fraction (90-1000 μm) can the separate minima of the two features be resolved. For all bands, the depths decrease from the coarsest grain size (90-1000 μm) to the finest (<45 μm) by more than 50%. However, all band depths do not decrease uniformly; for most samples, the ratio of the ~2.2 μm band depth to ~1.9 μm band depth decreases with smaller grain sizes. This change may be due to the increased surface area at small grain sizes, which allows a larger fraction of molecular H_2O to become adsorbed onto silica surfaces. The variation may also be due in part to changes in volume versus surface scatter at different grain sizes.

The OPA002 spectra exhibit broad absorptions centered near 0.9 μm, likely due to the iron impurities that give the samples their yellow to reddish hues (these samples contain 0.19-0.32 wt. % Fe_2O_3). This band obscures the subtle ~0.95 μm H-$_2$O and/or OH feature in the spectra of these samples; however, the ~0.95 μm feature can be resolved in the spectra of coarse-grained OPA001 and SIL115 (band depths 0.013-0.023; Table 11a). The weak ~1.14 μm feature can also be resolved in the spectra of the coarse grained fraction of all samples (band depths 0.005-0.018). Sample SIL106 contains a large fraction of calcium (35.11 wt. % CaO), and calcite has been identified as a mineral phase by XRD (Table 9); thus a ~2.3 μm calcite band due to the $3\nu_3$ overtone of C-O is the likely cause of the band minimum near 2.31 μm.

4.1.4 Quartz and cristobalite

The spectra of macrocrystalline quartz varieties (amethyst, quartz, rose quartz and sulfur-bearing quartz; Figure 7) and high-temperature SiO_2 polymorphs (cristobalite) are largely featureless in Vis-NIR wavelengths, with the exception of absorptions in the visible range due to the impurities that give amethyst and rose quartz their characteristic violet and pink hues (see Table 3). The spectra of coarse-grained (90-1000 μm) amethyst, cristobalite, rose quartz and sulfur-bearing quartz also exhibit weak, broad absorptions centered near 1.91μm (band depths up to 0.077) that may be due to molecular H_2O adsorbed on the mineral grains and/or incorporated into the silica framework (e.g., Flörke et al., 2000); these samples do contain small amounts of H_2O (0.30-0.68 wt. % H_2O; Table 8c). In the spectra of the fine-grained (< 45 μm) fraction for these samples, however, these features are not observed. The

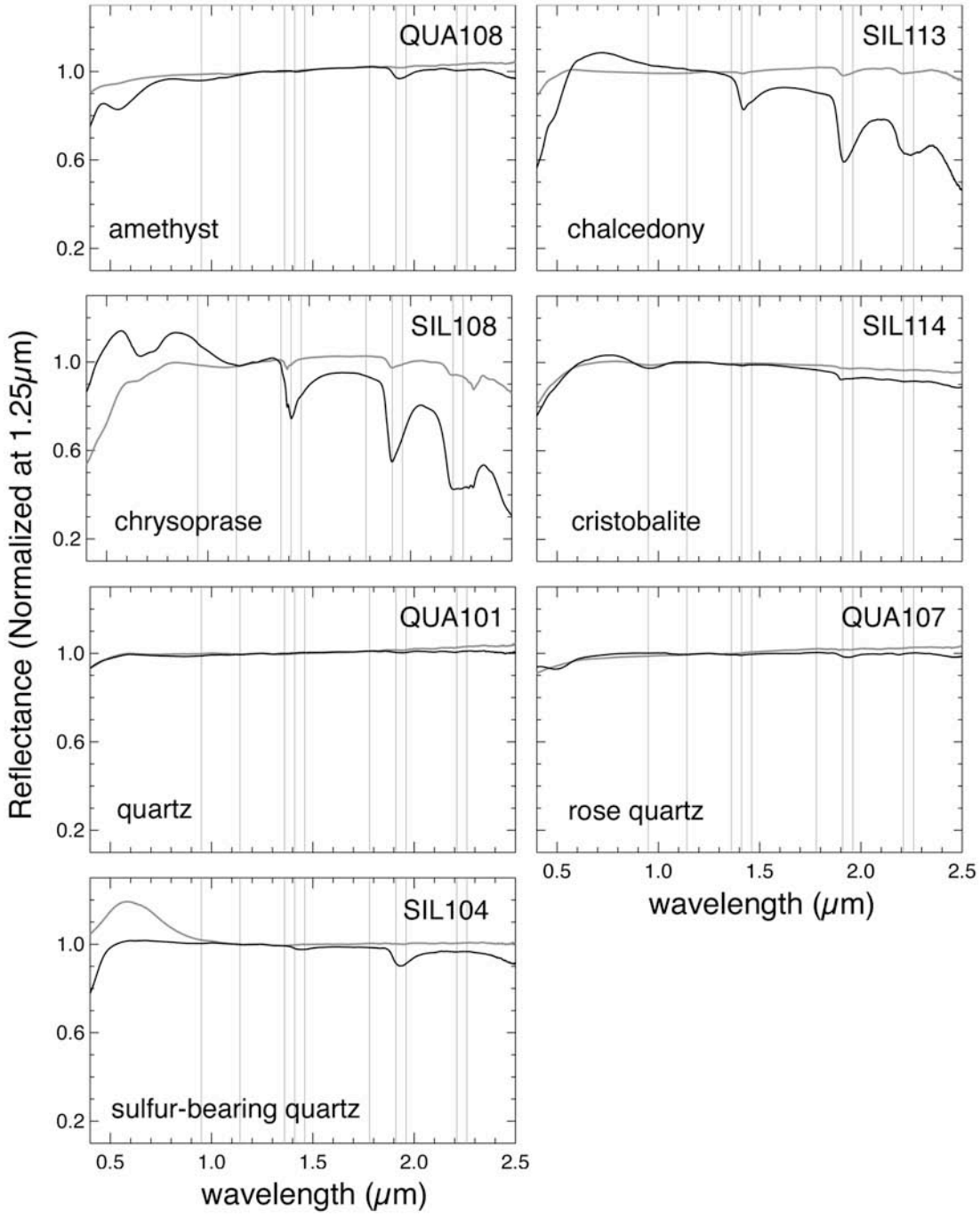

Figure 7. Scaled reflectance spectra (0.35-2.5 μm; normalized to 1 at 1.25 μm) of quartz and cristobalite samples at varying grain sizes: 90-1000 μm (solid black line) and <45 μm (solid gray line). Sample information provided in Table 5.

reflectance maximum near 0.6 μm in the spectrum of the fine-grained SIL104 (sulfur-bearing quartz) sample may be due to UV metal-oxygen charge transfers coupled with longer-wavelength absorptions (see *Section 4.1.1*) and/or the presence of sulfur; previous studies of the spectra of sulfur-coated volcanic glasses have shown similar reflectance maxima in their Vis-NIR spectra (e.g., Minitti et al., 2007).

The spectra of cryptocrystalline quartz varieties (chalcedony and chrysoprase; Figure 7) exhibit features in the ~1.4, 1.9 and 2.2 μm regions indicative of hydrated silica. These samples contain larger amounts of H_2O than macrocrystalline quartz (1.86-2.82 wt. % H_2O; Table 8c). Although the shape of the wide ~1.4 μm feature in the coarse-grained chalcedony (SIL113) spectrum indicates a significant contribution from the 1.46 μm H_2O combination band (1.41/1.46 band depth ratio = 1.81; Table 11b), the relative contribution of this band is less in the coarse-grained chrysoprase (SIL108) spectrum (where the 1.41 μm OH overtone dominates; 1.41/1.46 band depth ratio = 1.25). This discrepancy may be attributed to a greater fraction of the H_2O in the chrysoprase sample incorporated as SiOH (as opposed to molecular H_2O). The relative depths of the ~2.2 μm (SiOH) vs. ~1.9 μm (H_2O) features are consistent with this interpretation (the ~2.2/1.9 band depth ratio is nearly 1.0 for chrysoprase, but less than 0.5 for chalcedony).

The spectrum of coarse-grained chrysoprase (SIL108) exhibits a visible reflectance maximum near 0.55 μm due to a broad absorption centered at ~0.7 μm due to Ni^{2+} in octahedral co-ordination (Graetsch, 2011), and this is responsible for giving this mineral its distinctive green color. In the fine-grained (<45 μm) fraction, however, this band is no longer present. The impurities in the chrysoprase sample also

give rise to an absorption centered at 2.35 μm which broadens the long-wavelength edge of the ~2.2 μm SiOH band; this specific feature may be attributable to serpentine (the sample contains 2.78 wt. % MgO (Table 8c) and serpentine has been identified by XRD (Table 9)).

4.1.5 Sinters

The spectra of natural sinters exhibit a range of behaviors in the ~1.4, 1.9 and 2.2 μm regions (Figures 8-9). The separate 1.41 and 1.46 μm bands are clearly discernible in the spectra of coarse-grained (90-1000 nm) and whole-rock samples of opal-A sinters (SIL206, Geysir-02, SIL200, SIL201 and SIL203). In the sinters consisting of other silica polymorphs (opal-CT, opal-C, quartz and/or cristobalite), however, the ~1.4 μm feature is more symmetrical (the 1.41/1.46 band depth ratio is closer to 1.0; Table 11b), and the distinct minimum of the 1.46 μm band is not resolvable. The ~1.9 μm feature also appears highly asymmetrical in spectra for the opal-A samples, with a narrow band centered at 1.897-1.901 μm and a weaker 1.96 μm feature contributing to the band profile. The 1.91/1.96 band depth ratios for the spectra of the other silica polymorphs are lower, and the band profiles are wider and more symmetrical. We discuss possible correlations between these band behaviors and the specific silica polymorph (opal-A vs. opal-CT) further in *Section 6*.

The short-wavelength H_2O features at ~0.95 and 1.14 μm are seen in the spectra of some whole rock sinters (ICE102, Geysir-02, Geysir-04, SIL200 and SIL203); the near-infrared profiles of other H_2O-bearing whole rock sinters, however, are featureless. For all samples, these bands cannot be resolved for the fine-grained

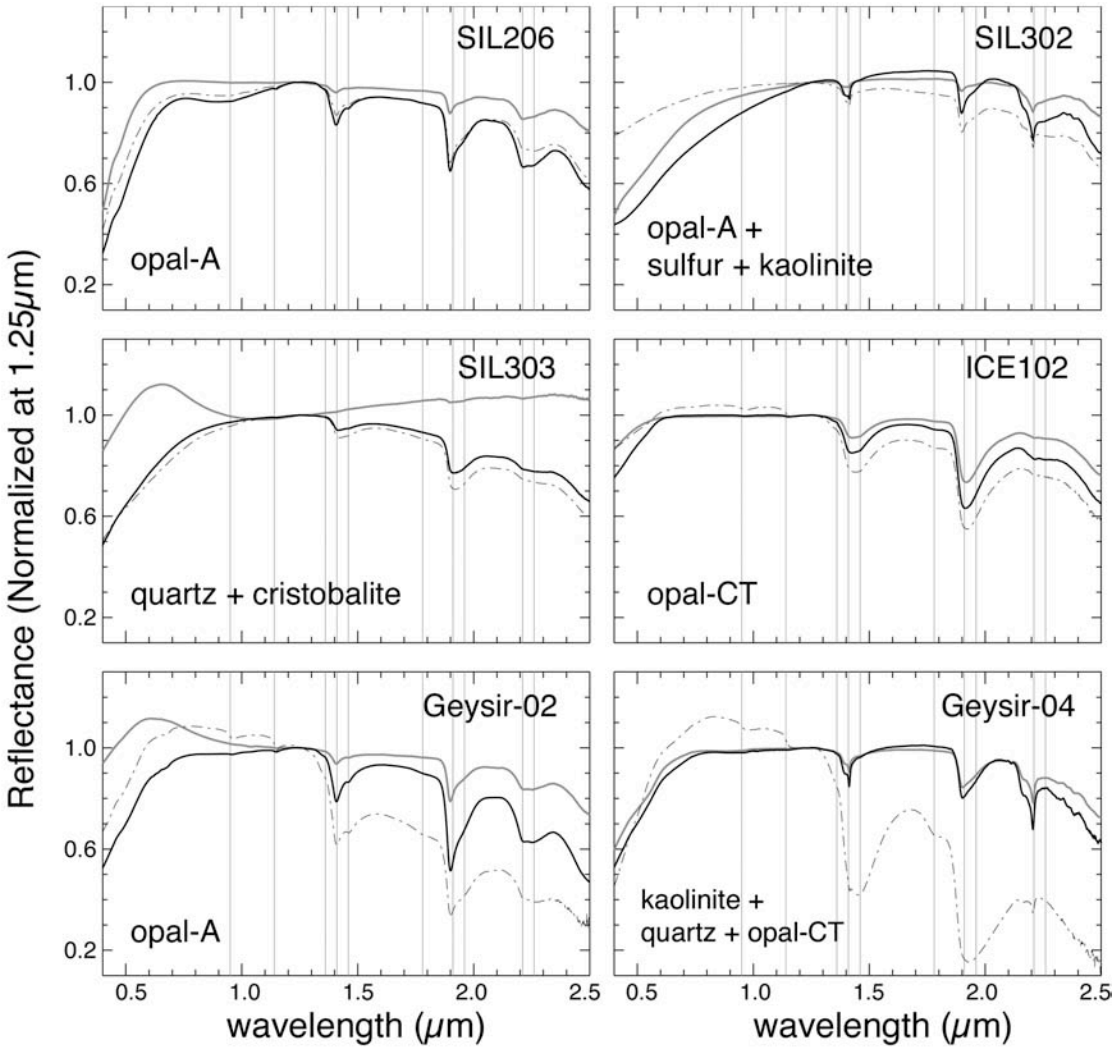

Figure 8. Scaled reflectance spectra (0.35-2.5 μm; normalized to 1 at 1.25 μm) of silica sinter samples (1 of 2) at varying grain sizes: whole rock (dashed line), 90-1000 μm (solid black line) and <45 μm (solid gray line). The silica type identified by XRD (Table 9) is provided for each sample. Sample information provided in Table 5.

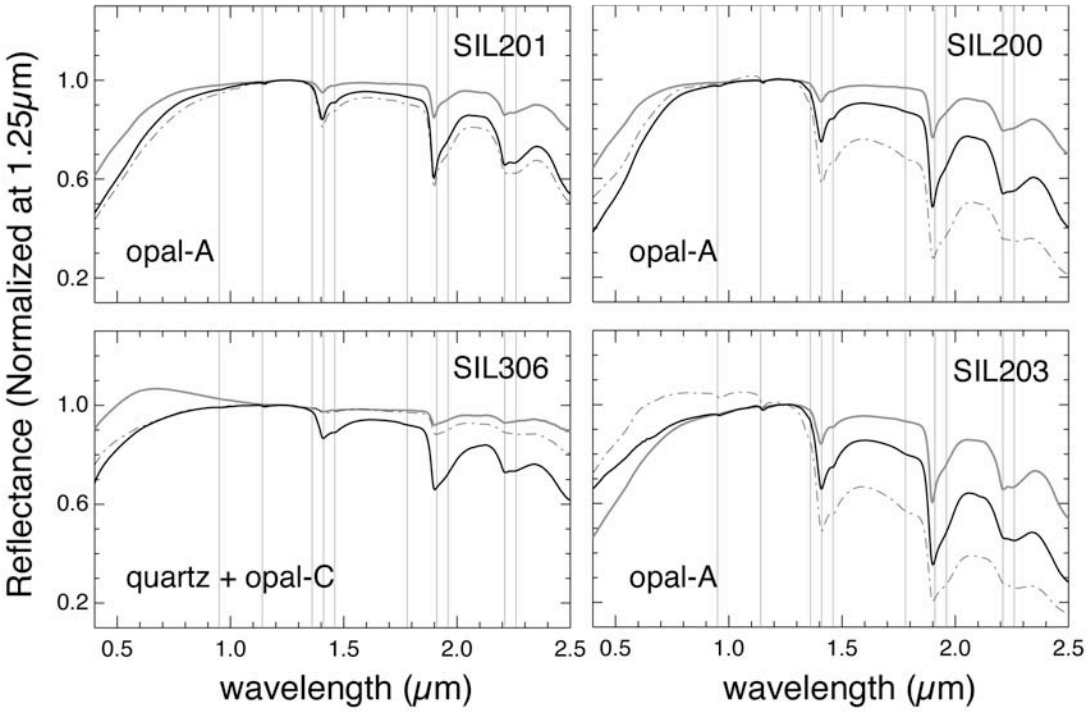

Figure 9. Scaled reflectance spectra (0.35-2.5 μm; normalized to 1 at 1.25 μm) of silica sinter samples (2 of 2) at varying grain sizes: whole rock (dashed line), 90-1000 μm (solid black line) and <45 μm (solid gray line). The silica type identified by XRD (Table 9) is provided for each sample. Sample information provided in Table 5.

(<45 μm) fraction. The band depths of most features decrease with grain size; however, as also observed in the spectra of opals, all bands do not decrease uniformly. For example, the depth of the ~2.2 μm feature is greater in the spectra of each sinter sample at 90-1000 μm than it is in the corresponding whole rock spectra (Table 11b). Consequently, the ratio of the depths of the bands in the ~2.2 and ~1.9 μm regions decreases with smaller grain sizes, possibly due to additional H_2O adsorbed onto silica surfaces at smaller grain sizes (because of increased surface area). In the spectrum of Geysir-04 as whole rock, the ~2.2 μm feature disappears almost entirely as the overall spectral profile becomes dominated by the ~3 μm H_2O band.

The sample Geysir-04 contains a large fraction of kaolinite (Table 9), and the anomalous shapes of the ~1.4 μm and 2.2 μm features (Figure 8) in its spectra can be attributed to the doublets that arise from Al-OH overtones in kaolinite (e.g., Clark et al., 1990). The spectra of sample SIL302 exhibit similar structures in the ~1.4 and 2.2 μm regions, which may also arise from kaolinite. The sample is enriched in Al_2O_3 (5.01 wt. %; Table 8d), and the XRD data confirm the presence of kaolinite in this SIL302. We note that we are unable to address the influence of moganite on the spectra of our silica samples for this study (moganite is a polymorph of SiO_2 that is present in most natural sinters but is not clearly distinguishable from quartz in XRD data) (Rodgers et al., 2002).

4.1.6 Synthetic Silica

Like the spectra of opals and natural sinters, the spectra of synthetic silica samples (silicic acid and silica gel; Figure 10) exhibit the characteristic overlapping features in the ~1.4, 1.9 and 2.2 μm regions. However, the spectra of synthetic samples are distinct in the prominence of the short-wavelength H_2O features at ~0.95 and 1.14 μm. The spectra of these materials exhibit the largest band depths for these features (up to 0.073 and 0.097, respectively; Table 11c) of any silica-rich material examined in this study. These spectra are also distinct in that they exhibit the weak ~1.78 μm feature (band depth up to 0.05 for coarse-grained silica gel). As observed in the spectra of all other materials, the depths of these features decrease significantly with decreasing grain size. Unlike for other materials, however, the shapes of individual bands can also change significantly with grain size. For example, the

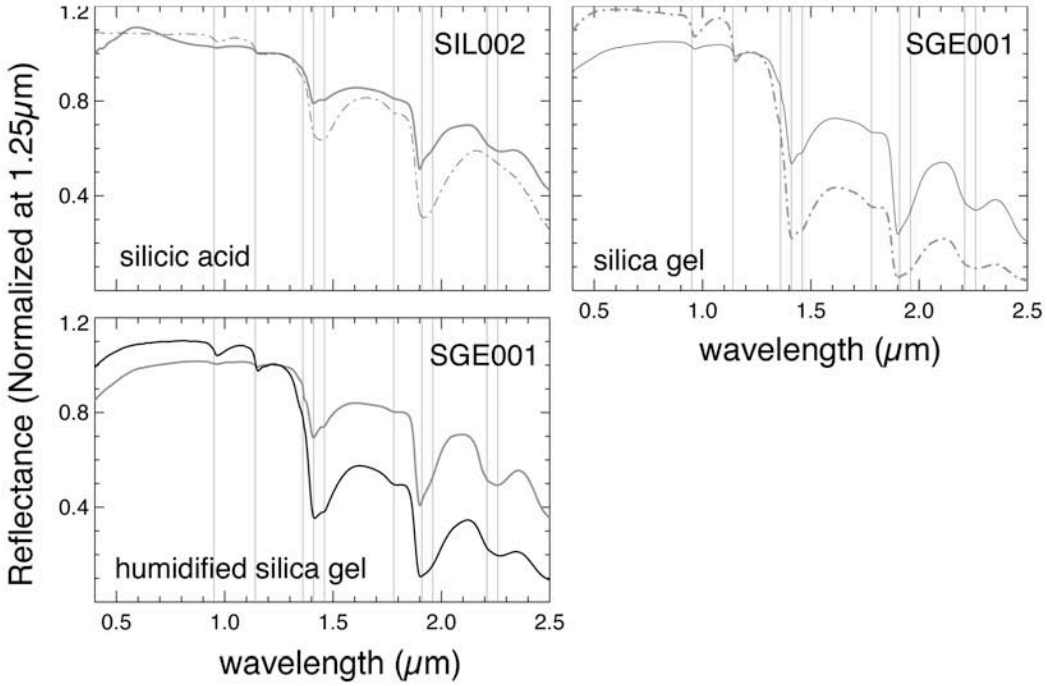

Figure 10. Scaled reflectance spectra (0.35-2.5 μm; normalized to 1 at 1.25 μm) of synthetic silica samples at varying grain sizes: (a) unsorted (dashed line) and <45 μm (solid gray line); (b) 250-1000 μm (solid gray line) and < 250 μm (dashed line); (c) <90 μm (solid gray line) and <1000 μm (solid black line). Sample information provided in Table 5.

symmetries and band minimum positions of the ~1.4 and 1.9 μm features are clearly different between the unsorted and <45 μm fractions of silicic acid (SIL002); this may be indicative of the same rearrangement of H_2O during the grinding and sieving process that leads to the increased ~2.2/1.9 band depth ratios in spectra of the finer-grained fractions. These relative differences may also be caused by band saturation in the course-grained samples.

4.2 Low-temperature experiments

Spectra of quartz samples (Figure 11), opals (Figure 12), silica gels (Figure

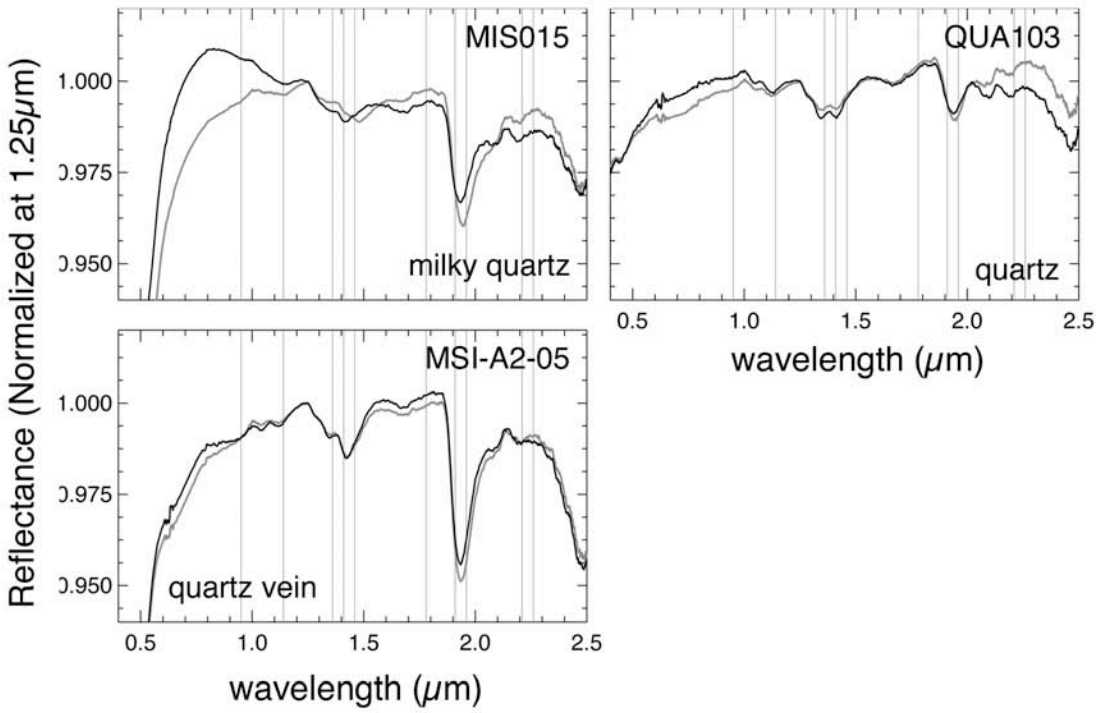

Figure 11. Scaled reflectance spectra (0.35-2.5 μm; normalized to 1 at 1.25 μm) of quartz samples at room temperature (black line) and at -13° C (gray line). All samples were crushed and sieved to <250 μm. (a) Milky quartz (MIS015); (b) Quartz (QUA103); (c) Quartz vein (MSI-A2-05). Details of the experimental runs are given in Table 6. Compositions of the samples are given in Table 8.

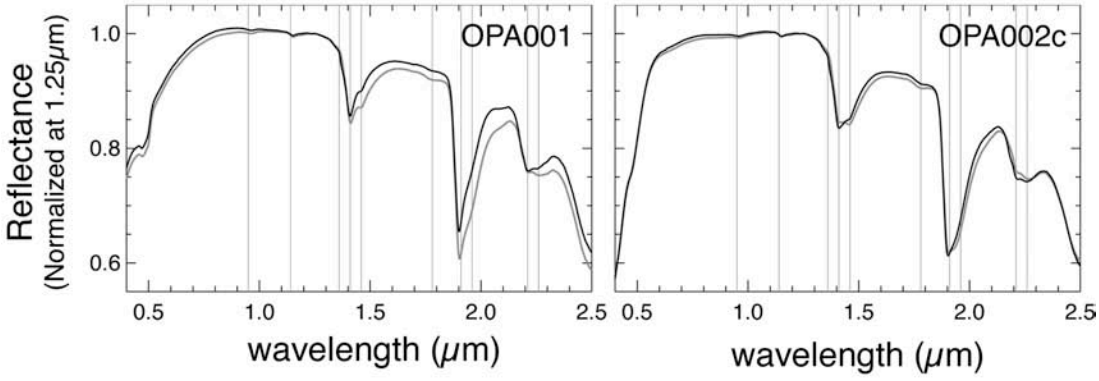

Figure 12. Scaled reflectance spectra (0.35-2.5 μm; normalized to 1 at 1.25 μm) of opal samples at room temperature (black line) and at -13° C (gray line). All samples were crushed and sieved to <250 μm. (a) OPA001; (b) OPA002c. Details of the experimental runs are given in Table 7. Compositions of the samples are given in Table 8.

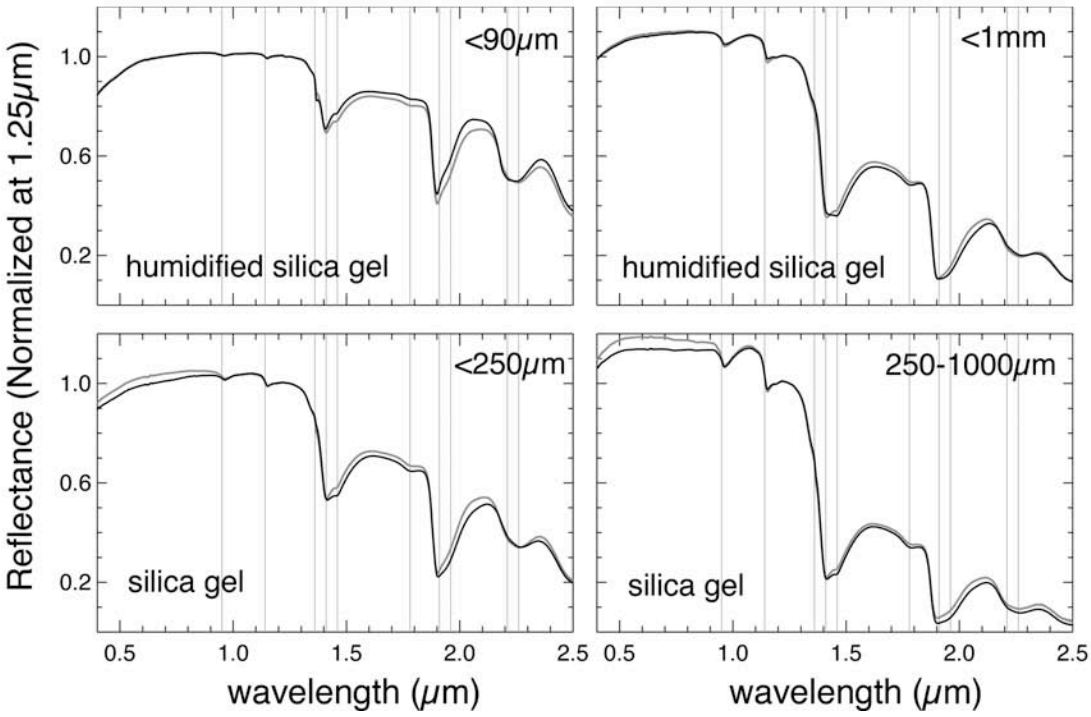

Figure 13. Scaled reflectance spectra (0.35-2.5 μm; normalized to 1 at 1.25 μm) of synthetic silica samples at room temperature (black line) and at -13° C (gray line). (a) <90μm fraction of humidified silica gel (SGE001); (b) < 1mm fraction of humidified silica gel (SGE001); (c) <250μm fraction of silica gel (SGE001); (d) 250-1000μm fraction of silica gel bathed in water (SGE002).

13), and water-saturated samples (Figure 14) were acquired at -13° C +20° C. Upon freezing, H_2O molecules in larger clusters can assume an ice-like structure, which has different band positions than liquid H_2O (Aines et al., 1984; Table 2). All spectral features move to longer wavelengths at lower temperature (-13° C) for all silica samples, by 0.01-0.24 μm (Table 12). The shapes of the ~1.4, 1.9 and 2.2 μm features also change when the samples are frozen. For example, the strength of the 1.96 μm B-type H_2O band increases relative to that of the 1.91 μm A band when opal samples are frozen (Figure 12), increasing the symmetry of the ~1.9 μm feature and thus

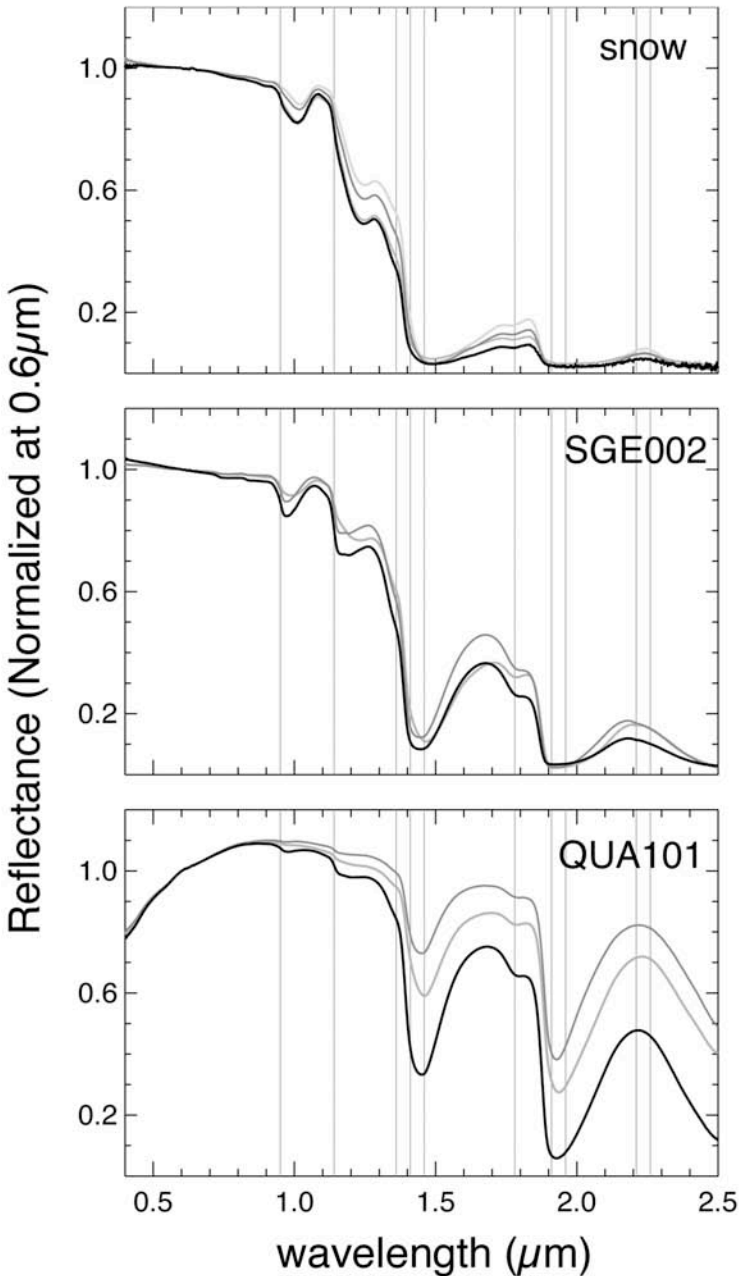

Figure 14. Scaled reflectance spectra (0.35-2.5 μm; normalized to 1 at 0.6 μm) of water-saturated samples when frozen (black line) and at times after exposure to +20° C (gray lines). (a) fresh snow observed at -10° C, and 30, 60 and 90 seconds after exposure to ambient temperature; (b) silica gel (SGE002; unsorted) bathed in water observed at -13° C, and 3, 5, 9 and 20 minutes after exposure to ambient temperature; (b) quartz (QUA101; <45 μm) bathed in water observed at -13° C, and 3 and 5 minutes after exposure to ambient temperature.

Table 12. Band position and depth analyses for temperature experiments.

Material	Sample ID	Temp. (°C)	~ 0.95 µm Position	~ 0.95 µm Depth	~ 1.14 µm Position	~ 1.14 µm Depth	~ 1.41 µm Position	~ 1.41 µm Depth	1.41/1.46 Ratio	~ 1.78 µm Position	~ 1.78 µm Depth	~ 1.91 µm Position	~ 1.91 µm Depth	1.91/1.96 Ratio	~ 2.21 µm Position	~ 2.21 µm Depth	2.21/2.26 Ratio	~2.2/1.9 Ratio
milky quartz	MIS015	-13	0.945	-0.001	1.154	0.002	1.438	0.008	0.812	1.819	0.000	1.943	0.034	0.806	2.200	0.000	0.224	0.005
		23	0.942	-0.001	1.139	0.002	1.414	0.008	1.456	1.820	0.000	1.934	0.024	1.093	2.186	0.003	-3.114	0.105
quartz	QUA103	-13	0.924	-0.001	1.124	0.003	1.416	0.008	2.015	1.820	0.000	1.949	0.015	0.759	2.189	0.001	0.086	0.072
		23	0.910	-0.001	1.131	0.003	1.414	0.010	2.157	1.820	0.000	1.940	0.011	1.026	2.188	0.002	-0.320	0.147
quartz vein	MSI-A2-05	-13	0.924	0.001	1.125	0.002	1.427	0.013	1.204	1.820	0.000	1.934	0.046	0.948	2.204	0.000	0.152	0.008
		23	0.927	0.001	1.131	0.002	1.424	0.015	1.291	1.820	0.000	1.934	0.043	1.041	2.188	0.001	0.001	0.026
opal	OPA001	-13	0.966	0.000	1.152	0.008	1.411	0.135	1.339	1.773	0.004	1.903	0.324	1.439	2.211	0.066	1.323	0.204
		23	0.963	0.000	1.150	0.007	1.409	0.127	1.659	1.778	0.001	1.901	0.284	1.689	2.209	0.092	1.424	0.324
opal	OPA002c	-13	0.958	0.005	1.152	0.006	1.413	0.130	1.029	1.776	0.006	1.905	0.299	1.215	2.215	0.052	1.039	0.174
		23	0.963	0.005	1.150	0.006	1.410	0.143	1.199	1.778	0.004	1.903	0.311	1.342	2.213	0.074	1.202	0.238
humidified silica gel[b]	SGE001	-13	0.962	0.009	1.150	0.014	1.409	0.261	1.347	1.778	0.009	1.901	0.473	1.497	2.225	0.206	1.011	0.435
		23	0.959	0.008	1.149	0.012	1.407	0.252	1.478	1.780	0.005	1.899	0.442	1.649	2.217	0.249	1.113	0.562
humidified silica gel[c]	SGE001	-13	0.964	0.044	1.152	0.061	1.414	0.578	1.108	1.778	0.036	1.903	0.765	1.195	2.250	0.265	0.860	0.346
		23	0.964	0.036	1.154	0.047	1.420	0.557	1.006	1.776	0.044	1.907	0.762	1.117	2.250	0.199	0.724	0.261
silica gel	SGE001	-13	0.963	0.021	1.152	0.029	1.411	0.401	1.229	1.776	0.017	1.901	0.624	1.356	2.246	0.242	0.935	0.388
		23	0.963	0.020	1.152	0.028	1.414	0.401	1.113	1.776	0.024	1.903	0.637	1.251	2.250	0.194	0.824	0.305
silica gel	SGE001	-13	0.963	0.073	1.152	0.097	1.412	0.720	1.105	1.778	0.050	1.903	0.821	1.162	2.246	0.400	0.940	0.486
		23	0.963	0.063	1.152	0.085	1.413	0.728	1.073	1.777	0.058	1.903	0.885	1.114	2.250	0.425	0.893	0.480
fresh snow	fresh snow	-10	0.990	0.022	1.180	-0.045	1.450	0.870	0.672	1.780	0.038	1.932	0.842	0.994	2.170	-0.578	0.889	-0.686
		+ 30s[a]	0.990	0.052	1.180	-0.014	1.450	0.827	0.845	1.776	0.040	1.936	0.655	0.988	2.170	-0.284	0.948	-0.434
		+ 60s[a]	0.990	0.037	1.180	-0.026	1.450	0.873	0.759	1.779	0.044	1.921	0.794	1.008	2.170	-0.459	0.909	-0.578
		+ 90s[a]	0.990	0.072	1.180	0.016	1.450	0.877	0.873	1.777	0.056	1.927	0.692	0.958	2.173	-0.360	0.943	-0.520
silica gel slurry[a]	SGE002	-13	0.985	0.046	1.180	0.039	1.450	0.801	0.823	1.778	0.060	1.932	0.902	1.000	2.170	-0.362	1.001	-0.402
		+ 3m[a]	0.969	0.081	1.158	0.104	1.439	0.815	0.958	1.780	0.072	1.916	0.917	1.031	2.170	-0.245	1.025	-0.268
		+ 5m[a]	0.972	0.107	1.158	0.130	1.439	0.856	0.969	1.778	0.092	1.907	0.837	1.036	2.170	-0.265	1.078	-0.317
quartz slurry[a]	QUA101	-13	0.980	-0.003	1.178	0.011	1.450	0.370	0.698	1.779	0.018	1.934	0.636	0.988	2.170	-0.105	0.979	-0.165
		+ 3m[a]	0.978	-0.004	1.161	0.011	1.447	0.275	0.823	1.778	0.011	1.927	0.556	1.079	2.170	-0.066	0.956	-0.118
		+ 5m[a]	0.976	0.009	1.162	0.029	1.448	0.621	0.864	1.779	0.038	1.925	0.896	1.033	2.170	-0.195	0.978	-0.217

[a] time after sample preparation

decreasing the 1.91/1.96 band depth ratio (Table 12). The spectra of the water-saturated samples (fresh snow, silica gel and quartz bathed in water; Figure 14) are dominated by the H_2O features, and no SiOH absorption near ~2.2 μm is observed. The ~1.4 and 1.9 μm features are saturated in these spectra, but the ~0.95 and 1.14 μm features can be more clearly observed than in other silica-rich spectra, as they are significantly deeper. These and all other H_2O and OH features occur at longer wavelengths in the water-saturated samples, where the spectra are dominated by H_2O ice, than in spectra of hydrated silica materials.

4.3 Humidity experiments

Figure 15 shows spectra of silica-rich materials after exposure to 100% RH and under ambient conditions for comparison. The major spectral differences are the depths of the ~1.4 and 1.9 μm H_2O features, which increase for the samples under increased humidity. The shapes of these features also appear to be affected by humidity, as those under 100% RH conditions exhibit smaller 1.41/1.46 and 1.91/1.96 band depth ratios in the opal and silica gel samples (Table 13). The shape of the ~2.2 μm SiOH feature does not change consistently with humidity, nor does the band depth in this region. Therefore the ~2.2/1.9 μm band depth ratio tends to decrease with humidity for hydrated silica, by as much as 35% (Table 13). These spectral changes are consistent with adsorbed molecular H_2O being added to the samples under high humidity conditions (as indicated by the increased ~1.4 and 1.9 μm band depths) and becoming hydrogen-bonded to silica surfaces (as indicated by the increased 1.96 type-

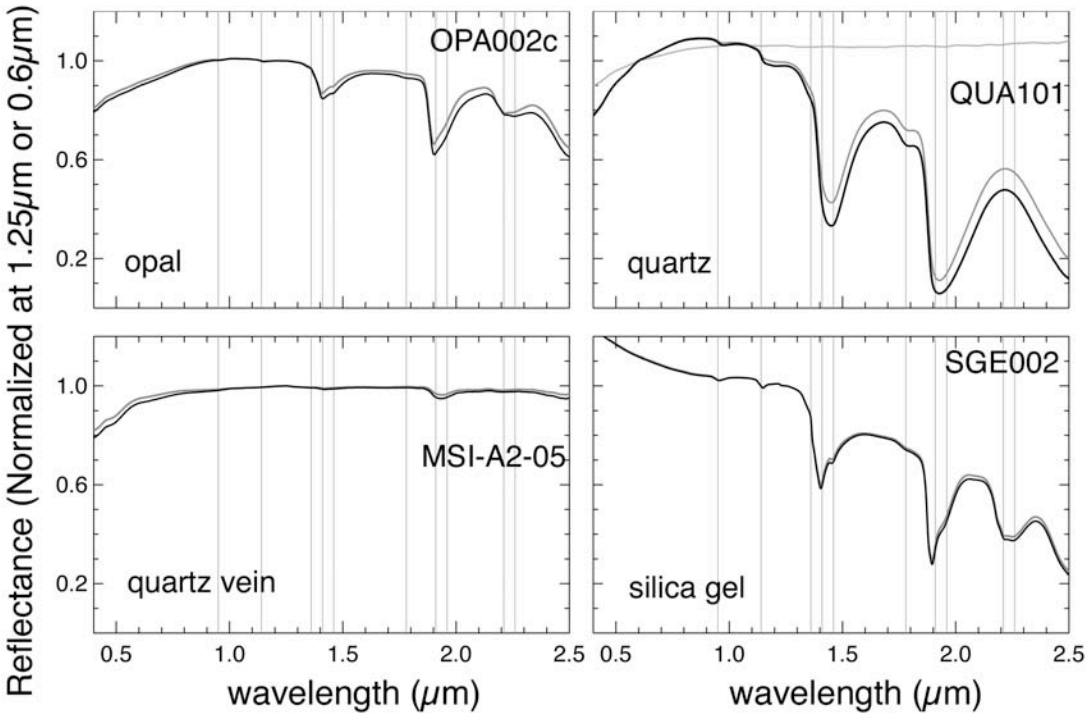

Figure 15. Scaled reflectance spectra (0.35-2.5 μm; normalized to 1 at 1.25 μm for all spectra except for those of QUA101, which are normalized to 0.6 μm) of silica-rich materials after being exposed to 100% relative humidity (RH) (black lines) and under ambient conditions (gray lines). (a) opal (OPA002c) crushed and sieved to <250 μm; (b) quartz (QUA101) crushed and sieved to <45 μm, observed under ambient conditions (flat spectrum), at 100% RH (black line) and 5 minutes after sample preparation; (c) quartz vein (MSI-A2-05) crushed and sieved to <250 μm; (d) unsorted silica gel (SGE002).

B feature) without much apparent incorporation into the silica structure (as indicated by no change to the ~2.2 μm SiOH feature).

These results are in contrast to those of previous studies, which show that hydration in high-humidity environment led to increases in the number of Si-OH bonds in silica-rich materials (more so in opal-CT than opal-A), mainly as an increase in the type-A 2.21 μm band (Langer and Flörke, 1974). In that previous study, this spectral change reversed after reequilibration at room temperature, implying that H_2O

Table 13. Band position and depth analyses for humidity experiments.

	Sample	RH	~ 0.95 µm		~ 1.14 µm		~ 1.41 µm		1.41/1.46	~ 1.78 µm		~ 1.91 µm		1.91/1.96	~ 2.21 µm		2.21/2.26	~2.2/1.9
Material	**ID**		**Position**	**Depth**	**Position**	**Depth**	**Position**	**Depth**	**Ratio**	**Position**	**Depth**	**Position**	**Depth**	**Ratio**	**Position**	**Depth**	**Ratio**	**Ratio**
opal	OPA002c	ambient	0.980	-0.006	1.150	0.007	1.409	0.119	1.403	1.776	0.001	1.901	0.286	1.515	2.212	0.087	1.339	0.305
		100%	0.980	-0.007	1.150	0.008	1.411	0.137	1.264	1.776	0.003	1.903	0.318	1.417	2.215	0.063	1.201	0.197
quartz	QUA101	ambient	0.949	-0.003	1.150	0.003	1.370	0.004	1.238	1.820	0.000	1.950	0.004	0.520	2.196	0.003	-3.609	0.662
		+7m[a]	0.977	0.004	1.162	0.023	1.448	0.530	0.855	1.779	0.029	1.926	0.824	1.046	2.170	-0.148	0.984	-0.179
		in H_2O	0.976	0.009	1.162	0.029	1.448	0.621	0.864	1.779	0.038	1.925	0.896	1.033	2.170	-0.195	0.978	-0.217
quartz		ambient	0.942	0.002	1.150	0.001	1.416	0.008	1.420	1.820	0.000	1.932	0.029	1.020	2.201	0.004	-5.644	0.138
vein	MSI-A2-05	100%	0.914	0.001	1.128	0.001	1.419	0.011	1.210	1.820	0.000	1.934	0.039	1.063	2.196	0.002	-1.131	0.057
silica gel	SGE002	ambient	0.957	0.020	1.148	0.025	1.404	0.353	1.569	1.781	0.002	1.896	0.584	1.603	2.215	0.302	1.125	0.516
		100%	0.956	0.019	1.148	0.024	1.404	0.369	1.537	1.778	0.003	1.896	0.599	1.561	2.215	0.308	1.115	0.514

[a] time after sample preparation.

diffused from the surface nearest layer of H_2O film into the silica matrix when exposed to high humidity. This process may have occurred to some extent during our experiment as well, but we observe the dominant effect of high-humidity to be simply the addition of surface H_2O layers. Such differences in spectral behavior could be related to differences in texture, porosity, or composition of the samples, or to the amount of SiOH initially present.

4.4 Low-pressure experiments

The spectra of the natural sinter SIL203 after 1 day, 215 days, and 294 days (including 35 days of UV) of exposure to simulated martian surface conditions (a 5 Torr CO_2 atmosphere), as well as under ambient conditions, are shown in Figure 16. The behavior of the ~1.4, 1.9, and 2.2 μm band centers, depths and and depth ratios with time after exposure are plotted in Figure 17 and listed in Table 14. The spectral changes include a shift of the ~1.4 μm absorption feature to shorter wavelengths, a decrease in the ~1.9 μm absorption feature depth, and an unmasking of the absorption feature near ~2.2 μm within one day of exposure (in the spectrum acquired under ambient conditions, the ~2.2 μm feature was likely masked by the short wavelength wing of the ~3 μm H_2O band). These trends continue during equilibration to 5 Torr conditions over the full 442 days of the experiment (Figure 17). Subsequently, the ~2.2/1.9 band depth ratio increases steadily from 0.18 towards 1.0 over the course of the experiment (Table 14). The shapes of the ~1.4 and 1.9 μm features also change with time during exposure to low-pressure conditions, as quantified by the increasing 1.41/1.46 and 1.91/1.96 band depth ratios plotted in Figure 17. Collectively, these

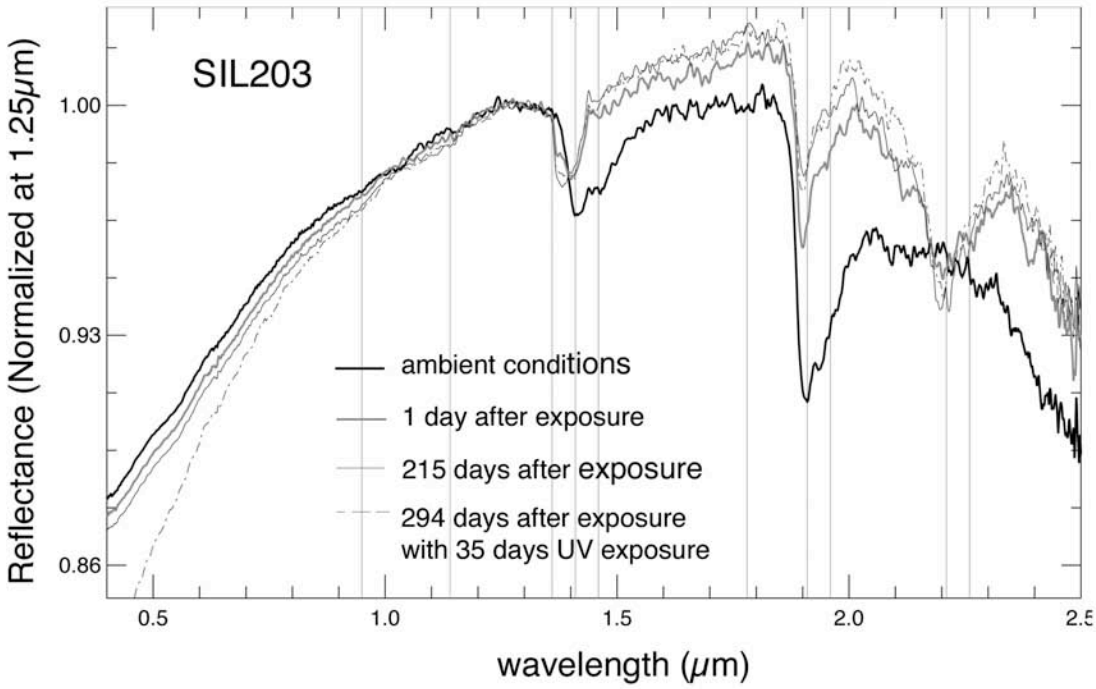

Figure 16. Scaled reflectance spectra of the silica sinter sample SIL203 (ground and sieved to <45 μm) during the low-pressure experiment, normalized to 1 at 1.25 μm. The sample was exposed to simulated martian surface conditions (5 Torr CO_2 atmosphere and temperatures below +20° C) for a total of 442 days. Major spectral changes include the shift of the ~1.4 μm H_2O/OH feature to shorter wavelengths, the decrease in the ~1.9 μm H_2O band depth, and the appearance of the ~2.2 μm SiOH feature. See text for further description of the experiment.

spectral changes suggest a change in the form of the H_2O (from the symmetry of the ~1.4 and 1.9 μm features) and a loss of molecular H_2O (from the depth of 1.9 μm feature). Previous work has shown that up to 80-90% of the total H_2O content can be removed from opals under low-pressure (Segnit et al., 1965). Our results also indicate that exposure of silica-rich materials to Mars surface conditions can have dramatic spectral effects due to loss and rearrangement of any preexisting H_2O. The exposure to UV radiation on day 259 of the experiment does not appear to have accelerated the observed spectra changes.

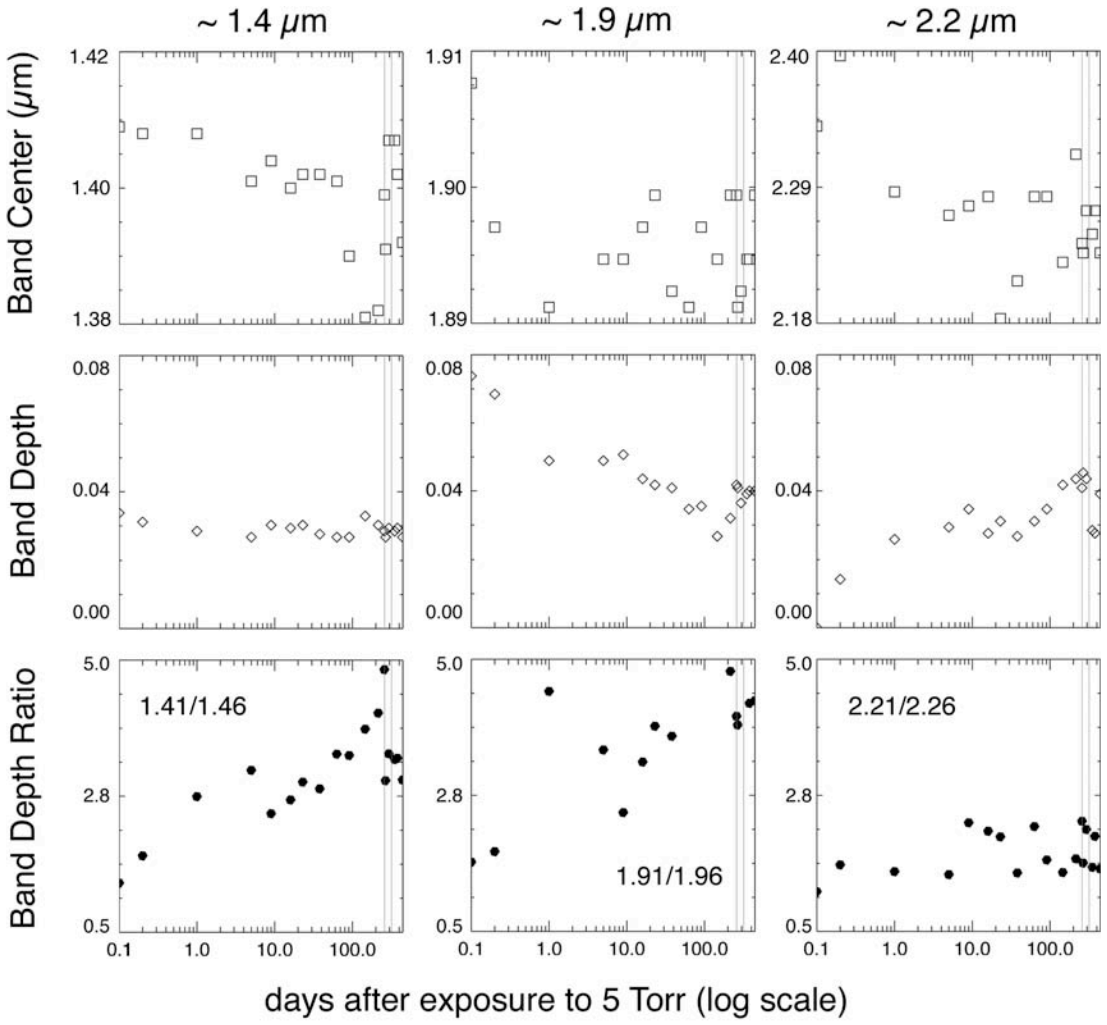

Figure 17. Changes to band centers, band depths and band depth ratios over time during the pressure-controlled experiment (see text for description of band measurements). Silica sinter sample SIL203 was exposed to simulated martian surface conditions (5 Torr CO_2 atmosphere and temperatures below +20^o C) for a total of 442 days. On day 259, the sample was illuminated with UV light until the bulb died on day 319; the measurements acquired during UV illumination (on days 267 and 294) are indicated by the vertical lines in the plots. Band measurements are also provided in Table 14.

Table 14. Band position and depth analyses for the spectra of SIL203 during exposure to a 5 Torr CO_2 environment over a period of 442 days.

Days after	~ 1.41 µm		1.41/1.46	~ 1.91 µm		1.91/1.96	~ 2.21 µm		2.21/2.26	~2.2/1.9
exposure	Position	Depth	Ratio	Position	Depth	Ratio	Position	Depth	Ratio	Ratio
0[a]	1.411	0.117	1.390	1.903	0.287	1.477	2.219	0.052	1.011	0.181
0[b]	1.409	0.033	1.313	1.910	0.078	1.645	2.221	-0.005	1.156	-0.065
0.2	1.408	0.030	1.764	1.901	0.072	1.819	2.236	0.011	1.600	0.158
1	1.408	0.027	2.743	1.896	0.050	4.468	2.207	0.024	1.488	0.480
5	1.401	0.025	3.178	1.899	0.050	3.500	2.202	0.028	1.439	0.569
9	1.404	0.029	2.461	1.899	0.052	2.465	2.204	0.034	2.296	0.653
16	1.400	0.028	2.688	1.901	0.044	3.300	2.206	0.026	2.156	0.596
23	1.402	0.029	2.983	1.903	0.042	3.892	2.180	0.030	2.063	0.731
38	1.402	0.026	2.871	1.897	0.041	3.727	2.188	0.025	1.466	0.620
63	1.401	0.025	3.445	1.896	0.034	7.743	2.206	0.030	2.233	0.888
91	1.390	0.025	3.423	1.901	0.035	15.577	2.206	0.034	1.681	0.975
146	1.381	0.032	3.858	1.899	0.025	-26.143	2.192	0.042	1.474	1.682
215	1.382	0.029	4.123	1.903	0.031	4.799	2.215	0.044	1.700	1.409
258	1.399	0.027	4.842	1.903	0.042	4.056	2.196	0.041	2.321	0.975
267[c]	1.391	0.025	3.006	1.896	0.041	3.912	2.194	0.046	1.630	1.115
294[d]	1.407	0.028	3.451	1.897	0.036	6.319	2.203	0.044	2.185	1.218
350	1.407	0.027	3.357	1.899	0.039	5.991	2.198	0.027	1.560	0.689
379	1.402	0.028	3.377	1.899	0.040	4.271	2.203	0.026	2.072	0.666
442	1.392	0.025	3.018	1.903	0.040	4.312	2.194	0.039	1.534	0.958

[a] Sample in ambient conditions outside of Mars chamber
[b] Sample in ambient conditions inside of Mars chamber (through the sapphire window)
[c] 8 days of UV exposure
[d] 35 days of UV exposure

5. Discussion

5.1 Absorption in the 1 µm region: Implications for MER Pancam and MSL Mastcam observations

The ~0.95 µm H_2O and/or OH feature is the only spectral feature associated with hydrated silica that occurs in the Vis-NIR wavelength range accessible to the MER Pancam and MSL Mastcam instruments. This feature is seen as a weak absorption (band depth < 0.08) in the spectra of some natural sinters (ICE102, Geysir-02, Geysir-04, SIL200 and SIL203), two opal samples (OPA001 and SIL115) and all synthetic silica samples (SGE001, SGE002 and SIL002) included in this study. While we would expect the ~0.95 µm band to be present in all hydrated samples (those with strong ~1.4 and 1.9 µm absorptions), we only observe it a subset of our spectra; it may

be that this weak band is only resolvable in the spectra of the most transparent samples that contain the most water and/or samples with surficial water.

Because this band center occurs between the wavelengths of the two longest-wavelength Pancam filters (934 and 1009 nm; Bell et al., 2003) and the two longest-wavelength Mastcam filters (937 and 1035 nm; Malin et al., 2010) for all samples, it may be undetectable with these instruments. Although some of the integrated area of the Pancam R6 and Mastcam R5 filters extend past 950 nm, and thus could be sensitive at some level to the ~950 nm band, whether the band affects the NIR profiles of these instruments will depend on the strength of the H_2O/OH absorption and the signal to noise ratio of the data. Figure 18 shows example spectra of whole-rock sinters convolved to Pancam and Mastcam bandpasses, and the feature centered at 0.95-0.96 μm does not appear to affect the NIR profiles. We also do not expect these materials to influence Pancam or Mastcam spectra at the lower pressure and temperature conditions of the martian surface; although the band center of the ~0.95 μm feature moves to longer wavelengths at lower temperatures, these shifts (typically < 0.02 μm) are insufficient to move the band into the bandpass of the ~1009 nm Pancam filter or that of the ~1035 nm Mastcam filter. Only the spectra of water-saturated silica (e.g., SGE002 in Figure 18a) reproduce the spectral downturn at 1009 nm that characterizes the Pancam spectra of silica-rich materials at Gusev Crater (shown in Figure 1). This result adds credence to the interpretation by Rice et al. (2010) that the silica-rich materials observed by MER Spirit must contain large amounts of free H_2O contained in voids or adsorbed onto the silica surface. At Mastcam wavelengths, the spectra of water-saturated silica (e.g., SGE002 in Figure

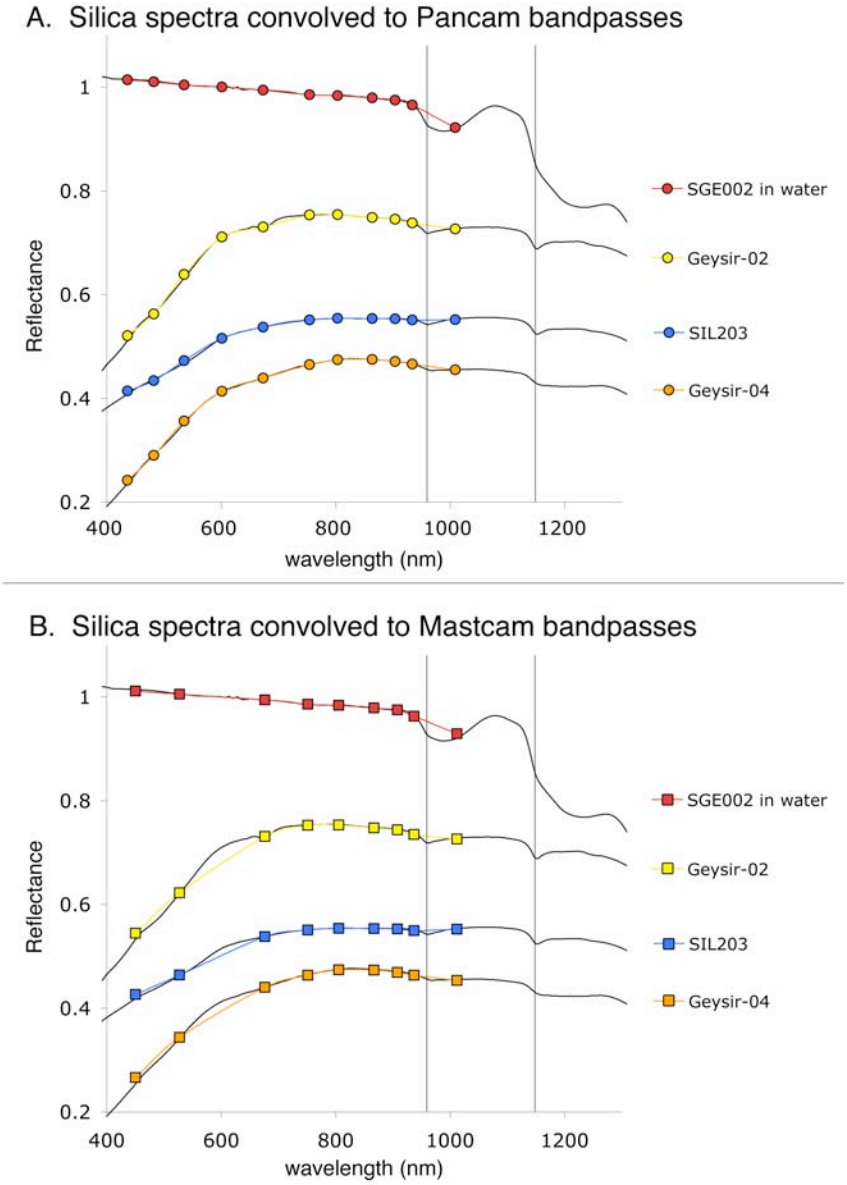

Figure 18. Example spectra of silica-rich materials exhibiting ~0.95 µm and ~1.14 µm absorption bands: whole rock natural sinters (Geysir-02, Geysir-04 and SIL203) and silica gel (SGE002) bathed in water and frozen to -13° C. Measured laboratory reflectance spectra are shown as black lines. (a) Spectra convolved to Pancam bandpasses (Bell et al., 2003) are shown as colored circles. (b) Spectra convolved to Mastcam bandpasses (Malin et al., 2010) are shown as colored squares. The SGE002 spectrum was normalized to 1.0 at 1.25 µm. For all spectra except that of SGE002, the ~0.95 µm feature occurs between the two longest-wavelength Pancam and Mastcam filters and is undetectable to these instruments. The wet SGE002 spectrum, however, exhibits the ~1009 nm downturn in Pancam bandpasses that characterizes the spectra of silica-rich materials at Gusev Crater (Figure 1). SGE002 also exhibits a ~1012 nm downturn in Mastcam bandpasses.

18b) are also the only spectra that exhibit a significant downturn in the longest-wavelength filter.

For those materials that do exhibit a ~0.95 μm absorption, the depth of this feature correlates with the measured H_2O content of the sample (Figure 19). However, whether or not hydrated silica-rich materials exhibit a ~0.95 μm absorption does not seem to be a function of the H_2O content (for example, the spectra of the sinter with the largest H_2O content (SIL302) exhibit featureless profiles between 0.8 and 1.2 μm). The 1.14 μm H_2O absorption is stronger than the ~0.95 μm feature and occurs in every spectrum where the ~0.95 μm feature is observed. The observed depth of this feature also correlates ($R^2 = 0.76$) with the H_2O content of the sample (Figure 19).

5.2 Absorptions in the 1.4, 1.9 and 2.2 μm regions: Implications for CRISM and OMEGA observations

The measured depths of the ~1.4 and 1.9 μm features, like those of the weaker ~0.95 and 1.14 μm bands, weakly correlate with the H_2O content of the silica-rich material (R^2 values between 0.39-0.49) (Figure 19). The band depth ratios (1.41/1.46, 1.91/1.96 and 2.21/2.26) do not appear to correlate with H_2O content as well as the absolute band depth measurements (Figure 19); this result is expected, as our laboratory study has revealed that the band depth ratios are mostly sensitive to differences in the style of hydrogen bonding (not total H_2O or SiOH content). The 1.91/1.96 band depth ratio weakly correlates with H_2O content for all materials except the synthetic materials, though, suggesting that the relative strength of the type-A 1.91 μm band to the type-B 1.96 μm band may be an indicator of the overall amount of

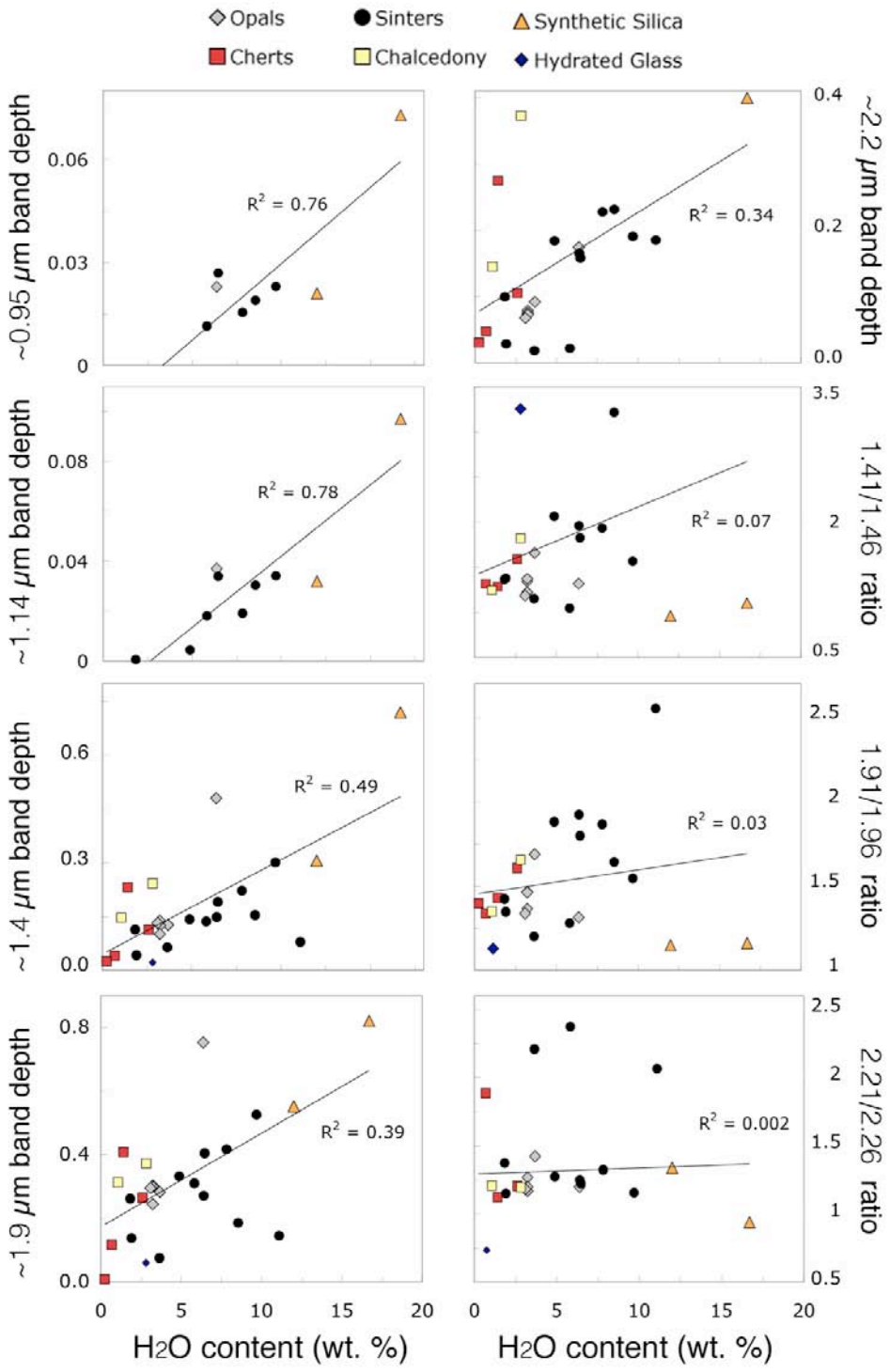

Figure 19. Plots of band measurements vs. water content (given as wt. % H_2O) for silica-rich materials (all crushed and sieved to 90-1000 μm). For all band measurements (~0.95, 1.14, 1.4, 1.9 and 2.2 μm), the band depth correlates with water content (the weakest correlation is with the depth of the ~2.2 μm SiOH feature). The band depth ratios (1.41/1.46, 1.91/1.96 and 2.21/2.26) do not correlate well with water content, with the possible exception of the 1.91/1.96 ratio for natural silica materials.

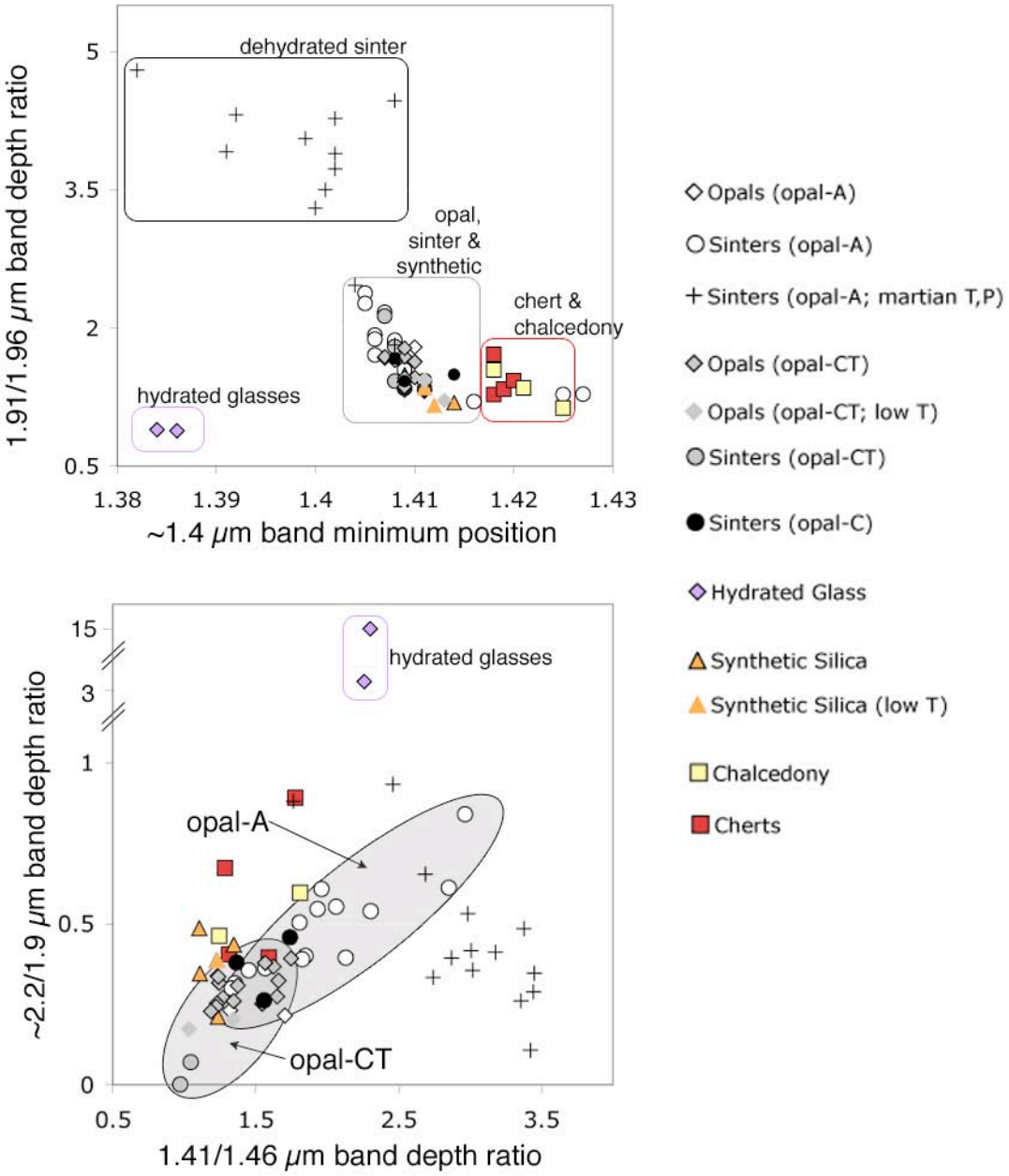

Figure 20. Parameter space plots of the band measurements of silica-rich materials. Top: ratio of the 1.91 to 1.96 µm band depths vs. the position of the ~1.4 µm band minimum. Hydrated glass, cryptocrystalline quartz (chert and chalcedony), amorphous silica (opal, sinter and synthetics) and dehydrated silica materials fall into distinct regions of this parameter space. Bottom: ratio of the ~2.2 to 1.9 µm band depths vs. the ratio of the 1.41 to 1.46 µm band depths. Opal-A and opal-CT silica varieties fall into separate, yet overlapping, regions of this parameter space. See text for further discussion.

H_2O present for most silica-rich materials.

However, the LOI value that we use to estimate H_2O content may be influenced by the presence of other volatiles in the sample. During the heating process, which is similar to TGA (thermogravimetric analysis) except without the incremental heating, SO_3, CO_2, CH_4, and NH_3 can also be expelled with a concomitant loss in weight. Furthermore, the LOI determination is complicated by oxidation (e.g., of Fe, Mg, or Cr) during the heating process, which can produce a weight gain. The measured LOI, therefore, is the sum of the weight loss due to volatile release and the weight gain due to oxidation, and will provide a more accurate estimate of H_2O content for our nearly-pure SiO_2 samples than for those with more varied chemistries.

In addition to using band measurements of silica-rich materials to infer the amount of H_2O in the sample, a major objective of this study is to identify spectral parameters that can be used to distinguish between different types of silica-rich materials. Table 15 lists the ranges of spectral parameters measured for each type of silica-rich material that exhibits strong H_2O, OH, and SiOH spectral features. The parameters we have identified that best distinguish between these materials are plotted in Figure 20. In the plot of the ratio of the 1.91 to 1.96 μm band depths (1.91/1.96 depth) vs. the position of the ~1.4 μm band minimum (Figure 20, top), the hydrated glass, cryptocrystalline quartz (chert and chalcedony), non-crystalline silica (opal, sinter and synthetics), and dehydrated silica materials fall into distinct regions of this parameter space.

Our results (Table 15) disagree with the band attributions of Milliken et al. (2008), who interpreted spectra with bands centered at 1.38–1.39 μm as being most

Table 15. Generalizations of band positions and ratios for possible discrimination of different silica-rich materials. The ranges presented here are only from spectra with resolvable bands in the relevant wavelength regions, and include all grain sizes and temperatures measured.

Material	Water Content	~1.4 µm Position	1.41/1.46 Ratio	~1.9 µm Position	1.91/1.96 Ratio	~2.2 µm Position	2.21/2.26 Ratio	~1.9/2.2 Ratio
Chalcedony	1.06	1.418-1.421	1.245-1.810	1.912-1.912	1.349-1.808	2.200-2.214	1.208-1.516	0.463-0.906
Cherts	0.68-2.60	1.418-1.420	1.285-1.776	1.903-1.925	1.280-1.715	2.198-2.219	1.123-1.919	0.396-0.890
Hydrated Glass	0.5	1.386-1.384	0.025-0.275	1.932-1.943	0.887-0.901	2.210-2.211	1.695-1.722	2.706-15.648
Opals (opal-A)	6.37	1.410-1.411	1.317-1.702	1.901-1.903	1.315-1.797	2.213-2.215	1.199-1.343	0.216-0.232
Opals (opal-CT)	3.09-3.22	1.407-1.413	1.029-1.746	1.901-1.905	1.215-1.784	2.209-2.216	1.039-1.612	0.174-0.392
Opals (all)	**3.09-9.96**	**1.405-1.413**	**1.029-1.746**	**1.901-1.905**	**1.215-1.797**	**2.209-2.216**	**1.039-1.612**	**0.174-0.392**
Sinters (opal-A; martian pressure)	unknown	1.381-1.411	1.313-4.842	1.896-1.910	1.645-7.743	2.180-2.236	1.156-2.321	0.260-0.932
Sinters (opal-A)	4.88-9.96	1.405-1.411	1.332-2.966	1.897-1.901	1.346-2.381	2.209-2.217	1.045-1.406	0.400-0.871
Sinters (opal-C)	1.83	1.408-1.414	1.364-1.738	1.901-1.905	1.423-1.672	2.209-2.213	1.078-1.546	0.263-0.458
Sinters (opal-CT)	5.82	1.425-1.431	0.972-1.045	1.914-1.920	1.202-1.280	2.206-2.212	-0.271-2.374	0.001-0.070
Sinters (all)	**1.83-9.96**	**1.405-1.431**	**0.972-2.966**	**1.897-1.920**	**1.202-2.381**	**2.206-2.217**	**-0.271-2.374**	**0.001-0.871**
Synthetic Silica	16.69-59.71	1.409-1.412	1.105-1.234	1.899-1.903	1.162-1.491	2.246-2.250	0.841-0.940	0.212-0.486
Opal-A (all)	**4.88-9.96**	**1.405-1.411**	**1.317-2.966**	**1.897-1.903**	**1.315-2.381**	**2.209-2.217**	**1.039-1.406**	**0.216-0.871**
Opal-CT (all)	**3.09-5.82**	**1.407-1.431**	**0.972-1.746**	**1.901-1.920**	**1.202-1.784**	**2.206-2.216**	**-0.271-2.374**	**0.001-0.392**

consistent with opaline silica, and those with bands centered at 1.41 μm as being most consistent with hydrated impact and/or volcanic glasses. Our sample set included two hydrated glasses exhibiting ~1.4 μm features in their spectra (the lechatelierites SIL131 and SIL130), both of which were centered at 1.38-1.39 μm. Our collective results (Figure 20 top) suggest that spectra with bands centered at 1.38-1.40 μm are consistent with hydrated glasses and dehydrated silica, whereas those with bands centered at 1.40-1.43 μm are consistent with opaline and cryptocrystalline silica. The nature of the disagreement between our results and those of Milliken et al. (2008) may be due to differences in sample characteristics or spectral resolutions.

Although the ~1.4 μm band positions and 1.91/1.96 band depth ratios can be used to broadly distinguish broadly between different types of silica-rich materials, based on our sample set we note that these parameters cannot be used to uniquely identify a material as opal-A, opal-CT, opal-C, or cryptocrystalline quartz. The chert and chalcedony samples appear spectrally distinct from the opals, sinters and synthetics (the non-crystalline silica samples) in that their ~1.4 μm features are typically centered at longer wavelengths (~1.42 μm, as opposed to ~1.41 for opals). However, a ~1.4 μm band minimum at wavelengths longer than 1.418 μm does not uniquely identify a cryptocrystalline silica-rich material, as some opal-A bearing sinters exhibit this band at wavelengths as long as 1.43 μm (Figure 20). The forms (opal-A vs. opal-CT) of the opal and sinter samples also cannot be uniquely distinguished in this parameter space.

Based on our measurements of the ~2.2 μm SiOH feature in a wide variety o f samples, we find that the position, width, and number of absorptions in the ~2.2 μm

region cannot be used to distinguish reliably between different types of silica-rich materials. Although multiple studies of silica-rich materials on Mars have used the position and shape of the ~2.2 μm feature in CRISM spectra to distinguish between hydrated glasses and opaline silica phases (e.g., Milliken et al., 2008; Ehlmann et al., 2009; Skok et al., 2010), our measurements indicate that the ranges of ~2.2 μm position and 2.21/2.26 band depth ratios for different materials overlap considerably (Table 16 and Figure 21). The only exceptions are the spectra of synthetic silica samples, which exhibit SiOH bands centered at anomalously long wavelengths (~2.25 μm, as opposed to < 2.24 μm for all other materials), and the spectra of dehydrated silica, which have SiOH bands at anomalously short wavelengths (as low as 2.18 μm) due to the diminished influence of the type-B 2.26 μm band as H_2O is removed. Although the spectra of synthetic, unaltered glasses exhibit a single band in the ~2.2 μm region, as opposed to overlapping 2.21 and 2.26 μm bands (e.g., Moroz et al., 2009), the natural glasses analyzed in this study do exhibit structure in their ~2.2 μm SiOH bands (Figure 5) indistinguishable from that of other silica-rich materials. We have identified no means of distinguishing between chert, chalcedony, opal-A, opal-CT, opal-C, and hydrated glass using the ~2.2 μm behavior. Although many detections of silica-rich materials on Mars from CRISM spectra are based solely on the presence and width of the ~2.2 μm feature (e.g., Figure 2b), we caution against using the band position and symmetry of this feature to draw conclusions about the type of silica-rich material present.

We also caution against using any single band position to attempt to make detailed interpretations about the type of silica-rich material. Based on the large band

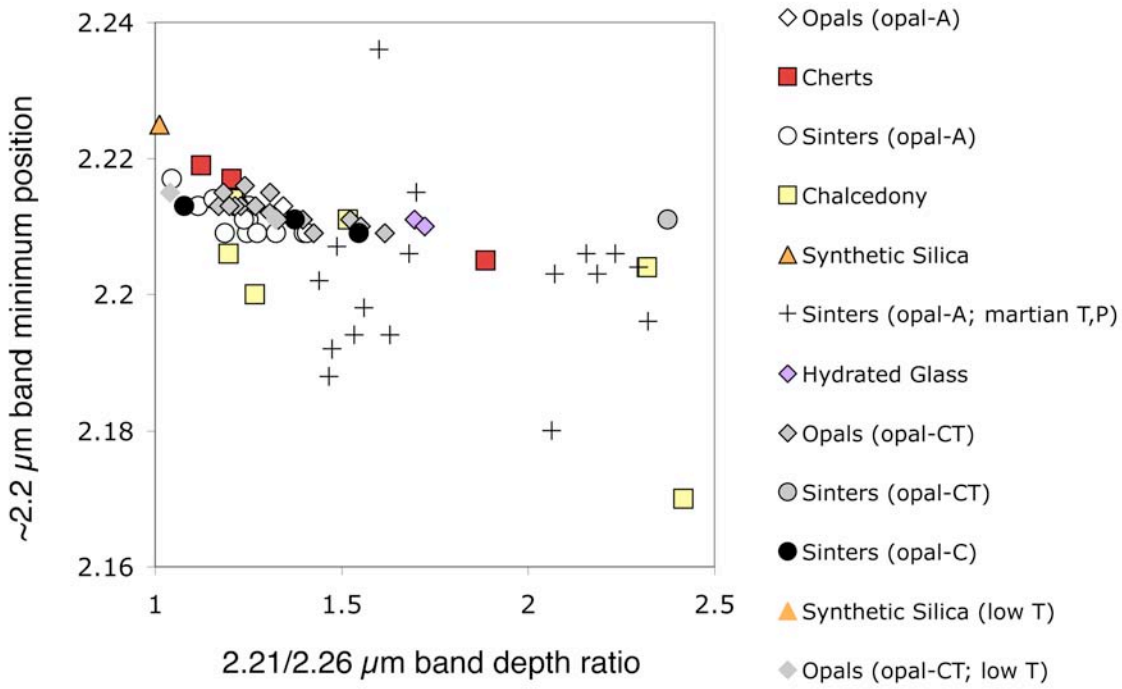

Figure 21. Parameter space plot of the ~2.2 μm band measurements of silica-rich materials. The various forms of silica do not fall into distinct regions of this parameter space (see Figure 20 for comparison), and thus we caution against use the position of the ~2.2 μm band minimum or the 2.21/2.26 μm ratio as tools for distinguishing between various types of silica-rich materials. See text for further discussion.

position shifts observed for the sample of opal-A exposed to martian surface conditions (Figure 17 and Table 14), we conclude that the spectra of silica-rich materials on Mars may not be the same as those observed in terrestrial laboratories under ambient conditions. More studies of silica varieties exposed to low temperature and pressure conditions for extended periods are needed to better quantify the expected band positions on the surface of present-day Mars.

Langer and Flörke (1974) found that opal-A and opal-CT can be distinguished in Vis-NIR spectra based on the shape of the ~1.9 μm feature. Specifically, the band area of the type-A (1.91 μm) absorption relative to the band area of the type-B (1.96 μm) absorption was found to be larger in opal-A spectra than in opal-CT spectra. In our analysis, we measure band depth as a proxy for band area, but we find that the measured ratios of the 1.91 to 1.96 μm band depths are not diagnostically larger for our opal-A samples than the opal-CT samples (Table 16). We find that the depth of the ~2.2 μm feature relative to that ~1.9 μm region is a better indicator of opal type. This band depth ratio is an approximation of the ratio of SiOH to molecular H_2O in the sample. Langer and Flörke (1974) quantitatively determined the amounts of SiOH and molecular H_2O from the integral absorbances of the ~2.2 μm and ~1.9 μm features, and found that opal-A materials contained greater amounts of SiOH (0.8-0.9 wt. %) than opal-CT materials (0.2-0.4 wt. %). Therefore, we hypothesize that the spectra of opal-A sinters and opals included in this study should exhibit greater ~2.2/1.9 band depth ratios than the opal-CT samples.

The ratio of the ~2.2 to 1.9 μm band depths vs. the ratio of the 1.41 to 1.46 μm band depths for all samples is plotted in Figure 20 (bottom). The opal-A and opal-CT

samples fall into separate, yet overlapping, regions of this parameter space, with opal-A materials typically exhibiting larger ~2.2/1.9 band depth ratios than opal-CT materials as expected. These opals typically exhibit differences in the shapes of their ~1.4 μm bands as well, as the 1.41/1.46 band depth ratio for opal-A materials is typically larger than for opal-CT materials. These differences are consistent with disordered silica (opal-A) containing proportionately more SiOH than more ordered silica (opal-CT). The overlap between the ranges of the ~2.2/1.9 band depth ratio for opal-A and opal-CT materials (i.e., the fact some opal-A materials plot with opal-CT materials) may be attributed to textural irregularities in the natural sinters (e.g., bubbles, voids and fissures) that could contain relatively large amounts of liquid H_2O and hence decrease the ~2.2/1.9 band depth ratio. Very little (<1 wt. %) SiOH has been shown to be present in cryptocrystalline quartz varieties as well (Scholze, 1960), and the ~2.2/1.9 band depth ratios we measured for cherts and chalcedony samples fall within the full range of those observed for opal-A and opal-CT.

Among the different opal-A materials, we observe that the ~2.2/1.9 band depth ratios are larger for the sinter samples (0.22-0.23) than for the opal samples (0.40-0.87) (Table 16). We ascribe this to differences in the formation mechanisms of these materials (summarized in Table 3). For example, sinters result from the rapid precipitation of silica from high-temperature solutions onto colder substrates in hydrothermal environments, and this process incorporates relatively large amounts of H_2O into the silica matrix and many OH groups are retained. Opals that form in rock fissures at low-temperatures, however, incorporate fewer OH groups into the silica structure because they form more slowly (e.g., Flörke et al., 2000). Among the

different opal-CT materials, however, the sinters exhibit lower ~2.2/1.9 band depth ratios than the opals formed at low temperatures.

6. Conclusions and Future Work

We have observed a great amount of diversity in the spectra of silica-rich materials at varying grain sizes, temperatures, relative humidity conditions and pressures. Based on our analyses of the band depths, positions and symmetries of the characteristic spectral features of hydrated silica (the bands listed in Table 4), we draw the following conclusions that can aid in the interpretation of the form and content of H_2O associated with silica detections on Mars:

1. The depths of all bands decrease with grain size, and the weakest features at ~0.95 and 1.14 μm are only observed in course-grained or whole-rock samples of opals, natural sinters, and synthetic silica.
2. The only spectra that reproduce the ~1 μm absorption in Pancam wavelengths observed by MER Spirit are those of water-saturated materials.
3. At low temperatures, all spectral features move to longer wavelengths, and the shapes of the ~1.9 and 2.2 μm features change as the relative strengths of the type-B bands increase.
4. At high humidity, the depths of the H_2O features at ~1.4 and 1.9 μm increase, yet a lack of changes to the ~2.2 μm region implies that very little H_2O is adsorbed onto or diffuses into the silica matrix.

5. Under simulated martian surface conditions (low pressure and temperature), the ~1.4 μm feature shifts to lower wavelengths (from 1.411 to 1.381 μm) and the ratio of the ~2.2 and 1.9 μm features increases as molecular H_2O is lost and SiOH dominates. These results suggest that, more generally, the spectra of silica-rich materials on Mars may not be the same as those obtained in terrestrial laboratories under ambient conditions.
6. The depths of features at ~0.95, 1.14, 1.4 and 1.9 μm correlate with H_2O content, as does the ratio of the type-A to type-B bands that comprise the ~1.9 μm absorption feature.
7. Based on our data, the ~2.2 μm band depth and shape cannot be used to reliably distinguish between chert, chalcedony, opal-A, opal-CT, opal-C, and hydrated glass.
8. The position of the ~1.4 μm feature and the symmetry of the ~1.9 μm feature can be used to discern between various forms of silica-rich materials (hydrated glass vs. non-crystalline silica vs. cryptocrystalline silica vs. dehydrated silica) in our sample set.
9. The ratio of the ~2.2 μm and ~1.9 μm band depths, and the symmetry of the ~1.41 μm feature, can be used to distinguish between opal-A and opal-CT materials (although not unambiguously).
10. The ratio of the ~2.2 μm and ~1.9 μm band depths can be used to distinguish between opal-A materials formed under high-temperature conditions (sinters) and those formed at low temperatures (opals).

Our future work on the spectral diversity of silica-rich materials will include using mathematical models of absorption bands (e.g., Sunshine et al., 1990) to more accurately quantify the relative contributions of the overlapping type-A and type-B bands in the ~1.9 and 2.2 μm regions, and the overlapping OH and H_2O features in the ~1.4 μm region (for example, the shape of OH bands in opals has been described as Gaussian by Langer and Flörke, 1974). We also plan to reverse the low-pressure experiment and quantify the spectral changes to silica that accompany rehydration as the sample reequilibrates to ambient pressure and temperature conditions. We predict that some spectral changes will be irreversible, based on heating experiments by Morris et al. (2010) that show irreversible changes to the ~1.4 and 1.9 band depths for nontronite samples. XRD analysis of the reequilibrated sample will indicate whether the structural ordering has increased during exposure to simulated martian surface conditions (e.g., whether the silica polymorph evolved from opal-A to opal-CT or opal-C), which may have implications for future detections of silica on the surface of Mars.

REFERENCES

Adams, J. B., Pieters, C., McCord, T. B., 1974. Orange glass: Evidence for regional deposits of pyroclastic origin on the moon. Lunar Planet. Sci. Conf. V, 171-186.

Adams, S.J., Hawkes, G.E., Curzon, E.H., 1991. A solid state ^{29}Si nuclear magnetic resonance study of opal and other hydrous silicas. Am. Mineral. 76, pp. 1963-1871.

Aines, R.D., Rossman, G.R., 1984, Water in minerals? A peak in the infrared. Journal of Geophysical Research 89, 4059-4071.

Aines, R.D., Kirby, S.H., Rossman, G.R., 1984, Hydrogen speciation in synthetic quartz. Physics and Chemistry of Minerals 11, 204-212.

Anderson, J.H., Wickersheim, K.A., 1964. Near infrared characterization of water and hydroxyl groups on silica surfaces. Surface Science 2, pp. 252-260.

Bandfield, J.L., Glotch, T.D., Christensen, P.R., 2003. Spectroscopic identification of carbonate minerals in the martian dust. Science 301, 1084–1087. doi:10.1126/science.1088054.

Bandfield, J.L., 2008. High-silica deposits of an aqueous origin in western Hellas Basin, Mars. Geophys. Res. Lett. 35, 142–147. doi:10.1029/2008GL033807.

Bayliss, P., Males, P.A., 1965. The mineralogical similarity of precious and common opal from Australia. Mineral. Mag. 35, pp. 429-431.

Bayly, J.G., Kartha, V.B., Stevens, W.H., 1963. The absorption spectra of liquid phase H_2O, HDO and D_2O from 0.7 μm to 10 μm. Infrared Phys. 3, 211-223.

Bell III, J.F., and 24 colleagues, 2003. Mars Exploration Rover Athena Panoramic Camera (Pancam) investigation. J. Geophys. Res. 108, E12. doi:10.1029/2003JE002070.

Benesi, H.A., Jones, A.C., 1959, An infrared study of the water-silica gel system. J. Chem. Phys. 63, 179-182.

Bibring, J.-P., and 10 colleagues, 2006. Global mineralogical and aqueous Mars history derived from OMEGA/Mars Express data. Science 312, 400–404. doi:10.1126/science.1122659.

Bishop, J.L., Murad, E., Lane, M.D., Mancinelli, R.L., 2004. Multiple techniques for mineral identification on Mars: a study of hydrothermal rocks as potential analogues for astrobiology sites on Mars. Icarus 169, pp. 311–323. doi:10.1016/j.icarus.2003.12.025.

Bishop, J.L., and 12 colleagues, 2009. Mineralogy of Juventae Chasma: Sulfates in the light-toned mounds, mafic minerals in the bedrock, and hydrated silica and hydroxylated ferric sulfate on the plateau. J. Geophys. Res. 114, E00D09. doi:10.1029/2009JE003352.

Bishop, J.L., and 11 colleagues, 2008. Phyllosilicate Diversity and Past Aqueous Activity Revealed at Mawrth Vallis, Mars. Science 321, 830. doi:10.1126/science.1159699.

Bouška, V., Bell III, J.F., 1993. Assumptions about the presence of natural glasses on Mars, J. Geophys. Res., 98, 18719-18726.

Buijs, K., Choppin, G.R., 1963. Near-infrared studies of the structure of water. I. Pure water. J. Chem. Phys. 39, pp. 2035-2041.

Buijs, K., Choppin, G.R., 1964. Assignment of the near-infrared bands of water and ionic solutions. J. Chem. Phys. 40, p. 3120.

Burns, R.G., Fisher, D.S., 1993. Rates of Oxidative Weathering on the Surface of Mars, J. Geophys. Res. 98, E2, pp. 3365–3372. doi:10.1029/92JE02055.

Cady, S.L., Farmer, J.D., 1996. Fossilization processes in siliceous thermal springs: Trends in preservation along thermal gradients. In: Bock, G., Goode, J. (Eds.), Evolution of Hydrothermal Ecosystems on Earth (and Mars?). Wiley, New York, pp. 150–170.

Channing, A., Butler, I.B., 2007. Cryogenic opal-A deposition from Yellowstone hot springs. Earth Planet. Sci. Lett. 257, 121–131. doi:10.1016/j.espl.2007.02.026.

Christensen, P. R., and 18 colleagues, 2003. Miniature Thermal Emission Spectrometer for the Mars Exploration Rovers, J. Geophys., Res. 108, 8064. doi:10.1029/2003JE002117.

Clark, R.N., King, T.V.V., Klewja, M., Swayze, G.A., 1990. High spectral resolution reflectance spectroscopy of minerals. J. Geophys. Res. 95, pp. 12653-12680.

Clark, R.N., Roush, T.L., 1984. Reflectance spectroscopy—Quantitative analysis techniques for remote sensing applications. J. Geophys. Res. 89, 6329–6340. doi:10.1029/JB089iB07p06329.

Clark, R.N., Swayze, G.A., Wise, R., Livo, E., Hoefen, T., Kokaly, R., Sutley, S.J., 2007. USGS digital spectral library splib06a: U.S. Geological Survey. Digital Data Series, 231.

Cloutis, E.A., Bell III, J.F., 2003. Mafic silicate mapping on Mars: Effects of palagonite, multiple mafic silicates, and spectral resolution, Icarus, 172, 233-254.

Cloutis, E., Craig, M., Kaletzke, L., McCormack, K., Stewart, L., 2006. HOSERLab: A new planetary spectrophotometer facility. Lunar Planet. Sci. Conf. XXXVII, Abstract 2121.

Cloutis, E.A., Craig, M.A., Kruzelecky, R.V., Jamroz, W.R., Scott, A., Hawthorne, F.C., Mertzman, S.A., 2008a. Spectral reflectance properties of minerals exposed to simulated Mars surface conditions. Icarus 195, 140–168. doi:10.1016/ j.icarus.2007.10.028.

Cloutis, E.A., McCormack, K.A., Bell III, J.F., Hendrix, A.R., Bailey, D.T., Craig, M.A., Mertzman, S.A., Robinson, M.S., Riner, M.A., 2008b. Ultraviolet spectral reflectance properties of common planetary minerals. Icarus, 197, 321–347. doi:10.1016/j.icarus.2008.04.018.

Cordier, P., Doukhan, J.C., 1991. Water speciation in quartz: A near infrared study. Am. Mineral. 76, 361-369.

Craig, M.A., Cloutis, E.A., Mueller, T., 2001. ME and Mini-ME: Two Mars environmental simulation chambers for reflectance spectroscopy, Lunar Planet. Sci. XXXII, Abstract 1368.

Craig, M.A., Osinski, G.R., Flemming, R.L., Cloutis, E.A., 2011. Spectral identification of impact glasses via NIR reflectance spectroscopy, Lunar Planet. Sci. XVII, Abstract 2411.

Dijkstra, T.W., Duchateau, R., van Santen, R.A., Meetsma, A., Yap, G.P.A., 2002. Silesquioxane models for geminal silica surface silanol sites. A spectroscopic investigation of different types of silanols. J. Am. Chem. Soc. 124, 9856-9864.

Doremus, R.H., 1998. Diffusion of water and oxygen in quartz: reaction-diffusion model. Earth Planet. Sci. Lett. 163, pp. 43-51.

Ehlmann, B.L., and 13 colleagues, 2008. Orbital identification of carbonate-bearing rocks on Mars. Science 322, 1828–1832. doi:10.1126/science.1164759.

Ehlmann, B.L., and 11 colleagues, 2009. Identification of hydrated silicate minerals on Mars using MRO-CRISM: Geologic context near Nili Fossae and implications for aqueous alteration. J. Geophys. Res. 114, E00D08. doi:10.1029/ 2009JE003339.

Eisenberg, D., Kauzmann, W., 1969. The Structure and Properties of Water, Oxford University Press, New York.

Elliott, C.R., Newns, G.R., 1971. Near infrared absorption spectra of silica: OH overtones, Appl. Spectrosc. 25, pp. 378-379.

Ellis, A.J., Mahon, W.A.J., 1977. Chemistry and Geothermal Systems. Academic Press, New York.

Farmer, J.D., 1996. Hydrothermal systems on Mars: An assessment of present evidence. In: Bock, G., Goode, J. (Eds.), Evolution of hydrothermal ecosystems on Earth (and Mars?). Wiley, New York, pp. 273–295.

Flörke, O.W., Köhler-Herbertz, B., Tönges, I., 1982. Water in microcrystalline quartz of volcanic origin: Agates. Contrib. Mineral. Petrol. 80, 324-333.

Flörke, O.W., and 15 colleagues, 2000. Silica. In *Ullmann's Encyclopedia of Industrial Chemistry*, Wiley-VCH Verlag GmbH & Co. KGaA. doi:10.1002/14356007.a23_583.pub3.

Frondel, C., 1982. Structural hydroxyl in chalcedony (type B quartz). Am. Mineral. 67, 1248-1257.

Gaillou, E., Fritsch, E., Aguilar-Reyes, B., Rondeau, B., Post, J., Barreau, A., Ostroumov, M., 2008. Common gem opal: An investigation of micro- to nano-texture. Am. Mineral. 93, pp. 1865-1873. doi:10.2138/am.2008.2518.

Gellert, R., and 10 colleagues, 2006. The Alpha Particle X-Ray Spectrometer (APXS): Results from Gusev Crater and Calibration Report, J. Geophys. Res. 111, E02S05. doi:10.1029/2005JE002555.

Ghaemi, F.T., 2009. Design and fabrication of lenses for the color science cameras aboard the Mars Science Laboratory rover, Opt. Eng. 48, 103002, doi:10.1117/1.3251343.

Gooding, J.L., Keil, K., 1978. Alteration of glass as a possible source of clay minerals on Mars. Geophys. Res. Lett. 5, 8, pp. 727-730.

Goreva, J.S., Ma, C., Rossman, G.R., 2001. Fibrous nanoinclusions in massive rose quartz: The origin of rose coloration. Am. Min 86, pp. 466–472.

Graetsch, H., 2011. Microstructure and origin of colour of chrysoprase from Haneti (Tanzania). Neues Jahrbuch für Mineralogie – Abhandlungen 188, 2, pp. 111-117(7). doi:10.1127/0077-7757/2011/0187.

Graetsch, H., 1994. Structural characteristics of opaline and microcrystalline silica minerals. In *Silica: Physical Behavior , Geochemistry and Materials Applications, Reviews in Mineralogy 29* (Heaney, P.J., Prewitt, C.T., and Gibbs, G.V., editors); Mineral. Soc. Am., Washington, DC, pp. 209-232.

Graetsch, H., Flörke, O.W., Miehe, G., 1985. The nature of water in chalcedony and opal-C from Brazilian agate geodes. Phys. Chem. Miner. 12, 300-306.

Grundy, W.M., Schmitt, B., 1998. The temperature-dependent near-infrared absorption spectrum of hexagonal H_2O ice. J. Geophys. Res. 103, pp. 25809-25822.

Guthrie, G.D., Jr., Bish, D.L., Reynolds, R.C., Jr., 1995. Modeling the X-ray diffraction pattern of opal-CT. Am. Min. 80, 869- 872.

Hambleton, F.H., Hockey, J.A., Taylor, J.A.G., 1966. Investigation by infra-red spectroscopic methods of deuterium exchange properties of aerosol silicas. Trans. Faraday Soc. 62, 801-807.

Herdianita, N.R., Browne, P.R.L., Rodgers, K.A., Campbell, K.A., 2000a. Mineralogical and textural changes accompanying ageing of silica sinter. Mineral. Deposita 35, pp. 48-62.

Herdianita, N.R., Rodgers, K.A., Browne, P.R.L., 2000b. Routine instrumental procedures to characterize the mineralogy of modern and ancient silica sinter. Geothermics 29, pp. 65-81.

Herzberg, G., 1945. Infrared and Raman Spectroscopy. Von Nostrand Reinhold Company, Inc., New York.

Hinman, N.W., 1990. Chemical factors influencing the rates and sequences of silica phase transitions. Geochim. Cosmochim. Acta 54, pp. 1563-1574.

Hockey, J.A., Pethica, B.A., 1961, Surface hydration of silicas. Trans. Faraday Soc. 57, 2247-2262.

Horgan, B., Bell, J.F. III, in press. Widespread weathered glass on the surface of Mars. Geology. doi:10.1130/G32755.1.

Hornig, D.F., 1964. On the spectrum and structure of water and ionic solutions. J. Chem. Phys. 40, pp. 3119-3120.

Irvine, W.M., Pollack, J.B., 1968. Infrared optical properties of water and ice spheres. Icarus 8, 324-360.

Jones, B., Renaut, R.W., 2004. Water content of opal-A: implications for the origin of laminae in geyserite and sinter. J. Sed. Res. 74, pp. 117-128. doi:10.1306/052403740117.

Jones, B., and Renaut, R.W., 2007. Microstructural changes accompanying the opal-A to opal-CT transition: new evidence from the siliceous sinters of Geysir, Haukadalur, Iceland. Sedimentology 54, 921-948.

Jones, B., Renaut, R.W., Torfason, H., Owen, R.B., 2007. The geological history of Geysir, Iceland: a tephrochronological approach to the dating of sinter. J. Geol. Soc. London 164, 1241-1252.

Jones, J.B., Segnit, E.R., 1966. The occurrence and formation of opal at Coober Pedy and Andamooka, Australian J. Sci. 29, pp. 129-133.

Jones, J.B., Segnit, E.R., 1971. The nature of opal: I. Nomenclature and constituent phases. J. Geol. Soc. Aust. 18-1, 57-68.

Kekulawala, K.R.S.S., Paterson, M.S., Boland, J.N., 1981. An experimental study of the role of water in quartz deformation. In *Mechanical Behavior of Crustal Rocks* (Carter, N.L., Friedman, M., Logan, J.M., and Stearns, D.W., editors), AGU, Washington, DC, pp. 49-60.

King, R.J., 1986. Minerals explained 4: Opal (silica). Geology Today Mar-Apr 1986, pp. 58-61.

Knauth, L.P., 1994. Petrogenesis of chert. . In *Silica: Physical Behavior, Geochemistry and Materials Applications,* Review in Mineralogy, 29; Mineralogical Society of America, Washington, DC, pp. 233-258.

Koeberl C., 1990. The geochemistry of tektites: An overview. Tectonophysics 171, pp. 405–422.

Konhauser, K.O., Jones, B., Reysenbach, A.-L., Renaut, R.W., 2003, Hot spring sinter: keys to understanding Earth's earliest life forms. Can. J. Earth. Sci. 40, pp. 1713-1724.

Langer, K., Flörke, O.W., 1974, Near infrared absorption spectra (4000-9000 cm^{-1}) of opals and the role of "water" in these $SiO_2 \cdot nH_2O$ minerals. Fortschritte der Mineralogie 52, 17-51.

Laschet, C., 1984, On the origin of cherts. Facies 10, 257-289.

Lowe, D.R., 1975. Regional controls on silica sedimentation in the Ouachita System. GSA Bulletin 86, 8, pp. 1123-1127. doi: 10.1130/0016-7606(1975)86<1123:RCOSSI>2.0.CO;2.

Malin, M.C., and 27 colleagues, 2010. The Mars Science Laboratory (MSL) Mast-mounted Cameras (Mastcams) flight instruments, Lunar Planet. Sci. XLI, Abstract 1123.

Marzo, G.A., Davila, A.F., Tornabene, L.L., Dohm, J.M., Fairén, A.G., Gross, C., Kneissl, T., Bishop, J.L., Roush, T.L., McKay, C.P., 2010. Evidence for Hesperian impact-induced hydrothermalism on Mars. Icarus 208, 2, pp. 667–683. doi:10.1016/j.icarus.2010.03.013.

Mastrapa, R.M., Bernstein, M.P., Sandford, S.A., Roush, T.L., Cruikshank, D.P., and Dalle Ore, C.M., 2008. Optical constants of amorphous and crystalline H_2O-ice in the near infrared from 1.1 to 2.6 μm. Icarus 197, pp. 307-320. doi:10.1016/j.icarus.2008.04.008.

McDowell, M.L., Hamilton, V.E., Cady, S.L., Knauth, P., 2009. Thermal infrared and visible to near-infrared spectral analysis of chert and amorphous silica. Lunar Planet. Sci. XL, Abstract 1419.

McKeown, N.K., Bishop, J.L., Noe Dobrea, E.Z., Ehlmann, B.L., Parente, M., Mustard, J.F., Murchie, S.L., Swayze, G.A., Bibring, J.-P., Silver, E.A., 2009. Characterization of phyllosilicates observed in the central Mawrth Vallis region, Mars, their potential formational processes, and implications for past climate, J. Geophys. Res. 114, E00D10. doi:10.1029/2008JE003301.

McLennan, S.M., 2003. Sedimentary silica on Mars. Geology 31, 315–318. doi:10.1130/0091-7613(2003)031<0315:SSOM>2.0.CO;2.

McSween H.Y., and 41 colleagues, 2006. Characterization and petrologic interpretation of olivine-rich basalts at Gusev Crater, Mars, J. Geophys. Res. 111, E02S10. doi:10.1029/2005JE002477.

Mertzman, S.A., 2000. K–Ar results from the southern Oregon-northern California cascade range. Oregon Geol. 62, 99–122.

Michalski, J.R., Kraft., M.D., Dietrich, T., Sharp, T.G., Christensen, P.R., 2003. Thermal emission spectroscopy of the silica polymorphs and considerations for remote sensing of Mars. Geophys. Res. Lett. 30, 19. doi:10.1029/2003GL018354.

Milliken, R.E., and 11 colleagues, 2008a. Opaline silica in young deposits on Mars. Geology 36, 847–850. doi:10.1130/G24967A.1

Ming, D.W., Morris, R.V., Clark, B.C., 2008a. "Aqueous Alteration on Mars," Chapter 23 in *The Martian Surface: Composition, Mineralogy, and Physical Properties* (J.F. Bell III, ed.), Cambridge University Press, pp. 519-540.

Ming, D.W., and 19 colleagues, 2008b. Geochemical properties of rocks and soils in Gusev Crater, Mars: Results of the Alpha Particle X-Ray Spectrometer from Cumberland Ridge to Home Plate. J. Geophys. Res., 113. E12S39. doi:10.1029/ 2008JE003195.

Minitti, M.E., Weitz, C.M., Lane, M.D., Bishop, J.L., 2007. Morphology, chemistry, and spectral properties of Hawaiian rock coatings and implications for Mars, J. Geophys. Res. 112, E05015. doi:10.1029/2006JE002839.

Moroz, L.V., and 13 colleagues, 2009. Spectral properties of simulated impact glasses produced from martian soil analogue JSC Mars-1. Icarus 202, pp. 336–353. doi:10.1016/j.icarus.2009.02.007.

Morris, R.V., Ming, D.W., Golden, D.C., Graff, T.G., Achilles, C.N., 2010. Evidence for interlayer collapse of nontronite on Mars from laboratory visible and near-IR reflectance spectra. Lunar Planet. Sci. XLI, Abstract 1368. 2156.

Morris, R.V., and 12 colleagues, 2010. Identification of carbonate-rich outcrops on Mars by the Spirit rover. Science 329, 5990, pp. 421-424. doi:10.1126/science.1189667.

Murchie, S.L., and 16 colleagues, 2009. A synthesis of martian aqueous mineralogy after 1 Mars year of observations from the Mars Reconnaissance Orbiter. J. Geophys. Res. 114, E00D06. doi:10.1029/2009JE003342.

Mustard, J.F., and 35 colleagues, 2008. Hydrated silicate minerals on Mars observed by the Mars Reconnaissance Orbiter CRISM instrument. Nature 454, 305–309. doi:10.1038/nature07097.

Nakata, Y., Suzuki, M., Okutani, T., Kikuchi, M., Akiyama, T., 1989. Preparation and properties of SiO_2 from rice hulls. J. Ceram. Soc. Jpn. 97, pp. 830-836.

Noe Dobrea, E.Z. and 14 colleagues, 2010. Mineralogy and stratigraphy of phyllosilicate-bearing and dark mantling units in the greater Mawrth Vallis/west Arabia Terra area: Constraints on geological origin, J. Geophys. Res. 115, E00D19. doi:10.1029/2009JE003351.

Osinski, G.R., Haldemann, A.F.C., Schwarcz, H.P., Smith, J.R., Kleindienst, M.R., Kieniewicz, J., Churcher, C.S., 2007. Impact glass at the Dakhleh Oasis, Egypt: Evidence for a cratering event or large aerial burst? Lunar Planet. Sci. XXXVIII, Abstract 1346.

Paterson, M.S., 1982. The determination of hydroxyl by infrared absorption in quartz, silicate glass and similar materials. Bulletin de Minèralogie 105, pp. 20-29.

Preston, L.J., Benedix, G.K., Genge, M.J., Sephton, M.A., 2008. A multidisciplinary study of silica sinter deposits with applications to silica identification and detection of fossil life on Mars. Icarus 198, 331–350. doi:10.1016/j.icarus.2008.08.006.

Proust, D., Fontaine, C., 2007. Amethyst-bearing lava flows in the Paraná Basin (Rio Grande do Sul, Brazil): cooling, vesiculation and formation of the geodic cavities. Geological Mag. 144, pp. 53-65. doi:10.1017/S001675680600269X.

Reich, M., Zúñiga, A., Amigo, A., Vargas, G., Morata, D., Palacios, C., Parada, M.A., Garreaud, R.D., 2009. Formation of cristobalite nanofibers during explosive volcanic eruptions. Geology 37, pp. 435-438. doi:10.1130/G25457A.1.

Rice, M.S., Bell, J.F. III, Cloutis, E.A., Wang, A., Ruff, S., Craig, M.A., Bailey, D.T., Johnson, J.R., de Souza Jr., P.A., Farrand, W.H., 2010. Silica-rich deposits and hydrated minerals at Gusev crater, Mars: Vis-NIR spectral characterization and regional mapping. Icarus 205, 375–395. doi:10.1016/j.icarus.2009.03.035.

Rice, M.S., Bell, J.F. III, Cloutis, E.A., Wray, J.J., Herkenhoff, K.E., Sullivan, R., Johnson, J.R., Anderson, R.B., 2011. Temporal observations of bright soil exposures at Gusev crater, Mars. J. Geophys. Res. 116, E00F14. doi:10.1029/2010JE003683.

Rodgers, A., Cressey, G., 2001. The occurrence, detection and significance of moganite (SiO_2) among some silica sinters. Min. Mag. 65, 157 - 167.

Rodgers, K., and 13 colleauges, 2004. Silica phases in sinters and residues from geothermal fields of New Zealand. Earth Sci. Rev. 66, 1–61. doi:10.1016/j.earscirev.2003.10.001

Rogers, K.A., Cook, K.L., Browne, P.R.L., Campbell, K.A., 2002.The mineralogy, texture and significance of silica derived from alteration by steam condensate in three New Zealand geothermal fields. Clay Minerals 37, 299-322.

Ruff, S.W., and 10 colleagues, 2011. Characteristics, distribution, origin, and significance of opaline silica observed by the Spirit rover in Gusev crater, Mars, J. Geophys. Res. 116, E00F23. doi:10.1029/2010JE003767.

Segnit, E.R., Stevens, T.J., Jones, J.B., 1965, The role of water in opal. J. Geol. Soc. Aust. 12, 211-226.

Skok, J.R., Mustard, J.F., Ehlmann, B.L., Milliken, R.E., Murchie, S.L., 2010. Silica deposits in the Nili Patera caldera on the Syrtis Major volcanic complex on Mars. Nature Geoscience 3, 12, pp. 838–841. doi:10.1038/ngeo990.

Smith, D.K., 1998. Opal, cristobalite, and tridymite: noncrystallinity versus crystallinity, nomenclature of the silica minerals and bibliography. Powder Diffraction 13, 2-19.

Smith, M.L., Bandfield, J.L., Gillespie, A.R., 2011. Felsic and Altered Mineral Suite in Antoniadi Crater, Mars as a Future Rover Landing Site. Lunar Planet. Sci. Conf. XLII, Abstract 1671.

Smith, P., and 35 colleagues, 2009. H_2O at the Phoenix landing site. Science 325, 58-61. doi:10.1126/science.1172339.

Squyres, S.W., and 17 colleagues, 2008. Detection of silica-rich deposits on Mars. Science 320, 1063–1067. doi:10.1126/science.1155429.

Sunshine, J.M., Pieters, C.M., Pratt, S.F., 1990. Deconvolution of mineral absorption bands - An improved approach. J. Geophys. Res. 95, 6955. doi:10.1029/JB095iB05p06955.

Thompson, W.K., 1965. An infrared study of water adsorbed on silica. Proc. Brit. Ceram. Soc. 5, 143-151.

Ugolini, F., 1986. Pedogenic zonation in the well-drained soils of the arctic regions. Quaternary Res 26, 100-120.

Van Thiel, M., Becker, E.D., Pimentel, G.C., 1957. Infrared studies of hydrogen bonding of water by the matrix isolation technique. J. Chem. Phys. 27, pp. 486-490.

Wang, A., and 15 colleagues, 2008. Light-toned salty soils and coexisting Si-rich species discovered by the Mars Exploration Rover Spirit in the Columbia Hills. J. Geophys. Res. 113, E12S40. doi:10.1029/2008JE003126.

Wang, Y., Merino, E., 1990. Self-organizational origin of agates: Banding, fiber twisting, composition, and dynamic crystallization model. Geochim. Cosmochim. Acta 54, pp. 1627-1638.

Webb, J.A., Finlayson, B.L., 1987, Incorporation of Al, Mg, and water in opal-A: Evidence from speleothems. Am. Mineral. 72, 1204-1210.

Weitz, C.M., Milliken, R.E., Grant, J.A., McEwen, A.S., Williams, R.M.E., Bishop, J.L., Thomson, B.J., 2010. Mars Reconnaissance Orbiter observations of light-toned layered deposits and associated fluvial landforms on the plateaus adjacent to Valles Marineris. Icarus 205, 1, pp. 73–102. doi:10.1016/j.icarus.2009.04.017.

Wendt, L., Gross, C., Kneissl, T., Sowe, M., Combe, J.-P., LeDeit, L., McGuire, P., Neukum, G., 2011. Sulfates and iron oxides in Ophir Chasma, Mars, based on OMEGA and CRISM observations. Icarus 213, pp. 86-103. doi:10.1016/j.icarus.2011.02.013.

White, D.E., Hutchinson, R.A., Keith T.E.C., 1988. The geology and remarkable thermal activity of Norris Geyser Basin, Yellowstone National Park, U.S. Geol. Surv. Prof. Pap. 1456.

Worley, J.D., Klotz, I.M., 1966. Near-infrared spectra of H_2O-D_2O solutions. J. Chem. Phys. 45, pp. 2868-2871.

Wray, J.J., and 13 colleagues, 2011. Columbus crater and other possible groundwater-fed paleolakes of Terra Sirenum, Mars. J. Geophys. Res. 116, E01001. doi:10.1029/2010JE003694.

Yamatera, H., Fitzpatrick, B., Gordon, G., 1964. Near infrared spectra of water and aqueous solutions. J. Mol. Spectrosc. 14, pp. 268-278.

CHAPTER 4

TEMPORAL OBSERVATIONS OF BRIGHT SOIL EXPOSURES AT GUSEV CRATER, MARS[1]

0. Abstract

The Mars Exploration Rover (MER) Spirit has discovered bright soil deposits in its wheel tracks that previously have been confirmed to contain ferric sulfates and/or opaline silica. Repeated Pancam multispectral observations have been acquired at four of these deposits to monitor spectral and textural changes over time during exposure to martian surface conditions. Previous studies suggested that temporal spectral changes occur due to mineralogic changes (e.g. phase transitions accompanying dehydration) (Wang et al., 2008). In this study, we present a multispectral and temporal analysis of eight Pancam image sequences at the Tyrone exposure, three at the Gertrude Weise exposure, two at the Kit Carson exposure, and ten at the Ulysses exposure that have been acquired as of sol 2132 (1 January 2010). We compare observed variations in Pancam data to spectral changes predicted by laboratory experiments for the dehydration of ferric sulfates. We also present a spectral analysis of repeated Mars Reconnaissance Orbiter (MRO) HiRISE observations spanning 32 sols, and a textural analysis of Spirit Microscopic Imager (MI) observations of Ulysses spanning 102 sols. At all bright soil exposures, we

[1] An edited version of this paper was published by AGU. Copyright 2011 American Geophysical Union. Full citation: Rice, M. S., J. F. Bell III, E. A. Cloutis, J. J. Wray, K. E. Herkenhoff, R. Sullivan, J. R. Johnson, and R. B. Anderson (2011), Temporal observations of bright soil exposures at Gusev crater, Mars, Journal of Geophysical Research - Planets, 116, E00F14, doi:10.1029/2010JE003683.

observe no statistically significant spectral changes with time that are uniquely diagnostic of dehydration and/or mineralogic phase changes. However, at Kit Carson and Ulysses, we observe significant textural changes, including slumping within the wheel trench, movement of individual grains, disappearance of fines, and dispersal of soil clods. All observed textural changes are consistent with aeolian sorting and/or minor amounts of airfall dust deposition.

1. Introduction and Background

The Mars Exploration Rover (MER) Spirit has excavated subsurface deposits of sulfate- and/or silica-rich materials in eighteen locations in the Columbia Hills of Gusev Crater, Mars. These deposits occur as anomalously high albedo soil exposures within the rover's wheel tracks, with white and/or yellow hues that vary over small length scales. Most of these deposits have been brought up from depths of ~10 cm by the dragging motion of Spirit's inoperative right front wheel, its actuator having failed on sol 779 of the mission. In-situ measurements with Spirit's Alpha Particle X-Ray Spectrometer (AXPS) have revealed that these soils have the highest sulfur concentrations (up to 38 wt.% SO_3) of any materials yet observed by either of the MER rovers (Ming et al., 2006, 2008; Arvidson et al., 2011). Mössbauer (MB) spectrometer data suggest the presence of ferric-bearing sulfates (e.g., Gellert et al., 2006; Morris et al., 2006, 2008b), and the soils' distinctive Panoramic Camera (Pancam) and Miniature Thermal Emission Spectrometer (Mini-TES) spectra are consistent with a heterogeneous mixture of hydrated ferric sulfates (e.g., Johnson et al., 2007; Lane et al., 2008; Parente et al., 2009).

At the soil exposure called Gertrude Weise, the highest albedo soil observed by Spirit, APXS measurements revealed a nearly pure silica composition (~98 wt.% SiO_2 when corrected for dust contamination) and minor TiO_2 (Squyres et al., 2008). Mini-TES measurements of this soil are consistent with the presence of hydrated amorphous silica (Squyres et al., 2008; Ruff et al., 2011), and a ~1 μm absorption feature in Pancam spectra indicates the presence of H_2O and/or OH (Rice et al., 2010a). While Gertrude Weise is the only nearly-pure silica soil yet discovered, the sulfate-bearing exposures at regions called Tyrone and Ulysses also contain a component enriched in SiO_2 (Squyres et al., 2008; Wang et al., 2008; Arvidson et al., 2011; Ruff et al., 2011).

The mineralogy, geochemistry, spatial variability, and geologic setting of the bright subsurface soils suggest that they likely formed in a hydrothermal environment from fumarolic condensates, precipitation from geothermal waters, and/or leaching of local basaltic rocks (e.g., Squyres et al., 2008; Yen et al., 2008; Morris et al., 2008b). The time of hydrothermal activity within Gusev Crater, when the sulfate- and silica-rich soils would have formed, is not well constrained; however, the processes that have sorted, transported and modified the bright soil material may be on-going. Indeed, the layered structure of the Ulysses soil, where soluble ferric-sulfate species appear to be segregated below a layer with a less soluble silica-rich component, all below an insoluble, cemented hematite and calcium-sulfate surface layer, suggests an on-going pedogenic modification from downward migration of soluble materials by gravity-driven water (Arvidson et al., 2011).

Some ferric sulfate species that have been proposed as possible components of the Spirit bright soil exposures, such as ferricopiapite

($Fe_{2/3}^{2+}Fe_4^{3+}(SO_4)_6(OH)_2 \cdot 20(H_2O)$) and fibroferrite ($Fe^{3+}(SO_4)(OH) \cdot 5H2O$) (Johnson et al., 2007; Lane et al., 2008; Parente et al., 2009), are known to be unstable under current martian surface conditions (Chipera et al., 2007; Cloutis et al., 2008; Freeman et al., 2009; Wang et al., 2011). If the relative humidity environment in the near subsurface differs from that of the surface (i.e., is buffered by hydrated minerals or ground ice), it is possible that buried soils are not in equilibrium with surface conditions at the Spirit site, and that some minerals could undergo dehydration and/or phase changes after exhumation by the rovers' wheels.

Spectral changes are known to accompany mineralogic changes among ferric sulfates and hydrated silica phases, resulting in modifications to their visible color (Cloutis et al., 2008; Rice et al., 2010b; Wang et al., 2011). Wang et al. (2008) suggested that such modifications occurred for the Tyrone soil, and they described changes in the blue-to-red (432 to 753 nm) spectral slope in Pancam observations spanning a period of ~150 sols. Textural changes, such as shrinkage and cracking, are also expected to accompany the dehydration of hydrated ferric sulfates based on laboratory experiments (e.g., Cloutis et al., 2008).

To test the hypothesis that the Spirit bright soils have undergone mineralogic changes upon exposure to the martian surface, we have performed a detailed analysis of Pancam multispectral images at the four sites where repeat observations have been made: Tyrone (sols 790-1062), Gertrude Weise (sols 1158-1198), Kit Carson (sols 1864-1866), and Ulysses (sols 1888-2132). We include a multispectral analysis of repeated Mars Reconnaissance Orbiter (MRO) High Resolution Imaging Science Experiment (HiRISE) observations of these soils for sols 1935 to 1967 and compare

the analyses to Pancam observations. We also compare temporal observations in both the Pancam and HiRISE multispectral data to the variations predicted from laboratory experiments on ferric sulfate minerals exposed to current martian surface conditions.

For the Pancam images with high enough spatial resolution to resolve soil texture (at Kit Carson and Ulysses), we describe textural changes observed with time and discuss whether they are indicative of mineralogic changes, aeolian sorting, and/or dust deposition within the soil trenches. Although detailed studies of the wind-driven mobility of basaltic sand and airfall dust have been performed at Gusev Crater (e.g. Greeley et al., 2006; Sullivan et al., 2008), no assessment has yet been made of the mobility of the bright soils, which we address here. We also use the available repeated observations of these soils from Spirit's Microscopic Imager (MI) to observe and document additional textural changes, allowing us to characterize temporal changes in the bright soils from the microscopic to orbital scale.

2. Methods

2.1 Pancam Observations

2.1.1 Pancam Instrument and Calibration

The Pancam instrument consists of two cameras at a 30 cm stereo separation, each using a 1024 x 1024 pixel charge-coupled device (CCD) detector with 0.27 mrad per pixel resolution (Bell et al., 2003; Bell et al., 2006). Pancam's 13 narrowband geology filters cover 11 specific wavelengths in the visible and near infrared (432 to 1009 nm; Table 1). Some of the images used in this study were acquired using lossy wavelet-based ("ICER") compression (Maki et al., 2003). Based on pre-launch tests,

Table 1. Pancam filter data.

Filter	Effective Wavelength (nm)[a]	Band Pass (nm)[a]	Camera
L7	432	32	LEFT
R1	436	37	RIGHT
L6	482	30	LEFT
L5	535	20	LEFT
L4	601	17	LEFT
L3	673	16	LEFT
L2	753	20	LEFT
R2	754	20	RIGHT
R3	803	20	RIGHT
R4	864	17	RIGHT
R5	904	26	RIGHT
R6	934	25	RIGHT
R7	1009	38	RIGHT

[a] from Bell et al. (2003)

compression effects on radiometric precision at the typical compression bit rates employed using the ICER compressor were estimated to be less than 1% (Bell et al., 2006).

We use near-simultaneous observations of the Pancam calibration target, as well as pre-launch calibration and modeling, to derive estimated reflectances of the scene relative to the standard reflectance materials on the calibration target (Bell et al., 2003; Bell et al., 2006). To correct for dust contamination of the calibration target, Pancam data are calibrated using a two-layer radiative transfer model (Sohl-Dickstein et al., 2005; Bell et al., 2006; Kinch et al., 2007). The Pancam reflectance products are called “IOF” images, where IOF (also known as the “radiance factor” or "I over F"; Hapke, 1993), is defined as the ratio of the bidirectional reflectance of a surface to that of a normally illuminated, perfectly diffuse surface. Dividing the Pancam IOF images

by the cosine of the solar incidence angle at the time of each observation gives the relative reflectance R* (Reid et al., 1999; Bell et al., 2006), also known as the "reflectance factor" or "reflectance coefficient" (Hapke, 1993). Bell et al. (2006) have estimated the relative filter-to-filter uncertainties in R* to be 1-5%, and the absolute reflectance levels to be accurate to within ~10%. Because diffuse component corrections are relatively minor at the solar incidence angles of our dataset (6^{o}-40^{o}; Table 2) (Johnson et al., 2006), we did not correct for diffuse illumination.

2.1.2 Extraction of Pancam Spectra

We have acquired visible to near-infrared (Vis-NIR) spectra of the soil targets by manually selecting pixels from common regions of interest (ROIs) in the right and left camera datasets and averaging the R* values of those regions for each filter. We have chosen ROIs for each target that include as many pixels as possible (to minimize instrumental artifacts and statistical noise), excluding shadowed regions. We also exclude pixels that are potentially approaching saturation to ensure that we only use data within the demonstrated linearity of the Pancam instrument (Bell et al., 2003). For the Tyrone, Kit Carson, and Ulysses soils, we have selected ROIs from both the "yellow" and "white" hue separations (indicated by the yellow and black outlines, respectively, in Figures 2, 6, 9 and 12). In all images, we also extracted representative spectra from other scene elements (undisturbed dusty soil and disturbed dark soil, indicated by the red and brown outlines). For the blue (432 and 436 nm) and red (753 and 754 nm) stereo filters, we have used the R* values acquired by the left camera (432 and 753 nm). The error bars represent the variance among the selected ROI

Table 2. Pancam full filter imaging sequences used for spectral characterization of bright soils.

Soil Exposure Name[a]	Sol	Site[b]	Position[b]	Sequence ID	Local True Solar Time[c]	Imaging Duration (seconds)	Incidence Angle (degrees)[c]	Emission Angle (degrees)[c,d]	Phase Angle (degrees)[c]	Sols After Exposure	Tau[e]	Saturated Filters[f]
Tyrone	790	126	142	P2531	11:56:05	236	26.9	28.2	41.5	8	0.342	L67
	864	128	0	P2547	12:37:47	231	38.3	5.8	64.0	82	0.256	L6
	922	128	0	P2552	12:02:10	288	39.9	5.4	71.6	140	0.295	L6
	959	128	0	P2560	12:07:35	249	38.9	5.4	70.7	177	0.302	---
	982	128	0	P2566	12:10:36	211	37.0	5.4	70.5	200	0.312	---
	1005	128	0	P2576	12:23:12	353	34.7	5.4	68.3	223	0.240	---
	1036	128	20	P2585	13:03:39	200	33.1	6.1	60.2	254	0.381	---
	1062	128	115	P2596	12:30:12	412	25.1	5.6	70.5	280	0.883	---
Gertrude Weise	1158	128	1318	P2581	12:29:46	274	7.3	12.0	74.9	10	0.800	---
	1187	129	112	P2533	12:16:34	261	6.4	19.6	64.6	39	0.939	---
	1198	129	140	P2539	12:11:16	394	7.4	42.2	55.1	50	0.943	---
Kit Carson	1864	136	614	P2562[g]	12:32:30	183	10.1	48.0	31.9	3	1.187	---
	1866	136	614	P2555	12:43:18	286	12.3	57.3	20.7	5	1.103	---
Ulysses	1888	137	130	P2559	14:01:10	878	30.0	65.6	42.1	2	0.875	---
	1892	137	178	P2560	13:07:52	254	18.7	54.6	34.3	6	0.823	---
	1894	137	182	P2560	13:04:35	252	18.1	54.6	34.1	8	0.792	---
	1897	137	195	P2562	12:24:41	262	11.6	58.3	24.6	11	0.768	---
	1933	137	249	P2382[h]	13:32:11	4372	23.8	58.5	40.4	47	0.470	---
	1982	137	249	P2547	13:15:13	254	18.3	66.3	26.3	96	0.377	R1
	2019	137	249	P2392[h]	11:41:49	4360	6.1	58.7	32.8	142	1.452	L567R1[i]

[a] Feature names are informal and not formally accepted by the International Astronomical Union;
[b] The surface coordinate frames utilized by MER (Maki et al., 2003);
[c] At the starting time of the Pancam observation and for the center of the image
[d] The INSTRUMENT_ELEVATION parameter stored in the image label;
[e] Visible optical depth observed with Pancam's L8 filter (Lemmon *et al.*, 2004)
[f] Where clusters of pixels in the raw image equal 4095 DN
[g] This sequence includes a reduced filter set: L257R12467
[h] These sequences contain five pointings to cover the extent of the soil exposure
[i] The saturated pixels in this sequence were over reflective portions of the spacecraft, not the soil exposures

Table 3. Spectral parameters used in this study

Parameter	Description
535 nm band depth	$1 - (R^*_{535} / [(0.573 \times R^*_{432}) + (0.427 \times R^*_{673})])$
753 nm to 432 nm ratio	$(R^*_{753}) / (R^*_{432})$
864 nm band depth	$1 - (R^*_{864} / [(0.387 \times R^*_{753}) + (0.613 \times R^*_{934})])$
934 to 1009 nm ratio	$(R^*_{934}) / (R^*_{1009})$

pixels, rather than from the formal instrumental noise (which is generally much lower) (Bell et al., 2006).

2.1.3 Comparisons of Spectral Parameters

To quantify spectral variations with time, we have chosen four spectral parameters to compare between image sequences (Table 3). Three of these parameters characterize distinctive regions of the Vis-NIR spectra of ferric sulfates: (1) the 753 to 432 nm ratio, which quantifies the overall "redness" of the sample's color; (2) the 535 nm band depth, which indicates the strength of Fe^{3+} absorptions near ~550 nm; and (3) the 864 nm band depth, which quantifies the diagnostic Fe^{3+}-related absorptions at ~850-900 nm. Strong 535 nm and 864 nm band depths have been used in previous studies to classify the Pancam spectra of sulfate-rich soils at Gusev Crater (Farrand et al., 2008; Parente et al., 2009). We have also acquired laboratory spectra of four candidate ferric sulfates during long-term exposure to martian surface conditions in order to characterize the temporal behavior of these spectral parameters for specific minerals (described in Section 2.4).

The fourth spectral parameter that we monitor is the 934 to 1009 nm ratio.

This parameter has previously been used to detect silica-rich materials along the rover's traverse in Gusev Crater (Wang et al., 2008; Rice et al., 2010a). A high 934 to 1009 nm ratio (or steeply negative 934 to 1009 nm slope) is attributed to a combinational mode of H_2O ($2v_1 + v_3$) and/or an OH overtone (3v) near ~970-1000 nm, and its magnitude is sensitive to the amount of OH/H_2O present in the mineral and/or adsorbed on mineral grains (Rice et al., 2010a). For a detailed explanation of the attribution of a negative 934 to 1009 nm slope to water and/or OH, as opposed to other factors that can affect the spectral slope (such as viewing geometry, dust coatings or an uncorrected diffuse component), we refer the reader to Rice et al. (2010a). Because the depths of all H_2O and OH absorption features in silica decrease during dehydration experiments (e.g. Cloutis et al., 2008; Rice et al., 2010b), an observed decrease in the magnitude of the 934 to 1009 nm ratio with time would be consistent with the soils dehydrating upon exposure.

We estimate the uncertainty in the spectral parameters by propagating the uncertainty in R* through the calculations shown in Table 3 by standard error analysis (e.g. the fractional uncertainty in the 753 to 432 nm ratio is calculated as the sum in quadrature of the fractional uncertainties in R^*_{753} and R^*_{432}).

2.1.4 Correction for Minor Dust Contamination of Camera Optics

All images used in this study exhibit some effects attributed to minor heterogeneous dust contamination on the front sapphire windows of the Pancam instruments. The effect is too small to be meaningful in individual filter images, but it is enhanced in the ratio and band depth maps used in this study, where top-to-bottom

brightness gradients of up to 5-10% have been observed in some scenes. This gradient does not affect our spectral comparisons when the ROIs are selected from the same region of the CCD in each image (as is the case for the Tyrone and Ulysses observations), but it must be accounted for when we compare spectra from different locations in each image.

In this study we account for dust contamination effects on the optics by considering the spectral parameters as ratios of the bright soil targets to dusty, undisturbed soils imaged in similar regions of the field of view (FOV), rather than as absolute values. We assume that the spectra of undisturbed, dust-covered surface soils should not change between image sequences under the same or nearly the same lighting conditions. Because undisturbed soils are primarily of basaltic composition (e.g., Sullivan et al., 2008; Morris et al., 2008a) and have likely been exposed to surface conditions for an extensive time, we assume that they are in equilibrium and do not undergo mineralogic changes during our short observation periods. Thus we can enhance our ability to detect changes in the sulfate- and silica-rich soils by observing them relative to unchanging, undisturbed materials. The uncertainty in these ratios is estimated by propagating the uncertainties in the values of the spectral parameters for the bright and undisturbed soils, which is a conservative but prudent overestimate of the true instrumental error.

2.1.5 Coregistration of Multiple Image Sequences

To monitor pixel-to-pixel changes between Pancam image sequences, we have coregistered the image sequences from Tyrone that were acquired from nearly

identical positions. During Spirit's second winter campaign, the rover was parked at Low Ridge in view of the Tyrone soil exposure at Low Ridge (Figure 1) and made five Pancam 13-filter observations from sols 864-1005 (Table 2). We have shifted each of those image sequences by an integer number of pixels in the x and y directions to coregister all images for direct spectral comparisons. In all cases the required shifts were small (< 30 pixels, <3% of the FOV), and thus there were no significant variations in emission angle geometry among these observations. The effect of coregistration on radiometric precision is minor given that the shifts were integer-only and the images were not re-sampled. Tyrone was the only soil target from which multiple Pancam observations were acquired from similar enough perspectives to perform a coregistration.

To illustrate trends in temporal variations of the spectral parameters listed in Table 3, we have calculated the percent change of each parameter for each pixel in the coregistered Tyrone image set. For every pixel, we have performed a linear regression fit to the spectral parameter vs. sol data, and we calculate the percent difference between the values of the linear function at the first and last sols of observation. We use the resulting "percent change maps" in addition to spectra from selected ROIs (*Section 2.1.2*) to look for systematic spectral variations relative to the rest of the scene in the Tyrone observations.

2.2 HiRISE Observations

2.2.1 HiRISE Instrument and Calibration

Orbital monitoring provides an independent view of the spectral evolution of bright soils exposed by Spirit, and enables monitoring to continue even after the rover has driven out of Pancam imaging range. Specifically, the MRO HiRISE camera (McEwen et al., 2007) has a sufficiently small pixel scale (~26.5 cm at the latitude of the Columbia Hills) to enable detection of the largest exposures of bright soils. HiRISE has three color filters: blue-green (BG; l_{eff}=502±157 nm), red (RED; l_{eff}=686±267 nm), and near-infrared (IR; l_{eff}=878±143 nm) (McEwen et al., 2007; Delamere et al., 2010), allowing detection of color changes over a limited portion of the spectrum. BG and IR data can only be acquired for a central strip covering 20% of each HiRISE RED image. In this study we compare the two observations with color coverage of the Home Plate vicinity during the period over which the Kit Carson soils were visible from orbit (Table 4).

The current state of radiometric calibration for HiRISE was recently described by Delamere et al. (2010). Uncertainties in absolute I/F values were estimated as ±20% absolute, whereas relative errors within a HiRISE image are typically only ~2% (~0.5% within a single CCD channel). This high relative precision can be exploited for change detection studies by observing not just the change in absolute I/F of a feature of interest, but also the change in I/F ratio between a feature of interest and an undisturbed homogeneous area of adjacent terrain within the same CCD channel. This technique has been used successfully to monitor color and albedo changes of 20-60% attributed to sublimation of subsurface water ice exposed by impact cratering (Byrne et al., 2009).

Table 4. HiRISE Observations of Kit Carson soils

Image ID	Sol	LTST	RED pixel scale (cm)	IR/BG pixel scale (cm)	Incidence angle (°)	Emission angle (°)	Phase angle (°)	Atmospheric opacity (τ)
ESP_013499_1650	1935	14:39	26.9	53.8	38.7	10.1	48.5	0.51
ESP_013921_1650	1967	14:28	26.5	26.5	35.8	8.5	27.4	0.39

To correct for the spectral contribution from atmospheric aerosols, which can either brighten or darken the apparent I/F of a given pixel depending on the surface albedo, we use the method described by Portyankina et al. (2010), which has previously been tested on the set of images used in this study and demonstrably reduces I/F discrepancies between them. We have performed our analysis with and without the Portyankina et al. dust correction, and find that the correction changes relative I/F values in the RED and IR filters by <1% and in the BG filter by 3-5% for both observations. The estimated added uncertainty in I/F due to the dust correction is ~1%.

2.2.2 Comparison of HiRISE color data

We resampled each HiRISE image (Table 4) to 50 cm/pixel so that they could be compared directly. This pixel size is large compared to the bright soil exposures, suggesting that most or all "bright soil" pixels are actually spatial mixtures of bright soil plus adjacent undisturbed soils and/or rocks (which are universally darker). We therefore measured I/F only for the brightest pixel within each soil exposure in a given image in order to minimize spectral contamination from other materials. There was no saturation in any HiRISE band for the soils observations. To reduce the effects of differing illumination and observation geometry between images (Table 4), we divided these bright soil I/F values by those extracted from nearby areas of the surface that appear relatively uniform and were not disturbed by Spirit. We tested several of these denominators (each an average of ~100 pixels) to confirm that our results do not depend on the choice of denominator.

Table 5. Microscopic Imager observations

Soil Exposure Name	Target Name	Sol	Starting Image ID	Relation to MB	Sols After Exposure
Kit Carson/ John Wesley Powell	John Wesley Powell	1863	2M291757231	post-MB	3
Ulysses	Sackrider	1922	2M296987659	post-MB	36
		1925	2M297265696	post-MB	39
		1982	2M302317675 2M302318000 2M302318330 2M302318917	no MB	96
	Penina	1936	2M298228753	post-MB	50
		1940	2M298597018	post-MB	54
		1941	2M298683977	post-MB	55
		1986	2M302672548 2M302672856	no MB	100
		2024	2M306051847	no MB	138

We measured the BG, RED and IR relative I/F for the Kit Carson, Gertrude Weise and Tyrone soils, which had been exposed to the surface for 74, 787 and 1153 sols, respectively, when the first HiRISE observation was made. For additional points of comparison, we extracted single-pixel I/F values for four nearby bright "calibration" outcrops undisturbed by Spirit, which would not be expected to undergo intrinsic spectral changes. We also measured the ratios of relative RED to relative BG for comparison with Pancam red to blue ratios (753 nm to 432 nm), as well as relative IR to relative RED.

2.3 Microscopic Imager Observations

The Microscopic Imager (MI) is a fixed-focus camera mounted on the instrument arm, with the same 1024 x 1024 CCD as the other MER cameras (Herkenhoff et al., 2003). The MI acquires panchromatic images at a scale of 31 microns/pixel over a broad spectral range (400 to 700 nm). The MI acquires images

using solar or diffuse skylight illumination of the target surface. The MI focal section merges used in this study combine the best-focused parts of images acquired at multiple distances from the target, separated by the 3 mm depth of field of the MI. Some MI images were merged with Pancam color data using the approach described by Herkenhoff et al. (2006). Details of all MI observations used in this study are provided in Table 5.

2.4 Laboratory Exposure of Ferric Sulfates to Martian Surface Conditions

To better characterize the expected spectral behavior of ferric sulfate materials as they dehydrate upon exposure to current martian surface conditions, and to predict the spectral changes observable to the Pancam and HiRISE instruments, we have subjected four ferric sulfate samples to long-duration (150+ days) simulated martian pressure and temperature conditions: (1) coquimbite ($Fe^{3+}_2(SO_4)_3 \cdot 9H_2O$); (2) ferricopiapite ($Fe_{2/3}^{3+}Fe_4^{3+}(SO_4)_6(OH)_2 \cdot 20(H_2O)$); (3) fibroferrite ($Fe^{3+}(SO_4)(OH) \cdot 5H2O$); and (4) rhomboclase ($HFe^{3+}(SO_4)_2 \cdot 4H_2O$). These specific ferric sulfates were chosen based on their identification as possible mineral constituents of the Gusev bright soil deposits from Pancam spectral deconvolution studies (Johnson et al., 2007; Lane et al., 2008; Parente et al., 2009). All samples were characterized by X-ray fluorescence and X-ray diffraction, and water contents were measured as the weight losses upon heating the samples to 900^o C for 1 to 1.5 hours, as described by Mertzman (2000). The compositions and phases of each sample are provided in Table 6.

Table 6. Composition of samples used in this study

Wt. %[a]	Coquimbite SPT126	Ferricopiapite SPT125	Fibroferrite SPT121	Rhomboclase SPT139
SiO_2	1.14	4.39	2.6	0.48
TiO_2	0.09	0.06	0.04	0.04
Al_2O_3	1.25	2.01	0.21	0.02
Fe_2O_3 (tot.)[b]	(94.05)	(27.01)	(95.02)	(98.24)
FeO[c]	0.34	0.00	0.00	0.28
Fe_2O_3[c]	93.67	27.01	95.02	97.93
MnO	0.08	0.01	0.04	0.01
MgO	1.34	0.27	0.31	0.02
CaO	0.34	0.41	0.7	0.22
Na_2O	0.44	4.25	0.58	0.08
K_2O	0.04	1.69	0.1	0.01
P_2O_5	0.04	0.07	0.03	0.01
SO_3		33.16		
Total	**99.77**[d]	**99.16**	**99.63**[d]	**99.63**[d]
LOI[e]	71.45	58.99	63.22	74.79
SO_3[f]	31.10		35.38	26.87
H_2O[g]	40.35	25.83	27.84	47.92
ppm				
Sr	6	<5	15	<2
Zr	<1	15	29	10
V	13	90	72	<1
Co			<2	
Cr	8	55	48	21
Ni			<2	
Rb			8	
Pb	65			5
Zn	2345			33
XRD[h]	coquimbite, paracoquimbite	ferricopiapite, minor jarosite	fibroferrite, minor butlerite	pure rhomboclase

[a] Analysed by X-ray fluorescence at Franklin and Marshall College by Stan Mertzman (March 2002).
[b] Total Fe expressed as Fe_2O_3.
[c] FeO determined by wet chemistry and Fe_2O_3 as difference between total Fe and FeO.
[d] Elemental totals expressed on a volatile-free basis.
[e] Loss on ignition represents percent weight loss after heating to 900°C for 1 to 1.5 hours.
[f] S expressed as SO_3 and determined by ignition at the University of Alberta (August 2000).
[g] H_2O is taken as the difference between the measured values of LOI and SO_3.
[h] Phases listed in order of abundance as measured by X-ray diffraction at the University of Manitoba Department of Geological Sciences in May and June of 1999. The samples were run in continuous scanning mode to provide information on the <45µm size samples and whether any accessory phases are present.

The samples were ground and sieved to <45 μm and exposed to simulated Mars surface conditions using the University of Winnipeg's miniature Mars Environment (mini-ME) chamber (Craig et al., 2001). A constant atmospheric pressure was maintained at 660 Pa CO_2 (6.6 mbar; 5 Torr), and the sample temperature was restricted to close to maximum surface temperatures on present-day Mars (~20 ^{o}C), as described by Cloutis et al. (2008). We note that the partial pressure of water vapor (pH_2O) was not monitored during the experiment; however a constant supply of dry CO_2 was supplied to the samples and Mars atmospheric pressure maintained with a vacuum pump, and thus the expected relative humidity is near zero.

Reflectance spectra were measured with an Analytical Spectral Devices (ASD) FieldSpec Pro HR spectrometer (at a viewing geometry of i=0° and e=0° using a bifurcated probe) through a 10 mm-thick sapphire window. Sample spectra were measured relative to a halon standard and corrected for minor (<2%) irregularities in its absolute reflectance. Spectra were collected every few days for the first month, and then on a roughly monthly basis (9 spectra acquired over 150 days of exposure). In every case, 1000 spectra of the dark current, standard and sample were acquired to provide sufficient signal to noise for subsequent interpretation.

During the experiment, the ferric sulfate samples exhibited various decreases in volume that resulted in sample surface shrinkage, the sample moving away from the sides of the well, and/or cracking. When coupled with the small path length of the ASD probe to the sample, the surface shrinkage sometimes caused a significant change in overall reflectance. Because the samples could not be accessed during the experimental run, we chose to analyze the results as scaled reflectance (all spectra

normalized to unity at 1250 nm), rather than in absolute reflectance. We note that normalizing the spectra has no effect on the calculated values of the spectral parameters used in this study, which are all based on relative, rather than absolute, reflectance levels.

To simulate MER Pancam observations of these minerals on the martian surface, we multiplied the high-resolution laboratory spectra by the solar spectrum, weighted the resulting radiance spectra by the Pancam spectral bands (Table 1) (Bell et al., 2003), and divided the radiance value at each band by the solar spectrum weighted by that band. This method provides 11-wavelength spectra that we can use for direct comparison with Pancam spectra in R^* values (see *Section 2.2.1* for an explanation of R^*). From each weighted spectrum, we calculated the values of the three spectral parameters described in *Section 2.1.3* that characterize distinctive regions of the Vis-NIR spectra of ferric sulfates (Table 3): (1) the 753 to 432 nm ratio; (2) the 535 nm band depth; and (3) the 864 nm band depth. We use the observed changes to these spectral parameters as predictors of how the Pancam instrument would detect spectral changes due to the dehydration of ferric sulfate soils on the martian surface. Laboratory spectra were also weighted by the three HiRISE bandpasses (Delamere et al., 2010) using the same procedure described above.

3. Observations of Spectral Variations

3.1 Pancam Observations

3.1.1 Tyrone Soil Exposure

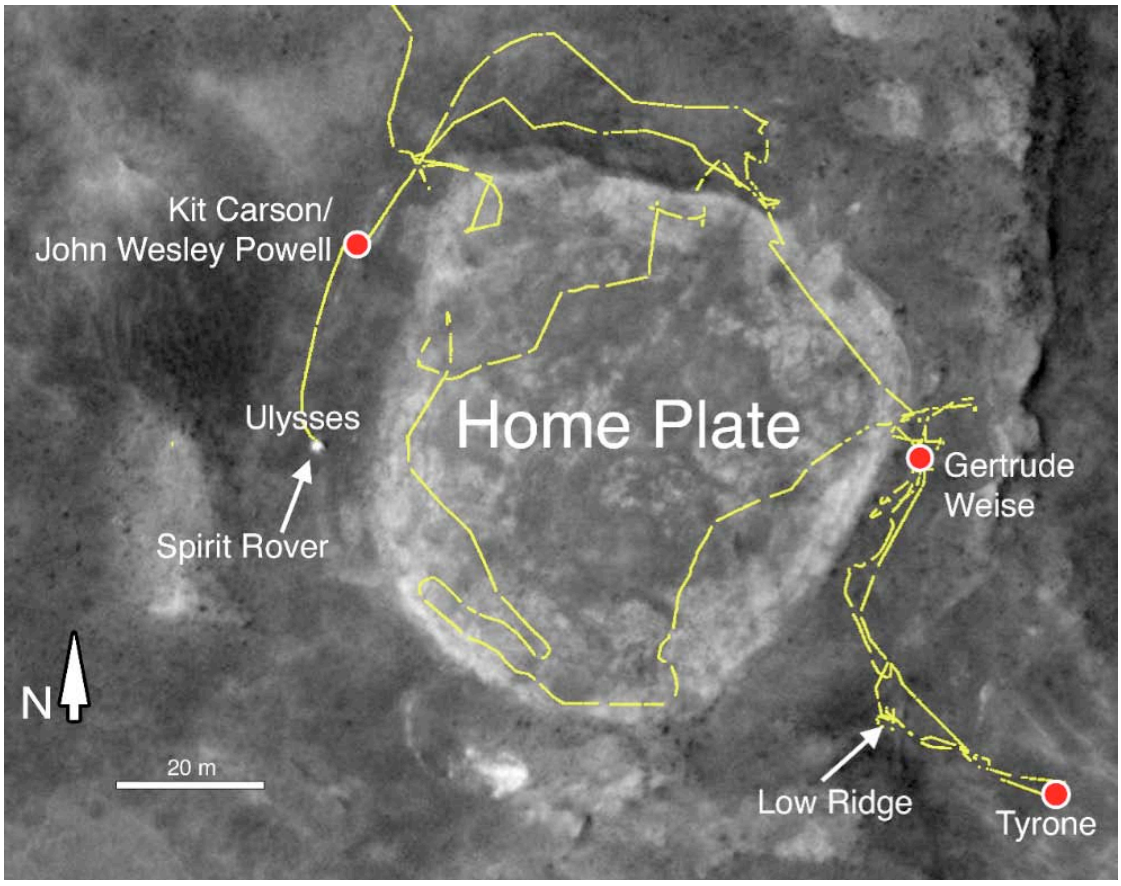

Figure 1. Spirit traverse map of the Home Plate vicinity (sols 743-2185) showing locations of the soil exposures discussed in this work and the Spirit rover embedded in the Ulysses soil as of sol 2185. Traverse is shown over a subframe of HiRISE image ESP_0013499_1650_red.

The Tyrone bright soil was excavated by Spirit's wheels on sol 782, after which the rover became temporarily stuck in the fine, unconsolidated materials. During the extraction process, Spirit's inoperative right front wheel exhumed yellow-hued soils from depths of ~11 cm, which appear to be segregated below the white-hued soils that are found in the shallower left wheel trench (Figure 2) (Wang et al., 2008). One Pancam 13-filter image sequence was acquired of the soils at the Tyrone site on sol 790, after which Spirit was directed to Low Ridge to park with a northerly tilt for the winter (Figure 1). From a distance of ~30 m, the team periodically imaged

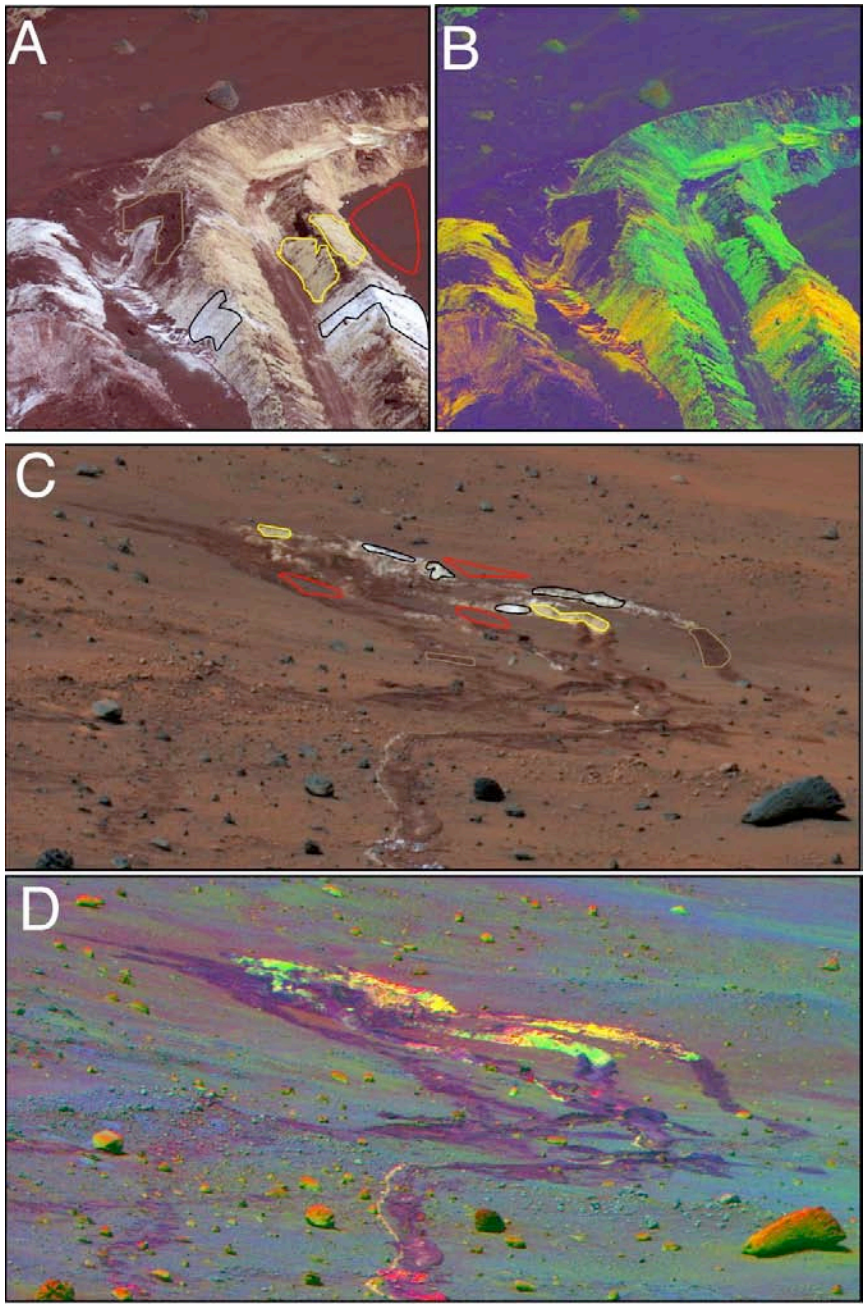

Figure 2. Pancam image products of the Tyrone soil exposure: (a) False color composite (blue = 432 nm, green = 535 nm, red = 753 nm) and (b) Decorrelation stretch (DCS) image (made from 432 nm, 535 nm and 753 nm filter images) from sol 790 (P2531), field of view is ~65 cm; (c) False color composite and (d) DCS image from sol 864 (P2547), wheel tracks are ~16 cm wide. Regions of interest (ROIs) from which spectra were acquired are enclosed by black, yellow, red and brown lines for the white and yellow soil hues, undisturbed soil, and dark disturbed soil, respectively.

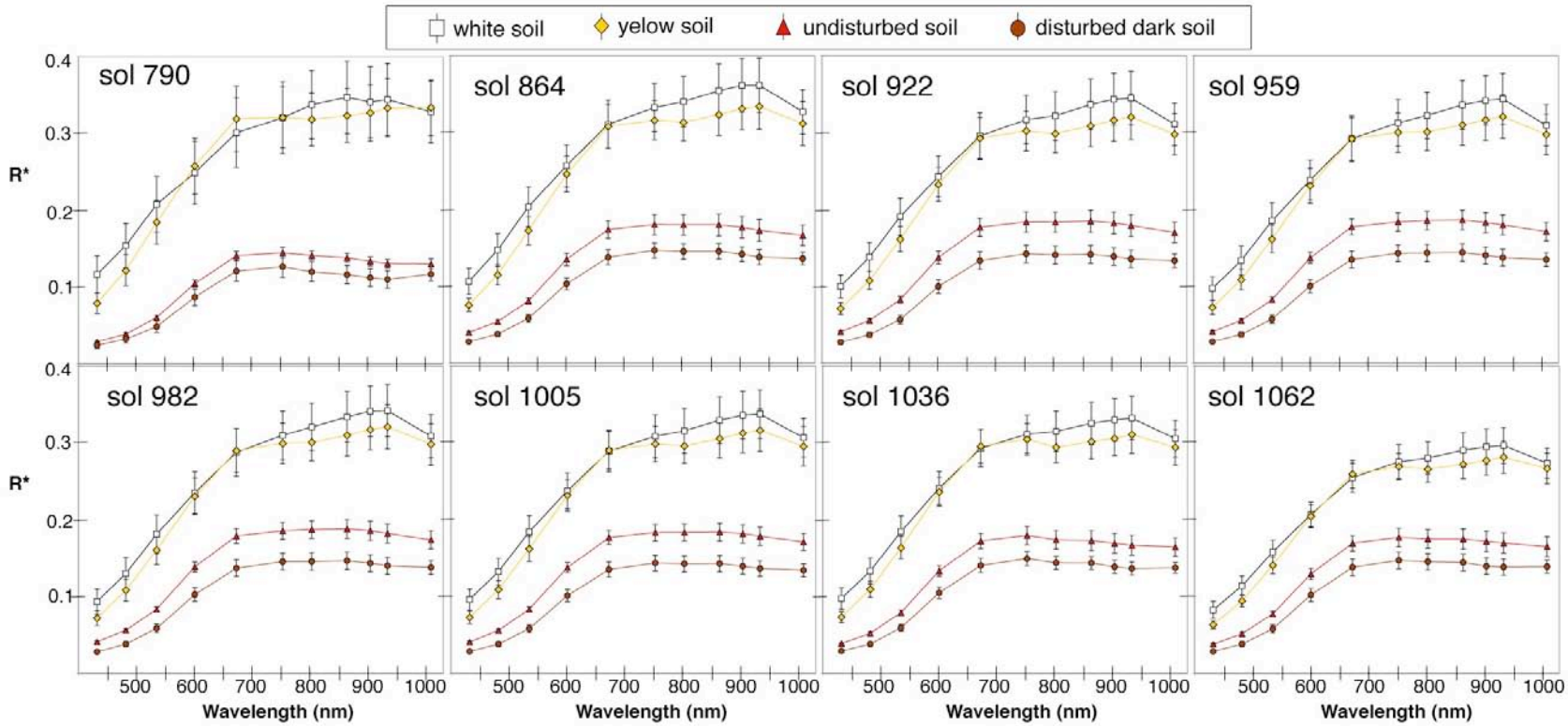

Figure 3. Pancam spectra from the eight 13-filter Tyrone observations: sol 790; sol 864; sol 922; sol 959; sol 982; sol 1005; sol 1036; sol 1062 (Table 2). The "white" and "yellow" soils, undisturbed soil, and dark disturbed soil are shown as white boxes, yellow diamonds, red triangles, and brown circles, respectively.

the Tyrone exposure, acquiring five images from sols 864 to 1005 (Table 2). We note that one additional Pancam 13-filter observation was acquired from Low Ridge on sol 856 (P2297), but because this observation is part of the larger McMurdo 360° panorama and the Tyrone exposure is located at the seam between two frames, and because six of the thirteen filter images have saturated pixels, we omit this observation from our analysis. At the end of its winter campaign, the team acquired two additional full-filter images of Tyrone on sols 1036 and 1062 as Spirit resumed its traverse.

We use decorrelation stretch (DCS) images (Gillespie et al., 1986) made from L7 (432 nm), L5 (535 nm) and L2 (753 nm) filter images to enhance the color variations within each scene and to identify spectral separations within the soil exposure (Figure 2b,d). Two hues are distinct within the Tyrone bright soil exposure, even in the observations acquired from ~30 m distance at Low Ridge: (1) the "white" soil (yellow in DCS images); and (2) the "yellow" soil (green in DCS images). Spectra of the "white" and "yellow" soil hue separations, in addition to spectra of undisturbed surface soil and disturbed, dark soil within the wheel tracks, are shown for each of the eight Pancam observations in Figure 3. As noted in previous studies, the "yellow" spectrum is characterized by a steep blue-to-red spectral slope and a minor absorption near 800-864 nm consistent with ferric sulfate minerals, while the "white" spectrum typically exhibits higher reflectance values at all wavelengths and a 934 to 1009 nm ratio greater than unity (Johnson et al., 2007; Wang et al., 2008; Lane et al., 2008; Parente et al., 2009; Rice et al., 2010a).

Of the eight full spectral observations at Tyrone, the largest temporal changes occur between the sol 790 and sol 864 observations, where the reflectance maximum

of the yellow hue at 670 nm decreases relative to the white hue (Figure 3). An increase in the 934 to 1009 nm ratio also appears between these sols in the "yellow" spectrum. We note that because of differences in viewing geometry (emission angle difference of 22.7^{o}; Table 2) and resolution (0.06 cm/pixel and 0.7 cm/pixel), the spectra from these two observations were not extracted from the exact same regions of the soil exposure or CCD image frame region (Figure 2). The five observations acquired between sols 864 and 1005 were acquired from the same position, however, and the sol 1036 and sol 1062 observations were acquired from a similar distance (~30 m) after short drives. Spectral comparisons of these last seven observations are therefore significantly more straightforward than comparisons between the first two observations.

The left column of Figure 4 shows the values of the 535 nm band depth, 734 to 432 nm ratio, 864 nm band depth and 934 to 1009 nm ratio for each observation. Variations in these spectral parameters for the white and yellow soil hue separations are often paralleled by variations in the undisturbed and dark disturbed soils, suggesting that some changes reflect systematic differences between entire images (such as airfall dust accumulation, or changes in viewing geometry and illumination angle; Table 3), rather than variations from region-to-region within individual images. To account for such image-to-image variations, we divide the spectral parameters of the bright soils by those of undisturbed soils in the same image, which we assume do not vary with time. Plots of these ratios vs. sol are shown in the right column of Figure 4. As ratios, the 535 nm band depths of the yellow and white soil hues increase

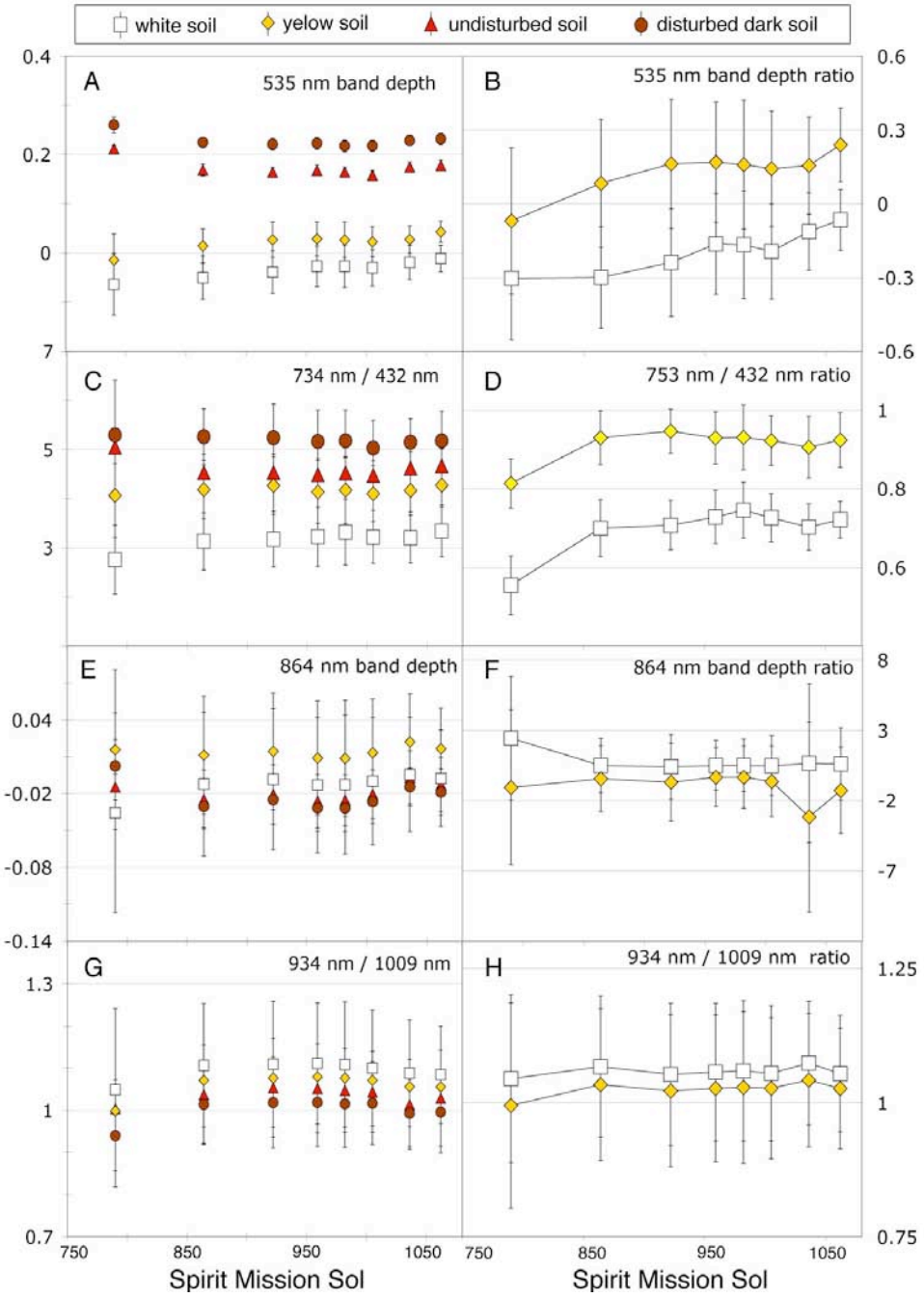

Figure 4. Pancam spectral parameters (Table 3) of the Tyrone "white" (white boxes) and "yellow" (yellow diamonds) soils, undisturbed soil (red triangles), and disturbed dark soil (brown circles) displayed as absolute values (left column) and as the ratios of the "white" and "yellow" soils to undisturbed soil (right column): (a-b) 535 nm band depth; (c-d) 753 to 432 nm ratio; (e-f) 864 nm band depth ratio; (g-h) 934 to 1009 nm ratio. Regions of interest (ROIs) from which spectra were acquired are shown in Figure 2.

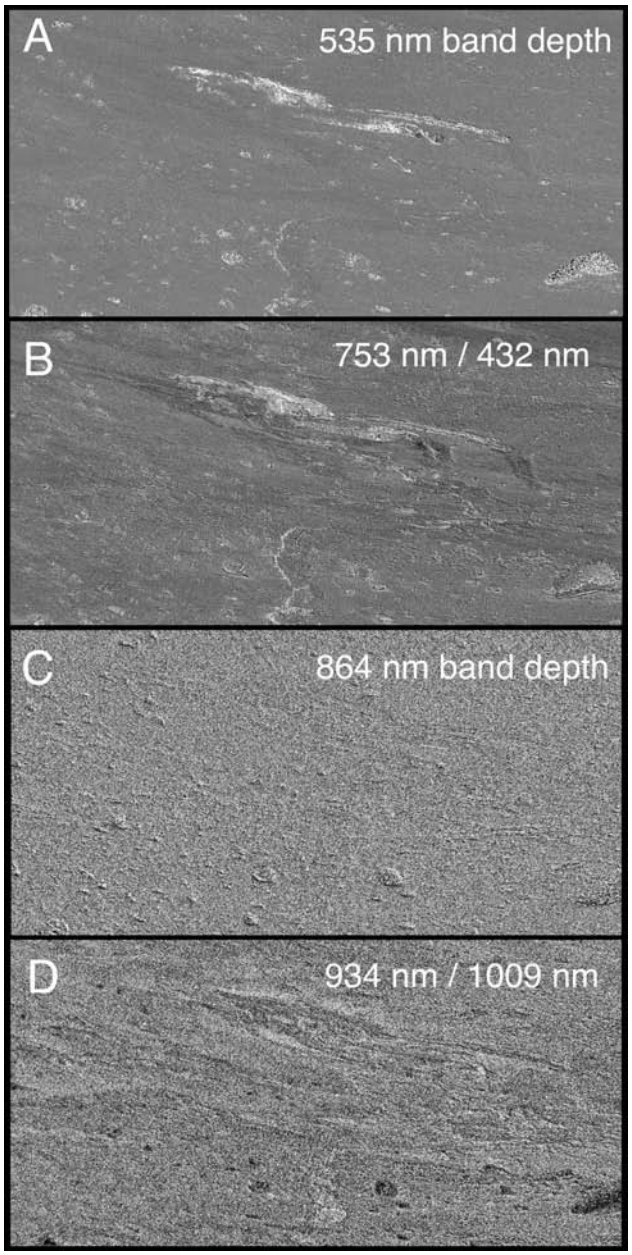

Figure 5. Percent change maps calculated from a linear regression fit to spectral parameter vs. sol data for the Pancam observations of Tyrone from sols 864 to 1005. Bright pixels indicate an overall increase of the spectral parameter with time; darker pixels correspond to an overall decrease of the spectral parameter with time: (a) 535 nm band depth (black corresponds to <-100%, white to >100%); (b) 753 nm / 432 nm (black corresponds to <-15%, white to >15%); (c) 864 nm band depth (black corresponds to <-15%, white to >15%); (d) 934 nm / 1009 nm (black corresponds to <-15%, white to >15%). False color and DCS images of this scene are shown in Figure 2c-d.

50-200% between sols 790 and 959, and 66-68% between sols 1005 and 1062; these variations are the same magnitude as the statistical errors shown in Figure 4b.

The most significant change in the spectra of the yellow and white soil hues relative to undisturbed soils is seen in the red to blue (753 to 432 nm) ratio between sols 790 and 864 (Figure 4d). The 26% and 15% changes to the white soil and yellow soil, respectively, represent a "reddening" of both materials over 74 sols that is larger than the size of the statistical errors. No statistically significant variations are observed in the bright soils relative to the dusty undisturbed soil in the 753 to 432 nm ratio after sol 864, nor in the 864 nm band depth, nor the 934 to 1009 nm ratio over all sols. The increase in the 934 to 1009 nm ratio for the yellow hue between sols 790 and 864, noted above and seen in Figure 3, falls within the range of statistical errors shown in Figure 4h.

For the five observations acquired from the same position (sols 864 to 1005), we have performed a pixel-to-pixel analysis to complement the image-based analysis discussed above. Our derived percent change maps (Figure 5; percent change maps are described in *Section 2.1.5*) highlight regions where spectral parameters are increasing (or decreasing) with time as bright (or dark) relative to the rest of the map. In the 535 nm band depth percent change map (Figure 5a), the Tyrone soil is brighter than surrounding materials, indicating that the 535 nm band depth increases systematically over the five observations. The average increase for the white and yellow Tyrone soil pixels is 120%. We note that dark, basaltic rocks also exhibit trends of increasing in 535 nm band depth with time (up to 100% increase). Portions of the Tyrone soil are also brighter than surrounding materials in percent change maps of the 753 to 432 nm

ratio (Figure 5b); the average change for the white soil is an increase of 4%, and the yellow soil is a decrease of 2%. The variability of percent change values among neighboring pixels is large, as the standard deviations of the white and yellow soil values are 6-7%. Percent change maps for the 864 nm band depth and 934 to 1009 nm ratio show no changes at the Tyrone soil relative to surrounding materials (Figure 5c-d). Interpretations of these observations are discussed in Section 5.

3.1.2 Gertrude Weise Soil Exposure

The silica-rich Gertrude Weise soil was exposed by Spirit's inoperative right front wheel on sol 1148 and Pancam full filter observations were acquired on sols 1158, 1187 and 1198 (Table 2). Because the three observations were acquired from different viewing geometries (Figure 6), they could not be coregistered for pixel-to-pixel comparisons. DCS images of Gertrude Weise reveal that, unlike the Tyrone exposure, the Gertrude Weise trench is spectrally homogeneous and only has one hue (right column of Figure 6); however, the shallower Lefty Ganote trench, exhumed by Spirit's left wheels and also visible in Figure 6, contains a mixture of silica-rich and basaltic soils and exhibits a range of hues. Spectra from the three Pancam observations are nearly identical (Figure 7), and are characterized by a steep slope from 432 nm to 864 nm, a flat near-infrared profile from 864 nm to 934 nm, and a steeply negative slope from 934 nm to 1009 nm (Wang et al., 2008; Rice et al., 2010a). The spectral parameters measured for the white soil (535 nm band depth, 753 nm to 432 nm ratio, 864 nm band depth and 934 nm to 1009 nm) vary slightly

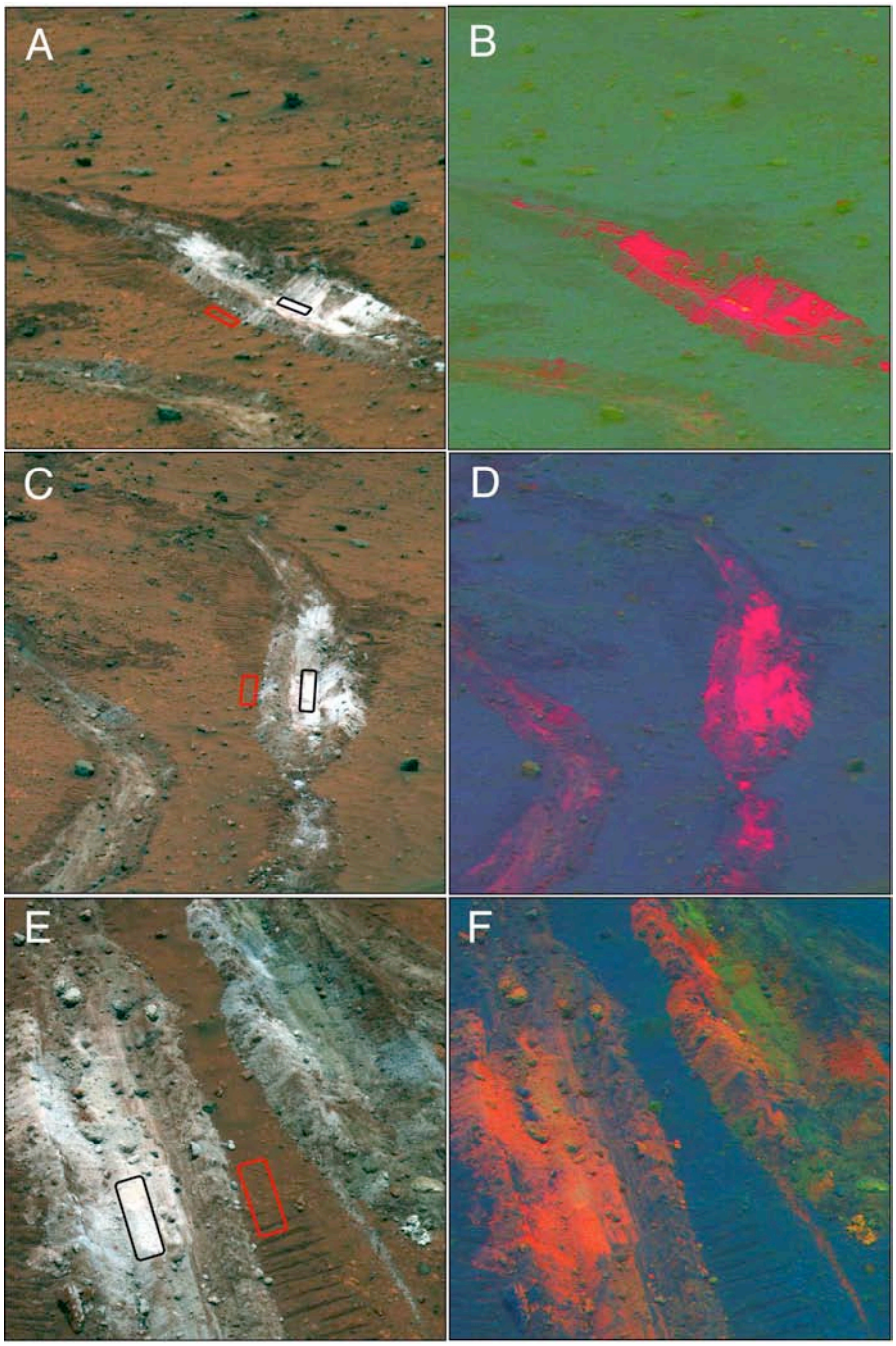

Figure 6. Pancam image products of the Gertrude Weise soil exposure (the rover's right wheel trench with ROIs outlined is Gertrude Weise; the rover's left wheel trench is Lefty Ganote, which is not considered in this study): (a) False color composite (blue = 432 nm, green = 535 nm, red = 753 nm) and (b) Decorrelation stretch (DCS) image (made from 432 nm, 535 nm and 753 nm filter images) from sol 1158 (P2581); (c) False color composite and (d) DCS image from sol 1187 (P2533); (e) False color composite and (f) DCS image from sol 1198 (P2539). Wheel tracks are ~16 cm wide. Regions of interest (ROIs) from which spectra were acquired are enclosed by black and red boxes for the white soil hue and relatively undisturbed soil, respectively.

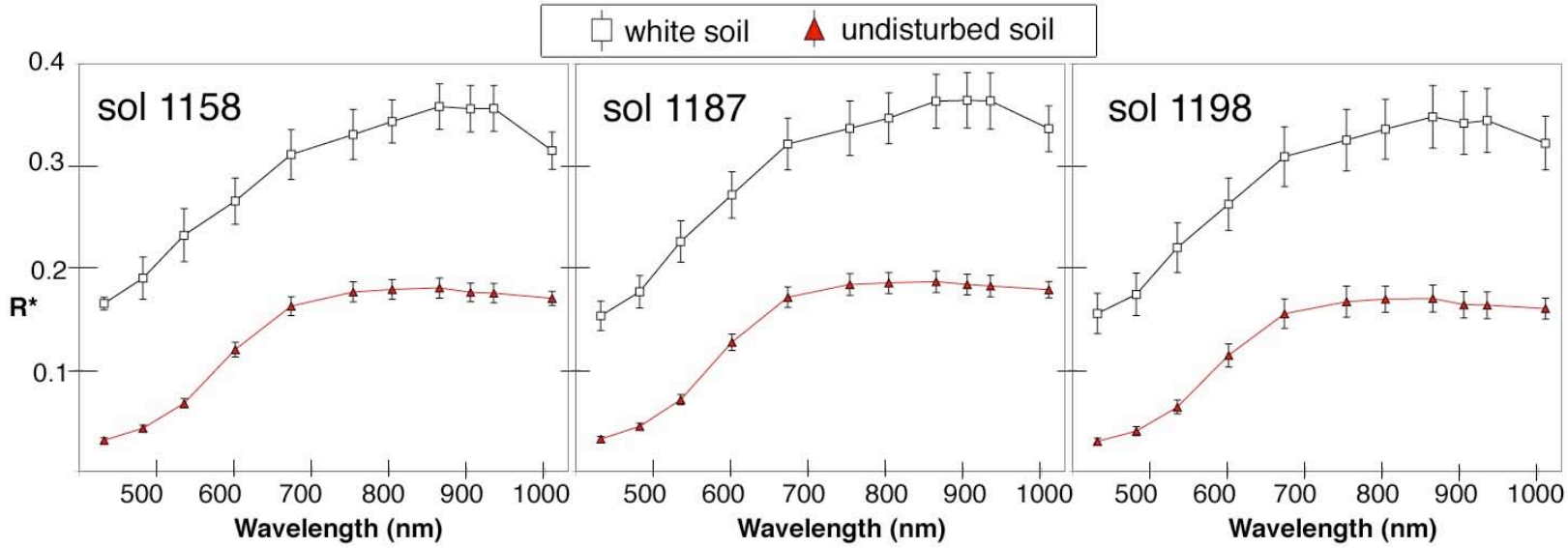

Figure 7. Pancam spectra from the three 13-filter Tyrone observations: sol 1158; sol 1187; and sol 1198. The "white" soil and undisturbed soil are shown as white boxes and red triangles, respectively.

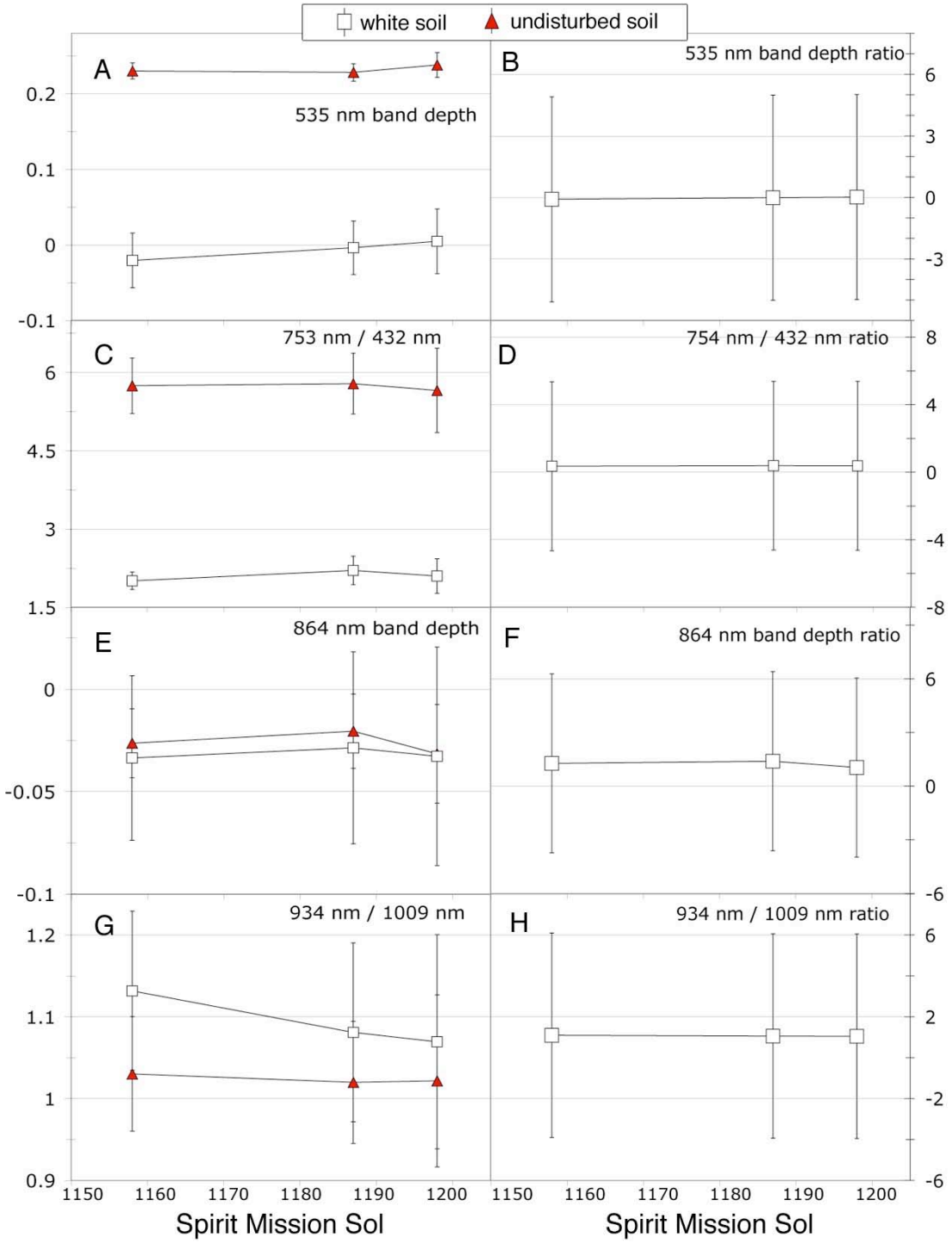

Figure 8. Pancam spectral parameters of the Gertrude Weise soil (white boxes) and undisturbed soil (red triangles) displayed as absolute values (left column) and as the ratios of the "white" soil to undisturbed soil (right column): (a-b) 535 nm band depth; (c-d) 753 to 432 nm ratio; (e-f) 864 nm band depth; (g-h) 934 to 1009 nm ratio.

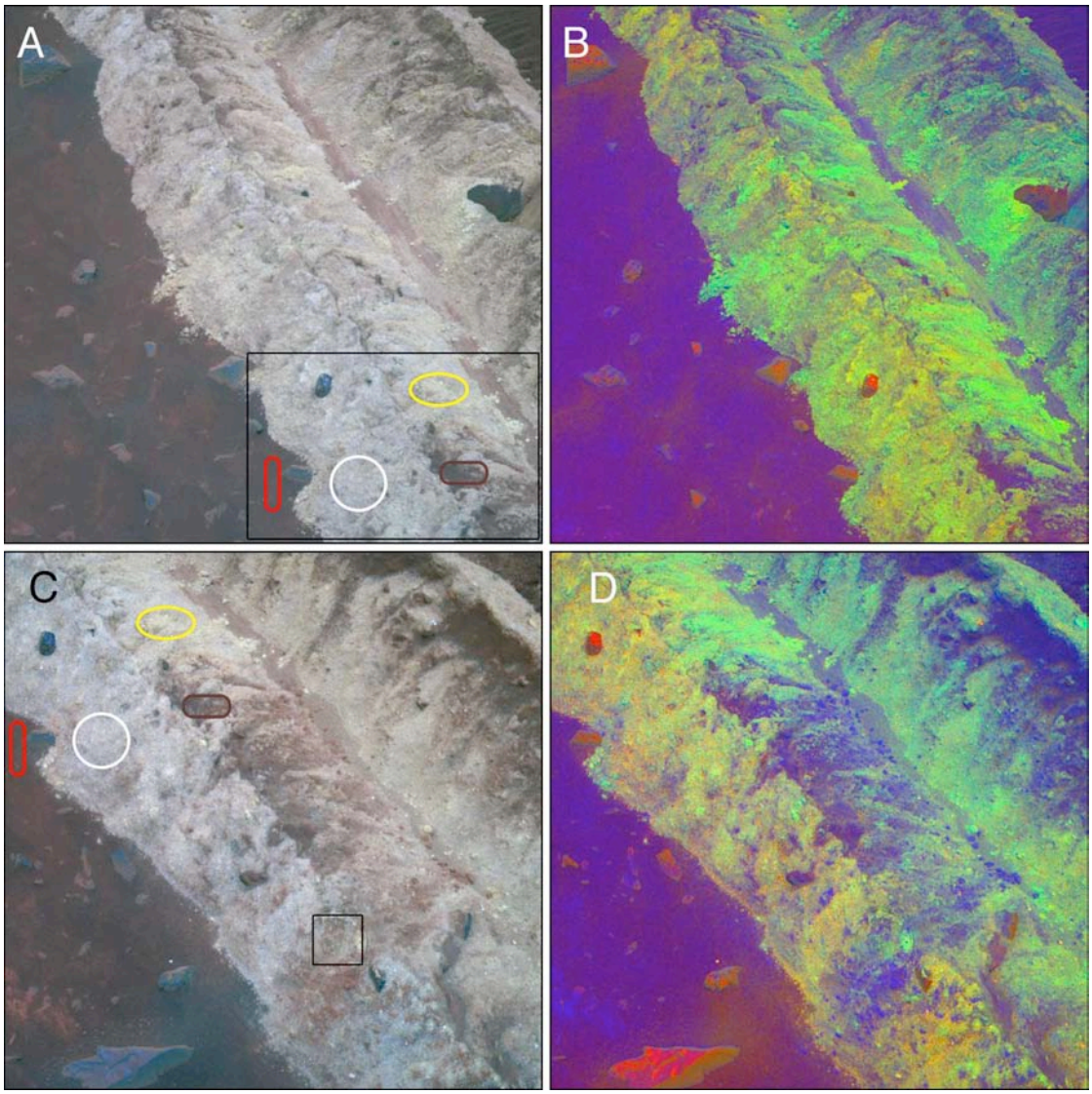

Figure 9. Pancam image products of the Kit Carson soil exposure: (a) False color composite (blue = 432 nm, green = 535 nm, red = 753 nm) and (b) Decorrelation stretch (DCS) image (made from 432 nm, 535 nm and 753 nm filter images) from sol 1864 (P2562), field of view is ~50 cm; (c) False color composite and (d) DCS image from sol 1866 (P2555), field of view is ~37 cm. Regions of interest (ROIs) from which spectra were acquired are enclosed by white, yellow, red and brown ovals for the white and yellow soil hues, undisturbed soil, and dark disturbed soil, respectively. The black box in (a) indicates the location of Figure 20a; the black box in (b) indicates the location for Figure 21.

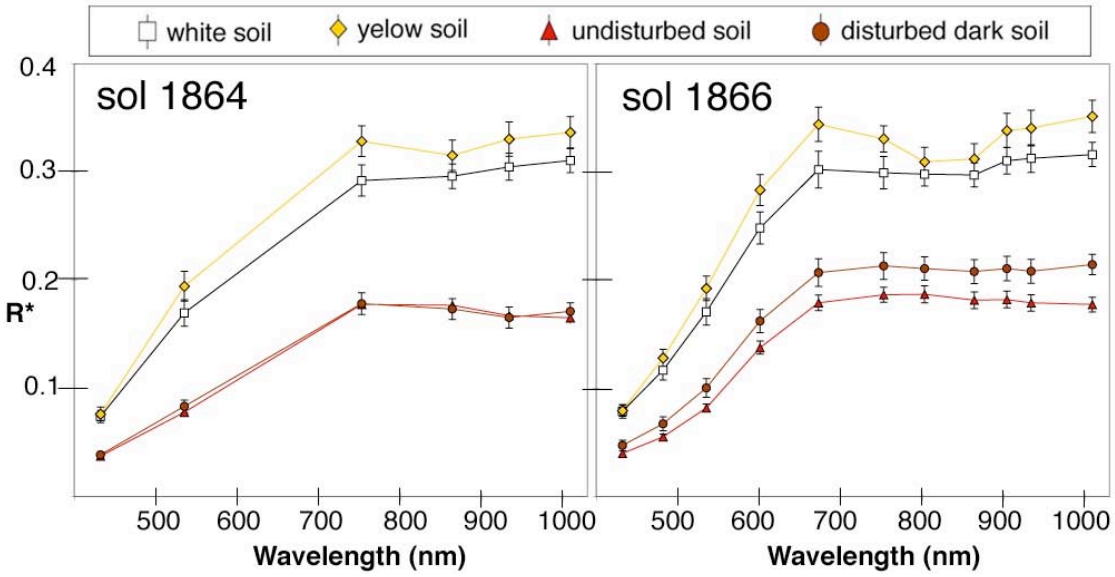

Figure 10. Pancam spectra from the 8-filter (sol 1864, P2562) and the 13-filter (sol 1866, P2555) observations of Kit Carson. The "white" and "yellow" soils, undisturbed soil, and dark disturbed soil are shown as white boxes, yellow diamonds, red triangles, and brown circles, respectively. Spectra were extracted form the regions of interest (ROIs) shown in Figure 13.

between observations, but when measured relative to undisturbed soil, we observe no statistically significant changes to any parameter (Figure 8).

3.1.3 Kit Carson Soil Exposure

Spirit's right front wheel exposed the bright Kit Carson soil on sol 1861, and Pancam acquired two observations on sols 1864 and 1866 as Spirit continued its traverse south (Table 2). Because a drive occurred between the two observations, there is a limited region of overlap for comparison between the two images (bottom right of Figures 9a-b and top left of Figures 9c-d). Spectra from the two observations

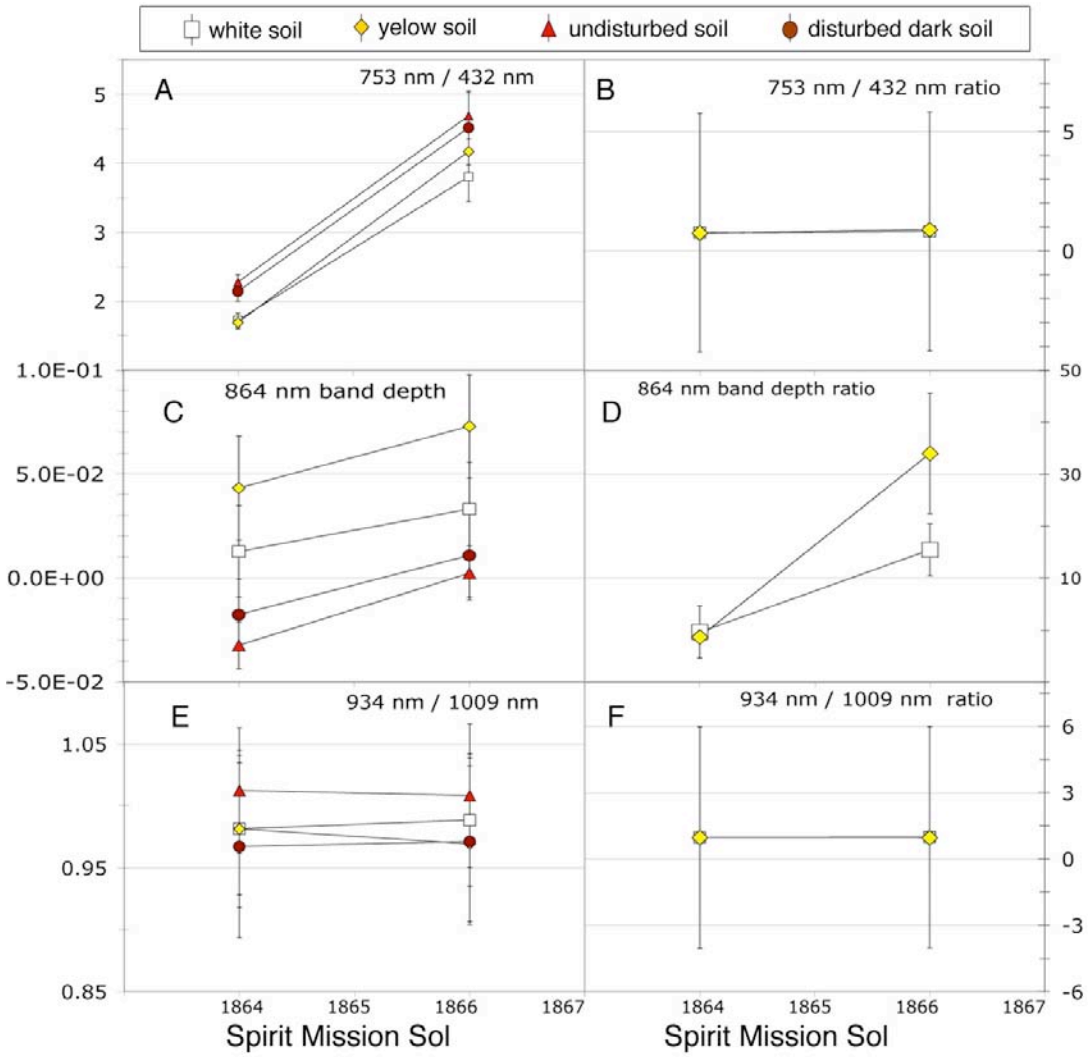

Figure 11. Pancam spectral parameters of the Kit Carson "white" (white boxes) and "yellow" (yellow diamonds) soils, undisturbed soil (red triangles), and disturbed dark soil (brown circles) displayed as absolute values (left column) and as the ratios of the "white" and "yellow" soils to undisturbed soil (right column): (a-b) 753 to 432 nm ratio; (c-d) 864 nm band depth; and (e-f) 934 to 1009 nm ratio.

were thus acquired from ROIs in different regions of the FOV, and are variably affected by the dust contamination described in Section 2.1.4.

In false color and DCS images (Figure 9), two color hue separations are visible within the trench, similar to those observed at the Tyrone exposure: (1) "white" soil (yellow in DCS images); and (2) "yellow" soil (green in DCS images). Spectra of these two hue separations, dark disturbed soil and undisturbed soil are shown in Figure 10. The observations from sol 1864 contain a reduced filter set due to limited time and power resources, so we cannot compute the 535 nm band depth for this observation as defined in Table 3. Observed changes to the bright soils include an increase in reflectance of dark disturbed soil, an increase in 864 nm band depth and increase in 753 nm to 432 nm ratio between sols 1864 and 1866 (Figure 10). Figures 11a and 11c show that increases in the 753 nm to 432 nm ratio and 864 nm band depth for the white and yellow soils are mirrored by changes in the dark and undisturbed soils in the same portion of the image, and the 753 nm to 432 nm ratio and 943 nm to1009 nm ratios for the bright soils do not change relative to the undisturbed soil (Figure 11b,f). The 864 nm band depth does increase relative to surrounding materials, however, by > 200% for both the yellow and white soil hues (Figure 11d). This observation implies that there is still a statistically significant increase in band depth even when we account for systematic image-to-image variations; possible causes of this change are discussed in Section 5.

3.1.4 Ulysses Soil Exposure

The Ulysses bright soil was exposed during Spirit's drive south from Kit Carson on sol 1886, when the rover became stuck in the fine-grained, unconsolidated material. Seven full filter Pancam observations of the exposure were acquired between sols 1888 and 2019 (Table 2). Three additional 13-filter subframes were acquired within the trench on sols 1901-3, but because these observations were acquired at high phase angles on only a small portion of the soil exposure, we do not include them in our analysis. During the extrication efforts, the rover changed position slightly between each Pancam observation until sol 1933 (Table 2), and we have been careful to select ROIs for our spectral analysis that are visible in each of the seven observations and that have not been further disturbed by the extrication activity (Figure 12). A detailed description of the measurement campaign at Ulysses with Spirit's full suite of instruments has been provided by Arvidson et al. (2011).

False color and DCS images from the first Pancam observation sol 1888 reveal two color hue separations within the trench (Figure 12a-b), as observed at the Kit Carson and Tyrone exposures: (1) "white" soil (yellow/red in DCS images); and (2) "yellow" soil (green in DCS images). By sol 1982, the color of the Ulysses soil had visibly changed (Figure 12c), and the two hues are no longer distinguishable in DCS images (Figure 12d). These changes are reflected in the spectra shown in Figure 13, where the "yellow" and "white" spectra, as well as the dark disturbed soil spectra, have converged to the same shape in the sol 1933-2019 observations; the negative 934 nm to 1009 nm slope characteristic of the "white" spectrum has flattened, and all spectra develop a reflectance maximum at 904 nm. We note that spectra from the Ulysses imaging campaign were acquired from a wider range of incidence angles than

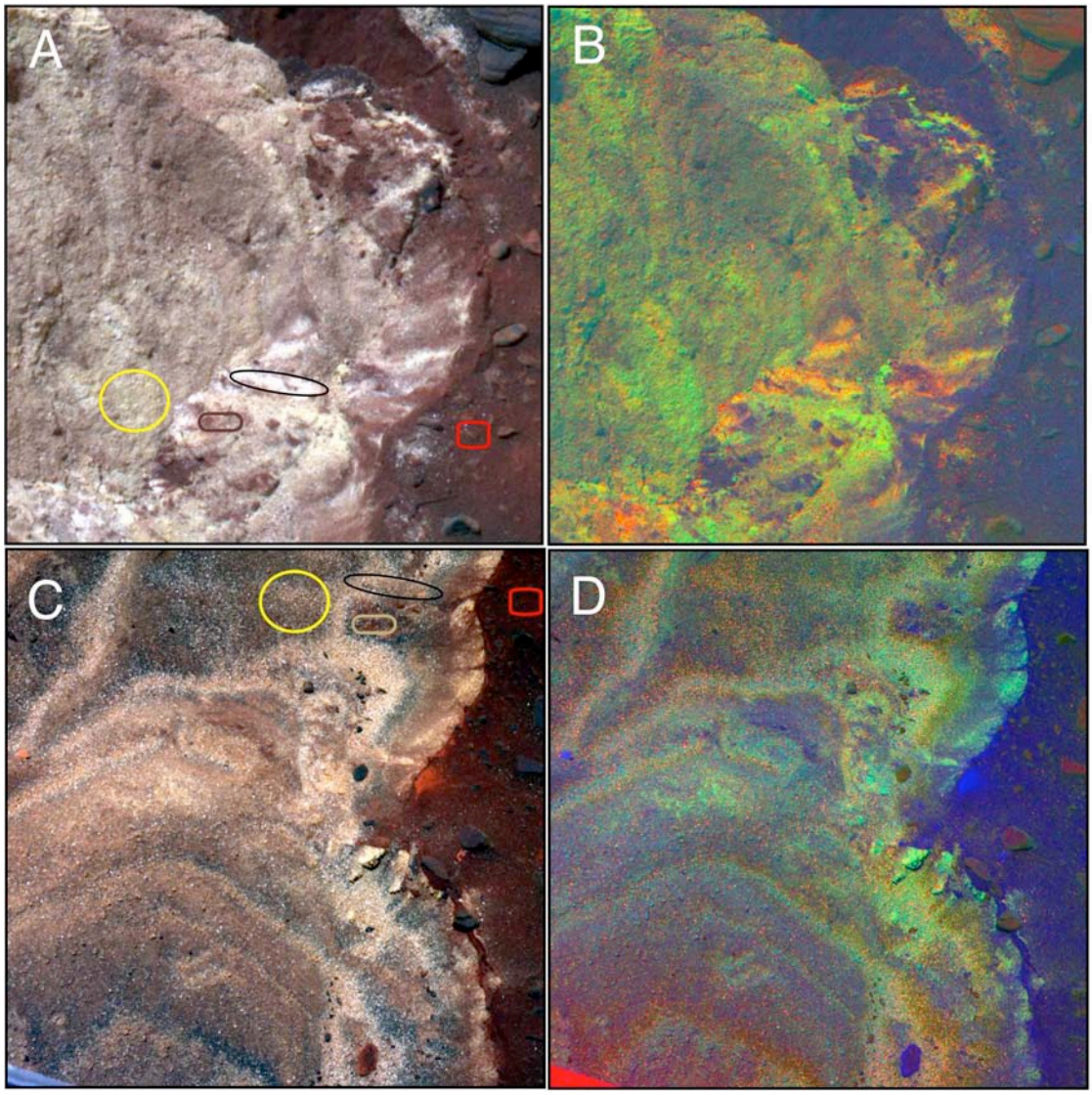

Figure 12. Pancam image products of the Ulysses soil exposure: (a) False color composite (blue = 432 nm, green = 535 nm, red = 753 nm) and (b) Decorrelation stretch (DCS) image (made from 432 nm, 535 nm and 753 nm filter images) from sol 1888 (P2559), field of view is ~24 cm; (c) False color composite and (d) DCS image from sol 1982 (P2547), field of view is ~34 cm. Regions of interest (ROIs) from which spectra were acquired are enclosed by white, yellow, red and brown ovals for the white and yellow soil hues, undisturbed soil, and dark disturbed soil, respectively.

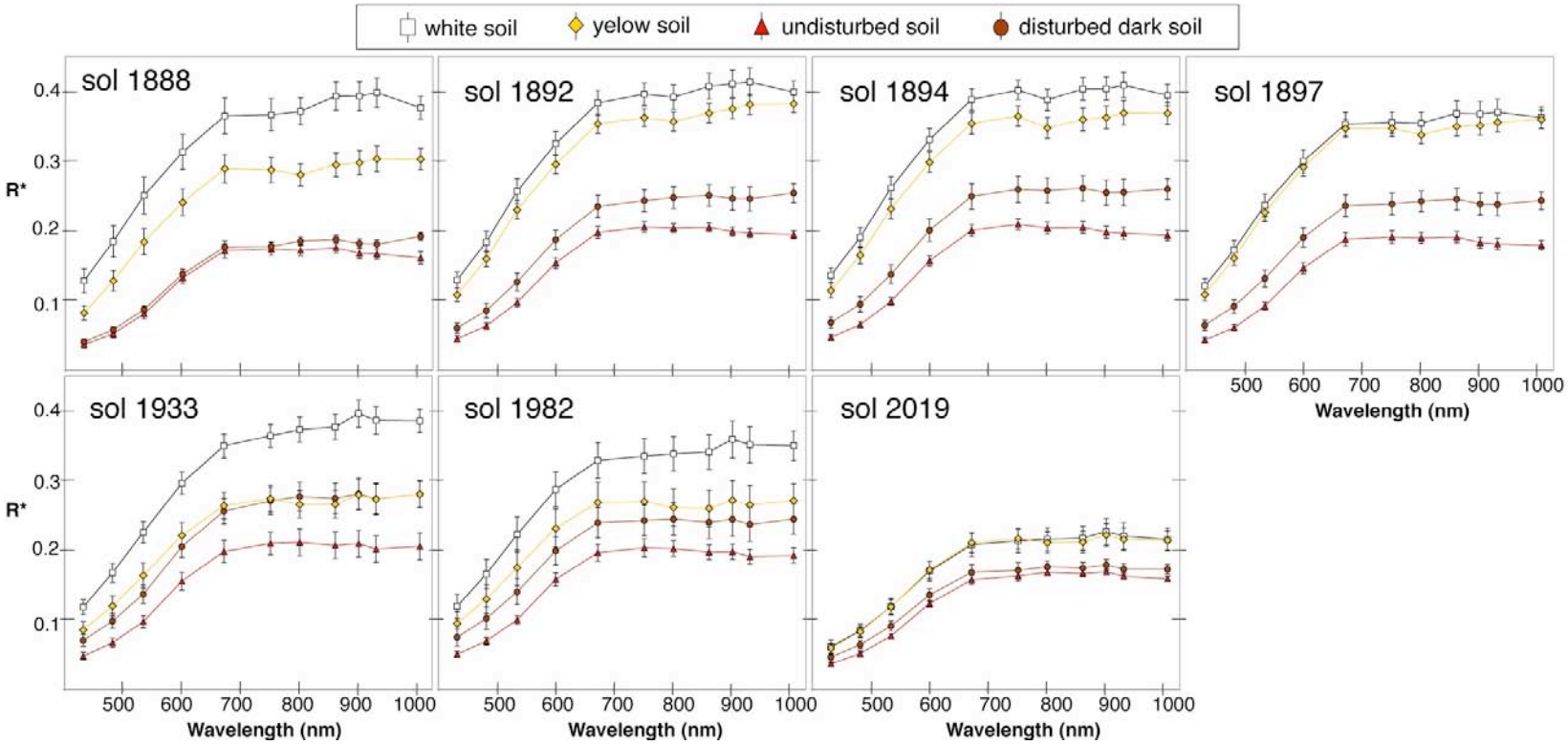

Figure 13. Pancam spectra from the seven 13-filter Ulysses observations: sol 1888; sol 1892; sol 1894; sol 1897; sol 1933; sol 1982; and sol 2019. The "white" and "yellow" soils, undisturbed soil, and dark disturbed soil are shown as white boxes, yellow diamonds, red triangles, and brown circles, respectively.

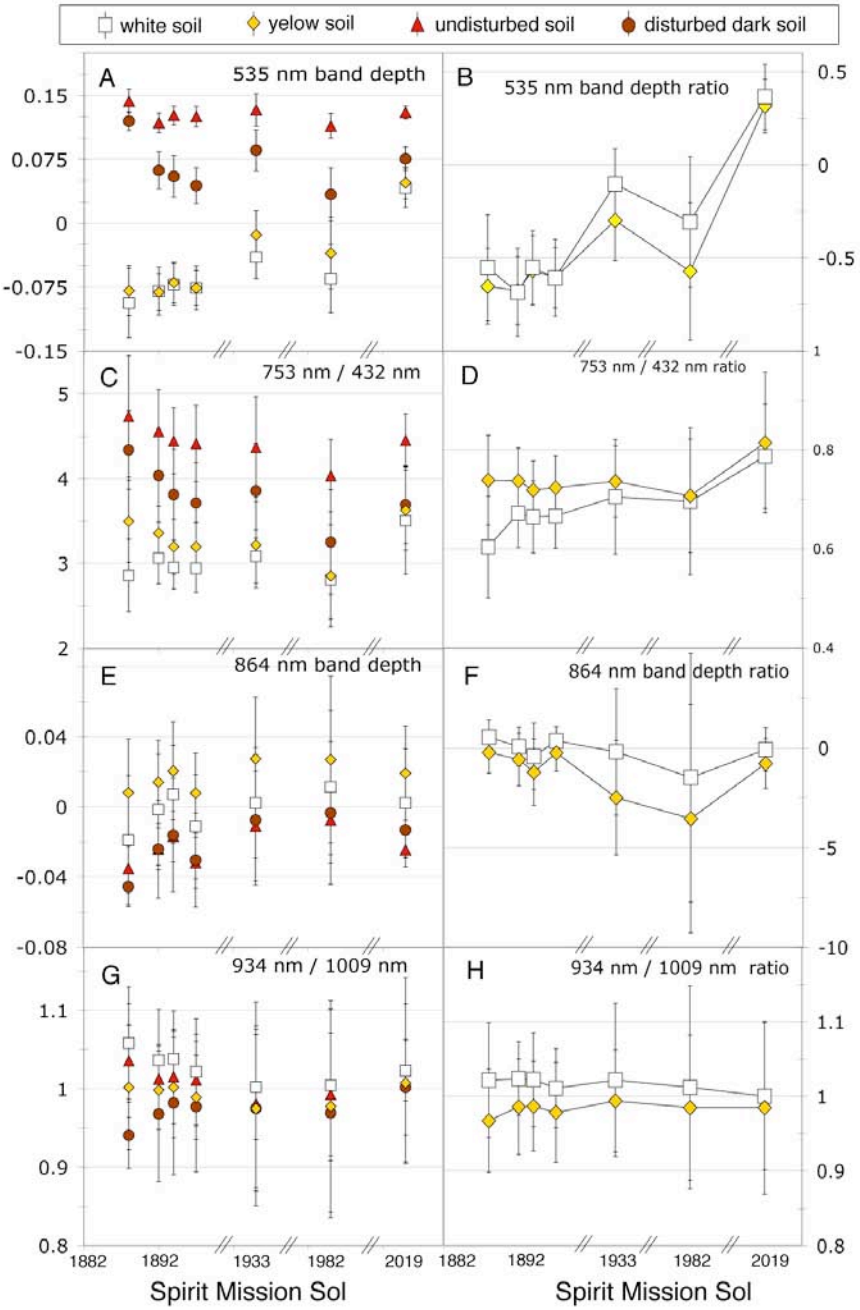

Figure 14. Pancam spectral parameters of the Ulysses "white" (white boxes) and "yellow" (yellow diamonds) soil hue separations, undisturbed soil (red triangles), and disturbed dark soil (brown circles) displayed as absolute values (left column) and as the ratios of the "white" and "yellow" soils to undisturbed soil (right column): (a-b) 535 nm band depth ratio; (c-d) 432 to 753 nm slope ratio; (e-f) 864 nm band depth ratio; (g-h) 934 to 1009 nm slope ratio.

other campaigns (Table 2), which results in the variability in overall reflectance between observations for all surface materials, most notably with the sol 2019 observation (Figure 13). In this study, however, we are concerned with changes to relative spectral features rather than changes in absolute reflectance.

Over the first nine sols of observation, the most significant change to the bright soils relative to the undisturbed soil is an increase in the 753 nm to 432 nm ratio for the white soil (Figure 14d). After sol 1897, the 934 to 1009 nm ratio does not change over the observation period (Figure 14h), but all other parameters vary considerably. By sol 2019, the 535 nm band depth, 753 to 432 nm ratio and 864 nm band depth of the bright soils approach the values for the dark disturbed surface soils (Figure 14a-f). Interpretations of these changes are provided in Section 5.

3.2 HiRISE Observations

The Kit Carson soils were exposed on sol 1861, and a HiRISE image acquired 20 sols later demonstrated that they could be seen from orbit in the RED filter (Figure 15a). A follow-up HiRISE imaging campaign was planned, including two three-color images on sols 1935 and 1967 (Table 4; Figure 15b); another image acquired on sol 1994 (ESP_014277_1650) provides additional coverage, but at lower resolution and only in the RED filter. Shortly thereafter, MRO entered an extended "safe mode" period during which all science instruments were powered off, preventing acquisition of additional images. A significant regional dust storm also occurred in Gusev crater during this period, with atmospheric opacity peaking at $\tau > 2.6$ on sol 2007 and subsequent dust settling on the surface (as measured by the reduced power output of

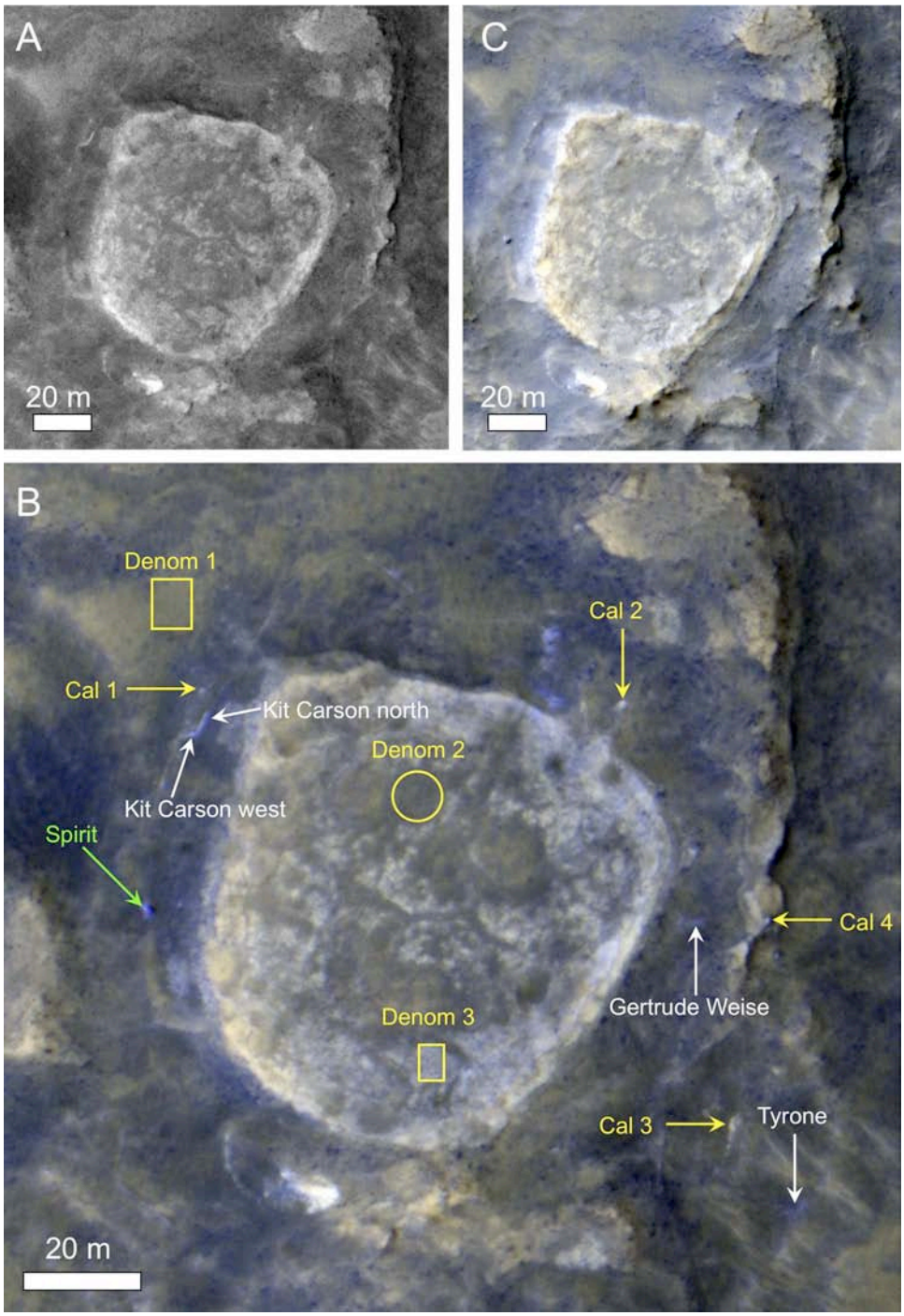

Figure 15. Orbital view of the region surrounding Home Plate in the Columbia Hills. (A) Portion of the first HiRISE image acquired after exposure of the Edgar Allen Poe and Kit Carson soils, ESP_012787_1650 (sol 1881). (B) "IRB" enhanced color composite [*McEwen et al.*, 2010] from ESP_013921_1650 (sol 1967); see section 5.3 for discussion. (C) IRB composite from ESP_016677_1650 (sol 2177), in which all bright soils are virtually invisible.

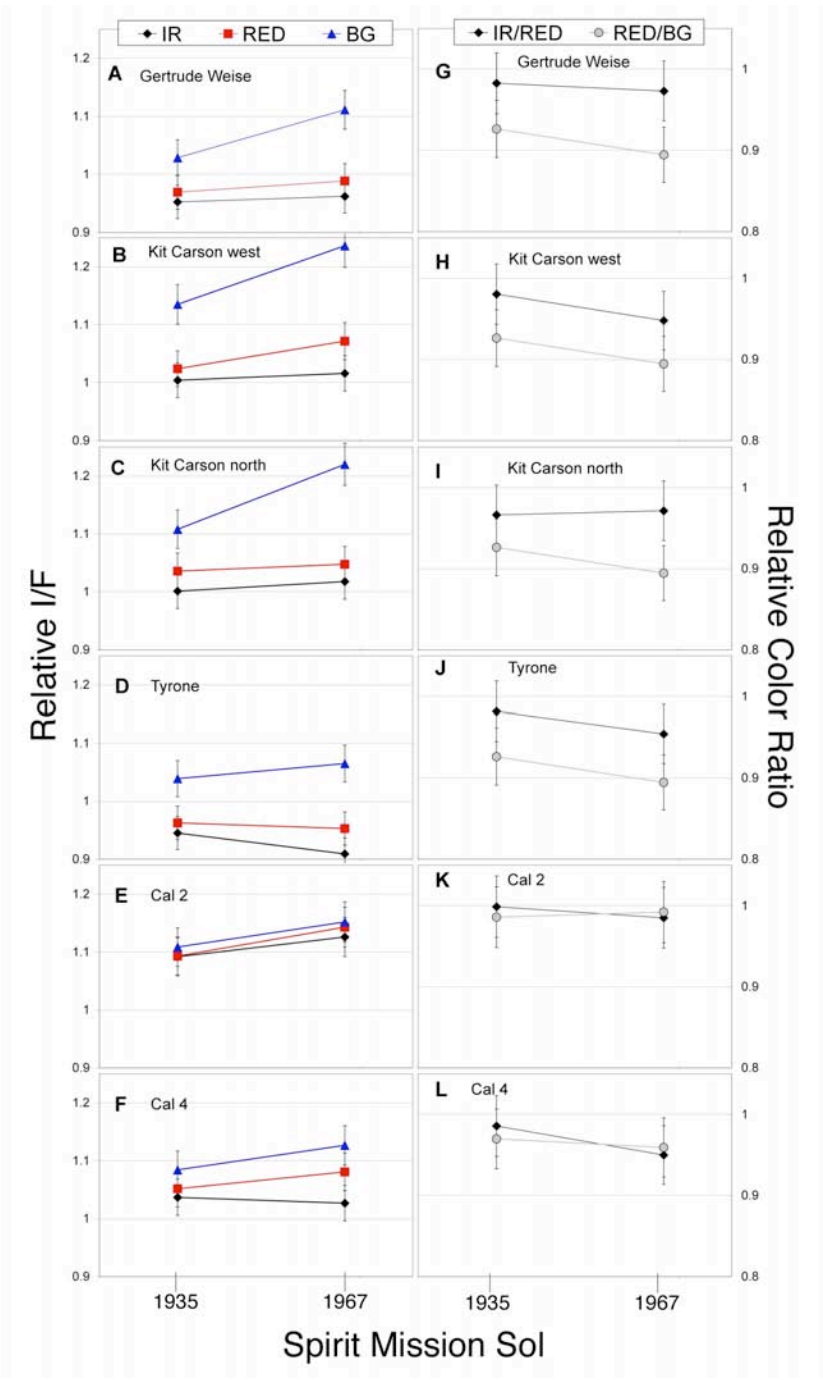

Figure 16. HiRISE spectral evolution of the Gertrude Weise, Kit Carson and Tyrone bright soils from sols 1935 to 1967. Two example calibration outcrops (Cal 2 and Cal 4, locations indicated in Figure 15b) are shown for comparison. Values in the left column are I/F for the three color filters of the feature of interest divided by that of a nearby undisturbed area (Denom 1 in Figure 15b). Values in the right column are color ratios (IR/RED and RED/BG) taken from the relative I/F values. Error bars are 2% of relative I/F.

Spirit's solar panels; Figure 25 and Arvidson et al. (2011)). Six months later, in the first HiRISE image acquired after MRO exited safe mode, Kit Carson and other bright soils were no longer visible in any filters (Figure 15c). Our change detection campaign is therefore limited to the two color images listed in Table 4.

Between sols 1935 and 1967, our four calibration outcrops (labeled "Cal" 1-4 in Figure 15) exhibited relative brightening of 2-4% in BG, 3-5% in RED, and 2–3% in the IR (relative I/F measurements for Cal 2 and Cal 4 are shown in Figure 16e-f). We calculated relative I/F values for two spots within the Kit Carson exposure (labeled as "west" and "north" in Figure 15b), Gertrude Weise, Tyrone, and four calibration outcrops using "Denominator 1" from Figure 15b. Using other denominators changed the results by 2% or less in all cases. Virtually all of the exposed soils and the calibration spots show similar spectral behavior: a relative brightening over 32 sols in the BG, IR and RED bands (by 4–10%, 1–4%, and 1–5%, respectively), with the exception of Tyrone and the Cal4 spot, which decrease in RED and/or IR (Figure 16, left column). As ratios (Figure 16, right column), IR/RED for the bright soils changes by -3% to 0.5% and RED/BG changes by -8% to -3%. All observed variations are within the size of the estimated instrumental errors.

3.3 Laboratory Experiments

Normalized spectra of coquimbite, ferricopiapite, fibroferrite and rhomboclase are shown in Figure 17 for days 1, 2, 24 and 125 of our laboratory experiment in a low temperature and low pressure environment. The major changes accompanying exposure to Mars surface conditions include changes in depth and wavelength position

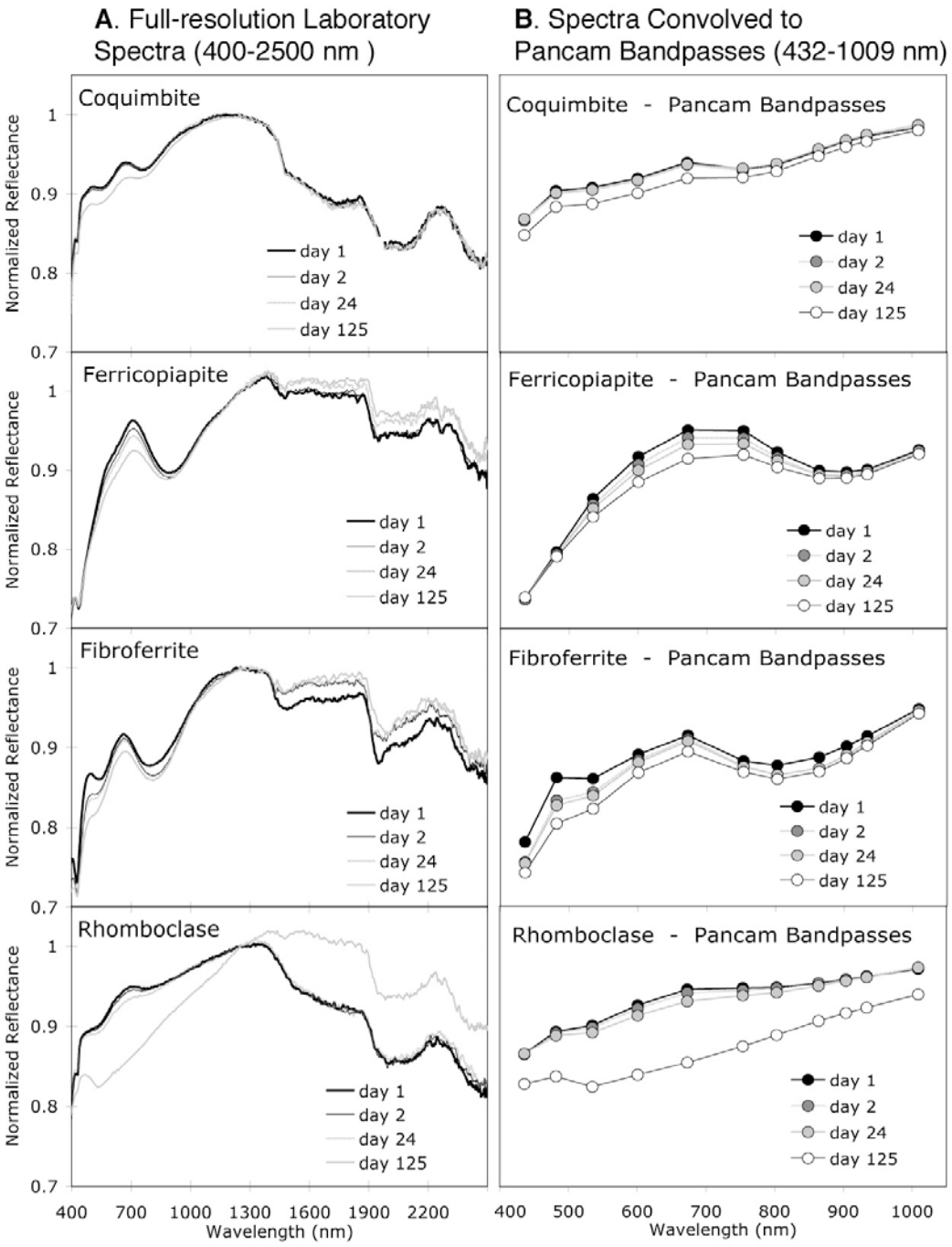

Figure 17. Spectra of ferric sulfate minerals (normalized to their value at 1250 nm) over the first 150 days of exposure to martian surface conditions (P = 5 Torr CO_2; T = 20°C): (a) Full resolution Vis-NIR spectra (400-2500 nm); (b) Spectra convolved to Pancam bandpasses. Spectra are shown for days 1, 2, 24 and 125 of the experiment; see text for experimental procedure.

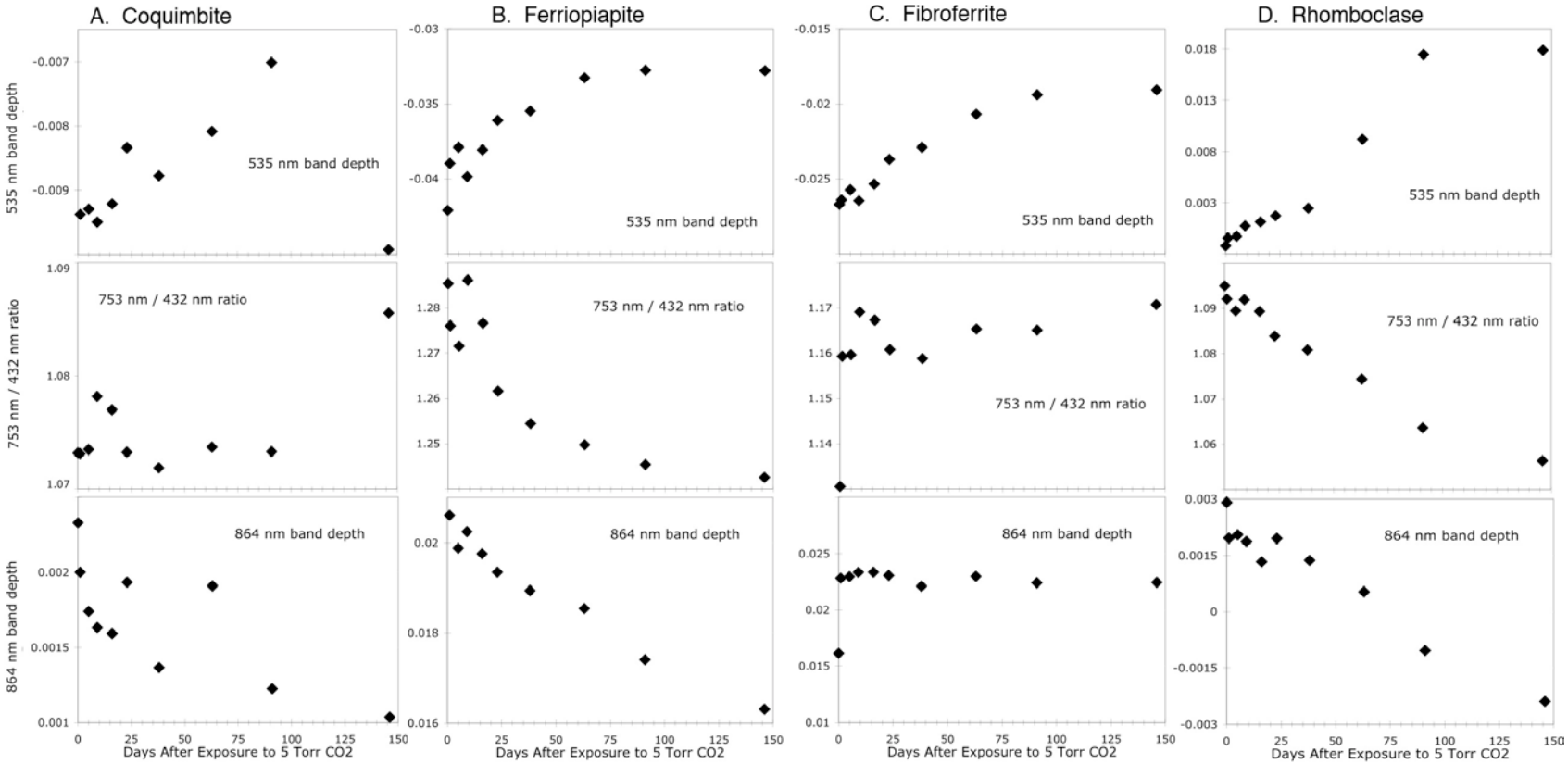

Figure 18. Spectral parameters (535 nm band depth, 753 nm/432 nm slope, and 864 nm band depth) measured from laboratory spectra of ferric sulfate minerals exposed to martian surface conditions (P = 5 Torr CO_2; T = 20°C) over the first 150 days of the experiment: (a) coquimbite; (b) ferricopiapite; (c) fibroferrite; and (d) rhomboclase. See text for experimental procedure.

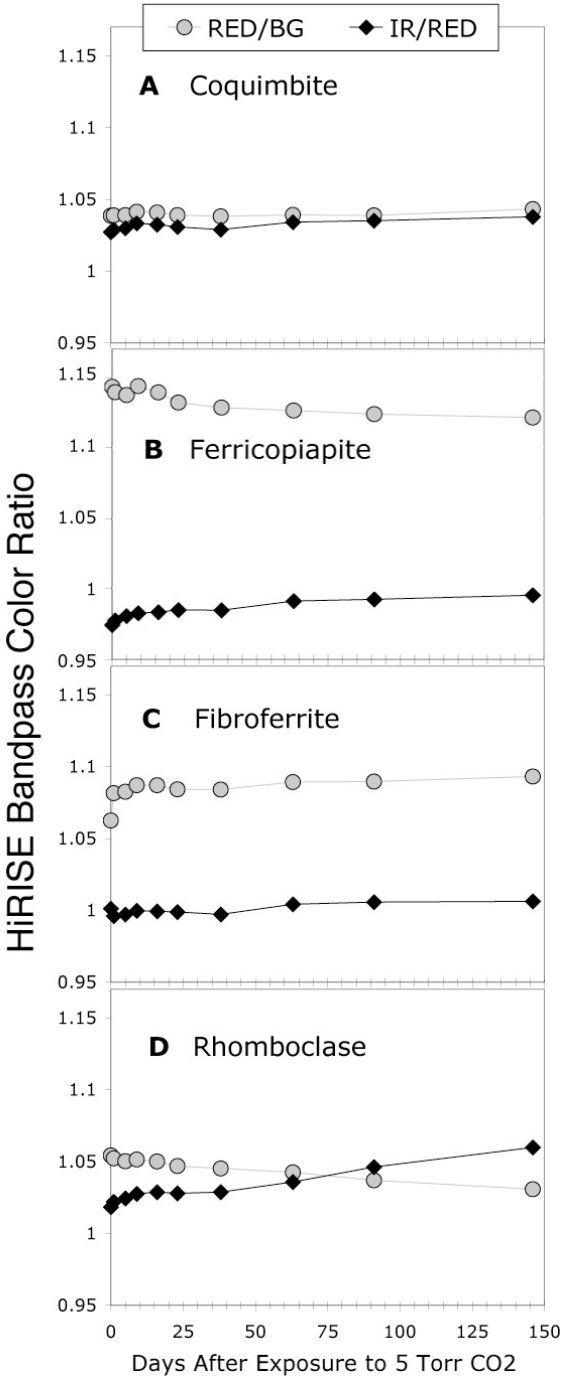

Figure 19. Color ratios (RED/BG and IR/RED) of HiRISE bandpasses (BG=502±157 nm; RED=686±267 nm; IR=878±143 nm) measured from laboratory spectra of ferric sulfate minerals exposed to martian surface conditions (P = 5 Torr CO_2; T = 20^{o}C) over the first 150 days of the experiment: (a) coquimbite; (b) ferricopiapite; (c) fibroferrite; and (d) rhomboclase. See text for experimental procedure.

of OH and H_2O features at ~1400 nm and ~1900 nm, respectively (Figure 17a). These changes reflect differential loss of OH vs. H_2O or OH/H_2O located in multiple sites (e.g., Cloutis et al., 2008). Changes in the visible region, which Pancam samples, can also be dramatic. For example, the ~430 nm Fe^{3+} band deepens in the coquimbite, ferricopiapite and fibroferrite spectra, and the ~790-900 nm Fe^{3+} features become less distinct for all samples. These spectral changes are linked to either a loss of H_2O and/or OH or a structural rearrangement of the OH that bridges between adjacent ferric irons (Cloutis et al., 2008). The modifications to the position and shape of the ~1.9 μm feature in the fibroferrite spectra further indicate a loss of H_2O and structural rearrangement.

In Pancam bandpasses (Figure 17b), the effect of exposure to martian conditions is primarily to decrease the contrast of spectral features. The changes to the Pancam spectral parameters listed in Table 3 are plotted against time in Figure 18 (excluding the 934 nm to 1009 nm ratio, which is an indicator of silica-rich materials, not ferric sulfates). Based on the observed trends, we predict that, if one or more of these candidate ferric sulfates are present in a bright soil deposit that is dehydrating upon exposure to surface conditions, the following changes could be observable in Pancam spectra: (1) an increase in the 535 nm band depth; (2) a decrease in the 753 to 432 nm ratio; and (3) a decrease in the 864 nm band depth. Because the spectral variations in Figure 18 reflect the samples equilibrating to Mars surface conditions from Earth surface conditions, whereas potential spectral variations observed by Spirit reflect an equilibration from Mars shallow subsurface conditions to a Mars surface

condition, we do not predict the magnitude of possible Pancam spectral changes from our observations and consider only the direction.

The HiRISE filters do not optimally sample the changes to the spectral features of ferric sulfates observed in Figure 17. The variations in the RED/BG and IR/RED ratios measured from the laboratory spectra weighted by the HiRISE bandpasses (Figure 19) are minor compared to the variations in the Pancam parameters observed over the 150 days of the experiment, exhibiting no changes greater than 5%. Thus we do not expect spectral changes due to the dehydration of coquimbite, ferricopiapite, fibroferrite or rhomboclase to be observed in HiRISE spectra.

4. Observations of Textural Variations

4.1 Kit Carson Soil Exposure

Several textural modifications to the bright Kit Carson soil material are observed in the region of overlap between the sol 1864 and 1866 Pancam observations (Figure 20). The dragging motion of Spirit's inoperative right front wheel squeezed bright material out to either side of the trench, resulting in narrow, parallel ridges resembling levees composed of unconsolidated material at the angle of repose. The "white" and "yellow" soil hues have been mixed with dark soils and basaltic pebbles by the trench excavation. Figure 20 shows examples of the observed modifications to soil texture: (b) partial disintegration of the soil clod in the bottom center of the image, and appearance of a "halo" of fine, bright material on undisturbed soil; (c) disappearance of bright material from small depressions in rounded pebble; (d) appearance of fine, bright material in dark portion of wheel trench; and (e)

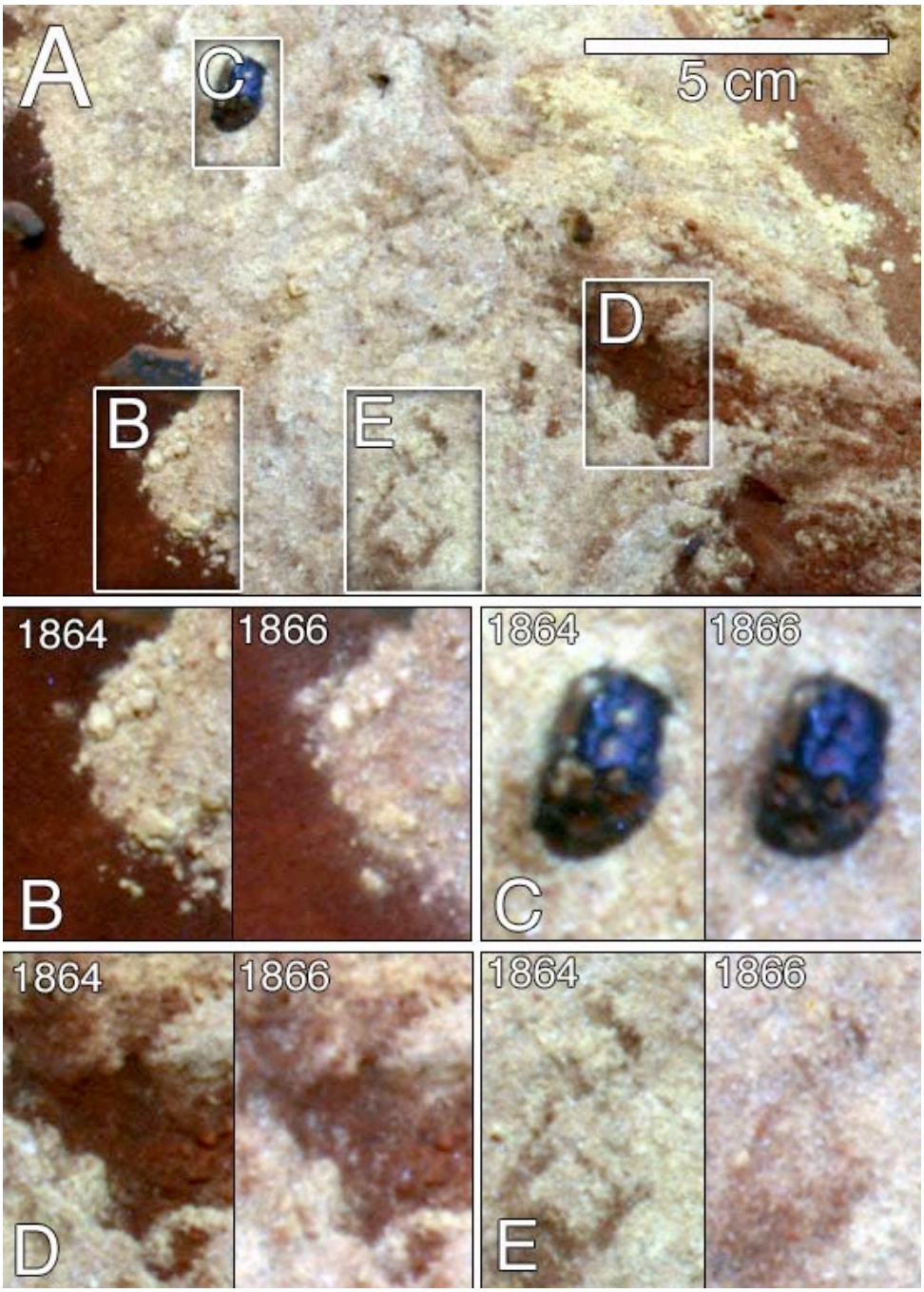

Figure 20. Examples of textural changes at the Kit Carson soil exposure between sols 1864 and 1866. (a) False color image (blue = 432 nm, green = 535 nm, red = 753 nm) from sol 1864 (P2562) showing the locations of b-e. (b) Partial disintegration of soil clod and movement of fines; (c) removal of fines from basaltic pebble; (d) appearance of light-toned material upon dark soil; and (e) disintegration of soil clods and homogenization of texture. Note that the two Pancam images are not shown at the same color stretch, and should only be used for textural comparisons, not color comparisons. Location of (a) is indicated in Figure 9a.

Figure 21. Merge of calibrated MI image 2M291757408, acquired on Sol 1863 when target was fully shadowed, and Pancam L257 enhanced color image, acquired on Sol 1866 of the John Wesley Powell target within the Kit Carson soil exposure. Location is shown in Figure 9c. Field of view is ~3 cm.

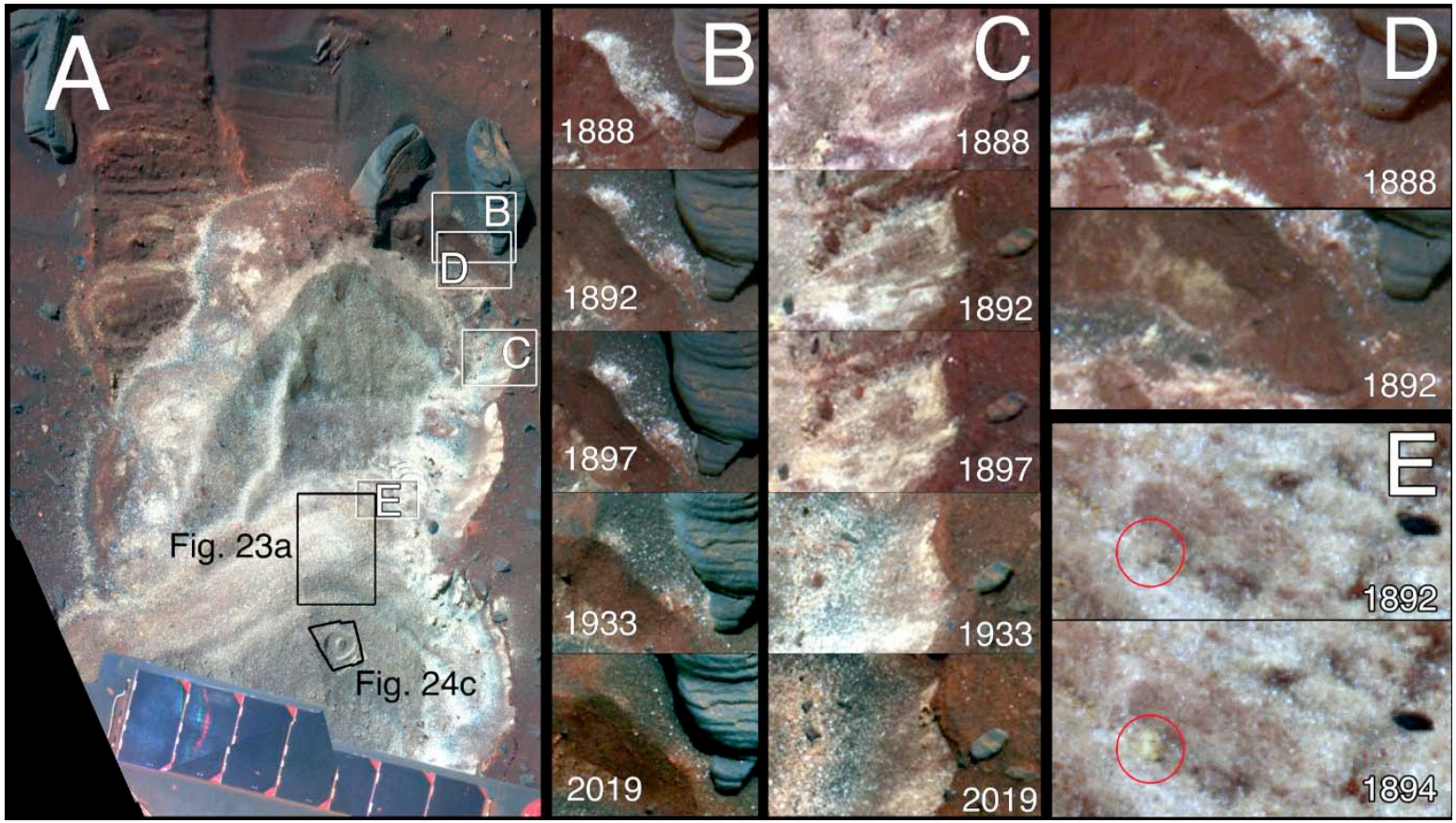

Figure 22. Examples of textural changes at the Ulysses soil exposure between sols 1888 and 2019. (a) False color image (blue = 432 nm, green = 535 nm, red = 753 nm) from sol 1933 (P2382) showing the locations of b-e, as well as Figure 23a and Figure 24a. The wheel track in the upper left is ~16 cm wide. (b) Disappearance of fine white material; (c) Dispersal and removal of light material along the cliff at the eastern edge of the exposure; (d) appearance of bright material in cliff at the northern edge of the exposure; (e) appearance of a bright soil clod (marked by the red circle) within the exposure.

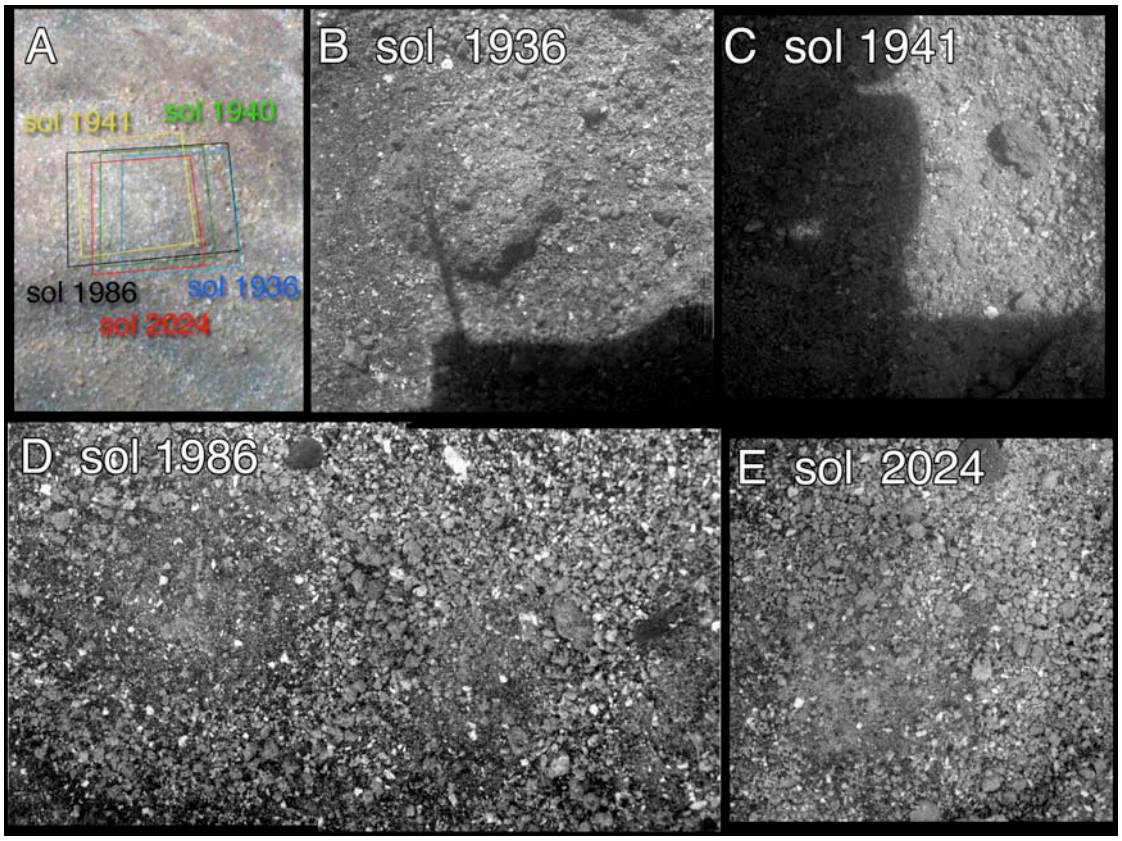

Figure 23. Observations of Penina. Each MI observation is ~3 cm high. (a) Pancam image with footprints of MI observations. (b) Merge of 6 MI images acquired on Sol 1936 when the target was partly shadowed. (c) Merge of 5 MI images acquired on Sol 1941 when the target was partly shadowed. (d) Mosaic of 2 MI images acquired on Sol 1986 when the target was fully shadowed. (e) MI image 2M306051999, acquired on Sol 2024 when target was fully shadowed. Location of (a) is shown in Figure 22a.

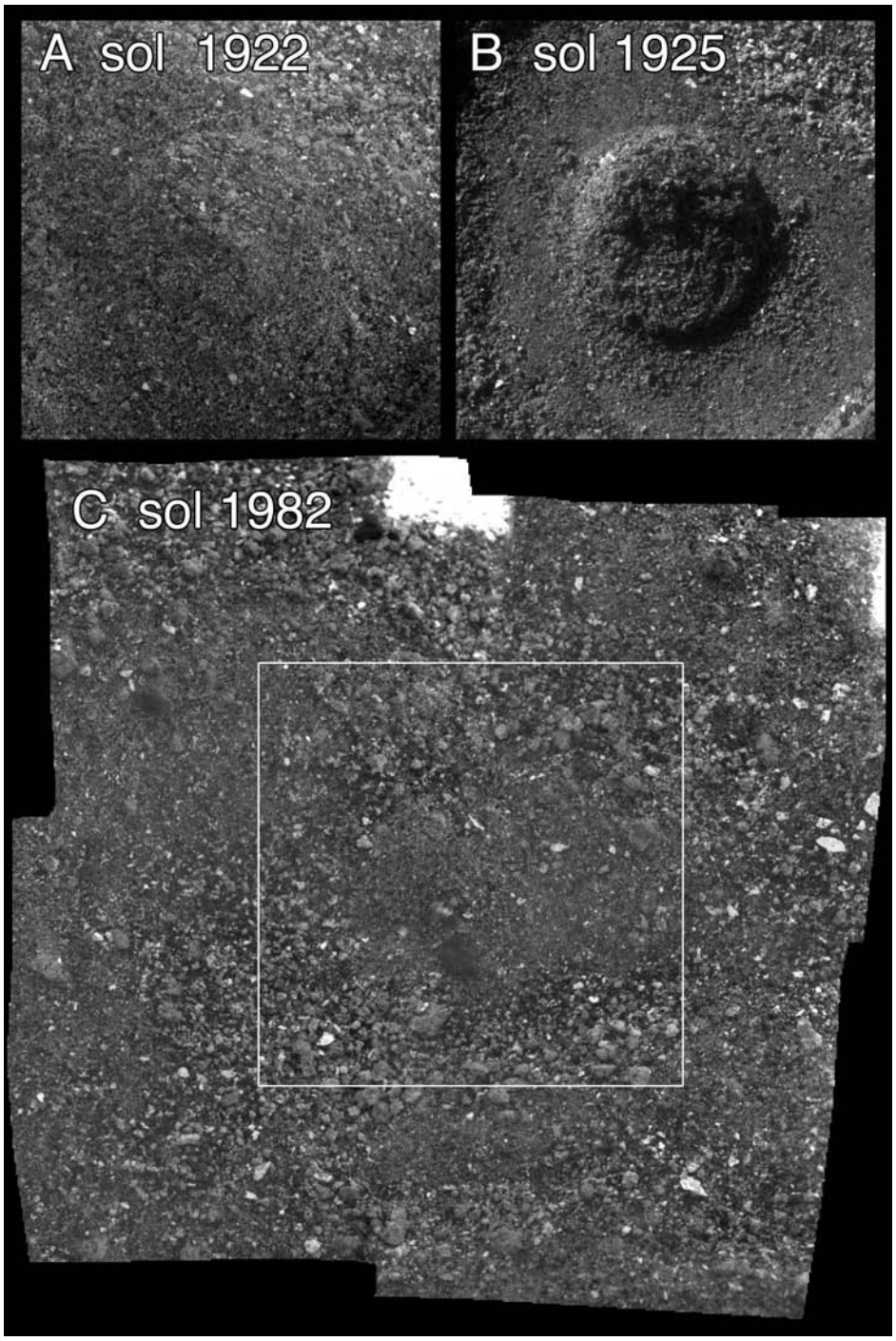

Figure 24. Microscopic Imager (MI) observations of Sackrider. (a) Merge of 5 MI images acquired on Sol 1922 when target was fully shadowed. Image is ~3 cm across. (b) Merge of 5 MI images acquired on Sol 1925 when target was illuminated from the upper left. Image is ~3 cm across. (c) Mosaic of 4 MI images acquired on Sol 1982 when target was mostly shadowed. White box in indicates location of (a) and (b); mosaic is ~5 cm across. Location of (c) is shown in Figure 22a.

modifications to small-scale topographic features within the trench. Note that the two Pancam false color images are not at the same stretch, and these images should only be used for textural comparisons, not color comparisons (Figure 9).

One MI observation of bright soil near the Kit Carson exposure was acquired on sol 1863 at the target called John Wesley Powell (Table 5; location shown in Figure 9); unfortunately, no additional MI observations were acquired at this site. A merge of this observation with Pancam false color is shown in Figure 21. The ring seen in this image is the impression of the Mössbauer (MB) contact plate, which had compressed the soil with a force of 1N. The soil in the MI observation is largely composed of 100-300 μm aggregates of grains smaller than the MI resolution limit. The "fluffy" aggregates are easily crushed by the MB contact, as seen by the dominance of <100 μm silt and fine-grained sand in the area compacted by the MB (Figure 21). The color variability in the image does not appear to correspond to any distinguishable textural variability among the color units.

4.2 Ulysses Soil Exposure

Pancam observations reveal extensive textural changes within the Ulysses soil exposure over 131 sols. Figure 22 shows examples of the observed modifications: (b) disappearance of fine bright material; (c) dispersal and removal of light material along the cliff at the eastern edge of the exposure; (d) appearance of bright material along a cliff at the northern edge of the exposure; and (e) appearance of a bright soil clod (marked by the red circle) within the exposure. The most dramatic changes to (b) and (c) occur between sols 1897 and 1933, but some change is observed between each pair

of observations. Within the bulk material, Pancam images show an increase in granularity with time as fine grained material appears to have been removed (Figure 12). The steep wall at the eastern edge of the exposure (Figure 22c) shows that the soil is weakly cohesive at the surface, with cohesion seeming to decrease within the bulk bright soil material a few millimeters below the surface.

Repeated MI observations within the Ulysses exposure were acquired at two targets called Penina (Figure 23) and Sackrider (Figure 24), locations of which are shown in Figure 22a. The four observations of Sackrider and three of Penina (Table 5) show that these targets are composed of angular, poorly sorted, sand-sized and finer particles (<300 μm), with some aggregates (mostly 500-700 μm) and a subpopulation of larger, rounded clasts (>800 μm). Most grains are opaque, but some grains that are bright or glinting are also observed (saturating the dynamic range of the MI camera). Some particles are two-toned, and appear to be dark clasts coated by bright, fine-grained material (see also Figures 13 and 17 of Arvidson et al. (2011)).

At both Penina and Sackrider, a removal of fine-grained material is observed (Figures 23-24). We note that the first MI observation at Ulysses was acquired 36 days after the material was exposed, when the texture may already have been modified to some extent. The later Penina observations (sol 1986 and 2024) show a marked decrease in 100-300 μm grains and aggregated particles, leaving a lag of larger, subangular sand particles (Figure 23). Grain size distributions measured at the Penina target confirm that the mean grain size increases between sols 1936 and 2024 (Siebach et al., 2010; Arvidson et al., 2011). At Sackrider, the initial MI observation (sol 1922) is dominated by 100-300 μm grains and aggregates which crush easily under the 1N

force of the MB, creating a high-fidelity cast of the smooth MB plate surface and a raised circle of uncompressed material in the center of the sol 1925 observation (Figure 24a-b). By the sol 1982 Sackrider observation (Figure 24c), the soil is dominated by a spatially heterogeneous distribution of >300 μm fine to medium sand particles.

5. Discussion

At the Tyrone soil exposure, the most significant changes observed in Pancam spectra were an increase in the 535 nm band depth over 152 sols (Figure 4b), and an increase in the red to blue (753 nm to 432 nm) ratio during the first 74 sols with no statistically significant change thereafter (Figure 4d). The percent change maps for these parameters (Figure 5a-b) agree with the image-based observations. The 535 nm band depth percent change map (Figure 5a) shows that this parameter systematically increased between sols 864 and 1005 by ~120% for both the white and yellow soil hues, which is the largest change observed for any material in the image. An increase in 535 nm band depth is consistent with dehydration based on our laboratory experiments (Figure 18), but is also consistent with contamination by airfall dust and/or aeolian mixing with surrounding dusty soils, which have relatively deep 535 nm features in Pancam spectra (e.g., Figure 3 and 4a). Because the 535 nm band depth is also observed to increase for dark, basaltic float rocks in the scene (Figure 5a), the effect of airfall dust may explain the observations. Therefore, on its own, an increase in 535 nm band depth is not a unique or definitive indicator of mineralogic change.

The 753 nm to 432 nm ratio percent change map (Figure 5b) indicates that this parameter increases at the Tyrone white soil with respect to other materials between sols 864 and 1005. However, the average magnitude of this change is only 4%, which is smaller than the typical pixel-to-pixel variations within the white soil deposit (± 7%). In the image-based analysis (Figure 4d), we observe that the only statistically significant change to the red to blue ratio occurred between sols 790 and 864. An increase in this ratio is inconsistent with the spectral changes associated with the dehydration of ferric sulfates (Figure 18); it is consistent, however, with dust contamination over 74 sols, which would "redden" the soil color. Thus, the effects of airfall dust contamination alone could explain the increases in the 535 nm band depth and red to blue ratio observed at the Tyrone soils.

The trends in Spirit's solar array energy can be used to infer dust deposition and wind activity over the period of observation (e.g., Landis et al., 2004). The power from the solar panels varies with season and atmospheric optical depth (tau in Table 2), degrades slowly from continual airfall dust accumulation, and increases sharply following strong wind events that remove dust from the solar panels. Over sols 790 to 1062 (Figure 25), no large solar panel cleaning events occurred during the Tyrone imaging campaign. The gradual decrease in solar array energy over the Tyrone imaging campaign (from 357 to 288 W-hrs), even after the winter solstice on sol 923 (when the solar insolation begins to increase), indicates a period of low winds and gradual dust deposition during Spirit's winter at Low Ridge. This decrease is consistent with the minor spectral variations observed at the Tyrone soil exposure

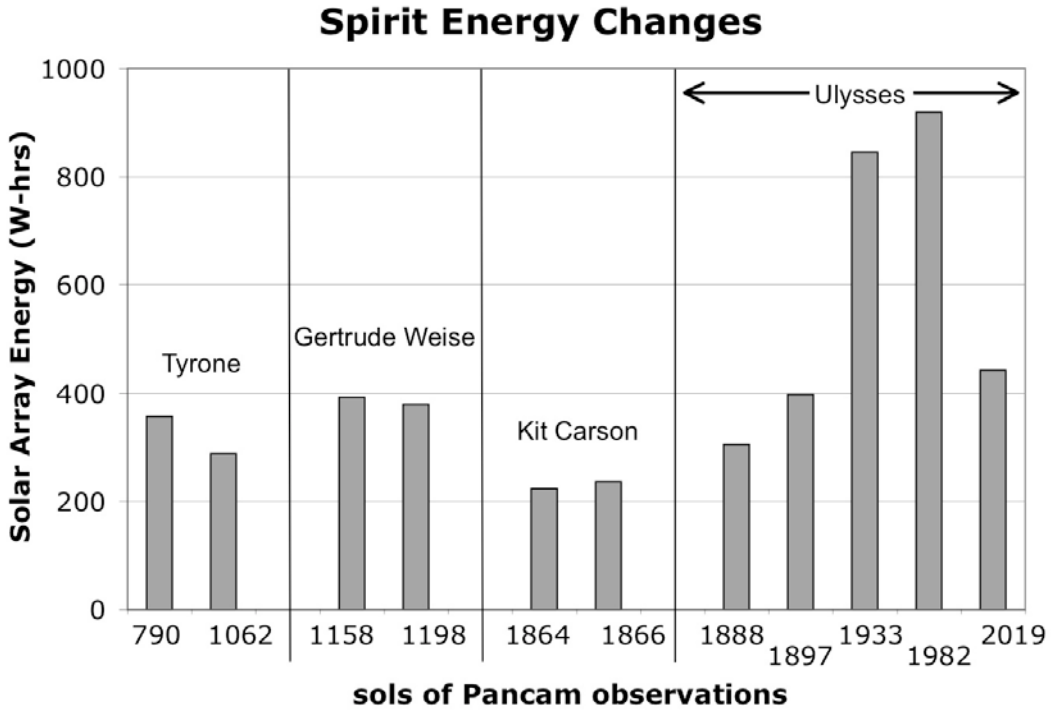

Figure 25. Spirit solar array energy for the sols of imaging campaigns considered in this study: Tyrone (sols 790-1062), Gertrude Weise (sols 1158-1198), Kit Carson (sols 1864-1866) and Ulysses (sols 1888-2019). The increase in array energy between sols 1897 and 1933 indicates a strong wind event that cleaned dust from the rover deck; decreases in array energy indicate dust deposition on the solar panels.

reflecting contamination by airfall dust, and not aeolian mixing or a mineralogic change.

Our results cannot confirm the initial Pancam-based study by Wang et al. (2008), who reported a decrease in the 432 to 753 spectral slope of the Tyrone yellow soil hue between sols 864 and 1062, with the largest change occurring between sols 922 and 959. Those spectral changes were interpreted as evidence for a mineralogic phase change of the exposed yellow soil. While we do observe a minor decrease in the 753 to 432 nm ratio between sols 922 and 959 (Figure 4d), we show above that

this difference is well within the statistical noise, as are all of the other variations of this parameter between sols 864 and 1062 for the yellow and white soils.

Wang et al. (2008) based their results on visual, qualitative analysis of 432 nm vs. 753 nm histograms from each observation, in which the data cloud containing pixels from the yellow soil was observed to change relative to the data cloud containing pixels from the white soil (Figure 27 of Wang et al. (2008)). However, small, qualitative variations in the shapes and positions of data clouds such as 2-dimensional histograms might not accurately represent the actual level of statistical variations within an individual image, or between sets of subsequent images. For example, visual methods for detecting changes in the centroid of a histogram data cloud are highly sensitive to how histogram frequency values are displayed on a plot. If all values in the histogram are displayed in the same or similar color or grayscale, for example, then outliers of relatively insignificant numbers of pixels could be perceived as having much greater statistical weight than they should actually have. More rigorous weighting of each histogram bin is critical in order to accurately assess variations in a data cloud.

At the Gertrude Weise exposure, we observed no statistically significant spectral changes, implying that Pancam detected no dehydration of the silica-rich material. The solar array energy data (Figure 25) indicates that no strong wind events or significant dust deposition occurred during the 50 sol period of observation, supporting the contention that aeolian mixing did not occur between sols 1158 and 1198.

The increase in 864 nm band depth of Kit Carson white and yellow soils is the most statistically significant spectral change observed by Pancam at any soil exposure (Figure 11). However, this increase is inconsistent with expected spectral changes from the dehydration of the ferric sulfates that we studied (Section 3.3), and is also inconsistent with dust deposition or aeolian mixing because all other scene materials have shallower 864 nm band depths than the bright soil (Figure 11). While an increase of this band depth could be consistent with the rehydration of a ferric sulfate mineral (in the case where pH_2O is greater at the martian surface than in the near subsurface), we consider this an unlikely scenario because the magnitude of the observed change is so large – the 200% increase in 864 nm band depth observed over two sols is greater than the largest change observed in our laboratory experiments of ferric sulfates equilibrating to martian conditions from Earth conditions over 150 days (130% decrease in 864 nm band depth for coquimbite). Furthermore, no other spectral changes that would be expected to accompany rehydration have been observed, such as a decrease in 535 nm band depth or an increase in 753 nm to 432 nm ratio (from the reverse of trends shown in Figure 18).

The observed 864 nm band depth increase at Kit Carson could instead represent an instrumental or observational effect rather than a physical change, because: (1) the magnitude of the observed change is so large; (2) it is the only significant spectral change observed; (3) an increase in 864 band depth is inconsistent with dust deposition, aeolian sorting or mineral dehydration; and (4) the spectra extracted from the two Pancam observations were variably affected by the dust contamination effects described in Section 2.1.4 (because the ROIs were extracted

from different regions of the FOV; Figure 9). We performed a first-order correction for dust contamination by considering the spectral parameters as ratios of the bright soil targets to undisturbed soils imaged in similar regions of the FOV, rather than as absolute values (see Section 2.1.4 above); however, our assumption that the contamination affects similar regions of the FOV by the same scale factor is incorrect. Further work is needed to understand the effects of dust contamination on the Pancam optics late in Spirit's mission.

No changes were observed in HiRISE color data over a 32-sol period that would indicate a mineralogic change, dust deposition, or aeolian sorting event; all measurements of relative color ratio for the Kit Carson, Gertrude Weise and Tyrone soils were <5% and smaller than the estimated errors (Figure 16). For comparison, the relative I/F decrease in the BG filter observed for exposed ice by Byrne et al. (2009) ranged from 20% to 60%. Based on convolutions of our laboratory spectra to HiRISE bandpasses (Figure 19), we would not expect the dehydration of ferric sulfate minerals following exposure to the martian surface to be detectable above the uncertainties in HiRISE observations. However, we would expect extensive dust deposition and/or aeolian mixing to be detectable as an increase in the RED/BG ratio. The non-detection of changes is consistent with the solar array data (Figure 25), which indicate no major dust deposition between sols 1935 and 1967. We note that later changes to the Gusev soils have been observed by HiRISE, as all bright soil exposures are no longer visible in the sol 2177 RED observation (Figure 15c).

The non-detection of mineralogic changes from Pancam and HiRISE data may indicate that highly hydrated ferric-sulfates are not actually present in the bright soil

exposures. None of Spirit's instruments have unambiguously identified the minerals used in our lab study at the Gusev bright soil exposures, and the Pancam spectral deconvolution studies did not include anhydrous ferric-bearing sulfates in their libraries (with the exception of yavapaiite) (Johnson et al., 2007; Lane et al., 2008; Parente et al., 2009), so it is a possibility that the sulfate-rich soils consist largely of anhydrous phases. The non-detection could also indicate that any hydrated mineral components of the Gusev bright soil exposures were in equilibrium with Martian surface conditions prior to exposure, or that the spectral changes accompanying mineral dehydration were below the instrument detection limits.

Alternately, the dehydration of the bright soils may be inhibited by slow reaction kinetics at low temperatures, as has been proposed for the Mg-sulfates of Candor Chasma by Roach et al. (2009). Using two years of Compact Reconnaissance Imaging Spectrometer (CRISM) and Observatoire pour la Minéralogie, l'Eau, les Glaces et l'Activite´ (OMEGA) observations, Roach et al. (2009) found no spectral changes indicative of changes in hydration state of the mono- or polyhydrated sulfates, although only one hydration state should be stable at a given time. The authors suggest that the thermodynamically predicted conversion between Mg-sulfate phases is limited by reaction kinetics at low Martian surface temperatures, which may be the case for ferric sulfate phases at Gusev Crater as well (the average surface temperature at Gusev crater is significantly lower than the $+20^{o}C$ used in our laboratory experiments).

The observed textural changes at Kit Carson directly reveal movement of fine particles by wind. Wind is the only explanation for the removal of material from

depressions on the small cobble, for example, and for the appearance of bright material on dark portions of the wheel trench (Figures 20c-d). Because there was no significant change in dust factor between sols 1864 and 1866 (Figure 25), the observed changes must have been caused by winds too small (or too close to the ground) to remove a significant amount of dust from the rover deck. The only textural change that would be consistent with dehydration is the dispersal of the soil clod in Figure 20b, which could occur upon desiccation. However, a weakly bound soil aggregate, such as those seen in the MI image in Figure 21, could also disperse if impacted by a particle traveling on a wind-driven trajectory (although no lineations or streaks of bright material, as would be expected from this scenario, are observed). Some spectral variations observed at Kit Carson have resulted from these textural changes, such as the increase in reflectance of dark disturbed soil from contamination by wind-blown, fine-grained, bright soil, as illustrated in Figure 20d.

The many spectral and textural changes observed at Ulysses are also related. The changes in the Pancam spectral parameters show that the white and yellow soils grew less distinct from the dark disturbed materials over time (Figure 14), and the spectra of white and yellow hues converged (Figure 13). This convergence is illustrated well in DCS images, where the two distinct hues seen in the sol 1888 observation are no longer distinguishable in the sol 1982 observation (Figure 12). These spectral and color changes are consistent with aeolian mixing of bright materials with basaltic soils in the trench. A large wind event(s) between the sol 1897 and sol 1933 observations, illustrated as an increase in solar array energy in Figure 25, likely mobilized and removed at least some of the finest grains. Monitoring of the

rover deck with Pancam images of the calibration target also showed significant cleaning after sol 1896 until sol 2003, when dust was again deposited on the deck. The Sackrider and Penina MI observations confirm the removal of fine, bright material, leaving behind the coarsest size fraction of the bright materials mixed with basaltic sand-sized grains.

We interpret some textural changes to result from the slumping of material at the angle of repose. Fine-grained bright material is seen to have moved down slope from the ridge at the west of the Kit Carson exposure (top of Figure 20b). The bright material that "appears" along the Ulysses trench wall between sols 1888 and 1982 (Figure 22d) has likely been exposed from underneath dark material along the wall that has slumped into the trench. This gravity-driven mobility exemplifies the unconsolidated nature of both the dark and bright exposed materials.

Textural modifications occur outside the bright deposits as well, such as softening of the imprints created by the wheel cleats in dusty surface soil at Ulysses (top of Figure 22a). We do not observe any wind-related changes to surfaces that have not been disturbed by wheels, however, because induration of the martian regolith in this area has apparently immobilized surface grains (e.g. Sullivan et al., 2008). As seen in the Ulysses eastern cliff (Figure 22c), the topmost soil layer consists of a series of ~1 cm crust-like layers of cohesive, perhaps cemented grains.

Our observations of wind-driven particle movement are consistent with previous studies of particle mobility at Gusev Crater. The majority of grain movement has been shown to occur in brief episodes of entrainment and saltation during strong wind events, and sand grains (~100 μm) have been noted to appear on Spirit's solar

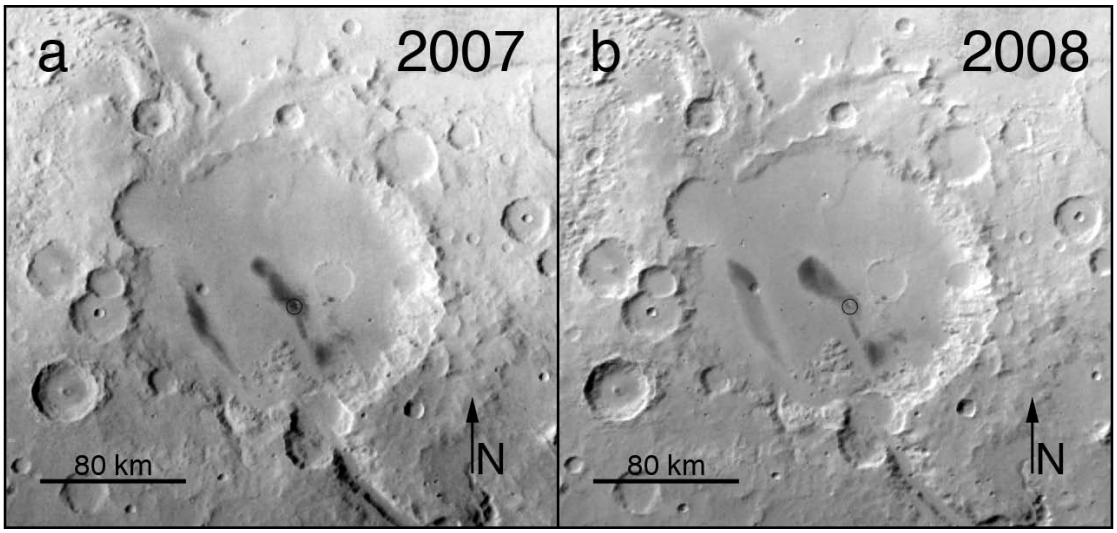

Figure 26. Mosaics of Gusev Crater from the Mars Reconnaisance Orbiter Mars Color Imager (MARCI) band 5 (718 ± 50 nm). The mosaics were generated by map-projecting all MARCI images of Gusev Crater in: (a) 2007 (sols 1064-1419); and (b) 2008 (sols 1420-1775) for which spacecraft pointing and ephemeris (SPICE) information was available. To minimize the effects of atmospheric dust, each pixel in the mosaic was assigned the lowest albedo value for that location from the list of overlapping map-projected images. The black circles indicate the location of the Columbia Hills and the Spirit rover. The changes to the low-albedo wind streaks exemplify the large-scale wind activity and dust movement that has occurred over the period discussed in this work.

panel deck 0.66 m above the ground following periods of high winds (Greeley et al., 2006). Sullivan et al. (2008) showed that low density, sand-sized (several hundred μm) aggregates of airfall dust are more easily mobilized than solid particles of the same size; in the MI observations at Ulysses, we observe that the same is true of porous bright soil aggregates, which are more easily mobilized than soil grains of the same size (the solid >300 μm grains remain in the trench as a lag deposit; Figures 23-24).

Spirit has observed hundreds of dust devils during its mission (Waller et al., 2009), and dust devil tracks in Gusev Crater have been observed from orbit (Greeley

et al., 2003). The strong wind events recorded in Spirit's solar array energy and seen in Pancam and MI data also caused dramatic changes in the low-albedo wind streaks in Gusev crater. This is apparent in repeated observations of the region by the Mars Reconnaissance Orbiter Mars Color Imager (MARCI) (Bell et al., 2009) (Figure 26). The observed dust devil and wind streak activity indicates that Gusev Crater was an active region of dust removal and deposition during the time period discussed in this work.

6. Conclusions

We have compared repeated multispectral observations of the Tyrone, Gertrude Weise, Kit Carson and Ulysses bright soils to test the hypothesis that the ferric sulfate and silica-rich materials undergo mineralogic changes upon exposure. In Pancam and HiRISE data, we observe no statistically significant spectral changes that are uniquely diagnostic of dehydration and/or mineralogic phase changes. In Pancam and MI observations of Kit Carson and Ulysses, we have also observed no textural changes that are consistent with the desiccation of a hydrated mineral. We conclude that there is no unique or statistically reliable evidence for mineralogic changes following the exposure of the Gusev bright soils. Our non-detections do not prove that no mineralogic changes occurred in the soils examined in this study. However, if any mineralogic changes did occur, they were below the detection threshold of the Pancam instrument.

We have observed several spectral and textural changes that are consistent with airfall dust deposition and wind-driven particle movement. The Tyrone bright soil

spectra converge toward the spectral characteristics of martian dust over the 272 sols of observation (e.g., the 753 nm to 432 nm ratio and the 535 nm band depth increase), consistent with contamination by airfall dust. The hue separations at Ulysses become less distinct over the 131 sols of observation, which we interpret as evidence of aeolian mixing within the trench. At Kit Carson and Ulysses, we observe significant textural changes, including slumping within the wheel trench, winnowing of fines, movement of soil aggregates, and dispersal of soil aggregates. Our observations are consistent with previous studies that have shown that strong wind events mobilize the <300 μm soil fraction and can entrain larger, porous soil aggregates (e.g., Greeley et al., 2006; Sullivan et al., 2008). Thus, to varying degrees, all of the observed changes to the spectra and textures of the bright Gusev soil exposures can be attributed to airfall dust deposition and aeolian sorting.

REFERENCES

Arvidson, R.E., and 36 colleagues, 2010. Spirit Mars Rover Mission to the Columbia Hills, Gusev Crater: Mission overview and selected results from the northern Home Plate Winter Haven to the side of Scamander Crater, J. Geophys. Res., 115, E00F03, doi:10.1029/2010JE003633.

Bell, J.F., III, and 24 colleagues, 2003. Mars Exploration Rover Athena Panoramic Camera (Pancam) investigation. J. Geophys. Res. 108, E12, doi:10.1029/2003JE002070.

Bell, J.F., III, Joseph, J., Sohl-Dickstein, J.N., Arneson, H.M., Johnson, M.J., Lemmon, M.T., Savransky, D., 2006. In-flight calibration and performance of the Mars Exploration Rover Panoramic Camera (Pancam) instruments. J. Geophys. Res. 111, E2, doi 10.1029/2005JE002444.

Bell, J.F., III, and 20 colleagues, 2009. Mars Reconnaissance Orbiter Mars Color Imager (MARCI): Instrument description, calibration, and performance (2009), J. Geophys. Res., 114 E08S92, doi: 10.1029/2008JE003315.

Byrne, S., and 17 colleagues, 2009. Distribution of mid-latitude ground ice on Mars from new impact craters, Science, 325, 1674, doi:10.1126/science.1175307.

Chipera, S., Vaniman, D., Bish, D.L., 2007, The Effect of Temperature and Water on Ferric-Sulfates, Lunar Planet. Sci. XXXVIII, Abstract 1409.

Cloutis, E.A., Craig, M.A., Kruzelecky, R.V., Jamroz, W.R., Scott, A., Hawthorne, F.C., Mertzman, S.A., 2008. Spectral reflectance properties of minerals exposed to simulated Mars surface conditions. Icarus 195, 140-168, doi: 10.1016/j.icarus.2007.10.028.

Craig, M.A., Cloutis, E.A., Mueller, T., 2001. ME and Mini-ME: Two Mars environmental simulation chambers for reflectance spectroscopy, Lunar Planet. Sci. XXXII, Abstract 1368.

Delamere, W.A., and 15 colleagues, 2010. Color imaging of Mars by the High Resolution Imaging Science Experiment (HiRISE), Icarus 205, 38–52, doi:10.1016/j.icarus.2009.03.012.

Farrand, W.H., Bell, J.F., III, Johnson, J.R., Arvidson, R.E., Crumpler, L.S., Hurowitz, J.A., Schröder, C., 2008. Rock spectral classes observed by the Spirit rover's Pancam on the Gusev Crater plains and in the Columbia Hills. J. Geophys. Res. 113, doi:10.1029/2008JE003237.

Freeman, J., Wang, A., Ling, Z., 2009. Ferric Sulfates on Mars: Mission Observations and Laboratory Investigations, Lunar Planet. Sci. XL, Abstract 2284.

Gellert, R., and 11 colleagues, 2006. Alpha particle X-ray spectrometer (APXS): Results from Gusev Crater and calibration report. J. Geophys. Res. 111, doi:10.1029/2005JE002555.

Gillespie, A., Kahle, A., Walker, R., 1986. Color enhancement of highly correlated images. I. Decorrelation and HSI contrast stretches. Remote Sensing of Environment, 20, 3 209-235.

Greeley, R., and 21 colleagues, 2006. Gusev crater: Wind-related features and processes observed by the Mars Exploration Rover Spirit, J. Geohphys. Res., 111, E02S09, doi:10.1029/2005JE002491.

Greeley, R., Kuzmin, R.O., Rafkin, S.C.R., 2003. Wind-related features in Gusev crater, Mars, J. Geophys. Res. 108, E12, 8077, doi:10.1029/2002JE002006.

Hapke, B., 1993. Theory of Reflectance and Emittance Spectroscopy, Cambridge Univ. Press, Cambridge, UK.

Herkenhoff, K.E., and 23 colleagues, 2003. Athena Microscopic Imager Investigation. J. Geophys. Res. 108, E12, 8065, doi:10.1029/2003JE002076.

Herkenhoff, K.E., and 41 colleagues, 2006. Overview of the Microscopic Imager Investigation during Spirit's first 450 sols in Gusev crater, J. Geophys. Res., 111, E02S04, doi:10.1029/2005JE002574.

Johnson, J.R., Bell, J.F., III, Cloutis, E., Staid, M., Farrand, W.H., McCoy, T., Rice, M., Wang, A., Yen, A., 2007. Mineralogic constraints on sulfur-rich soils from Pancam spectra at Gusev Crater, Mars. Geophys. Res. Lett. 34, 13202, doi:10.1029/2007GL029894.

Johnson, J.R., and 12 colleagues, 2006. Spectrophotometric properties of materials observed by Pancam on the Mars Exploration Rovers: 1. Spirit. J. Geophys. Res. 111, doi:10.1029/2005JE002494.

Kinch, K.J., Sohl-Dickstein, J., Bell III, J.F., Johnson, J.R., Goetz, W. and Landis, G.A., 2007. Dust deposition on the Mars Exploration Rover Panoramic Camera (Pancam) calibration targets, *J. Geophys. Res., 112,* CiteID E06S03, doi:10.1029/2006JE002807.

Landis, G.A., Kerslake, T.W., Jenkins, P. and Scheiman, D., 2004. Mars Solar Power. 2nd International Energy Conversion Engineering Conference, AIAA 2004-5555.

Lane, M.D., Bishop, J.L., Dyar, M.D., King, P.L., Parente, M., Hyde B.C., 2008. Mineralogy of the Paso Robles soils on Mars. Amer. Min. 93, 728-739, doi:10.2138/am.2008.2757.

Lemmon, M.T., and 14 colleagues, 2004. Atmospheric Imaging Results from the Mars Exploration Rovers: Spirit and Opportunity. Science 306, 1753, doi:10.1126/science.1104474.

Maki, J.N., and 21 colleagues, 2003. Mars exploration rover engineering cameras. J. Geophys. Res. 108, 8071, doi:10.1029/2003JE002077.

McEwen, A.S., and 14 colleagues, 2007. Mars Reconnaissance Orbiter's High Resolution Imaging Science Experiment (HiRISE). J. Geophys. Res. 112, E05S02. doi:10.1029/2005JE002605.

McEwen, A.S., and 69 colleagues, 2010. The High Resolution Imaging Science Experiment (HiRISE) during MRO's Primary Science Phase (PSP). Icarus 205, 2– 37. doi:10.1016/j.icarus.2009.04.023.Mertzman, S.A. (2000), K-Ar results from the southern Oregon-northern California cascade range: Oregon Geology, v. 62, p. 99-122.

Ming, D.W., and 16 colleagues, 2006. Geochemical and mineralogical indicators for aqueous processes in the Columbia Hills of Gusev Crater, Mars. J. Geophys. Res. 111, doi:10.1029/2005JE002560.

Ming, D.W., and 19 colleagues, 2008. Geochemical properties of rocks and soils in Gusev Crater, Mars: Results of the Alpha Particle X-Ray Spectrometer from Cumberland Ridge to Home Plate, J. Geophys. Res., 113, E12S39, doi:10.1029/2008JE003195.

Morris, R.V., and 19 colleagues, 2006. Mössbauer mineralogy of rock, soil, and dust at Gusev Crater, Mars: Spirit's journey through weakly altered olivine basalt on the plains and pervasively altered basalt in the columbia hills. J. Geophys. Res. 111, doi:10.1029/2005JE002584.

Morris, R. V. Klingelhöfer, G., 2008a. Iron mineralogy and aqueous alteration on Mars from the MER Mössbauer spectrometer, in The Martian Surface - Composition, Mineralogy, and Physical Properties, edited by J. F. Bell III, pp. 339-365, Cambridge Univ. Press, Cambridge, UK.

Morris, R.V., and 19 colleagues, 2008b. Iron mineralogy and aqueous alteration from Husband Hill through Home Plate at Gusev Crater, Mars: Results from the Mössbauer instrument on the Spirit Mars Exploration Rover. J. Geophys. Res. 113, E12S42, doi:10.1029/2008JE003201.

Parente, M., Bishop, J.L., Bell, J.F., III, 2009. Spectral unmixing for mineral identification in pancam images of soils in Gusev crater, Mars, Icarus 203, 421-436, doi:10.1016/j.icarus.2009.04.029.

Portyankina, G., Vincendon, M., Thomas, N., Aye, K.-M., 2010. Recovery of surface reflectance from atmospheric aerosol contribution: Application to HiRISE images, Lunar. Planet. Sci. XLI, Abstract 1582.

Reid, R.J., Rueffer, P., Gliem, F., Johnson, J.R., Maki, J.N., Herkenhoff, K.E., Singer, R.B., 1999. Imager for Mars Pathfinder (IMP) image calibration. J. Geophys. Res. 104, 8907-8926, doi: 10.1029/1998JE900011.

Rice, M.S., Bell, J.F. III, Cloutis, E.A., Wang, A., Ruff, S., Craig, M.A., Bailey, D.T., Johnson, J.R., de Souza Jr., P.A., Farrand, W.H., 2010a. Silica−rich deposits and hydrated minerals at Gusev crater, Mars: Vis−NIR spectral characterization and regional mapping. Icarus 205, 375–395. doi:10.1016/j.icarus.2009.03.035.

Rice, M., Cloutis, E.A., Crowley, J., 2010b. Spectral Reflectance Changes Accompanying Long-Duration Exposure of Silica Sinter and Fe-Sulfates to Simulated Mars Surface Conditions, Lunar. Planet. Sci. XLI, Abstract 2576.

Roach, L. H., Mustard, J.F., Murchie, S.L., Bibring, J.-P., Forget, F., Lewis, KW., Aharonson, O., Vincedon, M., Bishop, J.L., 2009. Testing evidence of recent hydration state change in sulfates on Mars, J. Geophys. Res. 114, E00D02, doi:10.1029/2008JE003245.

Ruff, S.W., and 10 colleagues, 2011. Characteristics, distribution, origin, and significance of opaline silica observed by the Spirit rover in Gusev crater, Mars, J. Geophys. Res. 116, E00F23. doi:10.1029/2010JE003767.

Siebach, K., Arvidson, R.E., Cabrol, N., Athena Science Team, 2010. Recent Spirit Results: Microscopic Imager Analysis of Particle Properties in Scamander Crater, West of Home Plate. Lunar. Planet. Sci. XLI, Abstract 2548.

Sohl-Dickstein, J., Johnson, J. R., Grundy, W. M., Guinness, E. A., Graff, T., Shepard, M. K., Arvidson, R. E., Bell, J. F.,III, Christensen, P. R., Morris, R. V., 2005. Modeling visible/near-infrared photometric properties of dustfall on a known substrate. Lunar Planet. Sci. XXXVI, Abstract 2235.

Squyres, S.W., and 17 colleagues, 2008. Detection of silica-rich deposits on Mars. Science 320, 1063, doi:10.1126/science.1155429.

Sullivan, R., Arvidson, R.E., Bell, J.F., III, Gellert, R., Golombek, M., Greely, R., Herkenhoff, K., Johnson, J.R., Thompson, S., Whelley, P., Wray, J.J., 2008. Wind-driven particle mobility on Mars: Insights from Mars Exploration Rover observations at “El Dorado” and surroundings at Gusev Crater. J. Geophys. Res. 113, E06S07 doi:10.1029/2008JE003101.

Waller, D.A., Greeley, R., Neakrase, L.D., Landis, G.A., Whelly, P., Thompson, S.D., 2009. Dust loading in Gusev crater, Mars: Results from two active dust devil seasons, American Geophysical Union Fall Meeting, Abstract EP21A-0579.

Wang, A., Ling, Z.C., 2011. Ferric sulfates on Mars: A combined mission data analysis of salty soils at Gusev crater and laboratory experimental investigations. J. Geophys. Res. 116, E00F17, doi:10.1029/2010JE003665.

Wang, A., and 15 colleagues, 2008. Light-toned salty soils and coexisting Si-rich species discovered by the Mars Exploration Rover Spirit in the Columbia Hills. J. Geophys. Res. 113, E12S40, doi:10.1029/2008JE003126..

Yen, A.S., and 13 colleagues, 2008. Hydrothermal processes at Gusev Crater: An evaluation of Paso Robles class soils. J. Geophys. Res. 113, E12, doi:10.1029/2007JE002978.

CHAPTER 5

INFLUENCE OF FAULT-CONTROLLED TOPOGRAPHY ON FLUVIO-DELTAIC SEDIMENTARY SYSTEMS IN EBERSWALDE CRATER, MARS[1]

0. Abstract

Eberswalde crater was selected as a candidate landing site for the Mars Science Laboratory (MSL) mission based on the presence of a fan-shaped sedimentary deposit interpreted as a delta. We have identified and mapped five other candidate fluvio-deltaic systems in the crater, using images and digital terrain models (DTMs) derived from the Mars Reconnaissance Orbiter (MRO) High Resolution Imaging Science Experiment (HiRISE) and Context Camera (CTX). All of these systems consist of the same three stratigraphic units: (1) an upper layered unit, conformable with (2) a subpolygonally fractured unit, unconformably overlying (3) a pitted unit. We have also mapped a system of NNE-trending scarps interpreted as dip-slip faults that pre-date the fluvial-lacustrine deposits. The post-impact regional faulting may have generated the large-scale topography within the crater, which consists of a Western Basin, an Eastern Basin, and a central high. This topography subsequently provided depositional sinks for sediment entering the crater and controlled the geomorphic pattern of delta development.

---

[1] An edited version of this paper was published by AGU. Copyright 2011 American Geophysical Union. Full citation: Rice, M.S., S. Gupta, J.F. Bell III, N.H. Warner (2011), Influence of Fault-Controlled Topography on Fluvio-Deltaic Sedimentary Systems in Eberswalde Crater, Mars, *Geophysical Research Letters*, doi:10.1029/2011GL048149.

1. Introduction

The identification of putative ancient fluvio-deltaic sedimentary systems on Mars has great significance for the astrobiological potential of martian sedimentary rocks; however, the context of how such systems have developed and built stratigraphy is poorly constrained. On Earth, the accumulation of sedimentary successions is commonly associated with tectonic subsidence controls, such as in fault-controlled sedimentary basins (Gupta et al., 1998). In these settings, there is commonly an intimate relationship between topography created by structures such as faults and folds, and the geometry, distribution, and sediment dispersal pathways of fluvio-deltaic systems (Gupta et al., 1999). On Mars, accommodation space for fluvio-deltaic systems is typically considered to be provided by impact crater topography; the role of intra-crater, structurally generated topography has not previously been recognized.

Here, we investigate the role of structurally controlled topography in creating intra-crater basins and topographic highs in Eberswalde crater, and we examine how this topography influences the distribution and sediment dispersal pathways of source-to-sink sedimentary systems within this proposed Mars Science Laboratory (MSL) landing site (Grant et al., 2011). We use images and Digital Terrain Models (DTMs) from the Mars Reconnaissance Orbiter (MRO) to: (1) map structural lineaments in Eberswalde crater; (2) characterize their topographic properties and identify structurally controlled topographic highs and basins; and (3) relate six proposed fluvio-deltaic systems to this structurally controlled topographic template. Our observations suggest that the spatial distribution and evolution of fluvio-deltaic

systems in Eberswalde crater may be strongly influenced by intra-crater structural topography, thus providing a new model for controls on these sedimentary systems. Furthermore, we can infer the distribution of deep-water environments where low energy deposits may be sampled from this topographic control.

2. Setting

Eberswalde crater is centered at 33^{o} W 24^{o} S within the Erythraeum region of Mars, immediately NNE of Holden crater along the Uzboi-Ladon-Morava (ULM) system (e.g., Grant and Parker, 2002). The network of valleys that traverse the intercrater plains north of Holden crater appear to have transported sediment into western Eberswalde crater, building a layered, fan-shaped landform interpreted as a lacustrine delta (Malin and Edgett, 2003; Moore et al., 2003; Wood, 2006; Lewis and Aharonson, 2006; Pondrelli et al., 2008) or possibly an alluvial fan (Jerolmack et al., 2004).

Elsewhere in Eberswalde crater, inverted channels and plateaus of layered rocks suggest a complex history of fluvial activity and deposition in the basin (Lewis and Aharonson, 2006; Pondrelli et al., 2008; Rice and Bell, 2010). Two lobate plateaus in the north of the crater have been interpreted as other remnant deltas (Pondrelli et al., 2008; Rice and Bell, 2010). Pondrelli et al. (2008) noted the presence of linear scarps at the front of the Eberswalde delta, which they interpreted as syn-sedimentary faults, and they proposed a large fault system cutting the crater's center; the extent of such faulting and its influence on sedimentation patterns, however, has not been recognized.

3. Data and Methods

We used images from the MRO Context Camera (CTX) (Malin et al. 2007) to generate a 6 m/pix mosaic base map of the crater, and we analyzed ~0.27 m/pix High Resolution Imaging Science Experiment (HiRISE) images (McEwen et al., 2007) covering the majority of the crater floor. To identify possible structural features, we mapped obvious linear features, noting stratigraphic and topographic evidence for lateral (strike-slip) or vertical (dip-slip) offset along these lineaments that could be suggestive of faulting. Mars Orbiter Laser Altimeter (MOLA) data (Zuber et al., 1992; Smith et al., 2001) provided regional-scale topographic context at ~1 m vertical resolution at a local grid spacing of ~ 0.86×0.43 km^2 (Figure 1a). We also used seven publicly available DTMs derived from HiRISE stereo pairs (Kirk et al., 2008; McEwen et al., 2010) to quantify the vertical offset along the identified structural features. Six fluvio-deltaic systems (inverted, sinuous landforms that, at lower elevations, terminate at fan-shaped plateaus of layered rock) were mapped and stratigraphic units were identified.

4. Results

4.1 Structural geometry and topography of Eberswalde crater

We have identified 233 linear features within Eberswalde crater that we interpret as faults (Figure 1a) based on vertical offsets (our map includes scarps taller than ~5 m). The rose plot in Figure 1a shows that two thirds of these features trend within 15° to 45^o from north. All of these features are characterized by near-vertical scarps; we observed no lateral offsets associated with these lineaments.

Figure 1. (a) MOLA elevation map (color scale: red = high = -1000 m; white = low = -1600 m), draped over a CTX mosaic, showing lineations interpreted as dip-slip faults (white lines), with rose plot indicating their orientations relative to compass directions (data binned at 5^{o} intervals; the circles indicate percentages of total faults at 2% intervals). White shaded regions indicate the faulted margins marked in Figure 1b. The black line from A to A' indicates the location of the topographic profile shown in Figure 1b. The location of Figure 1c is indicated by the black rectangle; (b) MOLA profile across crater (from A to A' as shown in (a), with detail from B to B' indicated in (c)); (c) HiRISE DTM (from PSP_008272_1560 and PSP_010474_1560, overlain on image PSP_010474_1560) showing detail of lineaments in central Eberswalde (color scale: red = high = -1200 m; white = low = -1600 m); (d-e) HiRISE images (from PSP_010474_1560) of linear scarps interpreted faults, locations shown in (c).

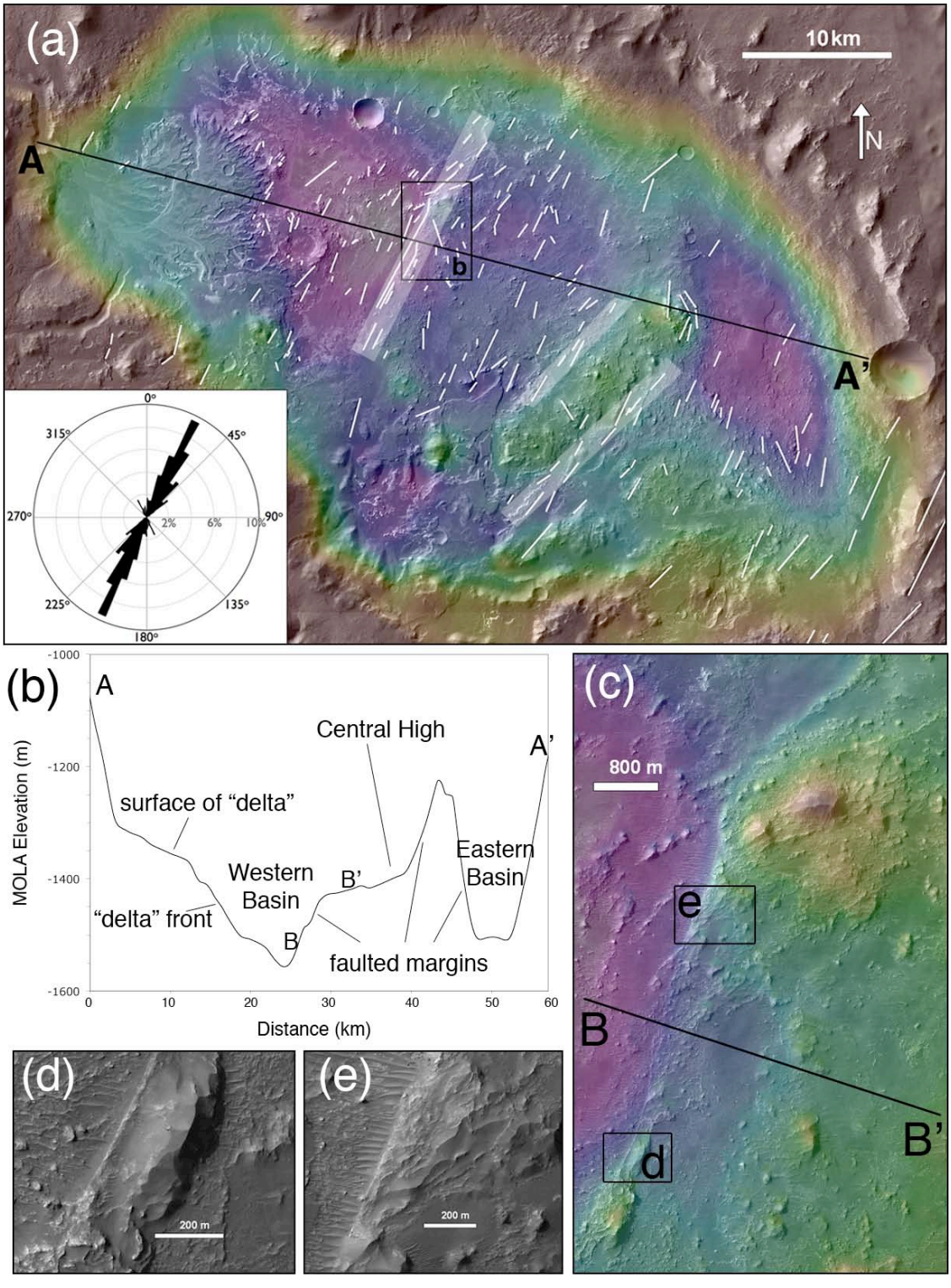
(a)
10 km
N
A
A'
b
0°
45°
90°
135°
180°
225°
270°
315°
2%
6%
10%
(b)
A
A'
Central High
surface of "delta"
Western Basin
B'
Eastern Basin
"delta" front
B
faulted margins
MOLA Elevation (m)
-1000
-1200
-1400
-1600
0
10
20
30
40
50
60
Distance (km)
(c)
800 m
e
B
B'
d
(d)
200 m
(e)
200 m

Analysis of MOLA, CTX and HiRISE topography data show that Eberswalde crater contains a ~100–300 m topographic high that separates two topographic lows: the "Western Basin" and the "Eastern Basin" (Figure 1). The boundary between the Western Basin and the topographic high is marked by a series of distinct lineaments (the most prominent shown in Figure 1c).

4.2 Fluvio-deltaic systems

Six putative fluvio-deltaic systems in Eberswalde crater (FDS1–6) are displayed in Figure 2a. These include the primary "delta," which extends 13 km by 11 km and covers 115 km^2 of the Western Basin (FDS1; Figure 2b), three systems in the north of the crater (FDS2-4), and two in the south (FDS5–6) that have not previously been reported. No evidence for fluvio-deltaic activity has been observed in the Eastern Basin. We focus our detailed analyses on FDS1 (Figure 3a–c), FDS3–4 (Figure 3d–f) and FDS6 (Figure 3g–i) because HiRISE stereo imaging has not yet been acquired for FDS2 and FDS5.

All six systems consist of the same three stratigraphic units: (1) an upper layered unit, conformable with (2) a subpolygonally fractured unit, unconformably overlying (3) a lower pitted unit (Rice and Bell, 2010). Examples of each unit are shown in Figure 4, and unit maps for FDS1, FDS3–4 and FDS6 are shown in Figure 3.

4.2.1 Western system (FDS1).

The front of FDS1, the main Eberswalde "delta" (Figure 2b), is characterized by a ~50 m stack of layered rock that forms cliff faces and "stair-step" geometries.

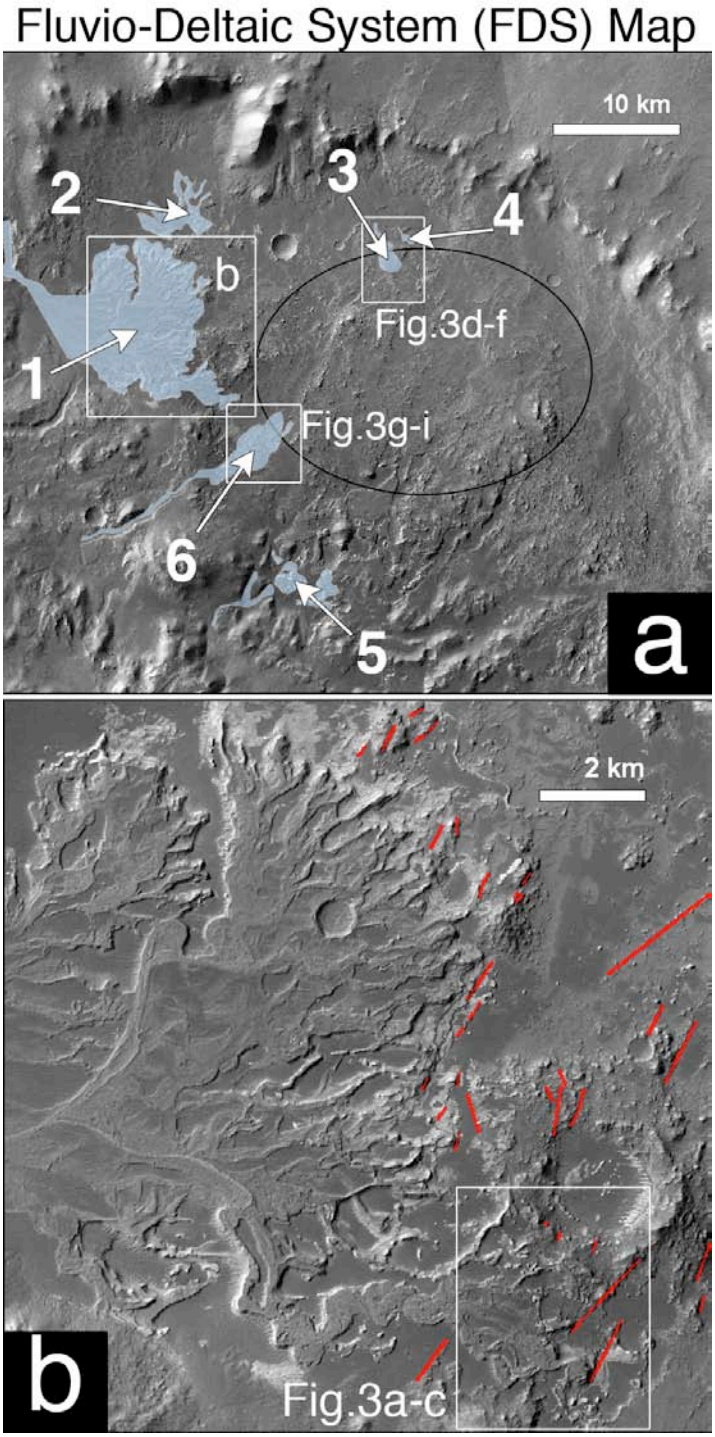

Figure 2. (a) Proposed fluvio-deltaic system (FDS) map for Eberswalde Crater overlain on a CTX mosaic (made from images P01_001336_1560_X1_24S033W and P01_001600_1560_X1_23S033W), showing the location and extents of FDS1-6; (b) detail of FDS1, with red lines indicating locations of linear scarps (CTX image P01_001336_1560_X1_24S033W). Location is indicated in (a).

Figure 3. Maps of individual proposed fluvio-deltaic systems: (a) HiRISE detail (image ESP_019757_1560) of the easternmost extent of FDS1 (location shown in Figure 2b); (b) unit map of the easternmost extent of FDS1; (c) HiRISE DTM (from ESP_019757_1560 and ESP_020034_1560) of the easternmost extent of FDS1; (d) CTX detail (P01_001600_1560_X1_23S033W) of FDS3 and FDS4 (location shown in Figure 2a); (e) unit map of FDS3 and FDS4; (f) HiRISE DTM (from ESP_019190_1560 and ESP_019335_1560) of FDS3 and FDS4.; (g) CTX detail (P01_001336_1560_X1_24S033W) of FDS6 (location shown in Figure 2a); (h) unit map of FDS6. The white arrow indicates the inferred direction of inflow; (i) HiRISE DTM (from ESP_019757_1560 and ESP_020034_1560) of FDS6. White outlines indicate extents of fluvio-deltaic sediments. Black arrows indicate relationships of sediments to potential faults. White arrows indicate inferred inflow directions.

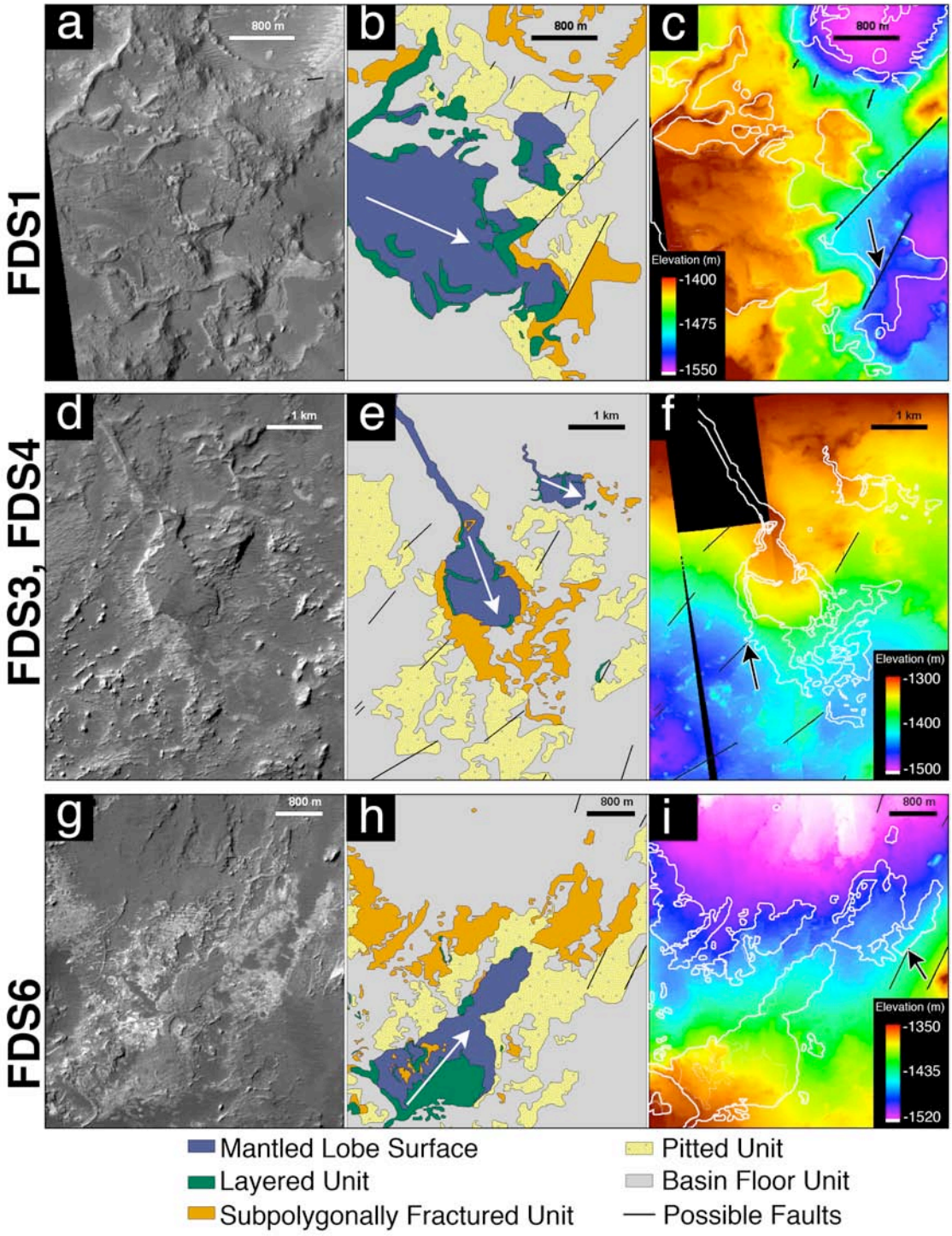
FDS1
FDS3, FDS4
FDS6
a
b
c
d
e
f
g
h
i
800 m
1 km
Elevation (m)
-1400
-1475
-1550
-1300
-1400
-1500
-1350
-1435
-1520
Mantled Lobe Surface
Layered Unit
Subpolygonally Fractured Unit
Pitted Unit
Basin Floor Unit
Possible Faults

These layers have measured dips of 1–3^{o} (Lewis and Aharonson, 2006), and some appear to be shedding boulders that have fallen to the bottom of cliff faces. This layered unit conformably overlies a thin (< 8 m) unit that consists of angular, subpolygonal blocks (with no observed hierarchical patterns) and extends ~2 km from the base of the layered unit toward the center of the crater. The subpolygonally fractured unit unconformably overlies a pitted unit, which covers a large portion of the crater floor and is characterized by quasi-circular depressions in light-toned rock, occurring as dense clusters of ~1–30 m pits.

The FDS1 deposits appear to have been transported into the crater via a large channel that cuts the western crater rim and enters the Western Basin. The layered unit is fan-shaped in planform and extends ~11 km east toward the deepest portion of the basin, preserving sinuous and meandering ridges on its surface covered by a thin mantling material. The ridges appear to be grouped into multiple deposits, which have been mapped in previous studies as three (Bhattacharya et al., 2005) or five (Wood, 2006; Pondrelli et al., 2008) distinct deltaic lobes.

The front of FDS1 is characterized by NNE-trending scarps (Figure 2b). At the easternmost extent of FDS1 (Figure 3a), which has been interpreted as some of the youngest deposits of this system (e.g., Wood, 2006), the layered and subpolygonally fractured units are bounded by a structural lineament (arrow in Figure 3c), while the pitted unit appears modified by the possible fault (Figure 3c). In places, the pitted unit is topographically higher than the subpolygonally fractured unit (Figure 3b–c), suggesting that the subpolygonally fractured deposits conformed to preexisting topography.

4.2.2 Northern systems (FDS3–4).

Two smaller, fan-shaped features in the north of the crater (Figure 3d–f) were noted by Pondrelli et al. (2008). FDS3 and FDS4 originate at the basinward ends of sinuous ridges along the northern crater wall and are superposed on the crater's central topographic high; the surface of FDS3 is at elevation -1385 m, roughly 50 m above the front surface of FDS1. The subpolygonally fractured and layered units at FDS3 overly a NNE-trending lineament that has formed a scarp in the pitted unit (arrow in Figure 3f).

4.2.3 Southwestern system (FDS6).

The FDS6 deposits appear to have been transported into the Western Basin via a channel that cuts the southwestern rim of Eberswalde crater. The surface of FDS6 (Figure 3g) preserves sinuous and digitate ridges that have eroded into a stair-step pattern of layered rock near the southwest crater rim; sinuous landforms and subpolygonally fractured material extend ~3.5 km toward the eastern edge of the Western Basin (Figure 3h). The layered and subpolygonally fractured units that comprise this system are oriented parallel to the NNE-trending lineaments that form the topographic divide immediately to the east (Figure 3i); these features modify the pitted unit and are overlain by the subpolygonally fractured unit.

5. Discussion

We interpret the lineaments in Eberswalde crater to be dip-slip faults because we observe vertical offsets and no lateral offsets. The dominant NNE directionality of

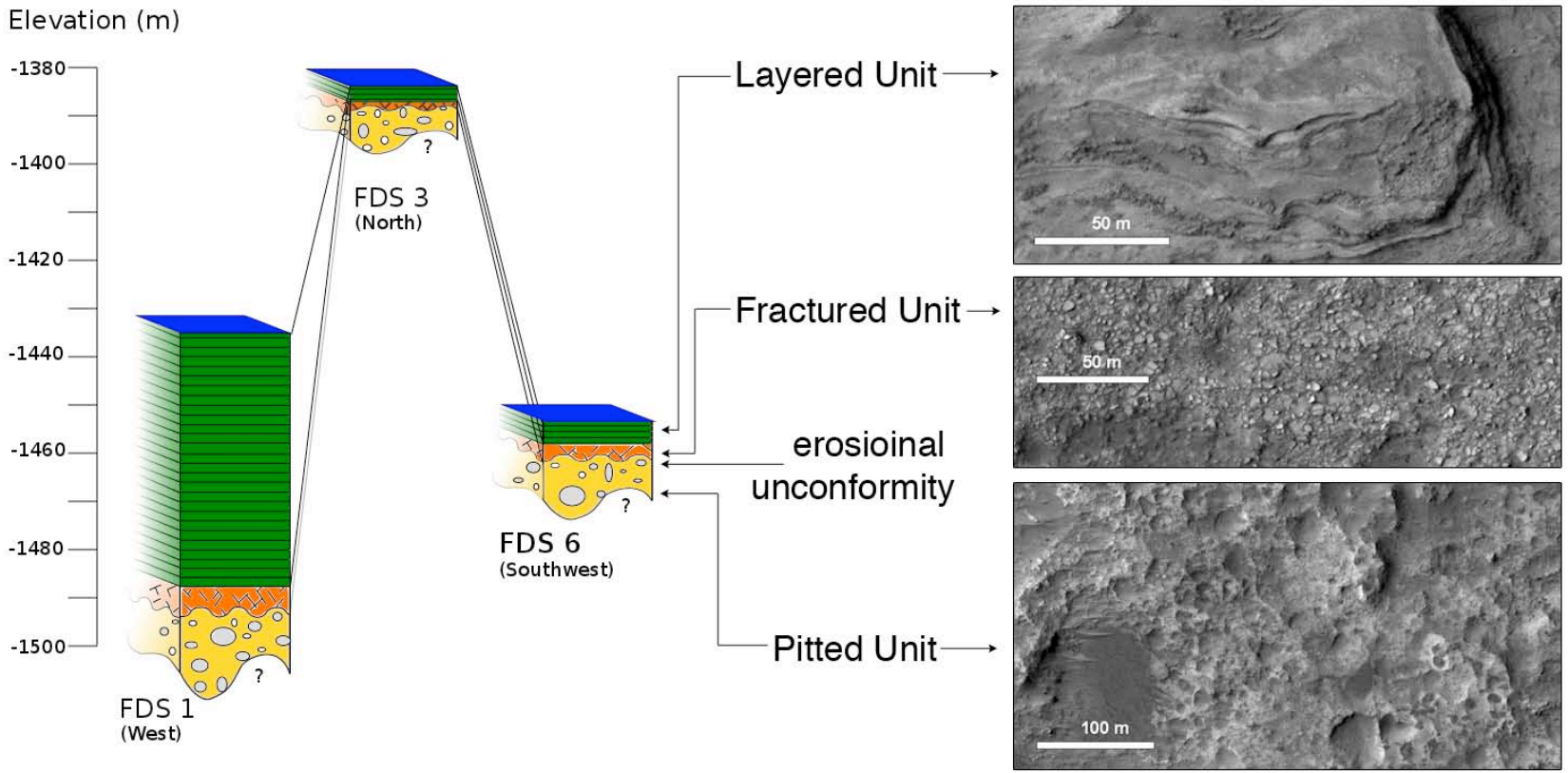

Figure 4. Simplified stratigraphic columns of proposed fluvio-deltaic systems FDS1 (in the Western Basin), FDS3 (on the central high) and FDS6 (southwestern in the Western Basin), indicating the elevations and inferred thicknesses of the lower pitted unit, the subpolygonally fractured unit, and the layered unit. These three units define the stratigraphy of all six fluvio-deltaic systems observed in Eberswalde Crater, and the colors correspond to those mapped in Figure 3. Dips measured at FDS1 are 1-3^{o} towards the center of the crater [*Lewis and Aharonson*, 2006]. HiRISE examples of each unit (ESP_019757_1560) are shown.

the faults is inconsistent with the stresses expected from the impact event that formed Eberswalde crater (which should be radial and parallel to the crater walls) (Melosh, 1989). Rather, the faults follow this NNE trend across the width of the crater floor and across its northern rim, onto the highland plains north of the crater, as well as south onto the divide between Holden and Eberswalde craters. We therefore infer that larger, regional post-impact stresses must be responsible for the observed faulting. For example, the NNE orientation is consistent with thrust faulting and wrinkle-ridge formation predicted in this region due to the loading-induced stresses from the formation of Tharsis (Anderson et al., 2001; Andrews-Hanna et al., 2008). Current age estimates for Tharsis place the bulk of its formation during the late Noachian (Fassett and Head, 2011), which predates age estimates of fluvio-lacustrine activity in Eberswalde crater (ranging from late Noachian/early Hesperian (Moore et al., 2003) to Amazonian (Grant and Wilson, 2011)). Alternatively, a regionally extensive extensional regime has been invoked to explain a similar NNE trend of extensional fractures associated with formation of Morava Valles and Iani Chaos (Warner et al., 2011). These chaos features occur north of Eberswalde crater and are part of the same ULM fluvial system.

The faults in Eberswalde bound a central high in the crater which may be a complex, up-faulted structure. The pitted unit, which covers most of the crater floor in both basins as well as the central high, is the lowest stratigraphic unit and the material in which most scarps occur. While Pondrelli et al. (2008) interpreted this unit as lacustrine sediments, we have observed no layering or other characteristics that support that hypothesis. Also, the pitted morphology is inconsistent with the observed

erosional morphology of other putative lacustrine sediments on Mars (e.g., Milliken and Bish, 2010; Wray et al., 2011). We therefore propose three possible interpretations for the pitted unit: (1) the pits result from heterogeneous erosion of an ancient surface saturated with small impact craters; (2) the pits formed from de-volatilization and degradation of an ancient, basal impact melt surface; or (3) the light-toned material may be the erosionally resistant matrix of a megabreccia (possibly from the Holden impact event (Grant et al., 2008)), and the pits are the "holes" left by removed/eroded megaclasts. In support of (3), 20–500 m of ejecta from the Holden impact is expected to have blanketed the floor of Eberswalde crater based on empirical expressions for the radial decay of ejecta thickness by Garvin and Frawley (1998). Consistent with all interpretations, the pitted unit is likely the exposed remnants of ancient impact crater floor material and unrelated to the younger, fluvio-deltaic systems.

We interpret the layered unit, which comprises the lobate units associated with each fluvio-deltaic system, to be deltaic sediments; and we interpret the extensive subpolygonally fractured unit, which lies conformably beneath each exposure of the layered unit, to be delta bottomset deposits and/or lacustrine sediments. Because the faults occur in the pitted unit but do not modify the overlying subpolygonally fractured or layered units, the fluvio-deltaic activity must have post-dated the faulting in Eberswalde crater and thus is unlikely the result of processes associated or contemporaneous with the Eberswalde impact itself. Indeed, the deposition of fluvio-deltaic sediments within Eberswalde appears to have been controlled by the fault-related topography. For example, the subpolygonally fractured unit associated with FDS3 overlies a faulted margin (Figure 3e), and the sinuous channels associated with

FDS6 appear to follow the NNE-trending fault system (Figure 3h). These relationships imply that the topographic character of Eberswalde crater (the two basins and a central high) was in place prior to fluvio-deltaic activity. Following this line of reasoning, a significant amount of material that once filled the crater must have been removed, as implied by the inverted channels and deltas.

The features we have mapped as fluvio-deltaic systems could be alluvial fans (e.g., Jerolmack et al., 2004); however, we note that the fan-shaped plateaus and layered deposits of FDS2–6 do not initiate at the break in slope associated with the wall of the crater, as might be expected for alluvial fan formation (e.g., Williams et al., 2006). Instead, channel bifurcation to create a fan-shaped sediment body occurs basinward of the crater rim implying that fluvially transported sediments were deposited along a shoreline and into a standing body of water. The multiple, bifurcating inverted channels preserved on FDS1, FDS3, and FDS6 are consistent with this interpretation.

The topographic high within the center of the crater therefore predates sedimentation and likely lake development. The question, then, is whether the water level in the western basin was sufficient to inundate the pre-existing central high. The putative deltas FDS3–4 occur on top of the central topographic high, where there is also evidence for inverted channels and isolated mesas of material that are morphologically similar to the subpolygonally fractured and/or layered units of other fluvio-deltaic systems. Based on these observations, we suggest that the lake in Eberswalde crater must have covered the central high to a minimum depth of -1385 m. Also, the margins of the central high are not eroded into drainage networks (unlike the

crater walls), suggesting that they may have been covered by water during the era of fluvial activity into Eberswalde crater. Although there are no crater rim fluvio-deltaic systems entering the Eastern Basin, a remnant of a sinuous channel network present along the topographic ridge separating the central high from the Eastern Basin provides evidence of possible overspill between the western lake system and the Eastern Basin. This overspill provides a possible means of stabilizing the water level, as the surface area rises considerably once the western sub-basin is flooded to this level.

The presence of multiple fluvio-deltaic systems in Eberswalde crater, all exhibiting a consistent stratigraphic sequence, has implications for its potential as a Mars landing site. A rover might have opportunities to examine the chemistry, mineralogy, and organic material preservation potential of remnant deltas and associated lacustrine deposits that preserve fine-grained sediments transported from multiple distinct source regions, potentially containing geochemical signatures of past habitability. For example, the layered unit associated with FDS3 lies within the proposed MSL landing ellipse, as does the subpolygonally fractured unit associated with FDS6; these systems are thus more readily accessible than FDS1 (the primary "go-to" target for MSL in Eberswalde), the closest deposits of which are ~2 km from the edge of the proposed landing ellipse (Figure 2). The largest faults in the crater lie within the proposed MSL landing ellipse as well, and thus they would make easily accessible science targets for hypothesis testing about the relationship between sedimentation and faulting in Eberswalde crater. Also, our results suggest that an Eberswalde lake extended over the area of the proposed MSL landing ellipse on the

central topographic high. Given the pre-existing topography, we predict that a rover could sample the deepest, lowest-energy sediments (that might best preserve organic materials) in the lowest, easternmost portion of the Western Basin.

6. Conclusions

We have mapped 233 NNE-trending linear scarps in Eberswalde crater that we interpret as dip-slip faults formed under regional stresses. We have also mapped the stratigraphic units associated with six fluvio-deltaic systems in the crater, and based on the relationships of these units to the faults, we infer the following sequence of events: (1) Eberswalde crater forms; (2) the pitted unit is deposited (potentially as modified Eberswalde basement rock or ejecta from the Holden crater impact), covering most of the crater floor; (3) extensive faulting, possibly from regional stresses related to the formation of Tharsis, creates the Western Basin, Eastern Basin, and central high within the crater; (4) at least six fluvio-deltaic systems form, with the geomorphic pattern of delta development controlled by the fault-induced topography; (5) crater fill material is excavated, leaving the inverted channels and deltas observed in present-day Eberswalde.

REFERENCES

Anderson, R.C., Dohm, J.M., Golombek, M.P., Haldemann, A.F.C., Franklin, B.J., Tanaka, K.L., Lias, L., Pee, B., 2001. Primary centers and secondary concentrations of tectonic activity through time in the western hemisphere of Mars. J. Geophys. Res. 106, E9. doi:10.1029/2000JE001278.

Andrews-Hanna, J.C., Zuber, M.T., Hauck, S.A., 2008. Strike-slip faults on Mars: Observations and implications for global tectonics and geodynamics. J. Geophys. Res. 113, E8. doi:10.1029/2007JE002980.

Bhattacharya, J.P., Payenberg, T.H.D., Lang, S.C., Bourke, M., 2005. Dynamic river channels suggest a long-lived Noachian crater lake on Mars. Geophys. Res. Lett. 32, L10201. doi:10.1029/2005GL022747.

Fassett, C.I., Head, J.W., 2011. Sequence and timing of conditions on early Mars, Icarus 211, 1204, doi:10.1016/j.icarus.2010.11.014.

Garvin, J.B., Frawley, J.F., 1998. Geometric properties of Martian impact craters: Preliminary results from the Mars Orbiter Laser Altimeter, Geophys. Res. Lett. 25, 24, 4405-440.

Grant, J.A., Parker, T.J., 2002. Drainage evolution in the Margaritifer Sinus region, Mars, J. Geophys. Res. 107, E9, 5066.

Grant, J.A., Wilson, S.A., 2011. Late alluvial fan formation in southern Margaritifer Terra, Mars. Geophys. Res. Lett. 38, L08201. doi:10.1029/2011GL046844.

Grant, J.A., Irwin, R.P., Grotzinger, J.P., Milliken, R.E., Tornabene, L.L., McEwen, A.S., Weitz, C.M., Squyres, S.W., Glotch, T.D., Thompson, B.J., 2008. HiRISE imaging of impact megabreccia and sub-meter aqueous strata in Holden crater, Mars. Geology 36, 3, 195-198. doi:10.1130/G24340A.1.

Grant, J.A., Golombek, M.P., Grotzinger, J., Wilson, S.A., Watkins, M.M., Vasavada, A.R., Griffes, J.L., Parker, T.J., 2010. The science process for selecting the landing site for the 2011 Mars Science Laboratory. Planet. Space Sci., 1-54. doi:10.1016/j.pss.2010.06.016.

Gupta, S., Cowie, P.A., Dawers, N.H., Underhill, J.R., 1998. A mechanism to explain rift basin subsidence and stratigraphic patterns through fault array evolution. Geology 26, 595–598.

Gupta, S., Underhill, J.R., Sharp, I.R., Gawthorpe, R.L., 1999. Role of fault interactions in controlling synrift sediment dispersal patterns: Miocene, Abu Alaqa Group, Suez Rift, Sinai, Egypt. Basin Research 11,167–189.

Jerolmack, D.J., Mohrig, D., Zuber, M.T., Byrne, S., 2004. A minimum time for the

formation of Holden Northeast fan, Mars. Geophys. Res. Lett. 31, L21701. doi:10.1029/2004GL021326.

Kirk, R., and 18 colleagues, 2008. Ultrahigh resolution topographic mapping of Mars with MRO HiRISE stereo images: Meter-scale slopes of candidate Phoenix landing sites. J. Geophys. Res. 113, E00A24, doi:10.1029/2007JE003000.

Lewis, K.W., Aharonson, O., 2006. Stratigraphic analysis of the distributary fan in Eberswalde crater using stereo imagery. J. Geophys. Res. 111, E06001. doi:10.1029/2005JE002558.

Malin, M.C., and 13 colleagues, 2007. Context Camera Investigation on board the Mars Reconnaissance Orbiter. J. Geophys. Res. 112, E05S04.

Malin, M.C., Edgett, K.S., 2003. Evidence for persistent flow and aqueous sedimentation on early Mars. Science 302, 1931–1934.

McEwen, A.S., and 14 colleagues, 2007. Mars Reconnaissance Orbiter's High Resolution Imaging Science Experiment (HiRISE). J. Geophys. Res. 112, E05S02. doi:10.1029/2005JE002605.

McEwen, A.S., and 69 colleagues, 2010. The High Resolution Imaging Science Experiment (HiRISE) during MRO's Primary Science Phase (PSP). Icarus 205, 2– 37. doi:10.1016/j.icarus.2009.04.023.

Melosh, H.J., 1989. Impact Cratering: A Geologic Process. Oxford UP, New York, N.Y.

Milliken, R., Bish, D., 2010. Sources and sinks of clay minerals on Mars, Philos. Mag. 90, 2293–2308. doi:10.1080/14786430903575132.

Moore, J.M., Howard, A.D., Dietrich, W.E., Schenk, P.M., 2003. Martian layered fluvial deposits: Implications for Noachian climate scenarios. Geophys. Res. Lett. 30, 24, 2292. doi:10.1029/ 2003GL019002.

Pondrelli, M., Pio Rossi, A., Marinangeli, L., Hauber, E., Gwinner, K., Baliva, A., di Lorenzo, S., 2008. Evolution and depositional environments of the Eberswalde fan delta, Mars. Icarus 197429. doi:10.1016/j.icarus.2008.05.018.

Rice, M.S., Bell, J.F., III, 2010. Geologic Mapping of the Proposed Mars Science Laboratory (MSL) Landing Ellipse in Eberswalde crater. Lunar Planet. Sci., XXXXI, Abstract 2524.

Smith, D.E., and 23 colleagues, 2001. Mars Orbiter Laser Altimeter: Experiment summary after the first year of global mapping of Mars. J. Geophys. Res. 106, 23689-23722. doi:10.1029/2000JE001364.

Warner, N. H., Gupta, S., Kim, J.-R., Muller, J.-P., Le Corre, L., Morley, J., Lin, S.-Y., McGonigle, C., 2011. Constraints on the origin and evolution of Iani Chaos, Mars. J. Geophys. Res. 116, E6. doi:10.1029/2010JE003787.

Williams, R.M.E., Zimbelman, J.R., Johnston, A.K., 2006. Aspects of alluvial fan shape indicative of formation process: A case study in southwestern California with application to Mojave Crater fans on Mars. Geophys. Res. Lett. 33, L10201, doi:10.1029/2005GL025618, 2006.

Wood, L., 2006. Quantitative geomorphology of the Mars Eberswalde delta. GSA Bulletin 118, 5–6, 557.

Wray, J.J., and 13 colleagues, 2011. Columbus crater and other possible groundwater-fed paleolakes of Terra Sirenum, Mars. J. Geophys. Res. 116, E01001. doi:10.1029/2010JE003694.

Zuber, M.T., Smith, D.E., Solomon, S.C., Muhleman, D.O., Head, J.W., Garvin, J.B., Abshire, J.B., Bufton, J.L., 1992. The Mars Observer laser altimeter investigation. J. Geophys. Res. 97, 7781-7797. doi:10.1029/92JE00341.

CHAPTER 6

A DETAILED GEOLOGIC CHARACTERIZATION OF EBERSWALDE CRATER, MARS[1]

0. Abstract

Eberswalde crater, selected as one of four finalist landing sites for the Mars Science Laboratory mission, is best known for the spectacularly preserved, inverted, fan-shaped deposit along its western margin. This feature has been interpreted as a lacustrine delta, although the timing and duration of an Eberswalde crater lake is poorly understood. The aim of this study is to place more broadly observed fluvio-lacustrine activity throughout the crater's floor within the larger context of Eberswalde's geologic history, and to infer the sequence of deposition and erosion of the observed stratigraphic and geomorphic units.

We have identified and mapped stratigraphic and geomorphic units within all of Eberswalde crater using orbital imagery from the HiRISE, MOC and CTX cameras, and we have calculated crater statistics to infer the relative ages of crater floor materials. Using topographic datasets derived from HiRISE, CTX and MOLA, we determine the unit associations, successions, and geometries and develop a model for the depositional and erosional history within the crater.

We have produced maps of ten stratigraphic and seven geomorphic units identified within Eberswalde crater. Our observations of the stratigraphy, geomorphology, topography and crater densities imply a complex relationship

[1] Submitted for publication in *Mars* as: M.S. Rice, J.F. Bell III, S. Gupta, N.H. Warner, K. Goddard, R.B. Anderson, A Detailed Geologic Characterization of Eberswalde Crater, Mars.

between deposition and exhumation within Eberswalde crater, and we infer the following sequence of major events: (1) Eberswalde crater forms in the Noachian (> 3.6 Ga); (2) Holden crater forms southwest of Eberswalde crater in the late Noachian to Early Hesperian, and its associated ejecta blanket covers the floor of Eberswalde crater and heavily modifies the southern rim; (3) Extensive faulting from regional stresses creates the first-order topography within the crater, and vein-like features form in some units from fracturing, fluid circulation, and cementation; (4) Valley features are carved in the crater walls as water flows into the crater, creating an Eberswalde lake in which delta formation occurs. The distribution of features interpreted as inverted channels and lacustrine deposits implies that the lake extended into the easternmost portion of the crater and at least six fluvio-deltaic systems formed; (5) Extensive exhumation and degredation of the crater floor materials occurs, perhaps simultaneously with the deposition of an airfall mantling unit; (6) Very little besides aeolian sediment transport activity occurs in the Amazonian.

1. Introduction

Ancient layered outcrops on Mars that could represent lacustrine sediments have been high priority targets of observation in recent decades (e.g., Malin and Edgett 2000; McEwen et al., 2007a; Malin et al., 2007; Murchie et al., 2007). Studies of these outcrops can both help to constrain the activity of liquid water on Mars during the planet's early history (the Noachian Period, before about 3.6 Ga) and to identify regions of potential astrobiologic interest for future landed missions. However, the distribution of water on Mars in space and time remains largely unresolved, in part

because of the scarcity of identified landforms that are clearly diagnostic of specific other aqueous processes (Malin and Edgett, 2000). Perhaps the most spectacularly preserved example of such a rare landform on Mars is the inverted fan-shaped deposit in Eberswalde crater that has been interpreted as the remnant of an ancient delta (e.g., Malin and Edgett, 2003). As described in the discovery paper by Malin and Edgett (2003), the location, form and structure of this landform "uniquely reflect materials deposited within an aqueous sedimentary environment."

1.1 Geologic Setting

Eberswalde crater is centered at 24^{o} S 33^{o} W within the Erythraeum region of Mars (Figure 1a). It is located immediately north-northeast of Holden crater along the Uzboi-Ladon-Morava system (Figure 1b), a proposed fluvial network of valleys and impact craters connecting Argyre Basin to Ares Vallis (e.g., Grant and Parker, 2002). Holden crater's continuous ejecta blanket extends across the degraded southern rim of Eberswalde crater indicating its younger relative age. Although earlier reports suggested a Noachian age for the Holden impact event (Moore et al., 2003), new constraints from crater statistics suggest formation during the Early to Late Hesperian period (Irwin and Grant, 2011). Both Holden crater and Eberswalde crater rest within the Holden basin, which is one of several large, Mid-Noachian-age, multi-ringed impact basins that pre-dates valley network formation in the Uzboi-Ladon-Morava system. Fluvial incision of the interior rim of Holden basin by branching valley networks and infilling of the basin by layered sediment has been constrained to the Late Noachian period, possibly extending into the Hesperian (Grant and Parker, 2002;

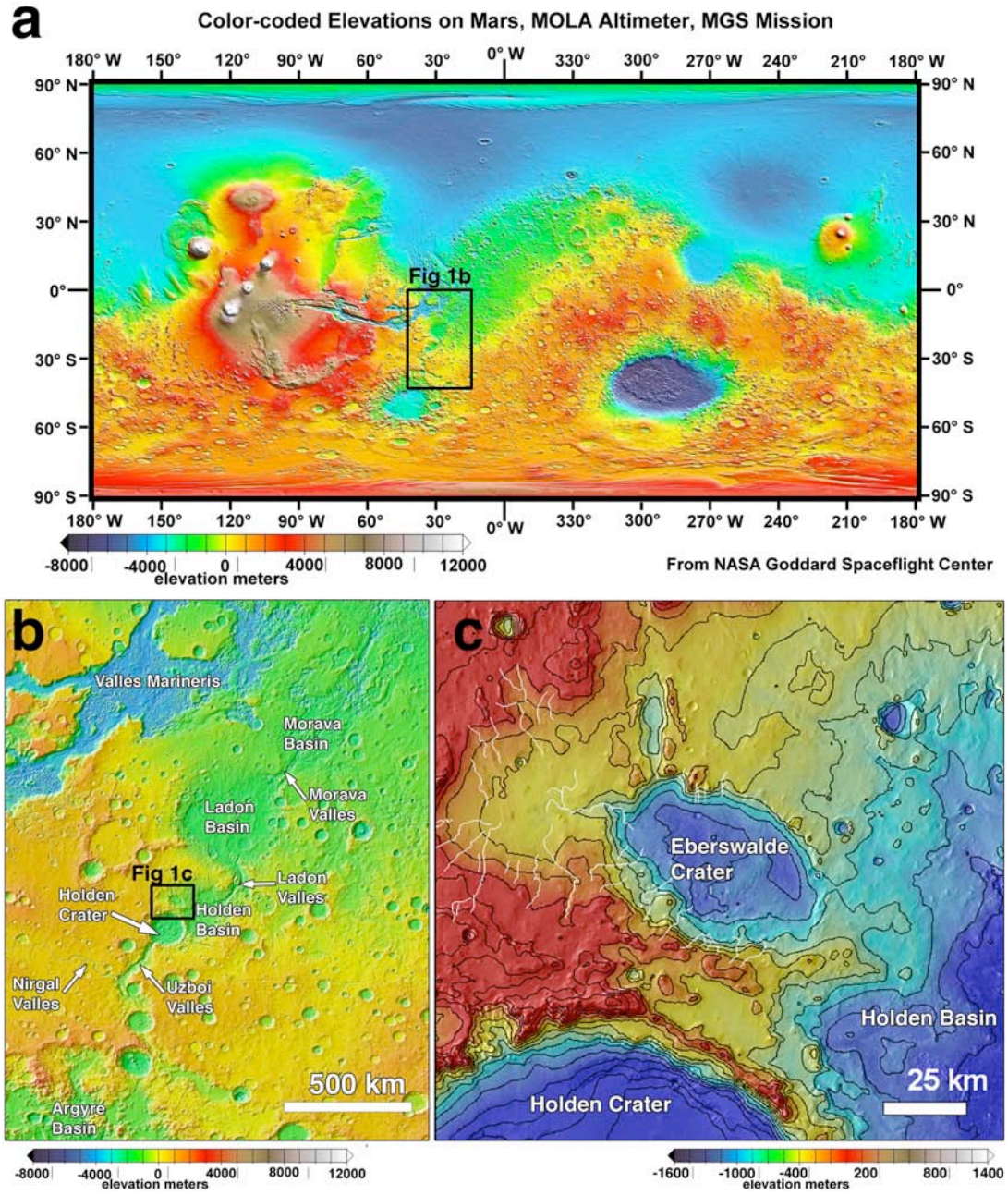

Figure 1. (a) Global topographic map of Mars based on MOLA data (Smith et al., 2001); (b) MOLA map of the Uzboi-Ladon-Morava system, with the location of Eberswalde crater indicated by the black box; (c) MOLA map of Eberswalde crater and immediate surroundings with 200 m contour lines drawn in black. Locations of major drainage channels are indicated by white lines. Note that the color scale of (c) is different from that of (a) and (b).

Irwin and Grant, 2011). These relative associations place the formation of Eberswalde crater to some time in the Late Noachian to Early Hesperian.

1.2 Fluvio-lacustrine activity

Valley networks traverse the intracrater plains north of Holden crater and appear to have transported sediment into the western portion of Eberswalde crater, building the layered, fan-shaped landform that has been interpreted as a lacustrine delta (Malin and Edgett 2003; Moore et al., 2003; Bhattacharya et al., 2005; Wood 2006; Lewis and Aharonson 2006; Pondrelli et al., 2008; Pondrelli et al., 2011) or as an alluvial fan (Jerolmack et al., 2004). These valley networks post-date Holden ejecta, indicating that fluvial activity into Eberswalde and delta development occurred at some point after the Early-Late Hesperian (Irwin and Grant 2011).

The Eberswalde fan, which extends 13 km by 11 km and covers 115 km^2 of the western basin floor, consists of at least three lobes of layered rock and cross-cutting, sinuous ridges (Malin and Edgett 2003). While Jerolmack et al. (2004) examined a scenario in which the fan was built subaerially (i.e., as an alluvial fan), Bhattacharya et al. (2005) note that alluvial fans should be dominated by sheet floods and debris flows, not the highly sinuous channelized flows observed at Eberswalde. Bhattacharya et al. (2005) also argued that the transition from laterally continuous and smooth basal layers to bifurcating channel networks in the upper layered strata suggests a complex evolution consistent with a deltaic origin.

Estimates of the time required to form the fan vary widely, ranging from ~100 years (in the alluvial fan scenario; Jerolmack et al., 2004) to ~10^5 years (in a deltaic

environment; Bhattacharya et al., 2005). While Wood (2006) argued that the sinuosity indexes, meander-bend migration, and ridge-and-swale point-bar topography infer stable deposition in a long-lived lake, Lewis and Aharonson (2006) concluded, based on a quantitative analysis of the stratigraphy, that the delta more likely formed during a small number of shorter lacustrine episodes.

The source of the water that transported fan building sediment into Eberswalde crater is also debated. Several branching fluvial systems enter Eberswalde crater from the terrain that borders the crater's western, northern, and southern rims, contributing sediment to several fans within the crater (Rice et al., 2011). No channels have been identified that enter from the east, although the terrain east of Eberswalde occurs within the Holden basin and has been disrupted by a chaos formation event (Irwin and Grant 2011). To the immediate south and southwest of Eberswalde crater, the channels clearly superimpose the continuous ejecta blanket of Holden crater indicating that fluvial incision post-dates the Holden impact. To the northwest and north, superposition relationships with Holden ejecta are less clear, although models of ejecta thickness indicate meters to tens of meters of ejecta at these locations (Garvin and Frawley 1998). From these relative associations and from the morphology of the channel systems, it has been suggested that runoff may have been related either to localized processes that are tied directly to the formation of Holden crater, or to longer term precipitation that was controlled by regional or global climate conditions (Moore et al., 2003).

There are three main mechanisms by which Holden impact induced runoff may have occurred: (1) release of ground water through localized, sustained impact-

induced hydrothermal activity (Ivanov and Piarazzo 2011); (2) through disruption of an existing liquid water aquifer leading to instantaneous fluvial activity (Wang et al., 2005; Harrison et al., 2010; Moore et al., 2003); or (3) melting of ground ice or surface snow by hot ejecta (Mangold 2011). Of the three hypotheses, the ejecta melting hypothesis fits best with the morphologic observation that most of the Eberswalde channels are derived only from within the mapped extent of Holden ejecta. However, Irwin (2011) suggests that impact induced runoff by ground ice melting would have led to overfilling of the crater, above the level of the preserved delta, as evaporation could not keep up with the initial pulse of runoff.

Irwin (2011) postulates that ephemeral and intermittent runoff production via precipitation over longer timescales is a more likely scenario in the broader context of the occurrence of valley networks, alluvial fans, and the putative deltas throughout this region. Irwin (2011) hypothesizes that the Eberswalde delta would have required conditions resembling an arid terrestrial desert over timescales of >103 to 104 years, in order for evaporation to keep up with runoff. By this model, precipitation occurred during a longer term global to regional climate change event. Alternatively, a lake may have formed within Holden crater immediately following the impact. The formation of small lake effect storms across this lake may explain localized precipitation and runoff in the area around Holden and Eberswalde craters (Kite et al., 2011). The presence of an ancient lake within Holden crater has been postulated based on the stratigraphic observations of finely-layered sediments that superimpose impact breccia floor materials of Holden crater (Grant et al., 2008).

Other fans and fan-form features have been recently identified in high-resolution imaging elsewhere on Mars; some have also been interpreted as potential deltas or deltaic landforms. For example, Weitz et al. (2006) interpreted a terraced fan deposit within one of the troughs of Coprates Catena as a delta deposited into a shallow, potentially Hesperian lake that formed in the trough. Di Achille et al. (2007) have interpreted a number of fan-shaped deposits at nearly constant topographic elevation within Shalbatana Vallis as late Hesperian deltas, deltaic deposits, and shorelines. However, Kraal et al. (2008) have questioned the evidence for persistent, long-duration flow associated with many of these features, instead favoring a model involving single, short-duration outflow events depositing sediments over previous (non-deltaic) fan-shaped deposits. These recent studies have helped to justify new observations of the Eberswalde fan deposit using higher resolution data sets.

A reinterpretation of the discharge into Eberswalde crater was made possible by new high-resolution (~25 cm/pix) images from the Mars Reconnaissance Orbiter (MRO) High Resolution Imaging Science Experiment (HiRISE) instrument (McEwen et al., 2007a). Boulders on the surface of the fan were interpreted by Schieber (2007) and Howard et al. (2007) as having been transported by the flow that deposited the fan. Kraal and Postma (2008) also interpreted the fan as having formed in a debris flow based on their analysis of the bend forms. However, Pondrelli et al. (2008) supported the deltaic interpretation based on the complex stratal organization visible in HiRISE images. Furthermore, Rice et al. (2011) identified a total of six fan-shaped plateaus in the crater which they interpreted as fluvio-deltaic systems because, as seen in the high-resolution images, channel bifurcation occurs basinward of the crater rim

implying that fluvially-transported sediments were deposited along a shoreline and into a standing body of water.

Because of the long-lived lake interpretation, Eberswalde crater was selected as a high-priority candidate landing site for the Mars Science Laboratory (MSL) mission, scheduled to launch in November 2011 and land in the summer of 2012 (Grant et al., 2011). The primary objective of the MSL mission is to search for past and present habitable environments on Mars (Grotzinger 2009). The selection of a candidate landing sites was based in part on their potential for having preserved biomarkers (Grant et al., 2011); sediment deposition in a low-energy environment, such as a quiescent lake, typically has very high preservation potential (Summons et al., 2011). The identification of phyllosilicate minerals at the fan terminus and in the crater basin, which may have formed *in-situ* or have been eroded from the source basin to the west (Milliken and Bish 2010), enhanced Eberswalde's appeal as a landing site. However, Gale Crater was selected as the final landing site over Eberswalde Crater in July 2011.

1.3 Objectives of this work

In this work, our aim is not to settle the long-standing debates about the duration of a lake in Eberswalde crater or the source of the water. Rather, we address a different question that has not been examined in the current literature: what are the depositional histories of all units within the crater? We do this by examining a variety of imaging and topographic datasets. Pondrelli et al. (2008) mapped units within the Eberswalde crater basin, but not at sufficient resolution to develop specific hypotheses

for all materials; Pondrelli et al. (2011) provided an analysis of the putative delta, but did not extend their analysis to the rest of Eberswalde crater. Schieber (2008) identified potential high-priority science targets in the center of the crater based on HiRISE imagery, and Rice et al. (2011) identified candidate fluvio-deltaic systems and mapped the distribution of putative faults, but neither study comprehensively mapped the full extents of crater floor units.

Here we present stratigraphic and morphologic unit maps of features within Eberswalde crater that directly bear on the fluvial and aqueous history of the basin, including the putative deltaic deposits. In the next section, we describe the orbital datasets used in the study and our mapping methodology. We then provide descriptions, depositional hypotheses, and interpretations of each inferred stratigraphic and morphologic unit; descriptions of the associations, successions and geometries of these units; and finally crater statistics and inferred relative ages of crater floor materials. In the discussion we present our inferred depositional and erosional history model within Eberswalde crater, with our conclusions summarized in the final section. While one goal of this work is to aid in the characterization of what is still an exciting potential future Mars landing site, the detailed mapping and interpretation of sedimentary units within Eberswalde crater are critical to understanding the geologic history of Mars in general.

2. Data and methods

2.2 Visible to near-infrared datasets: MOC, CTX and HiRISE

Our detailed investigation of Eberswalde crater was made possible through the

extensive imaging coverage of the crater by instruments on the Mars Global Surveyor (MGS) and MRO spacecraft. For the primary base map for this study, we used radiometrically-calibrated data from the MRO Context Camera (CTX) (Malin et al., 2007; Bell et al., 2011) to generate a 6 m/pixel mosaic of Eberswalde crater. CTX images cover the entire crater and surrounding drainage basin (a list of images is provided in the Appendix). We calibrated and projected these CTX observations using the USGS Integrated Software for Imagers and Spectometers (ISIS) software package (e.g., Eliason et al., 2001).

We also use CTX images to estimate the albedo of surface units (Eliason et al., 2001). Dividing the radiometrically-corrected CTX images by the cosine of the solar incidence angle at the time of each observation gives an estimate of the Lambert (isotropically scattering surface) albedo over the CTX bandpass (611±189 nm; Bell et al., 2011), which is essentially the ratio of the reflectance of a surface to that of a perfectly diffuse surface under the same viewing conditions. These Lambert-corrected images enable direct comparison between images taken in different viewing geometries; however, uncertainties still exist due to seasonal lighting variations, interannual differences in aeolian surface dust covering, and variable atmospheric dust opacity. Combining these uncertainties with the estimated accuracy of the CTX radiometric calibration (Bell et al., 2011), we estimate that the uncertainties on the CTX-derived Lambert albedo values reported here are around ±20%.

Because Eberswalde crater was selected as one of the four finalist MSL landing sites (Grant et al., 2010), it has been targeted repeatedly by the MRO HiRISE instrument (McEwen et al., 2007a). The ~0.27 m/pixel HiRISE data cover the majority

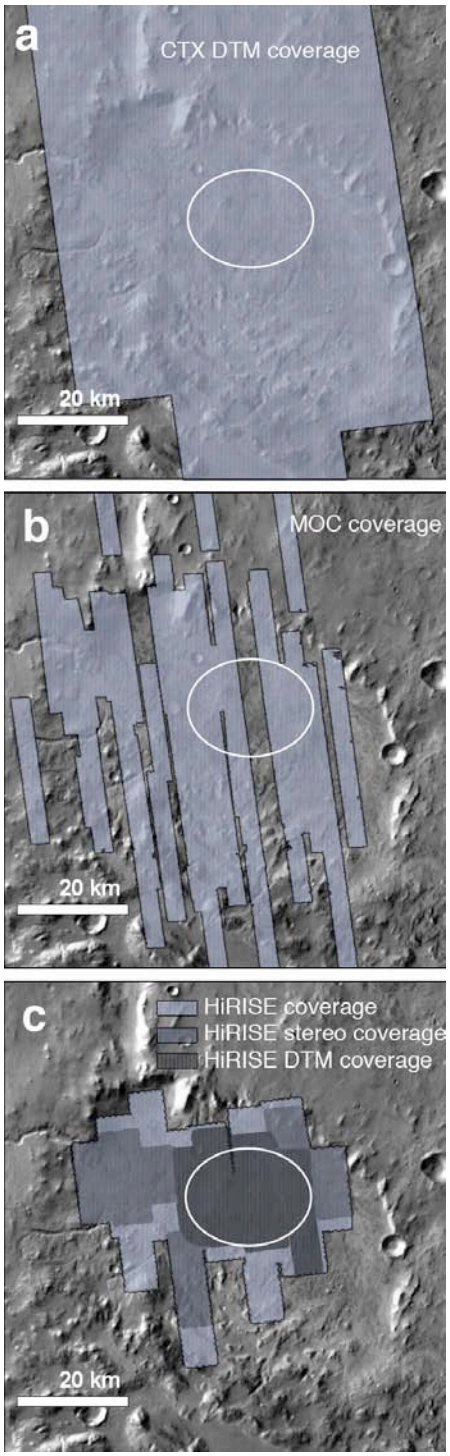

Figure 2. Footprint maps showing the imaging coverage of Eberswalde crater used in this study: (a) CTX DTMs; (b) MOC NA images; (c) HiRISE images, stereo anaglyphs, and DTMs. The location of the proposed landing ellipse is outlined in white. All footprints are shown over a THEMIS daytime IR basemap (Christensen et al., 2006).

of the north and center of the crater floor, including the entire area identified as the potential MSL landing ellipse (Figure 2c; a full list of images is given in the Appendix). HiRISE has three color filters: blue-green (BG; λeff=502±157 nm), red (RED; λeff=686±267 nm), and near-infrared (IR; λeff=878±143 nm) (McEwen et al., 2007a; Delamere et al., 2010); these filters enable the creation of false color images over a limited portion of the field of view (BG and IR data can only be acquired for a central strip covering 20% of each HiRISE RED image). We acquired map-projected HiRISE RED and false color observations from the Planetary Data System (PDS) (http://pds-imaging.jpl.nasa.gov/search/search.html), which we use as the primary dataset for our mapping.

In locations without HiRISE coverage, we have used MGS Mars Orbiter Camera (MOC) images (Malin and Edgett 2001; Malin et al., 2010) to study small-scale features at ~1.5 m/pixel resolution. MOC coverage of Eberswalde crater is shown in Figure 2b, and product IDs are listed in the Appendix. We radiometrically-calibrated and projected all MOC observations with ISIS using similar methods as for CTX.

2.2 Topography: MOLA, CTX DTMs and HiRISE DTMs

We used a topographic map based on MGS Mars Orbiter Laser Altimeter (MOLA) data (Zuber et al., 1992; Smith et al., 2001) to provide regional-scale topographic context for Eberswalde crater at ~1 m vertical resolution and a spatial grid resolution of 1/64o in latitude × 1/32o in longitude (~ 0.86 × 0.43 km2 at Eberswalde crater) (Figure 1). We augmented this topography with three digital terrain

models (DTMs) within the crater derived from the CTX stereo pair images listed in the Appendix (Edwards and Broxton, 2006; Broxton and Edwards, 2008). For topographic investigations of specific, smaller-scale features, we used DTMs derived from HiRISE stereo pairs (Kirk et al., 2008). HiRISE DTMs for candidate MSL landing sites have been made publically available as soon as possible following their production (McEwen et al., 2010), including four DTMs within Eberswalde crater as of October 2010 (from stereo pair images listed in the Appendix). The spatial coverages of the CTX and HiRISE DTMs used in this study are shown in Figure 2.

2.3 Identification and mapping of units

In this study we have identified and mapped the distribution of stratigraphic units based on CTX, HiRISE and MOC images. We define a stratigraphic unit as a sheetlike, wedgelike, or tabular body of rock that underlies the surface (or unconsolidated material on the surface) and exhibits consistent features that can be identified in orbital images. Each stratigraphic unit has a limited surface exposure, the horizontal extent of which can be mapped, and the vertical extent of which usually has to be inferred but in some cases can be constrained by topography. We identify stratigraphic units through the principles of photographic interpretation and planetary mapping originally defined for lunar geology (e.g., Shoemaker and Hackman, 1962; Wilhelms, 1974; 1990). These include the following geologic attributes: albedo, color, texture (the aggregate appearance of meter-scale features), pattern (the aggregate appearance of 10-100 m-scale features), relief (topography as determined by shading and DTM data), and retention of small (< 50 m) craters. Fortunately, because

the inferred surface dust cover (Ruff and Christensen 2002) is uniformly low throughout the Eberswalde crater region (Rogers et al., 2009), our mapping is only minimally hindered by the obscuring effects of surface dust that plague photogeologic studies of many other regions on Mars.

Our mapping of stratigraphic units and determination of relations between them is based on identification of specific contacts. All the terrain enclosed by a contact is interpreted to belong to one unit, and the geometric distributions of the contacts is inferred to reflect depositional patterns and age relationships of the units (e.g., Wilhelms, 1990). Also, we use the geometry of a contact itself to aid interpretation of the unit it bounds; for example, a cohesive rock unit will typically form sharp contacts along scarps and cliff faces, whereas unconsolidated material will often grade imperceptibly with subjacent units. We note that in the latter case, the transition between units can be ambiguous, and some simplifications and uncertainties are necessarily involved in mapping the distribution of units. Thus, dividing lines between our interpreted stratigraphic units is often a matter of judgment.

We take care to distinguish stratigraphic units from geomorphic units, which we define as landforms with consistent surface morphologies that can be identified in orbital images. We identify geomorphic units on the basis of their planimetric configurations (the two-dimensional shapes of features), albedo, color, and context (the relation of features to one another). Unlike stratigraphic units, geomorphic units do not necessarily occupy unique locations within the inferred stratigraphic column. In some cases, the composition of geomorphic units appears to be unique from that of stratigraphic units (e.g., the vein-like features); in other cases, geomorphic units

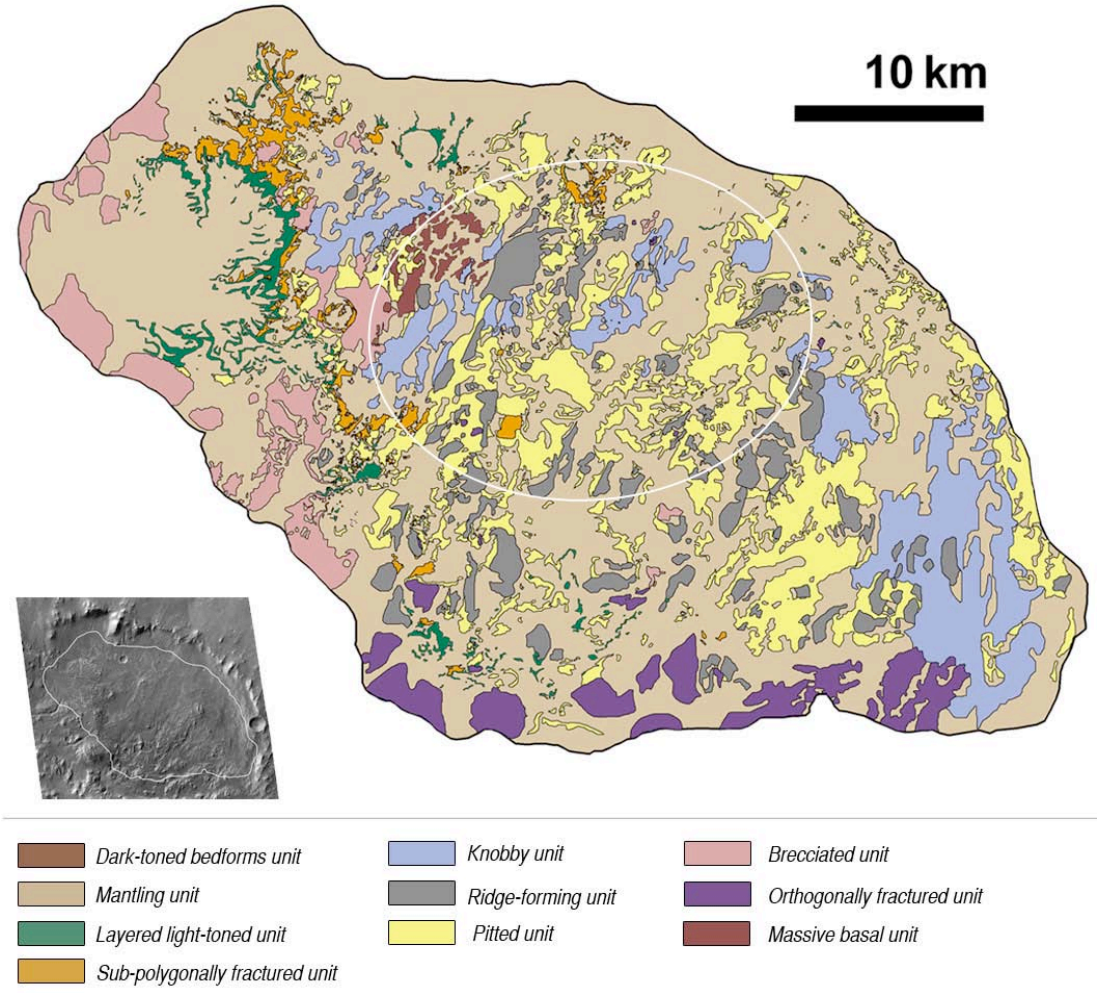

Figure 3. Map of inferred stratigraphic units inside Eberswalde crater. The boundary of the mapped region is defined by the -1200 m contour line. The white line indicates the location of the proposed MSL landing ellipse. See text for detailed descriptions of units.

Table 1. Summary of stratigraphic units

Stratigraphic Unit	Figures	Description	Contact Relationships	Interpretation*	Comparison to Previous Studies
Massive, basal unit	4	Massive; extensively fractured; distinct hues in HiRISE color	Obscured contact with the pitted unit; unable to discern the relationship	Fractured Eberswalde bedrock	[1,2]Lava flows and pyroclastic materials
Orthogonally-fractured unit	5	Massive; orthogonally-fractured	Obscured contact with the pitted unit; unable to discern the relationship	Megabreccia (allocthonous or parautocthonous)	[1,2]Lava flows and pyroclastic materials
Brecciated unit	6, 24, 25	Megaclasts encased in a light-toned, finer-grained matrix; in places cut by light-toned, vein-like lineations	Overlain by the layered, light-toned unit; Obscured contact with the discontinuous, light-toned unit	Megabreccia (allocthonous)	[1,2]Lava flows and pyroclastic materials; [3]Megabreccia
Pitted unit	7, 25, 26, 27	Light-toned; clusters of quasi-circular depressions	Cut by vein-like features; obscured contact with the brecciated, ridge-forming unit; overlain by the fractured and layered light-toned units	Erosional expression of the brecciated unit	[2]Lacustrine deposits
Ridge-forming unit	8	Massive; no systematic fractures; possible layering; boulder-shedding	Overlies the pitted unit	*Sedimentary rock? Outcrops of other units obscured by airfall deposits?*	[1,2]Lava flows and pyroclastic materials
Knobby unit	9	Isolated hillocks of light-toned rock, spaced >50 m apart	Contacts with other units obscured by the mantling unit	Eroded remnants of the sub polygonally fractured and/or layered light-toned units	none
Sub-polygonally fractured unit	10, 25, 26, 27	Sub-polygonally fractured; occurs as isolated mesas or extensive deposits; boulder-shedding	Overlies the discontinuous light-toned unit; underlies the fractured light-toned unit; onlaps the brecciated ridge-forming unit; overlies vein-like features	Lacustrine bottomset deposits	[2]Lacustrine deposits
Layered, light-toned unit	11-13, 23, 24	Layers < 10 m thick; sometimes sub-polygonally or orthogonally fractured; boulder-shedding; layers have variable resistances to erosion	Overlies the fractured and discontinuous light-toned units; onlaps the brecciated, ridge-forming unit (BR_3)	Deltaic and/or alluvial sediments	[2-10]Deltaic sediments; [11]Alluvial fan sediments
Mantling unit	14	Smooth; retains small craters; cliff-forming; grades into linear bedforms	Overlies and obscures all units but the dark-toned bedforms unit	Aeolian deposits	[2]Aeolian deposits
Dark-toned bedforms unit	15	Dark-toned; complex bedforms	Abuts the brecciated, ridge-forming unit	Modern aeolian deposits	none

Table 1 cont'd.

Stratigraphic Unit	Elevations (m)	Thickness (m)	Albedo	Mineralogy
Massive, basal unit	-1585 to -1495	> 30	0.13 to 0.15	[13]Olivine
Orthogonally fractured unit	-1405 to -1200	> 70	0.11 to 0.18	unknown
Brecciated unit	-1570 to -1200	> 60	0.11 to 0.17	[12,13]Fe/Mg phyllosilicates
Pitted unit	-1545 to -1200	> 130	0.11 to 0.16	unknown
Ridge-forming unit	-1540 to -1220	> 90	0.10 to 0.17	[12,13]Fe/Mg phyllosilicates
Knobby unit	-1580 to -1200	> 15	0.11 to 0.15	unknown
Sub-polygonally fractured unit	-1495 to -1300	< 9	0.12 to 0.15	[12,13]Fe/Mg phyllosilicates
Layered light-toned unit	-1465 to -1320	< 50	0.13 to 0.25	[12,13]Fe/Mg phyllosilicates; [13]Unidentified hydrated minerals; [13]High-calcium pyroxene
Mantling unit	-1585 to -1200	< 5	0.09 to 0.13	[13]High-calcium pyroxene; [13]Olivine
Dark-toned bedforms unit	-1500 to -1450	< 5	0.07 to 0.09	unknown

[*] See text for a description of alternate hypotheses

[1] Scott & Tanaka (1986); [2] Pondrelli *et al.* (2008); [3] Scheiber (2007) ; [4] Malin & Edget (2003); [5] Moore *et al.* (2003); [6] Bhattacharya *et al.* (2005); [7] Wood (2006); [8] Lewis & Aharaonson (2006); [9] Pondrelli *et al.* (2008); [10] Pondrelli *et al.* (2010); [11] Jerolmack *et al.* (2004); [12] Milliken & Bish (2010); [13] McKeown & Rice (2011)

appear to be comprised of multiple stratigraphic units (e.g., the fan-form plateaus).

3. Inferred stratigraphic units

We have identified ten stratigraphic units within Eberswalde crater, which we have mapped in Figure 3. Because the southern rim of the crater is severely degraded, we cannot objectively define where Eberswalde crater ends and the plains between Eberswalde and Holden craters begin; in this work, we have chosen to use the -1200 m contour line as the boundary of our mapping region. The detailed descriptions of our observations, hypotheses, and interpretations of each unit are given below, and a summary of all units is provided in Table 1.

3.1 Massive, basal unit

Observations. The massive, basal unit is distinct from other crater floor materials in that it is light-toned, extensively fractured (although with no apparent systematic pattern to the fractures) and has no visible layering. While most occurrences of this unit (mapped in Figure 3) are flat-lying and variably covered by the mantling unit, the most prominent examples are where the unit forms mounds with steep ridges (Figure 4). No outcrops appear be forming and/or shedding boulders; we observe no blocks that may have fallen from the high ridges. In false-color HiRISE images, this unit exhibits whitish to blueish hues that distinguish these outcrops from other crater floor units (Figure 4c).

Hypotheses and interpretations. These materials appear to have originated from the deeply-eroded, well-exposed basement of Eberswalde crater, and we interpret

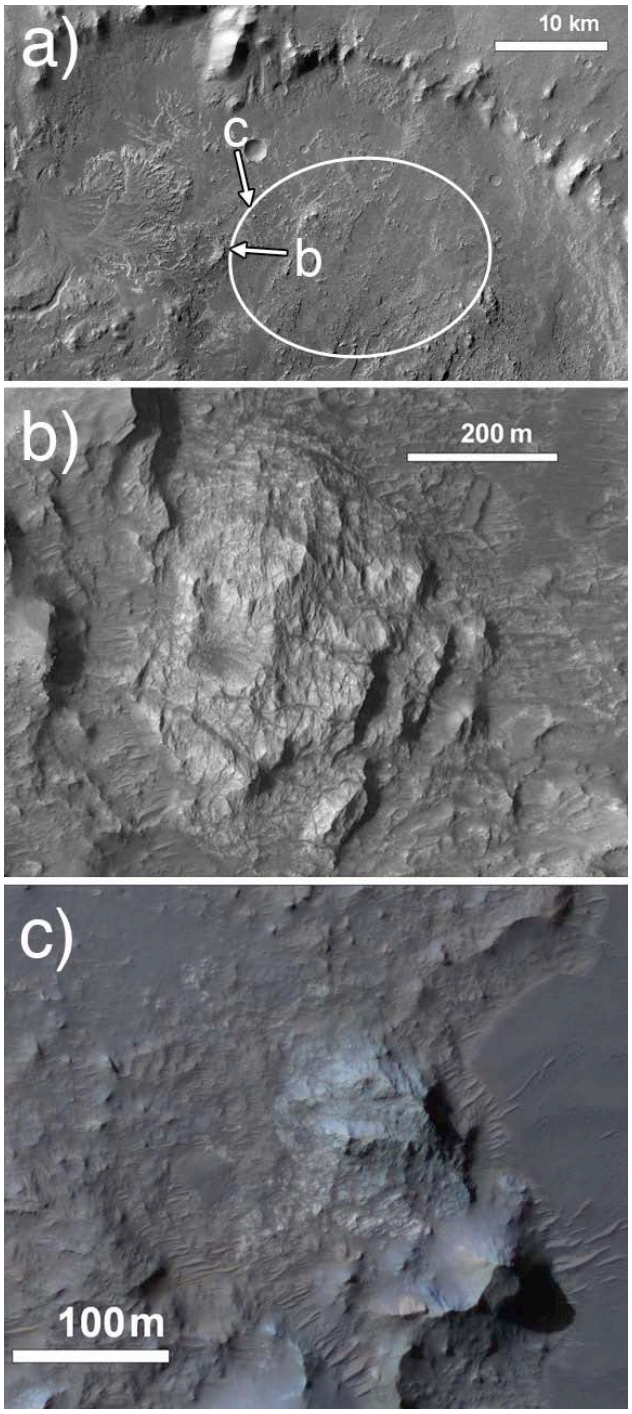

Figure 4. Examples of the massive, basal unit: (a) CTX mosaic of Eberswalde crater indicating the locations of 4b-c and the proposed MSL landing ellipse; (b) example of the massive, basal unit near the rim of an impact crater (from HiRISE observation ESP_020034_1560_RED); (c) Example of color variations within the massive, basal unit (from HiRISE observation PSP_010052_1560_COLOR). North is oriented at the top of the page in all images.

them as fractured, pre-Eberswalde bedrock. The colors, erosional expressions, and fracture patterns associated with the massive, basal unit are distinct from all other units within the crater, and there is no evidence suggesting that these outcrops are sedimentary or crater-fill deposits. Furthermore, they are only exposed in the topographically lowest, most deeply exhumed portion of the crater. We propose that this location in the western crater, where the massive, basal unit is exposed, is a "window" through the crater-filling units into the basement material that underlies the whole of the crater.

3.2 Orthogonally-fractured unit

Observations. The orthogonally-fractured unit is homogeneous, systematically fractured, and massive. It occurs as outcrops several kilometers wide along the eroded southern crater rim, and also as smaller (0.5-1 km) isolated outcrops (Figure 5). The fracture spacing ranges from 5-50 m, and orientations are typically NNW-SSE and ENE-WSW. In some locations, the fractures appear to have eroded deeply (Figure 5b), creating clusters of four-sided columns. In others, the fractures are filled by the darker mantling unit (Figure 5c), and only the surfaces of the separate four-sided forms are visible.

Hypotheses and interpretations. Like the massive, basal unit, the orthogonally-fractured unit can also be interpreted as Eberswalde basement material. In this scenario, the orthogonally-fractured outcrops would have undergone a different set of stresses than the massive, basal unit in order to create the fracture sets exemplified in Figure 5, and are composed of different mineralogies that do not exhibit the same

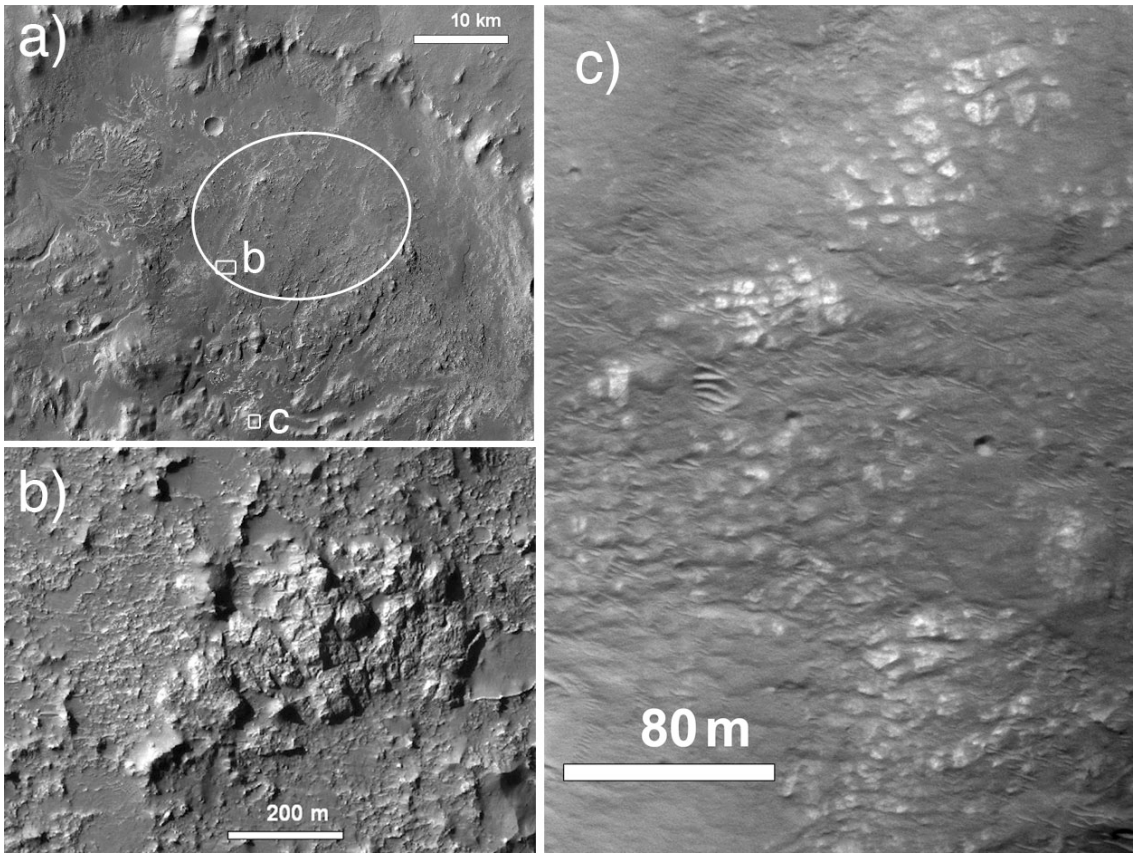

Figure 5. Examples of the orthogonally fractured unit: (a) CTX mosaic of Eberswalde crater indicating the locations of 5b-c and the proposed MSL landing ellipse; (b) example of an isolated, orthogonally fractured outcrop (from HiRISE observation PSP_010052_1560_RED); (c) example of the orthogonally fractured unit along the southern crater rim (from HiRISE observation ESP_018557_1560_RED). North is oriented at the top of the page in all images.

blueish hues in false color images.

An alternate hypothesis is that the orthogonally-fractured outcrops are large (>100 m) ejecta blocks from the Holden impact event. The large Holden crater to the southwest is younger than Eberswalde crater (e.g., Malin and Edgett 2003), and ejecta from the Holden impact event would likely have been deposited along the southern rim of Eberswalde crater and within the basin. The linear depression extending northward from the northwestern rim of Eberswalde crater (Figure 1c) may have formed from a Holden ejecta ray, implying that large blocks could have been ejected even further than the northern Eberswalde rim. It is plausible, therefore, that large outcrops of this unit were ejected from Holden and perhaps developed their orthogonal fracture patterns upon impact.

3.3 Brecciated unit

Observations. The brecciated unit is comprised of angular, partially- to fully-formed megaclasts (meters to tens of meters in size) encased in a light-toned matrix (e.g. Figure 6d-f). In false color HiRISE images, the megaclasts are heterogeneous and distinct in hue from the matrix and other crater floor materials (e.g., Figure 6f). Shadows cast by some megaclasts imply that they protrude from the matrix (Figure 6e inset); in some outcrops, however, shadows indicate pits in the matrix where megaclasts may have been removed.

Some outcrops of the brecciated unit contain long (up to 2 km) light-toned veins with variable widths (<1-20 m). In the western portion of the crater, the veins are aligned roughly parallel at the kilometer scale (Figure 6b) but appear random at

Figure 6. Examples of the brecciated unit: (a) CTX mosaic of Eberswalde crater indicating the locations of 6b-f and the proposed MSL landing ellipse; (b) example with sub-parallel, linear veins (from HiRISE observation ESP_012610_1560_RED); (c) close-up, color image of a vein in the brecciated unit (location shown in (b)); (d) color variations in megaclasts along a crater rim (from HiRISE observation PSP_04000 _1560_COLOR); (e) outcrop of the subunit BR_4 (from HiRISE observation PSP_019335_1560_RED), with the inset showing ~5-10 m megaclasts encased in a light-toned, fine-grained matrix (from HiRISE observation PSP_019190_1560_RED); (f) example of color variations of megaclasts in the eastern portion of the crater (from HiRISE observation ESP_011265_1560_COLOR). North is oriented at the top of the page in all images.

a)
10 km
b
e
d
f
b)
c
300 m
c)
50 m
d)
50 m
e)
100 m
25 m
f)
100 m

smaller scales (Figure 6c). Some wider veins (Figure 6c) are heterogeneous in color and texture, and appear to consist of angular clasts. Milliken and Bish (2010) detected phyllosilicate minerals within these outcrops using data from the MRO Compact Reconnaissance Imaging Spectrometer for Mars (CRISM); the spatial resolution of the instrument (~18 m/pix), however, did not allow them to determine whether the phyllosilicates were confined to the veins or to the darker, massive material or megaclasts.

Hypotheses and interpretations. Scott and Tanaka (1986) and Pondrelli et al. (2008) interpreted these crater floor materials as a series of eroded remnants of lava flows and pyroclastic materials. However, the lack of observable planform flow features, preserved lava surface textures, or volcanic constructs on or near Eberswalde crater make it difficult to confirm a volcanic hypothesis. In addition, given the observed size of the breccia blocks (meters to tens of meters), it is unlikely that these deposits are volcanic as they would have to have been derived from a proximal and explosive volcanic source that has not been detected. While a volcanoclastic interpretation cannot be completely ruled out for the brecciated unit, we consider the lack of primary volcanic morphologies within the crater as the best possible evidence against this hypothesis.

Our observations are more consistent with the interpretation by Schieber (2007) that these outcrops are megabreccia derived from impact events. In terrestrial impact craters, megabreccias have been described as poorly sorted deposits that are commonly lithified and consist of large (meter-scale) angular to subrounded clasts (e.g., French 1998). Based on their morphology and distribution, impact megabreccia

can be distinguished as parautocthonous (having formed nearly in-place) or allocthonous (consisting of rocks derived from elsewhere).

Ejecta from the Holden impact event would likely have been deposited along the southern rim of Eberswalde crater and within the basin as allocthonous megabreccia. Using empirical expressions for the radial decay of ejecta thickness by Garvin and Frawley (1998), we estimate that the entire floor of Eberswalde crater could have been covered by Holden ejecta (up to ~1.6 km thick in southern Eberswalde, and 100-200 m thick near the northern Eberswalde rim).

Because of the heterogeneous colors of megaclasts that we interpret as evidence for a heterogeneous lithology within this unit (e.g., Figure 6f), we suggest that these materials are allocthonous megabreccia comprised of blocks ejected during the Holden impact. These blocks are held in place by a matrix material, which may be more erosion-resistant than the blocks themselves, as indicated by the pits remaining in some place where blocks appear to have been removed. Alternatively, the blocks may be "falling out" of a more erodible matrix, as is suggested by the blocks protruding from the matrix (Figure 6e-f); however, a lag of boulders is not observed at the base of large outcrops.

The vein-cut outcrops, however, may be parautocthonous megabreccia formed nearly in-place during the Eberswalde crater impact event. Their color, morphology, and dissection by light-toned veins (e.g., Figure 6b) are consistent with parautocthonous megabreccia previously identified near the rim of Holden crater (Grant et al., 2008; Tornabene et al., 2009). The light-toned veins in megabreccia near Holden crater have been interpreted as breccia injection dikes formed by the

circulation of hydrothermal fluids following the impact event (Tornabene et al., 2009), and we adopt a similar interpretation for the veins observed in the Eberswalde.

3.4 Pitted unit

Observations. The pitted unit covers most of the floor of Eberswalde crater (Figure 3) and is overlain by the mantling unit and the dark-toned bedforms unit. This unit is light-toned and is characterized by a pitted morphology, which transitions over several hundred meters from dense clusters of < 30 m wide pits to isolated light-toned quasi-circular depressions < 10 m wide (e.g., Figure 7b). In places, the quasi-circular depressions are variably covered with and filled by the mantling unit (Figure 7c). The unit exhibits a range of topographic expressions: flat-laying, scarp-forming, ridge-forming, and undulating.

This unit appears to grade continuously into the brecciated unit, making it difficult to determine the boundary between these units; furthermore, the average CTX albedo of the pitted material (~0.14) is the same as the matrix material of the brecciated unit. Our mapping of these units (Figure 3) is thus rather equivocal. Ultimately, we distinguish this pitted, discontinuous, light-toned unit from the brecciated, ridge-forming unit by the absence of megaclasts entrained in the light-toned material.

Hypotheses and interpretations. While Pondrelli et al. (2008) interpreted this unit as lacustrine sediments that were emplaced in the deepest part of a possible Eberswalde lake, we have observed no evidence for layering that would support that hypothesis. Also, the pitted morphology is inconsistent with the observed erosional

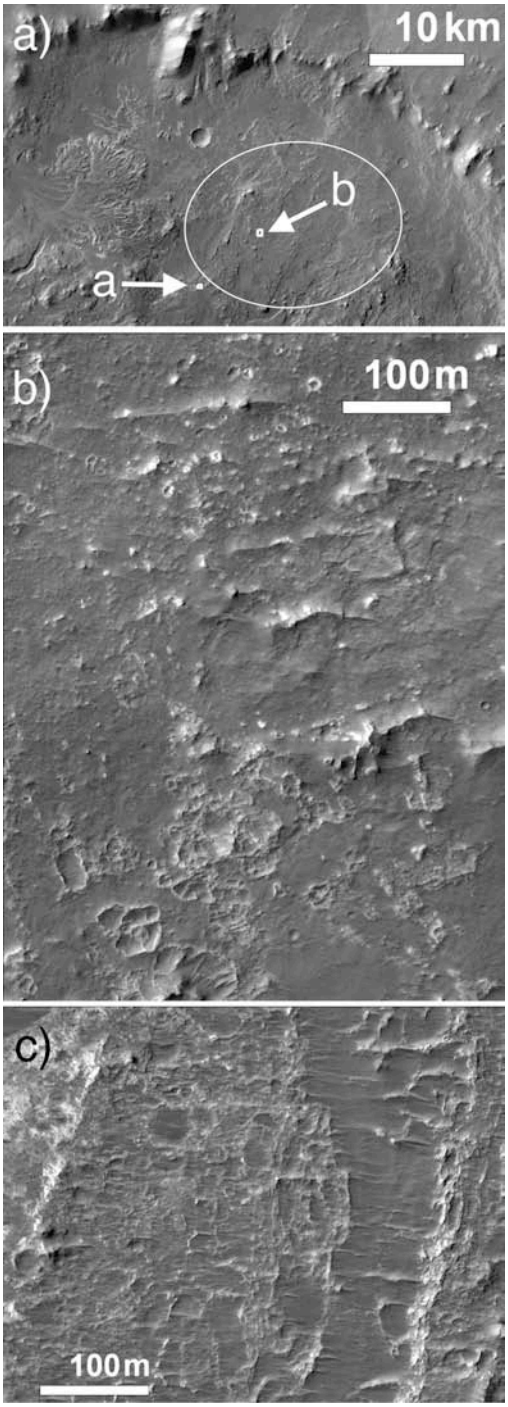

Figure 7. Examples of the pitted unit: (a) CTX mosaic of Eberswalde crater indicating the locations of 7b-c and the proposed MSL landing ellipse; (b) example of pitted, discontinuous light-toned material transitioning northward to isolated, light-toned, quasi-circular depressions (from HiRISE observation PSP_010474_1560_RED); (c) example of pitted material variably covered and filled by the darker-toned mantling unit (from HiRISE observation PSP_010052_1560_RED). North is oriented at the top of the page in all images.

morphology of other putative lacustrine sediments on Mars (e.g., Grant et al., 2008; Warner et al., 2010). We therefore support three possible alternate interpretations for this unit: (1) the depressions are the result of heterogenous erosion of an ancient surface saturated with small impact craters; (2) the pitted morphology formed as a result of de-volatilization and degradation of an ancient, basal impact melt surface; and (3) the light-toned material may be the erosionally resistant matrix of the brecciated unit and/or the vein-like features within the brecciated material, and the pitted morphology may result from the "holes" left by megaclasts that have since been removed. In the case of (3), there are similarities between the pitted, discontinuous light-toned unit and the brecciated unit, such as their albedos and the sizes of the pits/megaclasts, that support this hypothesis. The apparent gradational relationship between the pitted and brecciated units is consistent with this hypothesis as well.

In support of hypothesis (2), we note that for large, near-pristine impact craters on Mars, a pitted surface texture is often observed on the crater floor, within materials that immediately superpose the primary bedrock of the impact crater. A key example is the relatively pristine pitted terrain within the floor of the 50-km-wide, Hesperian to Early Amazonian-age Mojave crater (Williams and Malin 2008), which has pits covering the vast portions of the crater floor, terraces and rims (Boyce et al., 2011). This pitted material has been interpreted as impact melt that, upon cooling and solidification, underwent devolatilization (McEwen et al., 2007b; Tornabene et al., 2007; Williams and Malin 2008). According to that model, the pits would be regions of collapse formed by surface deflation due to volume loss within the cooled melt. The surface texture of the pitted unit within Eberswalde crater may therefore represent a

degraded example of such devolatalized terrain, with the possible addition of degraded, small impact craters. In this hypothesis, we would expect the pitted unit to predate and underlie the brecciated unit, which we interpret as allochtonous ejecta from the Holden impact; however, these types of contact relationships have not been clearly observed (see Unit Associations, Successions and Geometries below).

Pondrelli et al. (2011) termed this unit the "non-layered member" of the "Eberswalde Formation"; however, we do not associate this unit with the fan deposits based on observed contact relationships (see Unit Associations, Successions and Geometries for further discussion). Consistent with all interpretations, the pitted unit likely represents exposed remnants of ancient floor material that is unrelated to the younger, fluvio-lacustrine processes that formed the putative delta.

3.5 Ridge-forming unit

Observations. The ridge-forming unit (Figure 8) has the most extreme topographic relief of any material within Eberswalde crater, and it is characterized by sharp peaks, scarps and ridges. This unit includes outcrops that appear homogeneous in albedo and color, are not extensively fractured, and that contain horizontal lineations that may indicate layering (e.g., Figure 8c). It is often unclear whether the homogeneous appearance is due to a single composition of the outcrop or a uniform covering of dust and/or the mantling unit. In many occurrences, this unit exhibits steep cliffs along SW-NE-oriented linear scarps (e.g., Figure 8d). Boulders observed at the base of these cliffs likely have been shed from these outcrops (e.g., Figure 8f).

Figure 8. Examples of the ridge-forming unit: (a) CTX mosaic of Eberswalde crater indicating the locations of 8b,d and the proposed MSL landing ellipse; (b) example of the ridge-forming unit with extreme topography within the landing ellipse (from HiRISE observation PSP_010474_1560_RED); (c) close-up example showing possible layering, location shown in (b); (d) example of the ridge-forming unit along a topographic divide in the east of the crater (from HiRISE image ESP_016210_1560_RED); (e) close-up of a cliff shedding boulders, location shown in (d). North is oriented at the top of the page in all images.

a)
10 km
b
d
b)
c
c)
100 m
d)
1 km
e
e)
150 m

Hypotheses and interpretations. An hypothesis for the homogeneous appearance of the ridge-forming unit is that these outcrops are in fact other crater floor units (e.g., the brecciated unit and/or orthogonally fractured unit) that have been draped by the mantling unit. The mantling may be obscuring the light-toned veins, heterogeneous colors, or other defining characteristics of the underlying outcrop, and the layered appearance may result from fractures in the cemented mantling material. Light-toned material visible at the base of some outcrops is consistent with the hypothesis that these are outcrops of the pitted or brecciated units covered by mantling. Alternately, the ridge-forming unit may represent layered strata consisting of aeolian deposits, volcanic ash, or fluvial/lacustrine sediments.

3.6 Knobby unit

Observations. Much of the west-central portion of the Eberswalde crater floor is covered with isolated hillocks of light-toned rock which we have mapped as the "knobby" unit (Figure 3). The knobs are typically < 30 m wide, < 50 m high, and spaced > 50 m apart (Figure 9). While most consist of massive, light-toned rock-forming peaks or ridges along their tops, some knobs are rounded and covered with meter-size boulders (e.g., the knob in the center of Figure 9c).

Hypotheses and interpretations. It is unclear whether the meter-size boulders observed in HiRISE images represent formerly in-situ, eroded clasts or materials that were deposited on the surface of the knobby unit after it was emplaced. If the boulders are in place, one possible interpretation for the knobby unit is that it was derived from a laterally extensive ejecta deposit that was possibly associated with nearby impact

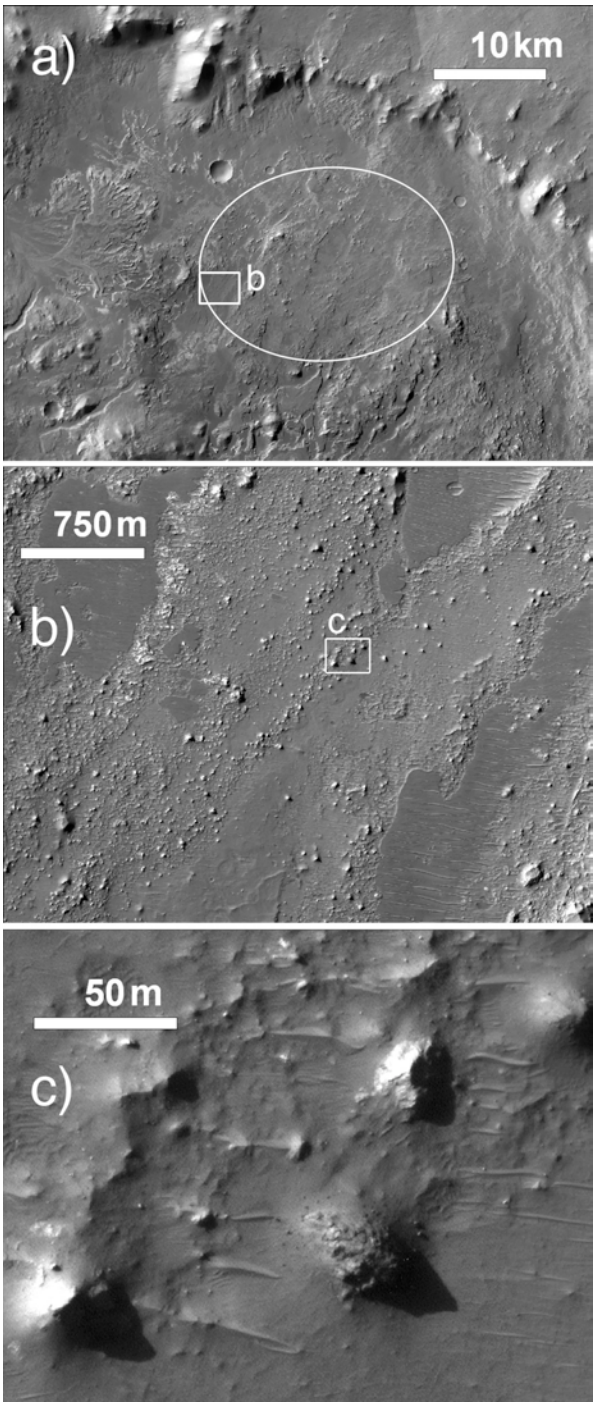

Figure 9. Examples of the knobby unit: (a) CTX mosaic of Eberswalde crater indicating the location of 9b and the proposed MSL landing ellipse; (b) a large extent of the knobby unit, covered by patches of the smooth mantling unit (from HiRISE observation PSP_010052_1560_RED). The white box indicates the location of 9c; (c) examples of knobs composed of massive, light-toned, ridge-forming material and a mound covered with meter-size boulders. North is oriented at the top of the page in all images.

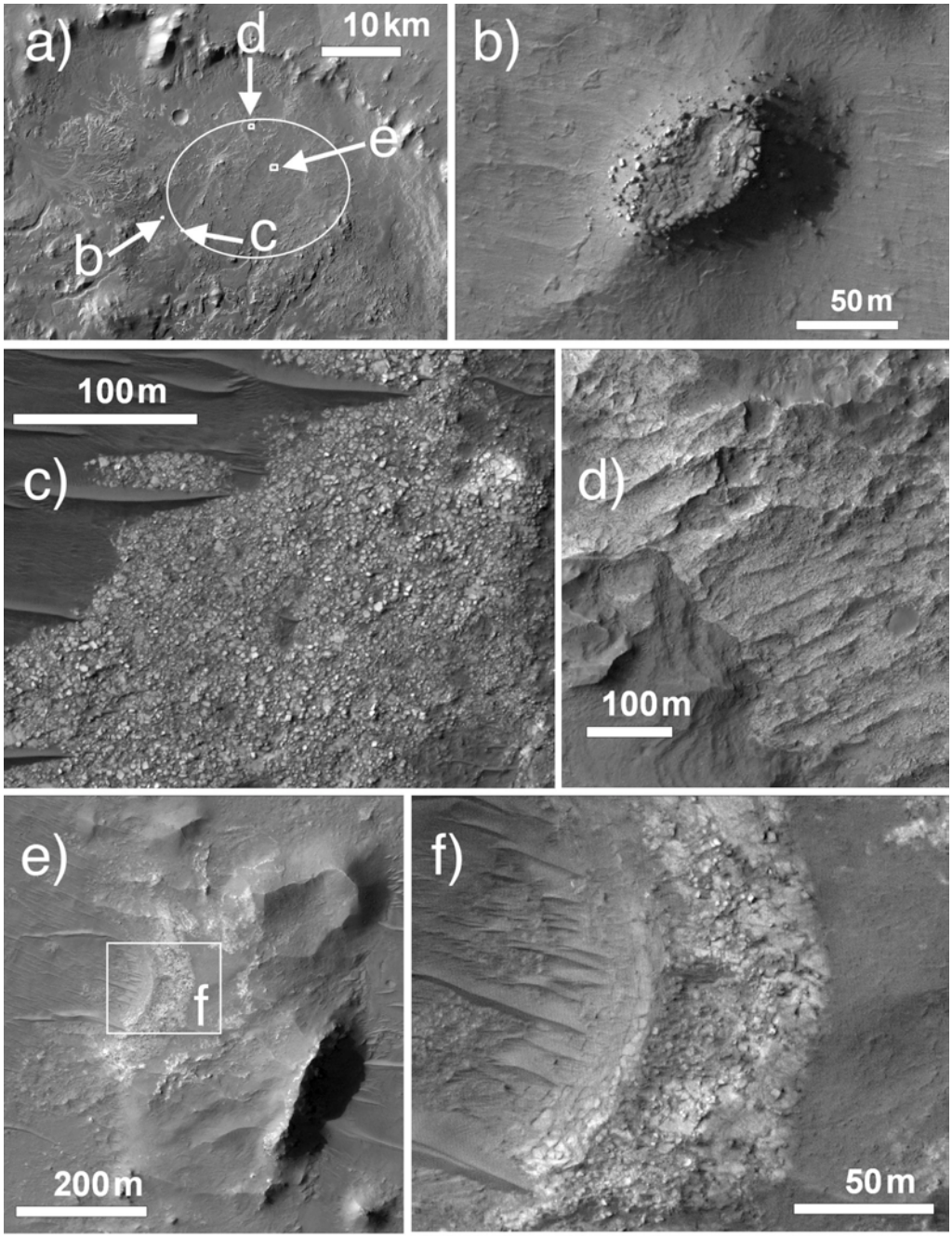

Figure 10. Examples of the sub-polygonally fractured unit: (a) CTX mosaic of Eberswalde crater indicating the locations of 10b-e and the proposed MSL landing ellipse; (b) an isolated mesa of the sub-polygonally fractured unit shedding boulders (from HiRISE observation PSP_010553_1560_RED); (c) an extensive outcrop at the edge of the landing ellipse (from HiRISE observation PSP_010052_1560_RED); (d) bedform features in the sub-polygonally fractured unit (from HiRISE observation PSP_010474_1560_RED); (e-f) fractured light-toned rock along the rim of a partially-preserved impact crater (from HiRISE observation ESP_019335_1560_RED). North is oriented at the top of the page in all images.

crater formation. If the boulders are not in place and are derived from elsewhere, the knobs likely represent a series of erosion-resistant mesas and hills that are remnants of a more extensive unit(s) that once covered the west-central portion of the Eberswalde basin floor, possibly including the sub-polygonally fractured unit and/or the layered light-toned unit (although no layering is observed in the knobs at the scale of HiRISE observations).

An alternate, albeit speculative, hypothesis is that the knobs may be erosional remnants of glacial or periglacial features like pingos or thermokarst-like hummocks that were formed in previously ice-rich terrain. For example, deflation of ice-rich terrain has been proposed as a possible explanation for "hummocky terrain" in Gusev Crater (Gregg et al., 2007); however, those hummocks typically have much closer spacing and consist of poorly consolidated debris, which is not consistent with our observations of this unit in Eberswalde.

3.7 Sub-polygonally fractured unit

Observations. Light-toned materials comprised of angular, sub-polygonal blocks outcrop in several major locations within Eberswalde crater (Figure 3). The polygons are ~1-6 m in diameter, and the shapes of adjacent polygons are complementary (i.e., the fractured forms fit together like puzzle pieces and are not chaotically organized) (Figure 10). In places, the fractured light-toned unit clearly is weathering into meter-scale blocks (such as in Figure 10b) where this unit outcrops as isolated mesas.

Over the spatial distribution of this unit (Figure 3), we observe an apparent degradation of the continuous, fractured rock into a lag of boulders on the surface. Figure 10c shows an example of an intermediate stage of degradation, where the unit consists mainly of boulders, although complementary edges are still observed. Outcrops in the center of the crater, however, consist mainly of light-toned boulders (Figure 10f)

While other stratigraphic units also exhibit extensive fracturing (such as the layered light-toned unit), we restrict our characterization of the sub-polygonally fractured unit to flat-lying, spatially extensive exposures. This unit may conform to topography in some instances, such as along the bedforms near the fan-form feature in the north of the crater (Figure 10d); however, it is unclear whether the fractured material drapes preexisting bedforms, or whether the bedforms are within this unit.

Hypotheses and interpretations. The complementary form of the fractures suggests that the light-toned material has been fractured in place, as opposed to having been deposited as a breccia (Pondrelli et al., 2008). The fracturing could represent desiccation cracks in dehydrated sulfate- or clay-rich strata. In support this hypothesis, CRISM data are consistent with the presence of phyllosilicate minerals (Milliken and Bish 2010). However, Schieber (2007) argued that desiccation cracks of clay-rich mudstones are typically much smaller than those observed in Eberswalde, and that the fracturing is more likely due to thermal contraction of sandstones encrusted by evaporite minerals. An alternate hypothesis is that the fracturing is due to tectonic stress; however, we have observed no preferred orientation to the fractures bounding polygons.

Jerolmack et al. (2004) extrapolated that, if the fan-shaped feature in western Eberswalde were an alluvial fan and not a delta, the fan sediments would have extended 45 km from the western rim past the center of the Eberswalde basin. Because all exposures of the fractured light-toned unit occur within this distance from the western rim (Figure 3), it is possible that these outcrops are the remnants of such extensive fan deposits. Alternately, if the fan-shaped feature is indeed a delta, the fractured light-toned unit may represent an extended delta bottomset and associated lacustrine sediments. This hypothesis is consistent with the detection of phyllosilicate minerals (Milliken and Bish 2010) and the unit's association with other fan-shaped features in Eberswalde.

An additional hypothesis is that the light-toned material consists of tephra (volcanic airfall) deposited subaerially or subaqueously within the crater. However, this interpretation cannot be confirmed from morphology alone, but will likely require in-situ observations of composition and stratigraphy. Fallout tephra deposits systematically thin away from the source and drape local topography. While we have observed no systematic trend in unit thickness, this does not rule out tephra deposits from multiple volcanic source regions or from regionally/globally extensive airfall. However, we also have identified no occurrences of this unit draped at varying elevations, which is the strongest observation against a subaerial volcanic airfall hypothesis. As we elaborate in the Unit Associations, Successions and Geometries section, the fractured light-toned material is restricted to occurrences below a common elevation in the Eberswalde basin.

Figure 11. Examples of the layered light-toned unit exposed at the putative Eberswalde delta: (a) the locations of 11b,d at the terminus of the putative delta (from CTX observation P01_001336), with the inset indicating the locations of the putative delta and the proposed MSL landing ellipse within Eberswalde crater; (b) context along the south rim of Eberswalde crater (from HiRISE observation PSP_004000_1560_RED), the white box indicates the location of 11c; (c) sub-polygonal fracturing in light-toned layers; (d) a possible downlap relationship in the north lobe (from HiRISE observation PSP_001534_1560_RED); (e) perspective view showing shadows cast by overhanging layers (from HiRISE observation PSP_004000_1560_RED draped over a DTM). North is oriented at the top of the page in all images unless otherwise noted.

a)
5 km
d
b
10 km
b)
300 m
c
c)
50 m
d)
100 m
e)

Figure 12. Examples of the layered light-toned unit in northern Eberswalde, with arrows indicating traceable layers: (a) CTX mosaic of Eberswalde crater indicating the location of 12b,d and the proposed MSL landing ellipse; (b) a lobate plateau of layered rocks in the north of Eberswalde crater (from HiRISE observation PSP_010764_1560_RED), the white box indicates the location of 12c; (c) layers exposed along the edge of a lobate plateau (from HiRISE observation PSP_010764_1560_RED); (d) context for layered rocks along the rim of a crater (from HiRISE observation PSP_010553_1560_RED), the white boxes indicate the locations of 12e-f; (e) a plateau of light-toned, layered rocks (from HiRISE observation PSP_010553_1560_RED); (f) layered rocks (partially mantled) (from HiRISE observation PSP_010553_1560_RED). North is oriented at the top of the page in all images.

a)
10 km
d
b
b)
1 km
c
c)
50 m
d)
1 km
f
e
e)
200 m
f)
100 m

Figure 13. Examples of the layered light-toned unit in southern Eberswalde, with arrows indicating traceable layers: (a) CTX mosaic of Eberswalde crater indicating the location of 13b,g and the proposed MSL landing ellipse; (b) context for layered deposits in southwest Eberswalde crater, white boxes indicate the locations of 13c-d (from CTX observation P21_009274); (c) example of light-toned layers exposed in a cliff face (from HiRISE observation PSP_010553_1560_RED); (d) example of a fan-like plateau comprised of light-toned layers and context for 13e-f (from HiRISE observation ESP_018056_1560_RED); (e) example of layers exposed at the edge of a sinuous landform (from HiRISE observation ESP_018056_1560_RED) (f) example of light-toned layers exposed along a digitate landform (from HiRISE observation ESP_018056_1560_RED); (g) context for layered deposits in southwest Eberswalde crater, white boxes indicate the locations of 13h-i (from HiRISE observation ESP_018056_1560_RED); (h) example of light-toned layers exposed in along a digitate landform; (i) example of light-toned layers exposed beneath a tabular mesa. North is oriented at the top of the page in all images.

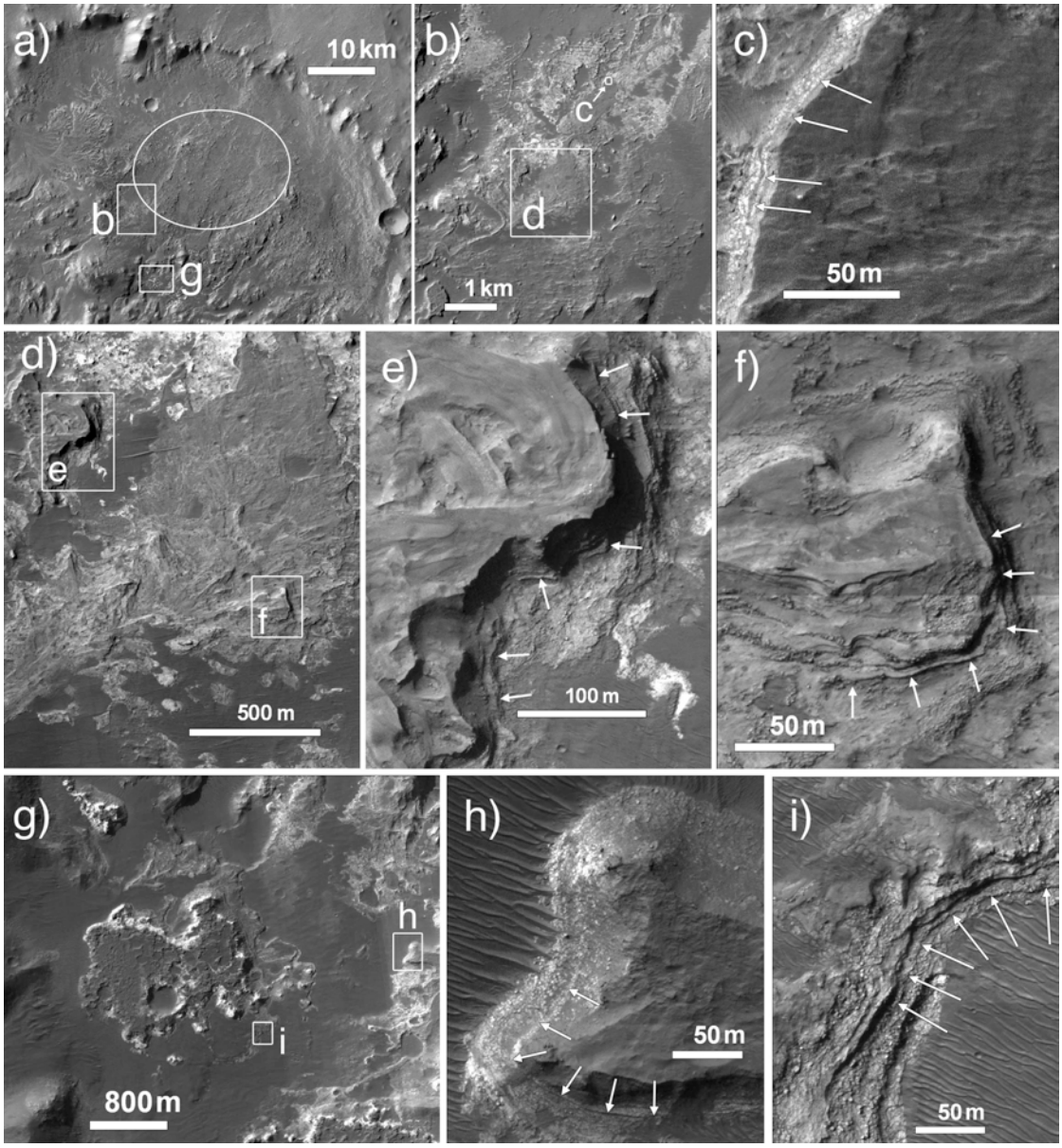
a)
10 km
b
g
b)
c
d
1 km
c)
50 m
d)
e
f
500 m
e)
100 m
f)
50 m
g)
h
i
800 m
h)
50 m
i)
50 m

3.8 Layered light-toned unit

Observations. Light-toned rock that is clearly layered at the scales of HiRISE and MOC images crops out near the north, west, and southern rims of Eberswalde crater, and the most extensive outcrops are associated with the putative delta in the west of the crater (Figures 11-13). This layered light-toned unit has the highest CTX albedo (up to 0.25) of any material within the crater. Because there are albedo variations between layers, it is possible that the unit consists of light and dark layers that represent lithologic or sedimentologic variations in the outcrop; however, we are often unable to discern whether the lower albedo is a true characteristic of the darker layers, or if these layers are more consistently covered by a mantling unit. Some layers at the edge of the putative delta are more erosionally resistant than others and form thin (< 50 cm) overhangs that cast shadows upon the layers below (Figure 11e). The layers have measured dips of 1-3o (Lewis and Aharonson 2006), and no clear clinoforms are observed at the front of the putative delta (e.g., Figure 11e). We have observed only one possible downlap relationship in the northern lobe of the putative delta (Figure 11d), although some layers appear to pinch out.

The upper layers of the putative delta have no obvious fracturing, while the lower layers are extensively polygonally fractured (Figure 11c) and appear to be forming and shedding boulders that have fallen to the bottom of the cliff face. These lower layers are morphologically similar to some outcrops of the sub-polygonally fractured unit described in the previous section. In some layers along the edge of the delta, randomly oriented blocks appear to be resting on or within a finer-grained, darker-toned material.

The distribution of layering in other locations is shown in Figure 3. In northern Eberswalde crater, the light-toned layered unit is visible along the edge of a fan-shaped feature and individual layers are traceable for < 100 m (Figures 12b-c). Layered rock also crops out along the rim of an impact crater (Figures 12d-f). In these locations, the light-toned layered unit is not as extensively fractured as in the putative delta, and where the uppermost surface is not covered by the mantling unit, the rock appears to have eroded into scalloped depressions (e.g., Figure 12e).

In southwest Eberswalde, the layered light-toned unit is associated with a more extensive exposure of other light-toned materials (Figure 13b) and exhibits a diverse range of morphologies (Figures 13c-f). The material is clearly fractured along the cliff face of a plateau of layered rock (Figure 13c), but ~2 km further south, where visible along the edges of sinuous landforms, the layers are not fractured and are covered more extensively by the mantling unit. The layered rock forms both cliff faces (i.e., Figure 13e) and "stair-step" geometries (i.e., Figure 13f). In southern Eberswalde (Figures 13g-i), the light-toned layers are sub-polygonally fractured and associated with 1-5 m boulders.

Hypotheses and interpretations. There is no clear evidence that the light-toned layered unit breaks into granule-sized particles (2-4 mm; Sharp, 1963), as we observe no light-toned dunes associated with the layered unit. Rather, we observe the layers to be fractured and shedding 1-10 m boulders. However, there is no extensive talus at the bottom of cliff faces. As Jerolmack et al. (2004) noted, a lack of talus may indicate that the unit erodes to sand-sized or finer grains (< 300 μm; Sharp, 1963) that are carried away by the wind. Given these observations, we interpret the light-toned,

layered unit as being composed largely of weakly lithified, fine-grained material that, due to its fracturing, sheds boulders that are easily disintegrated. This hypothesis is consistent with the identification of Mg/Fe-phyllosilicates within the layers of the putative delta (Milliken and Bish 2010; McKeown and Rice 2011).

Based on the analyses of stratal geometries and discussions in Malin and Edgett (2003), Moore et al. (2003), Bhattacharya et al. (2005), Wood (2006), Lewis and Aharonson (2006) and Pondrelli et al. (2008), we interpret the layered rock in western Eberswalde crater to be deltaic sediments. We interpret the layers in the northern (Figure 12), southwestern (Figures 13b-f), and southern (Figures 13g-i) portions of the Eberswalde basin as deltaic sediments as well due to their morphology, their association with possible fluvial features such as sinuous ridges and valleys, as well as their confinement to the margins of the crater (Rice et al., 2011).

Additional hypotheses are that the layers are volcanic ash (deposited either subaqueously or subaerially), aeolian deposits, or potentially impact-generated base surge deposits (from large impacts which scatter enormous amounts of debris distally, as has been suggested for the layered rock in Meridian Planum by Knauth et al., 2005).

3.9 Mantling unit

Observations. The mantling unit consists of a dark (albedo 0.09-0.13), fine-grained, smooth material that covers the majority of the Eberswalde basin (Figure 3). Many small craters and clusters of craters are preserved in this unit (e.g., Figure 14d), and in places the smooth mantling grades into aeolian bedforms with E-W trending

Figure 14. Examples of the mantling unit: (a) CTX mosaic of Eberswalde crater indicating the locations of 14b-e and the proposed MSL landing ellipse; (b) extensive occurrence of the mantling unit with the inset showing its cliff-forming nature (from HiRISE observation PSP_010052_1560_RED); (c) occurrence of the mantling unit where it onlaps underlying units; the arrow indicates a fresh impact crater exposing darker material in its ejecta (from HiRISE observation ESP_012610_1560_RED); (d) a cluster of fresh impact craters preserved in the mantling unit (from HiRISE observation PSP_010474_1560_RED); (e) the mantling unit covering a sinuous landform, the inset shows that the unit is thin enough to reveal the fractured nature of the material it covers (from HiRISE observation PSP_010052_1560_RED). North is oriented at the top of the page in all images.

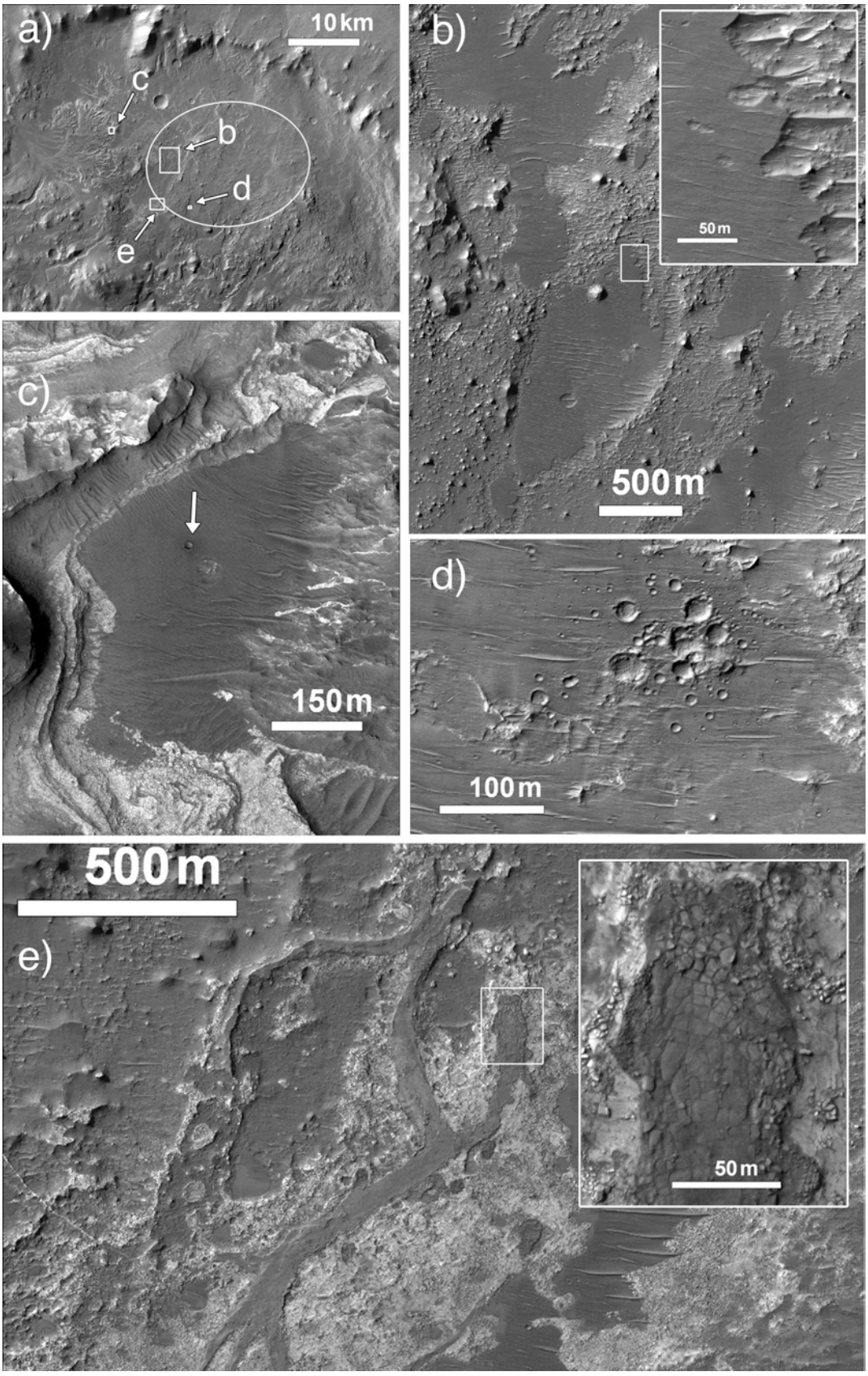
a)
10 km
c
b
d
e
b)
50 m
500 m
c)
150 m
d)
100 m
500 m
e)
50 m

crests typically ~100 m in length with ~40 m spacing (e.g., Figures 14c-d). Near topographic obstacles, the bedforms are oriented perpendicular to cliff faces.

The mantling unit generally obscures the underlying topography, and it can terminate directly against another unit (e.g., Figure 14c) or form cliffs along an erosional surface (e.g., Figure 14b inset). No boulders are observed at the base of these cliffs, and no bedding planes have been observed along their edges. In places, the mantling is thin enough to reveal the form of the sub-polygonally fractured rock (Figure 13e) or sinuous landforms beneath (e.g., Figure 11e). A fresh crater in the mantling unit near the terminus of the putative delta (Figure 13c) reveals that the underlying material has an even lower albedo than most surficial deposits.

Hypotheses and interpretations. Similar mantling deposits elsewhere on Mars have been interpreted as airfall dust deposits (e.g., Christensen 1986; Bridges et al., 2009; Malin et al., 2010). Because of the preservation of small craters and its cliff-forming nature, we interpret the mantling unit as at least partially lithified. This implies that the bedforms are not recent; old, inactive, indurated bedforms have been widely observed across the planet (e.g., Malin and Edgett, 2001). The absence of talus at the base of cliffs, however, implies that the indurated mantling material easily disintegrates into grain sizes small enough to be transported away by wind. The observation that the underlying material has a lower albedo than the surficial deposits suggests that the indurated mantling is covered by a thin layer of higher-albedo dust or has been altered at the surface, at least in places.

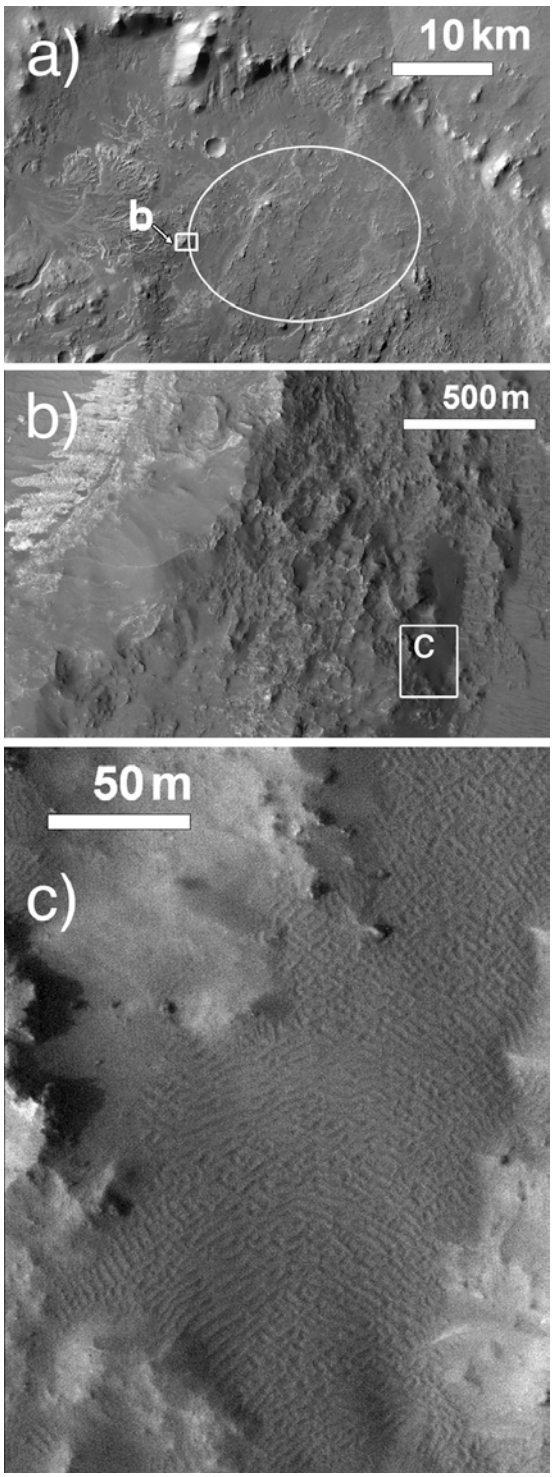

Figure 15. Examples of the dark-toned bedforms unit: (a) CTX mosaic of Eberswalde crater indicating the location of 15b and the proposed MSL landing ellipse; (b) context for the bedforms shown in 15c against the rim of an impact crater (from HiRISE observation ESP_012610_1560_RED); (c) dark-toned, complex bedforms preserving no small craters. North is oriented at the top of the page in all images.

3.10 Dark-toned bedforms unit

Observations. In a few isolated locations in the western portion of the crater, dark-toned (albedo 0.07-0.09), complex bedforms abut east-facing topographic obstacles (such as the brecciated ridge forming unit in Figure 15b). The dark-toned bedform unit does not preserve small impact craters and is the only unit that is not covered in part by the mantling unit.

Hypotheses and interpretations. The dark-toned bedforms appear to be the youngest deposits in Eberswalde crater, and the paucity of impact craters superposed on them suggests that the bedform material has been recently reworked. We interpret this unit as modern aeolian bedforms, similar to the El Dorado dunes observed by the Mars Exploration Rover Spirit in Gusev Crater (Sullivan et al., 2008).

4. Inferred geomorphic units

We have identified seven geomorphic units within Eberswalde crater, which we have mapped in Figure 16. The detailed descriptions of our observations, hypotheses, and interpretations of each unit are given below, and a summary of all units is provided in Table 2.

4.1 Vein-like features

Observations. Several stratigraphic units within Eberswalde crater are cut by light-toned vein-like features < 5 m in width, ranging from 10 to 1000 m in length (Figure 17). In the brecciated unit, these features can be either linear with parallel orientations or randomly aligned with varying thicknesses (Figure 6b-c). Within other

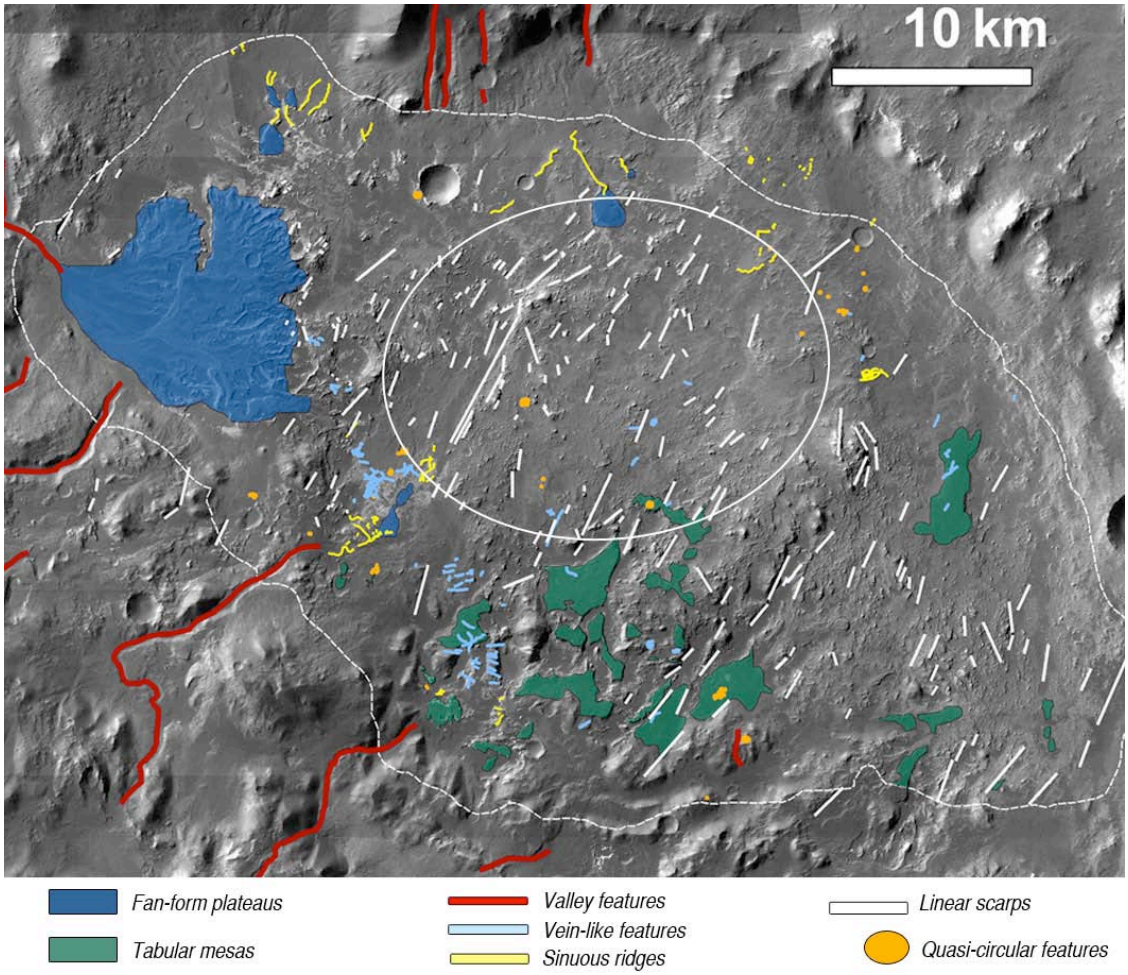

Figure 16. Map of inferred geomorphic units inside Eberswalde crater. The white line indicates the location of the proposed MSL landing ellipse. See text for detailed descriptions of units.

Table 2. Summary of geomorphic units

Geomorphic Unit	Figures	Description	Topography (m)	Contact Relationships	Process Interpretation*	Comparison to Previous Studies
Vein-like features	17, 24	Narrow; linaer to arcuate ridges; meet at right angles; some networks	-1500 to -1280	Found in the brecciated and pitted units	Breccia injection dikes; cemented fracture fill	none
Channel-like features	18, 25	Linear to sinuous valleys; 200-800 m wide	> -1330	Incising the brecciated unit at the margins of the crater; partially filled by the mantling unit	Fluvial channels	[1-8] Fluvial channels
Sinuous ridges	14e, 19, 25	Sinous with raised relief; 10^1-10^3 m long; light-toned material at base; sometimes meandering or branching	-1490 to -990	Above the brecciated unit, the sub-polygonally fractured unit, and/or the pitted unit; covered by the mantling unit	Inverted, fluvial channels	[6-9] Inverted, fluvial channels
Fan-like plateaus	11a, 12b, 12c, 20b, 25	Fan-shaped, layered plateaus; preserve sinuous landforms; light-toned rock exposed in cliff faces	-1490 to -1250	Onlapping the brecciated unit and/or the pitted unit; covered by the mantling unit	Remnant deltas	[1-9] Remnant deltas; [10]Remnant alluvial fans
Tabular mesas	13g, 20c-d	Irregular-shaped mesas; pitted, scalloped surfaces; preserve small craters; light-toned material exposed in cliff faces	-1510 to -1205	Above the brecciated unit and/or the pitted unit; covered by the mantling unit	*Fluvial deposits? Lacustrine sediments?*	none
Concentric, quasi-circular features	21	Small (<500 m), concentric, quasi-circular; some fracturing; largely obscured by the mantling	-1495 to -1260	Above the brecciated unit and/or the pitted unit; covered by the mantling unit	Filled craters	none
Linear scarps	8, 22	NNE-SSW trending lineations; form cliff faces > 5 m high	> -1570	Found in the massive basal, orthogonally fractured, brecciated, pitted, sub-polygonally fractured, and light-toned layered units; in places overlain by the sub-polygonally fractured, light-toned layered, and mantling units	Dip-slip faults	[6] Faults; [9] Dip-slip faults

* See text for a description of alternate hypotheses

[1] Malin & Edget (2003); [2] Moore *et al. (*2003); [3] Bhattacharya *et al. (*2005); [4] Wood (2006); [5] Lewis & Aharaonson (2006); [6] Pondrelli *et al. (*2008); [7] Pondrelli *et al. (*2010); [8] Scheiber (2007); [9] Rice *et al. (*submitted); [10] Jerolmack *et al. (*2004).

Figure 17. Examples of vein-like features: (a) CTX mosaic of Eberswalde crater indicating the location of 17b-e and the proposed MSL landing ellipse; (b) a ~1 km linear, isolated vein-like ridge near the center of the landing ellipse (from HiRISE observation ESP_012610_1560_RED); (c) complex pattern of vein-like features (from HiRISE observation PSP_017845_1560_RED); (d) arcuate, vein-like ridges; the inset shows where polygonally fractured material overlies a ridge (from HiRISE observation PSP_004356_1560_RED); (e) arcuate, vein-like features in southwest Eberswalde; the arrows indicate a double-ridged levee (from HiRISE observation PSP_004356_1560_RED). North is oriented at the top of the page in all images.

a)
10 km
e
b
d
c
b)
200 m
c)
50 m
100 m
d)
20 m
e)
200 m

units, the vein-like features are typically narrower and can occur as isolated, linear (e.g., Figure 17b) to arcuate (e.g., Figure 17e) forms. Where these features meet, they consistently do so at right angles (e.g., Figures 17d-e). Shadows cast by these features indicate that, in some cases, they are ridges with positive relief; in other examples, no relief can be inferred and a dark-toned line is observed along the center of the light-toned features (Figure 17e). Within some outcrops of the pitted, discontinuous light-toned unit, the vein-like features occur as networks of polygonal patterns (Figure 17c). We have observed no large-scale patterns associated with the alignments of the vein-like features, with the exception of the linearly aligned features at the kilometer-scale within some occurrences of the brecciated unit.

Hypotheses and interpretations. We interpret the vein-like features as fracture-fills within the brecciated ridge-forming and other stratigraphic units. The dark-toned line observed dividing some features (Figure 17e) could be the fracture itself, while the lighter-toned ridges consist of the erosion-resistant material filling or cementing a fracture. In locations such as these, where the light-toned ridges occur in parallel pairs, they may also be the arched up antiform margins of megapolygons (or "teepees") (Kendall and Warren 1987). The origin of the fractures within multiple units may be regional stresses or residual stresses from the formation of Eberswalde crater. In the latter case, the fractures would be expected to be aligned radially from the center of the impact and parallel to the crater rim (e.g., Melosh 1989); however, because we observe no large-scale pattern in the alignment of features, we cannot distinguish large-scale impact-induced stresses from smaller-scale regional (including possible impact-related) stresses.

The composition and origin of the fracture-filling material is unknown; however, on Earth, a variety of fracture filling minerals, derived from precipitation of fluids, can be found in basaltic settings. These include carbonate, clay, silica (opaline and quartz), zeolites, or sulfates, the occurrence of which are dependent on the host rock composition, source of the precipitating fluids, pH, water-rock ratio, and temperature (e.g., Kendall and Warren 1987). Fracture-fills have been observed within martian meteorites (e.g. Rao et al., 2008), and have previously been identified elsewhere on Mars with in-situ (Knoll et al., 2008) and orbital (Okubo and McEwen 2007) observations.

The vein-like features could also be dikes formed by igneous intrusions (which have been proposed for similar features in other martian craters by Head and Mustard 2006) or pressurized/fluidized sediment (e.g., mud-sand dikes). The vein-like features within megabreccias associated with Holden crater have been interpreted as breccia injection dikes (Grant et al., 2008; Tornabene et al., 2009), and are morphologically similar to those observed with the brecciated ridge-forming unit in Eberswalde. Igneous dike swarms tend to be parallel, en echelon, or radially oriented (Neuendorf et al., 2005), which is consistent with some (but not all) of those observed within the brecciated unit (Figure 6b-c). Another possibility is that the veins represent fractures that captured loose/transported sediment and debris, potentially of differing composition, which was then buried and lithified and is now being exhumed and preserved in inverted relief.

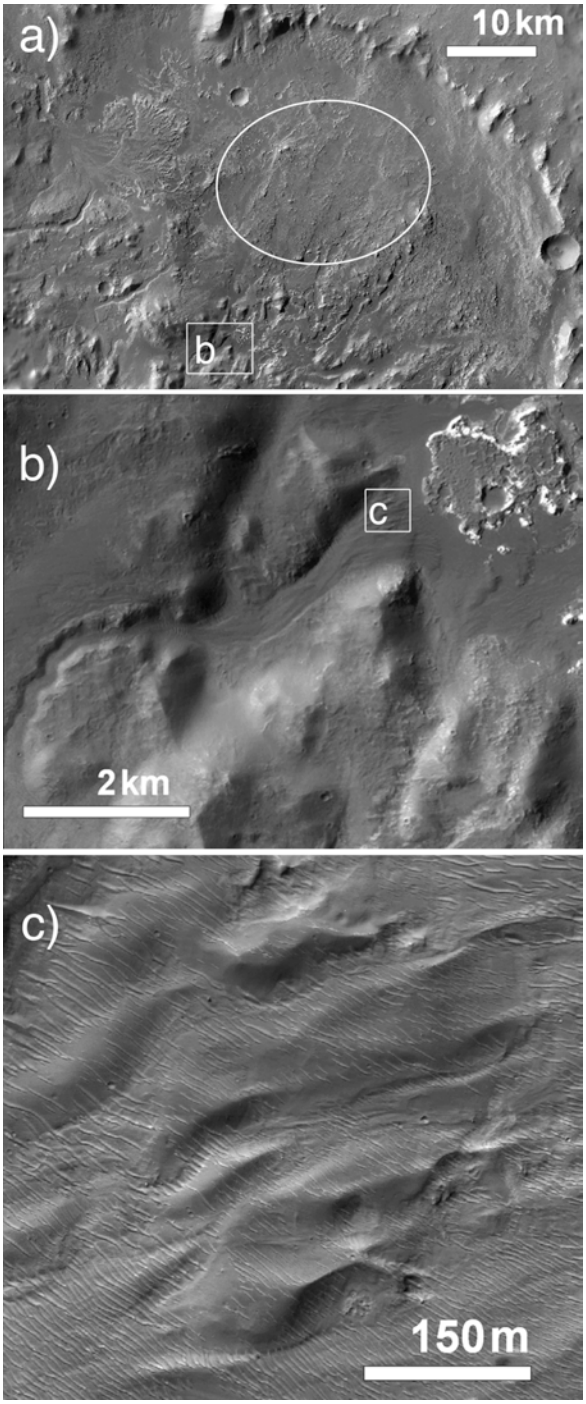

Figure 18. Example of a channel-like feature in southern Eberswalde: (a) CTX mosaic of Eberswalde crater indicating the location of 18b and the proposed MSL landing ellipse; (b) a channel-like feature cutting the south rim of Eberswalde crater, the white box shows the location of 18c (from HiRISE observation ESP_018056_1560_RED); (c) detail of yardangs and bedforms at the end of the valley. North is oriented at the top of the page in all images.

4.2 Valley features

Observations. Several valley features are observed on the northern, western, and southern rims of Eberswalde crater. These features are 200-800 m wide, linear to sinuous valleys that originate on the plains surrounding Eberswalde and terminate within the crater. The valley-fill material is mapped as the mantling unit in Figure 3, which is fluted with grooves parallel to the valley walls (e.g., Figure 18b). Near the basinward terminations of these features, the valley-fill material is eroded into linear ridges that resemble yardangs. Throughout the valleys, the dark valley-fill material is superposed by linear bedforms spaced ~10 m apart and aligned perpendicular to the valley walls (e.g., Figure 18c).

Hypotheses and interpretations. Sinuous valleys similar to those along the walls of Eberswalde crater have been observed on Mars since the Mariner 9 mission, and have been interpreted to have been carved by the movement of liquid water (e.g., Carr 1996). The linear grooves parallel to the valley walls are morphologically similar to the lineated valley fill observed near the northern dichotomy boundary (Squyres 1978) that has been interpreted as debris-covered glaciers (Morgan et al., 2009). However, we have observed no lobate debris aprons at the valley termini that would support the presence of glaciers. Instead, we interpret the grooved features present where the valleys meet the basin as yardangs (e.g., McCauley et al., 1977) carved from the valley floor materials by wind erosion.

4.3 Sinuous ridges

Observations. We have identified many sinuous features with raised relief

Figure 19. Examples of sinuous ridges in Eberswalde crater: (a) CTX mosaic of Eberswalde crater indicating the location of 19b-e and the proposed MSL landing ellipse; (b) sinuous ridges within the landing ellipse, with the inset showing light-toned material exposed beneath the ridge (from HiRISE observation PSP_016065_1560_RED); (c) branching, sinuous ridge structure in eastern Eberswalde (from HiRISE observation PSP_001600_1560_RED); (d) sinuous ridge in southwest Eberswalde with layers visible (from HiRISE observation ESP_018056_1560_RED); (e) highly sinuous ridges on the northern crater wall (from HiRISE observation PSP_001600_1560_RED). North is oriented at the top of the page in all images.

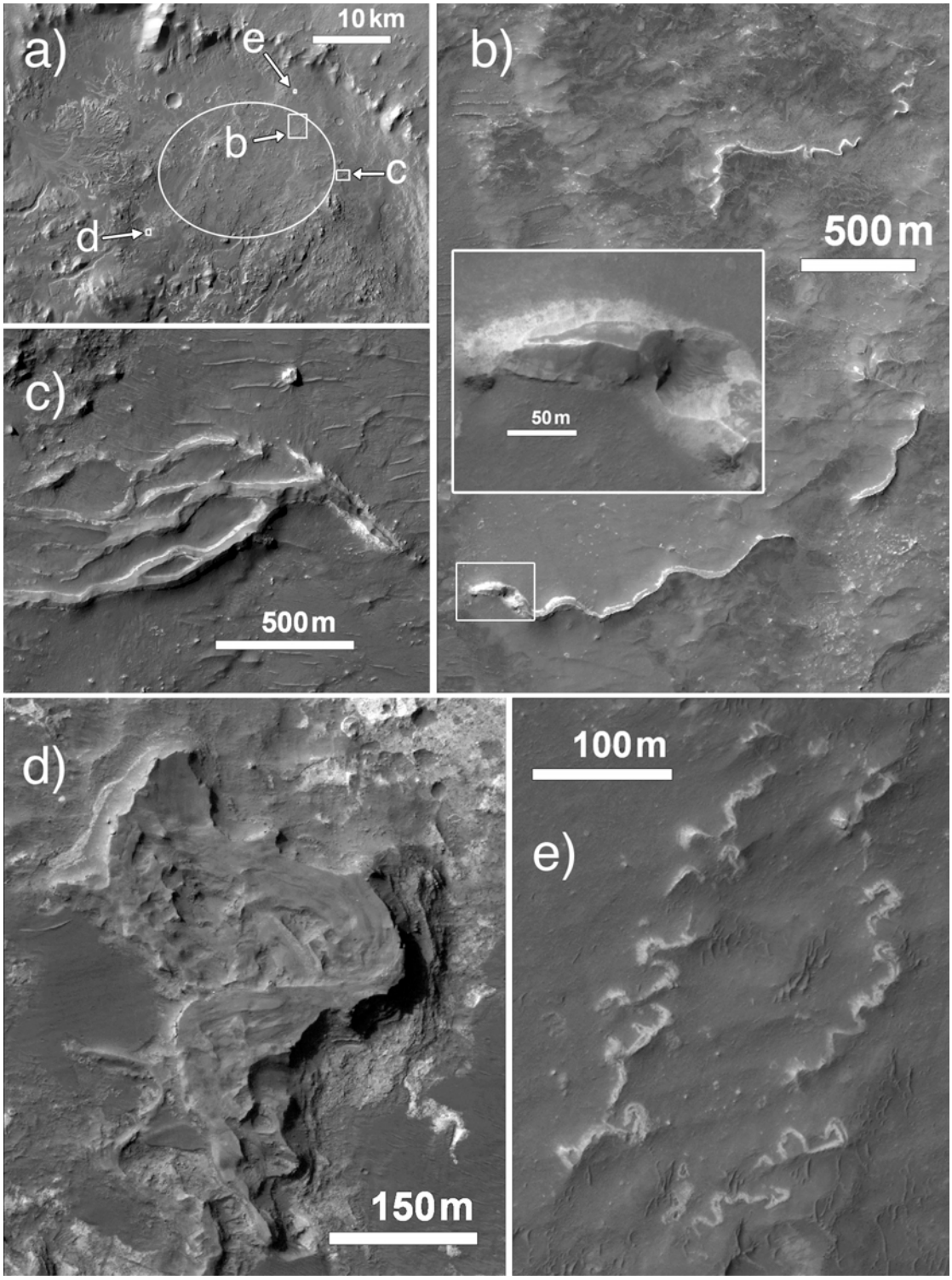
a)
10 km
e
b
c
d
b)
500 m
50 m
c)
500 m
d)
150 m
100 m
e)

(locations shown in Figure 16), with lengths ranging from 10 m to 3 km and widths ranging from 10-100 m. These ridges occur as thin forms (e.g., Figure 19b,e), wider meander-like forms (e.g., Figure 19d), or networks of branching features (e.g., Figure 10a, Figure 14e, Figure 19c). All sinuous ridges observed are covered by the mantling unit along the ridge, and expose lighter-toned material to varying degrees along their edges.

The sinuous features in different regions of Eberswalde crater have distinct morphologies. Those in the northern and eastern portions of the crater, for example, form sharp ridges covered by the mantling unit and revealing the massive light-toned unit at their bases (Figure 19b-c). Those in the south and western portions of the crater are wider plateaus covered by the mantling unit and exposing the layered light-toned unit (e.g., Figure 19d) or the fractured light-toned unit (e.g., Figure 15c) along cliff faces. The northern crater wall is covered with sinuous ridges distinct from those observed elsewhere in the Eberswalde basin in that they are extremely narrow, highly sinuous, and often occur as chains of elongated mesas (e.g., Figure 19e).

Hypotheses and interpretations. Sinuous ridges similar to those observed in Eberswalde crater are common on Mars (Edgett 2005) and have been interpreted as inverted channels similar to those observed in Oman (Maizels 1990) and the Colorado Plateau (Williams et al., 2009). In arid environments on Earth, ancient fluvial channels become inverted in relief when they are filled with a material that is more erosion resistant than the surrounding terrain, either by chemical cementation, "armoring" by course grains, or infilling by lava flows (Pain et al., 2007; Williams et

al., 2009). The surrounding, less resistant material erodes before the channel-fill, and the channel remains as a raised ridge or a chain of mesas/hills.

An alternate hypothesis is that some ridges are an erosion-resistant fracture-fill material, similar to the vein-like features. The sinuosity of the ridges, however, is distinct from the vein-like features, which are linear to actuate, and are typically much narrower. Furthermore, the sinuous ridges often branch and anastomose (e.g. Figures 10e, 19c), which is also more consistent with the morphology of fluvial channels.

We interpret the sinuous ridges as inverted fluvial channels composed of cemented and/or course-grained material. Because we observe no accumulations of boulders or talus at the base of these features, we suggest that the ridge-forming material weathers into sand-sized grains (< 300 μm; Sharp 1963) that are transported away by winds.

The sinuous ridges near the margins of the basin that are associated with valley features may be fluvial sediments that have been deposited either subaerially or subaqueously (within an Eberswalde basin lake), and may have been transported from the plains surrounding Eberswalde crater via the valleys. Some ridges, however, are not associated with valley features (such as those on the northern rim and those within the basin) and thus their sediment source regions are less easily inferred.

4.4 Fan-form plateaus

Observations. The most significant fan-form plateau in Eberswalde crater is the famous "delta" in the west (Figure 11) that has been extensively examined in previous studies (Malin and Edgett 2003; Moore et al., 2003; Bhattacharya et al.,

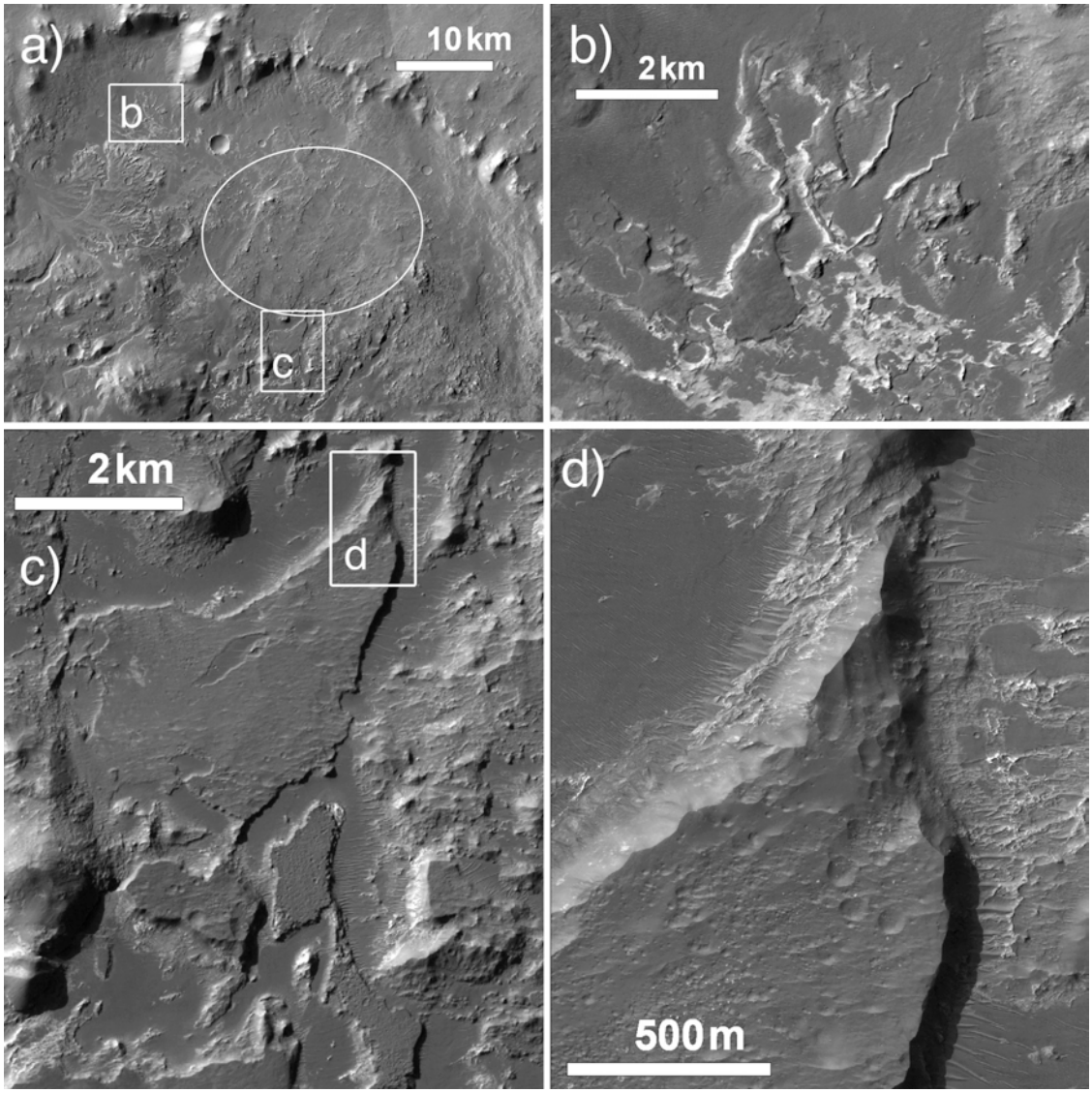

Figure 20. Examples of fan-like plateaus and tabular mesas in Eberswalde crater: (a) CTX mosaic of Eberswalde crater indicating the location of 20b-d and the proposed MSL landing ellipse; (b) fan-like mesas associated with sinuous ridges in northwest Eberswalde (from CTX observation P01_001336); (c) tabular mesas in southern Eberswalde (from HiRISE observation PSP_009274_1560_RED); (d) edge of a mesa showing the cratered and scalloped morphology and the discontinuous, light-toned unit exposed below (from HiRISE observation PSP_010474_1560_RED). North is oriented at the top of the page in all images.

2005; Jerolmack et al., 2004; Wood 2006; Lewis and Aharonson 2006; Pondrelli et al., 2008; 2011; Rice et al., 2011). This plateau of layered rock (with the layered, light-toned unit exposed along its edges) originates at a valley feature in the west of the crater and extends ~12 km into the basin (Figure 11a). The surface of this feature preserves sinuous ridges with measured sinuosities of 1.1 to 1.8 (Wood 2006). As described by Pondrelli et al. (2008), the forms of the preserved sinuous features range from rectilinear to meandering. They also appear to be grouped into multiple deposits, and have been mapped in previous studies as three (Bhattacharya et al., 2005) or five (Wood 2006; Pondrelli et al., 2008) separate lobes.

A smaller (~1.5 km wide), fan-shaped plateau of layered rocks in the north of the crater (Figure 12b) was noted by Schieber (2008). The layers are not traceable around the entire plateau, due to obscuration by the mantling unit, but are visible for ~100 m along its edge (Figure 12c). A ~300 m wide fan-shaped feature immediately northeast (Figure 12b) terminates at the end of a highly sinuous ridge. Due north of the proposed Eberswalde delta, two fan-form plateaus are associated with a network of sinuous ridges (Figure 20b). These features were mapped as an extension of the putative Eberswalde delta by Pondrelli et al. (2008). An additional fan-form plateau is located in the southwest of the crater (Figure 13d). This feature preserves sinuous and digitate ridges that appear to have eroded into a stair-step pattern of layered rock (e.g., Figure 11f). Further descriptions of these fans are provided by Rice et al. (2011).

Hypotheses and interpretations. Based on its morphology, association with a valley feature, lithology, and mineralogy, the largest fan-form plateau in the west of the crater has been widely interpreted as a lacustrine delta (Malin and Edgett 2003;

Moore et al., 2003; Bhattacharya et al., 2005; Wood 2006; Lewis and Aharonson 2006; Pondrelli et al., 2008; Pondrelli et al., 2011). Schieber (2008) hypothesized that the fan-form plateau in northern Eberswalde crater was the erosional remnant of an additional delta, and Rice et al. (2011) interpreted this and the other fan-shaped features in Eberswalde as deltaic as well.

Jerolmack et al. (2004) proposed that the largest fan-shaped feature was an alluvial fan, and the other features in Eberswalde could be alluvial fans as well. However, the fan-shaped plateaus and layered deposits of the other features do not initiate at the break in slope associated with the wall of the crater, as might be expected for alluvial fan formation (e.g., Williams et al., 2006). Instead, channel bifurcation to create a fan-shaped sediment body occurs basinward of the crater rim, implying that fluvially transported sediments were deposited along a shoreline and into a standing body of water. The multiple, bifurcating inverted channels preserved on the fan-shaped features are consistent with this interpretation.

4.5 Tabular mesas

Observations. The southern rim of Eberswalde crater is partially covered with mesas that, like the fan-form plateaus, are obscured by the dark mantling unit but expose light-toned material at their bases and at cliff faces. Unlike the possible fans, however, these tabular mesas do not preserve sinuous ridges and do not exhibit any layering at the scale of HiRISE resolution (~25 cm/pix). The distribution of these features is shown in Figure 16. The surfaces of the mesas preserve many small craters and exhibit pitted, scalloped morphologies (e.g., Figure 20c-d). Some of these mesas

expose the layered light-toned unit beneath their mantled surfaces (e.g., Figure 13), while others in the south of the crater appear to be comprised of the pitted unit (Figure 20d). The tabular mesas have been eroded into irregular shapes (e.g., Figure 20d) with no apparent preferred orientation.

Hypotheses and interpretations. Although the tabular mesas could be interpreted remnants of fan-form plateaus, we infer that these features have a separate depositional history because of their distinct surface morphologies (pitted and scalloped), preservation of small craters, and lack of visible layering. The mesas comprised of the layered light-toned unit may be eroded lacustrine sediments. Those comprised of the pitted unit are more difficult to interpret, as the pitted unit covers much of the Eberswalde basin (Figure 4) and is only associated with the tabular mesas in the south of the crater. We hypothesize that the mesas of the pitted unit are the eroded remnants of a more continuous, crater-filling unit. The mesas may remain because they are protected by a resistant capping unit.

It is possible that the tabular mesas are landforms carved by glacial movement, similar to the mesas interpreted to be associated with debris-covered glaciers in Deuteronilus Mensae (Dickson et al., 2008). Although there is no evidence for present glaciation in Eberswalde crater (such as lobate debris aprons), it may be that past glaciation had modified the southern rim of the crater and carved the irregular-shaped landforms. However, this hypothesis is speculative.

4.6 Concentric, quasi-circular features

Observations. In several locations within the Eberswalde basin, we have

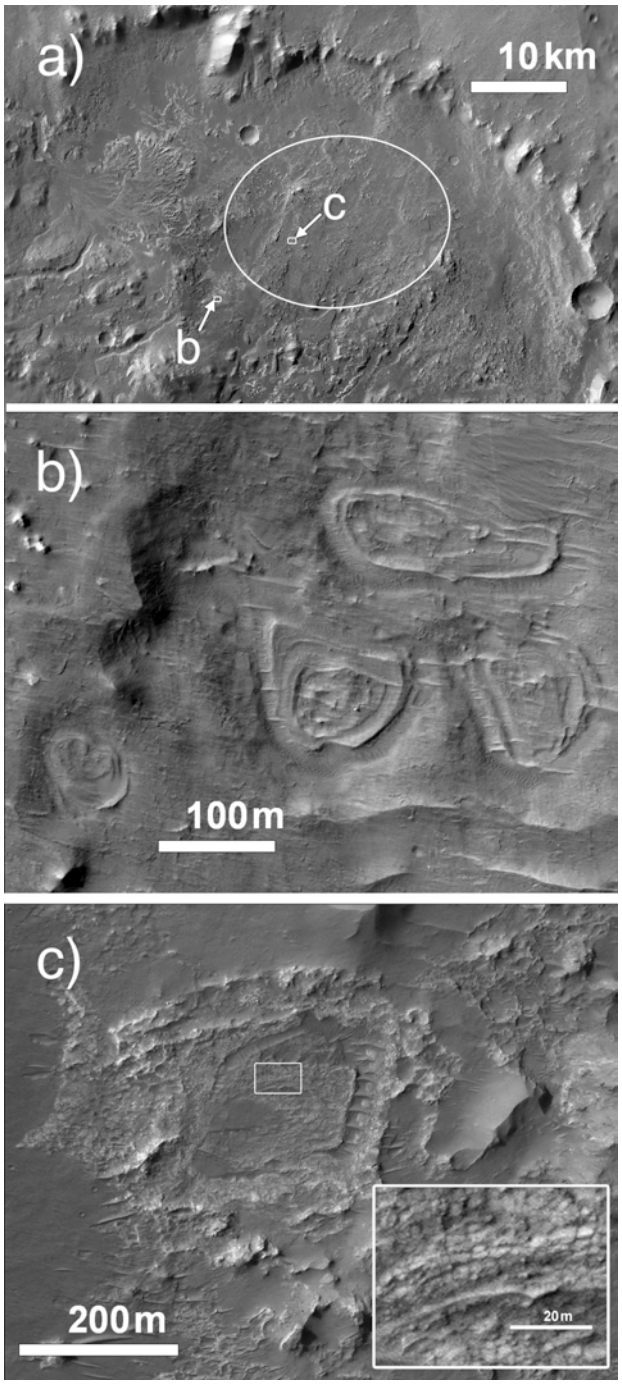

Figure 21. Examples of concentric, quasi-circular features in Eberswalde crater: (a) CTX mosaic of Eberswalde crater indicating the location of 21b-c and the proposed MSL landing ellipse; (b) features in southwest Eberswalde covered by the mantling unit (from HiRISE observation ESP_018056_1560_RED); (c) feature within the landing ellipse, with the inset showing fractured, light-toned material (from HiRISE observation PSP_007481_1560_RED). North is oriented at the top of the page in all images.

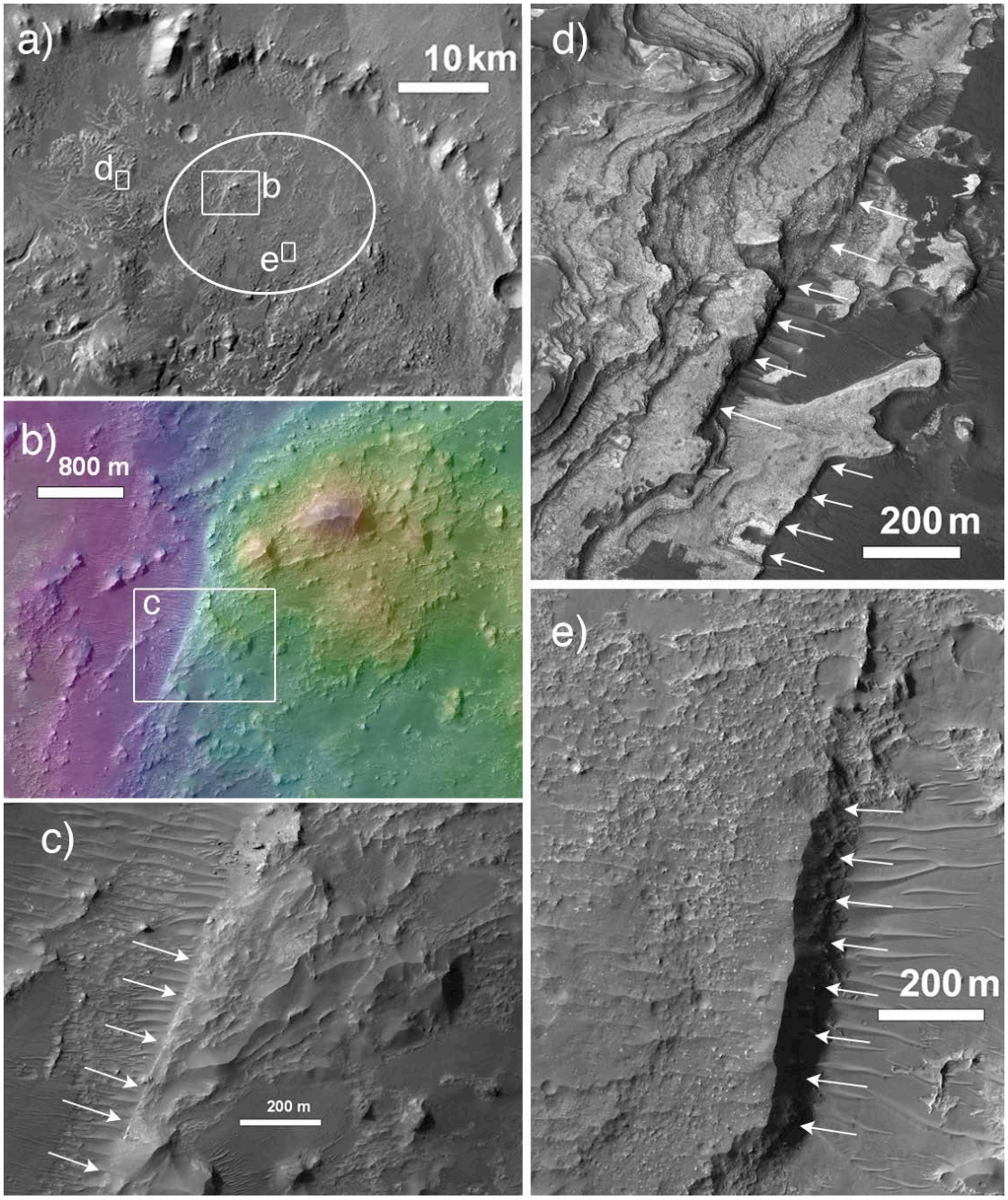

Figure 22. Examples of linear scarps in Eberswalde crater: (a) CTX mosaic of Eberswalde crater indicating the location of 22b,d,e and the proposed MSL landing ellipse; (b) HiRISE DTM (from PSP_008272_1560 and PSP_010474_1560, overlain on image PSP_010474_1560) showing topography of a prominent scarp in central Eberswalde (color scale: red = high = -1000 m; white = low = -1600 m); (c) HiRISE image (from PSP_010474_1560) of a linear scarp, location shown in (b); (d) linear scarps at the front of the "delta" (from HiRISE image PSP_04000_1560_RED); (e) linear scarp in the pitted unit (from HiRISE image ESP_019335_1560_RED). North is oriented at the top of the page in all images.

observed small (<500 m diameter), quasi-circular features with apparent layering. These features are mostly covered by the mantling unit and superposed by bedforms (e.g., Figure 21b), but other features appear to be comprised of the sub-polygonally fractured unit (e.g., Figure 21c).

*Hypotheses and interpretation*s. We interpret the concentric, quasi-circular features as small, infilled impact craters, such as those observed elsewhere on Mars by Malin and Edgett (2000). Concentric crater fill has been interpreted as evidence for glaciations at high latitudes (e.g., Squyres and Carr 1986), but at much larger scales than observed within Eberswalde crater (~100 m radii). Furthermore, there is no evidence for glacial flow into these features. More likely, we hypothesize that preexisting depressions (degraded impact craters) were once filled with sediment and entirely buried; as sediment was eroded and the craters were exhumed, the infilling layers were exposed such that they form concentric rings in plan view. Zimbelman et al. (1989) have interpreted similar features as aeolian crater fill materials.

4.7 Linear scarps

Observations. We have identified 233 linear scarps within Eberswalde crater (Rice et al., 2011), mapped in Figure 16. These features are characterized by cliff faces taller than ~5 m, and the lineations trend predominantly NNE-SSW (Figure 23); nearly two-thirds of these features trend within 15 to 45 degrees from north (Rice et al., 2011). All of these features are characterized by near-vertical scarps; we observe no lateral offsets associated with these lineaments. The linear scarps modify most crater floor materials, including the massive basal, orthogonally fractured, brecciated,

pitted,and sub-polygonally fractured units. The light-toned layered unit is cut by these scarps in some places as well (Figure 23), but in others this unit overlies the linear scarps (Rice et al., 2011).

Hypotheses and interpretations. Pondrelli et al. (2008) noted the presence of linear scarps at the front of the Eberswalde delta, which they interpreted as syn-sedimentary faults, and proposed a large fault system cutting the crater's center. We interpret the lineaments in Eberswalde crater to be dip-slip faults because we observe vertical offsets and no lateral offsets. The dominant NNE-SSW orientation of the faults is inconsistent with the stresses expected from the impact event that formed Eberswalde crater (which should be radial and parallel to the crater walls) (Melosh 1989). Rather, the faults follow this NNE-SSW trend across the width of the crater floor and across its northern rim, onto the highland plains north of the crater, as well as south onto the divide between Holden and Eberswalde craters. We therefore infer that larger, regional post-impact stresses must be responsible for the observed faulting, such as those expected from the formation of Tharsis, for example (Rice et al., 2011).

5. Unit associations, successions and geometries

The spatial distributions of stratigraphic units (Figure 3) and geomorphic features (Figure 16), their relationships to the present basin topography (Figure 23), and their contact relationships can aid our interpretations of the depositional history within Eberswalde crater. The elevation restrictions of each unit are provided in Tables 1 and 2. Below we describe the unit associations, successions and geometries, and use these observations to infer a stratigraphic sequence.

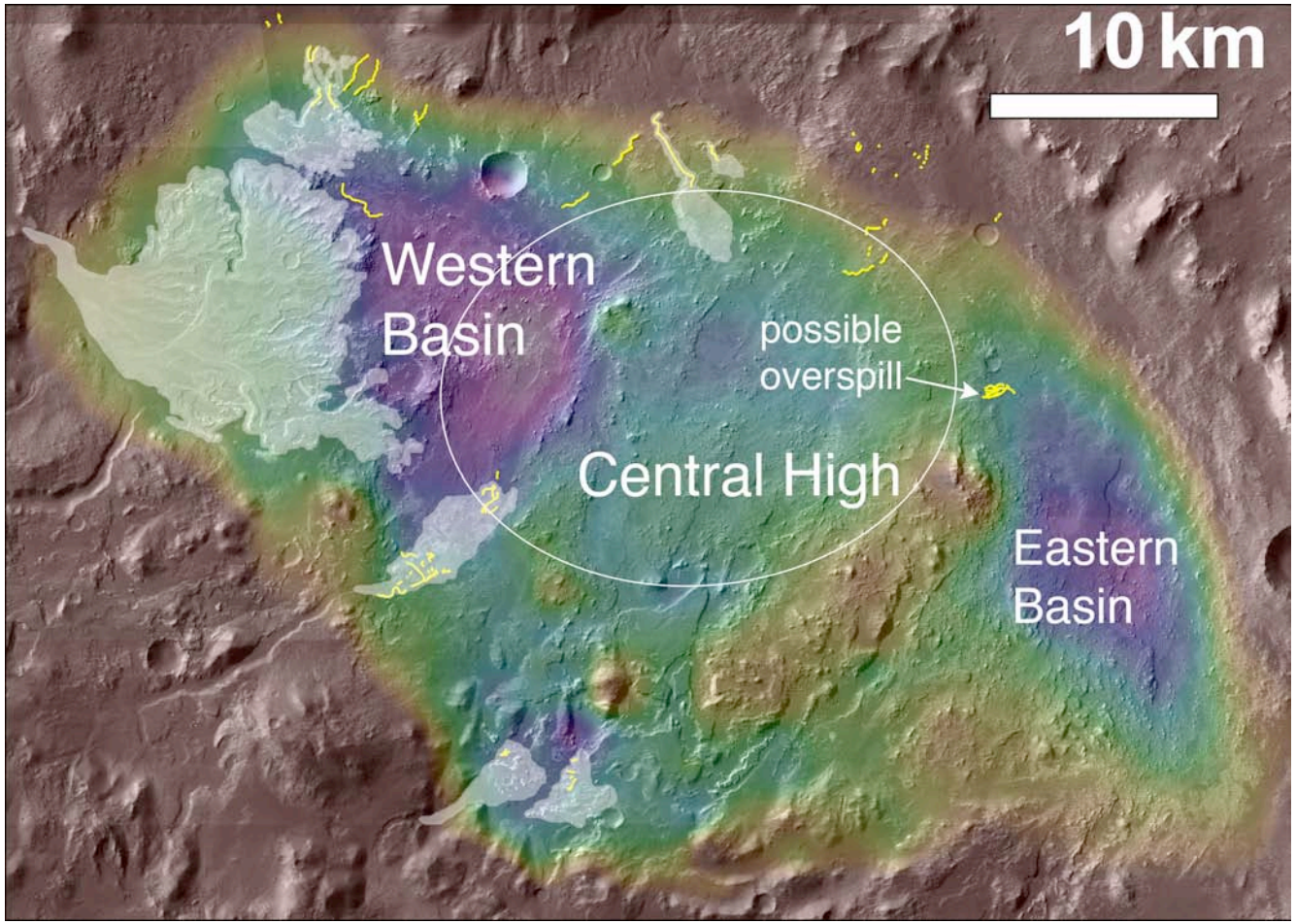

Figure 23. MOLA elevation map (color scale: red = high = –1000 m; white = low = –1600 m) draped over a CTX mosaic, showing the first-order topography within Eberswalde crater: Western Basin, Central High, and Eastern Basin. White regions indicate the fluvio-deltaic systems identified by Rice et al. (2011); yellow lines indicate locations of features interpreted as inverted channels.

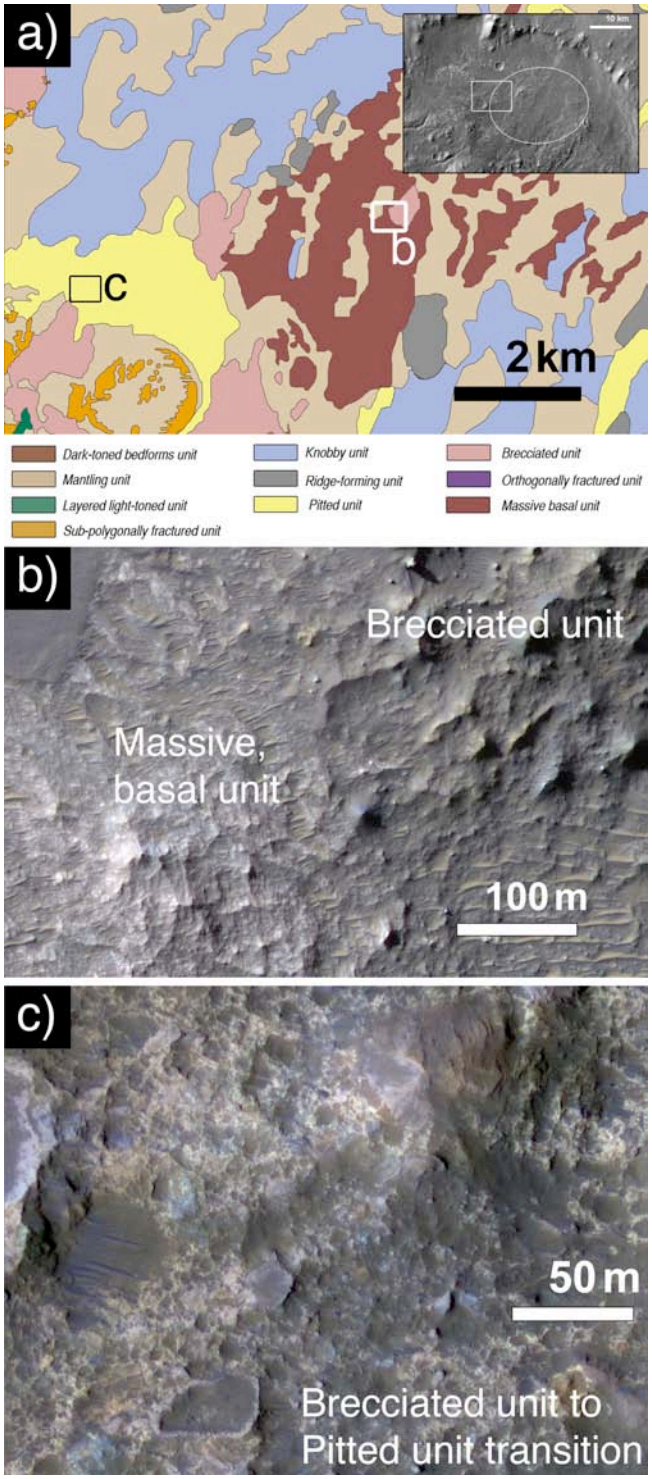

Figure 24. Relationship of brecciated unit to the massive, basal unit and the pitted unit. (a) Detail of stratigraphic unit map, location shown in the inset; (b) Contact between the brecciated and massive units (HiRISE PSP_004000_1560_COLOR); (c) Gradational contact between the brecciated and pitted units (HiRISE PSP_010052_1560_COLOR.

5.1 Observations

The large-scale topography in Eberswalde (Figure 23) divides the crater into three prominent regions: a Western Basin, a Central High, and an Eastern Basin (Rice et al., 2011). These regions are bounded by the linear scarps that trend NNE across the full extent of the crater. Topographically, the massive, basal unit is lower than any other stratigraphic unit; the exposed outcrops are restricted to below the -1495 m contour line. While this unit is variably covered by the mantling material, making contacts with other units difficult to infer, there are some locations where it clearly underlies the brecciated unit (Figure 24b) or the knobby unit.

The brecciated unit crops out at all but the very lowest elevations within the crater (> 1570 m). While this unit clearly superposes the massive, basal unit (Figure 24b), its relationship to the pitted unit is less clear. We have not observed contact relationships between the brecciated and pitted units; rather, one unit always appears to grade continuously into the other. Many outcrops that we have mapped as the brecciated unit in Figure 3 contain pits, and, conversely, many outcrops mapped as the pitted unit contain occasional clasts entrained within pits. Figure 24c shows an example of a transitional region between the brecciated and pitted units, where heterogeneous clasts and pits in the light-toned matrix material are found in close proximity. In this example, the outcrop to the north is predominantly pitted, and the outcrop to the south is predominantly brecciated (as shown in the unit map in Figure 24a).

The vein-like features clearly cut the pitted and brecciated units, but no other crater floor material. Figure 25 shows an example of vein-like ridges within the pitted

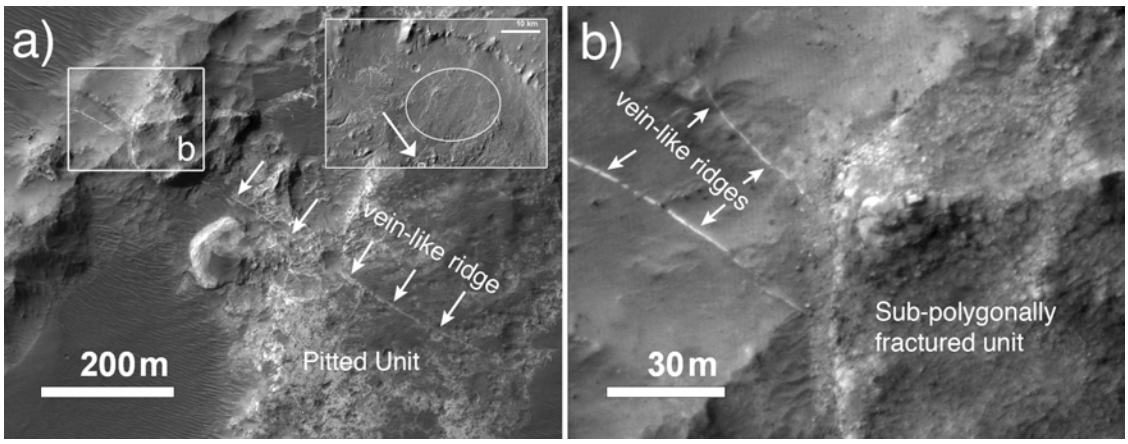

Figure 25. Example of contact relationships between the vein-like features and stratigraphic units. (a) Vein-like ridge cross-cutting the pitted unit but overlain by the sub-polygonally fractured unit (HiRISE ESP_018056_1560), location within Eberswalde crater shown in the inset; (b) Closer view of the sub-polygonally fractured unit overlying the vein-like features, location shown in (a).

unit, with the sub-polygonally fractured unit overlying them. The inset in Figure 17d provides a further example of sub-polygons overlying a vein-like ridge.

The stratigraphic context of the knobby unit is difficult to infer, as contacts with other units are obscured by the mantling unit. The knobs are also not restricted by elevation; they occur at all elevations within the mapped region of the crater (except for the lowest 5 m where the massive, basal unit crops out).

The layered light-toned and sub-polygonally fractured units are restricted to elevations below -1300 and -1320 m, respectively. These two units both appear to unconformably overlay the brecciated and pitted units. At the front of the fan-form plateau in the western portion of the crater (the Eberswalde "delta"), for example, the light-toned layers onlap against the brecciated unit (Figure 26). At this location, and at the other fan-form plateaus associated with valley features at the margins of the crater, we observe a repeated package of three stratigraphic units: (1) the layered light-toned

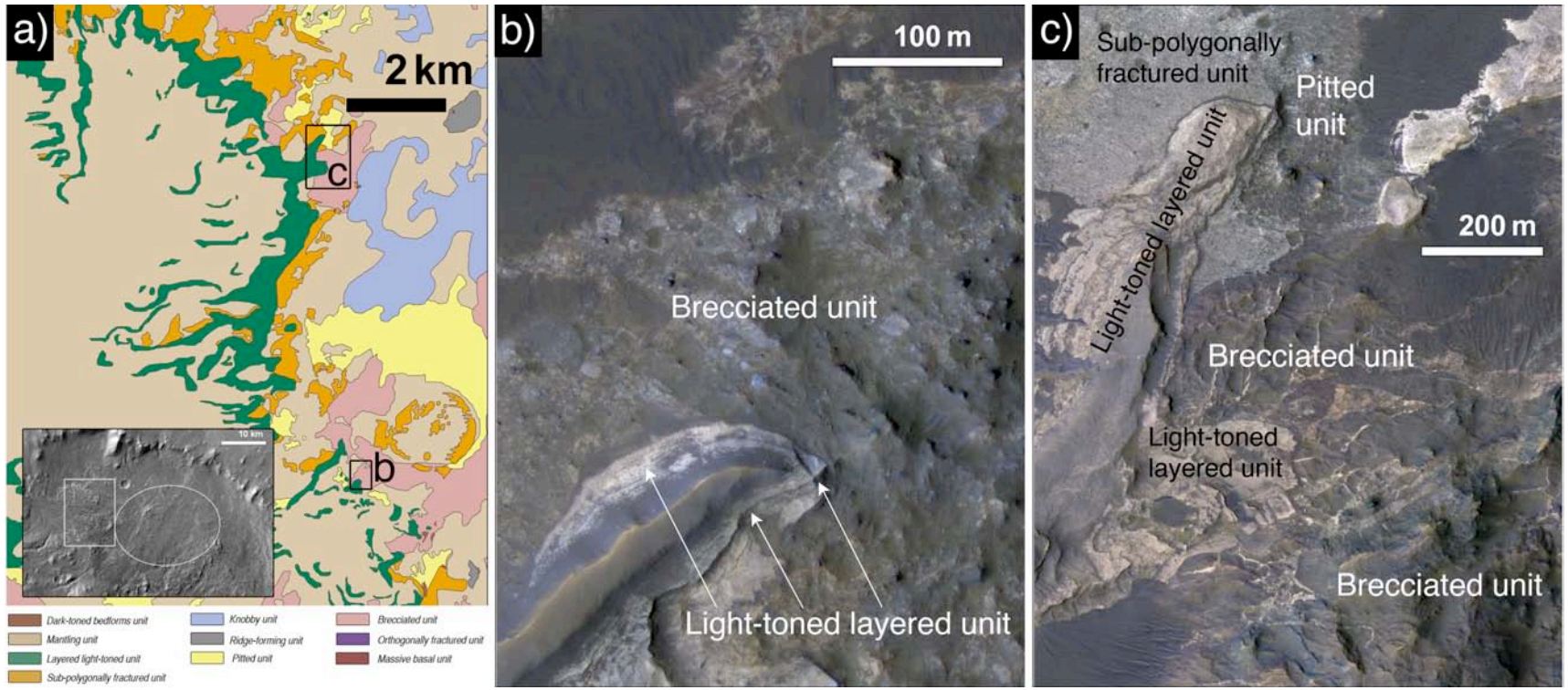

Figure 26. Examples of the light-toned layered unit in contact with other units at the front of the Eberswalde "delta". (a) Detail of stratigraphic unit map, location shown in the inset; (b) Light-toned layers unconformably overlying the brecciated unit; (c) The layered light-toned and sub-polygonally fractured units directly overlying the brecciated and pitted units at the delta front (HiRISE PSP_004000_1560_COLOR).

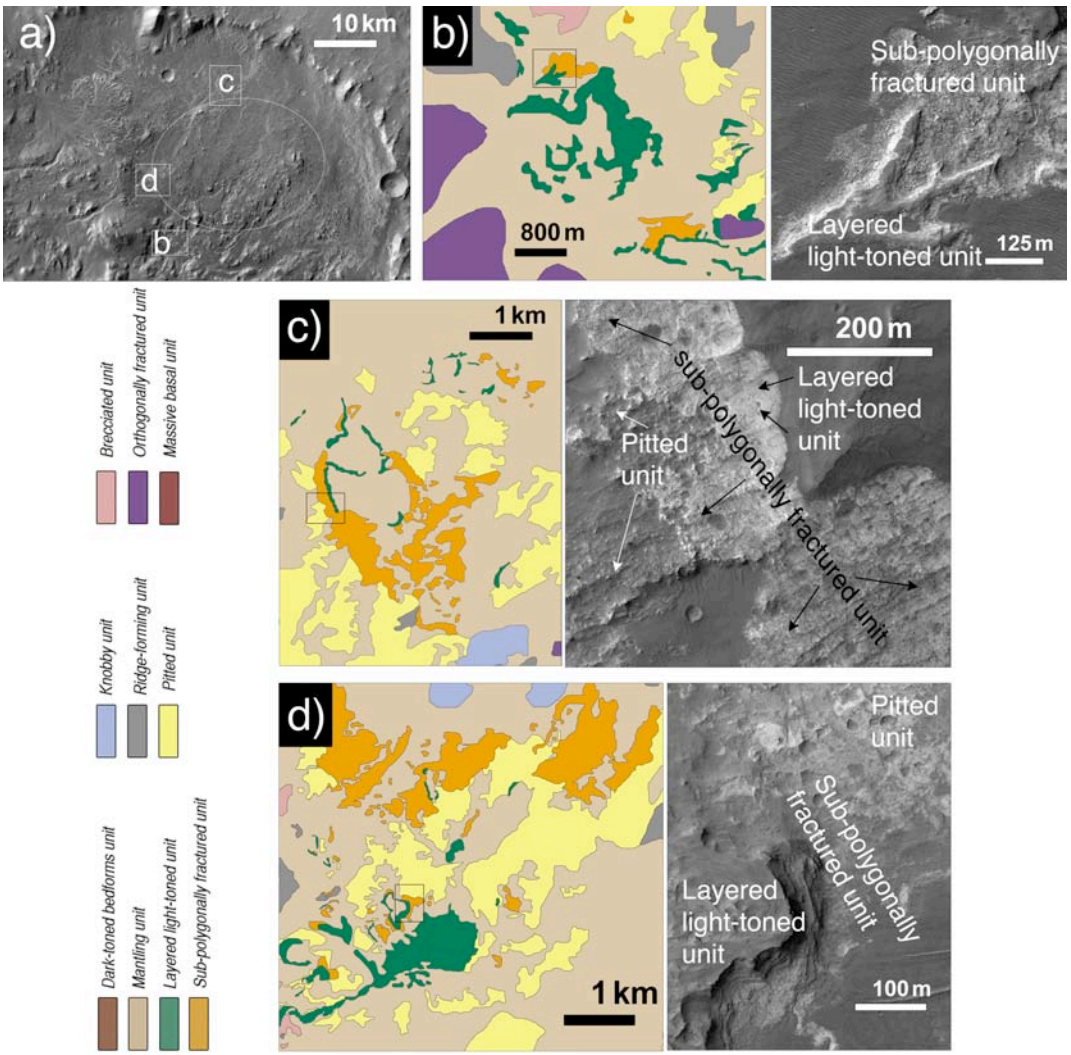

Figure 27. Examples of the three-unit pattern observed in association with channels that cut the Eberswalde crater walls: (1) the layered light-toned unit (mapped in green) conformably overlying (2) the sub-polygonally fractured unit (mapped in orange) unconformably overlying (3) the pitted unit (mapped in yellow). (a) CTX mosaic of Eberswalde crater indicating the location of 27b-d and the proposed MSL landing ellipse; (b) Detail of stratigraphic unit map in the south of the crater (left) where light-toned layers are in contact with the sub-polygonally fractured unit (right; HiRISE ESP_018056_1560_COLOR) and topographically above the pitted unit; (c) Detail of stratigraphic unit map at fan-form plateau interpreted as a remnant delta in the north of the crater (left) where light-toned layers are in contact with the sub-polygonally fractured unit, which overlies the pitted unit (right; HiRISE PSP_005556_1560_COLOR); (d) Detail of stratigraphic unit map at fan-form plateau interpreted as a remnant delta in southwest Eberswalde (left) where the light-toned layers exposed at the edge of a sinuous ridge are in contact with the sub-polygonally fractured unit, which overlies the pitted unit (right; HiRISE ESP_018056_1560_COLOR).

unit conformably overlying (2) the sub-polygonally fractured unit unconformably overlying (3) the pitted unit. At each of the six systems of outcrops associated with valleys that Rice et al. (2011) interpreted as fluvio-deltaic systems (mapped in Figure 23), these three units are observed in succession. Examples from the northern, southwestern and southern systems are shown in Figure 27.

The sinuous ridges in Eberswalde crater, which we interpret as inverted channels, are restricted to elevations above -1490 m. The distribution of these features with respect to the crater topography is provided in Figure 23; with one notable exception, all sinuous ridges are confined to the margins of the crater and/or are associated with a drainage valley and a proposed fluvio-deltaic system. The exception (Figure 19c) occurs along the boundary of the Central High and the Eastern Basin (location shown in Figure 23).

The mantling unit is the only unit observed in contact with every other crater floor unit. We observe that the mantling material consistently overlies every unit except for the dark-toned bedforms unit. No stratigraphic unit appears to overlay the mantling unit, with the possible exception of the layered light-toned unit (it is possible that the lower-albedo layers observed within this unit are interbedded mantling deposits).

5.2 Hypotheses and interpretations

Based these observations, we infer the following stratigraphic sequence for the units in Eberswalde crater (illustrated in Figure 28): (1) the dark-toned bedforms unit overlies (2) the mantling unit, which may be interbedded with (3) the light-toned

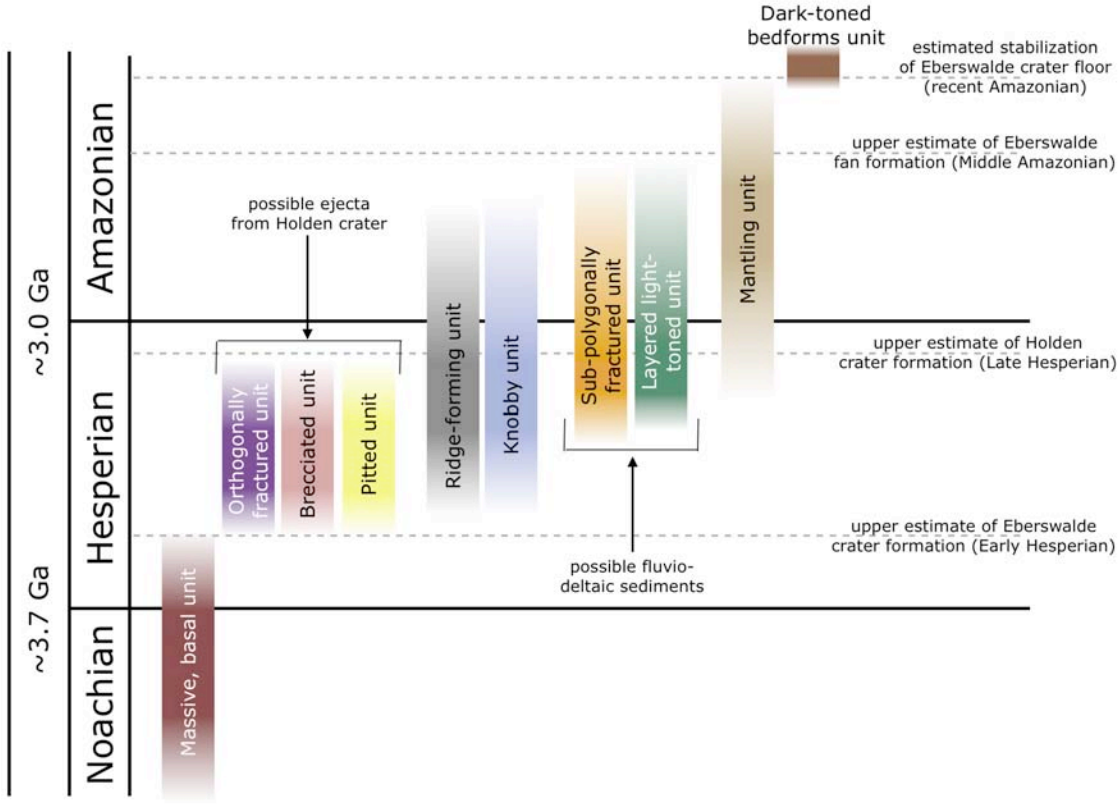

Figure 28. Inferred stratigraphy of the Eberswalde crater units mapped in Figure 3. Estimates of the Noachian, Hesperian and Amazonian periods as well as the approximate model ages that define the boundaries between them are shown in the left columns. Dashed lines indicate age estimates for major events in Eberswalde's geologic history: the crater's formation (upper estimate of Early Hesperian, as shown by this work); the formation of Holden crater (upper estimate of Late Hesperian; Irwin and Grant, 2011); the formation of the Eberswalde fan (Middle Amazonian; Grant and Wilson, 2011); and the stabilization of the Eberswalde crater floor (recent Amazonian, as shown by this work). Interpretations of unit successions and depositional age estimates are discussed further in the text.

layered unit. This unit conformably overlies (4) the sub-polygonally fractured unit, but the relationship between (3-4) and (5) the ridge-forming unit and (6) the knobby unit remains unclear. However, (3-6) all uncomformably overlay (7) the pitted unit, which grades continuously into (8) the brecciated unit, which may have been

emplaced contemporaneously with (9) the orthogonally fractured unit. The deepest unit is (10) the massive, basal unit, which unconformably underlies (7-8).

6. Impact crater statistics and chronology of Eberswalde crater floor materials

6.1 Observations

Our crater counts within Eberswalde crater include all craters with diameters (D) > 100 m, and are plotted in Figure 29a. The total area of the crater floor is 1188 km2 and includes 571 counted impact craters. For craters with D > 700 m (only 7), the cumulative frequency curve roughly follows the 3.5 Ga isochron. For craters with D < 700 m, we see a reduction in the slope of the cumulative frequency curve that is indicative of a process of crater resurfacing. A resurfacing correction (Michael and Neukum 2010) was therefore applied to the data at D < 700 m and indicates a crater retention age of ~360 Ma. To reveal variation in impact crater density across Eberswalde crater, and to therefore identify lateral heterogeneity in material properties and crater retention ages, we generated a crater density map (Figure 29b) by assigning the center of each crater to a point shapefile in ArcGIS. The density map indicates that the center of Eberswalde crater, in the region where we map the most extensive aeolian mantle, has the lowest impact crater density. The crater density throughout the majority of the crater floor appears fairly uniform, aside from pockets of high density in the southeast portion of the crater where we have observed well-indurated tabular mesas.

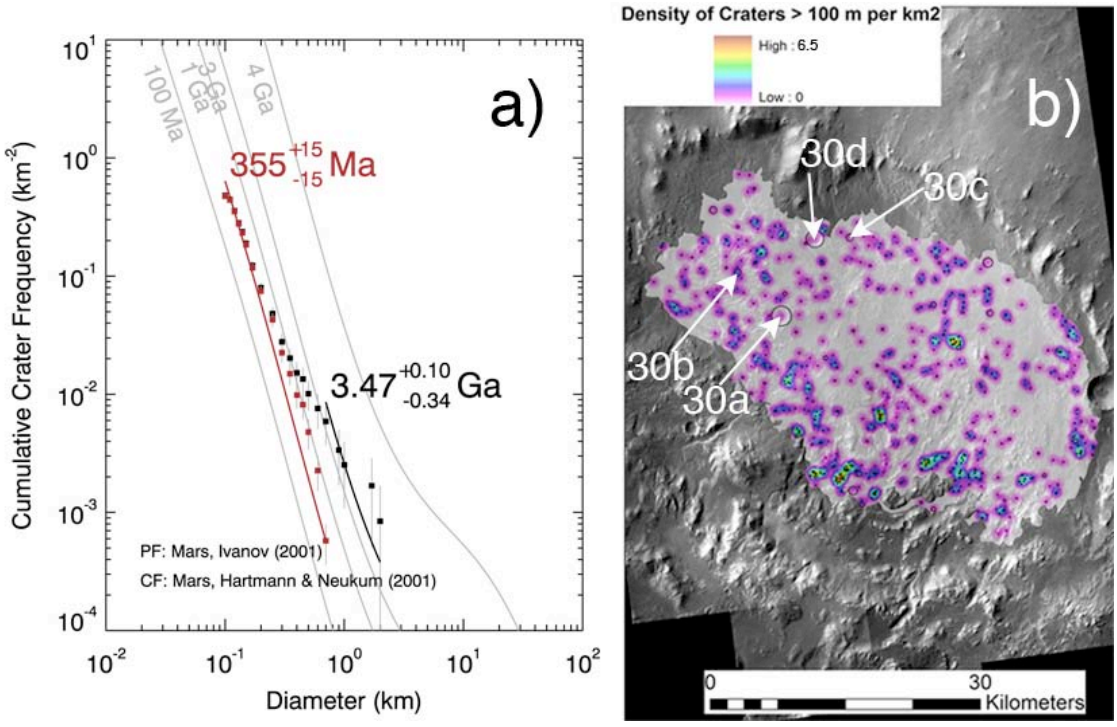

Figure 29. (a) Crater size-frequency distribution for the Eberswalde crater floor materials. CF is chronology function (Hartmann and Neukum, 2001), PF is a production function (Ivanov, 2001). (b) Crater density map of the 1188 km^2 region within Eberswalde crater discussed in this study, overlain on a CTX basemap (north is up). The largest craters are indicated by black outlines, and arrows indicate the locations of Figure 30a-d.

6.2 Hypotheses and interpretations

The small area and small number of craters counted in this analysis limits our ability to obtain absolute model ages for specific units (e.g., the fluvial-deltaic units). We therefore obtained a crater model age (Figure 29a) for the entire floor of Eberswalde crater including all craters that have impacted into the geologic units described in this analysis. Crater model ages obtained from a bulk analysis may be deceiving if the crater statistics are included from several spatially distinct geologic formations that have broad differences in formation ages and/or crater retention characteristics. If both old basement rock and younger infilling units are present, for

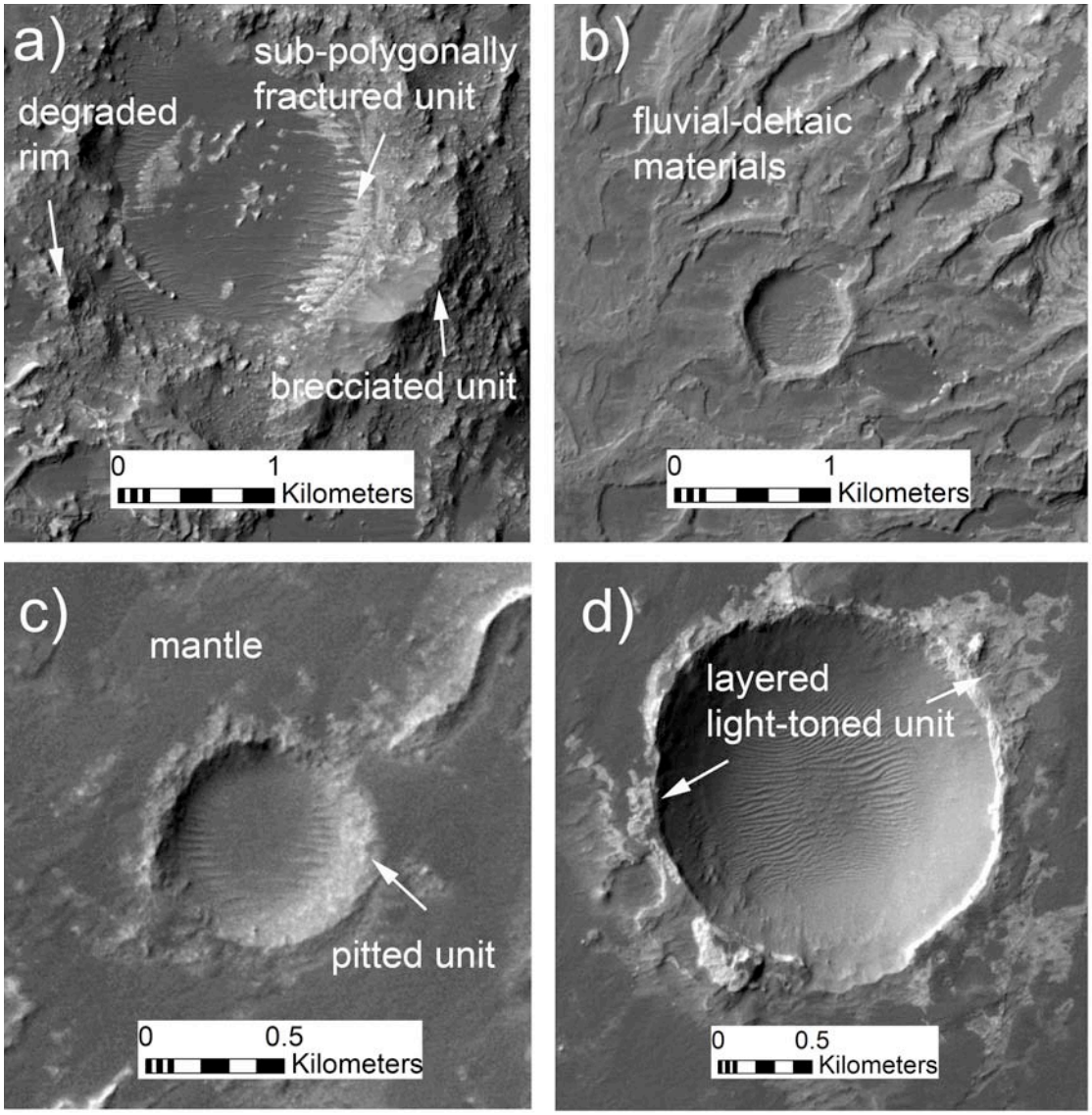

Figure 30: CTX image montage of large (D > 700 m) impact craters on the floor of Eberswalde crater. a) 2-km-diameter impact crater that sits within Eberswalde crater floor materials. Light-toned units that are part of the fluvial-deltaic sequences of the putative delta rest on the floor of the crater. The rim is highly degraded and the crater contains significant aeolian infill. b) 700-m-diameter impact crater that rests on top of the putative delta. This crater exhibits significant rim degradation. c) 700-m-diameter crater that rests on the floor materials of Eberswalde crater. Low-albedo mantling material obscures the crater rim and ejecta blanket. d) 1.8-km-diameter crater on the floor of Eberswalde crater. Isolated remnants of layered light toned materials rest on top of the crater rim.

example, there may be an overall shift in the cumulative frequency curve, providing an age estimate that is not truly representative of either material. However, crater statistics that are separated for individual geologic units that cover small areas (on the order of 100 km2 at CTX resolution), by probability of surface crater density, may exclude the large crater population (only 12 craters within Eberswalde with D > 500 m). Small area crater counts therefore provide a model age that may only include the population of small diameter impact craters that is most susceptible to processes of resurfacing, thus providing erroneously young ages (Neukum et al., 2010). Here, instead of focusing on absolute age estimates we instead use the shape of the cumulative frequency curve for Eberswalde crater to provide general information about the overall geologic history of the crater floor materials and to demonstrate that the craters are recording a very complex history of deposition and degradation since the Early Hesperian.

The kink in the slope of the cumulative frequency curve for craters with D < 700 m (Figure 29a) is consistent with small crater resurfacing, most likely the result of preferential burial (e.g., by airfall deposits) or preferential erosion of smaller craters. Both processes have likely operated within different regions of the Eberswalde crater floor since the basin formed, as we observe both degraded rims on craters across this region and crater-infilling by a low-albedo mantling unit that obscures the smallest craters in the center and western regions of Eberswalde crater (Figure 29b). The gradual decline in slope between D = 100 m and 700 m is more typical of a steady state, long-term resurfacing process where larger craters are better preserved relative to smaller craters (e.g., dust burial or wind erosion), rather than an instantaneous

resurfacing (such as a volcanic event) or an exhumation process upon which a new, younger population is established (Neukum et al., 2010). A fairly good fit is re-established for D < 200 m (including 480 craters), suggesting that there has been limited crater degradation in the recent Amazonian.

There are only seven craters larger than 700 m in diameter on the floor materials within Eberswalde crater. From these seven, an Early Hesperian crater retention age of ~3.5 Ga (+0.1/-0.3 Ga) can be estimated. Several of these craters have highly degraded rims that indicate some process of crater destruction that is also likely responsible for complete resurfacing of the smaller crater population (Figure 30). Due to the poor preservation of their crater rims and ejecta blankets, the geologic context of this crater population relative to Eberswalde crater floor materials is difficult to determine visually. We observed that the fluvial-deltaic materials both bury and are impacted by members of this population (Figure 30a-b). The presence of these sub-polygonally fractured and/or layered light-toned units within and on top of the rims of some of the larger craters (Figure 30a, d) suggests that they may have been present at least before the most recent era of fluvio-lacustrine activity (there is, however, no way to determine how much time passed between the crater formation and their infilling by the light-toned deposits). Furthermore, in the center of Eberswalde crater, several of the largest craters have elevated rims that appear to exhume at least part of the stratigraphic sequence of the Eberswalde crater floor materials (e.g., the orthogonally fractured, brecciated and pitted units), possibly including the basement materials (the massive, basal unit) (Figure 30a, c).

We therefore hypothesize that this > 700 m crater population could either represent: (1) impacts that include those most ancient craters that formed entirely within the primary bedrock floor material of Eberswalde crater; or (2) impacts that occurred entirely on top of the secondary fill materials (e.g., Holden ejecta). For case (1), the Early Hesperian model age represents an estimate for the formation age of Eberswalde Crater. This age is chronologically consistent with previous age estimates for the younger Holden crater (Early-Late Hesperian) (Irwin and Grant 2011). In the case of (2), infill of Eberswalde crater by Holden ejecta or other secondary materials would have been of sufficient thickness to obscure all the basement bedrock craters of Eberswalde crater (100 m – 1.6 km of ejecta is expected to cover the entire Eberswalde floor, based on expressions for the radial decay of ejecta thickness by Garvin and Frawley 1998). In that model, the 3.5 Ga model age would not represent the time of Eberswalde crater formation, but the time of resurfacing by some secondary process (e.g., Holden impact).

7. Discussion

Following the formation of Eberswalde crater, the first major event inferred by our observations is the infilling of some or all of the crater by ejecta from the Holden crater impact. We favor the interpretation that the orthogonally fractured unit, the brecciated unit, and the pitted unit are various expressions of megabreccia related to the Holden event. It is possible that the deposits covering the Eberswalde crater floor could have derived from other nearby impacts, but the proximity of Holden crater and

the extensive modification of Eberswalde's southern rim suggests that Holden had an important role in the geologic history of Eberswalde crater.

Long periods in Eberswalde crater's history remain unaccounted for, such as the time before the formation of Holden crater. It is possible for example that the Holden ejecta deposits are obscuring a record of Noachian fluvio-lacustrine sedimentation in Eberswalde; the most deeply exhumed portion of the crater reveals only the massive, basal unit beneath the inferred megabreccia deposits. What underlies these putative megabreccias in the central and eastern portions of the crater, however, remains unknown.

Because we observe the vein-like features in the inferred megabreccia deposits, but not in the massive, basal unit, we interpret that some process of fracturing and cementation created the vein-like features after – or perhaps concurrent with – the formation of Holden crater. If these features are indeed hydrothermal, they could have important implications for the habitability potential of Eberswalde crater before the deposition of the fluvio-lacustrine sediments (the sub-polygonally fractured and layered light-toned units); Summons et al. (2011) list hydrothermal systems as among the best known environments for supporting the synthesis, concentration and preservation of organic matter.

The linear scarps also occur predominantly in the brecciated, pitted and orthogonally-fractured units. The relationship of these candidate faults to the crater floor materials suggests that regional faulting occurred after the formation of Holden. The largest of these features defines the first-order topography within the crater (Figure 23). The fluvio-deltaic systems conform to this topography (Rice et al., 2011),

except for the western delta, which has linear scarps along its front (Figure 22); this feature may have formed contemporaneously with the faulting, implying multiple eras of deltaic deposition and/or faulting.

The relationship of the large-scale topography to the distribution of units in Eberswalde crater has implications for the presence of an ancient lake. For example, if the ridge-forming unit is interpreted as lacustrine sediments (rather than as other units obscured by airfall), an Eberswalde lake would have to have risen above the tallest ridges on the Central High (-1220 m). This height exceeds the estimate of -1400 m by Lewis and Aharonson (2008), and would imply that a lake was higher than the topographic divide separating the Central High from the Eastern Basin. Therefore, the lake in this scenario would have filled the Eastern Basin to the -1220 m contour as well. The presence of the knobby unit in this portion of the crater – which may be remnants of a formerly extensive sub-polygonally fractured or ridge-forming units – is consistent with this hypothesis. The various elevations of the different features, however, suggest that the lake-level history may have been complex.

The sinuous ridges interpreted as inverted channels may be sublacustrine or may have formed subareally after the lake level dropped. The prominent feature on the drainage divide (Figure 19c) may indicate a "spillover" from a western lake into the Eastern Basin. If this feature is an overspill, it could have provided a possible means of stabilizing the water level, as the lake's surface area would have risen considerably once the western sub-basin was flooded to this level.

We have not observed any direct evidence for layered material with a similar stratigraphy and crater density to the Eberswalde delta along the margins of the

Central High or along the eastern wall of the crater. This may indicate that (1) the layered materials were present here but have since been stripped away and/or degraded to become the knobby unit; (2) the layered materials are still present, but are buried beneath the mantling unit; or (3) the layered materials were never deposited toward the center of the crater or in the Eastern Basin. The relationships between the candidate fluvio-deltaic systems at the margins of the crater and the knobby and ridge-forming units in the central portion of the crater are unclear. These may be sediments that formed in the lake at the same era of fluvio-deltaic deposition, or perhaps much later. The preservation of impact craters on the central crater floor units (the ridge-forming and knobby units) is poor, and we are unable to constrain relative ages of these materials. Toward the center of the crater, for example, the impact density (Figure 29b) is very low.

Extensive removal of crater floor materials has occurred within Eberswalde crater, as evidenced by the prevalence of the knobby unit (which we interpret as remnants of a continuous floor-covering unit) and the inverted channels. The kink in the fit on the crater-frequency plot (Figure 29a) supports this interpretation of the geomorphology. Perhaps the most extreme example of exhumation is in the Western Basin, where the massive, basal unit is visible beneath the brecciated unit. We see no reason why there would have been "holes" left here during the deposition of the brecciated and pitted units that cover most of the rest of the crater floor, especially given our favored interpretation of them as Holden crater ejecta. More likely, this portion of the crater has been subjected to the most removal.

In this western region, we also see extensive cover by the mantling unit, which likely obscures the older crater population; however, the mantle also appears to be degrading in places (e.g., Figure 15b). Importantly, a fairly good fit on the crater-frequency plot (Figure 29a) is re-established for D < 200 m, suggesting that there has been limited crater degradation in the Amazonian, which may explain why the bedforms associated with the mantling unit appear to be stable, showing evidence for intact impact craters.

Evidence for geologic processes occurring in the late-Amazonian to the present includes the presence of dark-toned bedforms. These may still be active, as we have observed no small impacts or significant dust cover. The disintegration of the sub-polygonally fractured, layered light-toned, knobby and ridge-forming units (which appear to be actively shedding boulders) and the mantling unit (which appears to be indurated and developing cliffs) likely has continued into the present day as well.

8. Conclusions

Observations of the stratigraphy, geomorphology, topography and crater densities within Eberswalde crater allow us to infer the following sequence of major events:

1) From regional geologic relationships, Eberswalde crater forms in the Late-Noachian to Early Hesperian with impact crater statistics indicating a possible Early Hesperian formation age (perhaps around 3.5 Ga);

2) Holden crater forms in the Early Hesperian to Late Hesperian, and the associated ejecta blanket covers much or all of the floor of Eberswalde crater and heavily modifies the southern rim. The orthogonally fractured and brecciated units, which are interpreted as allochthonous and/or parautochthonous megabreccias, are deposited during this event;

3) Extensive faulting from regional stresses creates the Western Basin, Eastern Basin and Central High within the crater. Fracturing and cementation occurs within the brecciated unit, forming the vein-like features (timing of this relative to faulting is unconstrained);

4) Valley features are carved in the crater walls as water flows into the crater, creating an Eberswalde lake. Delta formation occurs within the lake, depositing the sub-pologyonally fractured unit (possible lacustrine bottomset beds) and the layered light-toned unit (deltaic sediments) along the margins of the crater. Faulting may have continued during the formation of the main Eberswalde delta, but the smaller fluvio-deltaic systems in the north and south of the crater conform to the fault-controlled topography. The ridge-forming unit forms, possibly as lacustrine deposits;

5) After the lacustrine era, extensive exhumation and degradation of the crater floor materials occurs, perhaps simultaneously with the deposition of the airfall mantling unit. The brecciated unit degrades into a pitted expression (the pitted unit), the sedimentary crater-fill material (the layered light-toned, sub-polygonally fractured, and/or

ridge-forming units) degrades into isolated hillocks (the knobby unit), and fluvial channels are exhumed with inverted relief. The deepest exhumation occurs in the Western Basin, exposing the Eberswalde basement rock (the massive, basal unit) beneath the brecciated unit. The mantling unit becomes indurated and degrades as well;

6) Very little geologic activity has occurred in the Amazonian, and includes the formation and movement of dark-toned aeolian bedforms and some degredation/exhumation of other crater floor units that likely continues in present-day Eberswalde crater.

Appendix

The data products used in this study listed in Table A1 (MOC), Table A2 (CTX), Table A3 (HiRISE), Table A4 (images used in CTX DEMs), Table A5 (images used in HiRISE DEMs), and Table A6 (THEMIS).

Table A1. CTX images of Eberswalde Crater

Product ID
P01_001336_1560_XI_24S033W*
P01_001534_1559_XI_24S033W
P01_001600_1561_XI_23S033W*
P03_002233_1558_XI_24S033W
P06_003222_1561_XI_23S033W
P13_005978_1543_XI_25S032W
P16_007125_1530_XN_27S033W
P16_007270_1546_XI_25S033W
P17_007481_1544_XI_25S033W
P18_008127_1548_XI_25S034W
P19_008272_1545_XI_25S033W
P21_009274_1558_XN_24S033W*
B01_010052_1559_XI_24S033W
B01_010197_1545_XI_25S032W
B02_010263_1557_XI_24S034W
B02_010408_1548_XI_25S033W
B02_010474_1558_XI_24S033W
B02_010553_1558_XI_24S033W
B02_010619_1561_XI_23S033W
B03_010764_1560_XI_24S033W
B03_010830_1560_XI_24S033W
B04_011265_1558_XI_24S033W
B04_011331_1558_XI_24S033W
B07_012465_1559_XN_24S033W
B10_013533_1560_XN_24S033W
B16_016065_1558_XN_24S033W
B17_016210_1558_XN_24S033W

* indicates images included in the mosaic used for this study

Table A2. MOC images of Eberswalde Crater

Product ID		
E14-01039	R09-01067	S11-01980
E17-01341	R10-02155	S12-01927
E18-00401	R11-02067	S13-02008
E20-001420	R13-02140	S14-01406
E21-00076	R14-00769	S14-02900
E21-00454	R18-01627	S14-02902
E21-01153	R19-02022	S15-02083
E22-01159	R20-00176	S16-01405
E23-00003	R22-00520	S18-01890
M15-00319	R23-00038	S18-02542
M18-00020	R23-01163	S19-01794
R06-00324	S01-00795	S19-01974
R06-00726	S03-00196	S20-00003
R06-01110	S03-01417	S20-00505
R07-00821	S04-01110	S20-00616
R07-01352	S05-00866	S20-01501
R07-01859	S07-02812	S21-01273
R08-01104	S09-01262	S22-01189

Table A3. HiRISE images of Eberswalde Crater

Product ID	
PSP_001336_1560	ESP_016210_1560
PSP_001534_1560	ESP_016777_1560
PSP_001600_1560	ESP_017845_1560
PSP_002233_1560	ESP_018056_1560
PSP_004000_1560	ESP_018267_1560
PSP_004356_1560	ESP_018412_1560
PSP_005556_1560	ESP_018557_1560
PSP_007270_1560	ESP_019111_1560
PSP_007481_1560	ESP_019190_1560
PSP_008272_1560	ESP_019335_1560
PSP_010052_1560	ESP_019757_1560
PSP_010474_1560	ESP_020034_1560
PSP_010553_1560	ESP_020324_1555
PSP_010764_1560	ESP_020390_1555
ESP_011265_1560	ESP_020891_1560
ESP_011331_1560	ESP_021669_1560
ESP_012465_1560*	ESP_022025_1560
ESP_012610_1560	ESP_022236_1560
ESP_013533_1560	ESP_022447_1560
ESP_016065_1560	

* cloud-covered image; not included in the HiRISE coverage map shown in Figure 2.

Table A4. List of images used in CTX DTMs

CTX Stereo Pair Product IDs	
P17_007481_1544_XI_25S033W_080301	P19_008272_1545_XI_25S033W_080502
P01_001336_1560_XI_24S033W_061108	P01_001534_1559_XI_24S033W_061123
P01_001600_1561_XI_23S033W_061129	P06_003222_1561_XI_23S033W_070404

Table A5. List of HiRISE stereo pairs

HiRISE Stereo Pair Product IDs	
PSP_001336_1560	PSP_001534_1560
PSP_004356_1560	PSP_012610_1560
PSP_010052_1560	PSP_010553_1560*
PSP_008272_1560	PSP_010474_1560*
ESP_011265_1560	ESP_011331_1560*
ESP_016065_1560	ESP_016210_1560*
ESP_016777_1560	ESP_018412_1560
ESP_018056_1560	ESP_018557_1560
ESP_019190_1560	ESP_019335_1560*
ESP_019757_1560	ESP_020034_1560*
ESP_020324_1560	ESP_020390_1560*

* indicates pairs that have been used to derive publically released DTMs

REFERENCES

Anderson, J.A. Sides, S.C., Soltesz, D.L., Sucharski, T.L, Becker, K.J., 2004. Modernization of the Integrated Software for Imagers and Spectrometers. Lunar. Planet. Sci. XXXV, p. 2039.

Bell, J.F. III, Rice, M.S., Johnson, J.R., Hare, T.M., 2008. Surface albedo observations at Gusev Crater and Meridiani Planum, Mars. J. Geophys. Res. 113, E06S18 doi:10.1029/2007JE002976

Bhattacharya, J.P., Payenberg, T.H.D., Lang, S.C., Bourke, M., 2005. Dynamic river channels suggest a long-lived Noachian crater lake on Mars. Geophys. Res. Lett. 32, L10201. doi:10.1029/2005GL022747.

Boyce, J.M., Mouginis-Mark, P., Tornabene, L., Allen, J., Wilson, L., 2011. Pitted deposits in fresh Martian impact craters. Lunar. Planet. Sci. XXXXII, p. 2701.

Bridges, N.T., and 11 colleagues, 2010. Aeolian bedforms, yardangs, and indurated surfaces in the Tharsis Montes as seen by the HiRISE Camera: Evidence for dust aggregates. Icarus 205, 165-182. doi:10.1029/JB091iB03p03533

Broxton, M.J., Edwards, L.J., 2008. The Ames Stereo Pipeline: Automated 3D Surface Reconstruction from Orbital Imagery. Lunar. Planet. Sci. XXXIX, p. 2419.

Carr, M. H., 1996. Water on Mars New York: Oxford University Press

Christensen, P.R., 1986. Regional dust deposits on Mars - Physical properties, age, and history. J. Geophys. Res. 91, 3533-3545.

Delamere, W.A., and 15 colleagues, 2010. Color imaging of Mars by the High Resolution Imaging Science Experiment (HiRISE), Icarus 205, 38–52, doi:10.1016/j.icarus.2009.03.012.

Di Achille, G., Ori, G.G., Reiss, D., 2007. Evidence for late Hesperian lacustrine activity in Shalbatana Vallis, Mars. J. Geophys. Res. 112, E07007 doi:10.1029/2006JE002858

Dickson, J.L., Head, J.W., Merchant, D., 2008. Late Amazonian glaciation at the dichotomy boundary on Mars: Evidence for glacial thickness maxima and multiple glacial phases Geology, vol. 36, Issue 5, p.411-414 doi:10.1130/G24382A.1

Edwards, L. Broxton, M., 2006., Automated 3D Surface Reconstruction from Orbital Imagery', AIAA, Space 2006, San Jose California, Sep. 19-21

Edgett, K.S., 2005. The sedimentary rocks of Sinus Meridiani: Five key observations from data acquired by the Mars Global Surveyor and Mars Odyssey orbiters Mars, Vol. 1, p. 5-58. doi:10.1555/mars.2005.0002

Eliason, E.M., Anderson, J.A., Barrett, J.M., Becker, K.J., Becker, T.L., Cook, D.A., Soderblom, L.A., Sucharski, T.L., Thompson, K.T., 2001. ISIS Image Processing Capabilities for MGS/MOC Imaging Data. Lunar. Planet. Sci. XXXII, p. 2081

French, B.M., 1998. Traces of Catastrophe: A Handbook of Shock-Metamorphic Effects in Terrestrial Meteorite Impact Structures Technical Report, LPI-Contrib-954

Gaddis, L., and 13 colleagues, 1997. An Overview of the Integrated Software for Imaging Spectrometers (ISIS). Lunar. Planet. Sci. XXVIII, p. 387.

Garvin, J.B., Frawley, J.J., 1998. Geometric properties of Martian impact craters: Preliminary results from the Mars Orbiter Laser Altimeter. Geophys. Res. Lett. 25, 4405-4408 doi:10.1029/1998GL900177

Gillespie, A., Kahle, A., Walker, R., 1986. Color enhancement of highly correlated images. I. Decorrelation and HSI contrast stretches. Remote Sensing of Environment, 20, 3 209-235.

Grant, J.A., Parker, T.J., 2002. Drainage evolution in the Margaritifer Sinus region, Mars. J. Geophys. Res. 107, 5066 doi:10.1029/2001JE001678

Grant, J.A., Wilson, S.A., 2011. Late Alluvial Fan Formation in Southern Margaritifer Terra, Mars. Geophys. Res. Lett., 38, L08201 doi:10.1029/2011GL046844

Grant, J.A., Irwin, R.P., Grotzinger, J.P., Milliken, R.E., Tornabene, L.L., McEwen, A.S., Weitz, C.M., Squyres, S.W., Glotch, T.D., Thompson, B.J., 2008. HiRISE imaging of impact megabreccia and sub-meter aqueous strata in Holden crater, Mars. Geology 36, 3, 195-198. doi:10.1130/G24340A.1.

Grant, J.A., Golombek, M.P., Grotzinger, J., Wilson, S.A., Watkins, M.M., Vasavada, A.R., Griffes, J.L., Parker, T.J., 2010. The science process for selecting the landing site for the 2011 Mars Science Laboratory. Planet. Space Sci., 1-54. doi:10.1016/j.pss.2010.06.016.

Gregg, T., Briner, J., Paris, K., 2007. Ice-rich terrain in Gusev Crater, Mars. Icarus 192, 2, 348–360. doi:10.1016/j.icarus.2007.08.010.

Grotzinger, J., 2009. Beyond water on Mars Nature Geoscience, Volume 2, Issue 4, pp. 231-233 (2009). doi:10.1038/ngeo480.

Hamilton, V.E. Osterloo, M.M., McGrane, B.S., 2007. THEMIS Decorrelation Stretched Infrared Mosaics of Candidate 2009 Mars Science Laboratory Landing Sites: Evidence for Significant Spectral Diversity. Lunar. Planet. Sci. XXXVIII, p. 1725.

Harrison, T.N. Malin, M., Edgett, K.E., Shean, D.E., Kennedy, M., Lipkaman, L., Cantor, B.A., Posiolova, L., 2010. Impact-induced overland fluid flow and channelized erosion at Lyot Crater, Mars. Geophys. Res. Lett. 37, L21201 doi:10.1029/2010GL045074

Hartmann, W.K. Neukum, G., 2001. Cratering Chronology and the Evolution of Mars Space Science Reviews, v. 96, Issue 1/4, p. 165-194, 2001).

Hartmann, W.K., 2005. Martian cratering 8: Isochron refinement and the chronology of Mars. Icarus 174, 294-320. doi:10.1016/j.icarus.2004.11.023

Howard, A.D., Moore, J., Irwin, R.P. III, Dietrich, W.E., 2007. Boulder Transport Across the Eberswalde Delta. Lunar. Planet. Sci. XXXVIII, p. 1168.

Head, J.W., Mustard, J.F., 2006. Breccia dikes and crater-related faults in impact craters on Mars: Erosion and exposure on the floor of a crater 75 km in diameter at the dichotomy boundary Meteoritics and Planetary Science, vol. 41, Issue 10, p.1675-1690 doi:10.1111/j.1945-5100.2006.tb00444.x

Irwin, R.P. III, 2011. Timing, duration and hydrology of the Eberswalde crater paleolake, Mars. Lunar. Planet. Sci. XXXXII, p. 2748

Irwin, R.P. III, Grant, J.A., 2011. Geologic map of MTM −15027, −20027, −25027 and −25032 quadrangles, Margaritifer Terra region of Mars, scale 1:500,000 U.S. Geol. Surv. Sci. Invest. Map, in press

Ivanov, B.A., 2001. Mars/Moon Cratering Rate Ratio Estimates Space Science Reviews, v. 96, Issue 1/4, p. 87-104.

Ivanov, B.A. Pierazzo, E., 2011. Impact cratering in H2O-bearing targets on Mars: Thermal field under craters as starting conditions for hydrothermal activity Meteoritics & Planetary Science, Volume 46, Issue 4, pp. 601-619. doi:10.1111/j.1945-5100.2011.01177.x

Jerolmack, D.J., Mohrig, D., Zuber, M.T., Byrne, S., 2004. A minimum time for the 262formation of Holden Northeast fan, Mars. Geophys. Res. Lett. 31, L21701. doi:10.1029/2004GL021326.

Kendall, C.G.S.C., Warren, J., 1987. A review of the origin and setting of tepees and their associated fabrics Sedimentology 34, p. 1007–1027 doi:10.1029/2007JE003000

Kite, E. S. Michaels, T.I., Rafkin, S. Manga, M., Dietrich, W.E., 2011. Localized precipitation and runoff on Mars. J. Geophys. Res. 116, E07002 doi:10.1029/2010JE003783

Kirk, R., and 18 colleagues, 2008. Ultrahigh resolution topographic mapping of Mars with MRO HiRISE stereo images: Meter-scale slopes of candidate Phoenix landing sites. J. Geophys. Res. 113, E00A24, doi:10.1029/2007JE003000.

Knauth, L.P., Burt, D.M., Wohletz, K.H., 2005. Impact origin of sediments at the Opportunity landing site on Mars Nature 438, 1123-1128. doi:10.1038/nature04383

Knoll, A.H., and 17 colleagues, 2008. Veneers, rinds, and fracture fills: Relatively late alteration of sedimentary rocks at Meridiani Planum, Mars. J. Geophys. Res. 113, E06S16 doi:10.1029/2007JE002949.

Kraal, E.R. van Dijk, M., Postma., G., Kleinhaus, M.G., 2008. Martian stepped-delta formation by rapid water release. Nature 451, 973-976. doi:10.1038/nature06615.

Kraal, E.R., Postma, G., 2008. The Challenge of Explaining Meander Bends in the Eberswalde Delta. Lunar. Planet. Sci. XXXIX, p. 1897.

Lewis, K.W., Aharonson, O., 2006. Stratigraphic analysis of the distributary fan in Eberswalde crater using stereo imagery. J. Geophys. Res. 111, E06001 doi:10.1029/2005JE002558.

Maizels, J., 1990. Raised channel systems as indicators of palaeohydrologic change: a case study from Oman Palaeogeography, Palaeoclimatology, Palaeoecology 76, 3-4, p. 241–277.

Malin, M.C., and 13 colleagues, 2007. Context Camera Investigation on board the Mars Reconnaissance Orbiter. J. Geophys. Res. 112, E05S04. doi:10.1029/2006JE002808.

Malin, M.C., Edgett, K.S., 2001. Mars Global Surveyor Mars Orbiter Camera: Interplanetary cruise through primary mission. J. Geophys. Res. 106, 23429-23570. doi:10.1029/2000JE001455

Malin, M.C., Edgett, K.S., 2003. Evidence for Persistent Flow and Aqueous Sedimentation on Early Mars Science 302, 1931-1934. doi:10.1126/science.1090544.

Malin, M.C, Edgett, K. S., 2000. Sedimentary Rocks of Early Mars Science 290, 1927-1937. doi:10.1126/science.290.5498.1927 .

Malin, M.C., Edgett, K.S., Cantor, B.A., Caplinger, M.A., Danielson, G.E., Jensen, E.H., Ravine, M.A., Sandoval, J.L., Supulver, K.D., 2010. An overview of the 1985-2006 Mars Orbiter Camera science investigation. Mars 5, 1-60 doi:10.1555/mars.2010.0001.

Mangold, N., 2011. Post-early Mars fluvial landforms on mid-latitude impact ejecta. Lunar. Planet. Sci. XXXXII, p. 1370

McEwen, A.S., and 14 colleagues, 2007. Mars Reconnaissance Orbiter's High Resolution Imaging Science Experiment (HiRISE). J. Geophys. Res. 112, E05S02. doi:10.1029/2005JE002605.

McEwen, A.S., and 69 colleagues, 2010. The High Resolution Imaging Science Experiment (HiRISE) during MRO's Primary Science Phase (PSP). Icarus 205, 2– 37. doi:10.1016/j.icarus.2009.04.023.

McCauley, J.F., Grolier, M.J., Breed, C.S., 1977. Yardangs. In: Doehring, D.O. (Ed.), Geomorphology in Arid Regions. Allen and Unwin, Boston, p. 33–269.

McKeown, N.K., Rice, M.S., 2011. Detailed mineralogy of Eberswalde crater. Lunar. Planet. Sci. XXXXII, p. 2450

Melosh, H.J., 1989. Impact Cratering: A Geologic Process, Cambridge University Press.

Michael, G. Neukum, G., 2008. Surface Dating: Software Tool for Analysing Crater Size-Frequency Distributions Including Those Showing Partial Resurfacing Events. Lunar. Planet. Sci. XXXIX, p. 1780.

Michael, G.G., Neukum, G., 2010. Planetary surface dating from crater size-frequency distribution measurements: Partial resurfacing events and statistical age uncertainty Earth and Planetary Science Letters 294, 223-229. doi:10.1016/j.epsl.2009.12.041

Milliken, R.E., Bish, D.L., 2010. Sources and sinks of clay minerals on Mars Philosophical Magazine, vol. 90, issue 17, pp. 2293-2308 doi:10.1080/14786430903575132

Moore, J.M., Howard, A.D., Dietrich, W.E., Schenk, P.M., 2003. Martian layered fluvial deposits: Implications for Noachian climate scenarios. Geophys. Res. Lett. 30, 24, 2292. doi:10.1029/ 2003GL019002.

Morgan, G.A. et al., 2009. Lineated valley fill (LVF) and lobate debris aprons (LDA) in the Deuteronilus Mensae northern dichotomy boundary region, Mars: Constraints on the extent, age and episodicity of Amazonian glacial events. Icarus 202, 22-38. doi:10.1016/j.icarus.2009.02.017

Murchie, S., and 49 colleagues, 2007. Compact Reconnaissance Imaging Spectrometer for Mars (CRISM) on Mars Reconnaissance Orbiter (MRO). J. Geophys. Res. 112, E11, doi: 10.1029/2006JE002682.

Neukum, G. et al., 2010. The geologic evolution of Mars: Episodicity of resurfacing events and ages from cratering analysis of image data and correlation with radiometric ages of Martian meteorites Earth and Planetary Science Letters 294, 204-222. doi:10.1029/2006JE002682

Neuendorf, K.K.E.; Mehl, J.P., Jr.; Jackson, J.A. (Eds.), 2005. Glossary of Geology, 5th Edition, American Geological Institute, Alexandria, Virginia.

Okubo, C.H., McEwen, A.S., 2007. Fracture-Controlled Paleo-Fluid Flow in Candor Chasma, Mars Science 315, 983. doi:10.1126/science.1136855

Pain, C.F., Clarke, J.D.A., Thomas, M., 2007. Inversion of relief on Mars. Icarus 190, 478-491. doi:10.1016/j.icarus.2007.03.017

Pondrelli, M., Pio Rossi, A., Marinangeli, L., Hauber, E., Gwinner, K., Baliva, A., di Lorenzo, S., 2008. Evolution and depositional environments of the Eberswalde fan delta, Mars. Icarus 197429. doi:10.1016/j.icarus.2008.05.018.

Pondrelli, M. Pio Rossi, A., Marinangeli, L., Hauber, E., Gwinner, K., Baliva, A., di Lorenzo, S. Geological, Geomorphological, Facies and Allostratigraphic Maps of the Eberswalde Fan Delta Planetary and Space Science, v. 59, Issue 11, 1166-1178. doi:10.1016/j.pss.2010.10.009

Rao, M.N., Nyquist, L.E., Sutton, S.R., Dreibus, G., Garrison, G.H., Harrin, J., 2008. The nature of Martian fluids based on mobile element studies in salt-assemblages from Martian meteorites. J. Geophys. Res. 113. doi:10.1029/2007JE002958

Rice, M.S., Gupta, S., Bell, J.F. III, Warner, N.H., 2011. Influence of fault-controlled topography on fluvio-deltaic sedimentary systems in Eberswalde crater, Mars. Geophys. Res. Lett., 38, L16203. doi:10:1029/2011GL048149

Rogers, A.D., Bandfield, J.L., 2009. Mineralogical characterization of Mars Science Laboratory candidate landing sites from THEMIS and TES data. Icarus 203, 437-453. doi:10.1016/j.icarus.2009.04.020

Ruff, S.W., Christensen, P.R., 2002. Bright and dark regions on Mars: Particle size and mineralogical characteristics based on Thermal Emission Spectrometer data. J. Geophys. Res., 107, E12, 5127 doi:10.1029/2001JE001580

Schieber, J., 2007. Reinterpretation of the Martian Eberswalde Delta in the Light of New HiRISE Images. Lunar. Planet. Sci. XXXVIII, p. 1982.

Scott, D.H., Tanaka, K.L., 1986. Geologic map of the western equatorial region of Mars U.S. Geol. Surv. Misc. Invest. Ser., Map I-1802-A.

Sharp, R.P., 1963. Wind ripples Journal of Geology, vol. 71, no. 5, p. 617-36.

Shoemaker, E.M., Hackman, R.J., 1962. Stratigraphic Basis for a Lunar Time Scale IN: THE MOON, (KOPAL,Z., AND MIKHAILOV,Z.K., EDITORS) IAU SYMPOSIUM 14, ACADEMIC, P. 289-300.

Simpson, J.I., Kim, J.P., Muller, J.-P., 2008. 3D crater database production on Mars by automated crater detection and data fusion, in The International Congress of the Photogrammetry, Remote Sensing and Spatial Information Sciences, edited, pp. 1049-1054, Beijing.

Smith, D.E., and 23 colleagues, 2001. Mars Orbiter Laser Altimeter: Experiment summary after the first year of global mapping of Mars. J. Geophys. Res. 106, 23689-23722. doi:10.1029/2000JE001364.

Squyres, S.W., 1978. Martian fretted terrain - Flow of erosional debris. Icarus 34, 600-613. doi:10.1016/0019-1035(78)90048-9

Squyres, S.W., Carr, M.H., 1986. Geomorphic evidence for the distribution of ground ice on Mars Science (ISSN 0036-8075), vol. 231, p. 249-252. doi:10.1126/science.231.4735.249

Sullivan, R., Arvidson, R.E., Bell, J.F., III, Gellert, R., Golombek, M., Greely, R., Herkenhoff, K., Johnson, J.R., Thompson, S., Whelley, P., Wray, J.J., 2008. Wind-driven particle mobility on Mars: Insights from Mars Exploration Rover observations at “El Dorado” and surroundings at Gusev Crater. J. Geophys. Res. 113, E06S07 doi:10.1029/2008JE003101.

Summons, R.E. and 9 colleagues, 2011. Preservation of Martian Organic and Environmental Records: Final Report of the Mars Biosignature Working Group Astrobiology 11, 2, doi:10.1089/ast.2010.0506

Tornabene, L.L., McEwen, A.S., Grant, J.A., Mouginis-Mark, P.J., Squyres, S.W., Wray, J.J., 2007. Evidence for the Role of Volatiles on Martian Impact Craters as Revealed by HiRISE. Lunar. Planet. Sci. XXXVIII, p. 2215.

Tornabene, L.L., Osinski, G.R., McEwan, A.S., 2009. Parautochthonous Megabreccias and Possible Evidence of Impact-induced Hydrothermal Alteration in Holden crater, Mars. Lunar. Planet. Sci. XL, p. 1766

Torson, J.M., Becker, K.J., 1997. ISIS - A Software Architecture for Processing Planetary Images. Lunar. Planet. Sci. XXVIII, p. 1443.

Wang, C. Manga, M., Wong, A., 2005. Floods on Mars released from groundwater by impact. Icarus 175, 551-555. doi:10.1016/j.icarus.2004.12.003

Warner, N. Gupta, S., Lin, S.-Y., Kim, J.-R., Muller, J.-P., Morley, J., 2010. Late Noachian to Hesperian climate change on Mars: Evidence of episodic warming from transient crater lakes near Ares Vallis. J. Geophys. Res. 115, E06013 doi:10.1029/2009JE003522

Weitz, C.M., Anderson, R.C., Bell, J.F., Farrand, W.H., Herkenhoff, K.E., Johnson, J.R., Jolliff, B.L., Morris, R.V., Squyres, S.W., Sullivan, R.J., 2006. Formation of a terraced fan deposit in Coprates Catena, Mars. Icarus 184, 436-451. doi:10.1016/j.icarus.2006.05.024

Wilhelms, D.E., 1990. Geologic Mapping Planetary Mapping Edited by Ronald Greeley, and Raymond M. Batson. Cambridge, GB: Cambridge University Press, 1990., p.208

Wilhelms, D.E., 1974. Interagency report: astrogeology 55, geologic mapping of the second planet. Part 1: Rationale and general methods of lunar geologic mapping. Part 2: Technicalities of map conventions, format, production mechanics, and reviewing. Part 3: History of the US Geological Survey lunar geologic mapping program In NASA. Ames Res. Center A Primer in Lunar Geology p 199-238 (SEE N75-13730 04-91)

Williams, R.M.E., Malin, M.C., 2008. Sub-kilometer fans in Mojave Crater, Mars. Icarus 198, 365-383. doi:10.1016/j.icarus.2008.07.013

Williams, R.M.E. et al., 2006. Aspects of alluvial fan shape indicative of formation process: A case study in southwestern California with application to Mojave Crater fans on Mars. Geophys. Res. Lett. 33, L10201 doi:10.1029/2005GL025618

Williams, R.M.E. et al., 2009. Evaluation of paleohydrologic models for terrestrial inverted channels: Implications for application to martian sinuous ridges Geomorphology 107, 3-4, p. 300–315. doi:10.1016/j.geomorph.2008.12.015

Wood, L., 2006. Quantitative geomorphology of the Mars Eberswalde delta Geological Society of America Bulletin 118, 5-6, 557 doi:10.1130/B25822.1

Zimbelman, J.R. Clifford, S.M., Williams, S.H., 1989. Concentric crater fill on Mars - an aeolian alternative to ice-rich mass wasting. Lunar. Planet. Sci. , p. 397.

Zuber, M.T., Smith, D.E., Solomon, S.C., Muhleman, D.O., Head, J.W., Garvin, J.B., Abshire, J.B., Bufton, J.L., 1992. The Mars Observer laser altimeter investigation. J. Geophys. Res. 97, 7781-7797. doi:10.1029/92JE00341.

CHAPTER 7

SYNTHESIS AND FUTURE WORK

The work described in this dissertation has provided insights into the water-rich past that is preserved at two key locations on Mars: (1) Gusev crater, the landing site of the Mars Exploration Rover (MER) Spirit; and (2) Eberswalde crater, a candidate landing site for the Mars Science Laboratory (MSL) Curiosity. In all of these investigations, the driving motivation has been to understand whether the planet is, or was ever, a habitable world. The goal of this final chapter is to review and synthesize the results of the presented studies. *Section 1* reviews the new techniques that have been developed in this work and describes how they can be applied to other datasets from past, current and future missions. *Section 2* provides a review of the major results, along with a discussion of the possible future work that could be motivated by these studies. *Section 3* concludes with a summary and synthesis of this work.

1. New techniques developed and applicability to other missions

1.1 The "hydration signature"

A major contribution of this work has been the development of the "hydration signature" described in Chapter 2, which has aided in the remote identification, interpretation, and mapping of hydrated materials on the surface of Mars by the Spirit Pancam instrument. The detection of the $2\nu_1 + \nu_3$ H_2O combination band and/or the $3\nu_{OH}$ overtone centered near ~1000 nm has expanded the known capabilities of the

instrument, as the Pancam bandpasses were originally selected to optimally characterize the ferrous and ferric mineralogies expected at the MER landing sites (Bell et al., 2003). Beyond the work presented here, mapping with the "hydration signature" has been employed by other authors to interpret results from the Spirit mission (e.g., Ruff et al., 2011).

The "hydration signature" mapping technique has also been applied to Pancam data from MER Opportunity at Meridiani Planum. While occurrences of the ~1000 nm feature are less widespread along Opportunity's traverse than has been observed along Spirit's traverse in the Columbia Hills, the presence of the "hydration signature" in a few key locations has aided in geologic and mineralogic interpretations of the Meridiani Planum site. Namely, Arvidson et al. (2011) presented "hydration signature" maps of the stratigraphy in Victoria crater (Figure 1), showing that the "Smith" layer is compositionally distinct from other units exposed in the crater wall. More recently, the "hydration signature" has been detected in association with the "Homestake" vein-like feature at Cape York, on the rim of Endeavour crater (Figure 2). The presence of the H_2O and/or OH feature longward of ~980 nm, in combination with data from the Alpha Particle X-ray Spectrometer (APXS) instrument that suggest a calcium-sulfate composition, has allowed for the interpretation that the vein contains the mineral gypsum. This result was presented at the December 2011 Fall Meeting of the American Geophysical Union.

The "hydration signature" technique can further be applied to observations from Mars Science Laboratory (MSL) Mast-mounted Cameras (Mastcams) when the rover lands in Gale crater in August 2012. Mastcam is a two-instrument suite of fixed-

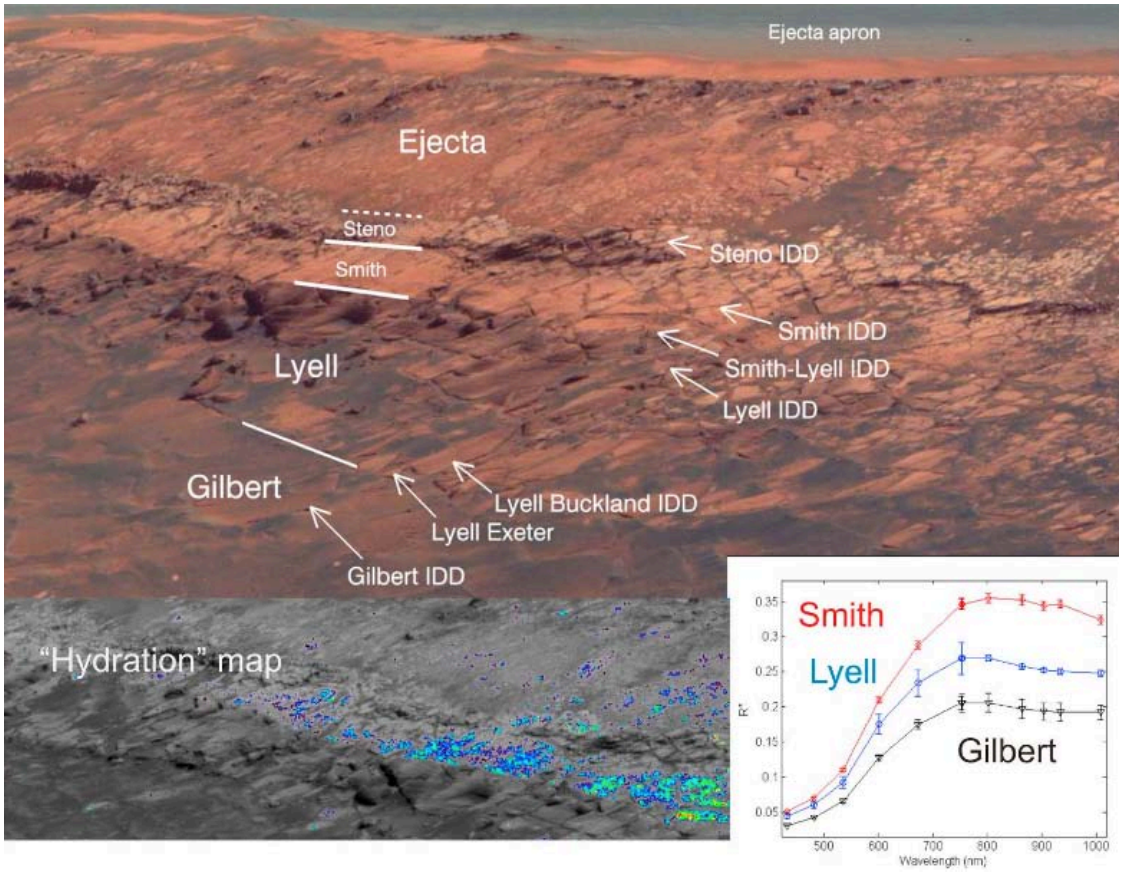

Figure 1. Application of the "hydration signature" mapping technique to the stratigraphy of Victoria crater, as presented by Arvidson et al. (2010). The "hydration signature" is associated with the "Smith" layer, and the ~1000 nm H_2O and/or OH feature is seen in the Smith spectrum in the lower right.

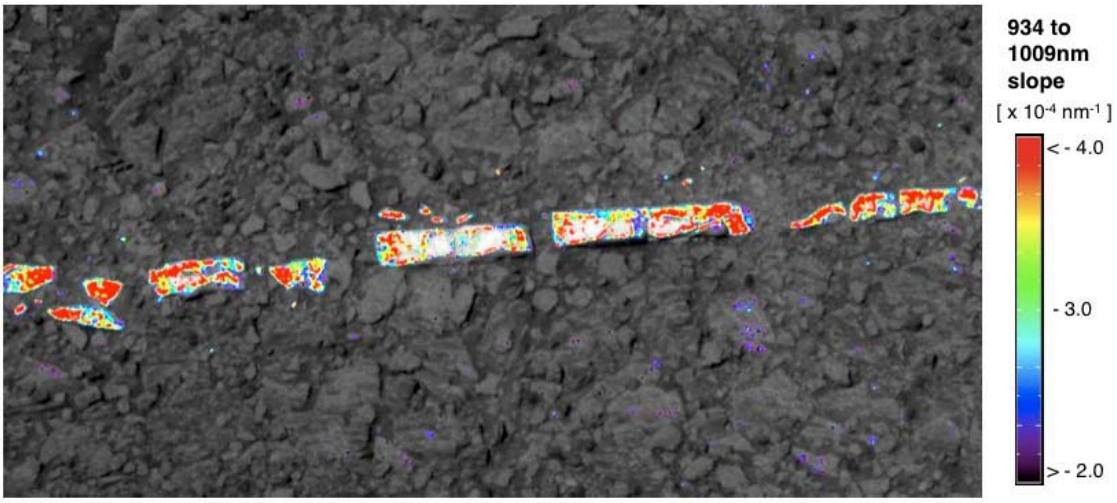

Figure 2. "Hydration signature" map of the vein-like feature "Homestake" observed by the Opportunity rover at Cape York (sol 2796, P2574). The presence of the ~1000 nm feature, in combination with the APXS data, suggests the presence of gypsum.

focal length (FFL) cameras, one with a 15° field of view (FOV) and the other with a 5.1° FOV. Mastcam's narrowband filters cover 9 unique wavelengths in the visible and near-infrared (band centers at 440, 525, 675, 750, 800, 865, 905, 935, and 1035 nm), and are distributed between the two FFL cameras (Ghaemi et al., 2009; Malin et al., 2010). Full-filter multispectral observations of the region of overlap between the two cameras can be used to perform "hydration signature" mapping, and the results of the spectroscopy study in Chapter 3 suggest that Mastcam's sensitivity to the H_2O and/or OH feature should be comparable to that of Pancam.

"Hydration signature" mapping can also be applied retroactively to datasets from the Imager for Mars Pathfinder (IMP) instrument (using its 968 and 1003 nm bands) (Smith et al., 1997) and the Phoenix Surface Stereo Imager (SSI) instrument (using its 968 and 1002 nm bands) (Lemmon et al., 2008). In previous studies with Phoenix SSI, the hydration feature near ~1000 nm has been observed at the ice exposures in the lander's trenches (Cull et al., 2009).

1.2 Spectral parameters for interpreting silica-rich materials

The classification of the spectra of silica-rich materials described in Chapter 3 can aid in characterizing the compositional diversity of silica-bearing deposits on Mars. Specifically, the parameter space plots shown in Figure 20 of Chapter 3 demonstrate how the position of the ~1.4 μm band minimum, in combination with the 1.91/1.96 μm, 1.41/1.46 μm, and ~2.2/1.9 μm band depth ratios can be used to help distinguish between different forms of silica. An application of these parameters to datasets from the Mars Reconnaissance Orbiter (MRO) Compact Reconnaissance Imaging Spectrometer for Mars (CRISM) and the Mars Express Observatoire pour la Minéralogie, l'Eau, les Glaces, et l'Activité (OMEGA) can aid in interpretations of silica-rich materials. However, it should be noted that many hyperspectral observations from Mars may not have a high enough signal to noise ratio to properly resolve the fine structure in the ~1.4 and ~1.9 μm regions, and the effects of low-temperature and pressure conditions on these features at the surface of Mars are still poorly constrained. Based on the results presented in Chapter 3, we caution against using the symmetry and position of the ~2.2 band to draw conclusions about the type of silica-rich material present. Given these considerations, however, a careful application of our results could give information about trends in the formation or degradation of silica (e.g., regional or stratigraphic trends in silica crystallinity, such as variations from opal-A to opal-CT).

2. Major results and future work

2.2 Gusev crater investigations

The mapping of the "hydration signature" across MER Spirit's traverse has shown that hydrated materials are widespread in the Columbia Hills of Gusev crater. Where observed in the spectra of silica-rich materials, the Pancam "hydration signature" is attributed to the substantial amounts of H_2O and/or OH, either bound in the mineral structure of the silica, trapped in fluid inclusions, or adsorbed onto the surface. Several questions remain, however, about the nature of the false "hydration signature" detections at high phase angles described in Chapter 2. Spectral studies of ferric-coated basalts by Fischer and Pieters (1993) suggest that the near infrared (NIR) spectral slope is effected by phase angle, with negative NIR slopes occurring for backscattering geometries. As suggested in Chapter 2, it is possible that a negative NIR slope observed in similar geometries can induce the ~1009 nm Pancam absorption seen on dusty rock surfaces. Ongoing work will quantify these effects in laboratory spectra and address how to correct for them in future "hydration signature" mapping.

The development of the "hydration signature" (Chapter 2) and the detailed classification of the ~950-1000 nm absorption in the spectra of silica-rich materials (Chapter 3) have been some of the first studies to examine the $2\nu_1 + \nu_3$ H_2O combination band and the $3\nu_{OH}$ overtone in detail. The role of this feature in CRISM visible spectra, however, has not yet been examined. An identification of this feature in the spectra of silica, gypsum, ice, or other hydrated materials detected from orbit is a goal of our ongoing studies.

Temporal observations of the spectra of silica- and sulfate-rich soils at Gusev crater (Chapter 4) reveal that no statistically significant changes occurred that are

consistent with mineralogic changes, implying that the soils have not undergone observable dehydration after their exposure. A major outstanding question for these materials, however, is their formation mechanism, the timing of the putative hydrothermal activity that led to their deposition in the Columbia Hills, and the regional extent of this activity. In future studies, hyperspectral observations from CRISM and/or OMEGA can be used to map the regional extent of alteration minerals that may be indicative of hydrothermal activity. The extensive dust cover in the region makes such detections difficult, but it may be possible if observations acquired in spatial and temporal "windows" of low dust are used.

2.2 Eberswalde crater investigations

At Eberswalde crater, this work has revealed a more complex story of fluvio-deltaic activity than had previously been acknowledged for the site. Six fluvio-deltaic systems have been identified through our mapping (Chapter 5), including the famous "Eberswalde delta" that led the crater to be a final candidate landing site for MSL. The geomorphic analyses presented in Chapter 5 also show that system of faults controlled the large-scale Eberswalde basin topography and the pattern of delta development. From detailed mapping of stratigraphic and geomorphic units throughout the crater (Chapter 6), a sequence of major events in the geologic history of the crater can be inferred: the formation of Eberswalde crater, followed by emplacement of ejecta from the Holden impact, followed by regional faulting, followed by a potentially extensive period of fluvio-deltaic activity, and finally a period of erosion of the crater floor concurrent with the deposition of an airfall mantling.

A major remaining question for Eberswalde crater, and an extremely important one for constraining the site's past habitability potential, is the timing and duration of the lake. A continuation of our stratigraphic and geomorphic mapping to the larger region, which includes the source channels surrounding Eberswalde crater and its drainage basin, could shed further light into this issue. Another outstanding question pertains to the mineralogy of the individual units described in this work (Chapter 6). Previous studies using observations from CRISM have shown that spectra of the layers of the "Eberswalde delta" are consistent with phyllosilicates (Milliken and Bish, 2010); these results enhanced the crater's appeal as a candidate landing site for MSL. However, the mineralogy of the layered materials in the other fluvio-deltaic systems identified in this study (Chapter 5) has yet to be constrained. Furthermore, a comprehensive study of all available CRISM images from the crater floor has not yet been performed. A correlation of mineralogic units with the units identified in this work could help refine the larger story of aqueous alteration at Eberswalde crater.

3. Conclusions

This body of work examined evidence for the surface of Mars having once been more water-rich than is currently observed. At Gusev crater, multiple occurrences of silica- and sulfate-rich materials indicate that a hydrothermal system may have been active at this site. The studies presented here have shown that hydration is widespread in the Columbia Hills, and is not only associated with the bright soils studied *in-situ* by the Spirit rover. Regional imaging studies have identified many features geomorphically similar to those observed in the Columbia

Hills, suggesting that geologic processes that occurred at the Spirit site may have been widespread. At Eberswalde crater, the discoveries of fluvio-deltaic systems beyond the famous "Eberswalde delta" have allowed a more complex story of lake-level history and duration to emerge. The mapping of the oldest crater floor units and identifications of vein-like features have suggested that the story of aqueous alteration in Eberswalde crater likely begins long before the deltas formed. Combined, the evidence presented in this dissertation suggests that the history of water at these key locations – and their potentials as former habitable environments – is richer and more complex than had previously been understood.

REFERENCES

Arvidson, R.E., and 33 colleagues, 2011. Opportunity Mars Rover Mission: Overview and Selected Results from Purgatory Ripple to Traverses to Endeavour Crater. J. Geophys. Res. 116, E00F15, doi:10.1029/2010JE003746.

Bell III, J.F., and 24 colleagues, 2003. Mars Exploration Rover Athena Panoramic Camera (Pancam) investigation. J. Geophys. Res. 108, E12. doi:10.1029/ 2003JE002070.

Cull, S., Arvidson, R.E., Mellon, M.T., Skemer, P., Shaw, A., Morris, R.V., 2009. Compositions of subsurface ices at the Mars Phoenix landing site. Geophys. Res. Lett. 37, L24203, doi:10.1029/2010GL045372.

Ghaemi, F.T., 2009. Design and fabrication of lenses for the color science cameras aboard the Mars Science Laboratory rover, Opt. Eng. 48, 103002, doi:10.1117/1.3251343.

Malin, M.C., and 27 colleagues, 2010. The Mars Science Laboratory (MSL) Mast-mounted Cameras (Mastcams) flight instruments, Lunar Planet. Sci. XLI, Abstract 1123.

Milliken, R.E., Bish, D.L., 2010. Sources and sinks of clay minerals on Mars. Philosophical Magazine 90, 17, 2293-2308. doi:10.1080/14786430903575132.

Ruff, S.W., and 10 colleagues, 2011. Characteristics, distribution, origin, and significance of opaline silica observed by the Spirit rover in Gusev crater, Mars, J. Geophys. Res. 116, E00F23. doi:10.1029/2010JE003767.

Smith, P.H., and 18 colleagues, 1997. The Imager for Mars Pathfinder experiment, J. Geophys. Res. 102, 4003–4025.